Precision measurements in neutral current Drell-Yan production at ATLAS

Dissertation
zur Erlangung des Grades

Doktor der Naturwissenschaften

am Fachbereich Physik, Mathematik und Informatik
der Johannes Gutenberg-Universität
in Mainz



Julian Blumenthal, geb. Fischer
geboren in Kaltenkirchen

Mainz, den 01. September 2023

CERN-THESIS-2023-373
01/02/2024

Julian Blumenthal, geb. Fischer
Precision measurements in neutral current Drell-Yan production at ATLAS
1. Berichterstatter: [In der elektronischen Version aus Datenschutzgründen entfernt]
2. Berichterstatter: [In der elektronischen Version aus Datenschutzgründen entfernt]
Johannes Gutenberg-Universität, Mainz
Datum der mündlichen Prüfung: 01. Februar 2024

Kurzfassung

Der Large Hadron Collider (LHC) am CERN ermöglicht den experimentellen Zugang zu Prozessen, die in Kollisionen von Protonen oder anderen Hadronen auftreten. Durch die hohe instantane Luminosität des Beschleunigers können große Datensätze aufgenommen werden. In der vorliegenden Dissertation wird der Datensatz von $139\,\mathrm{fb}^{-1}$, der am ATLAS Experiment von 2015-2018 bei $\sqrt{s} = 13\,\mathrm{TeV}$ in Proton-Proton-Kollisionen aufgenommen wurde, mit Blick auf den Drell-Yan Prozess untersucht. Zum ersten Mal werden dabei alle acht sogenannten *Winkelkoeffiezienten* des Z/γ^* Bosons in diesem Datenset differentiell in der Rapidität und dem transversalen Impuls des resultierenden Elektron/Positron bzw. Myon/Anti-Myon Paares gemessen. Zusätzlich wird der differentielle Wirkungsquerschnitt des Drell-Yan Prozesses bestimmt. Die Messung mittels einer statistischen Regression ist dabei konsistent zwischen beiden untersuchten Zerfallskanälen. Zudem werden vorige Messungen anderer Publikationen, beispielsweise nicht-verschwindende Koeffizienten A_5, A_6 und A_7, durch die Ergebnisse dieser Arbeit unterstützt.
Da der Winkelkoeffizient A_4 sensitiv auf den schwachen Mischungswinkel ist, wird dieser im zweiten Teil dieser Dissertation auf Simulationsbasis untersucht, um die zu erwartende Sensitivität einer Messung des effektiven leptonischen schwachen Mischungswinkels mit den zuvor analysierten Daten zu bestimmen. Die Untersuchung basiert dabei auf Elektron/Positron bzw. Myon/Anti-Myon Paaren aus der sogenannten zentralen Region des ATLAS Detektors. Eine Verbesserung der Senitivität von etwa 26% gegenüber der letzten Messung des ATLAS Experimentes in diesen Zerfallskanälen ist dabei zu erwarten. Die Sensitivität lässt sich durch Hinzuziehen eines weiteren Zerfallskanals, in dem Elektronen bzw. Positronen in der Detektor-Region nah der Strahlachse liegen, weiter erhöhen.
Aus diesem Grund werden im letzten Teil dieser Arbeit Algorithmen entwickelt, die Elektronen, Positronen und Photonen als Teil des ATLAS Trigger Systems auf dem sogenannten *forward feature extractor* für das Phase-II Upgrade für den High-Luminosity LHC effektiv identifizieren sollen. Dabei wird gezeigt, dass die Nutzung von Variablen, welche die Form der Teilchenschauer im Detektor beschreiben sowie von neuronalen Netzen eine Verbesserung darstellen gegenüber einfacheren Ansätzen, die in der Vergangenheit in solchen Systemen genutzt wurden. Diese Verbesserung schlägt sich in einer effektiveren Identifikation von Signalobjekten sowie einer verbesserten Unterdrückung des Untergrundes, in der Regel Jets, nieder.

Abstract

The Large Hadron Collider (LHC) at CERN is a powerful machine to facilitate collisions of hadrons such as protons. Its high instantaneous luminosity allows to collect large datasets of proton-proton collisions. In this thesis the data taken at the ATLAS experiment from 2015-2018 at $\sqrt{s} = 13\,\mathrm{TeV}$, amounting to $139\,\mathrm{fb}^{-1}$ is analysed in the context of the Drell-Yan process. In particular, for the first time the full set of eight so-called *angular coefficients* of the Z/γ^* boson using electron/positron and muon/anti-muon pairs are extracted from this data differentially in dilepton rapidity and transverse momentum. In addition, the differential cross section of the Drell-Yan process is determined. Results of the template fits using electrons/positrons and muons/anti-muons are predominantly consistent with each other. Additionally, previous measurements, in particular non-zero angular coefficients A_5, A_6 and A_7 as well as the breaking of the Lam-Tung relation are supported by the results presented. The angular coefficient A_4 is closely connected to the weak mixing angle. For this reason, in the second part of this dissertation, A_4 is studied in simulation to assess its expected sensitivity on the effective leptonic weak mixing angle emulating the statistical accuracy and uncertainties of the data. The study is focussed on electron/positron and muon/anti-muon pairs in the so-called central region of the ATLAS detector. The resulting expected sensitivity improves the previous ATLAS measurement of the weak mixing angle using this method in these decay channels by about 26%. The sensitivity of such a measurement benefits from the addition of electrons or positrons from the so-called forward region of ATLAS.
For this reason, in the final part of this thesis different options for algorithms to trigger on electrons, positrons or photons are evaluated using the so-called *forward feature extractor* module as part of the planned Phase-II upgrade of ATLAS for the High-Luminosity LHC era. It is shown that exploiting information about particle shower shapes in neural networks provides the best performance in identifying signal objects and rejecting backgrounds, the majority of which are jets, and proves to be superior to simpler approaches that rely on fixed selection criteria.

To my parents.
For your unconditional love and support.

Contents

I Introduction **1**

II Theoretical and Experimental Foundations **5**

1 Theoretical Introduction **7**
1.1 The Standard Model . . . 7
1.1.1 Phenomenological Overview . . . 7
1.1.2 Mathematical Formalism . . . 11
1.1.2.1 Quantum Electrodynamics . . . 11
1.1.2.2 Feynman Calculus . . . 13
1.1.2.3 Quantum Chromodynamics . . . 14
1.1.2.4 Electroweak Theory and Spontaneous Symmetry Breaking . . . 16
1.1.3 Limitations . . . 20
1.2 Proton-Proton Collisions . . . 21
1.2.1 Scattering Processes . . . 21
1.2.2 Parton Model . . . 22
1.2.3 Parton Distribution Functions . . . 23
1.2.4 Hadronisation . . . 24
1.2.5 The Drell-Yan Neutral Current Process . . . 25
1.3 High-Precision Tests of the Standard Model . . . 27
1.3.1 Motivation . . . 27
1.3.2 Angular Coefficients of the Drell-Yan Neutral Current . . . 28
1.3.2.1 Production Cross Section . . . 29
1.3.2.2 Collins-Soper Rest Frame . . . 30
1.3.2.3 Helicity Cross Sections . . . 31
1.3.2.4 Predictions . . . 34
1.3.2.5 Current Measurements . . . 36
1.3.3 The Weak Mixing Angle . . . 39
1.3.3.1 Forward-Backward Asymmetry . . . 40
1.3.3.2 Current Measurements . . . 42

2 Experimental Setup **45**
2.1 The Large Hadron Collider . . . 45

2.2 The ATLAS Experiment . . . 48
2.2.1 Coordinate System . . . 48
2.2.2 Tracking . . . 50
2.2.2.1 Pixel Detector and Insertable B-Layer . . . 50
2.2.2.2 Semi-Conductor Tracker . . . 51
2.2.2.3 Transition Radiation Tracker . . . 52
2.2.3 Calorimeter System . . . 52
2.2.3.1 Electromagnetic Calorimeter . . . 53
2.2.3.2 Hadronic Calorimeter . . . 55
2.2.4 Muon System . . . 56
2.2.5 Luminosity Detectors . . . 57
2.2.6 Trigger and Data Acquisition . . . 58
2.2.7 Data Formats and Offline Computing . . . 59
2.3 Object Reconstruction and Identification in ATLAS . . . 61
2.3.1 Electron Objects . . . 63
2.3.1.1 Reconstruction . . . 63
2.3.1.2 Identification . . . 65
2.3.2 Muon Objects . . . 66
2.3.2.1 Reconstruction . . . 67
2.3.2.2 Identification and Isolation . . . 68

3 Simulation **71**
3.1 Monte Carlo Method . . . 71
3.2 Event Generation . . . 72
3.2.1 Accuracy . . . 72
3.2.2 Monte Carlo Generators . . . 72
3.3 Detector Simulation . . . 74
3.3.1 Corrections . . . 75

III Measurement of the Angular Coefficients of the Z Boson **77**

4 Motivation and Strategy **79**

5 Data Analysis **83**
5.1 Datasets . . . 83
5.2 Monte Carlo Simulation . . . 83
5.2.1 Signal Process . . . 84
5.2.2 Background Processes . . . 85
5.3 Event and Object Selections . . . 87
5.3.1 Trigger . . . 87
5.3.2 Data Quality . . . 88
5.3.3 Preselection . . . 88

5.3.4 Electrons . . . 89
5.3.5 Muons . . . 91
5.3.6 Pair Selection and Binning . . . 93
5.3.7 Selection Acceptance and Efficiency . . . 93
5.4 Data-driven Multijet Background Estimate . . . 97
5.4.1 Methodology . . . 97
5.4.2 Estimate Results . . . 102
5.5 Uncertainties . . . 102
5.5.1 Statistical Uncertainties . . . 104
5.5.2 Experimental Uncertainties . . . 104
5.5.2.1 Electrons . . . 104
5.5.2.2 Muons . . . 106
5.5.3 Theory Uncertainties . . . 107
5.6 Comparison of Data to Expectation . . . 108
5.6.1 Single Lepton Distributions . . . 110
5.6.2 Dilepton Distributions . . . 113
5.7 Collins-Soper Variables in Data and Expectation . . . 118
5.7.1 Differential Effects of Rapidity and Transverse Momentum . . . 125

6 Extraction of the Angular Coefficients 129
6.1 Strategy . . . 129
6.1.1 Binning . . . 129
6.1.2 Template Method . . . 131
6.2 Statistical Methods . . . 134
6.3 Maximum Likelihood Fit . . . 140
6.4 Validation . . . 140
6.5 Fit Quality . . . 141
6.6 Uncertainties . . . 143
6.6.1 Electron Channel . . . 143
6.6.2 Muon Channel . . . 145
6.7 Compatibility . . . 151
6.7.1 Validation . . . 151
6.7.2 Data Compatibility . . . 153
6.8 Individual Results . . . 156
6.9 Combined Results . . . 159
6.9.1 Uncertainties . . . 162
6.9.2 Final Results . . . 164
6.10 Outlook . . . 170

IV Towards the Weak Mixing Angle 173

7 Motivation and Strategy 175

8 Expected Sensitivity of the Weak Mixing Angle Extraction **177**
8.1 Methodology . . . 177
8.2 Extraction of the A_4 Coefficient . . . 180
8.3 Expected Sensitivity of a Weak Mixing Angle Measurement . . . 185
8.4 Outlook . . . 194

9 Conclusion of the Study **197**

V Preparation for the High-Luminosity Era **199**

10 Future Upgrades to ATLAS for the High-Luminosity Large Hadron Collider **201**
10.1 The High-Luminosity LHC . . . 201
10.2 Upgrades to the ATLAS Detector . . . 202
10.3 Upgrades to the ATLAS Trigger System . . . 203
10.4 The Forward Feature Extractor . . . 205
10.4.1 The ATLAS Forward Region . . . 206
10.4.2 Firmware Considerations . . . 210

11 Development of Trigger Algorithms for the Forward Feature Extractor Module **215**
11.1 Trigger Algorithms . . . 215
11.1.1 Technical Prerequisites . . . 216
11.1.2 Sliding Window Algorithms . . . 216
11.1.3 Legacy-like Sliding Window Algorithm . . . 219
11.1.4 Geometry-aware Sliding Window Algorithm . . . 222
11.1.5 Shower Shape Variables . . . 224
11.1.6 Neural Networks . . . 227
11.2 Performance Evaluation . . . 229
11.3 Outlook . . . 234

VI Conclusion **237**

Bibliography **241**

A Datasets and Monte Carlo Simulation **271**

B STDM4 Preselection **273**

C Acceptance and Efficiency **275**

D Cutflows **277**

E Binning of 2D Collins-Soper Distributions **283**

F Additional Pull Distributions **291**

G Detailed Breakdown of Combined Measured Angular Coefficients and Cross Section **299**

H Shower Shape Variables **307**
H.1 Legacy Shower Shape Variables 307
H.2 Definition of Shower Shape Variables 309
H.3 Correlation Matrices 310

Part I

Introduction

> *Maybe we have 2500 years ahead of us before we get to the next big step.*
>
> **— Steven Weinberg**

When asked in an interview in the CERN Courier [1] about tackling some of the open problems of the so-called *Standard Model*, Steven Weinberg, theoretical particle physicist and nobel laureate, responded with the cautious words above. His remark illustrates the unpredictability of fundamental research, which, by its nature, explores the unknown. This exploration is driven by the curiosity inherent to human nature, which manifests in striving to understand the world we live in. In the aforementioned interview Weinberg draws a parallel to Democritus who, already in 400 BC, proposed the existence of atoms, a theory which has been rigorously adopted only in the 20th century. This demonstrates that, while new concepts and understanding might take a long while to be tested and understood, some theories preserve in the end.

Particle physics is the most foundational area of research and exploration which aims to describe and understand the most fundamental processes of the universe. The Standard Model of particle physics is the culmination of human understanding of these processes and has been a very successful theory standing experimental tests over decades. One of its most recent and most impactful breakthroughs was the discovery of the Higgs boson in 2012 [2, 3], which had already been proposed to exist almost 50 years earlier.

While the Standard Model is the most comprehensive theory of human fundamental understanding of the universe to date, numerous experimental observations, such as neutrino oscillations at Super-Kamiokande [4] and SNO [5], clearly show that the model is incomplete. A rich experimental programme is dedicated to explore

observations incompatible with the theory and challenge it in new experimental approaches. Measurements of previously untested areas of the Standard Model can be achieved for instance by increasing the energy of colliding particles in collision experiments. While this is a direct access to potential new phenomena, economically it is not possible to increase the energy of collision experiments and the infrastructure required indefinitely[1]. A second gateway to test the theory and access potential new phenomena beyond its scope are precision measurements of its predictions. Such precision measurements are feasible with current experimental setups or at least with relatively few changes compared to completely new setups. They rely on both a very good understanding of the experiment, methods used and theoretical assumptions as well as a large dataset which enables a high statistical accuracy.

This thesis focusses on such precision measurements, using the ATLAS detector at the Large Hadron Collider (LHC), a machine capable of colliding protons and other hadrons at very high energies. The results of these collisions can be recorded at detectors such as ATLAS. In particular, the discussions in this thesis centre around the so-called *Drell-Yan neutral current* studied in proton collisions. In the Drell-Yan neutral current, Z bosons or virtual photons γ^* are created from a quark and an anti-quark and decay into an oppositely charged lepton and anti-lepton. The cross section of this process can be parametrised in a way that factorises the production mechanism from the decay into the lepton/anti-lepton pair. In this factorisation, the polarisation of the Z boson or the photon are contained in angular coefficients, which can be used to probe the production process precisely. The measurement presented in this thesis uses the full Run 2 dataset recorded by ATLAS at a centre-of-mass energy of $\sqrt{s} = 13\,\text{TeV}$. For the first time the full set of eight angular coefficients as well as the total cross section are measured at $\sqrt{s} = 13\,\text{TeV}$ differentially, both as a function of the rapidity and the transverse momentum of the Z/γ^* around the Z boson pole mass. These measurements can be used to increase the accuracy of theoretical predictions as they are provided unfolded, i.e. with all detector effects removed. The angular coefficients are not only useful to study production processes of the Z/γ^*, but are also connected to the so-called *forward-backward asymmetry* and the *weak mixing angle*. As experimental tensions have been observed between the two most precise measurements [6] of the weak mixing angle, it is crucial to explore this apparent challenge to the Standard Model further. Exploiting the unprecedentedly large ATLAS Run 2 dataset allows for a very high statistical accuracy. An estimate for the sensitivity of such a measurement is derived using one of the angular coefficients, A_4, which is very sensitive to the weak mixing angle.

To further boost the sensitivity of measurements such as the angular coefficients and the weak mixing angle in the future, numerous upgrades to the detector are

[1] Assuming current technological standards and costs.

planned. As a preparation for the ATLAS Phase II upgrade, a project for the High-Luminosity upgrade of the LHC, algorithms are developed that can be used to trigger electrons/positrons or photons in the ATLAS forward region, i.e. the region close to the beam pipe. As electrons and positrons in this region are part of decay topologies of Z/γ^* bosons, which are especially sensitive to the weak mixing angle due to reduced dilution effects, an effective trigger system is crucial for the highest sensitivity measurements possible.

The thesis is structured as follows: In chapter 1 the theoretical foundations of relevance for the measurements are explained, followed by chapter 2 where the experimental setups of ATLAS and the LHC are introduced. In chapter 3 the simulations used throughout the thesis are discussed. The strategy and motivation of a measurement of the angular coefficients is provided in chapter 4, followed by a detailed study of the data and the predictions in chapter 5. This culminates in the actual measurement of the coefficients in chapter 6. Chapter 8 shows the study of the expected sensitivity of a measurement of the weak mixing angle, enclosed by chapters 7 and 9 providing context on the strategy, motivation and finally the outlook of such a measurement. After discussing the ATLAS upgrade in chapter 10, the development of trigger algorithms for the upgrade is discussed in chapter 11. An overall conclusion is drawn at the end of the thesis.

Part II

Theoretical and Experimental Foundations

1 Theoretical Introduction

> *It doesn't stop being magic just because you know how it works.*
>
> **— Terry Pratchett**

This chapter is intended to provide the theoretical foundation for the measurements presented in this thesis. As such the mathematical groundwork of the Standard Model in particle physics is provided and set into the context of proton-proton collisions. Finally, in order to highlight how relevant measurements of angular coefficients of the Z boson and the weak mixing angle are, their theoretical context and importance are described in detail. If not stated otherwise, the foundations for this chapter have been taken from Griffiths, Peskin, Schroeder and Kulesza [7, 8, 9].

1.1 The Standard Model

One of the most successful theories in physics has been the Standard Model of particle physics [10, 11, 12, 13]. Its predictions have been tested and confirmed in numerous experiments across many decades of research to ever greater precision. Below this model is theoretically described, followed by an overview of its known shortcomings and limitations. To be consistent with literature, natural units are used throughout this thesis, which define $c = \hbar = 1$.

1.1.1 Phenomenological Overview

The Standard Model of particle physics is a non-abelian gauge theory that builds upon the premise that all visible matter and three of the four known fundamental forces can be described by point-like particles and their interactions. For this reason a distinction is made between particles that describe matter, particles that are force carriers and the Higgs boson. They can be differentiated by their spin. The former carry a half-integer spin and are called *fermions*, while the latter carry an integer spin and are called *gauge bosons*.

Gauge Bosons

Four fundamental forces are currently known: The electromagnetic, strong, weak and the gravitational force. Of those, gravitation might be one of the most tangible, but it is not described within the formalism of the Standard Model. Its strength over short distances is also many orders of magnitude below the other three known forces. A summary of the gauge bosons in the Standard Model can be found in table 1.2.

The electromagnetic force can be experienced at all times, for instance in the form of visible light. It is mediated by a massless, electrically neutral spin-1 particle, called *photon*, usually denoted as γ and couples to the electric charge. The theory of *Quantum Electrodynamics* and its interactions are described in detail in section 1.1.2.1.

The weak force is prevalent for example in processes such as the β-decay of radioactive elements and is mediated by three spin-1 bosons: the $W^{\pm}$ and the Z bosons[1]. The former carry a positive or negative electric charge, while the latter is electrically neutral. The three bosons are some of the heaviest particles in the Standard Model. The W bosons have a pole mass of $(80.377 \pm 0.012)\,\mathrm{GeV}$ (world average without recent CDF II results) [14] and the Z boson has a pole mass of $(91.1876 \pm 0.0021)\,\mathrm{GeV}$ [14]. The gauge bosons of the weak force couple to the weak isospin T_3 and are described in the unification of the electromagnetic and the weak forces, the *Electroweak Theory*, which is dealt within section 1.1.2.4.

Lastly, the strong force is of particular relevance over short distances where its strength depending on the energies involved can easily surpass those of the other forces. Its massless spin-1 mediators called *gluons* couple to the colour charge. This quantum number can assume six states: red, green, blue and each anti-colour. Since each gluon carries two colour charges, there are a total of eight gluon mediators. Gluon interactions are described in *Quantum Chromodynamics* in section 1.1.2.3. Due to *confinement* only colour-less states can be observed experimentally, which means gluons can only be accessed indirectly.

Fermions

The fermions in the Standard Model can broadly be divided in two ways. This is also indicated in table 1.1. Firstly, there are *quarks* and *leptons*, each with their corresponding anti-particle. Secondly, there are three known *generations* of

[1] The example of the β-decay is only mediated by the $W^{\pm}$ bosons but not the Z boson.

fermions, each containing two quarks and two leptons (or either corresponding anti-particle).

Quarks Quarks and anti-quarks are the building blocks of all *hadrons*, a combination of which are composite particles of either quark/anti-quark pairs (called *mesons*) or three quarks or anti-quarks (called *baryons*) held together by the strong force. There are also states that involve more quarks/anti-quarks such as *tetraquarks* and *pentaquarks*, which have first been discovered by the Belle [15] and LHCb collaborations [16], respectively. Quarks and anti-quarks interact with all known fundamental forces as they carry an electric charge of $\pm\frac{1}{3}e$ or $\pm\frac{2}{3}e$ (where e is the elementary charge), a colour charge and a weak isospin. They can be distinguished by their weak isospin T_3, which is $+\frac{1}{2}$ for up-type quarks and $-\frac{1}{2}$ for down-type quarks. In total there are three generations of quarks/anti-quarks known as shown in table 1.1, where the second and third generation are identical to the first with respect to the quantum numbers presented, but they have a higher mass and different *flavours*.

Leptons In the same way as the quarks, leptons and anti-leptons can be arranged into three generations, where the second and third generation are identical copies of the first but with a higher mass[2]. The electron, the muon and tau all carry an electric charge of $-1e$, while their anti-particles carry an electric charge of $+1e$. Neutrinos in the Standard Model are massless and electrically neutral. All leptons interact with the weak force as they carry a weak isospin of $-\frac{1}{2}$ and $+\frac{1}{2}$ for the charged leptons and the uncharged leptons (neutrinos), respectively.

Higgs Boson

The latest addition to the Standard Model is the Higgs boson which has only been discovered in 2012 by the ATLAS [2] and CMS collaborations [3]. The Higgs mechanism is essential in the process of *spontaneous symmetry breaking* and has already been proposed in the 1960s by Higgs, Englert and Brout et al. [17, 18, 19, 20, 21, 22]. The Higgs boson is an electrically neutral scalar boson, so it has a spin of 0. The Higgs is produced as an excitation of the *Higgs field*, which is the mechanism that gives mass to all massive fundamental particles as described in section 1.1.2.4. Consequently, the Higgs boson couples to the mass of a particle and thus to most fundamental particles with the exception of the photon and the gluons. Its basic properties are summarised in table 1.2.

[2] In the Standard Model neutrinos are actually massless, but it has been observed to be incorrect due to neutrino oscillations, i.e. neutrinos changing their flavour. Whether the neutrinos follow the same mass hierarchy as the charged leptons has not been shown definitively.

Generation	1		2		3	
	Quarks					
	Up	Down	Charm	Strange	Top	Bottom
Symbol	u	d	c	s	t	b
Mass [GeV]	$2 \cdot 10^{-3}$	$5 \cdot 10^{-3}$	1	$95 \cdot 10^{-3}$	173	4
El. charge Q/e	$2/3$	$-1/3$	$2/3$	$-1/3$	$2/3$	$-1/3$
Weak isospin T_3	$1/2$	$-1/2$	$1/2$	$-1/2$	$1/2$	$-1/2$
	Leptons					
	Electron	Electron neutrino	Muon	Muon neutrino	Tau	Tau neutrino
Symbol	e	ν_e	μ	ν_μ	τ	ν_τ
Mass [GeV]	$0.5 \cdot 10^{-3}$	$< 3 \cdot 10^{-6}$	$11 \cdot 10^{-6}$	$< 2 \cdot 10^{-3}$	2	$< 16 \cdot 10^{-3}$
El. charge Q/e	-1	0	-1	0	-1	0
Weak isospin T_3	$-1/2$	$1/2$	$-1/2$	$1/2$	$-1/2$	$1/2$

Tab. 1.1.: Overview of fermion properties in the Standard Model by fermion type and generation. All values have been taken from the Particle Data Group [14] and mass values are rounded. The *current quark mass* values used for the Up, Down and Strange quarks are quoted in the $\overline{MS}$ scheme (which will be discussed in more detail in section 1.1.2.2), while the Top quark mass has been measured from decays.

	Photon	$W^\pm$ bosons	Z boson	Gluons	Higgs boson
Symbol	γ	$W^\pm$	Z	g	H
Coupling	El. charge	Weak isospin	Weak isospin	Colour charge	Mass
Mass [GeV]	0	~ 80.4	~ 91.2	0	~ 125.2
Spin	1	1	1	1	0

Tab. 1.2.: Overview of bosons and their properties in the Standard Model. All values have been taken from the Particle Data Group [14].

1.1.2 Mathematical Formalism

For a complete understanding of the Standard Model it is necessary not only to study its phenomenological aspects introduced in the previous chapter, but also to highlight the mathematical foundation behind it.

The Standard Model is a quantum field theory based on the principle of local gauge symmetry given by the group symmetry of

$$SU(3)_C \times SU(2)_L \times U(1)_Y. \tag{1.1}$$

Each particle is described as the excitation of a field that extends everywhere throughout space time. Quantum Chromodynamics is formed by the $SU(3)_C$ group[3], and electroweak theory can be described as a $SU(2)_L \times U(1)_Y$ group[4] that is spontaneously broken to a $U(1)_Q$ group[5] describing Quantum Electrodynamics. These mechanisms will be described in more detail assuming a basic understanding of relativistic quantum field theory. Additionally, the Feynman mechanism will be introduced, which is an essential aspect of theory calculations and predictions.

1.1.2.1 Quantum Electrodynamics

The theory of Quantum Electrodynamics (QED), sparked by research of Paul Dirac [23] and later refined e.g. by Fermi and others [24, 25, 26, 27], is a quantum field theory that describes interactions by electrically charged fermionic particles and bosonic photons as mediators of the electromagnetic force. It follows a $U(1)_Q$ group symmetry and is a useful example of applied quantum field theory.

A free, charged fermionic field $\psi(x)$ (where x is space-time) with a mass m is described by the *Dirac equation*

$$(i\gamma^\mu \partial_\mu - m)\psi(x) = 0, \tag{1.2}$$

where γ^μ are the Dirac matrices and ∂_μ the four gradient. The corresponding Lagrangian can thus be expressed as

$$\mathcal{L}_{\text{Dirac}} = \bar{\psi}(x)(i\gamma^\mu \partial_\mu - m)\psi(x), \qquad \text{where } \bar{\psi}(x) = \psi^\dagger(x)\gamma^0 \tag{1.3}$$

[3] The C is for the *colour charge*.
[4] The L is for the coupling of *weak isospin* couplings to left-handed fermions (or right-handed anti-fermions) and the Y for the *hypercharge* couplings.
[5] The Q is for the *electric charge*.

which is invariant under unitary transformations $U(1)$ that introduce a global phase

$$\psi(x) \to e^{i\alpha}\psi(x) \text{ and } \bar{\psi}(x) \to e^{-i\alpha}\bar{\psi}(x), \qquad \text{where } \alpha = \text{const.} \tag{1.4}$$

However, it is not invariant under a local gauge transformation of the form

$$\psi(x) \to e^{i\alpha(x)}\psi(x) \text{ and } \bar{\psi}(x) \to e^{-i\alpha(x)}\bar{\psi}(x) \tag{1.5}$$

due to the space-time dependence of the phase $\alpha(x)$ which introduces a non-vanishing term $-\bar{\psi}(x)\gamma^\mu\partial_\mu\alpha(x)\psi(x)$. The introduction of a *covariant derivative* D_μ, where

$$D_\mu := \partial_\mu + igA_\mu(x) \tag{1.6}$$

replaces the derivative ∂_μ, restores the gauge invariance of the Dirac Lagrangian

$$\mathcal{L}_{\text{Dirac}} = \bar{\psi}(x)(i\gamma^\mu D_\mu - m)\psi(x) \tag{1.7}$$

with the introduction of a new field $A_\mu(x)$. The Dirac Lagrangian of equation 1.7 in its full form can be written as

$$\mathcal{L}_{\text{Dirac}} = \bar{\psi}(x)(i\gamma^\mu\partial_\mu - m)\psi(x) - g\bar{\psi}(x)\gamma^\mu\psi(x)A_\mu(x) \tag{1.8}$$

by inserting equation 1.6. The new vector field $A_\mu(x)$ transforms under local gauge transformations as

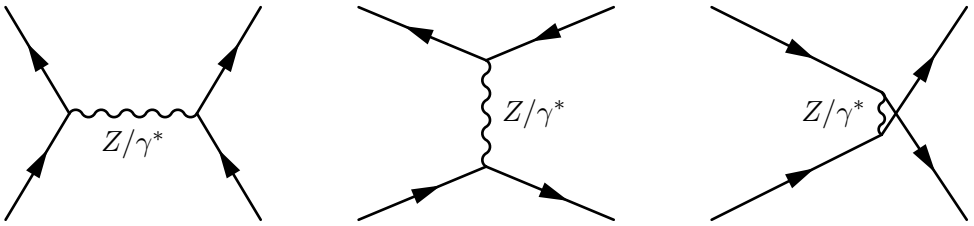
$$A_\mu(x) \to A_\mu(x) - \frac{1}{g}\partial_\mu\alpha(x). \tag{1.9}$$

This gauge boson field is identified as the *photon* field. Following Noether's theorem [28] the gauge symmetry leads to a conservation of the charge g by the fermion field $\psi(x)$ which can be identified as the electric charge e. This coupling strength is defined by the fine-structure constant[6] $\alpha_{\text{e.m.}}(\mathcal{O}(\text{MeV})) = \frac{e^2}{4\pi} \approx \frac{1}{137}$ [14]. The second part of equation 1.8 represents the interaction of the fermions with the photon field. In order to obtain the full Lagrangian for Quantum Electrodynamics, the Maxwell Lagrangian describing the kinematics of the photon field $A_\mu(x)$ needs to be added, so that

$$\mathcal{L}_{\text{QED}} = \bar{\psi}(x)(i\gamma^\mu\partial_\mu - m)\psi(x) - g\bar{\psi}(x)\gamma^\mu\psi(x)A_\mu(x) - \frac{1}{4}F^{\mu\nu}(x)F_{\mu\nu}(x) \tag{1.10}$$

is obtained, where $F^{\mu\nu}(x) = \partial^\mu A^\nu(x) - \partial^\nu A^\mu(x)$ is the electromagnetic field tensor which is also invariant under local phase transformations.

[6] This is a historical naming convention. Within the context of quantum field theory it depends on the energy scale at which a process it probed.



(a) Leading order s-channel interaction. **(b)** Leading order t-channel interaction. **(c)** Leading order u-channel interaction.

Fig. 1.1.: Examples of Feynman diagrams of the reaction $f\bar{f} \to Z/\gamma^* \to f'\bar{f}'$. Diagrams depicted possess identical initial and final states but can be distinguished by the type of interaction, i.e. scattering or annihilation processes.

1.1.2.2 Feynman Calculus

Before discussing Quantum Chromodynamics and Electroweak Theory in the next sections, it is useful to introduce one fundamental tool in quantum field theory, the *Feynman Diagrams* [29] originated in *pertubation theory* to calculate particle interactions. They form a powerful theoretical framework to describe fundamental particle interactions, such as the annihilation of a charged fermion f and anti-fermion $\bar{f}$ to create a photon[7] γ^* or Z boson in figure 1.1(a), which subsequently decays into a charged fermion f' and an anti-fermion $\bar{f}'$. Throughout this thesis, the time axis of Feynman diagrams is assumed to flow from left to right. The types of interactions in a Feynman diagram are defined by the Lagrangian of the theory under consideration, in this case equation 1.10 where the interaction of the fermion fields and photon fields are defined.

Diagrams are constructed from lines representing particles or anti-particles and vertices representing couplings between particles. In case of the diagram depicted in figure 1.1(a) a fermion (indicated by the arrow towards the positive time axis) and an anti-fermion (indicated by the arrow towards the negative time axis) annihilate into a Z/γ^* which in turn creates another fermion/anti-fermion pair. For simplicity, arrows are often not drawn but only implied as – following the basic principle of quantum mechanics – all processes that can occur will occur (and thus contribute to the overall observation). In case of the simple example discussed here, externally, other processes with the same final state cannot be distinguished from the one shown in 1.1(a) since the examples shown in figures 1.1(b) and figure 1.1(c) have identical initial and final states. Moreover, the processes shown so far are at *leading order* in the electromagnetic coupling. *Higher order* processes such as *next-to-leading order* (NLO) or *next-to-next-to-leading order* (NNLO) depicted in figure 1.2 contribute to the process as well due to the quantum mechanical principle that all possible contributions to an observed reaction will contribute and thus need to be considered.

[7] As photons are massless, the type of photon created in this reaction is *virtual*, which means it does not adhere to the energy-mass relation and has a non-zero invariant mass.



(a) Next-to-leading order example diagram.

(b) Next-to-next-to-leading order example diagram.

Fig. 1.2.: Examples of higher order contributions to the process $f\bar{f} \to Z/\gamma^* \to f'\bar{f}'$.

As it is impossible to calculate the infinite number of processes that contribute to a reaction (for instance $f\bar{f} \to Z/\gamma^* \to f'\bar{f}'$), perturbation theory is used to expand the analytical but incalculable description of a process into individual subprocesses such as depicted in figures 1.1 and 1.2. In case of the electromagnetic interaction, due to the small coupling of the electromagnetic coupling constant $\alpha_{\text{e.m.}}$, higher order contributions become ever smaller. Calculating physical observables from these Feynman diagrams will be discussed in more detail in section 1.2. Doing this it becomes clear that infinite values occur that need to be accounted for in a *renormalisation* procedure, where an unphysical scale μ_R is introduced to enforce finite values of measurable quantities leading to the dependence of the fine structure constant on the momentum transfer Q^2. How infinities are absorbed in the renormalisation depends on the scheme chosen. Typical examples of renormalisation schemes are the *on-shell* scheme and the modified minimal subtraction ($\overline{MS}$) scheme [30, 31]. In the on-shell renormalisation scheme the renormalised mass m_R is set to the pole mass m_P of a particle. This is not the case for the $\overline{MS}$ scheme where an arbitrary scale μ is introduced instead. The advantage of the latter is the necessity that physical observables must be independent of this scale leading to the renormalisation group equation [32]. As such it is typically simpler to compute amplitudes in the $\overline{MS}$ and thus it is often preferred.

1.1.2.3 Quantum Chromodynamics

The theory of Quantum Chromodynamics (QCD) was developed from a general field theory of Chen Yang and Robert Mills in the 1950s [33] into modern QCD by numerous researchers such as Harald Fritzsch [34], Murray Gell-Mann [35], Yuval Ne'eman [36] and others. It describes interactions of particles via the strong force, specifically *quarks/anti-quarks* and *gluons* as an $SU(3)_C$ group symmetry. The charges carried by quarks/anti-quarks and gluons are called *colour charges*. A fundamental difference of Quantum Chromodynamics to Quantum Electrodynamics are the self-interactions of the mediators of the force, the gluons. This fundamentally changes its behaviour as will be shown below, based on Brock, Peskin, Schroeder

and Skands [37, 8, 38], although the structure of the Lagrangian is very similar to the one of Quantum Electrodynamics in equation 1.10.

The invariant Lagrangian of Quantum Chromodynamics, a special case of Yang-Mills theory [33], can be expressed as

$$\mathcal{L}_{\mathrm{QCD}} = \bar{\psi}_{q,j}(x)(i\gamma^{\mu}(D_{\mu})_{ji} - m_q\delta_{ji})\psi_{q,i}(x) - \frac{1}{4}G_{\mu\nu,a}G_a^{\mu\nu}. \tag{1.11}$$

In this expression the sum of repeated indices is implicitly taken. The fields $\psi_{q,i}(x)$ describe quarks of flavour q and mass m_q. Interactions in Quantum Chromodynamics occur via the coupling to colour charges described before. The sums of indices i and j are added over all $N_C = 3$ colour types. The covariant derivative is defined as

$$(D_{\mu})_{ij} := \partial_{\mu}\delta_{ij} + ig_sA_{\mu,a}(T_a)_{ij} \tag{1.12}$$

and the gluon field strength tensor as

$$G_{\mu\nu,a} := \partial_{\mu}A_{\nu,a} - \partial_{\nu}A_{\mu,a} - g_sC_{abc}A_{\mu,b}A_{\nu,c}. \tag{1.13}$$

The indices a, b, c take values defined by the $N_C^2 - 1 = 8$ group components of the $SU(3)_C$ group so that $a, b, c \in [1, 2, ...8]$. This is also reflected in the vector fields $A_{\mu,a}$. The totally anti-symmetric structure constants C_{abc} also depend on these indices and define a Lie algebra. Furthermore, the strong coupling g_s is often expressed as the strong coupling constant[8] $\alpha_s = \frac{g_s}{4\pi}$ analogously to the electromagnetic coupling constant. Finally, the 3×3 matrices, the generators of the $SU(3)_C$ group, $(T_a)_{ij}$ fulfil the commutation relations

$$[T_a, T_b] = iC_{abc}T_c \tag{1.14}$$

that define the algebra. Crucially, the Lagrangian contains terms of self-interactions[9] of the gluons (terms that contain multiple of the vector field A_{μ} terms) in contrast to Quantum Electrodynamics.

Since QCD must be renormalisable, its coupling constant is found to be strongly dependent on the momentum transfer Q^2 of the process at each vertex. Specifically, $\alpha_s = \alpha_s(Q^2) \propto (\ln Q^2)^{-1}$, which means it obtains large values at small momentum transfers and small values at large momentum transfers, called *asymptotic freedom*. At the scale of the Z boson pole mass M_Z, for instance, $\alpha_s(M_Z^2) \approx 0.12$ [40].

[8] It is actually not a constant but strongly depends on the energy scales involved.

[9] Note that the necessity of gauge invariance leads to the definition of additional non-physical objects called *Faddeev-Poppov ghosts* [39], which are not identified as particles, but they are used as an auxiliary mechanism in QCD to remove unphysical polarisations.

1.1.2.4 Electroweak Theory and Spontaneous Symmetry Breaking

While the electromagnetic and the weak forces have been introduced separately in section 1.1.1, their description within the Standard Model emerges from a more fundamental unification of forces, the *electroweak force* first put forward by Glashow, Weinberg and Salam [10, 11, 12]. It is described as a $SU(2)_L \times U(1)_Y$ theory which is spontaneously broken by the *Higgs mechanism* to the $U(1)_Q$ group of electromagnetic theory. Before discussing electroweak theory in detail (following Dawson, Hays, Pich, Peskin and Schroeder [41, 42, 43, 8]), it is important to clarify the concept of *chirality* of particles, which is a fundamental aspect of the theory. The chirality can be determined from the eigenstates of the $\gamma^5 := i\gamma^0\gamma^1\gamma^2\gamma^3$ matrix. In the relativistic limit where the mass of a particle is negligible, the chirality is equal to the helicity of a particle, which defines how a particle behaves under mirror-transformations, i.e. the inversion of spatial coordinates. For example, polar vectors such as the position and momentum of a particle are inverted by such a transformation, while axial vectors like the angular momentum or spin remain unchanged. However, chirality itself cannot be interpreted in such a simple physical way as it represents abstract eigenstates. Nevertheless, particles can be classified by two chiral properties, *left-handedness* (denoted with the subscript L) and *right-handedness* (denoted with the subscript R). In the case of fermions this means that left-handed fermions form a *doublet* with a weak isospin component $T_3 = \pm\frac{1}{2}$ and right-handed fermions form a *singlet* with $T_3 = 0$, while the inverse is true for anti-fermions. Using the example of the first quark generation (u and d) of the Standard Model, the corresponding spinors can be defined as

$$\psi_1 = \begin{pmatrix} u \\ d \end{pmatrix}_L, \psi_2 = u_R \text{ and } \psi_3 = d_R. \tag{1.15}$$

Here, ψ_1 is the doublet and $\psi_{2,3}$ are the singlets. While the same holds true for the other quark generations, the Standard Model does not contain right-handed neutrinos ν_R.

In order to fully describe electroweak theory, it is again necessary to define a Lagrangian that defines all properties and interactions of particles in the theory. It can be grouped into three categories

$$\mathcal{L}_{\text{EW}} = \mathcal{L}_{\text{fermion}} + \mathcal{L}_{\text{gauge}} + \mathcal{L}_{\text{Higgs}}. \tag{1.16}$$

The first part, $\mathcal{L}_{\text{fermion}}$, defines fermion properties

$$\mathcal{L}_{\text{fermion}} = \sum_{i=1}^{3} \left(\bar{\psi}^q_{i,\alpha} \left(i\gamma^\mu \partial_\mu \right) \psi^q_{i,\alpha} \right) + \sum_{j=1}^{3} \left(\bar{\psi}^l_{j,\alpha} \left(i\gamma^\mu \partial_\mu \right) \psi^l_{j,\alpha} \right). \tag{1.17}$$

In this equation ψ_i are defined as outlines in equation 1.15, but this time using the different quark q and lepton l fields of each generation α, which is also summed over via i and j. The coupling to the weak isospin T_3 means that the electroweak force does not interact with right-handed particles or left-handed anti-particles.

While the chirality is integral to the $SU(2)_L$ group (having the weak isospin as generator), the generator of the $U(1)_Y$ group is the electroweak *hypercharge*, which relates the electromagnetic charge Q and the weak isospin T_3 as

$$Y = 2(Q - T_3). \tag{1.18}$$

The gauge requirements of both groups result in four vector boson fields which make up the gauge part of the Lagrangian, which is defined as

$$\mathcal{L}_{\text{gauge}} = -\frac{1}{4} W^{i,\mu\nu} W^i_{\mu\nu} - \frac{1}{4} B^{\mu\nu} B_{\mu\nu}, \tag{1.19}$$

where $i = \{1, 2, 3\}$. Tensors $W^{i,\mu\nu}$ are the field tensor of the $SU(2)_L$ group and $B^{\mu\nu}$ represents the field tensor of the $U(1)_Y$ group. They are defined as

$$W^{i,\mu\nu} = \partial^\mu W^{i,\nu} - \partial^\nu W^{i,\mu} + g\epsilon^{ijk} W^{j,\mu} W^{k,\nu} \qquad \text{and} \tag{1.20}$$

$$B^{\mu\nu} = \partial^\mu B^\nu - \partial^\nu B^\mu. \tag{1.21}$$

The $W^{i,\mu}$ can be identified as the three weak isospin fields of the $SU(2)_L$ group that only couple to left-handed particles (or right-handed anti-particles), and B^μ is identified as the weak hypercharge field of the $U(1)_Y$ group that couples to the hypercharge with coupling strength g'. The self-interaction of the $W^{i,\mu}$ fields can be seen in the second part of the $W^{i,\mu\nu}$ field tensor. Its sign depends on the fields involved due to the anti-symmetric tensor ϵ^{ijk} and possesses the coupling strength g. The fields $W^{i,\mu\nu}$ and B^μ do not correspond to the mass eigenstates known from the weak and electromagnetic interactions. The mass eigenstates of the $W^\pm$ bosons are constructed as linear combinations of $W^{1,\mu}$ and $W^{2,\mu}$ as

$$W^{\pm,\mu} = \frac{1}{\sqrt{2}} (W^{1,\mu} \mp i W^{2,\mu}). \tag{1.22}$$

The neutral Z boson and the photon are obtained by a rotation of the $W^{3,\mu}$ and B^μ fields

$$\begin{pmatrix} A^\mu \\ Z^\mu \end{pmatrix} = \begin{pmatrix} \cos\theta_W & \sin\theta_W \\ -\sin\theta_W & \cos\theta_W \end{pmatrix} \begin{pmatrix} B^\mu \\ W^{3,\mu} \end{pmatrix}, \tag{1.23}$$

where the angle θ_W is called the *weak mixing angle* (also known as *Weinberg angle*) that describes the mixing. It is also connected to the electric charge e and the couplings g and g' via

$$e = g \sin\theta_W = g' \cos\theta_W. \tag{1.24}$$

The angle is also closely connected to the two massive bosons

$$\cos\theta_W = \frac{M_W}{M_Z}, \tag{1.25}$$

where M_W and M_Z are the masses of the W bosons and the Z boson, respectively. Note that both equations 1.24 and 1.25 are valid at leading order in electroweak theory and do not include higher order corrections. In electroweak theory, charged and uncharged currents can be differentiated as the former are mediated by the W bosons and the latter by the photon and the Z boson. Photons and Z bosons mediate similar interactions, however their coupling is different. Specifically, it is important to compare the coupling of the photon defined in section 1.1.2.1 in Quantum Electrodynamics to fermionic fields f defined as

$$\mathcal{L}_{\mathrm{QED}} = eA_\mu \sum_f \bar{f}\gamma^\mu f \tag{1.26}$$

to the interaction of the Z boson in the neutral current (NC)

$$\mathcal{L}_{Z,\mathrm{NC}} = \frac{e}{2\sin\theta_W \cos\theta_W} Z_\mu \sum_f \bar{f}\gamma^\mu (v_f - a_f\gamma_5) f, \tag{1.27}$$

where $v_f = T_3^f(1 - 4|Q_f|\sin^2\theta_W)$ (vector component) and $a_f = T_3^f$ (axial vector component). Here, T_3^f and Q_f are the third component of the weak isospin and the electric charge of each fermion, respectively. This highlights the different coupling types: The Z boson has an *axial vector* component leading to its *vector - axial*, or *V-A*, coupling nature (depending on the magnitude of the weak mixing angle) compared to the purely vectorial coupling of photons. Thus, photons couple to particles/anti-particles of any chirality, while the Z boson couplings are different for left-handed and right-handed particles/anti-particles for instance in only coupling to left-handed neutrinos or right-handed anti-neutrinos.

On their own, the $\mathcal{L}_{\mathrm{gauge}}$ and $\mathcal{L}_{\mathrm{fermion}}$ components of the electroweak Lagrangian do not allow massive fermions or heavy weak gauge bosons as they are observed in experiments. The solution to this problem has been first proposed by Brout, Englert and Higgs et al.[10] [17, 18, 19, 20, 21, 22] with the introduction of a complex field, a

[10] In order to attribute all original authors, the mechanism is sometimes also called *Brout-Higgs-Guralnik-Hagen-Kibble mechanism*.

ϕ doublet which gives rise to fermion and $W^{\pm}$ and Z boson masses and is composed of charged (+) and uncharged (0) field components

$$\mathcal{L}_{\text{Higgs}} = (D^{\mu}\phi)^{\dagger}\,(D_{\mu}\phi) - V(\phi) + \mathcal{L}_{\text{Yukawa}}. \tag{1.28}$$

Here,

$$D^{\mu} = \partial^{\mu} + ig\frac{\sigma^{i}}{2}W^{i,\mu} - \frac{i}{2}g'B^{\mu} \tag{1.29}$$

is the covariant derivative (with σ^{i} as the Pauli-matrices) of the Higgs field ϕ which is expressed as the two components

$$\phi = \begin{pmatrix}\phi^{+}\\ \phi^{0}\end{pmatrix}. \tag{1.30}$$

The *Yukawa* [44] term $\mathcal{L}_{\text{Yukawa}}$ of the Lagrangian explicitly contains the couplings of the Higgs field to fermions with a coupling strength proportional to their masses. The potential $V(\phi)$ is required to follow the form

$$V(\phi) = -\mu^{2}\phi^{\dagger}\phi + \lambda\left(\phi^{\dagger}\phi\right)^{2} \quad \text{with} \quad \lambda > 0 \tag{1.31}$$

in order to adhere to renormalisability and follow the $SU(2)_L \times U(1)_Y$ symmetry. For $\mu^2 > 0$ the vacuum state ϕ_{vac} is found to be degenerate with an infinite number of solutions $\phi_{\text{vac}} = \sqrt{\frac{\mu^2}{2\lambda}}e^{i\theta}$ with $\theta \in \mathbb{R}$. The $SU(2)_L \times U(1)_Y$ symmetry is spontaneously broken by the choice of an arbitrary value of θ. It is convenient to choose $\theta = 0$, so that

$$\langle\phi_{\text{vac}}\rangle = \frac{1}{\sqrt{2}}\begin{pmatrix}0\\ v\end{pmatrix} \qquad \text{with } v = \sqrt{\frac{\mu^2}{\lambda}} \tag{1.32}$$

is the vacuum expectation value leading to the $U(1)_Q$ symmetry. Due to the conservation of the electric charge Q within the universe, only the uncharged part of the vacuum expectation value is non-zero. The choice of a unitary gauge for the ϕ doublet leads to

$$\phi = \frac{1}{\sqrt{2}}\begin{pmatrix}0\\ v + H\end{pmatrix} \tag{1.33}$$

with H the real, scalar *Higgs field*. It couples to the mass of particles. In case of fermions this is defined by the Yukawa coupling

$$y_f = \frac{m_f}{v}, \tag{1.34}$$

where m_f is the mass of the fermion. The masses of the heavy gauge bosons of electroweak theory can be determined as

$$m_W = \frac{gv}{2} \qquad \text{and} \qquad m_Z = \frac{v}{2}\sqrt{g^2 + g'^2}. \tag{1.35}$$

Due to its self-coupling, it also gives rise to the *Higgs boson*, which has been first observed by the ATLAS and CMS experiments [2, 3].

1.1.3 Limitations

Even though the Standard Model describes many phenomena of particle physics to a high precision that has been tested numerous times, it is apparent that it is not a complete description of fundamental physics. Three major limitations will be briefly outlined below.

Firstly, as mentioned previously, the gravitational force is not included in its description of quantised fundamental forces due to the challenges of formulating a comprehensive theory that combines quantum field theory and general relativity. Its inclusion would also give rise to the existence of a *graviton* as the force carrier of gravitation which would be difficult to detect due to its much weaker interaction strength compared to the other forces.

Secondly, neutrinos have been observed to change their flavour in a process called *neutrino oscillations* [4, 5]. Standard Model neutrinos are expected to be massless, however, the changing of flavour states can only occur if neutrinos are actually massive particles. Probing the precise nature of neutrinos is a vast area of modern research.

Thirdly, from observations of rotational speeds of galaxies [45] and the expansion of the universe [46] it has been determined that there is a vast amount of mass and energy of a type that is currently not understood. In fact, about 25% of the matter-energy content in our universe is called *dark matter* due to its apparent invisibility to the electromagnetic force. Additionally, the continued acceleration of the expansion of the universe is currently attributed to so-called *dark energy*, which contributes about 70% to the matter-energy content of the universe.

Finally, in addition to these examples of limitations of the Standard Model there are numerous experiments that have reported statistically significant deviations of certain fundamental properties between themselves and other experiments or to Standard Model expectations. A subset of these measurements that are particularly relevant to the motivation of the measurement presented in this thesis will be discussed in section 1.3.

1.2 Proton-Proton Collisions

The Standard Model Lagrangian introduced in the previous sections contains all information necessary to describe particle interactions within the limitations outlined. However, it is not possible to explicitly measure the Lagrangian since many fundamental particles and interactions cannot be observed directly. Nonetheless, its individual components are accessible via derived observables that can be measured in experiments. Proton-proton collisions as a means of access to such observables will be described in this chapter.

1.2.1 Scattering Processes

Detectors are useful tools to measure particles which are the result of scattering processes. In the context of collision experiments the most fundamental observable is the *rate* of an observation. It is directly proportional to the *cross section* σ of the process under consideration as well as the *instantaneous luminosity* L of the collider. The former is related to the probability of a specific type of interaction to occur, while the latter is a measure of the density of particles that cross each other in the interaction region of a detector. This leads to the definition of the rate as

$$\frac{\mathrm{d}N}{\mathrm{d}t} = \sigma L. \tag{1.36}$$

The rate is defined as the number of events of interest per time interval, i.e. $\frac{\mathrm{d}N}{\mathrm{d}t}$. It is convenient to consider the total number of events observed for a fixed *integrated luminosity* $\mathfrak{L}$. Since the number of events can be counted and the integrated luminosity can also be measured, this allows for a measurement of a cross section of interest

$$\sigma = \frac{N}{\mathfrak{L}}. \tag{1.37}$$

Most measurements are also sensitive to different regions in phase space $\mathrm{d}\Omega$ such that the *differential cross section*[11] is defined as

$$\frac{\mathrm{d}\sigma}{\mathrm{d}\Omega} = \frac{\mathrm{d}N}{\mathrm{d}\Omega}\frac{1}{\mathfrak{L}}. \tag{1.38}$$

Using nomenclature as defined in Griffiths [7], such cross sections can be calculated employing *Fermi's golden rule* [47, 23], which connects the measurable initial state i and final state f (both of which reside in the measurable phase space Ω) using an amplitude $\mathcal{M}_{fi}$. In case of a collision of two particles it is convenient to express their initial energy within the *centre-of-mass* frame as $s = \sqrt{(p_1 + p_2)^2}$, where $p_{1,2}$ are the

[11] In experimental contexts measured cross sections are not strictly mathematically differential, i.e. using infinitesimally small $\mathrm{d}\Omega$, but limited in resolution and typically grouped into *bins* of finite size $\Delta\Omega$.

four-momenta of the initial state particles. Considering an interaction of the type $1 + 2 \rightarrow 3 + 4$ in the centre-of-mass reference frame, the cross section of the process can then be expressed using Fermi's golden rule as

$$\frac{\mathrm{d}\sigma}{\mathrm{d}\Omega} = \frac{1}{64\pi^2 s}\frac{|\vec{p}_f|}{|\vec{p}_i|}|\mathcal{M}_{fi}|^2. \tag{1.39}$$

In this equation $\vec{p}_f$ and $\vec{p}_i$ are the three-vectors of the outgoing and incoming particles, respectively. The matrix element $\mathcal{M}_{fi}$ is calculated by

$$\mathcal{M}_{fi} = \int \bar{\psi}_f(x)\hat{V}\psi_i(x)\mathrm{d}x, \tag{1.40}$$

where $\psi_{f,i}$ represent the final and initial states and $\hat{V}$ represents the operator of the interaction of both particles. This so-called *amplitude* can be calculated from the Feynman diagrams introduced in section 1.1.2.2.

1.2.2 Parton Model

The interactions of colliding protons as depicted in figure 1.3 can be described using the *parton model*. Protons are composite objects which contain *valence quarks* and a dynamic *sea* of quarks, anti-quarks and gluons. Protons are baryons and built from two up quarks and a down quark as valence quarks. The sea is dynamically changing due to the strong force in which gluons are exchanged and pairs of quarks and anti-quarks are created and annihilated.

In the collision of two protons A and B at sufficiently high energies such as at the Large Hadron Collider, the interaction between the protons actually occurs between two of the fundamental particles within, called *partons* a and b as depicted in figure 1.3. This interaction is called *hard scattering* and is defined by the initial states of the participating partons. In particular, parton distribution functions $f_{a/A}$ and $f_{b/B}$ describe the probability of partons carrying a certain fraction x_a and x_b of the total proton momentum probed at a scale Q^2 [48]. The cross section $\sigma(AB \rightarrow X)$ of such an interaction where protons A and B collide to create final state X can be calculated as

$$\sigma(AB \rightarrow X) = \sum_{a,b}\int \mathrm{d}x_a \mathrm{d}x_b f_{a/A}(x_a, Q^2) f_{b/B}(x_b, Q^2)\hat{\sigma}_{ab\rightarrow X}(x_a, x_b, Q^2). \tag{1.41}$$

In this equation $\hat{\sigma}_{ab\rightarrow X}$ represents the cross section of the hard scattering between the two partons a and b to create final state X, calculated in a similar manner as equation 1.39. It is factorised from the parton density functions, which cannot be calculated from a theoretical perspective as perturbative QCD breaks down. This is discussed in the following section.

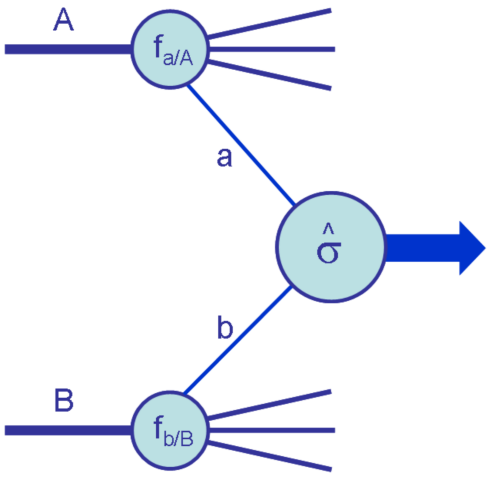
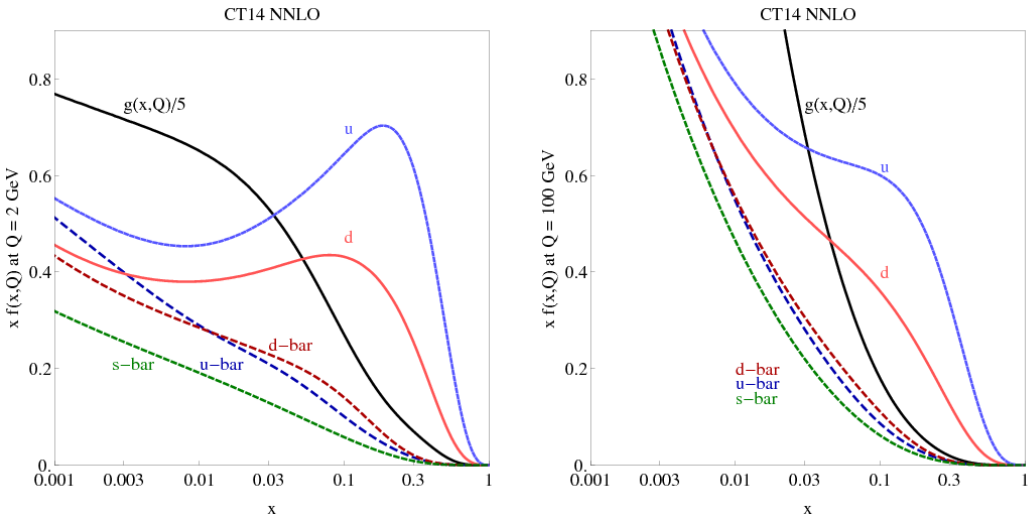


Fig. 1.3.: Schematic diagram of a collision of protons A and B [49].

1.2.3 Parton Distribution Functions

Precisely understanding parton distribution functions (PDFs) is a crucial aspect of formulating theoretical expectations of a given physical process in a hadron collision experiment. The collision of two protons does not allow to precisely understand the initial state of the interacting partons as the sea dynamically changes and thus the carried momentum fractions cannot be predicted. While the data gathered in such proton-proton collisions can still be utilised to understand its structure, typically, leptons are scattered with protons in *Deep Inelastic Scattering* (DIS) processes. As leptons are point-like particles, their initial state can be defined precisely and used to probe the inner structure of the proton.

To do this, a non-physical *factorisation scale* μ_F^2 is defined to distinguish between the hard scattering of the lepton and a quark or anti-quark and the actual parton distribution function (which effectively correspond to probability densities of momentum fractions) [50]. This is motivated by the factorisation theorem which explicitly separates short- and long-distance behaviour of physical processes (in particular in QCD) [51]. The PDFs can be probed at different momentum scales Q^2, an example of which is depicted in figure 1.4, where the CT14NNLO [52] PDF set is depicted at low $Q^2 = 4\,\mathrm{GeV}^2$ on the left and high $Q^2 = 10\,000\,\mathrm{GeV}^2$ on the right. This highlights how the contributions of the individual flavours of quarks, anti-quarks and the gluons evolve. While at low momentum the valence quarks (up and down quarks) statistically carry most of the momentum, this effect is reduced at higher momenta by the sea contributions and in particular by the gluon PDF which increases in dominance.



(a) $Q^2 = 4\,\mathrm{GeV}^2$. (b) $Q^2 = 10\,000\,\mathrm{GeV}^2$.

Fig. 1.4.: CT14NNLO parton density function at different momentum transfers Q^2 [52]. Uncertainties are not shown.

PDFs are determined by different groups such as CTEQ [53], MMHT [54], NNPDF [55] or HERAPDF [56], using different techniques of global fits on data of numerous processes. Typically, a scale μ_0 is chosen to then parametrise the parton distribution functions $f_{a/A}(x, \mu_0)$ for different partons $a = g, u, \bar{u}, ...$ etc. As the functions must follow e.g. momentum sum rules (i.e. the normalised sum over all momenta must equal 1), a starting set of parameters obeying these rules can be identified. Starting with $f_{a/A}(x, \mu_0)$, the function $f_{a/A}(x, \mu)$ for all μ is determined iteratively by evolution and comparison to data. The parameters fitted are thus fixed by the fit with uncertainties attached.

In order to be able to use PDFs to model physical interactions between two protons in a collider, it is vital to be able to provide a model of parton momenta at all momentum transfers Q^2. It is not possible to determine this experimentally. Instead, the evolution of the individual parton PDFs is described by the Dokshitzer-Gribov-Lipatov-Altarelli-Parisi (DGLAP) evolution equations [57, 58, 59, 60]. These equations can also be used for the determination of PDFs described before. The DGLAP equations are derived from the requirement that physical observables, such as the outgoing momenta of interacting partons, must be independent of the choice of the unphysical scale μ_F. They allow for a PDF description of the protons at arbitrary momentum transfers and thus to also use them for simulations of proton-proton interactions.

1.2.4 Hadronisation

The composite nature of protons means that the collision of two protons is a complex process during which not only the hard scattering takes place (as discussed in the

previous sections). Figure 1.5 is a stylised overview of how different aspects of a collision of two protons are modelled.

The black incoming objects from left and right represent the two incoming protons. Two gluons in the initial state interact in the hard scattering process, which produce a number of particles in the final state, mostly gluons, quarks and anti-quarks in this case. The cross section of this process can be calculated from the Feynman diagrams of the interactions and the PDFs of the participating protons. Particles, such as quarks, anti-quarks and gluons in the final state, radiate off gluons in a subsequent parton shower. The momentum of these radiated particles is smaller than the momentum of the final state particles. This process continues until the momentum is too small to apply perturbation theory and in the hadronisation quarks, anti-quarks and gluons form hadrons due to the confinement principle. These hadrons finally decay into stable particles which can be detected in an experiment such as ATLAS. Within such an experimental context "stable" refers to particles long-lived enough to pass into or through the detector. For example, muons or anti-muons are considered stable in this context even though they are short-lived. Finally, it is important to model another aspect of the proton-proton collision, which is the underlying event and represents interactions of the proton remnants. This process occurs simultaneously to the hard scattering and the subsequent steps and also follows through to a hadronisation and decaying step. This process is modelled to be mostly dominated by QCD interactions and not to contain additional hard scatterings. Experimentally, this results in a challenge to separate decay products of these interactions from products of the hard scattering of interest. In all stages of the process, photons can be radiated off changing the measured momenta of stable particles (which can also create pairs of electrons and positrons).

1.2.5 The Drell-Yan Neutral Current Process

The Drell-Yan process [62] depicted in figure 1.6 is a central process in hadron colliders to probe the partonic substructure of protons and to study the production of Z bosons or photons, which cannot be distinguished experimentally. This results from the factorisation of the PDF and the hard scattering process. The lepton/anti-lepton pair in the final state of the reaction provides a distinct signature that experiments can search for without the added challenge of the hadronisation of strongly interacting particles in the final state.

Naturally, besides the leading order Feynman diagram in figure 1.6, higher orders in QCD and electroweak theory need to be taken into account for theoretical predictions. This poses a computational challenge due to the exponentially rising number of processes to calculate. Overall, this process is a gateway to high-precision mea-

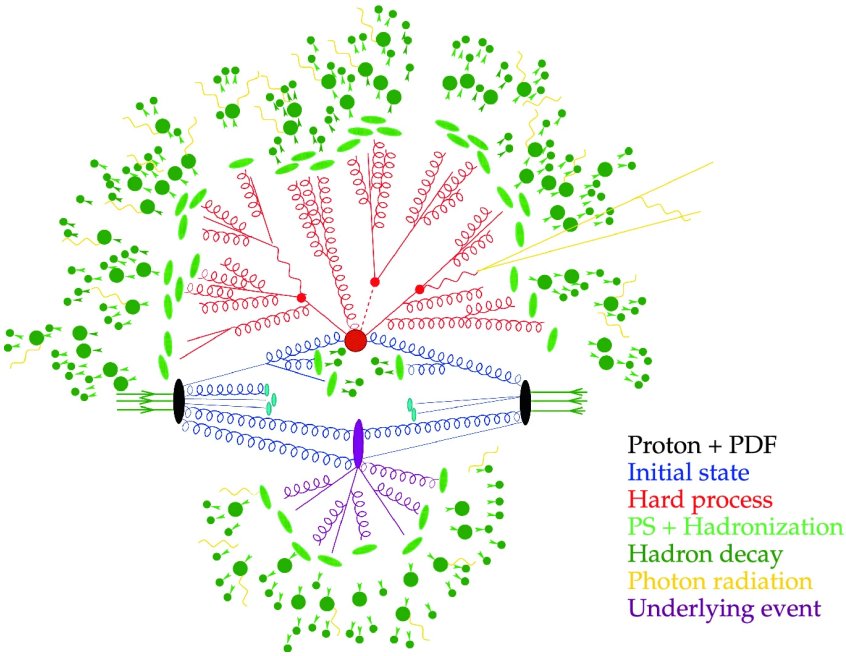


Fig. 1.5.: Schematic diagram illustrating a simplified overview of the different processes during and after a proton-proton interaction [61].

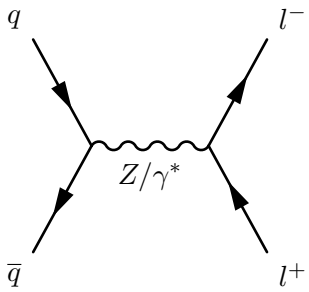


Fig. 1.6.: Leading order Drell-Yan neutral current process.

surements of QCD processes and electroweak theory and will be explored further in the following sections.

1.3 High-Precision Tests of the Standard Model

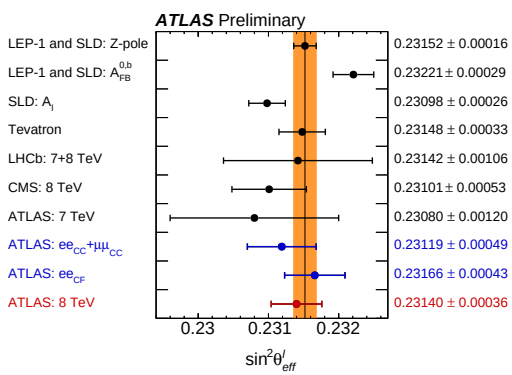
Although the Standard Model has been very successful in describing and predicting many phenomena, it currently does not describe a whole range of phenomena such as gravitation, dark matter, dark energy and massive neutrinos. This motivates highly precise measurements of Standard Model properties to challenge its predictions to a high accuracy.

1.3.1 Motivation

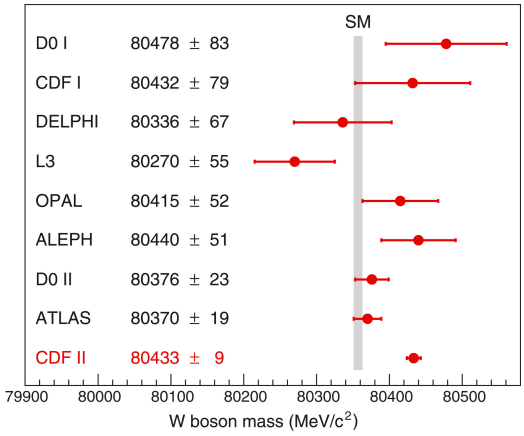
Direct searches for physics beyond the Standard Model (BSM) that focus on detecting resonances in kinematic distributions in collision experiments have been very successful for instance in the discovery[12] of the Higgs boson. However, they are oftentimes inherently limited by centre-of-mass energies, the number of recorded events and coupling strengths. Another approach to challenge the Standard Model are high-precision measurements of its parameters to search for potential deviations between predictions and measurements. Such measurements can then be used to improve the theoretical predictions or, in case measurements and theory are not compatible, indicate contributions from BSM physics processes. As such they are typically classified as *indirect searches* for physics beyond the standard model.

As mentioned in the introduction of the section, there are numerous aspects of the Standard Model where such a precision probing is crucial. This thesis focusses on two aspects that are connected in one measurement, namely predictions by perturbative Quantum Chromodynamics and electroweak theory. Perturbative QCD is an important cornerstone in particular at hadron colliders to better understand particle production processes and one of the foundations of most precision measurements at hadron colliders. Electroweak theory is a broad area of research where one of the most critical parameters is the weak mixing angle, which is directly connected not only to the masses of the $W^{\pm}$ and Z bosons but also the V-A couplings of the Z boson to fermions. Most notably, the two most precise measurements of this parameter shown in figure 1.7(a) deviate from another with a significance of approximately 3σ. Specifically, the measurement of $A_{\mathrm{FB}}^{0,b}$, which is the *forward-backward asymmetry* (see section 1.3.3.1), in unpolarised beams using the $e^+e^- \to b\bar{b}$ process at LEP 1 [6] deviates significantly from the measurement of the leptonic parity violating parameters

[12] Even though the Higgs boson was discovered in this direct way, indirect tests had constrained its mass to a specific window already before.



(a) Weak mixing angle measurements [65].



(b) W mass measurements [64].

Fig. 1.7.: Tensions of electroweak precision measurements.

A_l at SLD using polarised electron-positron beams for reactions $e^+e^- \to l^+l^-$, where $l \in \{e, \mu, \tau\}$ [63]. Consequently, a new precise measurement of this parameter is crucial to study this potential discrepancy in more detail. This is further supported by a recent measurement of the W boson mass by the CDF collaboration [64] with a tension of 7σ compared to the Standard Model expectation as shown in figure 1.7(b). As explained in section 1.25, both parameters are closely connected and due to the very precise measurement of the Z boson mass at LEP [6] they can be compared to a very high precision.

The next section will highlight a gateway to access both perturbative QCD and electroweak theory, which is a measurement of so-called *angular coefficients* of the Drell-Yan neutral current.

1.3.2 Angular Coefficients of the Drell-Yan Neutral Current

Angular distributions of charged lepton/anti-lepton pairs produced in neutral current Drell-Yan processes provide a portal to underlying QCD production processes exploiting spin correlation effects between final state leptons/anti-leptons and the initial state partons mediated by a spin-1 particle, predominantly the Z boson. The nature of this spin-1 exchange can be exploited by using spherical harmonics to decompose the cross section as will be discussed below.

1.3.2.1 Production Cross Section

Adopting a similar nomenclature as the basis used for the following discussion, i.e. the previous ATLAS analysis and Mirkes et al. [66, 67, 68], the Drell-Yan process[13] of interest can be expressed as $p_1(P_1) + p_2(P_2) \to Z(Q) + X \to l^+(L_1) + l^-(L_2) + X$, where P_i, L_i and Q are the momenta of the protons p_i, the leptons l_i and the Z boson, respectively. At leading order in the strong coupling constant α_s there are four Feynman diagrams contributing to the Z production: $q + \bar{q} \to Z$ if the Z boson does not have a transverse momentum, and $q + \bar{q} \to Z + g$, $q + g \to Z + q$ and $\bar{q} + g \to Z + \bar{q}$ if it is produced with transverse momentum[14]. In all cases it is assumed that the initial partons do not possess any transverse momenta.

At NLO in α_s there are five tree level diagrams and two loop diagrams contributing to the process. The number of Feynman diagrams at NNLO order and beyond increases dramatically with more combinatorial permutations and will not be shown here.

It is useful to exploit the so-called *Mandelstam* variables of the production process

$$\begin{aligned} s &= (P_1 + P_2)^2 \\ t &= (P_1 - Q)^2 \\ u &= (P_2 - Q)^2 \end{aligned} \tag{1.42}$$

in order to define the rapidity y_Z, the squared transverse momentum $p^2_{T,Z}$ and the squared mass m^2_Z of the Z boson as

$$\begin{aligned} y_Z &= \frac{1}{2}\ln\left(\frac{Q^2 - u}{Q^2 - t}\right) \\ p^2_{T,Z} &= \frac{(Q^2 - u)(Q^2 - t)}{s} - Q^2 \\ m^2_Z &= s. \end{aligned} \tag{1.43}$$

The hadron level cross section of the production process can then be obtained [66] by folding the parton level cross section with the respective parton densities as described in section 1.2:

$$\begin{aligned} &\frac{\mathrm{d}\sigma^{p_1 p_2}}{\mathrm{d}p^2_{T,Z}\mathrm{d}y_Z\mathrm{d}m^2_Z\mathrm{d}\Omega^*} = \\ &\sum_{a,b}\int \mathrm{d}x_1\mathrm{d}x_2 f_a^{p_1}(x_1,\mu_F^2) f_b^{p_2}(x_2,\mu_F^2)\frac{\mathrm{d}\hat{\sigma}_{ab}}{\mathrm{d}s\mathrm{d}t\mathrm{d}u\mathrm{d}\Omega^*}(x_1P_1, x_2P_2, \alpha_s(\mu_R^2)). \end{aligned} \tag{1.44}$$

[13] Since this thesis is focussed on a measurement around the Z pole mass, where the γ^* contributions are very small, further discussion also centres around the Z process.

[14] Depending on definition, this can also be classified as NLO due to the extra vertex. However, these are the lowest order diagrams contributing to non-zero transverse momenta processes.

In this equation, the sum is over all possible partons: $a, b \in q, \bar{q}, g$. The functions $f_a^{p_i}(x_i, \mu_F^2)$ denote the probability density functions for finding a parton a carrying momentum fraction x_i of the proton p_i when probed at scale μ_F^2. Finally, the parton level cross section is denoted as $\hat{\sigma}_{ab}$. Note that the strong coupling constant α_s depends on the renormalisation scale μ_R.

The differential solid angle is defined as $\mathrm{d}\Omega^* = \mathrm{d}\cos\theta_{\mathrm{CS}}\mathrm{d}\phi_{\mathrm{CS}}$ in a specific rest frame of the gauge boson, called the *Collins-Soper rest frame*.

1.3.2.2 Collins-Soper Rest Frame

A rest frame used as a cornerstone in the analysis is the so-called Collins-Soper rest frame [69]. In Z boson exchanges it is defined as the rest frame of the Z boson as depicted in figure 1.8 where figure 1.8(a) depicts a high-level view of the rest frame. The decay products, a lepton/anti-lepton l^-l^+ pair in case of this analysis, are by definition back-to-back, i.e. perfectly balanced. If the Z boson possesses a transverse momentum, the proton momenta $\vec{p}_B$ and $\vec{p}_{B'}$ are not collinear anymore and are used to define the hadron plane of the Collins-Soper frame. To construct the $\hat{z}$-axis of the frame, the angle between one of the proton momenta and the negative of the second proton momentum is bisected resulting in angle β. The sign of the $\hat{z}$-axis direction is defined by the direction of the Z boson in the laboratory frame (reconstructed by its decay products). Together with the lepton momenta the $\hat{z}$-axis forms the lepton plane. The $\hat{y}$-axis is then defined as the normal vector of the plane defined by the proton momenta, and finally the $\hat{x}$-axis is chosen to complete a right-handed Cartesian coordinate system. Note that in case of a vanishing transverse momentum of the Z boson the choice of a direction of the $\hat{y}$-axis is arbitrary.

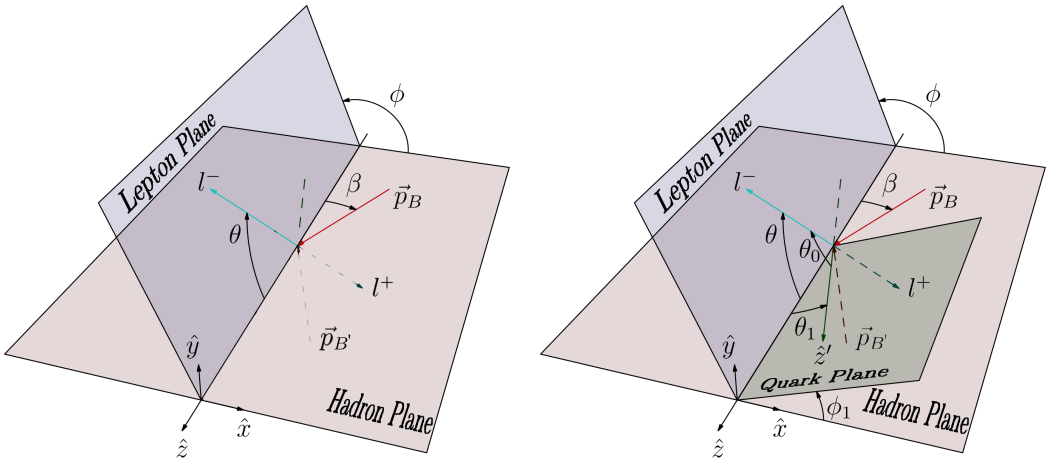
Two angles visible in figure 1.8(a) can directly be calculated from the lepton and anti-lepton momenta in the laboratory frame. The polar angle θ_{CS} is defined as the angle between the $\hat{z}$-axis and the lepton l^- momentum. It can be expressed in terms of the lepton/anti-lepton (laboratory-frame) momenta [71]:

$$\cos\theta_{\mathrm{CS}} = \frac{p_z(l^+l^-)}{|p_z(l^+l^-)|}\frac{2}{m_Z\sqrt{m_Z^2 + p_{T,Z}^2}}(P_1^+P_2^- - P_1^-P_2^+) \tag{1.45}$$

using

$$P_i^{\pm} = \frac{1}{\sqrt{2}}(E_i \pm p_{z,i}), \tag{1.46}$$

where E_i and $p_{z,i}$ are the energy and the momentum along the $\hat{z}$-axis of the lepton ($i = 1$) or anti-lepton ($i = 2$). $p_z(l^+l^-)$ represents the longitudinal momentum of the lepton/anti-lepton system, $p_{T,Z}$ the transverse momentum and m_Z the mass of the Z boson (determined from the measured l^+l^- pair).



(a) Collins-Soper frame without quark plane. **(b)** Collins-Soper frame with quark plane.

Fig. 1.8.: Schematic overview of Collins-Soper frame adapted from Peng et al. [70]. Note that angles θ and ϕ depicted here are defined as $\theta = \theta_{\mathrm{CS}}$ and $\phi = \phi_{\mathrm{CS}}$ in the text.

The azimuthal angle ϕ_{CS} is ambiguous in its definition but is chosen to follow the convention used in the previous ATLAS measurement [68]. It is chosen as the angle between the $\hat{x}$-axis and the lepton plane in $\hat{y}$ direction (i.e. the part of the lepton plane containing the lepton, rather than the anti-lepton). Conveniently, the definition of this frame only depends on the lepton/anti-lepton and the proton momenta and as such lends itself to usage in experiments where these quantities can be determined.

As the quark/anti-quark momenta do not necessarily align [70] with the proton momenta (for instance from non-zero transverse momenta within the proton), their momenta form a *quark plane* which is not identical to the hadron plane any more and is depicted in figure 1.8(b), where auxiliary angles are defined to describe this effect. Quark and anti-quark momenta are back-to-back in the Z rest frame. θ_1 describes the angle between the $\hat{z}$-axis and the newly defined $\hat{z}'$-axis, defined by the quark/anti-quark momentum unit vector. Additionally, the angle between the lepton l^- momentum and the $\hat{z}'$-axis is described by θ_0. Finally, ϕ_1 is used as a measure of the non-coplanarity of the quark-plane and the hadron plane depicted in figure 1.8(b) as it describes the angle between the quark- and the hadron-planes. These additional considerations are useful for formulating expectations and for understanding experimental observations.

1.3.2.3 Helicity Cross Sections

Mathematically the interaction $p + p \to Z + X \to l^- + l^+ + X$ is described by the contraction of the lepton tensor $L_{\mu\nu}$ with the hadron tensor $H^{\mu\nu}_{ab}$, where a, b are the

initial state partons . It is then possible to define nine helicity cross sections H_{ab}^{α} to extract the angular dependence [66]

$$\frac{1}{Q^2} L_{\mu\nu} H_{ab}^{\mu\nu} =: \sum_{\alpha \in \mathcal{M}} g_\alpha(\theta_{\mathrm{CS}}, \phi_{\mathrm{CS}}) H_{ab}^{\alpha}, \qquad \mathcal{M} := U+L, L, T, I, P, A, 7, 8, 9. \tag{1.47}$$

Here, g_α are (orthogonal) harmonic polynomials of second order, and H_{ab}^{α} are defined as linear combinations of density matrix elements

$$H_{ab}^{\sigma\sigma'} = \epsilon_\mu(\sigma) H_{ab}^{\mu\nu} \epsilon_\nu^*(\sigma'). \tag{1.48}$$

In this equation the polarisation vectors using $\sigma, \sigma' = \{0, +, -\}$ are defined as

$$\begin{aligned} \epsilon_\mu(\pm) &= \frac{1}{2}\sqrt{2}(0, \pm 1, -i, 0) \\ \epsilon_\mu(0) &= (0, 0, 0, 1). \end{aligned} \tag{1.49}$$

The angular cross section is summed over all initial states ab and can then be expressed [72, 68] as

$$\frac{\mathrm{d}\sigma}{\mathrm{d}p_{T,Z}\mathrm{d}y_Z\mathrm{d}m_Z\mathrm{d}\cos\theta_{\mathrm{CS}}\mathrm{d}\phi_{\mathrm{CS}}} = \sum_{\alpha \in \mathcal{M}} g_\alpha(\theta_{\mathrm{CS}}, \phi_{\mathrm{CS}}) \frac{3}{16\pi} \frac{\mathrm{d}\sigma^\alpha}{\mathrm{d}p_{T,Z}\mathrm{d}y_Z\mathrm{d}m_Z}, \tag{1.50}$$

where the helicity cross sections σ^α are determined by the (summed over a, b) density matrix elements $H^{\sigma\sigma'}$:

$$\begin{aligned} \sigma^{U+L} &\propto H^{00} + H^{++} + H^{--} \\ \sigma^{L} &\propto H^{00} \\ \sigma^{T} &\propto \frac{1}{2}(H^{+-} + H^{-+}) \\ \sigma^{I} &\propto \frac{1}{4}(H^{+0} + H^{0+} - H^{-0} - H^{0-}) \\ \sigma^{P} &\propto H^{++} - H^{--} \\ \sigma^{A} &\propto \frac{1}{4}(H^{+0} + H^{0+} + H^{-0} + H^{0-}) \\ \sigma^{7} &\propto \frac{-i}{2}(H^{+-} - H^{-+}) \\ \sigma^{8} &\propto \frac{-i}{4}(H^{+0} - H^{0+} + H^{-0} - H^{0-}) \\ \sigma^{9} &\propto \frac{-i}{4}(H^{+0} - H^{0+} - H^{-0} + H^{0-}) \end{aligned} \quad . \tag{1.51}$$

A total of 9 helicity cross sections (derived from 9 density matrix elements) are determined[15] and correspond to a full decomposition into 9 spherical harmonics determined by the spin-1 exchange. The unpolarised cross section is denoted as σ^{U+L}, all other cross sections describe the Z boson polarisation (in the Collins-Soper

[15] Note that the superscripts follow historical naming conventions used in literature by Mirkes et al. [66, 67].

rest frame). Specifically, σ^L denotes the longitudinal, σ^T the transverse and σ^I the transverse-longitudinal interference cross-section. Together with σ^9 these cross sections individually are proportional to the parity-conserving part of the hadron tensor, while $\sigma^{P,A,7,8}$ are proportional to the parity violating part [66].

Factorising out the unpolarised cross section σ^{U+L}, the cross section in equation 1.50 can be written as a sum of dimensionless angular coefficients A_{0-7} multiplied by polynomials P_i of $\cos\theta_{\mathrm{CS}}$ and ϕ_{CS}. The coefficients are defined as the ratio of the polarised cross sections to the unpolarised one:

$$\begin{aligned} A_0 &= \frac{2\mathrm{d}\sigma^L}{\mathrm{d}\sigma^{U+L}} & A_4 &= \frac{2\mathrm{d}\sigma^P}{\mathrm{d}\sigma^{U+L}} \\ A_1 &= \frac{2\sqrt{2}\mathrm{d}\sigma^I}{\mathrm{d}\sigma^{U+L}} & A_5 &= \frac{2\mathrm{d}\sigma^7}{\mathrm{d}\sigma^{U+L}} \\ A_2 &= \frac{4\mathrm{d}\sigma^T}{\mathrm{d}\sigma^{U+L}} & A_6 &= \frac{2\sqrt{2}\mathrm{d}\sigma^8}{\mathrm{d}\sigma^{U+L}} \\ A_3 &= \frac{4\sqrt{2}\mathrm{d}\sigma^A}{\mathrm{d}\sigma^{U+L}} & A_7 &= \frac{4\sqrt{2}\mathrm{d}\sigma^9}{\mathrm{d}\sigma^{U+L}} \end{aligned} . \tag{1.52}$$

Finally, the angular cross section can be expressed as

$$\frac{\mathrm{d}^5\sigma}{\mathrm{d}p_{T,Z}\mathrm{d}y_Z\mathrm{d}m_Z\mathrm{d}\cos\theta_{\mathrm{CS}}\mathrm{d}\phi_{\mathrm{CS}}} = \frac{3}{16\pi}\frac{\mathrm{d}\sigma^{U+L}}{\mathrm{d}p_{T,Z}\mathrm{d}y_Z\mathrm{d}m_Z}\left[\begin{array}{l} (1+\cos^2\theta_{\mathrm{CS}}) \\ + A_0\frac{1}{2}(1-3\cos^2\theta_{\mathrm{CS}}) \\ + A_1\sin 2\theta_{\mathrm{CS}}\cos\phi_{\mathrm{CS}} \\ + A_2\frac{1}{2}\sin^2\theta_{\mathrm{CS}}\cos 2\phi_{\mathrm{CS}} \\ + A_3\sin\theta_{\mathrm{CS}}\cos\phi_{\mathrm{CS}} \\ + A_4\cos\theta_{\mathrm{CS}} \\ + A_5\sin^2\theta_{\mathrm{CS}}\sin 2\phi_{\mathrm{CS}} \\ + A_6\sin 2\theta_{\mathrm{CS}}\sin\phi_{\mathrm{CS}} \\ + A_7\sin\theta_{\mathrm{CS}}\sin\phi_{\mathrm{CS}} \end{array}\right] . \tag{1.53}$$

In this equation the explicit dependence of the angular coefficients on $p_{T,Z}$, y_Z and m_Z is dropped for better readability. Crucially, this is a factorisation of the QCD production processes and the decay of the Z boson. The angular coefficients together with the unpolarised cross section completely describe the Z boson production and are thus of interest to probe experimentally for precision tests of calculations of perturbative QCD. The polynomials P_i, where $i = \{0, ..., 8\}$, in $\cos\theta_{\mathrm{CS}}$ and ϕ_{CS} fully contain the decay kinematics of the lepton/anti-lepton pair in full phase space. Importantly, some of the coefficients, A_3, A_4 and A_7, are closely connected to the effective weak mixing angle. This is explained in detail in section 1.3.3.

Before discussing the shape of the coefficients, it is useful to express the cross section in terms of the auxiliary angles in the Collins-Soper frame introduced in section 1.3.2.2. Following calculations from Peng et al. [70] the cross section can be expressed in terms of the angles defined before as well as a forward-backward asymmetry coefficient a which originates from the parity violating coupling of the leptons to the Z boson

$$\begin{aligned}\frac{\mathrm{d}^5\sigma}{\mathrm{d}p_{T,Z}\mathrm{d}y_Z\mathrm{d}m_Z\mathrm{d}\cos\theta_{\mathrm{CS}}\mathrm{d}\phi_{\mathrm{CS}}} \propto & (1+\cos^2\theta_{\mathrm{CS}}) \\ & + \frac{\sin^2\theta_1}{2}(1-3\cos^2\theta_{\mathrm{CS}}) \\ & + (\frac{1}{2}\sin 2\theta_1\cos\phi_1)\sin 2\theta_{\mathrm{CS}}\cos\phi_{\mathrm{CS}} \\ & + (\frac{1}{2}\sin^2\theta_1\cos 2\phi_1)\sin^2\theta_{\mathrm{CS}}\cos 2\phi_{\mathrm{CS}} \\ & + (a\sin\theta_1\cos\phi_1)\sin\theta_{\mathrm{CS}}\cos\phi_{\mathrm{CS}} \\ & + (a\cos\theta_1)\cos\theta_{\mathrm{CS}} \\ & + (\frac{1}{2}\sin^2\theta_1\sin 2\phi_1)\sin^2\theta_{\mathrm{CS}}\sin 2\phi_{\mathrm{CS}} \\ & + (\frac{1}{2}\sin 2\theta_1\sin\phi_1)\sin 2\theta_{\mathrm{CS}}\sin\phi_{\mathrm{CS}} \\ & + (a\sin\theta_1\sin\phi_1)\sin\theta_{\mathrm{CS}}\sin\phi_{\mathrm{CS}}.\end{aligned} \tag{1.54}$$

This alternate way of expressing the cross section is useful in order to formulate expectations about the kinematic shape of the angular coefficients and to highlight the connection of some of the coefficients to the forward-backward asymmetry.

1.3.2.4 Predictions

Having established the significance of the angular coefficients introduced in equation 1.53 it is useful to highlight how they can be calculated from observables used in experiments. The coefficients are not explicitly used in theoretical predictions or in Monte Carlo event generators (which will be discussed in section 3), but can be determined in such simulations from the two angular distributions following a procedure suggested by Mirkes et al. [67], called *moments method*. Conceptually, the average value of angular coefficients in a particular section of phase space (i.e. $m_Z \in [m_{\mathrm{low}}, m_{\mathrm{high}}]$, $p_{T,Z} \in [p_{T,\mathrm{low}}, p_{T,\mathrm{high}}]$ and $y_Z \in [y_{\mathrm{low}}, y_{\mathrm{high}}]$) are determined by calculating the moment of a polynomial $P_i(\cos\theta_{\mathrm{CS}}, \phi_{\mathrm{CS}})$ due to the orthogonality of the polynomials:

$$\langle P_i(\cos\theta_{\mathrm{CS}}, \phi_{\mathrm{CS}})\rangle = \frac{\int P_i(\cos\theta_{\mathrm{CS}}, \phi_{\mathrm{CS}})\mathrm{d}\sigma(\cos\theta_{\mathrm{CS}}, \phi_{\mathrm{CS}})\mathrm{d}\cos\theta_{\mathrm{CS}}\mathrm{d}\phi_{\mathrm{CS}}}{\int \mathrm{d}\sigma(\cos\theta_{\mathrm{CS}}, \phi_{\mathrm{CS}})\mathrm{d}\cos\theta_{\mathrm{CS}}\mathrm{d}\phi_{\mathrm{CS}}}. \tag{1.55}$$

This method allows to extract all reference coefficients and is only limited by the statistical accuracy of the simulation used. It is also important in the measurement of the coefficients in data, where the dependence of the simulation on the coefficients is removed, as will be discussed in chapter 6. The moments method cannot be applied to data directly since an integration over full phase space is required. Using this method both on the angular cross section in equation 1.53 and on the re-written cross section in equation 1.54, the coefficients are found [72, 70] to be

$$
\begin{aligned}
A_0 &= \langle 4 - 10\cos^2\theta_{\mathrm{CS}}\rangle = \langle \sin^2\theta_1\rangle \\
A_1 &= \langle 5\sin 2\theta_{\mathrm{CS}}\cos\phi_{\mathrm{CS}}\rangle = \langle \frac{1}{2}\sin 2\theta_1\cos\phi_1\rangle \\
A_2 &= \langle 10\sin^2\theta_{\mathrm{CS}}\cos 2\phi_{\mathrm{CS}}\rangle = \langle \sin^2\theta_1\cos 2\phi_1\rangle \\
A_3 &= \langle 4\sin\theta_{\mathrm{CS}}\cos\phi_{\mathrm{CS}}\rangle = a\langle \sin\theta_1\cos\phi_1\rangle \\
A_4 &= \langle \cos\theta_{\mathrm{CS}}\rangle = a\langle \cos\theta_1\rangle \\
A_5 &= \langle \sin^2\theta_{\mathrm{CS}}\sin 2\phi_{\mathrm{CS}}\rangle = \langle \frac{1}{2}\sin^2\theta_1\sin 2\phi_1\rangle \\
A_6 &= \langle \sin 2\theta_{\mathrm{CS}}\sin\phi_{\mathrm{CS}}\rangle = \langle \frac{1}{2}\sin 2\theta_1\sin\phi_1\rangle \\
A_7 &= \langle 4\sin\theta_{\mathrm{CS}}\sin\phi_{\mathrm{CS}}\rangle = a\langle \sin\theta_1\sin\phi_1\rangle .
\end{aligned}
\tag{1.56}
$$

The shape of predicted angular coefficients depends on the precision of the calculation in QCD. This is illustrated in figure 1.9, where NLO calculations are contrasted with NNLO calculations in QCD. Additionally, the figure depicts how the coefficients depend on the centre-of-mass energy of the protons. Note that only uncertainties from statistical limitations of the simulation used are shown. The coefficients are drawn as a function of the transverse momentum of the Z boson considering a mass range of $80\,\mathrm{GeV} < m_Z < 100\,\mathrm{GeV}$ and a rapidity range of $-6 < y_Z < 6$ (where the bulk of the Drell-Yan production occurs at the LHC). The overall energy scale is thus mostly defined by the mass range. The shape of A_0 approaches 0 at low transverse momentum $p_{T,Z}$ and increases at higher transverse momentum. Approaching $p_{T,Z} \approx 0$ means that no contributions arise from the misalignment of the quark-plane and the hadron plane which contributes more significantly at higher $p_{T,Z}$ (for instance due to non-zero transverse momenta in the initial state). In case of a perfect alignment of quark and hadron momenta A_0 is expected to be 0, thus it is an indicator of this misalignment [70]. For A_0 and A_2 the so-called *Lam-Tung relation* [73, 74] $A_0 - A_2 = 0$ is expected to hold until NLO in QCD and to be broken at NNLO and beyond which can be seen in the A_2 distribution. The coefficient A_2 is sensitive not only to the misalignment of quark and hadron momenta but also to the non-coplanarity (i.e. the dependence on ϕ_1) of their respective planes, which is why $A_2 \leq A_0$. This non-coplanarity affects all other coefficients as well, leading to generally increasing coefficients towards higher transverse momenta with the

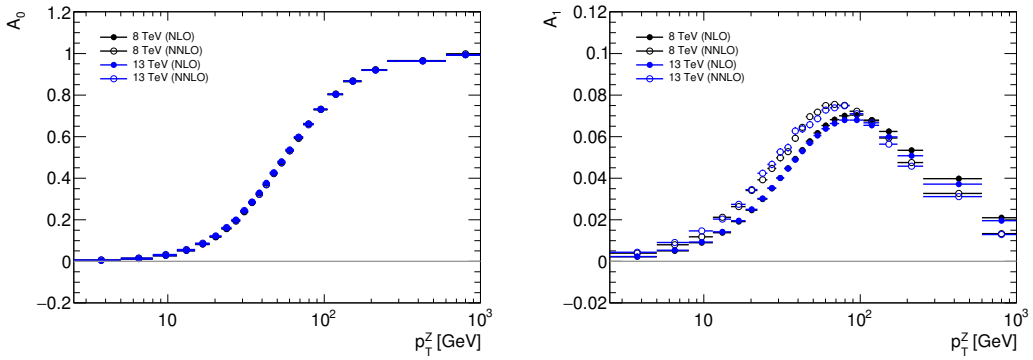
exception of A_4. The latter exhibits its parity violating coupling to the Z boson, which becomes diluted towards higher transverse momenta due to the misalignment of the quark/anti-quark and proton momenta [70]. Furthermore, coefficients A_5 to A_7 become non-zero only at NNLO in QCD or beyond as they carry information on higher-order effects. This is also visible in figure 1.9 where statistical and modelling effects from the simulation in fact lead to a slight deviation from zero in these coefficients already at NLO.

Finally, the difference in centre-of-mass energies $\sqrt{s} = 8\,\text{TeV}$ and $\sqrt{s} = 13\,\text{TeV}$, in particular in A_3 and A_4 shows that higher centre-of-mass energies lead to lower absolute values of these coefficients, which results from the *dilution* that is caused by the ambiguity in proton collisions on the direction of the quark and the anti-quark. This effect is enhanced by the higher collision energy as quark and anti-quark momenta statistically increase, thus statistically reducing the difference in momentum fractions carried, further contributing to this ambiguity as has been illustrated in figure 1.4. This effect can be partially mitigated by restricting the phase space to high absolute values of the rapidity as will be shown in chapter 6.

The strategy to determine these coefficients precisely is to perform a measurement of the Collins-Soper distributions $\cos\theta_{\text{CS}}$ and ϕ_{CS} in order to access the angular coefficients via the moments method. Unfolding these to full phase space (i.e. removing experimental effects) allows for a precise comparison of the data to expectations and thus directly enables a test of perturbative QCD predictions. This measurement will be shown in chapter 6.

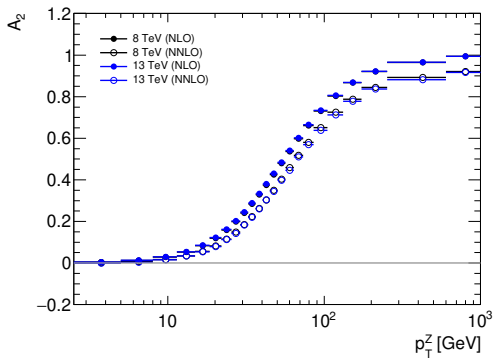
1.3.2.5 Current Measurements

There have been numerous measurements of angular coefficients of the Z boson in the past, typically focussing on a subset of parameters. The NA10 experiment has first studied A_0 and A_2 [77, 78]. The E615 collaboration first observed the violation of the Lam-Tung relation [79, 80] at the Tevatron. The advantage of a proton-anti-proton collider in measuring angular coefficients is the drastic reduction in dilution effects as statistically the quark will originate in the proton, while the anti-quark will originate in the anti-proton. The CMS collaboration has studied the coefficients A_0 to A_4 for the first time at the LHC at $\sqrt{s} = 8\,\text{TeV}$ [81], using muon/anti-muon pairs. This was followed by the first measurement of the full set of all angular coefficients at the same centre-of-mass energy by the ATLAS collaboration [68], using electron/anti-electron pairs as well as muon/anti-muon pairs. Finally, the most recent measurement has been performed by the LHCb collaboration, focussing on the A_0 to A_4 coefficients and using muon/anti-muon pairs at $\sqrt{s} = 13\,\text{TeV}$ in the forward rapidity region [82]. The full set of angular coefficients at $\sqrt{s} = 13\,\text{TeV}$

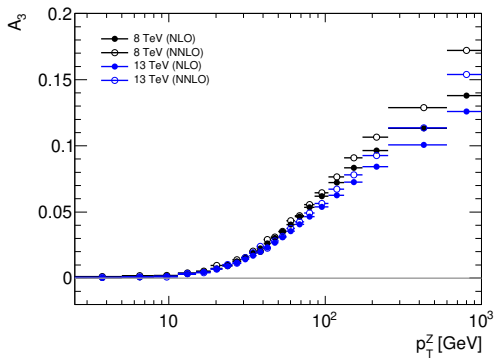


(a) A_0.

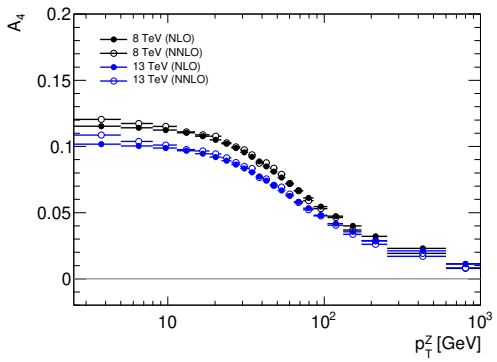
(b) A_1.



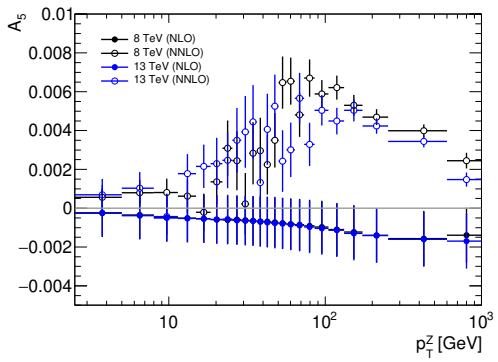
(c) A_2.



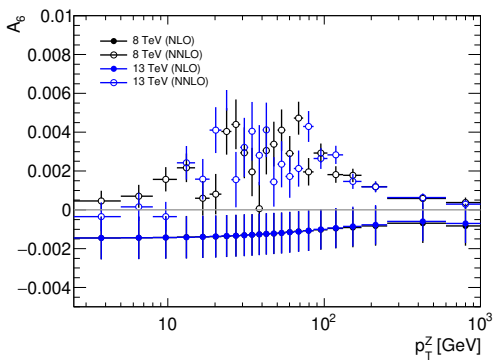
(d) A_3.



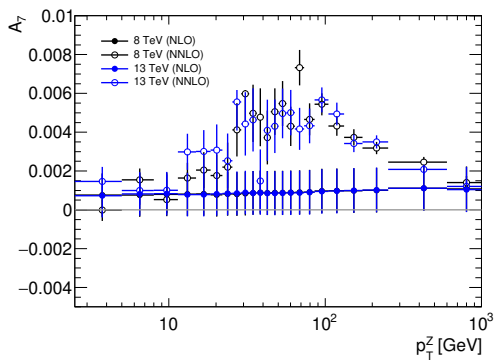
(e) A_4.



(f) A_5.

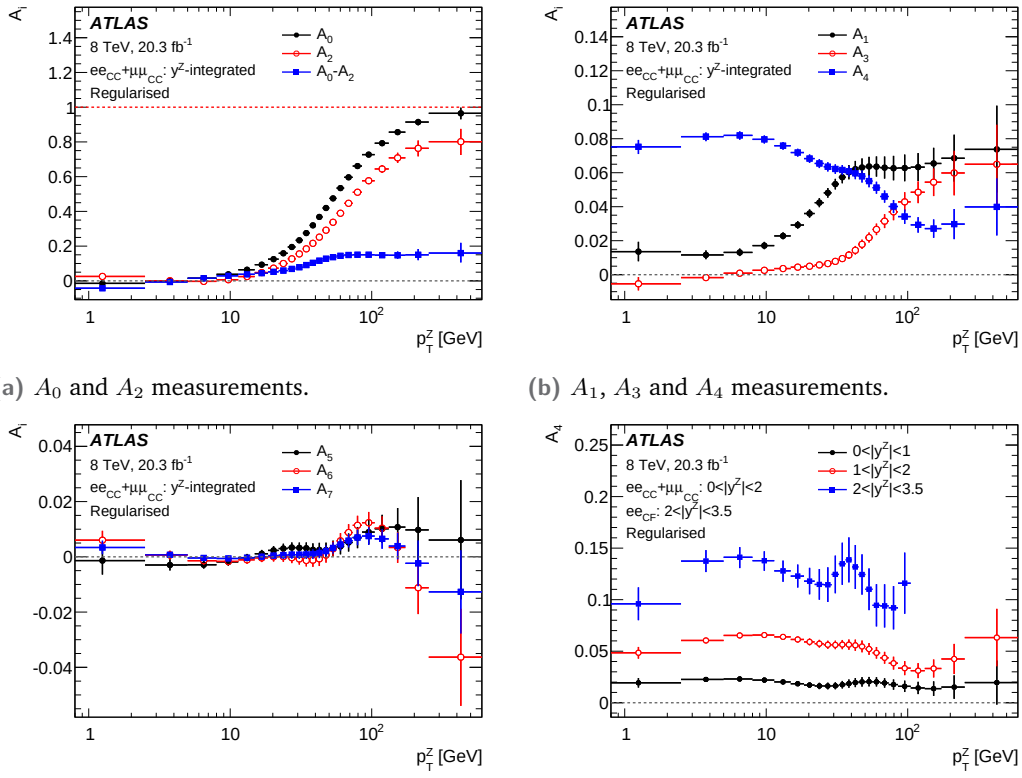


(g) A_6.



(h) A_7.

Fig. 1.9.: Predictions of all angular coefficients at NLO and NNLO compared between centre-of-mass energies of $8\,\text{TeV}$ and $13\,\text{TeV}$ provided by A. Vallier [75], using DYTURBO [76] and the CT14NNLO PDF set with electroweak input parameters $G_F = 1.166\,378\,7 \times 10^{-5}\,\text{GeV}^{-2}$, $M_Z = 91.1876\,\text{GeV}$ and $M_W = 80.379\,\text{GeV}$. Only statistical uncertainties of the simulation are shown.



(a) A_0 and A_2 measurements.

(b) A_1, A_3 and A_4 measurements.

(c) A_5,A_6 and A_7 measurements.

(d) Rapidity differential A_4 measurements.

Fig. 1.10.: Measurements of angular coefficients by the ATLAS collaboration at $\sqrt{s} = 8\,\text{TeV}$ [65].

has not been measured yet. As the previous ATLAS measurement has been the most comprehensive so far and closest to the measurement presented in this thesis, figure 1.10 highlights some of the measured distributions. Note that the coefficients depicted in data have been regularised, i.e. bin-to-bin correlations and fluctuations have been smoothed to give more insight into the shapes of the coefficients. As discussed before, the violation of the Lam-Tung relation can clearly be seen in the ATLAS data in figure 1.10(a). Furthermore, evidence for non-zero coefficients A_5, A_6 and A_7 has been observed as depicted in figure 1.10(c). The A_4 coefficient being non-zero at low transverse momentum is visible in the rapidity-integrated measurement in figure 1.10(b) together with the inversely behaving coefficients A_1 and A_3, which have been found to change with the rapidity. The same effect is observed in A_4 in figure 1.10(d), which shows the increase in dilution towards more centralised topologies (i.e. lower rapidity). This coefficient is particularly sensitive to the weak mixing angle as will be discussed in the following section.

1.3.3 The Weak Mixing Angle

One of the central parameters of electroweak theory is the *weak mixing angle*, which connects numerous quantities together and is thus particularly interesting for precision tests of the Standard Model.

As the broader context of electroweak theory has been set in chapter 1.1.2.4, this section is used to highlight its relevance as a quantity that is directly connected to many other parameters of the Standard Model, most of which are not predicted by the model but need to be measured. The weak mixing angle θ_W thus plays a crucial role in consistency tests of Standard Model measurements. This non-exhaustive discussion is based on the Review of Particle Physics [14].

One central role of the weak mixing angle is in the masses in electroweak theory, which arise from the coupling to the Higgs field. In case of the mass M_W of the W bosons at leading order this is

$$M_W = \frac{ev}{2\sin\theta_W}, \tag{1.57}$$

where e is the electric charge and $v \approx 246\,\mathrm{GeV}$ the vacuum expectation value of the Higgs field introduced in section 1.1.2.4. The masses of the two massive electroweak bosons are connected as

$$M_Z = \frac{M_W}{\cos\theta_W}, \tag{1.58}$$

where M_Z is the mass of the Z boson and has been measured at LEP 1 to a high precision $M_Z = (91.1875 \pm 0.0021)\,\mathrm{GeV}$ [6], while the mass of the W bosons is currently scrutinised to a high degree due to the deviation observed by the CDF collaboration as shown in figure 1.7(b). This demonstrates that the weak mixing angle plays a crucial role in a better understanding of this significant deviation of the W mass from the expectation.

Generally, the weak mixing angle can also be defined in different schemes which differ slightly depending on which parameter values are used for the calculation. In fact, both the weak mixing angle $\sin^2\theta_W$ and the mass of the W boson m_W, can be calculated from other electroweak parameters: the Z boson mass M_Z, the fine structure constant $\alpha_{\text{e.m.}}$, the masses of the Top quark m_t and the Higgs boson m_H and the Fermi constant G_F. Throughout this thesis, the discussion will focus on the *effective leptonic weak mixing angle* $\sin^2\theta^l_{\text{eff}}$ which is connected to the weak mixing angle in the $\overline{MS}$ scheme. The effective leptonic weak mixing angle at the Z pole mass is defined as

$$\sin^2\theta^l_{\text{eff}} = \kappa_l \sin^2\theta_W. \tag{1.59}$$

The factor κ_l is an effective scaling factor that includes higher order electroweak radiative corrections. Note that $\sin^2\theta^l_{\text{eff}}$ also depends on the scale μ at which it is probed, where $\mu = \sqrt{|q^2|}$ [83] and q^2 is the momentum transfer. This means that $\sin^2\theta^l_{\text{eff}}(\mu)$ needs to be measured at different scales which are briefly discussed in section 1.3.3.2. However, for the purpose of this thesis the discussion and the sensitivity study focus on the effective leptonic weak mixing angle at the Z pole mass $\sin^2\theta^l_{\text{eff}} = \sin^2\theta^l_{\text{eff}}(M_Z)$.

The effective weak mixing angle is sensitive to the V-A coupling nature of the Z boson [65]

$$\sin^2\theta^l_{\text{eff}} = \frac{1}{4}(1 - \frac{v_l}{a_l}), \tag{1.60}$$

where v_l and a_l are the vector and axial vector couplings to leptons, respectively. There are multiple gateways to measure the weak mixing angle. This is crucial to test its consistency in multiple contexts of the Standard Model. This thesis focusses on an extraction from the angular coefficients, one of which is closely related to the forward-backward asymmetry discussed in the next section. The focus of this discussion is on the effective leptonic aspect of the weak mixing angle as the asymmetry is only probed in leptonic decays of the Z/γ^* bosons.

1.3.3.1 Forward-Backward Asymmetry

Studying the decomposition of the Drell-Yan cross section in equation 1.53 at leading order in QCD, most terms vanish so that only

$$\frac{\mathrm{d}^5\sigma}{\mathrm{d}p_{T,Z}\mathrm{d}y_Z\mathrm{d}m_Z\mathrm{d}\cos\theta_{\text{CS}}\mathrm{d}\phi_{\text{CS}}} \propto 1 + \cos^2\theta_{\text{CS}} + A_4\cos\theta_{\text{CS}} \tag{1.61}$$

remains. The $1 + \cos^2\theta_{\text{CS}}$ term originates from the spin-1 nature of the exchanged boson, while the $A_4\cos\theta_{\text{CS}}$ term arises from interference effects between vector and axial vector couplings [84]. This effect can be seen in the simulation shown in figure 1.11, where A_4 is calculated for Z boson production only and for Z/γ^* interference for different invariant masses of the final state lepton/anti-lepton pair. The latter clearly shows the arising asymmetry once the interference is taken into account.

This asymmetry is commonly studied as the *forward-backward asymmetry* A_{FB}, which is closely connected to A_4 as

$$A_{\text{FB}} = \frac{3}{8}A_4 = \frac{N_{\text{F}} - N_{\text{B}}}{N_{\text{F}} + N_{\text{B}}} \tag{1.62}$$

where N_{F} is the number of forward decays, i.e. $\cos\theta_{\text{CS}} > 0$ and N_{B} the number of backward decays, i.e. $\cos\theta_{\text{CS}} < 0$ [85].

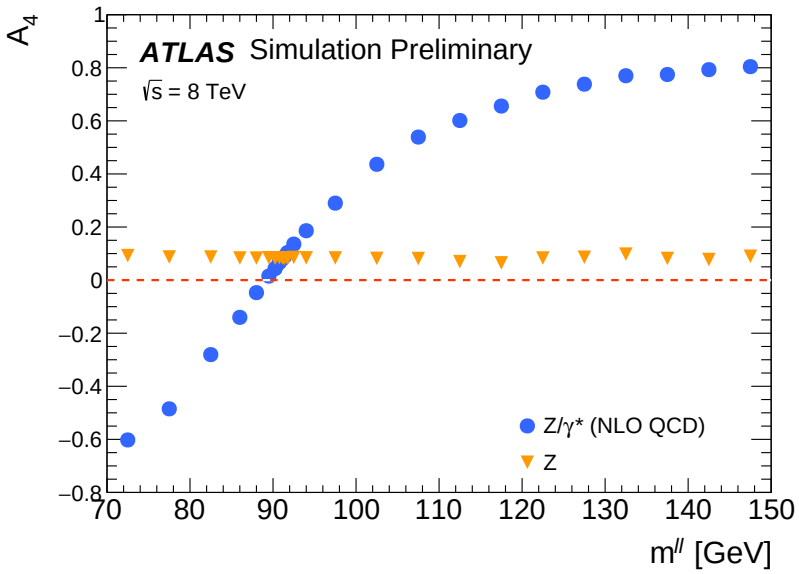


Fig. 1.11.: Simulated A_4 as function of the dilepton mass with and without Z/γ^* interference [65].

A_{FB} can also be computed from the fine structure constant $\alpha_{\mathrm{e.m.}}$, the Fermi constant G_F and the Z boson mass M_Z and decay width Γ_Z as well as the vector v and axial vector a couplings to leptons l and quarks q [84]:

$$A_{\mathrm{FB}} = \frac{6a_l a_q(8v_l v_q - k)}{16(v_l^2 + a_l^2)(v_q^2 + a_q^2) - 8v_l v_q k + k'}, \tag{1.63}$$

where k and k' are constants depending on the aforementioned constants and the invariant mass of the lepton/anti-lepton pair. Considering equation 1.60 together with equation 1.63, A_{FB} is found to be linearly correlated to the effective weak mixing angle[16].

Lastly, the alternative decomposition of the cross section shown in equation 1.54 together with the predicted values in equation 1.56 highlights that not only A_4 is connected to the forward-backward asymmetry (indicated by the asymmetry coefficient a) but also A_3 and A_7. However, for practical purposes it is useful to focus on A_4 because A_3 only becomes non-zero at high transverse momentum and A_7 is close to zero in all regions. Thus by far the highest sensitivity is achieved by exploiting A_4, which will be the focus of the study presented in section 8.

[16]This is under the assumption that the invariant mass of the lepton/anti-lepton in the final state are at the Z boson pole mass.

1.3.3.2 Current Measurements

As already indicated in section 1.3.1 and highlighted in figure 1.7(a), currently there are significant tensions between the two most precise measurements of the weak mixing angle (and consequently the effective weak mixing angle) at a significance of about 3σ [6].

Since this is unexpected, it is crucial to continue to study this parameter as precisely as possible to shed light onto the reason for this disagreement, which could be caused by physics beyond the Standard Model. Some of the most precise measurements to date shown in 1.7(a) are the combination from LEP experiments in $e^+e^- \to b\bar{b}$ resulting in $\sin^2\theta^l_{\text{eff}} = 0.23221 \pm 0.00029$ [6], while polarisation asymmetry measurements probing the left-right asymmetry A^0_{LR} (which is identical to A_{PV} in equation 1.64 at the Z pole mass) at SLC in $e^+e^- \to l^+l^-$, where $l \in \{e, \mu, \tau\}$, found $\sin^2\theta^l_{\text{eff}} = 0.23098 \pm 0.00026$ [6] and the Tevatron combination (in proton-anti-proton collisions) resulted in $\sin^2\theta^l_{\text{eff}} = 0.23148 \pm 0.00033$ [86]. One finds that the first two measurements are most precise, but they exhibit some statistical tension of 3σ. As the methods used to extract these results differ, it is vital to clarify if this deviation is a statistical effect only or whether it is statistically significant and thus hints at physics beyond the Standard Model.

So overall, this motivates additional experimental efforts to maximise sensitivity of a measurement of the weak mixing angle. A study of the expected sensitivity of such a measurement at ATLAS is presented in chapter 8 where the overall strategy is based on a linear parametrisation of the A_4 coefficient to extract $\sin^2\theta^l_{\text{eff}}$ from fitting the angular coefficients. Generally, measurements of the weak mixing angle in proton-proton collisions suffer more from dilution effects than measurements for instance at the Tevatron in proton-anti-proton collisions. However, as the study indicates a competitive sensitivity can still be achieved.

Beyond measurements at the Z boson pole mass, additional experimental efforts are ongoing to probe the running of the weak mixing angle studied by Erler et al. [83]. This is depicted in figure 1.12, where measurements discussed so far are clustered around the Z boson pole mass. Numerous experimental methods have been used for these measurements to establish the running of the weak mixing angle, such as atomic parity violation in Caesium [88], parity violating electron-electron [89] and electron-proton [90] scattering as well as deep inelastic scattering [91] and neutrino-nucleon scattering [92]. Additional experimental efforts beyond the Z pole mass intend to utilise Møller [93] and deep inelastic scattering [94]. In Mainz the prospective P2 experiment [95] aims for a precision measurement [87]

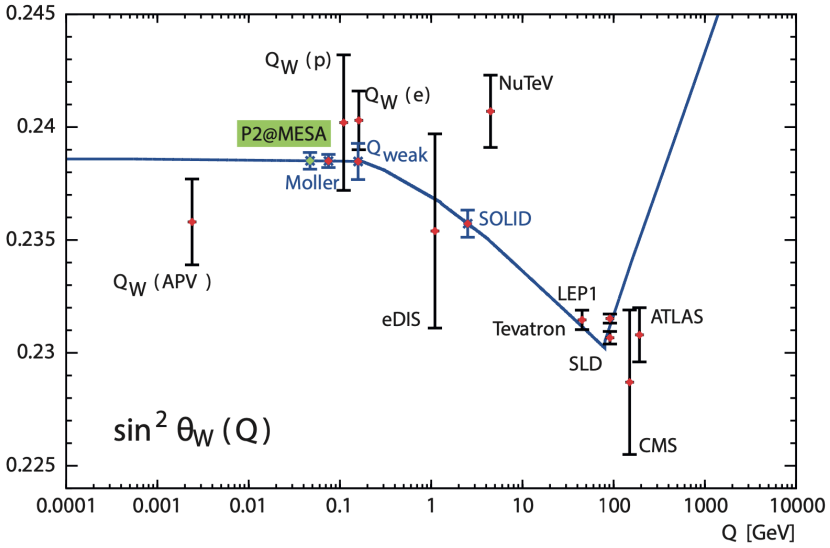


Fig. 1.12.: Scale dependence of the weak mixing angle illustrated [87] with completed measurements in black, prospective measurements in blue (centred on the theory prediction) and the theory prediction in dark blue.

using parity violating electron-proton scattering and left-handed and right-handed polarised electrons to determine the asymmetry

$$A_{\mathrm{PV}} = \frac{\sigma_{\mathrm{L}} - \sigma_{\mathrm{R}}}{\sigma_{\mathrm{L}} + \sigma_{\mathrm{R}}}, \tag{1.64}$$

where σ_{L} and σ_{R} are the left-handed and right-handed cross sections, respectively.

To summarise, a large number of experiments, such as ATLAS, aim to precisely probe the weak mixing angle at different scales to clarify deviations observed in the past and to continue to push the sensitivity ever lower for high-precision tests of the Standard Model.

2 Experimental Setup

> *We should remember that good fortune often happens when opportunity meets with preparation.*
>
> **— Thomas Edison**

The data that is analysed in this thesis was captured by the *ATLAS*[1] [96] experiment at the *Large Hadron Collider* (LHC) at CERN[2] in Geneva. This chapter will outline the experimental setup to provide the necessary context of the analysis. As a general-purpose detector ATLAS allows for a broad range of analyses, from direct searches to precision measurements. The setup described corresponds to the so-called *Run 2* of the LHC and its experiments, which entailed data taking periods between 2015 and 2018. The proton-proton collisions of interest occurred at a centre-of-mass energy of $\sqrt{s} = 13\,\mathrm{TeV}$. At the time of writing this thesis numerous upgrade projects both at the LHC as well as at ATLAS are being prepared for the currently ongoing *Run 3* at $13.6\,\mathrm{TeV}$ and for the High-Luminosity LHC (HL-LHC) near the end of the decade. The latter will be discussed in more detail in chapter 11.

2.1 The Large Hadron Collider

The LHC [97] at CERN is the largest and most powerful hadron collider ever constructed to date. It is part of a vast accelerator complex and a diverse experimental programme as the schematic overview in figure 2.1 indicates. It is constructed approximately $100\,\mathrm{m}$ underground with a circumference of approximately $27\,\mathrm{km}$.

Since the data in this thesis was taken from proton-proton collisions during the data taking period of 2015 to 2018 only, the following description of the different stages of acceleration focusses on protons only as for heavy ions the steps of acceleration differ slightly. In addition, changes to the accelerator complex and the ATLAS detector after 2018 are not discussed in this chapter. In order to reach energies of $6.5\,\mathrm{TeV}$, each proton beam passes through a total of five accelerator stages. A bottle of hydrogen serves as the source for protons by stripping the atoms from electrons with an electric field. The *Linear Accelerator 2* (LINAC2) serves as the first stage

[1] A ToroidaL ApparatuS
[2] Conseil européen pour la recherche nucléaire

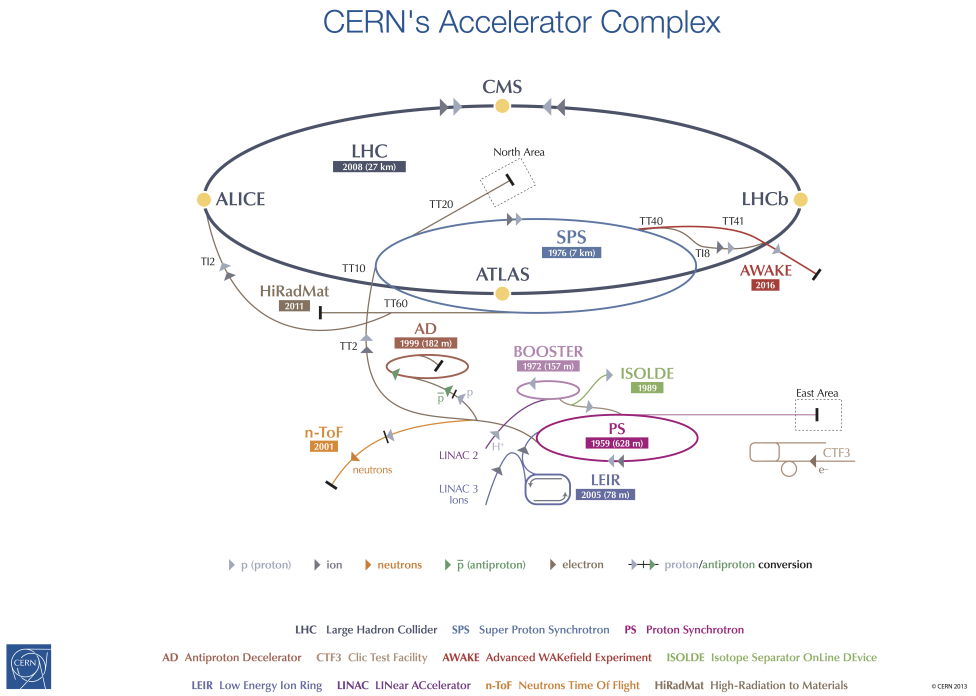


Fig. 2.1.: Overview of the accelerator complex at CERN, focussed on the Large Hadron Collider and its different stages [99].

of their acceleration up to $50\,\mathrm{MeV}$ and feeds into the *Proton Booster* (BOOSTER) synchrotron, where the energy of the protons is increased to $1.4\,\mathrm{GeV}$ for the injection to the *Proton Synchrotron* (PS). During this stage protons reach an energy of $26\,\mathrm{GeV}$ before they enter the *Super Proton Synchrotron* (SPS) where they are accelerated up to $450\,\mathrm{GeV}$. At last two opposing beams are accelerated in the LHC to reach $6500\,\mathrm{GeV}$ per beam.

The LHC finally delivers two opposing beams of proton bunches which are spaced approximately $25\,\mathrm{ns}$ apart. Bunches contain about 1.2×10^{11} protons so that bunch crossings in ATLAS at $40\,\mathrm{MHz}$ with approx. 40 collisions per crossing on average[3] result in more than 1 billion collisions per second, with a peak instantaneous luminosity of up to $L = 21.0 \times 10^{33}\,\mathrm{cm}^{-1}\,\mathrm{s}^{-2}$ [98].

In order to be able to achieve these conditions and to steer proton beams, the LHC uses 1232 [100] superconducting dipole magnets with a magnetic field strength of more than $8\,\mathrm{T}$. They are cooled by superfluid liquid helium at a temperature of $1.7\,\mathrm{K}$. The total number of magnets amounts to 9593, which includes quadrupoles and other types. Overall, a combination of sophisticated systems, such as the magnets, but also beam monitoring devices work together to enable a smooth operation of the

[3] Also called *pileup*.

Parameter	Design	Run 1	Run 2
Energy [TeV]	14	7/8	13
Bunch spacing [ns]	25	50	25
Bunch intensity [10^{11} protons per bunch]	1.15	1.6	1.2
Number of bunches (n_b)	2800	1400	2500
Emittance ϵ [μm]	3.5	2.2	2.2
Amplitude function β^* [cm]	55	80	30 to 25
Crossing angle [μrad]	285	240 to 290	300 to 260
Peak luminosity [$10 \times 10^{34}\,\mathrm{cm}^{-2}\,\mathrm{s}^{-1}$]	1.0	0.8	2.0
Peak number of simultaneous collisions	25	45	60

Tab. 2.1.: Technical parameters of the LHC comparing the design values to Run 1 and Run 2. Data taken from Duhr et al. [100]. Crossing angle for Run 1 taken from the dedicated ATLAS publication [104].

machine. The instantaneous luminosity L of the LHC given above is defined [97] by a number of factors as

$$L = \frac{n_b N_p^2 f_{rev} \gamma_r F}{4\pi\epsilon\beta^*}. \tag{2.1}$$

In this equation, n_b represents the number of bunches within the LHC, while N_p represents the number of protons in oppositely traversing bunches with a revolution frequency f_{rev} and relativistic gamma factor γ_r. Crucially, there are three additional parameters that significantly impact the luminosity. The emittance ϵ and the amplitude function β^* at the interaction point are measures of the transverse size of the beam at the interaction point. Hence, reducing their size leads to higher instantaneous luminosities. Finally, the factor F is a geometric factor taking into account the crossing angle of the two beams which reduces the instantaneous luminosity. This angle is needed as the two circulating beams traverse through the majority of the ring in parallel and are only crossed at the four interaction points of the large experiments, ATLAS [96], CMS[4] [101], LHCb[5] [102] and ALICE[6] [103]. Table 2.1 shows the parameters discussed as well as additional benchmark parameters comparing the design values and the achieved values in Run 1 and Run 2. The bunch spacing is a measure of the time between two bunches in the LHC ring. The table highlights the impressive performance of the LHC in both periods, but in particular how the Run 2 peak luminosity performance surpassed the design values by a factor of two due to reductions in the emittance, the amplitude function β^* and the bunch crossing angle as well as denser bunches (given by the bunch intensity) despite a lower than designed number of bunches n_b. It also illustrates the design value of the centre-of-mass energy of $14\,\mathrm{TeV}$ not yet achieved in Run 1 and Run 2 but targeted in future runs.

[4] Compact Muon Solenoid
[5] Large Hadron Collider Beauty
[6] A Large Ion Collider Experiment

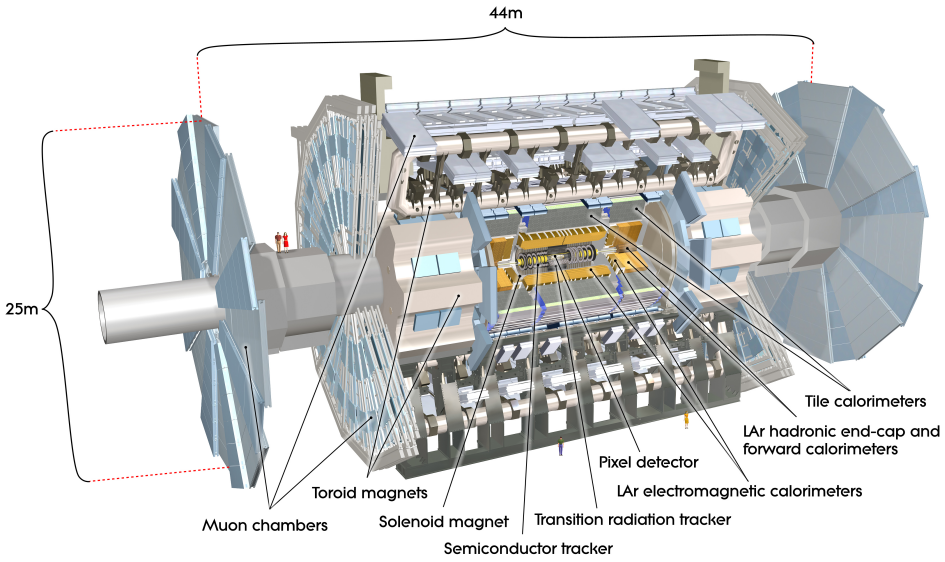


Fig. 2.2.: Computer generated overview of the ATLAS detector, shown here in a cut-away view with labels of major detector systems [105].

2.2 The ATLAS Experiment

As indicated in figure 2.1, the ATLAS experiment is one of four major experiments located at the LHC ring. It is a multi-purpose detector with capabilities to measure a broad spectrum of particles such as hadrons and charged leptons utilising its almost complete coverage of the full solid angle around the interaction point where the two proton beams cross. Its cylindrical construction, which is depicted in figure 2.2, allows for this close to 4π coverage and is built symmetrically around the interaction point in both directions of the colliding beams. In the following sections the purpose and function of the individual systems that make up the detector are described from inside to outside.

2.2.1 Coordinate System

For the purposes of this thesis it is convenient to adopt the right-handed coordinate system (centred at the interaction point *IP*) used in ATLAS [96]. A schematic overview is provided in figure 2.3: The positive x-axis is directed towards the centre of the LHC, the positive y-axis is oriented upwards (towards the surface above the LHC) and the positive z-axis consequently follows the beam pipe to complete the right-handed system. The azimuthal angle ϕ is defined starting from the positive x-axis around the z-axis between $[-\pi, \pi]$, and the polar angle θ is defined from the z-axis between $[0, \pi]$.

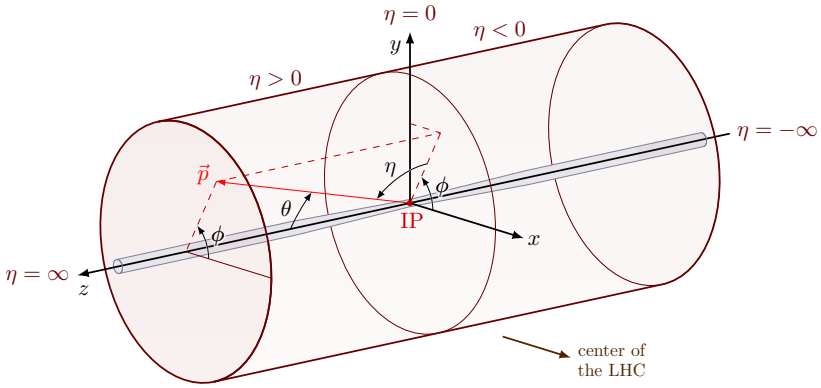


Fig. 2.3.: Coordinate system used for the ATLAS detector. Adapted from Neutelings [106].

The transverse plane is defined as the x-y plane orthogonal to the beam axis[7]. This allows to define object properties such as the *transverse momentum* (p_T), which is the momentum of the object projected onto the transverse plane. Its advantage is the invariance under Lorentz-boosts along the (longitudinal) z-axis. It is convenient to define the *transverse energy* $E_T = \sqrt{p_T^2 + m^2}$, where m is the mass of the object under consideration. To describe positions within the detector, it is also convenient to use the *pseudorapdity* η instead of the polar angle θ. It is defined as $\eta = -\ln(\tan(\frac{\theta}{2}))$. Its absolute values are within $|\eta| \in [0, +\infty)$, where 0 describes objects perfectly perpendicular to the beam axis and ∞ would be along the beam axis. In cases of very high energies where masses m of an object are negligible compared to their momentum $\vec{p}$, i.e. $m \ll |\vec{p}|$, the pseudorapidity approximates the *rapidity* $y = \frac{1}{2} \ln\left(\frac{E+p_z}{E-p_z}\right)$, where E is the energy and p_z the longitudinal momentum of a particle. This is usually the case for electrons or positrons[8] in ATLAS. The rapidity is a useful measure at collider experiments since differences Δy and thus $\Delta\eta$ are invariant under Lorentz-boosts along the longitudinal axis.

To describe detector parts, it is useful to distinguish between two major regions within the detector as *barrel* region and *end-cap* region. This nomenclature is used in multiple technical figures. The former describes the barrel or cylinder-like construction around the beam pipe in the centre of the detector, while the latter denotes systems constructed as a "cap" on either side of the barrel.

[7] The position of an object in this plane can be described by the azimuthal angle ϕ and its radial position $r = \sqrt{x^2 + y^2}$.

[8] In the following, particles and their anti-particles will not be explicitly distinguished, i.e. the term *leptons* also includes anti-leptons unless explicitly stated otherwise.

2.2.2 Tracking

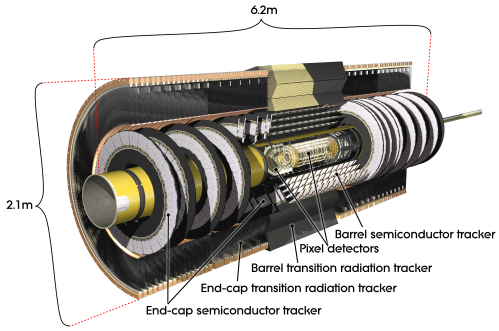
Closest to the beam axis is the tracking system [107] of ATLAS, which aims to accurately position charged particle trajectories. It is made up of three major tracking subsystems that are shown in figure 2.4 using different technologies, all permeated by a strong magnetic field. Particles are passing through multiple layers of tracking material, bent by the magnetic field. The collection of space-points in the tracker is then fitted to individual tracks that are associated to primary vertices or secondary vertices of particle interactions or decays in the *track to vertex association* (TTVA) step. This allows to reconstruct charged particle trajectories in the detector. A crucial aspect of the tracking system is a very high precision to resolve tracks and also a low material budget in order to minimise energy loss by particles traversing through the systems.

The solenoid magnet surrounds the inner detector that contains the tracking system. Its magnetic field has a strength of $2\,\mathrm{T}$ using super-conducting niobium-titanium wires embedded in aluminium strips. As the magnetic field lines are parallel to the beam axis, charged particles are bent within the transverse plane due to the Lorentz-force.

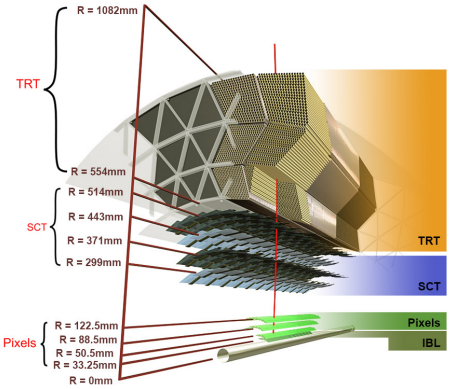
The resolution of the tracking system is $\sigma_{P_T}/p_T = 0.05\% \times p_T[\mathrm{GeV}] \oplus 1\%$ [108] in transverse momentum. Additionally, a resolution of better than $10\,\mu\mathrm{m}$ in the impact parameter (the closest approach of a track to a vertex in either the transverse or longitudinal direction) for particles with a high momentum and low pseudorapidity values is achieved. At lower momenta the resolution of the impact parameters decreases as uncertainties in associating the correct tracks to vertices increases. At the same time, the resolution of particle momenta improves as bending effects in the magnetic fields are stronger than at higher momenta. In all tracking systems a balance was struck to keep the material as low as possible while still ensuring high accuracy in order to avoid a significant energy reduction of incident particles before entering the calorimeters.

2.2.2.1 Pixel Detector and Insertable B-Layer

The innermost layer of the tracking system is the pixel detector [107], which consists of four layers of doped silicon pixels toroidally arranged around the beam pipe at radii between $33.25\,\mathrm{mm}$ to $122.5\,\mathrm{mm}$ as well as three disks around the beam pipe [96]. It covers a range in pseudorapidity of $|\eta| < 2.5$. The layer closest to the beam pipe is called *insertable B-layer* [110] as it has been installed after the first run of ATLAS and is particularly suited to improve the resolution of vertex positions, i.e.



(a) Cut-away view of the inner detector.



(b) Cross-sectional view of the different layers of the tracking systems.

Fig. 2.4.: Computer generated images of the ATLAS tracking system [109].

the position of primary interactions between protons as well as secondary vertices where long-lived particles (in particular b-mesons) decay.

The pixel detector as well as the insertable b-layer are constructed from doted silicon pixel modules. The pixel detector consists of 1744 modules, each containing 16 front-end chips with 2880 electronic channels, i.e. *pixels*, of sizes of $50 \times 400\,\mu\mathrm{m}^2$ or larger in $(r-\phi) \times z$ (i.e. in terms of their size on the surface of the cylinder) for a total of about 80.4 million read-out channels. The insertable b-layer adds another 6.02 million pixels with a size of $(r-\phi) \times z = 50 \times 250\,\mu\mathrm{m}^2$.

Particles traversing individual pixels create electron-hole pairs that travel in opposite directions within the pixel due to an electric field. The resulting current can be measured and comprises a *hit* in the pixel detector in case specified criteria are met.

2.2.2.2 Semi-Conductor Tracker

The Semi-Conductor Tracker (SCT) [107] is the second tracking subsystem in ATLAS and consists of four layers in radii between $299\,\mathrm{mm}$ and $514\,\mathrm{mm}$ in the barrel region in addition to nine disks each in the end-caps [96]. It covers the same $|\eta| < 2.5$ range as the pixel detector and consists of 4088 individual modules of silicon-strip detector elements. In the barrel region each module is built from four rectangular silicon-strip sensors, each with a pitch of $80\,\mu\mathrm{m}$. In the endcap each strip is oriented radially with constant azimuthal angle and a mean pitch of $80\,\mu\mathrm{m}$. Modules are designed to have an overlap to ensure hermetic coverage. In the barrel each module has a resolution of $17\,\mu\mathrm{m}$ in $r-\phi$ (i.e. in circular direction around the beam pipe)

and $580\,\mu\mathrm{m}$ in z and in the end-cap disks each module has a resolution of $17\,\mu\mathrm{m}$ in $r-\phi$ and $580\,\mu\mathrm{m}$ in r [108].

Charged particles passing through enable electric currents in reversed biased p-n-junction silicon diodes in the sensors. This signal can be measured to define a hit. A total of approximately 6.3 million read-out channels are attached to the SCT.

2.2.2.3 Transition Radiation Tracker

The Transition Radiation Tracker (TRT) [107] is the outermost tracking system of the inner detector and is positioned at radii between $554\,\mathrm{mm}$ and $1082\,\mathrm{mm}$ with a coverage of $|\eta| < 2.0$ [96]. It is built from individual straw tubes of about $4\,\mathrm{mm}$ diameter. Each tube has a coating used as a cathode such that the combination of a gold-plated tungsten wire and the cathode can be used as a drift chamber filled with gas. In it, charged particles ionise the gas such that resulting electrons and ions create a measurable electric current. There are 96 modules containing $52,544$ straw tubes each in the barrel and 20 modules with $122,880$ straw tubes per side in the end-cap region. Straw tubes are arranged in parallel to the beam axis in the barrel region and radially in the end-cap regions. Due to its construction the TRT only provides spatial information in the $r-\phi$ plane with an accuracy of approximately $130\,\mu\mathrm{m}$ per tube. A total of approximately $351,000$ read-out channels are connected to the TRT.

2.2.3 Calorimeter System

In addition to an accurate tracking system it is essential to have a precise measurement of particle energies in the detector. The calorimeter system of the ATLAS detector is designed to completely stop most particles emerging from interactions. Only muon and neutrino energies cannot be determined with the calorimeter system. The former are detected in the muon spectrometer (see section 2.3.2), while the latter do not interact with the detector at all. ATLAS uses a sampling calorimeter technology which alternates absorber and detector materials. Two major subsystems can be defined. The *electromagnetic calorimeter* is used to measure energies of mostly electrons, positrons and photons, while the *hadronic calorimeter* is constructed specifically to determine the energies of hadrons. A detailed description of the calorimeter functionality is given in the next sections.

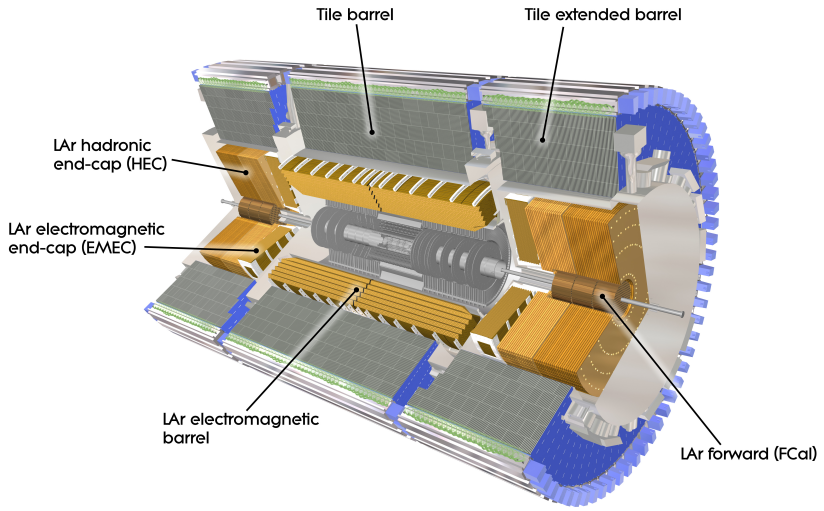


Fig. 2.5.: Computer generated cut-away view of the ATLAS calorimeter systems [111].

2.2.3.1 Electromagnetic Calorimeter

The electromagnetic calorimeter [112] in ATLAS is a liquid argon (LAr) sampling calorimeter. An incident, primarily electromagnetically interacting particle, i.e. electrons, positrons and photons, is decelerated by the calorimeter lead absorber material [113]. Highly energetic electrons and positrons emit photons as bremsstrahlung, whereas photons create electron-positron pairs via pair production. This causes a cascade of particles, the *electromagnetic shower* to occur in the calorimeter. This cascade continues until energies decrease to a level where ionisation or Coulomb scattering for electrons or positrons dominate and for photons where the photoelectric effect or Compton scattering dominate such that the shower stops. This threshold is called the *critical energy* and depends on the material used, described by the *radiation length* X_0, which is the mean length of an electron in a given material after which its energy is reduced by a factor of $1/e$.

To capture the energy deposits by this cascade of particles, layers of absorber material (lead) are alternated with active layers of liquid argon. Lead is chosen as a dense material to increase the probability of interactions, while liquid argon is chosen as material that gets ionised by incoming particles. The free electrons and ions created this way are collected at electrodes in the liquid argon layers and can be measured as electric current. The total number of particles depends on the critical energy E_c (which in turn depends on the material) and the incident energy of an incoming particle.

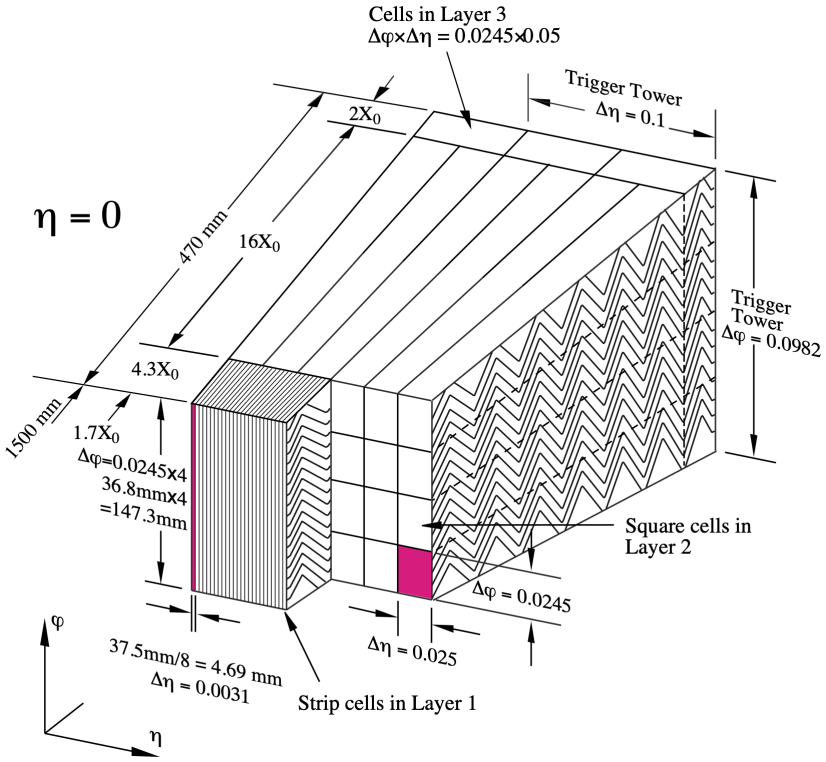


Fig. 2.6.: Schematic overview of a section of the liquid argon calorimeter highlighting the accordion structure and the segmentation into individual cells [96].

As can be seen in figure 2.5, there are multiple sections of the electromagnetic calorimeter in ATLAS. The *electromagnetic barrel* (EMB) region covers a range of $|\eta| < 1.475$. The *electromagnetic endcap* (EMEC) consists of two coaxial wheels, the outer wheel covering $1.375 < |\eta| < 2.5$ and the inner wheel with a coverage of $2.5 < |\eta| < 3.2$. Finally, in the range of $3.1 < |\eta| < 4.9$ the *forward calorimeter* (FCAL) is positioned. In the barrel and endcap regions an accordion geometry of the calorimeter was chosen to ensure full coverage over the angle ϕ. A schematic of a cut-out section of the barrel and end-cap modules in figure 2.6 highlights this accordion structure in which lead and liquid argon layers are alternated and which also shows individual calorimeter *cells*, the granular substructure of the system in which energy deposits are determined individually. This geometry provides a hermetic coverage in ϕ. The structure in the forward region is different and will be described in more detail in chapter 11 in the context of the ATLAS upgrade. Due to its closeness to the beam pipe it is built from copper absorber material containing thin tubes in parallel to the beam axis containing an electrode at their centre with their gap filled by liquid argon as active medium.

The energy resolution of the liquid argon barrel and end-cap calorimeters can be determined as $\sigma_E/E = \frac{10\%}{\sqrt{E}[\text{GeV}]} \oplus 0.7\%$ [114] and for the FCAL as $\sigma_E/E =$

$\frac{100\%}{\sqrt{E[\text{GeV}]}} \oplus 10\%$. A constant term due to electronic and other noise sources of 0.7% [114] (or 10% for the FCAL) cannot be reduced. However, the resolution that depends on the energy scale improves with higher energies due to larger numbers of particles that can be measured in the electromagnetic shower.

2.2.3.2 Hadronic Calorimeter

The hadronic part of the ATLAS calorimeter system is designed to measure energies of mostly strongly interacting particles such as hadrons. The hadrons dominantly interact inelastically with the nuclei of the calorimeter material [113]. Subsequently, additional hadrons are produced as secondary particles that go through the same process. This leads to a cascade, the *hadronic shower*, which typically reaches further into the detector material and is wider than electromagnetic showers. Once the energy of particles is below the production energy of a pion (which is the lightest hadron) the remaining hadrons decay. The precise process depends on the products involved, but they include electromagnetic decays such that an electromagnetic shower evolves. Furthermore, other particles decay weakly or cause nuclear spallation or fission processes until the shower is fully stopped. This process is characterised by the *nuclear interaction length* λ_A, which is the mean length a particle travels before undergoing an inelastic scattering with a nucleus. Since λ_A is typically significantly larger than the radiation length X_0, hadronic calorimeters are usually deeper than electromagnetic ones.

The hadronic calorimeter system is composed of three separate technologies. The *tile calorimeter* [115] is a sampling calorimeter composed of steel plates as absorber and scintillators as active layers. As visible in figure 2.5, it encloses the liquid argon electromagnetic calorimeter and covers a range of $|\eta| < 1.7$. Its construction is subdivided into a barrel region and two extended barrel regions. The scintillators are oriented radially from the beam pipe in alternation with the steel absorber plates.

The *hadronic endcap calorimeter* (HEC) is a liquid argon calorimeter [112] that uses the same technology as the electromagnetic liquid argon calorimeters and is located around the electromagnetic endcap calorimeters covering a range of $1.5 < |\eta| < 3.2$.

Finally, the second and third layer of the liquid argon forward calorimeter use tungsten as absorber material and are located behind the electromagnetic layer that uses copper. They cover a range of $3.1 < |\eta| < 4.9$ and are thus closest to the beam axis. Their construction follows the same principle as the electromagnetic part of the forward calorimeter.

Some products of the hadronic shower decay invisibly, for instance into long-lived neutral particles or muons. A fraction of the shower energy is also deposited by breaking up nuclear bonds, where fragments are re-absorbed before detection. This means that the resolution of the hadronic calorimeters is not as precise as the resolution of the electromagnetic calorimeter. Specifically, the HEC achieves an energy resolution of approximately $\sigma_E/E = \frac{50\%}{\sqrt{E[\mathrm{GeV}]}} \oplus 3\%$ [116] and the Tile calorimeter reaches a resolution of approximately $\sigma_E/E = \frac{47\%}{\sqrt{E[\mathrm{GeV}]}} \oplus 4.7\%$ (in this case measured for pions) [117].

2.2.4 Muon System

Measurements of muons in ATLAS rely on the eight-coiled toroid magnet system [118] that creates a magnetic field of a strength between $2.0\,\mathrm{T}$ to $6.0\,\mathrm{T}$, where field lines are oriented to be mostly orthogonal to muon trajectories in the $r-z$ plane. Three individual toroid magnets make up the overall system: The barrel toroid covers a range of $|\eta| < 1.4$, while for the range $1.6 < |\eta| < 2.7$ two endcap toroids rotated by $22.5\,\mathrm{deg}$ provide coverage with their magnetic fields. The transition region in $1.4 < |\eta| < 1.6$ is permeated by a superposition of both barrel and either endcap toroids.

The muon trajectories leave tracks in the inner detector system, but they only deposit little energy in the calorimeter systems due to their momentum (as they typically are minimum ionising particles) such that they escape. For this reason the ATLAS detector is encased by the muon system that is constructed to measure muon trajectories to reconstruct their momenta. The system is built from individual chambers that are constructed in three layers in the barrel region at radii of approximately $5\,\mathrm{m}$, $7.5\,\mathrm{m}$ and $10\,\mathrm{m}$. Additionally, on either side of the detector the chambers are arranged orthogonally to the beam axis in four disks at distances from the interaction point of approximately $7.4\,\mathrm{m}$, $10.8\,\mathrm{m}$, $14\,\mathrm{m}$ and $21.5\,\mathrm{m}$. At $|\eta| \approx 0$ there is a small gap in the system to allow service access to the toroid magnet, the calorimeters and the inner detector. A cross-sectional view of the system in the $y-z$ plane is given in figure 2.7. Part of the barrel and the end-cap systems are visible highlighting the different layers of chambers for maximum coverage.

Four types of muon chambers are used for the measurement of track coordinates. The different technologies all use the same fundamental principle of proportional chambers, which use one or more wires as anodes and the surrounding wall as cathodes. The chambers are filled with a gas that gets ionised by particles passing through creating avalanches of free electrons and ions that propagate to the oppositely charged poles and thus create a measurable current. Monitored Drift Tubes (MDTs) used in the central barrel and Cathode Strip Chambers (CSCs) in the

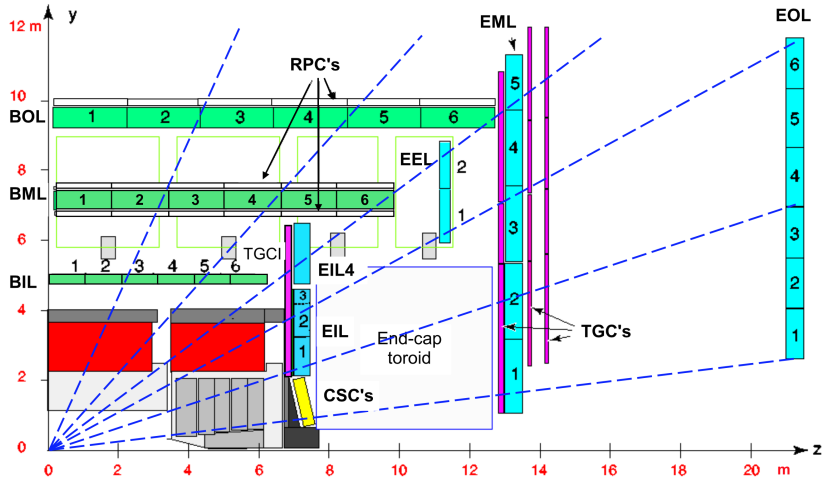


Fig. 2.7.: Cross-sectional schematic diagram [96] of a part of the muon system in the ATLAS detector. The barrel (B) and end-cap (E) inner (I), middle (M) and outer (O) layers (L) are coloured. Dashed lines indicate the hypothetical path of an infinite-momentum muon.

endcap regions are used to reconstruct muon tracks with a resolution of $\Delta z = 35\,\mu\mathrm{m}$ and $\Delta r \times \Delta\phi = 40\,\mu\mathrm{m} \times 5\,\mathrm{mm}$, respectively. For the trigger system, which will be explained in more detail in section 2.2.6, Resistive Plate Chambers (RPCs) and Thin Gap Chambers (TGCs) are used in the barrel and endcap regions, respectively, both of which provide only a coarser resolution but a fast response time. The overall resolution [119] of the muon spectrometer is approximately 3% for muons over a large range of transverse momenta up to approximately 10% for muons with a $p_T = 1\,\mathrm{TeV}$.

2.2.5 Luminosity Detectors

For precise measurements it is essential to determine the integrated luminosity delivered by the LHC and measured by ATLAS as accurately as possible. The *LUminosity measurement using Cherenkov Integrating Detector* (LUCID) [96] systems are positioned at $z = \pm 17\,\mathrm{m}$ on either side of the interaction point and are vital for a precise luminosity measurement. They contain 16 photomultiplier tubes with a diameter of $d = 10\,\mathrm{mm}$ each that use quartz fibre bundles and are covered by quartz windows used as Cherenkov medium. In addition, four photomultiplier tubes are situated $1.5\,\mathrm{m}$ closer to the interaction point inside the muon shielding. The determination of the luminosity is based on Cherenkov radiation caused by particles passing through the quartz media of LUCID. The emitted photons are measured in the photomultiplier tubes. The integral of the pulses in these tubes is proportional to the integrated luminosity of a so-called *luminosity block* of the LHC.

A luminosity block is defined [120] as a short time period (about 1 minute) during which the instantaneous luminosity is assumed to be approximately constant, i.e. it has not been degraded significantly.

A second system, the ATLAS *Beam Conditions Monitor* (BCM) [121], can be used for luminosity measurements. The BCM system is designed to very quickly identify and abort scenarios in which multiple proton bunches hit collimators in front of the experiment, thus potentially damaging sensitive detector components. At the same time it provides a complementary measurement of the luminosity conditions in ATLAS. Two detectors are positioned at $z = \pm 1.9\,\mathrm{m}$ on either side of the interaction point. They use electrodes to quickly detect electron-hole pairs created by charged particles in a diamond medium.

For the absolute calibration of the luminosity measurements, dedicated *van-der-Meer* beam separation scans at very low pileup are performed [122], where beams are swept transversally in different directions across each other. Naturally, this method is affected by uncertainties which originate from the method used, in beam parameters and mostly in the transfer of the calibration from low-pileup data to instantaneous luminosities three orders of magnitude higher such as during Run 2. Together with the methods described above, the integrated luminosity can be determined precisely for short luminosity blocks, which is essential for the overall normalisation of expected numbers of events in any analysis.

2.2.6 Trigger and Data Acquisition

During the period of data taking between 2015 and 2018 by ATLAS, called *Run 2*, the collision rate at the interaction point was approximately $40\,\mathrm{MHz}$. If every bunch crossing (also called *event*) was recorded, rates of $\mathcal{O}(\mathrm{PB\,s^{-1}})$ would be achieved and needed to be read out and stored. This vastly exceeds current speeds of storage systems and would also result in a very large amount of data unsuitable for analyses as events for precision measurements or searches typically require one or multiple specific topologies within the detector that only occur rarely during an inelastic scattering process in ATLAS. It is therefore essential to reduce the rate of data taking to a more manageable level and to apply a broad preselection of events to only record bunch crossings during which predefined criteria are met. This is done using the two-staged *trigger system* [123] of ATLAS, which is split into the hardware based *Level-1 Trigger* (L1) [124] and the software based *High-Level Trigger* (HLT) [125]. The system is depicted in figure 2.8.

The hardware-based level-1 trigger reduces the data rate from $40\,\mathrm{MHz}$ to $100\,\mathrm{kHz}$. To achieve this, the so-called *Central Trigger Processor* (CTP) receives information

from the muon system (*L1Muon*), as discussed before, as well as coarse calorimeter information (from the L1Calo, containing the *Jet/Energy-sum Processor* (JEP) and the *Cluster Processor* (CP)). The calorimeter information is used to compute properties such as energy sums, isolation and identification variables, while muon momenta and positions are determined from the muon trigger chambers. Together with the topological trigger processor this allows for a selection of more complex topologies in the detector that involve multiple objects and their properties such as angular separations or invariant masses. All calculations are done on field programmable gate arrays (FPGAs) for maximum speed. Different selection criteria can be applied to specify individual trigger requirements that are combined into *trigger chains*, which are logical `OR` combinations of individual trigger requirements. A latency of approximately $2.5\,\mu\mathrm{s}$ is allowed for the first level trigger to reach a decision.

If an event is accepted, the *front-end* (FE) detector elements read out the full detector. *Read-out Drivers* (RODs) process the signals and apply formatting and subsequently the *Read-out System* (ROS) buffers the data to be passed onto the software-based high-level trigger. This second stage of the trigger is located on a CPU farm using $400,000$ cores to calculate complex selection criteria and to reduce the event rate received from the first level to an average of $1.2\,\mathrm{kHz}$ of interesting events within approximately $200\,\mathrm{ms}$ [123]. The high-level trigger uses the *ATLAS Athena* [126] offline software framework, which itself is based on the *Gaudi* framework [127]. Events accepted by the high-level trigger are send by the *Sub-Farm Output* (SFO) to permanent storage for further processing at the so-called *Tier-0* facility at CERN, which is part of the worldwide computing grid discussed in the next section. Data throughput at this final stage is approximately $1.2\,\mathrm{GB\,s^{-1}}$ as each event is approximately $1\,\mathrm{MB}$ in raw size [123].

2.2.7 Data Formats and Offline Computing

The data collected at the ATLAS experiment as well as simulations used for comparisons require a very large amount of storage and computing capacities. The *Worldwide LHC Computing Grid* (WLCG) [129] is designed to provide these resources in a globally distributed way. As mentioned previously, the CERN Data Centre is called *Tier-0* and stores a copy of all data taken at ATLAS. It is connected to thirteen large computing centres (Tier-1) worldwide via the *LHC Optical Private Network*, which is a network of optical-fibre links working at rates between $10\,\mathrm{Gbit\,s^{-1}}$ to $100\,\mathrm{Gbit\,s^{-1}}$ used exclusively for data exchange between these centres. Moreover, approximately 160 Tier-2 centres are connected to the other Tiers and each other using regular internet connections. These centres are usually computing and storage facilities at universities and scientific institutes. Individual scientists access the grid resources via local Tier-3 systems, such as individual PCs. However, there is no

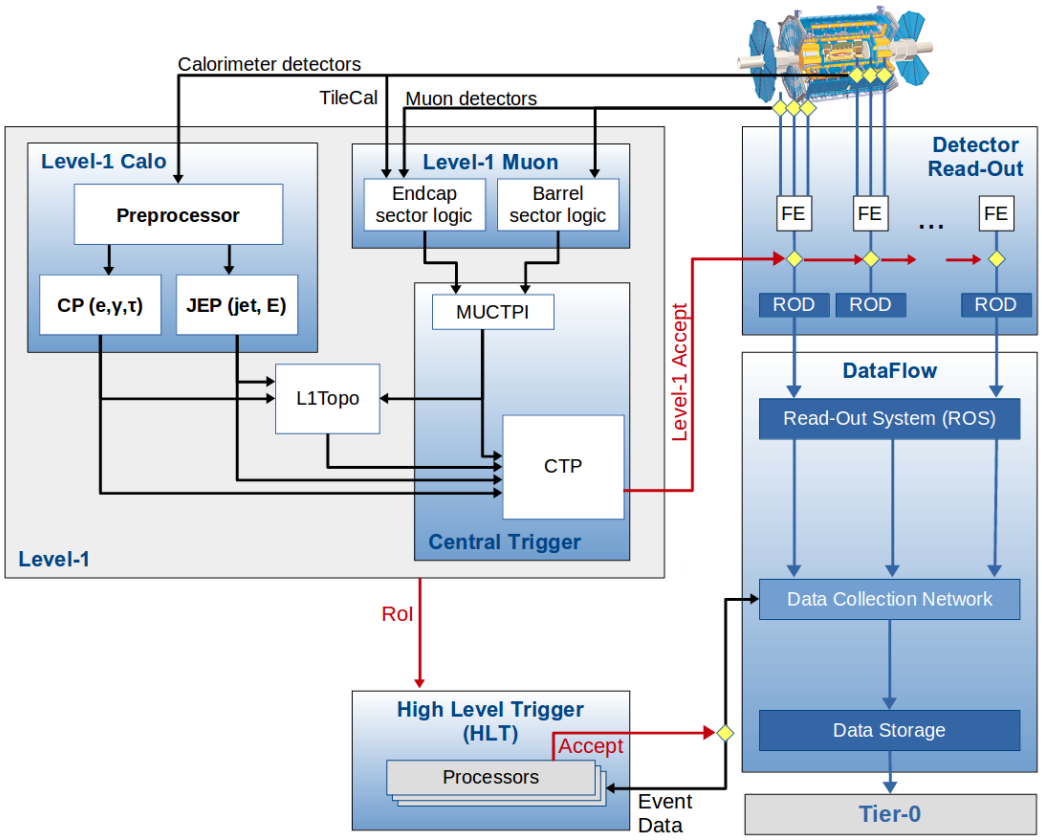


Fig. 2.8.: Schematic overview of the trigger and data acquisition system in ATLAS during Run 2. Adapted from ATLAS [128].

formal connection between the grid system and Tier-3 resources. The load of storage of data and simulations as well as processing of data and simulations is shared between the Tier-0, Tier-1 and Tier-2 systems.

After data has been recorded at ATLAS, it is stored permanently at the Tier-0 facility and other facilities for redundancy. It is stored in raw format, where, for instance, individual hits in the tracking system or signal shapes of calorimeter cells are saved in a digitised format, `RAW`. This is done using the ATLAS Athena framework, which is a C++ software framework using ROOT [130] for data storage and manipulation. In a second step, algorithms, such as the ones explained in the following section, are used to reconstruct particle tracks and showers and finally objects such as electrons, positrons, photons etc. Depending on how much of the original raw detector information is kept, such events are stored as `ESD` (Event Summary Data) or `AOD` (Analysis Object Data) files. The former retains parts of the original detector data, while the latter requires less storage capacity by removing most of the raw information. This results in a reduction of size per simulated (data) event from approximately $3.7\,\mathrm{MB}$ ($2.7\,\mathrm{MB}$) in the ESD format to approximately $0.6\,\mathrm{MB}$ ($0.4\,\mathrm{MB}$) in the AOD, respectively [129].

For analyses it is usually essential to reduce data sizes even further to reduce storage and computing costs. Consequently, the `DAOD` (Derived Analysis Object Data) format is used in most analyses including the measurements in this thesis. A reduction in size is achieved by skimming (removing events that do not fulfil certain basic requirements), slimming (removing individual unneeded objects from events) and thinning (removing unnecessary information from objects). For the analysis presented in this thesis the ATLAS DAOD format `STDM4` has been used (see section 5.3.3) whereas the algorithm studies have been based on the ESD format.

2.3 Object Reconstruction and Identification in ATLAS

As mentioned in the previous section, the reconstruction and identification of objects in the ATLAS detector from fundamental properties is essential to enable high-precision analyses such as the one presented in this thesis. Particles are reconstructed and identified by their signature in the detector, that is the combination of tracks and energy deposits in the respective detector parts as shown in figure 2.9.

In proton collisions at the LHC particles most abundantly created are quarks, anti-quarks and gluons and their subsequent hadronic daughter products. As explained in section 2.2.3.2, the particles cannot be measured directly but only as a hadronic

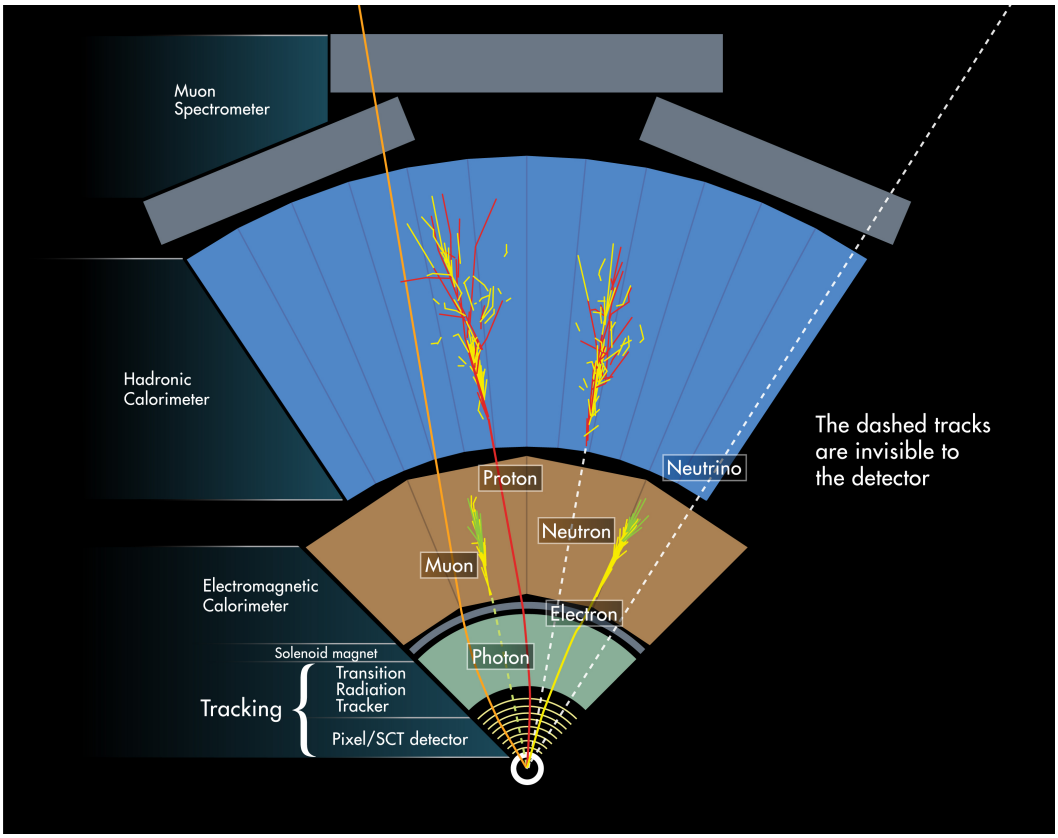


Fig. 2.9.: Schematic overview of expected signatures of different types of particles in the ATLAS detector [131].

shower in the calorimeter. Hence, it is necessary to define so-called *jets* as objects that collect energy deposits in the calorimeters to form a composite object. Since jets are not directly used in the analyses presented, they will not be discussed in detail, but it is important to note that jets are algorithmically defined objects that aim to capture the correct amount of deposited energy of a hadronic shower. Jets can be differentiated by their charge (shown as an example for protons and neutrons in figure 2.9) and flavour, that is their particle of origin. Reconstruction techniques can be employed to distinguish between gluon- or quark-originated jets and to some degree also quark flavours for example by utilising reconstructed vertices [132]. Jets can only be defined within the context of the jet clustering algorithm used to construct them. These algorithms are based on different techniques to determine which objects are counted towards a jet.

In contrast, electrons and muons can be defined more precisely due to the nature of their interactions with the detector. In this chapter the reconstruction and identification of these two types of objects will be outlined in more detail. Note that tau leptons are explicitly excluded in this description and the analysis due to their short lifetime and mostly hadronic decay, which leads to jet-like energy deposits in the detector. In figure 2.9 a clear distinction can be seen in the expected signature of an electron (which is charged and thus leaves a track as well as energy deposits in the electromagnetic calorimeter), photons (which generally do not leave a track as they are uncharged) and muons (which leave tracks but are not stopped by the calorimeters).

Lastly, neutrinos of all flavours only interact very weakly with matter and thus escape the detector undetected. Consequently, they are challenging to reconstruct, which can only be done indirectly using momentum conservation in the transverse plane and a property called *missing transverse energy* E_T^{miss}.

2.3.1 Electron Objects

Electron candidates reconstructed in ATLAS are built from multiple individual components. This section focusses on electron candidates in the central, high-precision region of ATLAS ($|\eta| < 2.47$), where the inner detector provides tracking coverage. The reconstruction and identification procedures will be outlined, but isolation criteria will not be discussed in detail as they are not used explicitly in the analysis.

2.3.1.1 Reconstruction

The electromagnetic shower explained in section 2.2.3.1 initiated by bremsstrahlung of an electron can already develop before hitting the electromagnetic calorimeter,

such as in the tracking system or the beam pipe. Consequently, an electron candidate will leave one or more tracks in the inner detector before interacting with the calorimeter material. In the electromagnetic calorimeter a compact shower further develops (or is initiated if it has not started) such that energy is deposited in the individual cells of the calorimeter. The energy deposition is first reconstructed using a *seed-cluster* algorithm, during which localised energy deposits are identified as seeds and local maxima criteria remove duplicate reconstruction candidates.

Electron candidate tracks are built from individual hits in individual layers of the tracking system. Only track candidates with a $p_T > 400\,\mathrm{MeV}$ are fitted using the ATLAS Global χ^2 Fitter [133], which also removes any ambiguities that may occur between track candidates.

The path of an electron candidate is visualised in figure 2.10, which highlights the trajectory of an electron candidate that emits a photon in the tracking system from the primary vertex to the energy deposit in the calorimeter. A second fit employing a Gaussian-sum filter (GSF) is used to spatially match (in η and ϕ) track candidates and clusters in the electromagnetic calorimeter taking into account energy losses in the material. This also improves the determination of the transverse impact parameter d_0, defined as the shortest distance between a track and the primary vertex (i.e. the interaction point) in the transverse plane [134]. In the last step the first matching between tracks and clusters is re-done with stricter requirements and reconstructed topological clusters are determined around the original seed clusters in a wider window of considered cells.

In order to be able to determine electron candidate energies reliably, a calibration procedure is performed on the data. Multiple steps are taken to maximise the resolution and ensure an accurate calibration. Energy deposits of electrons are estimated by relying on properties that describe the shower development in a multivariate approach. In addition, the relative energy scales between different layers of the calorimeters are unified and non-uniformities in the detector response are closely studied and adjusted. The overall energy scale is determined using the Z boson as a standard candle to calibrate measured energies in electron-positron pairs in data. Finally, results are verified by comparing simulation and data probing J/Ψ decays into electron-positron pairs. The systematic uncertainty resulting from this procedure is typically between 0.03% and 0.8%, depending on the transverse momentum of the electron candidate [135]. The efficiency $\epsilon_{reco} = \frac{\text{No. of reconstructed electrons}}{\text{No. of all electrons}}$ to reconstruct electron candidates is very high and typically exceeds 99% for electrons with a transverse momentum higher than $15\,\mathrm{GeV}$ [136]. The reconstructed properties of the position inside the detector using the pseudorapidity and the energy deposition inside the calorimeters together with the known electron mass then allow to completely reconstruct the four-vector of an electron candidate.

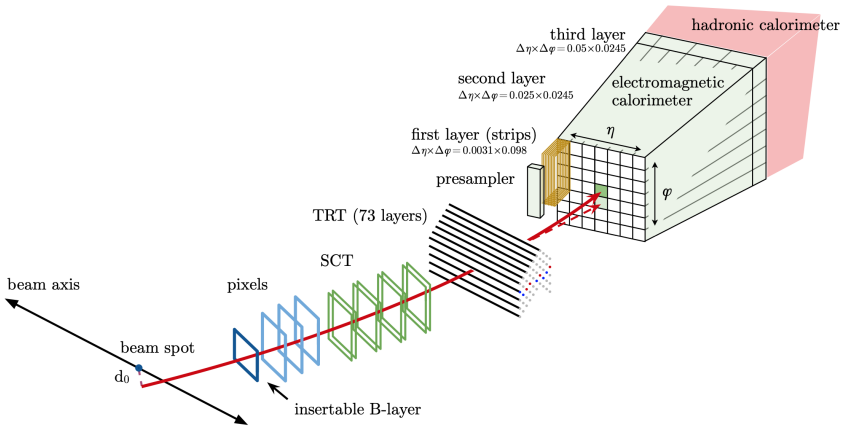


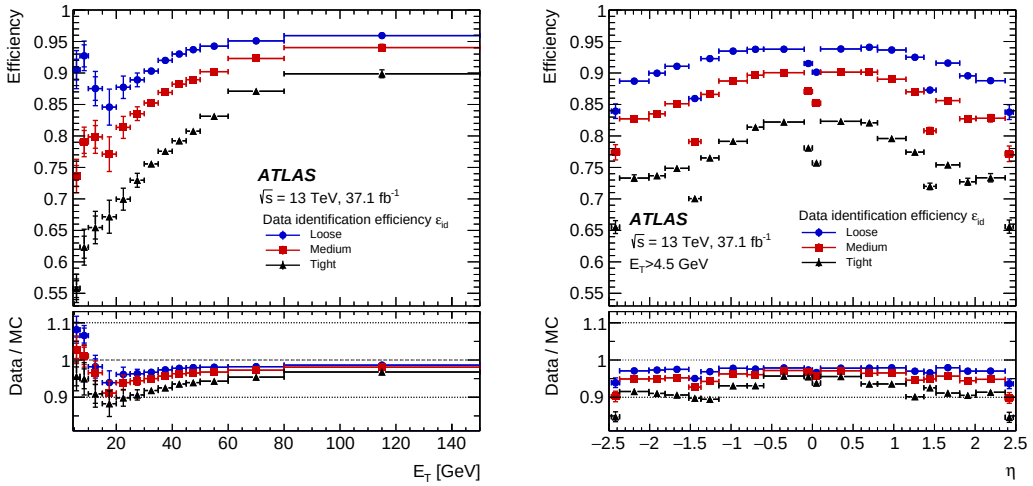
Fig. 2.10.: Schematic overview [136] of the different components of an electron candidate signature in the ATLAS detector used in the reconstruction. The solid red line represents an electron, while the dashed red line represents a photon emitted by the electron in the tracker. The beam spot is the region where the two colliding beams interact.

2.3.1.2 Identification

After electron candidates are reconstructed, likelihood-based methods are employed to sort them into different identification criteria depending on information from the tracking system, the calorimeters and combined quantities. Likelihood functions $L_{S,B}$ are constructed of Poissonian PDFs for real electrons (S for signal) and fake electrons (B for background, for instance from jets) and used to determine a discriminant [136]:

$$d_L = \frac{L_S}{L_S + L_B}. \tag{2.2}$$

Operating points that specify a value of signal efficiency and background rejection are defined as thresholds on the discriminant. The various variables used to built the likelihood functions can be found in a dedicated ATLAS publication [136] and aim at exploiting different signatures between real electrons and backgrounds such as photons or hadrons that can be misidentified. Four operating points are most commonly used and called *very loose*, *loose*, *medium* and *tight* in ascending order of background suppression and descending order of signal efficiency ϵ_{ID}. They vary between different regions in η and transverse energy E_T. In particular the transition region between the barrel and the endcap cryostats in the calorimeters suffer from significant efficiency drops. Each looser working point fully contains all stricter working point candidates. For instance, electron candidates with a transverse momentum of $40\,\mathrm{GeV}$ are identified at $\epsilon_{ID}(\text{loose}) = 93\%$, $\epsilon_{ID}(\text{medium}) = 88\%$ and $\epsilon_{ID}(\text{tight}) = 80\%$ [136] at the different operating points. Generally, the efficiencies increase towards higher transverse momenta and lower $|\eta|$ as shown in figure 2.11. While the efficiency decreases going from loose to tight, the background rejection behaves inversely and increases.



(a) Electron identification efficiencies as a function of the electron transverse energy.

(b) Electron identification efficiencies as a function of the electron pseudorapidity.

Fig. 2.11.: Electron identification efficiencies for different working points [136].

The charge of an electron is determined by its bending direction in the detector. At high energies or pseudorapidities the tracks they leave become straighter and thus more difficult to identify in their bending direction. A boosted decision tree is used to suppress the misidentification of electron charges using variables related to the track quality, the lateral shower development in the calorimeter and combined quantities. Generally, the chance of a misidentification of the charge increases towards higher pseudorapidity to approximately 3% at $|\eta| = 2.5$ for tightly identified electron candidates with an $E_T > 25\,\mathrm{GeV}$ compared to 0.03% in the most central $|\eta| < 0.5$ region [136].

Eventually, there are different methods of electron isolation which are based on either maximum energy sums around the candidate cluster in the calorimeter or a limit on high-p_T tracks around the candidate track. Both are evaluated within a cone around a candidate and can be adjusted to analysis or trigger needs.

2.3.2 Muon Objects

Unlike electrons, muons at the energies produced in proton collisions are usually minimum-ionising particles (MIPs). Hence, their signature typically consists of tracks in the muon spectrometer and in the inner detector tracking system as well as little energy deposited in the calorimeter systems.

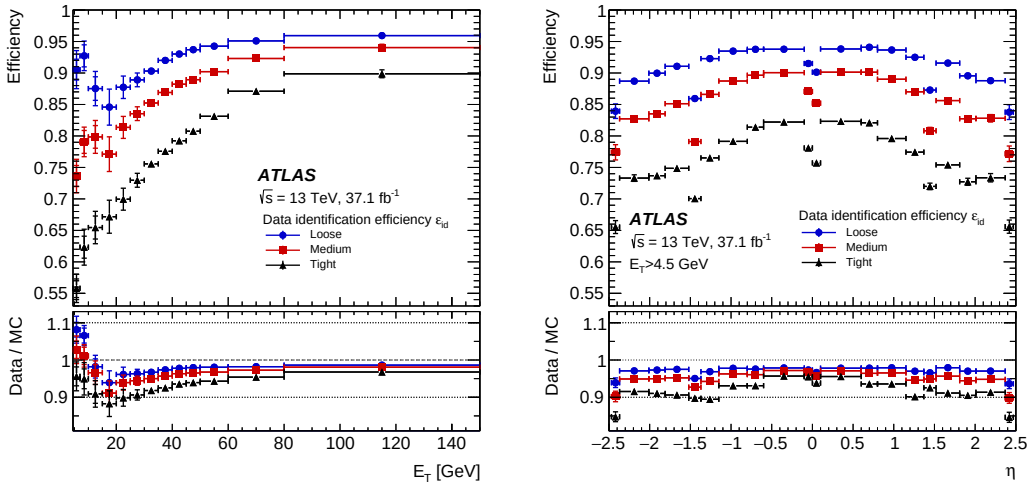
2.3.2.1 Reconstruction

Muon candidates based on using the full detector information are reconstructed following five main strategies. This is to maximise the reconstruction efficiency which might be lost if only one strategy was used. *Combined muons* are reconstructed by matching tracks in the muon spectrometer to tracks in the inner detector taking into account the energy loss in the calorimeters. *Inside-out combined* muons do not require an independently reconstructed track in the muon spectrometer, but they are built from tracks in the inner detector that are extrapolated to the muon spectrometer and combined with loosely identified tracks in the muon spectrometer and the energy loss in the calorimeters to a combined track fit. If a track in the muon spectrometer cannot be matched to a track in the inner detector, it is extrapolated to the beamline to define a *muon-spectrometer extrapolated* candidate[9]. In the second to last scenario a track in the inner detector can be extrapolated to the muon spectrometer following strict angular matching requirements to one or more reconstructed muon spectrometer segments to form a *segment-tagged* muon candidate. Lastly, *calorimeter-tagged* candidates are found by an extrapolation of tracks in the inner detector through the calorimeter to search for energy deposits compatible with a minimum-ionising particle. As mentioned before, since the transverse momentum of muons is determined by their track curvature, the precision and thus resolution of the transverse momentum decreases at very high momenta due to straighter tracks that are fitted. Overall, the reconstruction efficiency ϵ_{reco} has been measured to be close to 99% [137].

Similarly to electrons, the muon momentum scale and resolution are determined by using Z boson and J/Ψ decays to muon/anti-muon pairs where the decays are used as standard candles to determine the absolute momentum scale[10]. The momenta determined from the individual detector sections, inner detector (ID) and muon spectrometer (MS), are corrected for individually by determining several correctional factors depending on the kinematic region. Combined muons, which are constructed from information of both detector parts, benefit from the precise calibration of both systems to provide the final momentum as a weighted average of both. The momentum resolution has been determined to be 1.7% for muons from J/Ψ decays and 2.3% for muons from Z boson decays [137].

[9] These candidates extend the range of muon acceptance to $|\eta| = 2.7$, which is not used in the analysis presented that covers $|\eta| < 2.5$.

[10] In contrast to the electron calibration, the muon calibration corrects the simulation used to derive predictions discussed in the following chapter.



(a) Muon identification efficiencies as a function of the muon transverse energy.

(b) Muon identification efficiencies as a function of the muon pseudorapidity.

Fig. 2.12.: Muon identification efficiencies for different working points [137]. The efficiency in data is shown and compared to a Monte Carlo simulation for reference.

2.3.2.2 Identification and Isolation

Muon candidates are also categorised depending on specific identification and isolation criteria they fulfil. The identification relies on requirements for the number of hits in the different tracking subdetectors and the muon spectrometer parts as well as fit properties of the track and variables that test the compatibility between the two detector systems. The three identification working points *loose*, *medium* and *tight* are defined to efficiently identify muons from the hard scattering interaction and to reject muons from delayed decays of light or heavy hadrons. As for electrons each looser working point fully contains all candidates that fulfil the stricter requirements. The efficiencies for muons with a transverse momentum between $20\,\mathrm{GeV}$ and $100\,\mathrm{GeV}$ are $\epsilon_{ID}(\text{loose}) = 99\%$, $\epsilon_{ID}(\text{medium}) = 97\%$ and $\epsilon_{ID}(\text{tight}) = 93\%$ [119]. Similarly to the electron identification, muon identification efficiencies discussed increase towards higher transverse momentum, but in contrast they remain mostly flat for most $|\eta|$ regions with the exception around $|\eta| \approx 0$ where the efficiency drops due to a small gap in the muon system. This behaviour is visualised in figure 2.12. Besides these working points, two additional working points, *Low-*p_T and *High-*p_T, have been optimised for specific regions, with efficiencies in the same p_T region of $\epsilon_{ID}(\text{Low-}p_T) = 97\%$ and $\epsilon_{ID}(\text{High-}p_T) = 80\%$, respectively [119].

Since muons are reconstructed mostly from their tracks, it is important to allow certain isolation criteria to be applied, which aim to discriminate muons from a hard scattering event and muons that originate from hadronic decays. The latter is expected to result in a significantly larger energy deposit around the extrapolated muon track in the calorimeter systems, which is thus used as a means of discrim-

ination between the two types. This is defined in the *calorimeter-based isolation* $E_T^{\text{topocone20}}$, which is the sum of transverse energy E_T deposited in the topological cell clusters in a cone of size $\Delta R = \sqrt{(\Delta\eta)^2 + (\Delta\phi)^2} = 0.2$ around the reconstructed muon position in the calorimeters after subtracting the energy deposit of the muon itself. It is also possible to employ a *track-based isolation*, which is the scalar sum of transverse momenta of reconstructed tracks in the inner detector associated with the primary vertex around the reconstructed muon position in a cone of specified size. These variables can be used to select muon candidates with either higher or lower isolation. Multiple working points are defined that use the information presented before, such as *loose* or *FixedCutLoose* [137]. For instance, for muons that pass the *medium* identification working point with a transverse momentum between $20\,\text{GeV}$ and $100\,\text{GeV}$ the *loose* isolation has an efficiency of $\epsilon_{Iso}(\text{loose}) = 97\%$ and the *tight* isolation working point has an efficiency of $\epsilon_{Iso}(\text{tight}) = 89\%$ [119].

3 Simulation

> *We can only see a short distance ahead, but we can see plenty there that needs to be done.*
>
> **— Alan Turing**

Measurements of physical properties in particle physics rely on accurate predictions which the data can be compared to. Complex processes from the collision of protons to the response of the detector are simulated individually to allow precise comparisons to data. This chapter outlines the principles of the so-called *Monte Carlo method* used as a basis for the simulation. Additionally, the two main components of simulations at ATLAS, the *event generation* and the *detector simulation*, are explained in detail.

3.1 Monte Carlo Method

Many particle physics experiments, such as ATLAS, are experiments which store individual events and within each event a large quantity of different objects and properties. In order to accurately compare data taken at an experiment to the expectation it is necessary to rely on simulations. To this end real world randomness needs to be emulated to a high accuracy and in large quantities to formulate statistically stable predictions for probabilistic processes that often cannot be calculated analytically.

The usage of computers for these tasks is essential given the large amount and the complexity of simulations needed. However, as computers are strictly deterministic, true randomness cannot be achieved. Algorithms generating a sequence of numbers are used to generate pseudorandom numbers which repeat after a specific period. In order to resemble real randomness, modern algorithms used to create random numbers have a period of repetition of more than 10^{43} [138]. Such a period is many orders of magnitude larger than sizes of simulations used for instance in ATLAS, and thus they approximate true randomness to a very good degree.

In order to generate complex distributions rather than a uniform distribution of random numbers, so-called *Monte Carlo methods* such as von Neumann's acceptance-rejection method [139] are used. The probabilistic simulation of each step starting from the interaction of two protons to the generation of electric signals in the

detector are generated to a high accuracy using software libraries that implement Monte Carlo methods.

3.2 Event Generation

As described in section 1.2, there are numerous processes that occur during and following the interaction of two protons. The PDFs provide the probabilistic description of parton momenta within the proton. Subsequently, the physics simulation emulates the hard scattering, parton shower, hadronisation, underlying event and particle decays using so-called *event generators* and shower programs. In addition, in some cases individual calculations are also done by interfacing external computer programs. While the simulated result of an individual event or interaction might not provide much value, the power of these simulations is in the ability to produce large numbers of events that should, as described before, statistically resemble the real world.

3.2.1 Accuracy

As already stated in chapter 1, most calculations in quantum field theory can only approximate reality due to the quantum mechanical principle that all Feynman diagrams which can be written also contribute to a process.

This is particularly relevant in Quantum Chromodynamics where the coupling constant is large such that higher-order sums of Feynman diagrams diverge. While normalisation and factorisation scales introduced in chapter 1.1.2 alleviate some of the computational challenges, the accuracy of predictions in QCD still strongly depends on the order of precision in QCD, i.e. how many strong vertices are taken into account. Computational requirements increase exponentially with higher orders. Besides the baseline processes at *leading order* (LO) without additional vertices, typically at least *next-to-leading order* (NLO) can be calculated, as is the case for most of the generators used in this thesis. Calculations at *next-to-next-to-leading order* (NNLO) are already significantly more expensive, while N3LO (NNNLO) calculations are currently actively developed for instance by Camarda et al. or Duhr et al. [140, 141, 142].

3.2.2 Monte Carlo Generators

In most cases it is convenient to use different Monte Carlo generators for different purposes since some are specialised on specific types of calculations. Generally,

most generators simulate events with specific *Monte Carlo Event Weights* w^{MC}. The sum of these weights is the normalisation of a set of simulations. They are used to more accurately reflect the shape of the appropriate statistical distribution of a simulated process. In addition, some processes are filtered at generator level to save computational time if, for instance, only certain decay modes are of interest. If such a filter is applied, then this is corrected for in the normalisation of the simulation by multiplication of the respective efficiency ϵ_{filter}. Finally, most generators to date are not yet capable to simulate processes at high orders in QCD. However, in order to at least reflect the effect on the total normalisation going from NLO to NNLO (or from LO to NLO) in QCD, a *k-factor* k is applied, which corrects the total cross section σ to the next higher order. In total, this means any simulated event i receives the weight

$$w_i^{\text{evt}} = \frac{\mathfrak{L} \cdot \sigma \cdot k \cdot \epsilon_{\text{filter}}}{\sum_{i=1}^{N_{\text{MC events}}} w_i^{\text{MC}}}, \tag{3.1}$$

where $N_{\text{MC events}}$ is the total number of Monte Carlo events in a simulated sample and $\mathfrak{L}$ the target integrated luminosity (in case of this analysis $\mathfrak{L} = 139\,\text{fb}^{-1}$).

In order to be able to interface with other generators, a common format, the *Les Houches Event Files* [143], is used. This maximises compatibility and modularity between generators. Generators typically have a set of fundamental physical parameters as input that are either pre-set or can be tuned for accurate simulation of physical properties. They can differ between the type of program used. However, properties such as the weak mixing angle and boson masses (or equivalent replacements) are usually set in the program configuration. The following overviews provide information on the generators used in this thesis:

- PYTHIA [144] is a general-purpose event generator used to simulate high-energy particle physics interactions. It is able to compute energies and other particle properties for fundamental particles such as electrons or positrons but also for composite objects such as protons. It can be used as a stand-alone application from collisions to the hadronisation, but it can also be interfaced with other programs. Calculations in QCD and electroweak theory are performed at leading order.

- POWHEGBOX [145] is a program to calculate NLO hard scattering processes. It can be interfaced to parton shower generators such as Pythia as it is not a general-purpose generator.

- EVTGEN [146] is a generator used to calculate decays of heavy flavour particles. As such it is typically interfaced to the event generation process to simulate the decay of unstable heavy-flavoured particles.

- PHOTOS [147] is an algorithm and program used to calculate radiative corrections of quantum electrodynamical effects to any particle. As such it is typically interfaced to other generators.

- LPAIR [148] is a generator to simulate lepton pair creation in lepton-lepton, lepton-hadron or hadron-hadron interactions via two-photon processes.

- HERWIG [149] is another general-purpose generator to simulate lepton and hadron collisions. It can simulate all steps of the interaction process from the hard scattering to the decays of instable particles.

3.3 Detector Simulation

The previous section introduced simulations of interactions without the presence of a detector. This part will be discussed in the following section.

Since measurements by definition rely on detectors to record data, an accurate description of all types of processes that occur is needed. They take place not only between incident particles and the detector material but also in the signal formation, in electric noise and other real world influences. Consequently, they need to be simulated as precisely as possible to allow for a comparison between real data and simulations. At ATLAS this is done using the program `Geant 4` [150] to create a virtual representation of the detector which is used to model its response to the events that have been simulated in the event generation step.

Detector simulations are very computationally intensive due to their complexity. While a single event on one CPU in ATLAS can typically be generated within $90\,\mathrm{s}$, the detector simulation of the same event takes almost four times as long [151]. Generally, the simulation follows the steps outlined in chapter 1.2.2. First the hard scattering is simulated, then the parton shower and hadronisation as well as the underlying event. The output of this simulation is in the ATLAS `EVNT` format. This is interfaced to the Geant 4 simulation to model the detector response. First, the actual interaction of particles with the detector (stored in the ATLAS `HITS` format) is simulated, and second the detector output of these interactions is simulated and stored in the ATLAS `RDO` format [152]. The latter corresponds to the `RAW` format of the data explained in section 2.2.7. To account for multiple collisions during the same bunch crossing, two different approaches are used [153]. One approach is to specifically simulate bunch crossings with the appropriate ratio of interesting hard scattering events to pileup (i.e. mostly low energetic QCD originated) events. The second approach is to use a method called *pileup overlay* to combine the collision

of interest (i.e. the hard scattering) with specially recorded *zero-bias*, randomly triggered real data to emulate the pileup effect.

Finally, the output of the detector simulation is then treated identically to real detector output for object reconstruction, further processing and analysis.

3.3.1 Corrections

The detector simulation relies on a very detailed model of the detector and its systems, which is complemented by detailed measurements of detector properties to get the most accurate description possible. Nonetheless, it is impossible to create a perfect description of the detector. Such imperfections become apparent in dedicated analyses that aim to provide correctional factors applied to individual objects or events to resemble the actual detector response more correctly. Thus, correctional factors that have been derived are applied in the analysis of the angular coefficients and the weak mixing angle presented in this thesis. These corrections are discussed below.

Pileup The number of simultaneous collisions during a bunch crossing in ATLAS varies between each event. Measurements of the number of collisions using LUCID and the BCM show that simulated samples such as the ones used in this thesis do not reflect the actual distribution perfectly as they are generated before the data is taken and the distribution of simultaneous collisions can be assessed precisely. For this reason the distribution of simultaneous collisions is reshaped in the simulation to the actual data distribution by applying a weight w_{PU} to each event.

Efficiencies The application of selection criteria on objects that are triggered, reconstructed and identified in ATLAS is inherently done with a selection efficiency different from 100%. Since the detector simulation is not capable of delivering a detector response perfectly akin to the actual detector, minor deviations between the efficiencies in data and in simulation are expected. This is visible, for instance, in figure 2.12, where deviations between the data and the simulation are clearly apparent. These differences are corrected for by applying additional weights onto each object, called *scale factors* w_{SF}, which correct the simulated efficiencies to the ones measured from data. These scale factors are derived for the reconstruction, charge identification, object identification, isolation, track-to-vertex association and trigger efficiencies as a function of the pseudorapidity and the transverse momentum.

Impact Parameters As introduced in section 2.2.2, impact parameters are the closest approach of a track to the interaction point and can be calculated longitudinally or transversally. The resolution of this method is finite and differs between simulation and data. Thus, correctional factors are applied to simulated reconstructed objects to resemble the real efficiency more accurately.

Energy/Momentum Scale and Resolution Besides the electron energy calibration applied on data explained in the previous chapter, the muon momentum is corrected in the simulation to reflect data observations. Furthermore, electron energy responses are smeared to reflect the real resolution of the ATLAS detector.

Muon Sagitta Correction The *sagitta* of a particle track is a measure for its curvature in the magnetic field. If a track follows an arc with radius R due to the magnetic field over a length L, then the sagitta s can be approximated as $s = \frac{L^2}{8R}$ [154]. The ATLAS detector is affected by gravity effects which slightly distort its circular cross section. This is particularly noticeable in the muon system and results in deviations of the measured sagitta between positively charged and negatively charged muons [155]. A correction following recommendations of the ATLAS Muon Group is applied to data, which alleviates this distortional effect.

Part III

Measurement of the Angular Coefficients
of the Z Boson

4 Motivation and Strategy

> *Try to make sense of what you see and wonder about what makes the universe exist.*
>
> **— Stephen Hawking**

In the first chapter the general theoretical relevance of the angular coefficients of the Z boson has already been pointed out. The analysis presented in this thesis aims to present a first measurement of the full set of coefficients at $\sqrt{s} = 13\,\text{TeV}$ differentially in the Z boson rapidity and transverse momentum around its pole mass. This allows for a detailed study of their behaviour as a function of those two kinematic variables and is only possible due to the large dataset available from ATLAS during the full Run 2 amounting to approximately $139\,\text{fb}^{-1}$. It enables a precise comparison of reference calculations and subsequently potential refinements in perturbative QCD.

The outline of this analysis follows a two-staged approach. First, the data is analysed in detail and compared to predictions from Monte Carlo simulations and data-driven predictions. This is done in two channels, one using electron/positron pairs and one using muon/anti-muon pairs. To be able to accurately reflect theoretical expectations, multiple sets of Monte Carlo simulations are used to account for all background processes that contribute to detector signatures used in this measurement of the Drell-Yan signal process. These other contributions are mostly driven by the production of top quarks as well as multiple electroweak bosons resulting in two leptons in the final state. In addition, in the electron channel a small contribution from mostly low-energetic QCD dominated processes is determined using data and a so-called *fake factor method* as this contribution cannot be simulated. It accounts for signatures that involve one or two fake electrons originating from jets. The data is compared to the sum of the predictions to ensure that any deviations are understood and corrected for since they influence the shape of the Collins-Soper distributions and subsequently the angular coefficients. These comparisons are presented in different kinematic regions and also integrated over the rapidity to maximise the statistical sensitivity of the comparison.

At the same time sources of uncertainties need to be studied and understood as they are elemental to the sensitivity of the measurement. Different groups of uncertainties are identified and categorised into statistical, experimental and theoretical uncer-

tainty sources. In particular, their behaviour across different regions in phase space is studied in order to understand their potential impact on the measurement.

After establishing that data behaviour is understood and well described by the predictions, the second step is the actual statistical procedure to extract the angular coefficients from the Collins-Soper distributions $\cos\theta_{\mathrm{CS}}$ and ϕ_{CS}. This is achieved by constructing so-called *templates* that reflect the individual polynomials introduced in section 1.3.2. They are obtained by dividing the prediction by the differential cross section, which results in distributions affected by experimental effects but devoid of information of the angular coefficients. Reweighting them to the polynomials then allows for a likelihood fit of all templates in all analysis bins to result in unfolded distributions of the coefficients across the entire phase space of interest. This presentation of results is important to enable comparisons to other measurements or theoretical predictions without introducing specific experimental features. At the same time the differential cross section in the Z boson rapidity and transverse momentum is extracted as an overall normalisation. All these results reflect the high statistical accuracy possible with the large ATLAS Run 2 dataset and also serve as a baseline for future measurements of these coefficients and the weak mixing angle in particular, a study of which will be presented in chapter 8.

Notes on Contributions of the Author Analyses of the scope and complexity presented in this chapter always rely on collaborative efforts with contributions from a large number of scientists starting at the actual detector, its construction and the data taking all the way to colleagues working together at the data analysis shown here. The work presented in this chapter has been conducted by the author unless stated otherwise. However, due to the nature of collaborative work it is important to point out specific areas of focus. Firstly, the data and the simulation have been provided centrally by ATLAS as well as software such as Athena [126] and other dedicated tools related to calibrations, efficiencies etc. Two major frameworks are maintained by the "ZAi group" within the collaboration, which the author has been a part of: The `ntuplemaker_13TeV` [156] and `aidy` [157] programs built in C++ using ROOT and python are key to this work and have been developed by members of the group over numerous years.

A central aspect of the work presented in this thesis has been the co-development of these frameworks to facilitate the analysis presented in this dissertation. Within the context of this thesis these existing frameworks have been actively developed and expanded by the author. Furthermore, for the data analysis, a particular focus was placed on developing the central electron channel, the analysis of its systematic uncertainties, the data-driven estimate of QCD background contributions as well as detailed studies of kinematic and experimental features such as a detailed

understanding of correctional factors. Not explicitly discussed is additional effort spent on establishing a first understanding of an additional analysis channel using one central and one forward electron ($|\eta| > 2.5$), in particular the correction of numerous detector effects in this region. However, active development is still ongoing. The extraction of the angular coefficients utilises a custom fitting framework developed by A. Armbruster [158]. Most effort was spent on adapting the `aidy` framework to the requirements of this analysis, in particular with respect to the central electron channel, the treatment and understanding of systematic nuisance parameters in the likelihood fit both in simulation and in data fits and a close scrutiny of the results obtained.

5 Data Analysis

> *Anything can happen, in spite of what you're pretty sure should happen.*
>
> **— Richard P. Feynman**

This chapter outlines the first part of the analysis. The datasets are described and expectations that are derived from Monte Carlo simulations and data-driven methods to estimate contributions of different processes are introduced. After applying a set of selection criteria and corrections, the data is compared to the expectation in the relevant kinematic variables and in particular in angles of the Collins-Soper reference frame. Eventually, uncertainty sources are studied and broken down.

5.1 Datasets

The data used in this thesis has been taken in proton-proton collisions at the ATLAS experiment between 2015 and 2018 at a centre-of-mass energy of $\sqrt{s} = 13\,\text{TeV}$ in multiple periods. A detailed list of these datasets and the corresponding periods can be found in appendix A. The total integrated luminosity delivered by the LHC and recorded by ATLAS is shown in figure 5.1.

Differences in luminosity delivered and recorded arise from detector conditions, during which the detector is not capable of data-taking, for instance due to *dead time* of the trigger system. The integrated luminosity of $139\,\text{fb}^{-1}$ actually useable for analyses is slightly reduced due to quality criteria to ensure faultless operations of all detector parts using a *Good Runs List*, which will be explained in more detail in chapter 5.3.

The datasets have been processed centrally and were provided in the DAOD format by ATLAS according to the computing chain described in chapter 2.2.7.

5.2 Monte Carlo Simulation

Multiple sets of Monte Carlo simulations are used to compare the data to expectations. The processes of interest are labelled *signal*, while other processes are called

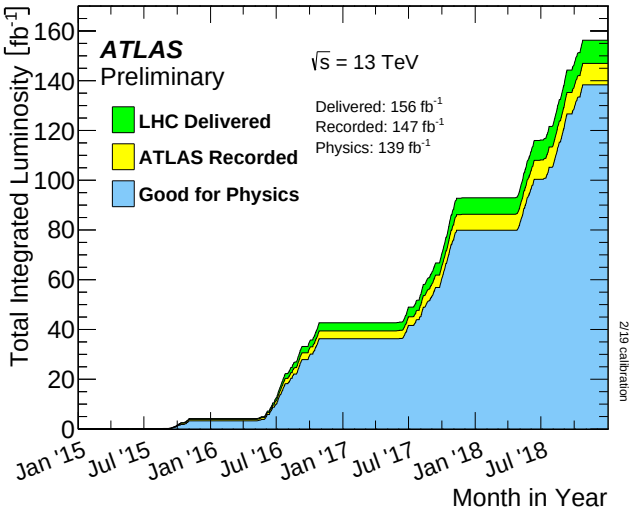


Fig. 5.1.: Integrated luminosity delivered by the LHC (green), recorded by ATLAS (yellow) and useable for analysis (blue) over the whole data-taking period [159].

background. Backgrounds need to be considered due to similar or identical final states and signatures in the detector. Some types of background processes cannot be simulated due to the divergence of the strong coupling constant at low scales and are consequently derived in a data-driven method in chapter 5.4.

The simulations have been produced centrally by ATLAS and were also provided in the DAOD format following the simulation chain described in chapter 3. A summary of the different sets of simulations is presented in table 5.1. An overview of all technical names of the simulations used can be found in the appendix in table A.2.

5.2.1 Signal Process

The dominating Drell-Yan process $pp \to Z/\gamma^* + X$, and $Z/\gamma^* \to l^+l^-$, was generated in POWHEGBOX V1 [145] with the CT10 NLO PDF [160] at NLO in α_s. The subsequent parton shower and hadronisation as well as the underlying event were simulated using PYTHIA version 8.186 [144] and the AZNLO parameter tune [161]. For the parton shower PDF set CTEQ6L1 [162] was used. The simulation was interfaced to PHOTOS v3.52 [147] for the simulation of final state radiation of the Z/γ^* decay. The decay of bottom or charm hadrons was simulated using the EVTGEN generator version v1.2.0 [146]. A complete list of the signal samples used can be found in appendix A. Since the focus of this analysis is on a fiducial region around the Z boson pole mass, the dominating process is $Z \to l^+l^-$. Consequently, in the following descriptions the signal will be denoted as Z only as it is expected to be the dominant contribution around the Z pole mass.

5.2.2 Background Processes

The Drell-Yan signal process contributes less than $\frac{1}{1000}\%$ [163] to the total cross section of a proton-proton interaction at the LHC at $\sqrt{s} = 13\,\mathrm{TeV}$, which means that other processes dominate by far. The main fraction of these interactions is filtered at trigger level already, however, still a large number of particles leave indistinguishable signal-like signatures in the detector. The event and object selection in the following chapter 5.3 efficiently suppresses these types of backgrounds, but it is ultimately limited by imperfect identification and reconstruction efficiencies, detector resolution and coverage. Nonetheless, the total contribution of these types of backgrounds is small, between 0.3% and 0.9% in the Z pole region for muons and electrons, respectively.

Overall backgrounds are categorised to be either *reducible* or *irreducible*. Reducible backgrounds are mainly caused by objects that produce a fake signal-like signature in the detector, e.g. light jets that are identified as leptons. By applying stricter identification or isolation criteria these can typically be drastically reduced. Events that contain identical final state products and potentially similar kinematic properties as the signal process are classified as irreducible backgrounds. The complete list of simulated samples used can be found in table 5.1. In the following, different types of background contributions will be discussed.

Non-fiducial Background Since this analysis aims to extract the angular coefficients in specific regions of phase space in the rapidity and transverse momentum of the Z boson, contributions of signal events that have been generated outside of the reconstructed phase space are classified as background. These contributions are caused by migration effects due to the finite detector resolution and the energy calibration of the detector. Especially at the boundaries of the chosen binning in rapidity and transverse momentum this migration leads to significant contributions as can be seen in figures 5.12 and 5.14. It can be quantified by spatially matching generator-level leptons to reconstructed leptons and evaluating whether the reconstructed fiducial phase space region aligns with the generated one or not.

Top Quark Backgrounds The production of a Top quark and an Anti-Top quark ($t\bar{t}$) is the leading contribution to Top quark production at the LHC [164]. Additionally, to a lesser degree Top quarks are also produced in association with lighter quarks or $W^{\pm}$ bosons. Since the Top quark almost exclusively decays into a Bottom quark and a $W^{\pm}$ boson, the decay of these particles can lead to real leptons in the detector. Consequently, these contributions are taken into account when comparing the data to the expectation.

Process	Generator	PDF	σ_{tot} [pb]
$Z/\gamma^* \to l^+l^-$	POWHEGBOX + PYTHIA 8	CT10nlo [160]	1901.10
$t\bar{t}$ pair	POWHEGBOX + PYTHIA 8	NNPDF23LO [166]	729.76
Single Top (tW)	POWHEGBOX + PYTHIA 8	NNPDF23LO [166]	3.29
Single Top (tq)	POWHEGBOX + PYTHIA 8	NNPDF23LO [166]	60.08
Diboson	POWHEGBOX + PYTHIA 8	CT10nlo [160]	80.02
$\gamma\gamma \to l^+l^-$ (Single Diss.)	LPAIR	N/A	2.06
$\gamma\gamma \to l^+l^-$ (Budnev)	HERWIG 7	MMHT2014lo68cl [54]	1.26
$\gamma\gamma \to l^+l^-$	PYTHIA 8	NNPDF23_QED [167]	3.58
Multijet	N/A	N/A	$> 78.40\,\text{mb}$

Tab. 5.1.: List of all processes generated using the Monte Carlo method with their respective generators, PDF sets and cross section σ_{tot} as set in the generator. Processes are generated for different lepton flavours separately and contain at least one lepton in the final state. Note that all processes use EVTGEN to more accurately reflect particle decays. An estimate of the cross section of the multijet contribution which includes dijet production, production of W bosons with jets etc. is also shown. The estimate is based on dijet production alone, which dominates the total cross section[1].

Electroweak Backgrounds Since this analysis is aimed at measuring the angular coefficients in electron and muon pairs, the production of a tau/anti-tau pair is included in the background expectation. As tau leptons can decay into lighter leptons, signal-like signatures can originate from this process. The generators used for this process are identical to the generators used for the signal simulation.

Another contribution of signal-like signatures is expected by diboson production processes. $W^{\pm}$ and Z bosons can decay not only into real charged leptons but also into quark pairs and neutrinos. This can lead to combinations of real and fake lepton signatures. Contributions from the latter are estimated in data in section 5.4.

Photon-Induced Background Quarks within the protons that partake in a collision can emit photons which carry a fraction of the proton momentum. Furthermore, since charged particles are accelerated in electric fields in the LHC photon radiation occurs. These photons can produce a Z boson that decays into a pair of leptons. The contribution of this background is expected to be very small in comparison to the signal or other background processes due to the magnitude of the expected photon PDF of the proton [165].

[1] Although the cross sections of these processes vastly dominate over all other cross sections shown here, most of their contribution is at low energies. The analysis selection presented later in the chapter very effectively eliminates these contributions by selections on lepton transverse momenta and identification. The estimate for the cross section is taken from JZ0W ATLAS simulations.

5.3 Event and Object Selections

Since the aim of this measurement relies on a very precise understanding of the data, it is paramount to carefully apply selections on the recorded events and the objects contained within to study the phase space regions of interest. These selections are designed to maximise the signal content and minimise the background contributions as well as other background contaminations from detector imperfections. The analysis is split into an *electron channel* and a *muon channel* depending on which decay products of the Z boson are studied. It is based on the ATLAS software release `AnalysisBase 21.2.188` (part of the ATLAS Athena software [126]).

5.3.1 Trigger

The trigger represents the first stage of the event selection that is applied live during the data taking process, as explained in chapter 2.2.6. Identical selections are applied on the simulations. The selection of trigger chains is aimed at maximising the number of events that are available for further processing while reducing the large number of events recorded to a subset that contains at least one (*single lepton trigger*) or two candidates (*dilepton trigger*) of real leptons. In all cases it is sufficient that one criterion is met for an event to be considered. A detailed list of the precise names of the trigger chains can be found in tables 5.2 and 5.3. Generally, to maximise the number of signal events captured by the analysis trigger thresholds are selected as low as possible. Due to hardware limitations outlined in section 2.2.6, it is not possible to select an arbitrarily low threshold, which is why the lowest single-lepton thresholds must fulfil the tightest identification criteria and are supplemented by higher trigger thresholds with subsequently looser identification (or isolation) criteria. Dilepton thresholds can typically set to lower thresholds of transverse momenta as their rate is drastically lower than single-lepton rates, due to their lower fake rate caused by misidentified background as leptons. The precise selection thresholds of the transverse momentum are chosen to be as low as possible to maximise selection efficiency while at the same time to correspond to the binning of the correctional scale factors of the trigger introduced in section 3.3.1.

In the electron channel the dilepton trigger aims at selecting pairs of electron candidates with a transverse momentum of at least $12\,\mathrm{GeV}$ to $17\,\mathrm{GeV}$, depending on the year, which pass the *loose* identification criteria at trigger level. The single lepton trigger requires a transverse momentum of at least $24\,\mathrm{GeV}$ or $26\,\mathrm{GeV}$, where at least the *medium* or *tight* identification criteria have to be fulfilled, respectively. Supplementing higher trigger thresholds aims to maximise the number of available events.

Muon signatures can be distinguished more clearly from other particles due to their distinct signature in the tracking and muon systems. This is exploited by ATLAS in the construction by surrounding the inner detector and the calorimeters with the muon chambers, and it allows for lower thresholds in muon candidate transverse momenta in the trigger. The dilepton trigger thresholds in transverse momentum are at $10\,\mathrm{GeV}$ and $14\,\mathrm{GeV}$ in different data taking periods, but they also allow for asymmetric thresholds of $18/22\,\mathrm{GeV}$ and $8\,\mathrm{GeV}$, respectively. The single lepton trigger requires transverse momenta of at least $20\,\mathrm{GeV}$ to $26\,\mathrm{GeV}$ with *loose* and *medium* isolation criteria, respectively. Subsequently higher thresholds with looser requirements supplement the trigger selection for the largest amount of data possible.

5.3.2 Data Quality

As explained in chapter 2.2.5, each cycle of data taking is split into luminosity blocks. If all detector parts relevant to analyses are running during a luminosity block, it will be stored in the so-called *Good Runs List*. All events in this analysis must pass this requirement, following this list[2]. Additional quality criteria include error-free states of the calorimeters and tracking systems. Finally, only events in which at least one primary vertex has been successfully reconstructed are considered for further analysis. The effect of these ATLAS standard requirements can be seen in table 5.4 and 5.5.

5.3.3 Preselection

The STDM4 DAOD format that is used to create the ROOT trees relies on a preselection to reduce the number of events that require processing. Specifically, to pass the STDM4 selection, an event must contain at least one central ($|\eta| < 2.6$) lepton that passes basic identification criteria or pass a loose single-lepton trigger[3]. The reconstructed transverse momentum is required to be larger than $p_T > 15\,\mathrm{GeV}$ or $p_T > 20\,\mathrm{GeV}$ for electrons or muons, respectively.

[2] 2018: `data18_13TeV.periodAllYear_DetStatus-v102-pro22-04_Unknown_PHYS_StandardGRL_All_Good_25ns_Triggerno17e33prim.xml`,
2017: `data17_13TeV.periodAllYear_DetStatus-v99-pro22-01_Unknown_PHYS_StandardGRL_All_Good_25ns_Triggerno17e33prim.xml`,
2016: `data16_13TeV.periodAllYear_DetStatus-v89-pro21-01_DQDefects-00-02-04_PHYS_StandardGRL_All_Good_25ns.xml`,
2015: `data15_13TeV/20170619/data15_13TeV.periodAllYear_DetStatus-v89-pro21-02_Unknown_PHYS_StandardGRL_All_Good_25ns.xml`

[3] A table of these trigger chains can be found in appendix B.

5.3.4 Electrons

To pass the selections in the electron channel, in addition to the trigger and the preselection requirements electron candidates must pass the *medium* identification criterion. These candidates must pass additional object quality criteria that ensure electrons are only selected if the detector subsection they are located in did not malfunction during a particular run, in particular to remove objects from faulty read-out boards and noise bursts in calorimeter cells.

The kinematic selections on electron candidates are designed to maximise the acceptance and the efficiencies of the trigger, the reconstruction and the identification. Consequently, the thresholds of transverse momenta are $1\,\mathrm{GeV}$ above the trigger threshold of the single-electron High-Level Trigger, which corresponds to thresholds of $21\,\mathrm{GeV}$, $24\,\mathrm{GeV}$ and $27\,\mathrm{GeV}$ matching the binning of the trigger scale factors explained in section 3.3.1. Table 5.2 presents the detailed list of thresholds used. Each candidate has to be spatially matched to the trigger object that fired the trigger chain for it to be passed on[4]. In addition, the pseudorapidity of electron candidates must be in $|\eta| < 2.47$, which corresponds to the coverage of the tracking system. The region of $1.37 < |\eta| < 1.52$ is called the *crack region* in the calorimeter since it contains cabling and other infrastructure for the detector and thus only has a degraded energy response. For this reason this region is removed as well.

Finally, the tracks associated to the electron candidate must fulfil two criteria with respect to their impact parameter. The absolute value of the longitudinal impact parameter[5] z_0 projected onto the beam axis is required to be smaller than $0.5\,\mathrm{mm}$ and additionally, the significance of the transversal impact parameter[6] must be smaller than 5 to ensure the correct association of tracks to electron candidates.

[4] This is to ensure trigger scale factors can be applied correctly, i.e. knowing which trigger chain was executed.
[5] This is the closest approach of a track to a vertex in the longitudinal direction.
[6] The significance is defined as the measured value d_0 divided by its spread $\sigma(d_0)$.

Year	Single-electron trigger ($\text{SLT}_{\text{lead,sublead}}$)	Di-electron trigger (DLT)	p_T[GeV] thresholds	
			$\{\text{lead}, \text{sublead}\}$	Trigger requirement
2015	HLT_e24_lhmedium_L1EM20VH $\vee$ HLT_e60_lhmedium $\vee$ HLT_e120_lhloose	HLT_2e12_lhloose_L12EM10VH	$\{> 25, > 25\}$ $\{> 25, [21; 25]\}$ $\{[21; 25], [21; 25]\}$	$\text{SLT}_{\text{lead}} \vee \text{SLT}_{\text{sublead}} \vee$ DLT $\text{SLT}_{\text{lead}} \vee$ DLT DLT
			$\{\text{lead}, \text{sublead}\}$	Trigger requirement
2016	HLT_e26_lhtight_nod0_ivarloose $\vee$ HLT_e60_lhmedium_nod0 $\vee$ HLT_e140_lhloose_nod0	HLT_2e17_lhvloose_nod0	$\{> 27, > 27\}$ $\{> 27, [21; 27]\}$ $\{[21; 27], [21; 27]\}$	$\text{SLT}_{\text{lead}} \vee \text{SLT}_{\text{sublead}} \vee$ DLT $\text{SLT}_{\text{lead}} \vee$ DLT DLT
			$\{\text{lead}, \text{sublead}\}$	Trigger requirement
2017	HLT_e26_lhtight_nod0_ivarloose $\vee$ HLT_e60_lhmedium_nod0 $\vee$ HLT_e140_lhloose_nod0	DLT17: HLT_2e17_lhvloose_nod0_L12EM15VHI (skipped in Period B5 to B8) $\vee$ DLT24: HLT_2e24_lhvloose_nod0	$\{> 27, > 27\}$ $\{> 27, [25; 27]\}$ Else if $\{> 21, > 21\}$	$\text{SLT}_{\text{lead}} \vee \text{SLT}_{\text{sublead}} \vee$ DLT24 $\text{SLT}_{\text{lead}} \vee$ DLT24 DLT17
			$\{\text{lead}, \text{sublead}\}$	Trigger requirement
2018	HLT_e26_lhtight_nod0_ivarloose $\vee$ HLT_e60_lhmedium_nod0 $\vee$ HLT_e140_lhloose_nod0	DLT17: HLT_2e17_lhvloose_nod0_L12EM15VHI $\vee$ DLT24: HLT_2e24_lhvloose_nod0	$\{> 27, > 27\}$ $\{> 27, [25; 27]\}$ Else if $\{> 21, > 21\}$	$\text{SLT}_{\text{lead}} \vee \text{SLT}_{\text{sublead}} \vee$ DLT24 $\text{SLT}_{\text{lead}} \vee$ DLT24 DLT17

Tab. 5.2.: Selection of transverse momenta p_T in the electron channel, split into the leading and subleading candidates with respect to the trigger chains that have been fulfilled. The subscripts indicate which electron candidate fulfilled the single-electron trigger (SLT), while DLT24 and DLT17 differentiate which di-electron trigger has been fulfilled.

5.3.5 Muons

The selection in the muon channel is very similar to the selection in the electron channel. Firstly, after passing the trigger and the preselection requirements muon candidates must fulfil the *medium* quality criterion and fulfil the *FixedCutLoose* isolation working point.

Closely aligned with the method used to select the electron transverse momentum, muons must also pass different thresholds of transverse momentum at least $1\,\mathrm{GeV}$ above the single-muon trigger threshold depending on which trigger chain has been passed. This results in thresholds of $20\,\mathrm{GeV}$, $21\,\mathrm{GeV}$, $23\,\mathrm{GeV}$ and $27.5\,\mathrm{GeV}$ matching the binning of the trigger scale factors explained in section 3.3.1. A detailed list of trigger chains and the corresponding thresholds can be found in table 5.3. Additionally, a spatial matching between the objects that triggered specific chains and reconstructed muon candidates has to be fulfilled as well. Furthermore, pseudorapidities of up to $|\eta| < 2.4$ are accepted, corresponding to the coverage of the muon spectrometer. The highest pseudorapidity region is excluded, for which precision descriptions in the simulation were not available at the time of writing this thesis.

Lastly, to ensure the correct association of tracks to vertices that have been identified, the significance of the transverse impact parameter has to be smaller than 3 and the longitudinal impact parameter projected onto the beam axis is required to be smaller than $0.5\,\mathrm{mm}$ for muons in $|\eta| < 2.5$.

Year	Single-muon trigger (SLT)	Di-muon trigger (DLT)	Transverse Momentum [GeV]	
			$\{\text{lead}, \text{sublead}\}$	Trigger requirement
2015	`HLT_mu20_iloose_L1MU15` $\vee$ `HLT_mu40`	`HLT_mu18_mu8noL1` $\vee$ `HLT_2mu10`	$\{> 21, > 21\}$	$\text{SLT}_{\text{lead}} \vee \text{SLT}_{\text{sublead}}$
			$\{> 21, [20; 21]\}$	SLT_{lead}
			$\{[20; 21], [20; 21]\}$	DLT
			$\{\text{lead}, \text{sublead}\}$	Trigger requirement
2016/ 2017/ 2018	`HLT_mu26_ivarmedium` $\vee$ `HLT_mu50`	DLT22: `HLT_mu22_mu8noL1` $\vee$ DLT14: `HLT_2mu14`	$\{> 27.5, > 27.5\}$	$\text{SLT}_{\text{lead}} \vee \text{SLT}_{\text{sublead}}$
			$\{> 27.5, [20; 27.5]\}$	SLT_{lead}
			$\{[23; 27.5], [20; 27.5]\}$	DLT22
			$\{[20; 23], [20; 23]\}$	DLT14

Tab. 5.3.: Selection of transverse momenta p_T in the muon channel, split into the leading and subleading candidates with respect to the trigger chains that have been fulfilled. The subscripts indicate which muon candidate fulfilled the single-muon trigger (SLT), while DLT22 and DLT14 differentiate which di-muon trigger has been fulfilled.

5.3.6 Pair Selection and Binning

For the purpose of this analysis at least two leptons must be found in an event. If more than two are reconstructed and pass all selection criteria, then the two candidates with the largest transverse momenta are chosen. These leptons must possess opposite electric charges.

This measurement is focussed on the region around the Z boson pole mass. If not explicitly stated otherwise, only events where the reconstructed invariant mass m_{ll} of the lepton pair is between $80\,\mathrm{GeV}$ and $102\,\mathrm{GeV}$ are considered. Furthermore, in the interest of comparability the upper boundary of the rapidity of the reconstructed Z boson is set to 2.4. As indicated in figure 5.2, this does not reduce the acceptance of the analysis in a noticeable way. The transverse momentum and the rapidity of the Z boson are also split into individual bins for the measurement. This will be discussed in section 6.1.1.

5.3.7 Selection Acceptance and Efficiency

It is useful to illustrate how the necessary selections reduce the number of events that are expected to be captured in the electron and the muon channels. This is done by comparing the simulated number of events in the full phase space in total to the number of events that pass all selections.

Tables 5.4 and 5.5 highlight the effects of the different selection criteria on the signal and background simulations[7] as well as the data in the rapidity integrated signal region. The simulation is normalised to the integrated luminosity of this analysis, i.e.$139\,\mathrm{fb}^{-1}$. Studying the two tables in detail is instructive to understand the effects of each selection step on data, signal and background simulation. The order of some selections (for instance **Lepton Kinematic** and **Lepton ID**) is chosen deliberately for technical reasons[8], but it does not affect the number of events and objects selected overall.

- **Initial** represents the total number of data events available in the STDM4 format used for this analysis.

[7] Note that the differences between the electron and muon channels in the first three selection steps are due to the usage of different simulated samples per flavour.

[8] Specifically, enforcing a loose identification requirement already reduces the number of events drastically and thus results in smaller files which can be used for exploratory studies.

- **Good Runs List (GRL)** reflects a filter of events included in runs that can be used for analyses, defined by accelerator and detector conditions. By definition the simulation is not affected by this.

- **Data Quality** includes all criteria outlined in section 5.3.2 to ensure high quality data. The simulation does not include "bad quality" data and as such is not affected by this step.

- **Two Leptons** is the selection step where at least two leptons are required to be reconstructed in events selected. This requirement affects the background simulation and the data most strongly, both of which are dominated by contributions from processes that create one lepton at most, but also fake leptons. The signal simulation always contains two real leptons and thus is only reduced due to limitations of acceptance and efficiency of the experiment.

- **Lepton Kinematic** represents stricter quality requirements on the leptons and the respective detector regions they are located in. Additionally, at this stage the trigger and transverse momentum selections (as well as the trigger matching) outlined in tables 5.2 and 5.3 are applied. Finally, at least the loose identification as well as the pseudorapidity requirements must be fulfilled by each lepton candidate. Expectedly, the data and background simulations (both of which contain mostly low energetic objects) are mostly affected by this and are reduced by more than one order of magnitude, while the signal is less strongly affected, due to its kinematic distribution around the Z boson pole.

- **Mass/Rapidity Window** is the actual selection of dilepton properties. The mass m_{ll} is required to be around the Z boson pole mass $80\,\mathrm{GeV} < m_{ll} < 102\,\mathrm{GeV}$ and the rapidity y_{ll} must be $|y_{ll}| < 2.4$. This affects the background simulation the most as its mass distribution in particular is independent of the Z boson mass and is thus reduced by almost an order of magnitude again.

- **Lepton ID** enforces the medium identification criteria outlined before to reduce potential fake lepton contributions as efficiently as possible. Its effect is visible in both data and simulation reflecting the removal of fake contributions (in data and background simulation) but also signal contributions that only fulfil the loose identification.

- **Opposite Sign** includes the requirement that the lepton candidates selected possess opposite electric charges as expected from a Z boson decay. This is to remove any events containing a fake and a real lepton candidate as well as background contributions, for instance from two W bosons carrying the same charge and decaying leptonically. As the electron channel is more affected

Selection	Event cutflow Data	Z/γ^*	Top + EW
Initial	555.3147×10^7	27.1239×10^7	935.8502×10^5
GRL	543.9675×10^7	27.1239×10^7	935.8502×10^5
Data Quality	543.5868×10^7	27.1239×10^7	935.8501×10^5
Two Leptons	138.2567×10^7	14.8822×10^7	292.1731×10^5
Lepton Kinematic	9.2496×10^7	8.4926×10^7	15.2340×10^5
Mass/Rapidity Window	7.9036×10^7	7.6365×10^7	3.3916×10^5
Lepton ID	7.5809×10^7	6.9521×10^7	3.0947×10^5
Opposite Sign	6.0420×10^7	5.7436×10^7	2.1615×10^5
Fake Removal	6.0420×10^7	5.7436×10^7	2.1483×10^5

Tab. 5.4.: Numbers of events in the electron channel after applying each selection step for $80\,\text{GeV} < m_{ll} < 102\,\text{GeV}$ and $0 < |y_{ll}| < 2.4$. Simulated events are scaled to $\mathfrak{L} = 139\,\text{fb}^{-1}$.

by potential fake contributions, this has a more significant impact than in the muon channel, where in the signal and the data the effect is a reduction of fewer than 10^4 events.

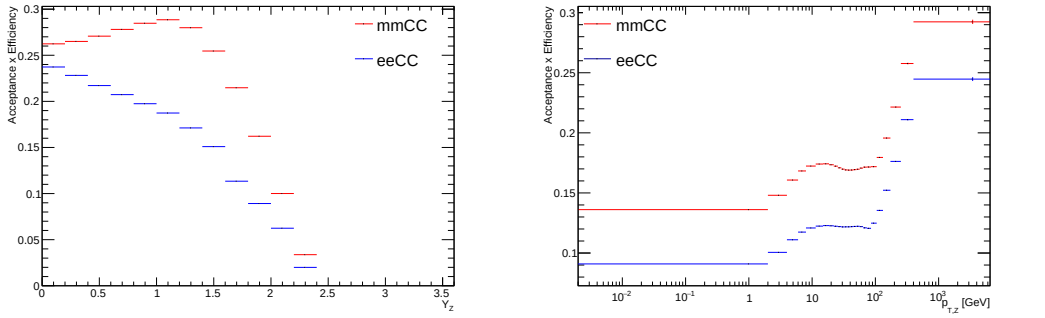
- **Fake Removal** finally represents a step where reconstructed objects in the simulation are spatially matched to their generator-level lepton counterparts to ensure the selection of true lepton candidates only. As such this step cannot be applied to data. This requirement ensures the removal of any residual fake contributions in both channels and in the signal and background contributions. This is important to estimate fake contributions in the electron channel in section 5.4 to avoid double-counting of fake objects.

It can be seen that the selections overall expectedly reduce the background and thus the data more drastically than the signal. Comparing the numbers of expected events to the number of observed events still exhibits a difference outside of statistical fluctuations. While part of this is expected due to uncertainties in the luminosity and the precision of the simulation, a fraction of this difference can be explained by multijet contributions which will be derived from data in the next section.

Additionally, figure 5.2 illustrates the product of acceptance and efficiency in both channels across the two dilepton properties of interest. Additional distributions of the acceptance and the efficiency alone can be found in appendix C. This parameter illustrates which fraction of $Z \to l^+l^-$ events produced in ATLAS are captured by this analysis. The dominant reason for values far below 100% is the acceptance of the detector, both spatially by its geometric coverage and technically by limitations of transverse momenta that can be resolved. The efficiencies of the reconstruction, identification and other analysis aspects individually are high (typically above 90%).

Selection	Event cutflow Data	Z/γ^*	Top + EW
Initial	555.3147×10^7	27.3266×10^7	944.7909×10^5
GRL	543.9675×10^7	27.3266×10^7	944.7909×10^5
Data Quality	543.5360×10^7	27.3266×10^7	944.7909×10^5
Two Leptons	137.9426×10^7	11.9647×10^7	297.3479×10^5
Lepton Kinematics	12.5750×10^7	10.8977×10^7	25.7151×10^5
Mass/Rapidity Window	9.3571×10^7	9.0248×10^7	3.1394×10^5
Lepton ID	8.4071×10^7	8.1605×10^7	2.7797×10^5
Opposite Sign	8.4066×10^7	8.1605×10^7	2.7566×10^5
Fake Removal	8.4066×10^7	8.1592×10^7	2.6679×10^5

Tab. 5.5.: Numbers of events in the muon channel after applying each selection step for $80\,\text{GeV} < m_{ll} < 102\,\text{GeV}$ and $0 < |y_{ll}| < 2.4$. Simulated events are scaled to $\mathfrak{L} = 139\,\text{fb}^{-1}$



(a) Acceptance × Efficiency as a function of the Z boson rapidity.

(b) Acceptance × Efficiency as a function of the Z boson transverse momentum.

Fig. 5.2.: Product of acceptance and efficiency in different dilepton variables for both analysis channels. The shapes of these distributions can be derived from the underlying kinematic distributions and constraints by the detector.

However, when multiplied they decrease the total number of events available for analysis noticeably. The difference between channels is solely driven by different efficiencies as the acceptance is identical due to identical kinematic regions under consideration, i.e. dilepton mass rapidity and transverse momentum.

Importantly, figure 5.2 illustrates an overall higher product of acceptance and efficiency for muons, which results from the higher efficiency in identification and reconstruction due to their distinct signatures in the detector compared to electrons as well as their lower limit on muon p_T which increases its selection efficiency. The electron channel also loses some efficiency because of the crack region, which the muons are not affected by. Overall, this is also reflected in their kinematic distributions in section 5.6, where the pseudorapidity is slightly less steeply falling for muons when compared to electrons.

5.4 Data-driven Multijet Background Estimate

As explained in the previous chapters, background contributions including one or two *fake leptons* are called *multijet background*. Such fake leptons are typically decay products from short-lived hadrons or charged hadrons that are mistakenly identified as leptons, but also leptons from photon conversions within hadronic jets. Since perturbative QCD calculations break down at lower energy scales, a data-driven method needs to be employed for accurate predictions. Overall the total contribution to the analysis is expected to be small (below 0.1% in the Z peak). The approaches taken in the electron channel and muon channel differ since fake muons occur less frequently due to their signature and the isolation criteria applied. Consequently, fake contributions in the muon channel can be disregarded for this measurement [68].

5.4.1 Methodology

To estimate contributions of QCD background in the electron channel, a *fake factor* method is employed.

The fake factor method is built on the assumption that the ratio between multijet contributions passing or failing certain identification criteria is identical in the pole region of the Z boson and in the background-enriched mass side bands[9], which are defined as $m_{ll} < 70\,\mathrm{GeV}$ and $m_{ll} > 125\,\mathrm{GeV}$ on either side. This allows to define multiple control regions to estimate the multijet contributions in the pole region. A precise definition of the assumptions and methodology is given below.

Signal and Control Regions In order to estimate the contribution of multijet events to the analysis region of interest, also called *signal region*, defined by the selections explained in chapter 5.3, it is necessary to define additional, orthogonal regions, called *control regions*. This is to avoid biasing the measurement by deriving a background estimate from the same region of interest that is later used in the extraction. The fundamental selections of the signal region are also applied in four additional control regions, with the exception of the mass window and the identification criteria. A conceptual overview of the four regions in total is given in figure 5.3. Since each electron signature individually could be falsely identified as electron candidate, it is necessary to evaluate each candidate individually with respect to the fraction of fake candidates.

[9] The reason for this is that electron identification efficiencies depend on kinematic properties of a single electron. Two electron candidates where one or both are fake are uncorrelated in their kinematic properties. Consequently, the *fake efficiency* ϵ_f can be assumed to be approximately constant across the invariant mass spectrum.

As events after selections in the data and simulation most dominantly have been triggered by one of the single-lepton triggers (less than 4% have been exclusively triggered by a dilepton trigger) there is an inherent bias per event. The electron candidate that caused the trigger to fire must fulfil stronger identification criteria compared to a second electron candidate in the event which must only fulfil a *very loose* identification criterion. Consequently, it is more likely for the electron candidate that has not been triggered to be fake. For this reason events are split using the single-lepton trigger requirement[10]. Figure 5.3 depicts the requirements in each of the four control regions. *On pole* and *off pole* refer to the dilepton mass of the electron pair to be either within $70\,\mathrm{GeV}$ to $125\,\mathrm{GeV}$ or outside of this mass window, respectively. *ID* refers to the fulfilment of the *medium* identification criterion used in the signal region, while *notID* refers to the fulfilment of the *anti-ID* criteria: The *medium* identification criterion must be failed and additional isolation criteria[11] must be failed to maximise the fake contributions. Crucially, the electron candidate that has not been triggered must always fulfil the *anti-ID* criteria.

Fake Factor Utilising the definition of multiple control regions above, it is possible to determine the contribution of multijet events in each region separately for each lepton $i \in \{1, 2\}$:

$$\begin{aligned} N_i^{\mathrm{MJ}}(\mathrm{CR}_{\mathrm{ID,On}}) &= N_i^{\mathrm{data}}(\mathrm{CR}_{\mathrm{ID,On}}) - \mu_i \cdot N_i^{\mathrm{real}}(\mathrm{CR}_{\mathrm{ID,On}}) \\ N_i^{\mathrm{MJ}}(\mathrm{CR}_{\mathrm{ID,Off}}) &= N_i^{\mathrm{data}}(\mathrm{CR}_{\mathrm{ID,Off}}) - \mu_i \cdot N_i^{\mathrm{real}}(\mathrm{CR}_{\mathrm{ID,Off}}) \\ N_i^{\mathrm{MJ}}(\mathrm{CR}_{\mathrm{notID,On}}) &= N_i^{\mathrm{data}}(\mathrm{CR}_{\mathrm{notID,On}}) - \mu_i \cdot N_i^{\mathrm{real}}(\mathrm{CR}_{\mathrm{notID,On}}) \\ N_i^{\mathrm{MJ}}(\mathrm{CR}_{\mathrm{notID,Off}}) &= N_i^{\mathrm{data}}(\mathrm{CR}_{\mathrm{notID,Off}}) - \mu_i \cdot N_i^{\mathrm{real}}(\mathrm{CR}_{\mathrm{notID,Off}}) \end{aligned}, \tag{5.1}$$

where N_i^{MJ} is the number of estimated multijet events, N_i^{data} the number of data events and N_i^{real} the number of events with only real leptons (taken from the simulations of signal and background) in each control region *CR* defined by on pole (*On*) or off pole (*Off*) dilepton masses and whether the lepton i that did not pass the single lepton trigger passed the medium identification criterion (*ID*) or the anti-ID criteria (*notID*). For multiple reasons (as discussed in section 5.3.7) the normalisation between data and simulation is expected to be slightly different. Consequently, the common normalisation factor μ_i is introduced. The foundational assumption of the fake factor method is that the ratio of multijet events that pass the

[10] The comparatively small fraction of events which have been selected *exclusively* by a dilepton trigger are disregareded in this procedure due to their small number and an even lower fake content (since the two leptons must fulfil specific ID criteria at trigger level already).

[11] Specifically, isolation in tracks and calorimeter energy deposits is vetoed by requiring the ratio of the reconstructed transverse momentum within a cone of $\Delta R = \sqrt{\Delta\phi^2 + \Delta\eta^2} = 0.2$ around a candidate to their p_T to be smaller than 0.14. Furthermore, the ratio of transverse energy $E_T = \sqrt{m^2 + p_T^2}$ deposited in the calorimeters around the candidate to their transverse energy must be smaller than 0.2. Both values have been studied and found to strike an appropriate balance between signal and fake content.

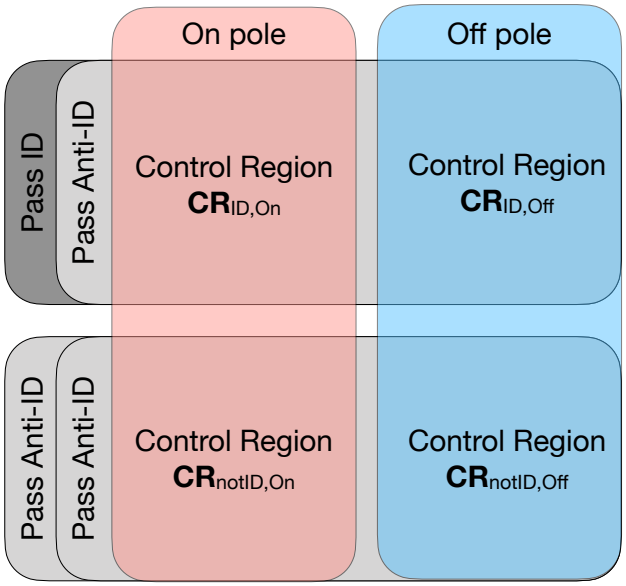


Fig. 5.3.: Schematic overview of the different regions used to determine the fake factors and their respective selection criteria. The *on pole* and *off pole* requirements are determined by the dilepton mass of the electron pair in an event. In contrast, the *pass ID* and *pass anti-ID* requirements are applied to the lepton of interest individually, while the second lepton must always fulfil the *pass anti-ID* requirement.

identification criteria to the number of multijet events that pass the anti-ID criteria is identical in on pole and off pole events:

$$\frac{N_i^{\mathrm{MJ}}(\mathrm{CR_{ID,On}})}{N_i^{\mathrm{MJ}}(\mathrm{CR_{notID,On}})} = \frac{N_i^{\mathrm{MJ}}(\mathrm{CR_{ID,Off}})}{N_i^{\mathrm{MJ}}(\mathrm{CR_{notID,Off}})}. \tag{5.2}$$

Utilising this relation the equation system can be solved for the number of multijet events in each region $N_i^{\mathrm{MJ}}(\mathrm{CR_{region}})$, where

$$\text{"region"} \in \{\text{"ID, On"}, \text{"ID, Off"}, \text{"notID, On"}, \text{"notID, Off"}\}. \tag{5.3}$$

The normalisation is denoted as μ_i and the fake factors f_i for each electron candidate are defined as

$$f_i = \frac{N_i^{\mathrm{MJ}}(\mathrm{CR_{ID,Off}})}{N_i^{\mathrm{MJ}}(\mathrm{CR_{notID,Off}})}. \tag{5.4}$$

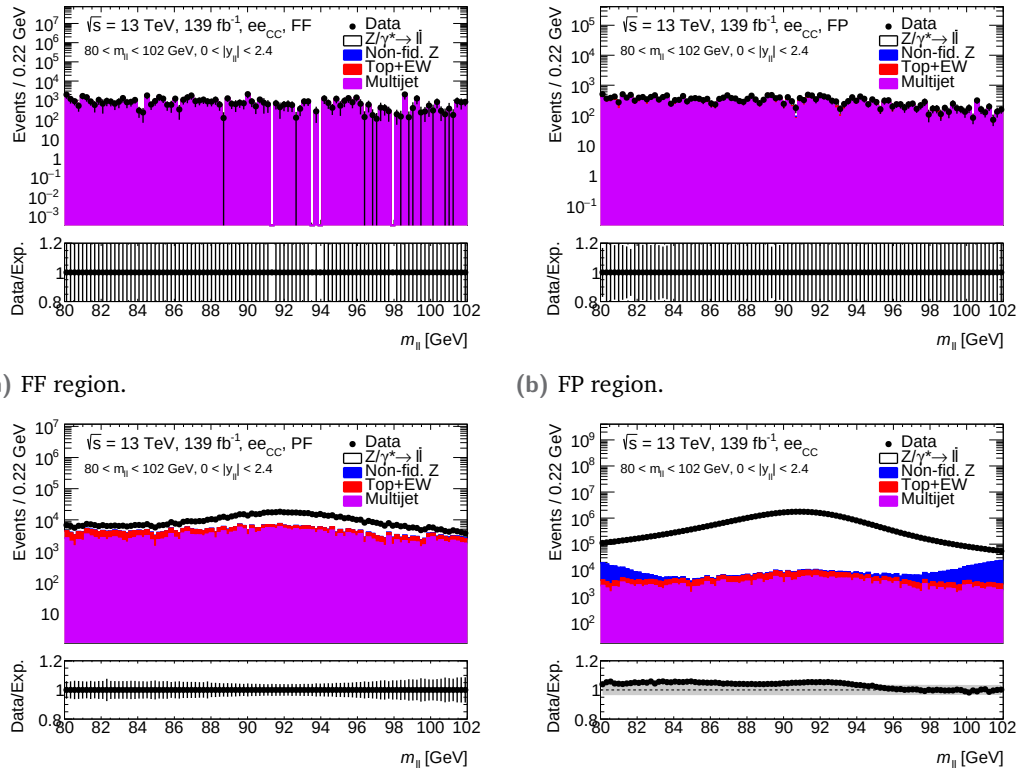
Fake Estimation To estimate the contribution of fake electrons to the signal region, it is necessary to determine all individual combinations of real and fake electrons. Specifically, aside from the signal region *SR* where both electrons are assumed to be real, contributions from regions where one or both electrons are fake are estimated using the previously determined fake factor

$$\begin{aligned}
\hat{N}^{\mathrm{data}}(\mathrm{SR}) &= N^{\mathrm{data}}(\mathrm{SR}) - f_1 \cdot N^{\mathrm{data}}(\mathrm{FP}) - f_2 \cdot N^{\mathrm{data}}(\mathrm{PF}) + f_1 \cdot f_2 \cdot N^{\mathrm{data}}(\mathrm{FF}) \\
\hat{N}^{\mathrm{real}}(\mathrm{SR}) &= N^{\mathrm{real}}(\mathrm{SR}) - f_1 \cdot N^{\mathrm{real}}(\mathrm{FP}) - f_2 \cdot N^{\mathrm{real}}(\mathrm{PF}) + f_1 \cdot f_2 \cdot N^{\mathrm{real}}(\mathrm{FF}).
\end{aligned} \tag{5.5}$$

In these equations $\hat{N}^{\mathrm{data}}(\mathrm{SR})$ and $\hat{N}^{\mathrm{real}}(\mathrm{SR})$ denote the fake subtracted data and simulation in the signal region. N^{data} and N^{real} denote the number of data and simulated events for each different category of event where either both leptons passed the anti-ID criteria (FF) or one of them passed the anti-ID and the other one the ID criteria (FP and PF). Note that each contribution is subtracted from the signal region. In particular the contribution from two fakes (FF) also needs to be subtracted from the contributions of single-fake events (FP and PF) to avoid double counting. Finally, the ratio of the fake subtracted data and signal $\hat{\mu} = \frac{\hat{N}^{\mathrm{data}}}{\hat{N}^{\mathrm{real}}}$ is used to normalise the signal in the subtraction from data to get an accurate estimate of the different fake contributions:

$$\begin{aligned}
N^{\mathrm{MJ}}(\mathrm{FF}) &= N^{\mathrm{data}}(\mathrm{FF}) - \hat{\mu} \cdot N^{\mathrm{real}}(\mathrm{FF}) \\
N^{\mathrm{MJ}}(\mathrm{PF}) &= N^{\mathrm{data}}(\mathrm{PF}) - \hat{\mu} \cdot N^{\mathrm{real}}(\mathrm{PF}) - N^{\mathrm{MJ}}(\mathrm{FF}) \\
N^{\mathrm{MJ}}(\mathrm{FP}) &= N^{\mathrm{data}}(\mathrm{FP}) - \hat{\mu} \cdot N^{\mathrm{real}}(\mathrm{FP}) - N^{\mathrm{MJ}}(\mathrm{FF}) \\
N^{\mathrm{MJ}}(\mathrm{SR}) &= N^{\mathrm{MJ}}(\mathrm{PF}) + N^{\mathrm{MJ}}(\mathrm{FP}) + N^{\mathrm{MJ}}(\mathrm{FF})
\end{aligned} \tag{5.6}$$

Each source of multijet events is calculated separately as $N^{\mathrm{MJ}}(\mathrm{permutation})$ removing double counting as before. The final estimate of multijet contributions to the



(a) FF region.

(b) FP region.

(c) PF region.

(d) Signal region.

Fig. 5.4.: Fake contribution in the four different regions used for the estimate. Coloured histograms are stacked and data is shown in black. The ratio of data and expectation (simulation and multijet estimate) is shown below. Note that in all regions except the signal region this is 1 by design. The signal region includes (statistical and systematic) uncertainties in the grey band.

signal region $N^{\mathrm{MJ}}(\mathrm{SR})$ can then be determined as the sum of each permutation. This is done for each bin individually. The mass distributions in different regions are depicted in figure 5.4 (only showing statistical uncertainties). By construction the data agrees perfectly with the sum of the simulated predictions and the multijet estimate in the FF, FP and PF regions as the multijet is extracted by the subtraction of the normalised true electrons from the data. The agreement between data and expectation (in particular the deviation from unity in the ratio) in the signal region will be discussed in detail in section 5.6. In the FF and FP regions the distributions are dominated by the multijet contributions. However, the PF region also exhibits a sizeable signal contribution as it contains true electrons that pass the single lepton trigger requirements. Due to the small fraction of events containing one or more fake electron candidates statistical fluctuations are significant. To avoid unphysical negative multijet contributions by statistical fluctuations in one of the control regions where the simulation might exceed the data, a lower limit of 0 is enforced, as visible for instance in some bins of the FF region in figure 5.4.

5.4.2 Estimate Results

The resulting factors are determined for each bin in the analysis. Figure 5.5 presents the factors as a function of the dilepton transverse momentum. The fake factors are determined in coarse bins in η and p_T of electron candidates as fake contributions are not expected to vary in a fine granularity. The figure presented illustrates this in showing the fake factors for different bins in electron η.

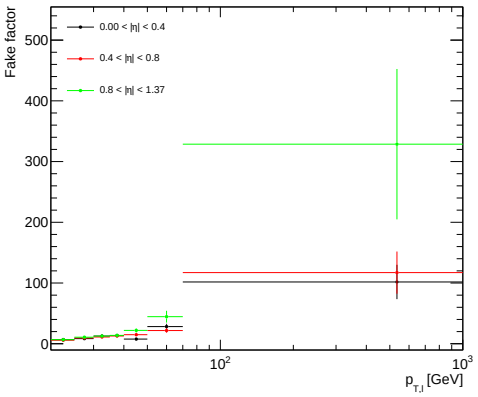
It is clearly visible that the trigger affects the overall fake factor dramatically. The fake factor determined for the electron which has been triggered is steeply rising towards higher transverse momenta of the lepton as the fraction of electrons passing the anti-ID criteria (and as such failing the identification criteria) decreases dramatically. At the same time the fake factor for the electron which has not been triggered is falling towards higher transverse momenta since objects failing electron identification and isolation criteria at higher transverse momenta are much more likely to be a jet. While some fluctuations can be observed for different regions in η in the detector, the overall behaviour is identical. Some bins are empty at high momenta for statistical reasons. In these edge cases no multijet contribution is estimated.

The uncertainties depicted in figure 5.5 correspond to the statistical uncertainties only. As the multijet contribution to the overall analysis is very small, a detailed study of individual uncertainty sources of the estimate does not contribute in a meaningful way to the overall result given that the statistical uncertainties cover minor variations in selection thresholds for different regions. Statistical fluctuations in the estimate are inherently large in sparsely populated kinematic regions and decrease in the most populated ones. The shapes and distributions of the multijet will be discussed in section 5.6.

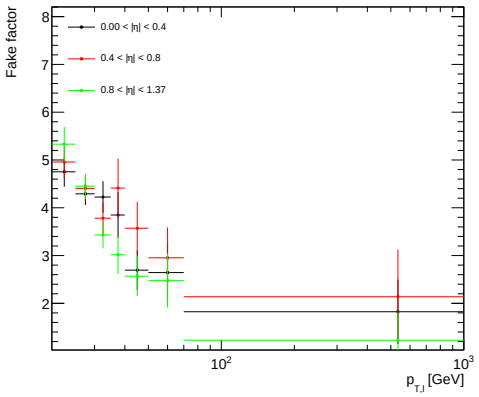
In the signal region used for this analysis, i.e. within $80\,\mathrm{GeV} < m_{ll} < 102\,\mathrm{GeV}$ and $|y_{ll}| < 2.4$ the total number of multijet events is estimated to 303612 ± 6449 (considering propagated statistical uncertainties only), which is about 0.5% of all data events passing the final selection. In individual bins the uncertainty increases drastically from 2% in the full signal region up to 250% in the most sparsely populated analysis bins.

5.5 Uncertainties

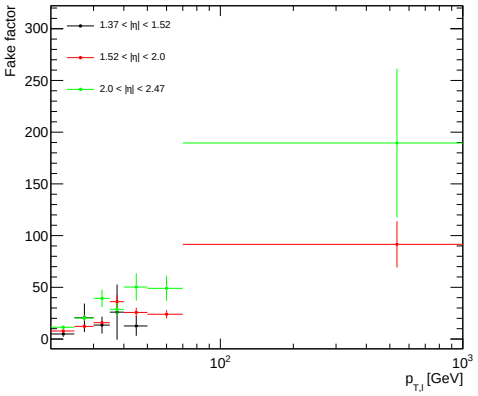
Naturally, the measurements performed in this thesis are affected by uncertainties. They can be broadly categorised as *statistical*, *experimental* and *theory* uncertainties depending on their origin. Below there is an overview and a discussion of these



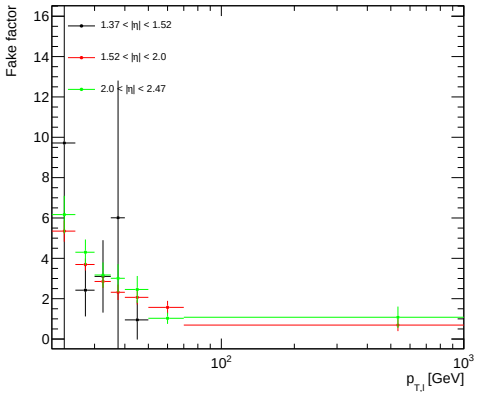
(a) Fake factor of electrons passing the single lepton trigger in the barrel region.



(b) Fake factor of electrons failing the single lepton trigger in the barrel region.



(c) Fake factor of electrons passing the single lepton trigger in the endcap region.



(d) Fake factor of electrons failing the single lepton trigger in the endcap region.

Fig. 5.5.: Fake factors with uncertainties as a function of the electron transverse momentum in different bins of the electron pseudorapidity. Fake factors for both leptons are shown, the one which has been triggered on the left and the one which has not been triggered on the right.

uncertainties and their impact on different kinematic distributions in both channels of the measurement.

5.5.1 Statistical Uncertainties

Counting experiments are inherently affected by statistical fluctuations. In particular, each bin that is studied follows a Poisson distribution with an expectation value of N_{events}. Consequently, the uncertainty per bin is $\sigma_{\text{stat}} = \sqrt{N_{\text{events}}}$ so that the relative uncertainty decreases with ever larger numbers of events.

In this analysis the statistical uncertainties vary between different regions of phase space, but overall they are the largest uncertainty in case of the rapidity binned measurement, as will be shown in section 6. In kinematic distributions the impact varies, depending on the population of an individual bin, as can be seen in the distributions in section 5.6, where its relative uncertainty varies between 0.1% in highly populated bins and more than 15% in sparsely populated ones.

5.5.2 Experimental Uncertainties

Due to imperfections of the ATLAS detector and the measurement methodologies as well as a finite detector resolution, the measurement is affected by a number of systematic uncertainties. They affect electrons and muons differently due to different signatures in the detector. The details are explained below.

Luminosity The measurement of the integrated luminosity in the ATLAS detector described in section 2.2.5 is affected by uncertainties. The effect of these is an uncertainty in the normalisation of the simulation, which uses the integrated luminosity as normalisation. For Run 2 this uncertainty has been determined[12] to be 1.7%, which means the luminosity used is found to be $(139.0 \pm 2.4)\,\text{fb}^{-1}$ [122].

5.5.2.1 Electrons

Energy Scale One of the major sources of uncertainty is the absolute energy scale of electron candidates. It relies on a calibration and estimates from simulation of Z boson decays to accurately match the electric current in individual calorimeter cells to the deposited energy. The largest uncertainties arise in the calibration procedure

[12] New developments briefly before this thesis was handed in have reduced the total luminosity uncertainty to 0.83% [122]. This does not influence the results presented in this thesis, but it will contribute to an overall higher sensitivity on the measurement of the cross section (the angular coefficients are unaffected by the total normalisation).

itself, inaccurate material descriptions as well as electronic noise and noise from products of other simultaneous collisions [135].

Due to the way the energy scale is determined, the size of the uncertainty depends on the pseudorapidity of the electron candidates. For instance, electron candidates in $|\eta| < 2.5$ with a transverse momentum close to $45\,\mathrm{GeV}$ have scale-related uncertainties between 0.03% and 0.2% [135]. These uncertainties increase for instance for electron candidates with a lower transverse momentum.

Energy Resolution Electron candidates are expected to deposit most of their energy in the electromagnetic calorimeters. As discussed in section 2.2.3, the energy measurement in these calorimeters has a finite resolution which depends on the type of calorimeter, especially the material and geometry, and the magnitude of the deposited energy. For electrons with lower transverse momenta, e.g. between $30\,\mathrm{GeV}$ to $60\,\mathrm{GeV}$ the resolution is known with a precision between $5 - 10\%$. Since the resolution improves at higher energies, the relative uncertainty on the resolution also increases to $20 - 50\%$ [135].

Trigger, Reconstruction and Identification Efficiencies As discussed in section 3.3.1, data and simulation are treated identically after the stage of electrical signals in the detector. The simulation provides a very good description of the detector, however, there are still differences after trigger chains have fired and objects reconstructed and identified. To correct for these deviations that manifest themselves in differences in efficiencies of these procedures, scale factors, as introduced in section 3.3.1, are applied. They depend on the transverse momentum as well as the pseudorapidity of electron candidates, i.e. their position in the detector.

Naturally, this correction introduces some uncertainties on the efficiencies they correct for. The dominant uncertainty is the one attached to the identification efficiency, which increases from the per-mille level up to 8% at electron transverse momenta of $200\,\mathrm{GeV}$ and higher as visible in figure 5.7, while the other efficiency-related uncertainties are below 0.5% in most regions.

Multijet Estimate Uncertainty The multijet contribution in the electron channel is very small, which is why only statistical uncertainties on the estimate are considered. They are propagated from the subtraction of data and simulation in control regions and vary drastically between analysis bins. The uncertainty covers other systematic sources, such as variations in selection thresholds or systematic variations in the simulation used. Depending on the analysis bin under consideration these relative uncertainties on the estimate itself range between 0.5% and 250%. In total,

their impact is at the per-mille level except in statistically very limited bins where uncertainties reach up to 1%.

5.5.2.2 Muons

Momentum Scale As discussed in chapter 2.3.2, the method to determine the momentum scale of muon candidates relies on studying Z boson and J/Ψ decays. In ATLAS, muon momenta are determined from the track curvature combining the inner detector and the muon spectrometers. Systematic uncertainties arise from the necessary calibration procedure and vary in different regions of pseudorapidity between 0.05% in the central barrel in $|\eta| < 1$ and up to 0.3% at high pseudorapidities of $|\eta| \approx 2.5$ [137].

Momentum Resolution Track reconstruction and the subsequent calculation of muon momenta is only possible at a finite resolution. It depends on the precision of the calibration procedure and on the momentum of the muons. In Z boson decays the uncertainty on the resolution varies with the transverse momentum of the muons and is typically within 0.5% for low momenta around the Jacobian peak and increases at higher momenta, as visible in figure 5.7.

Sagitta Correction If the detector is not precisely rotated as expected and implemented in the simulation, a bias is introduced that affects positively charged and negatively charged muons in an opposite way, as discussed in section 2.3.2. The effect on the reconstructed muon momentum is corrected for, however, this correction is affected by uncertainties of the procedure which are generally small below 0.1%.

Trigger, Reconstruction, TTVA and Isolation Efficiencies Since muons in this thesis are selected by their isolation properties, the scale factors needed to correct the simulation are another source of uncertainty. Together with the uncertainties on the efficiencies of the trigger and the reconstruction they are a minor contribution to the total uncertainty. They depend on the kinematic region of interest, in particular on the muon transverse momentum as visible in figure 5.7, where the trigger efficiency uncertainty drops from 3.5% at lower transverse momenta to 0.5% at higher ones. The isolation efficiency uncertainty is approximately 0.2% in most regions except at high p_T. Finally, the TTVA and reconstruction efficiency uncertainties affect the measurement at 0.05% and 0.2% to 0.4% depending on the region, respectively.

5.5.3 Theory Uncertainties

This measurement is generally dominated by theory uncertainties, in particular the statistical uncertainty of the simulation due to the detailed coverage of a large fraction of the phase space. Besides the uncertainties detailed below the uncertainty on the modelling of the Z boson transverse momentum is not explicitly shown. It is a modelling uncertainty which is effectively removed by the unfolding procedure into full phase space. In addition, the Z boson transverse momentum is a quantity which will be determined as part of this measurement and as such does not affect the overall result with any potential uncertainties.

Parton Density Functions The Monte Carlo simulations used throughout this analysis follow the simulation chain described in section 3. The PDF used to obtain the probabilities of specific parton interactions are extracted from measurements as they cannot be computed analytically. The uncertainties are decomposed into abstract eigenvectors. The `LHAPDF` tool [168] was used to extract the respective information. They mostly affect the total normalisation of the kinematic distributions. Since they are modelling-based uncertainties they will be drastically reduced in the actual full phase space extraction of the angular coefficients, which is also true for other kinds of modelling uncertainties. In the reconstructed distributions below, their uncertainty is typically around 3% depending on the precise region.

Statistical Uncertainty of the Simulation A significant fraction of computing time in the Worldwide LHC Computing Grid is dedicated to the simulation of events that are used to compare the data to expectations. Nonetheless, as discussed in section 3.3 especially the simulation of the detector response takes a significant amount of time. Consequently, the number of events in simulation is statistically limited. In this analysis almost 1 billion Z boson decays per lepton flavour (excluding $Z \to \tau^+\tau^-$) are used, but depending on the specific phase space region under consideration, the statistical uncertainty of the simulation is significant, in particular in more sparsely populated analysis bins. In most cases the statistical uncertainty on the simulation is the dominant systematic uncertainty.

Other Theory Uncertainties Additional sources of theory uncertainties are not explicitly shown here as they have been found to have a negligible impact on the extracted angular coefficients in the previous analysis [68]. This includes uncertainties arising from the choice of the factorisation and renormalisation scales μ_F and μ_R, the dependence on the choice of the event generator and parton shower as well as electroweak and QED corrections. As all of them are modelling-related, their impact is reduced drastically to a negligible level by the extraction procedure.

5.6 Comparison of Data to Expectation

Before it is possible to extract the angular coefficients from the data utilising the simulation, it is crucial to study and understand their agreement in detail. Tables 5.6 and 5.7 show the expected contents in each analysis region for the electron channel and the muon channel, respectively, as well as the ratio of data to expectation and in case of the electron channel the multijet (MJ) content and its ratio to the data. Depending on the region under consideration this shows a slightly closer agreement of the expectation and the data in the muon channel than in the electron channel in most cases. However, the overall normalisation does not critically influence the extraction of the angular coefficients and the cross section in the next chapter. In addition, the most important kinematic single lepton and dilepton distributions will be shown and discussed in detail. The focus will be on distributions that are integrated over the Z boson rapidity and transverse momentum to maximise statistical accuracy. If observations differ between this integrated case and a differential scenario, this will be stated explicitly[13]. In each histogram the data is shown as black data points, while the signal is represented by a white histogram, stacked with coloured histograms of each background contribution[14]. Below each distribution the ratio of the data and the sum of expected contributions is depicted with uncertainty bands in grey that include all systematic uncertainty sources. The uncertainties are shown in their 68% confidence level, which means $\pm 1\sigma$ variations around the central value as they are assumed to be Gaussian distributed. Separate distributions are provided to detail the breakdown of uncertainties excluding normalisation uncertainties from the luminosity and the multijet uncertainty for its small size.

[13] Comparisons for all analysis bins differentially in rapidity and transverse momentum can be found in appendix D.

[14] The photon-induced electron or muon production is included in the "Top + EW" category for simplicity. "EW" is short for the electroweak contributions.

Region	Data	Signal	Non-Fiducial	Top + EW	Multijet	Data/Exp.	MJ Fraction
Inclusive	60.4198×10^6	57.0579×10^6	37.7633×10^4	214.8300×10^3	30.9522×10^4	1.04	5.1×10^{-3}
$0 < \lvert y_{ll} \rvert < 0.4$	15.5570×10^6	14.6541×10^6	8.9061×10^4	62.3906×10^3	6.8776×10^4	1.05	4.4×10^{-3}
$0.4 < \lvert y_{ll} \rvert < 0.8$	14.0281×10^6	13.2074×10^6	8.5035×10^4	55.1321×10^3	6.6182×10^4	1.05	4.7×10^{-3}
$0.8 < \lvert y_{ll} \rvert < 1.2$	12.3983×10^6	11.7152×10^6	8.1342×10^4	43.9027×10^3	7.2466×10^4	1.04	5.8×10^{-3}
$1.2 < \lvert y_{ll} \rvert < 1.6$	10.0128×10^6	9.5096×10^6	6.6299×10^4	30.2633×10^3	5.2304×10^4	1.04	5.2×10^{-3}
$1.6 < \lvert y_{ll} \rvert < 2.0$	6.0703×10^6	5.7327×10^6	4.1474×10^4	17.3149×10^3	3.3468×10^4	1.04	5.5×10^{-3}
$2.0 < \lvert y_{ll} \rvert < 2.4$	2.3533×10^6	2.2389×10^6	1.4424×10^4	5.8265×10^3	1.6326×10^4	1.03	6.9×10^{-3}

Tab. 5.6.: Numbers of events in the electron channel after applying the full selection for $80\,\mathrm{GeV} < m_{ll} < 102\,\mathrm{GeV}$ and different bins in rapidity. Simulated events are scaled to $\mathfrak{L} = 139\,\mathrm{fb}^{-1}$. Ratios of data to the sum of expectations and the multijet fraction with respect to the data are listed.

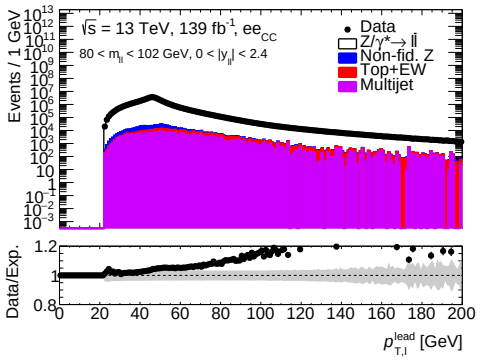
Region	Data	Signal	Non-Fiducial	Top + EW	Data/Exp.
Inclusive	84.0664×10^6	81.0863×10^6	50.5692×10^4	266.7850×10^3	1.03
$0 < \lvert y_{ll} \rvert < 0.4$	17.1465×10^6	16.5823×10^6	9.3359×10^4	62.0817×10^3	1.02
$0.4 < \lvert y_{ll} \rvert < 0.8$	17.6752×10^6	17.0668×10^6	9.9722×10^4	61.6342×10^3	1.03
$0.8 < \lvert y_{ll} \rvert < 1.2$	18.0469×10^6	17.4425×10^6	10.7730×10^4	57.8863×10^3	1.02
$1.2 < \lvert y_{ll} \rvert < 1.6$	16.3351×10^6	15.7449×10^6	10.3785×10^4	47.3547×10^3	1.03
$1.6 < \lvert y_{ll} \rvert < 2.0$	11.0968×10^6	10.6461×10^6	7.5198×10^4	28.9443×10^3	1.03
$2.0 < \lvert y_{ll} \rvert < 2.4$	3.7659×10^6	3.6036×10^6	2.5899×10^4	8.8839×10^3	1.04

Tab. 5.7.: Numbers of events in the muon channel after applying the full selection for $80\,\mathrm{GeV} < m_{ll} < 102\,\mathrm{GeV}$ and different bins in rapidity. Simulated events are scaled to $\mathfrak{L} = 139\,\mathrm{fb}^{-1}$. Ratios of data to the sum of expectations are listed.

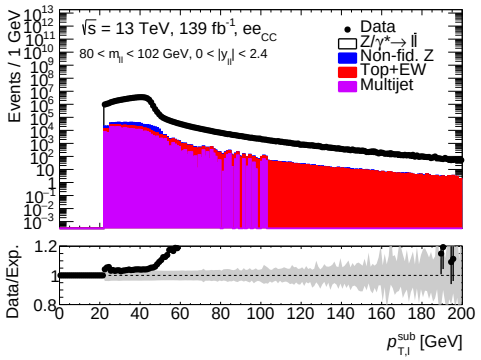
5.6.1 Single Lepton Distributions

Firstly, the distributions shown in the following figures all describe properties of the leptons from the Z boson decay individually. In each row the distributions of the lepton with the higher transverse momentum ("leading") are shown on the left.

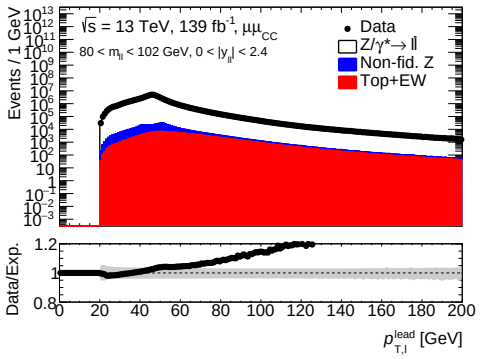
Transverse Momenta The first figure 5.6 shows the transverse momenta of each lepton. The cut-offs at $20\,\mathrm{GeV}$ and $22\,\mathrm{GeV}$ for electrons and muons, respectively, are caused by the trigger and analysis selection on the minimum transverse momentum. The distributions rise steeply towards a maximum at approximately $45\,\mathrm{GeV}$, called the *Jacobian peak*. This can be explained kinematically by a Z boson produced at rest or with very small transverse momentum decaying. Finally, towards high transverse momenta the distributions decrease quickly due to the exponentially falling production cross section of Z bosons with high transverse momenta. By definition it can be seen that the leading lepton is produced with higher transverse momentum on average than its counterpart, which explains the different shapes in the distributions. Strikingly in all cases the agreement between data and expectation is within uncertainties approximately until the Jacobian peak after which the data rises significantly above the expectation. This can be explained by the generator used for the simulations, POWHEGBOX. Its precision in QCD is NLO, however, as discussed in section 3.2 in order to produce a Z boson with non-zero transverse momentum an additional strong vertex in the Feynman diagram is needed. This means the generator is effectively at leading order in QCD when considering systems with a Z boson transverse momentum. This effect, also observed for instance in the ATLAS measurement of the Z boson production cross section [169], is directly propagated to the Z boson decay products, which is visible in their transverse momentum distributions. These major deviations do not affect the measurement of the angular coefficients, however, since a binning in the Z boson transverse momentum is chosen in such a way that within each bin the distribution is approximately flat. For a measurement of the weak mixing angle integrated in the transverse momentum of the Z boson this cannot be neglected, as will be discussed in chapter 8.
The corresponding uncertainties contained in the grey band are shown in detail in figure 5.7 with the exception of the flat luminosity uncertainty. Since the distributions shown are integrated in the rapidity, the dominant systematic uncertainty are the PDF uncertainties until at higher transverse momenta data and statistical uncertainties from simulation become dominant for the leading electron. Due to the more steeply falling distribution of the subleading lepton the statistical uncertainty from data becomes more dominant at higher transverse momenta compared to the case of the leading lepton which also results in larger contributions of the energy scale and resolution uncertainties. Energy scale and resolution uncertainties of the electrons follow a similar trend as the data statistical uncertainties, whereas muon momentum



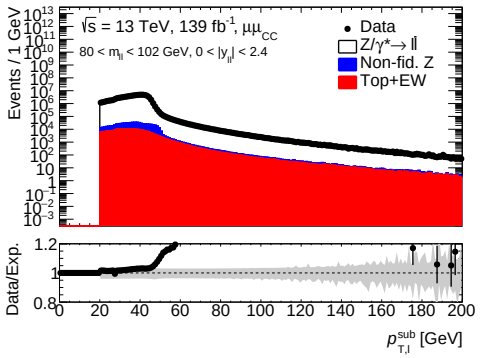
(a) Leading electron transverse momentum.



(b) Subleading electron transverse momentum.



(c) Leading muon transverse momentum.

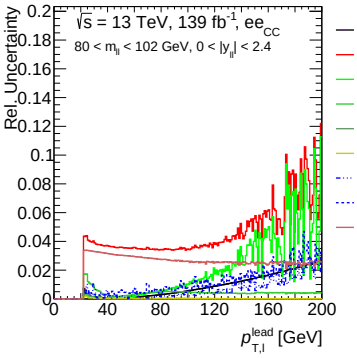


(d) Subleading muon transverse momentum.

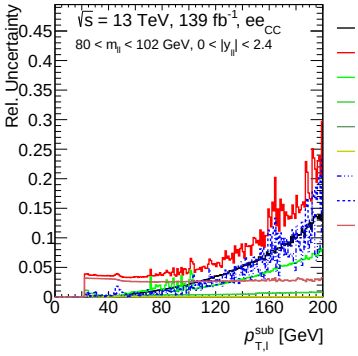
Fig. 5.6.: Comparison of data (black points) to expectation (stacked histograms) in the distributions of the transverse momentum of both leptons in both channels (the one with a larger p_T is shown in the left column, the other one in the right column, the electron channel is shown in the first row, the muon channel in the second row). The inclusive bin in the dilepton rapidity ($0 < |y_{ll}| < 2.4$) integrated over the dilepton transverse momentum in the mass window around the Z boson pole mass is depicted.
Below each histogram the ratio of the data and the sum of expectations is shown, where the grey band represents the combination of all uncertainties including the uncertainty on the integrated luminosity.

scale and resolution uncertainties follow a similar shape as the Monte Carlo statistical uncertainties due to the different methods of calibration. In case of the electrons the data is calibrated, while in case of the muons the simulation is calibrated.

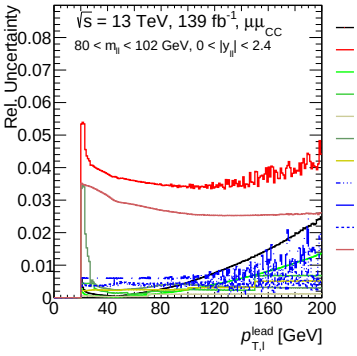
Pseudorapidities Figure 5.8 depicts the pseudorapidity distributions of the leptons individually. The distributions are bounded by the acceptance of the tracking system which ends at $|\eta| = 2.47$. In addition, a transition (crack) region between $1.35 < |\eta| < 1.52$ exhibits a significant drop in recorded electrons due to the transition between calorimeter parts, which provides only a degraded energy response and is thus removed from the selection. The pseudorapidities have a maximum at 0 and decrease towards higher absolute values of η as longitudinally boosted objects are produced less frequently due to the balanced proton momenta. The agreement of data and expectation is expectedly mostly flat and covered within uncertainties



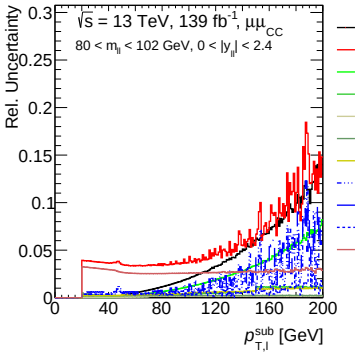
(a) Leading electron transverse momentum uncertainties.



(b) Subleading electron transverse momentum uncertainties.



(c) Leading muon transverse momentum uncertainties.



(d) Subleading muon transverse momentum uncertainties.

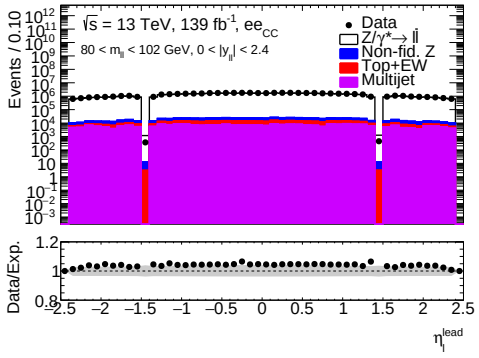
Fig. 5.7.: Comparison of uncertainties in the distributions of the transverse momentum of both leptons in both channels (the one with a larger p_T is shown in the left column, the other one in the right column, the electron channel is shown in the first row, the muon channel in the second row). The uncertainty on the integrated luminosity of about 1.7% is not shown as it affects only the normalisation. The inclusive bin in the dilepton rapidity ($0 < |y_{ll}| < 2.4$) integrated over the dilepton transverse momentum in the mass window around the Z boson pole mass is depicted.

except for some individual bins that fluctuate outside of this band, in particular in the sparsely populated crack region in the electron channel. There is a slight bowing effect in the ratio of the data to the expectation towards higher absolute values which is connected to small deviations between the efficiencies in the simulation and the data. This effect has been observed much more dominantly in earlier studies and was revealed to be connected to a coarse binning of electron identification scale factors. A finer binning provided in a new iteration significantly reduced the overall effect. The muon distributions exhibit a decrease at $\eta = 0$ due to a small gap in the muon system where two structures meet. Small fluctuations in the agreement of data and expectation in both channels are mostly covered by the mainly flat uncertainties depicted in figure 5.9, but there is a small overall shift in the normalisation between data and expectation. One reason for this is the mismodelling of the transverse momentum discussed in the previous section, but the largest contribution to this deviation comes from the precision in perturbative QCD of the generator used for the prediction (POWHEGBOX). As observed for instance in a Z boson cross section measurement by ATLAS [169] a shift of approximately 5% is expected at NLO POWHEGBOX predictions.

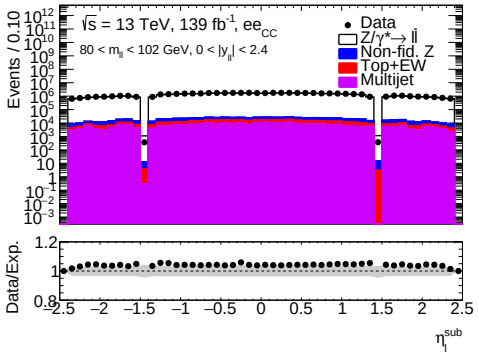
Azimuthal Angle From a perspective of the fundamental interactions during and after proton-proton collisions it is expected that the distributions in ϕ of the individual leptons are uniform and thus completely flat. However, as it is visible in figure 5.10 for both of the leptons in both channels in the ratio of data to expectation, there is a modulation in the azimuthal angle with opposite phases. This has been found to be caused by a slight deformation of the detector due to gravity and additional detector effects [170]. The effect in the electron channel is mainly caused by the angle at which the proton bunches are crossed in the detector, ϕ-dependant inefficiencies and in particular a slight variation in the absolute energy scale of electrons (mostly in the endcaps). In case of the muons this effect is also caused by ϕ-dependant inefficiencies as well as scale variations of the absolute transverse momentum. The overall effect is small and is not expected to influence the extraction of the angular coefficients, which does not directly rely on information from the azimuthal angle. Except for the small shift in the total normalisation also visible in other distributions this variation is covered by the uncertainties depicted in figure 5.11, which are expectedly flat in the azimuthal angle.

5.6.2 Dilepton Distributions

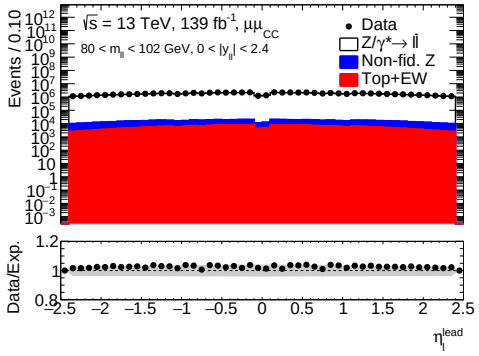
The kinematic distributions of the reconstructed Z boson are shown in figures 5.12 and 5.14 for the electron channel and the muon channel, respectively. In both cases the azimuthal angle exhibits a modulation in the ratio of data to expectation that is propagated by each single lepton modulation observed in the previous section.



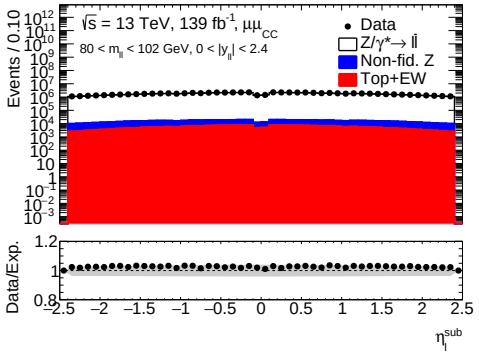
(a) Leading electron pseudorapidity.



(b) Subleading electron pseudorapidity.

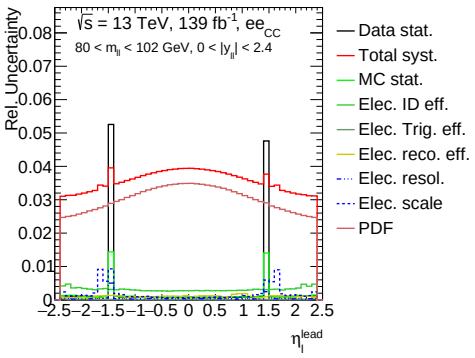


(c) Leading muon pseudorapidity.

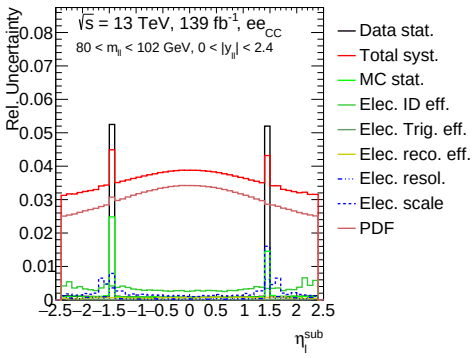


(d) Subleading muon pseudorapidity.

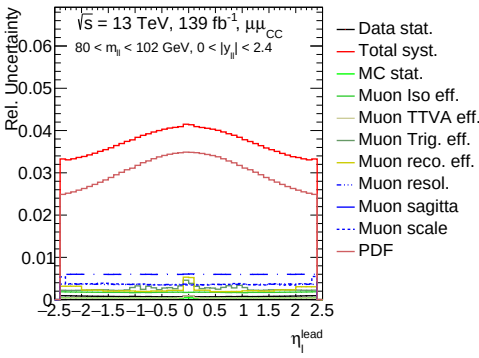
Fig. 5.8.: Comparison of data (black points) to expectation (stacked histograms) in the distributions of the pseudorapidity of both leptons in both channels (the one with a larger p_T is shown in the left column, the other one in the right column, the electron channel is shown in the first row, the muon channel in the second row). The inclusive bin in the dilepton rapidity ($0 < |y_{ll}| < 2.4$) integrated over the dilepton transverse momentum in the mass window around the Z boson pole mass is depicted.
Below each histogram the ratio of the data and the sum of expectations is shown, where the grey band represents the combination of all uncertainties including the uncertainty on the integrated luminosity.



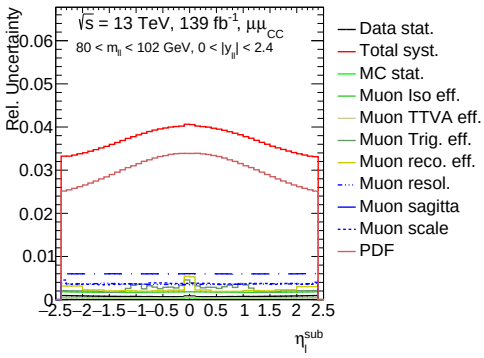
(a) Leading electron pseudorapidity uncertainties.



(b) Subleading electron pseudorapidity uncertainties.

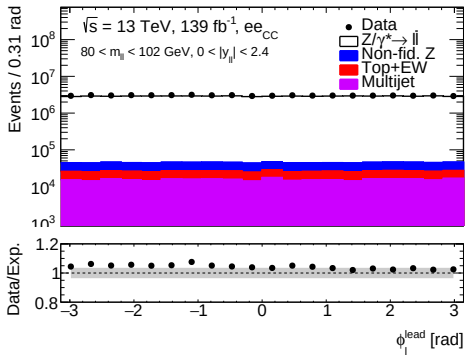


(c) Leading muon pseudorapidity uncertainties.

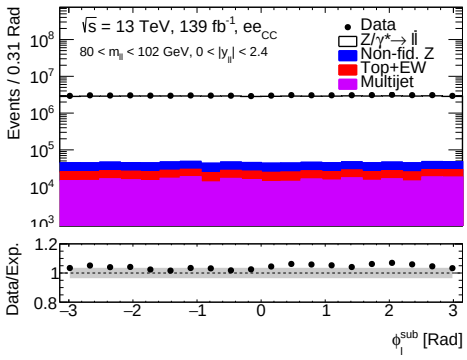


(d) Subleading muon pseudorapidity uncertainties.

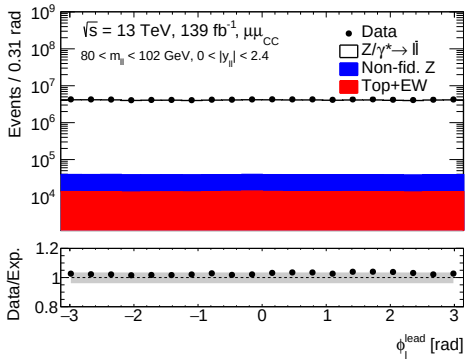
Fig. 5.9.: Comparison of uncertainties in the distributions of the pseudorapidity of both leptons in both channels (the one with a larger p_T is shown in the left column, the other one in the right column, the electron channel is shown in the first row, the muon channel in the second row). The uncertainty on the integrated luminosity of about 1.7% is not shown as it affects only the normalisation. The inclusive bin in the dilepton rapidity ($0 < |y_{ll}| < 2.4$) integrated over the dilepton transverse momentum in the mass window around the Z boson pole mass is depicted.



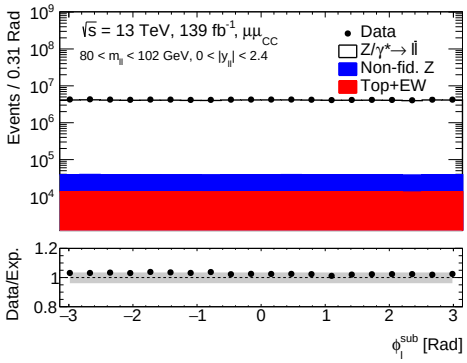
(a) Leading electron azimuthal angle.



(b) Subleading electron azimuthal angle.

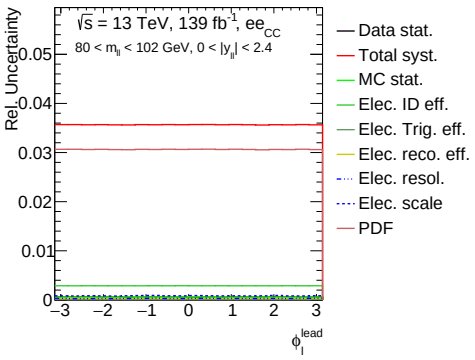


(c) Leading muon azimuthal angle.

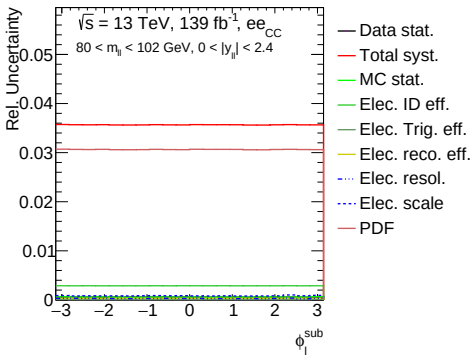


(d) Subleading muon azimuthal angle.

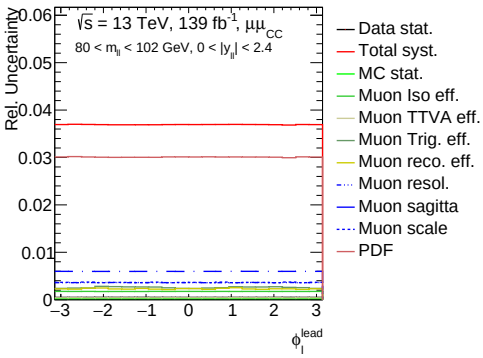
Fig. 5.10.: Comparison of data (black points) to expectation (stacked histograms) in the distributions of the azimuthal angle of both leptons in both channels (the one with a larger p_T is shown in the left column, the other one in the right column, the electron channel is shown in the first row, the muon channel in the second row). The inclusive bin in the dilepton rapidity ($0 < |y_{ll}| < 2.4$) integrated over the dilepton transverse momentum in the mass window around the Z boson pole mass is depicted.
Below each histogram the ratio of the data and the sum of expectations is shown, where the grey band represents the combination of all uncertainties including the uncertainty on the integrated luminosity.



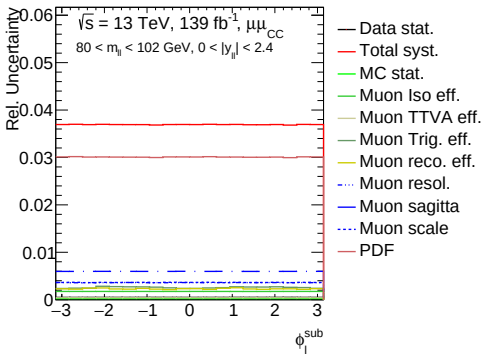
(a) Leading electron azimuthal angle uncertainties.



(b) Subleading electron azimuthal angle uncertainties.



(c) Leading muon azimuthal angle uncertainties.



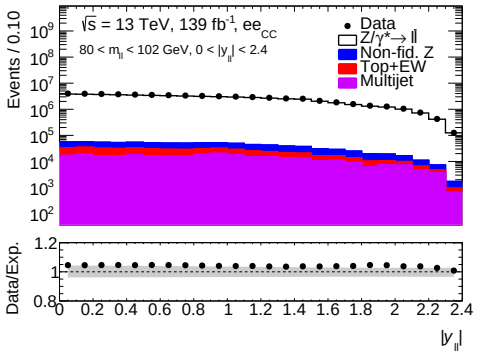
(d) Subleading muon azimuthal angle uncertainties.

Fig. 5.11.: Comparison of uncertainties in the distributions of the azimuthal angle of both leptons in both channels (the one with a larger p_T is shown in the left column, the other one in the right column, the electron channel is shown in the first row, the muon channel in the second row). The uncertainty on the integrated luminosity of about 1.7% is not shown as it affects only the normalisation. The inclusive bin in the dilepton rapidity ($0 < |y_{ll}| < 2.4$) integrated over the dilepton transverse momentum in the mass window around the Z boson pole mass is depicted.

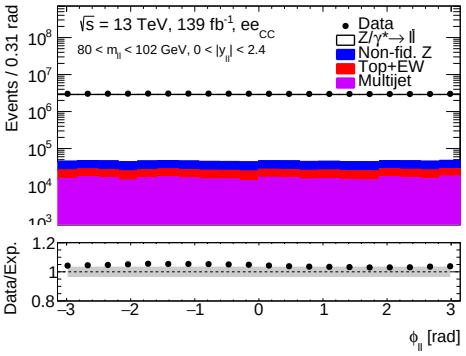
The rapidity of the reconstructed Z boson follows a falling distribution that is very similar in both channels. This is again due to the decreasing probability of a Z boson being produced at a high longitudinal boost. The agreement between data and prediction in both cases is expectedly mostly flat. The Z boson transverse momenta exhibit a maximum in their distribution at low momenta of approximately $10\,\mathrm{GeV}$ and a steeply falling distribution towards larger transverse momenta. The maximum is sculpted by the kinematic selections on the decay products of the Z boson, in particular by the minimum threshold on the p_T. As explained in the previous section and observed in other analyses as well, the ratio between data and expectation diverges at higher momenta due to a mismodelling in the generator used. Finally, the mass distributions in both channels exhibit the typical peak at approximately $91\,\mathrm{GeV}$ following a relativistic Breit-Wigner distribution. The agreement between data and expectation is flat in the muon channel. However, it shows some variance in the electron channel, but still within the uncertainties. The uncertainties depicted in figures 5.13 for the electron channel and 5.15 for the muon channel show a similar behaviour as in the single lepton distributions, which means that statistical uncertainties increase towards more sparsely populated regions of phase space and that the PDF uncertainties dominate overall. Crucially, in case of the mass distributions the scale and resolution related uncertainties are more relevant. Their shapes are in particular caused by the imperfect alignment of the Z boson peak and its width between simulation and data.

5.7 Collins-Soper Variables in Data and Expectation

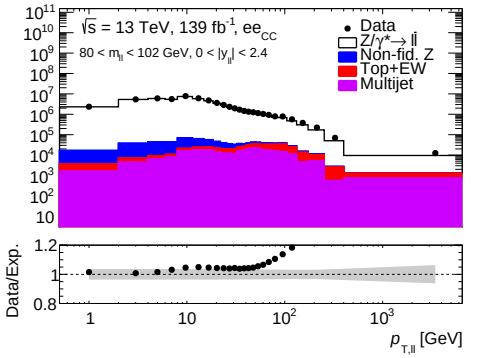
To extract the angular coefficients in the following chapter, a close inspection of the Collins-Soper variables $\cos\theta_{\mathrm{CS}}$ and ϕ_{CS} defined in chapter 1.3.2.2 is necessary as the method for the extraction is based on these distributions. They are depicted for both channels in figure 5.16 with their associated uncertainties in figure 5.17. Both distributions are sculpted by the kinematic selection applied in the analysis (differing significantly from generator-level distributions studied, for instance, by Kohl [170]). Importantly, the deviations in the ratio of data to expectation originates from a mismodelling of the transverse momentum of the Z boson discussed previously. In particular, high absolute values of $\cos\theta_{\mathrm{CS}}$ are correlated with high values of the transverse momentum of the Z boson. Since the extraction of the coefficients will be binned in the transverse momentum of the Z these shape deviations mostly disappear as shown in the next section where the differential effect of such a binning will be discussed. The uncertainties shown in figure 5.17 exhibit the same qualitative and quantitative behaviour as in other distributions discussed.



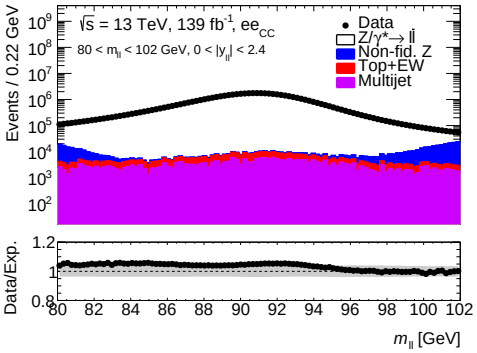
(a) Rapidity of the dielectron pair.



(b) Azimuthal angle of the dielectron pair.

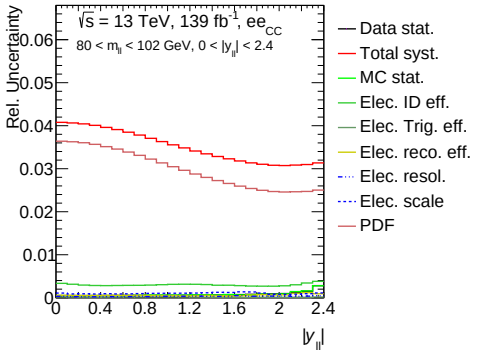


(c) Transverse momentum of the dielectron pair.

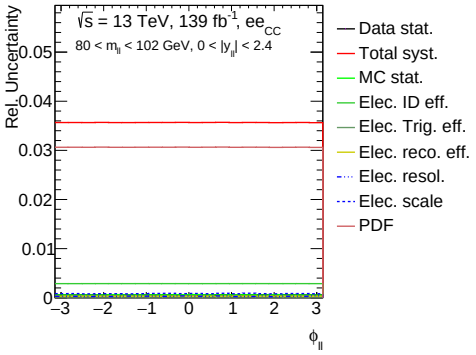


(d) Mass of the dielectron pair.

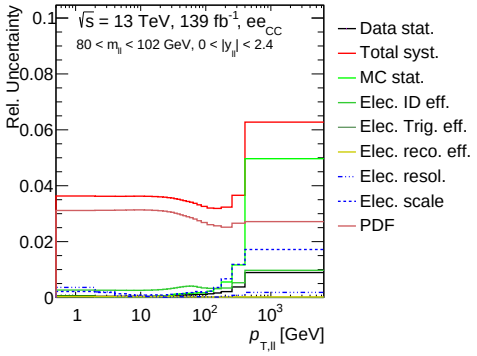
Fig. 5.12.: Comparison of data (black points) to expectation (stacked histograms) in the dilepton kinematic distributions in the electron channel. The inclusive bin in the dilepton rapidity ($0 < |y_{ll}| < 2.4$) integrated over the dilepton transverse momentum in the mass window around the Z boson pole mass is depicted. Below each histogram the ratio of the data and the sum of expectations is shown, where the grey band represents the combination of all uncertainties.



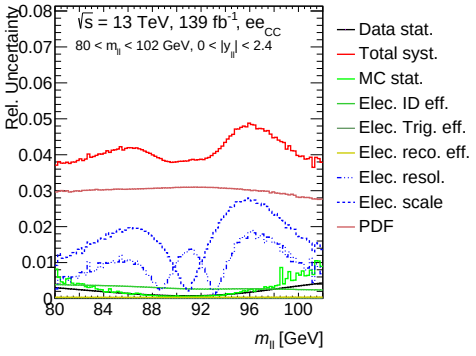
(a) Uncertainties on the rapidity of the dielectron pair.



(b) Uncertainties on the azimuthal angle of the dielectron pair.

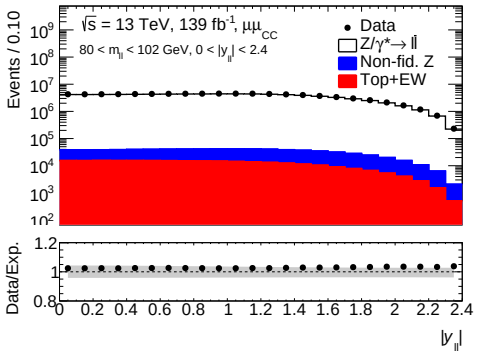


(c) Uncertainties on the transverse momentum of the dielectron pair.

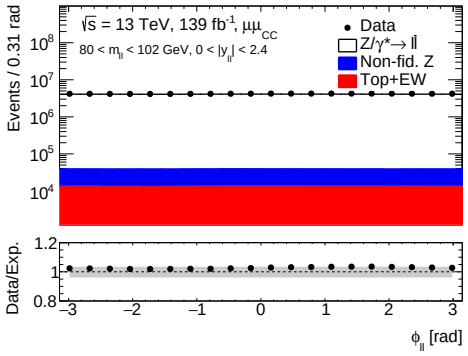


(d) Uncertainties on the mass of the dielectron pair.

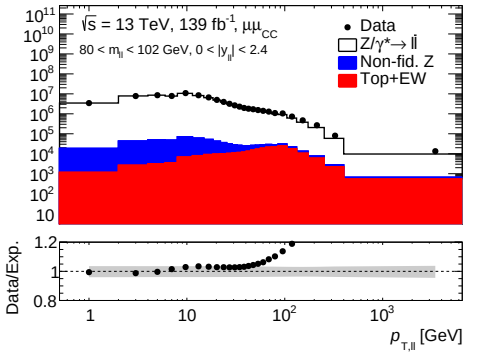
Fig. 5.13.: Comparison of uncertainties in dilepton distributions in the electron channel. The uncertainty on the integrated luminosity of about 1.7% is not shown as it affects only the normalisation. Depicted is the inclusive bin in the dilepton rapidity ($0 < |y_{ll}| < 2.4$) integrated over the dilepton transverse momentum in the mass window around the Z boson pole mass.



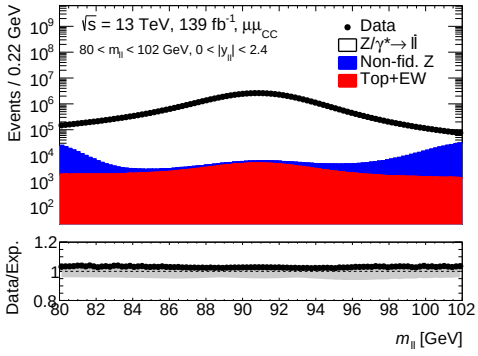
(a) Rapidity of the dimuon pair.



(b) Azimuthal angle of the dimuon pair.

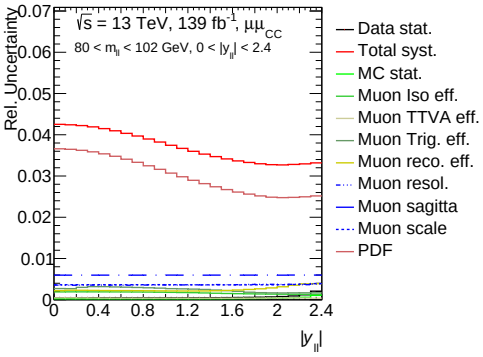


(c) Transverse momentum of the dimuon pair.

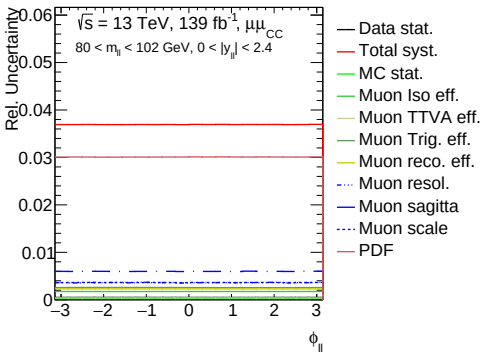


(d) Mass of the dimuon pair.

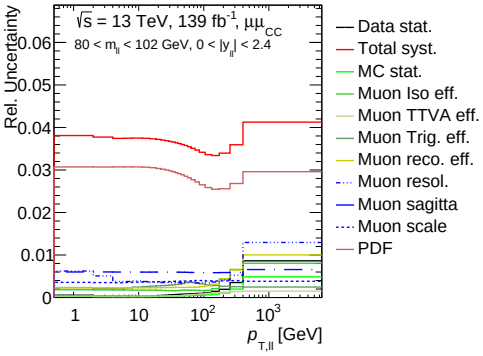
Fig. 5.14.: Comparison of data (black points) to expectation (stacked histograms) in the dilepton kinematic distributions in the muon channel. The inclusive bin in the dilepton rapidity ($0 < |y_{ll}| < 2.4$) integrated over the dilepton transverse momentum in the mass window around the Z boson pole mass is depicted. Below each histogram the ratio of the data and the sum of expectations is shown, where the grey band represents the combination of all uncertainties.



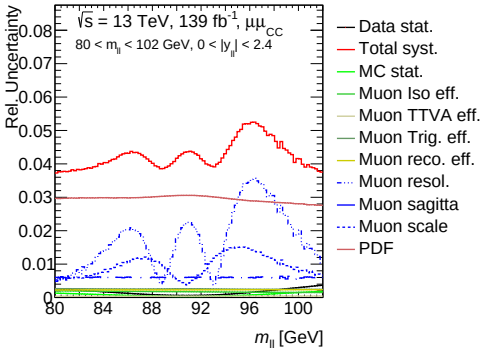
(a) Uncertainties on the rapidity of the dimuon pair.



(b) Uncertainties on the azimuthal angle of the dimuon pair.

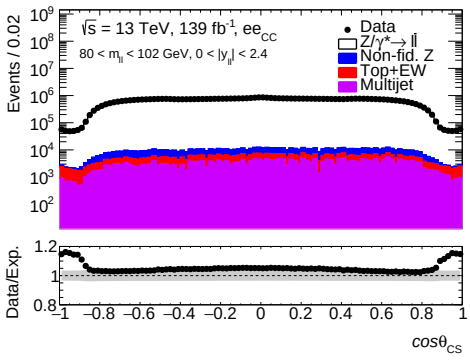


(c) Uncertainties on the transverse momentum of the dimuon pair.

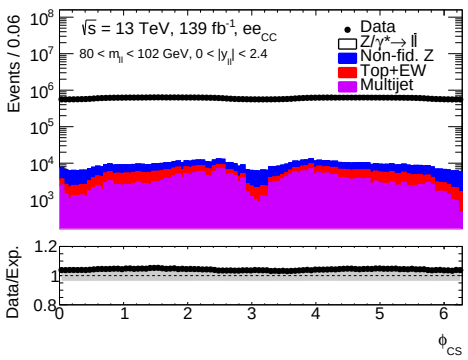


(d) Uncertainties on the mass of the dimuon pair.

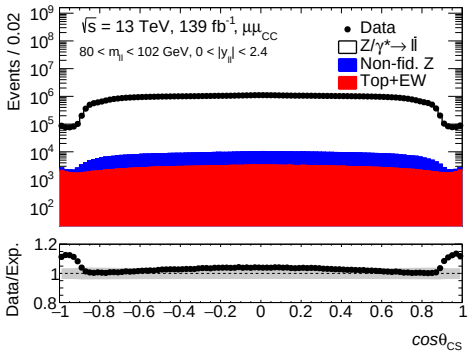
Fig. 5.15.: Comparison of uncertainties in dilepton distributions in the muon channel. The uncertainty on the integrated luminosity of about 1.7% is not shown as it affects only the normalisation. The inclusive bin in the dilepton rapidity ($0 < |y_{ll}| < 2.4$) integrated over the dilepton transverse momentum in the mass window around the Z boson pole mass is depicted.



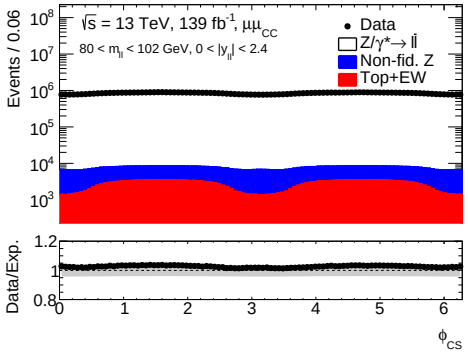
(a) Distribution of $\cos\theta_{\mathrm{CS}}$ in the Collins-Soper frame in the electron channel.



(b) Distribution of ϕ_{CS} in the Collins-Soper frame in the electron channel.

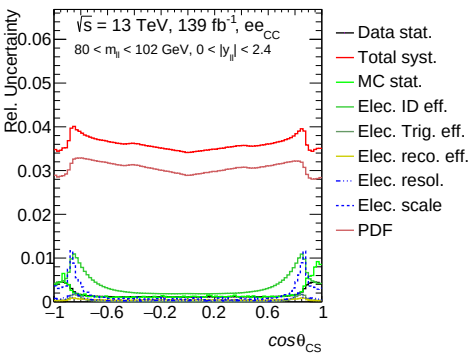


(c) Distribution of $\cos\theta_{\mathrm{CS}}$ in the Collins-Soper frame in the muon channel.

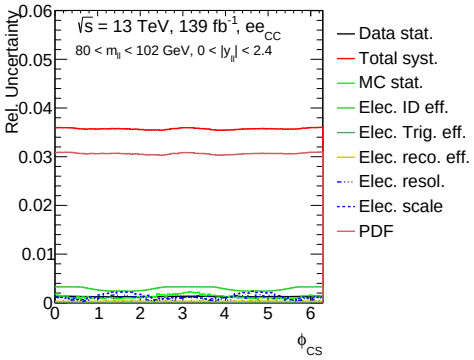


(d) Distribution of ϕ_{CS} in the Collins-Soper frame in the muon channel.

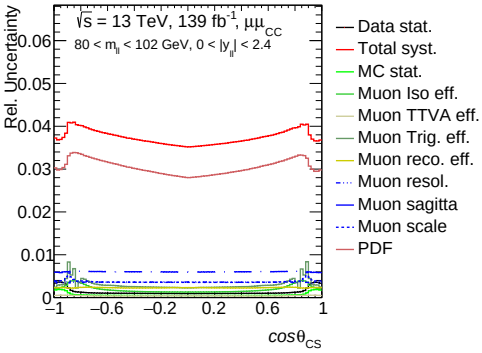
Fig. 5.16.: Comparison of data (black points) to expectation (stacked histograms) in the Collins-Soper distributions in both channels (the electron channel is shown in the first row, the muon channel in the second row). The inclusive bin in the dilepton rapidity ($0 < |y_{ll}| < 2.4$) integrated over the dilepton transverse momentum in the mass window around the Z boson pole mass is depicted.
Below each histogram the ratio of the data and the sum of expectations is shown, where the grey band represents the combination of all uncertainties.



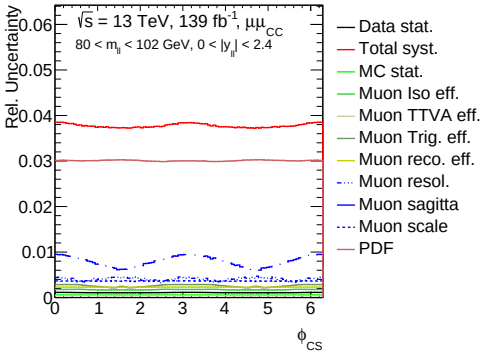
(a) Uncertainties on $\cos\theta_{\mathrm{CS}}$ in the Collins-Soper frame in the electron channel.



(b) Uncertainties on ϕ_{CS} in the Collins-Soper frame in the electron channel.



(c) Uncertainties on $\cos\theta_{\mathrm{CS}}$ in the Collins-Soper frame in the muon channel.



(d) Uncertainties on ϕ_{CS} in the Collins-Soper frame in the muon channel.

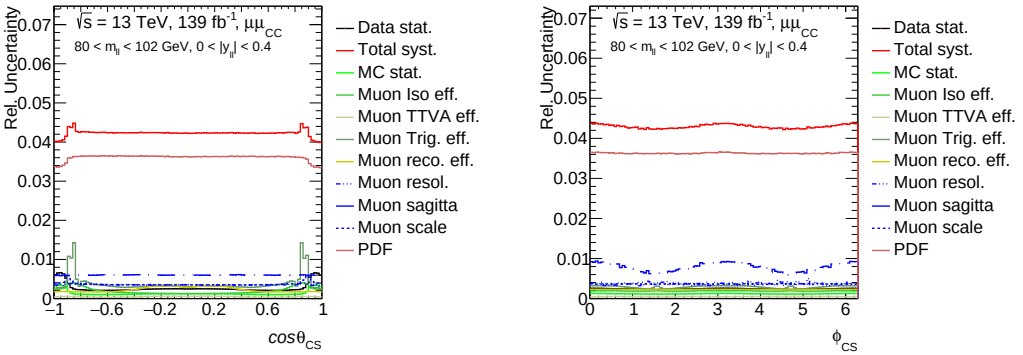
Fig. 5.17.: Comparison of uncertainties in the Collins-Soper distributions in both channels (the electron channel is shown in the first row, the muon channel in the second row). The uncertainty on the integrated luminosity of about 1.7% is not shown as it affects only the normalisation. The inclusive bin in the dilepton rapidity ($0 < |y_{ll}| < 2.4$) integrated over the dilepton transverse momentum in the mass window around the Z boson pole mass is depicted.

5.7.1 Differential Effects of Rapidity and Transverse Momentum

The distributions shown so far cover the full signal region, that is the mass window $80\,\mathrm{GeV} < m_{ll} < 102\,\mathrm{GeV}$, the rapidity region $|y_{ll}| < 2.4$ and the full transverse momentum of the Z boson $p_{T,ll} < 6500\,\mathrm{GeV}$. It is important to note the effects of the integration over the rapidity and the transverse momentum in particular. From a statistical perspective, both the data and the simulation benefit from the integration in these variables.

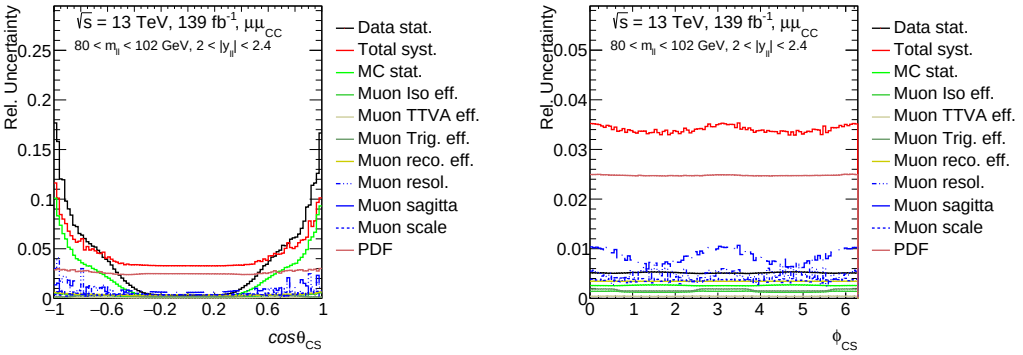
However, the integration over the rapidity does not highlight how the uncertainties of the PDFs depend on the rapidity. Parton momenta determine the longitudinal momentum of the Z boson most dominantly, which means they also significantly influence its rapidity. The Collins-Soper variables of centrally produced Z bosons (i.e. with small rapidity values) have a higher uncertainty from the PDF as they originate from partons with mostly balanced momenta. Hence, the definition of the Collins-Soper frame is ambiguous. Z bosons at higher rapidities mostly originate from partons with imbalanced momenta, thus reducing the ambiguity, also called *dilution*, and consequently also the PDF uncertainties. This is illustrated in an exemplary way in figure 5.18, where a decrease in PDF uncertainties between lower and higher rapidities can be seen. At the same time, the high rapidity region suffers from much larger statistical uncertainties in the data and the simulation since this phase space region is less densely populated. This effect occurs in both analysis channels. The significant contribution of PDF uncertainties will be reduced in the fitting procedure in the following chapter as this modelling uncertainty is effectively removed by the unfolding procedure.

Another effect to explain is the dependence of the Collins-Soper variables on the transverse momentum of the Z boson. As shown in figure 5.16, there are sizeable shape differences between data and expectation. They arise from the deviation at high transverse momenta as is shown in figure 5.19, where one bin at low momentum is compared with a bin at high momentum. It is immediately apparent that the shape differences mostly disappear with the exception of the ϕ_{CS} distribution at higher momentum. The normalisation differences between lower and higher transverse momenta are due to the increasing divergence in the simulation of the transverse momentum. This also explains that higher momentum bins still exhibit some shape deviations as the ratio between data and simulation can no longer be assumed to be completely flat within a single transverse momentum bin. However, the overall impact of this on the measurement is small, as the statistical power of these sparsely populated bins is significantly smaller than the one of bins at lower transverse momentum.



(a) Uncertainties on $\cos\theta_{\mathrm{CS}}$ in the Collins-Soper frame in $0 < |y_{ll}| < 0.4$.

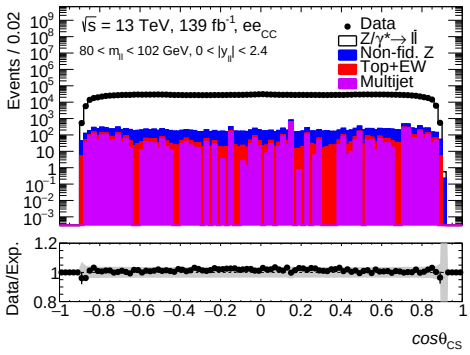
(b) Uncertainties on ϕ_{CS} in the Collins-Soper frame in $0 < |y_{ll}| < 0.4$.



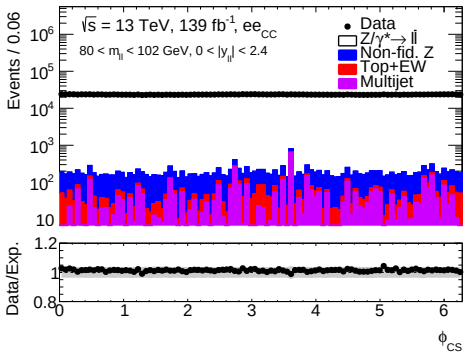
(c) Uncertainties on $\cos\theta_{\mathrm{CS}}$ in the Collins-Soper frame in $2.0 < |y_{ll}| < 2.4$.

(d) Uncertainties on ϕ_{CS} in the Collins-Soper frame in $2.0 < |y_{ll}| < 2.4$.

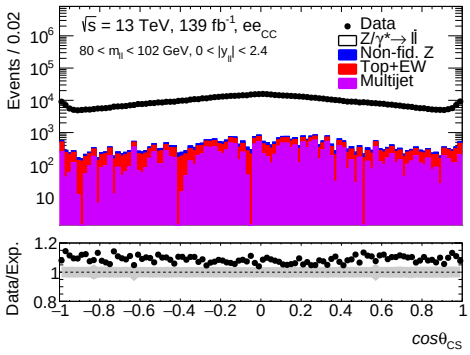
Fig. 5.18.: Comparison of uncertainties on Collins-Soper distributions in the muon channel between low dilepton rapidity and high dilepton rapidity regions.



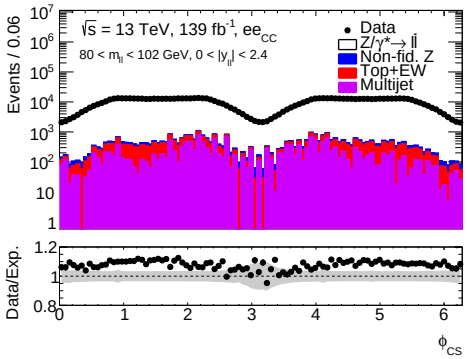
(a) Distribution of $\cos\theta_{\mathrm{CS}}$ in the Collins-Soper frame in $0\,\mathrm{GeV} < p_{T,ll} < 2.0\,\mathrm{GeV}$.



(b) Distribution of ϕ_{CS} in the Collins-Soper frame in $0\,\mathrm{GeV} < p_{T,ll} < 2.0\,\mathrm{GeV}$.



(c) Distribution of $\cos\theta_{\mathrm{CS}}$ in the Collins-Soper frame in $56.4\,\mathrm{GeV} < p_{T,ll} < 63.9\,\mathrm{GeV}$.



(d) Distribution of ϕ_{CS} in the Collins-Soper frame in $56.4\,\mathrm{GeV} < p_{T,ll} < 63.9\,\mathrm{GeV}$.

Fig. 5.19.: Comparison of Collins-Soper distributions in the electron channel between low dilepton momentum and high dilepton momentum regions.

To conclude, after this detailed inspection of the data and the predictions the few deviations observed have been explained by theoretical or experimental effects. Overall, a sound understanding has been established, which can be used in the following chapter to proceed with the actual extraction of the angular coefficients from the data.

6 Extraction of the Angular Coefficients

> *Learning never exhausts the mind.*
>
> **— Leonardo da Vinci**

In the previous chapter selections and corrections necessary for a measurement of the angular coefficients of the Z boson have been introduced. The data was analysed and compared to expectations. This chapter is used to discuss the actual extraction of the angular coefficients from the data using the Collins-Soper distributions and a Likelihood fit. After outlining the overall strategy and the methods used in the fitting procedure, uncertainties are studied and the final results in the different channels and their combination are shown. The measurement is performed using a custom software framework [157], which has been expanded and adapted for the purpose of the measurement presented in this thesis.

6.1 Strategy

Before laying out how the angular coefficients are extracted in detail, it is important to explain the over-arching methods and strategy used in this procedure. Since variables are used both in the context of reconstructed objects as well as in the full phase space, the following nomenclature (introduced in the previous ATLAS measurement [68]) is used: $p_{T,ll}$, y_{ll} and m_{ll} refer to properties of the reconstructed lepton pair, consistent with the nomenclature used throughout this thesis so far. The variables $p_{T,Z}$, y_Z and m_Z refer to the properties of the Z boson (or γ^*) in full phase space, devoid of any selections, acceptances or efficiencies.

6.1.1 Binning

As already indicated in chapter 5, the rapidity and the reconstructed transverse momentum of the diboson pair are binned. In each bin the Collins-Soper distributions are determined in data and simulation. Distributions of reconstructed variables or variables in full phase space generally share the same binning. The measurement

is done in four dimensions, which means the cross section of the Drell-Yan (DY) process is probed as

$$\frac{\mathrm{d}^4\sigma^{\mathrm{DY}}}{\mathrm{d}p_T\mathrm{d}y\mathrm{d}\cos\theta_{\mathrm{CS}}\mathrm{d}\phi_{\mathrm{CS}}}. \tag{6.1}$$

Mass To maximise the purity of the Z boson signal, a small mass window around the pole mass of the Z boson is chosen such that

$$m_{ll}^{\text{boundary}}, m_Z^{\text{boundary}} \in \{80\,\mathrm{GeV}, 102\,\mathrm{GeV}\}\,. \tag{6.2}$$

Transverse Momentum Some of the angular coefficients strongly depend on the transverse momentum of the Z boson. It is thus critical to use a fine binning that captures the shape over the full range of transverse momenta that can be produced at a centre-of-mass energy of $13\,\mathrm{TeV}$. Since the frequency of Z bosons produced with very high transverse momenta is exponentially falling, the bin width is increased towards higher transverse momenta to reduce the statistical uncertainty. The following bin boundaries have been chosen to fulfil these criteria and to be comparable to the previous measurement at $\sqrt{s} = 8\,\mathrm{TeV}$ [68]:

$$\begin{aligned} p_{T,ll}^{\text{boundary}}, p_{T,Z}^{\text{boundary}} \in \{&0,\ 2.0,\ 4.0,\ 6.0,\ 8.0,\ 11.4,\ 14.9,\ 18.5,\ 22.0,\ 25.5,\ 29.0,\ 32.6,\\ &36.4,\ 40.4,\ 44.9,\ 50.2,\ 56.4,\ 63.9,\ 73.4,\ 85.4,\ 105.0,\\ &132.0,\ 173.0,\ 253.0,\ 400.0,\ 6500.0\}\ \mathrm{GeV} \end{aligned} \tag{6.3}$$

Rapidity In order to study the cross section differentially in the absolute rapidity[1], an equidistant binning is introduced. Furthermore, some coefficients, in particular A_4, are expected to vary as a function of the absolute value of the rapidity. Finally, the weak mixing angle, which can be extracted from A_4, is sensitive to the rapidity due to a reduction of dilution effects at high y_Z, as shown in section 1.3.2.4. The following binning is used:

$$|y_{ll}^{\text{boundary}}|, |y_Z^{\text{boundary}}| \in \{0,\ 0.4,\ 0.8,\ 1.2,\ 1.6,\ 2.0,\ 2.4\}\,. \tag{6.4}$$

Collins-Soper Variables The functional forms of both $\cos\theta_{\mathrm{CS}}$ and ϕ_{CS} contain information of the decay kinematics of the Z boson. In particular it is essential to consider both variables simultaneously. The binning is chosen to be 8 bins in each variable (i.e. 64 bins in the 2-dimensional distribution). This is to reduce

[1] For symmetry reasons there is no differentiation between positive or negative rapidity regions expected or observed (within the limits of detector accuracy).

statistical uncertainties while preserving shape information. Bin boundaries have been optimised and are non-uniform to reduce statistical uncertainties in sparsely populated phase space regions, as defined in appendix E.

6.1.2 Template Method

The simulation is used to create so-called *templates* that contain the shape of the two-dimensional Collins-Soper distributions $\cos\theta_{\mathrm{CS}}$ and ϕ_{CS} following the technique used in the previous ATLAS measurement [68]. The technical description also follows the notation of this measurement outlined in detail in the corresponding technical report [72]. These templates are fitted to the data in all bins for all angular coefficients in a maximum likelihood fit. The normalisations of these templates are determined by the fit and correspond to the actual angular coefficients in full phase space. The global normalisation across all coefficients corresponds to the unfolded (i.e. devoid of any detector acceptance and efficiencies) double differential cross section in dilepton rapidity and transverse momentum, as discussed in detail in section 1.3.2. Using templates allows to obtain the angular coefficients in full phase space irrespective of any selections, acceptance and efficiencies.

This measurement relies on reconstructed leptons to determine the angular coefficients and the unpolarised cross section. Consequently, measured lepton kinematic distributions are sculpted by effects of the acceptance and efficiency of the ATLAS detector and the selections, as visible for instance in figure 5.2. To account for this, the method to extract these parameters of interest relies on effectively unfolding the measured coefficients to the full phase space. The conceptual strategy is based on the use of the polynomials of $\cos\theta_{\mathrm{CS}}$ and ϕ_{CS} which are normalised by the unpolarised cross section and the angular coefficients and define the fully differential cross section, as shown in section 1.3.2:

$$
\begin{aligned}
P_8(\cos\theta_{\mathrm{CS}},\phi_{\mathrm{CS}}) &= 1+\cos^2\theta_{\mathrm{CS}} \\
P_0(\cos\theta_{\mathrm{CS}},\phi_{\mathrm{CS}}) &= \frac{1}{2}(1-3\cos^2\theta_{\mathrm{CS}}) \\
P_1(\cos\theta_{\mathrm{CS}},\phi_{\mathrm{CS}}) &= \sin 2\theta_{\mathrm{CS}}\cos\phi_{\mathrm{CS}} \\
P_2(\cos\theta_{\mathrm{CS}},\phi_{\mathrm{CS}}) &= \frac{1}{2}\sin^2\theta_{\mathrm{CS}}\cos 2\phi_{\mathrm{CS}} \\
P_3(\cos\theta_{\mathrm{CS}},\phi_{\mathrm{CS}}) &= \sin\theta_{\mathrm{CS}}\cos\phi_{\mathrm{CS}}
\end{aligned}
\qquad
\begin{aligned}
P_4(\cos\theta_{\mathrm{CS}},\phi_{\mathrm{CS}}) &= \cos\theta_{\mathrm{CS}} \\
P_5(\cos\theta_{\mathrm{CS}},\phi_{\mathrm{CS}}) &= \sin^2\theta_{\mathrm{CS}}\sin 2\phi_{\mathrm{CS}} \\
P_6(\cos\theta_{\mathrm{CS}},\phi_{\mathrm{CS}}) &= \sin 2\theta_{\mathrm{CS}}\sin\phi_{\mathrm{CS}} \\
P_7(\cos\theta_{\mathrm{CS}},\phi_{\mathrm{CS}}) &= \sin\theta_{\mathrm{CS}}\sin\phi_{\mathrm{CS}}
\end{aligned}
\qquad (6.5)
$$

As the true polynomials cannot be measured directly in the data, the simulation is used to fold the analytical polynomials into templates, which are equivalent to the polynomials after the application of all selections and corrections. To show this, let $p(r|t)$ be the probability to observe a reconstructed observable r given a true

value t. Using the observables of interest, this means $r = \left\{\cos\theta^{ll}_{\mathrm{CS}}, \phi^{ll}_{\mathrm{CS}}, p_{T,ll}, y_{ll}\right\}$ and $t = \left\{\cos\theta^{Z}_{\mathrm{CS}}, \phi^{Z}_{\mathrm{CS}}, p_{T,Z}, y_{Z}\right\}$. The effects of the detector on reconstructed observables due to acceptance, efficiency and resolution will smear the true observables t. It is not possible to express these effects analytically. Hence, they are estimated by the Monte Carlo simulation to derive the probability $p^{MC}(r|t)$ [72]. To this end, the event weight $w^{\mathrm{evt}}(r|t)$ of each event in the simulation is divided by the expected differential cross section derived from the unpolarised cross section σ_j and the sum of the polynomials P_{ij} multiplied by the reference angular coefficients A^{ref}_{ij} of the corresponding bin j in $p_{T,Z}$ and y_Z:

$$p^{MC}_j(r|t) = \frac{w^{\mathrm{evt}}(r|t)}{f_j(\cos\theta^{Z}_{\mathrm{CS}}, \phi^{Z}_{\mathrm{CS}})}, \qquad \text{where} \tag{6.6}$$

$$f_j(\cos\theta^{Z}_{\mathrm{CS}}, \phi^{Z}_{\mathrm{CS}}) = \sigma_j \left\{\sum_{i=0}^{7} A^{\mathrm{ref}}_{ij} P_{ij}(\cos\theta^{Z}_{\mathrm{CS}}, \phi^{Z}_{\mathrm{CS}}) + P_{8,j}(\cos\theta^{Z}_{\mathrm{CS}}, \phi^{Z}_{\mathrm{CS}})\right\}. \tag{6.7}$$

The reference angular coefficients have been calculated by the moments method introduced in section 1.3.2. This method removes the dependence of the simulation on the angular cross section at generator level (i.e. before detector effects) in the full phase space. Crucially, the resulting distributions are only shaped by detector effects but without information on the cross section. Subsequently, these distributions are folded with the polynomial P_i of interest to yield the two-dimensional templates[2] corresponding to the two-dimensional polynomials accounting for selection acceptance and efficiency:

$$t^n_{ij} = \sum_{\mathrm{evt}\in\left\{(\Delta p_{T,Z}, \Delta y_Z)_j, (\Delta p_{T,ll}, \Delta y_{ll})_n\right\}} P_{ij}(\cos\theta^{Z}_{\mathrm{CS}}, \phi^{Z}_{\mathrm{CS}}) \cdot p^{MC}_j(r|t). \tag{6.8}$$

This way nine templates t^n_{ij} per analysis bin j in $p_{T,Z}$ and y_Z (i.e. the *true* bins) and reconstructed bin n in $p_{T,ll}$ and y_{ll} can be obtained. This amounts to a total of $N_{\text{nom. templates}} = (6 \cdot 25)^2 = 22500$ sets of nominal templates[3]. The polynomials are shown in figures 6.1 and 6.2 and their corresponding (exemplary) templates are shown in figures in 6.3 and 6.4. Generally, it is apparent that the shapes of the templates are much coarser due to their binning. In addition, smearing as well as acceptance and efficiency effects distort the analytical distributions. This is mostly noticeable in P_8 and its templated polynomial which is sculpted by kinematic selections.

[2] In the actual fit discussed in section 6.2 the templates are *unwrapped* into a single-dimensional histogram with 64 bins, retaining all information of the original two-dimensional template. This simplifies computational handling of the individual templates.

[3] These are calculated from 6 bins in rapidity and 25 bins in transverse momentum for reconstructed and true bins. To save computing time, a cutoff is enforced where migrations between bins are below 10^{-4}. This means bins that are significantly separated kinematically are not explicitly considered if the migration is below this level. For example, the first true $p_{T,Z}$ bin and the highest reconstructed $p_{T,ll}$ bin are not expected to suffer from measurable migration effects.

To account for background contributions, additional templates are constructed for all background sources explained in section 5.2.2: Multijet, Top, electroweak and non-fiducial backgrounds. The normalisation of the background templates T_B is defined by the product of their respective cross section and the integrated luminosity. The normalisation of the multijet background is derived by the data-driven method explained in section 5.4.

Sources of experimental and theoretical uncertainties have been decomposed into individual *nuisance parameters* during the generation of simulations. The decomposition allows to describe each uncertainty in detail and to assess their magnitude. To account for their impact, additional templates are constructed that reflect $\pm 1\sigma$ (standard deviation) variations of each individual nuisance parameter. The decomposition into nuisance parameters leads to a large number of variations. This will be shown in detail in section 6.6.

Technical Considerations Uncertainties are derived as variations of a *nominal* prediction in ROOT. Most of these variations, i.e. uncertainties on scale factors, can be constructed by a variation of the scale factor under consideration by $\pm 1\sigma$ of each respective nuisance parameter after all kinematic selections are already applied. However, some uncertainties (namely uncertainties related to the energy/momentum scale and resolution) affect the kinematic distributions of electrons or muons and thus impact the kinematic selection itself. This means for each nuisance parameter of this type, the kinematic selection has to be applied separately. While the effect of each nuisance parameter is small, the effect on the selection results in statistical differences between the set of events used for the nominal selection and the one used for each variation.

This has been studied closely to lead to unexpected variations in the content of each bin of the Collins-Soper distributions that exceed the variations caused by the nuisance parameter and even one-sided variations. As a consequence, nuisance parameters in such cases appear to be strongly constrained (i.e. reduced in size) by the fit although this is traced back to a purely statistical effect. To account for this, a symmetrisation is enforced which centres the $\pm 1\sigma$ variations around the nominal bin content to appropriately reflect its effect rather than artificially increasing the uncertainty due to statistical limitations of the Monte Carlo simulation. Furthermore, kinematically neighbouring bins are smoothed to reduce statistical fluctuations further by iteratively reducing the curvature between neighbouring bins.

Finally, even though the binning is optimised, some bins in the Collins-Soper distributions, in particular in sparsely populated kinematic regions such as at high rapidities and transverse momenta of the dilepton pair, exhibit very large statistical

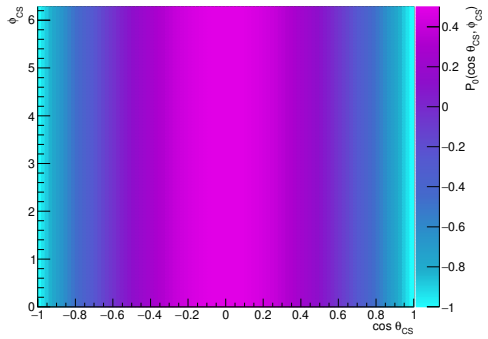
fluctuations. This can challenge the fit minimisation and lead to unexpectedly large χ^2 values. To account for this, individual outliers that are separated by more than 5 standard deviations from the median of the rest of the bins are removed from a template.

6.2 Statistical Methods

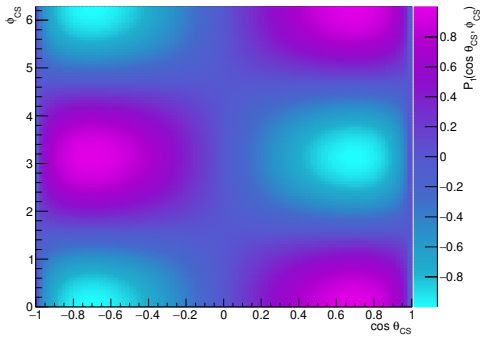
The statistical foundation of the extraction of the angular coefficients is a *likelihood function* that is constructed from the templates introduced in the previous section. Since each bin n observed in the analysis can be regarded as a Poissonian counting experiment where N^n_{exp} is the number of expected events within that particular bin, the likelihood function is defined as the product of each Poisson probability distribution from each bin.

Consequently, in each bin n a Poisson distribution describes the probability to observe N^n_{obs} events if N^n_{exp} events are expected: $P(N^n_{\text{obs}}|N^n_{\text{exp}})$. Given an integrated luminosity $\mathfrak{L}$ the expectation depends on the cross section σ, the set of all angular coefficients A and the nuisance parameters θ. The nuisance parameters are split into categories $\theta = \{\beta, \gamma\}$, where $\beta = \left\{\beta^0, ..., \beta^M\right\}$ and $\gamma = \left\{\gamma^0, ..., \gamma^{N_{\text{bins}}}\right\}$. The first category β represents experimental and theory systematic uncertainty sources. Each β^m corresponds to a nuisance parameter and is defined by a Gaussian probability distribution $G(0|\beta^m, 1)$, which is a normal distribution with an expectation value of 0 and a standard deviation of $\pm 1\sigma$, in which $\beta^m = \pm 1$ corresponds to the individual variations of the systematic templates that interpolate linearly between the nominal and the varied templates. M is the total number of variations: In case of the muon channel it is $M = 59$ and in the electron channel $M = 868$. These variations can change not only the normalisation, but also the shape of the templates. For the electron channel (before applying the cutoff to migration bins) this leads to a maximum of $1,953,0000$ systematic templates and for the muon channel to $132,750$ systematic templates. The large number of variations in the electron channel is driven by a very fine decomposition of systematic uncertainties on efficiency scale factors into high-granularity bins in lepton pseudorapidity and transverse momentum, whereas the muon systematic scheme in this thesis uses a coarser binning. The effects of this choice will be shown in section 6.6.

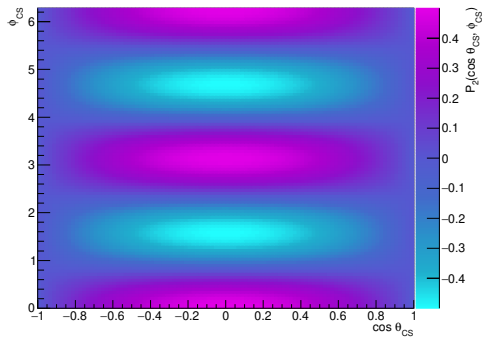
The second type of nuisance parameters γ^n represents the statistical limitation of the simulation in each analysis bin n. The number of simulated events per bin n is denoted as $N^n_{\text{MC,eff}}$ since the simulation is reweighted to an *effective* number of entries to account for corrections, the event generator weight and the desired integrated luminosity. Conversely, the statistical uncertainty of the simulation is constrained



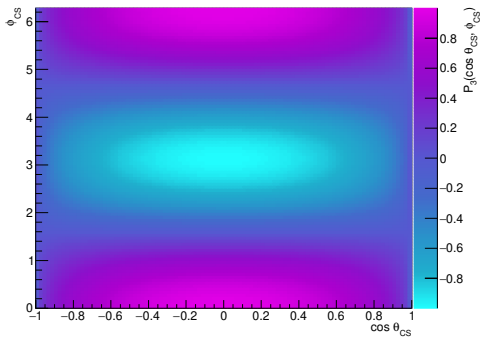
(a) $P_0(\cos\theta_{\mathrm{CS}}, \phi_{\mathrm{CS}})$.



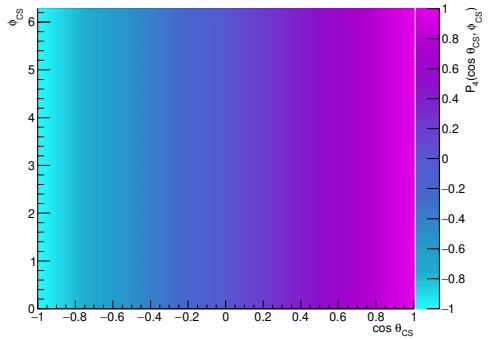
(b) $P_1(\cos\theta_{\mathrm{CS}}, \phi_{\mathrm{CS}})$.



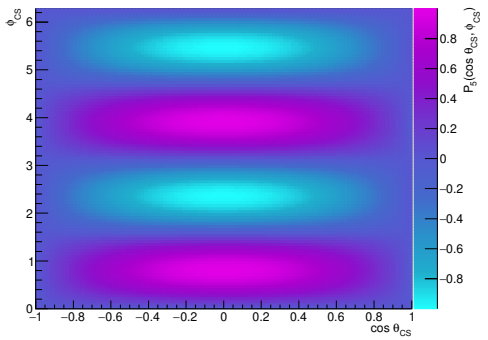
(c) $P_2(\cos\theta_{\mathrm{CS}}, \phi_{\mathrm{CS}})$.



(d) $P_3(\cos\theta_{\mathrm{CS}}, \phi_{\mathrm{CS}})$.

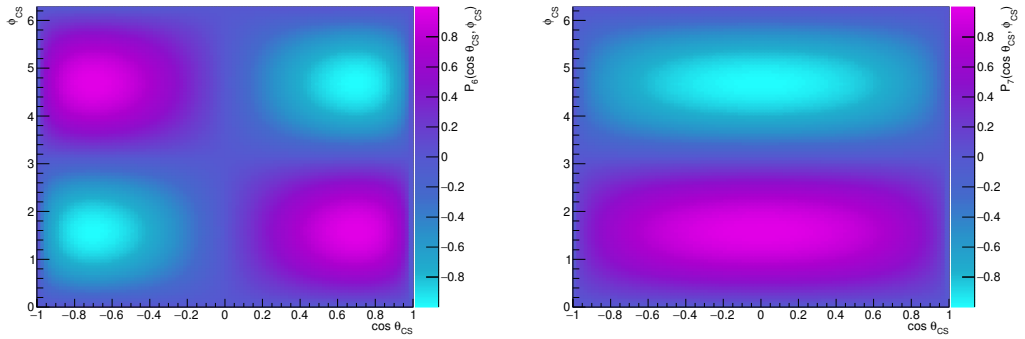


(e) $P_4(\cos\theta_{\mathrm{CS}}, \phi_{\mathrm{CS}})$.



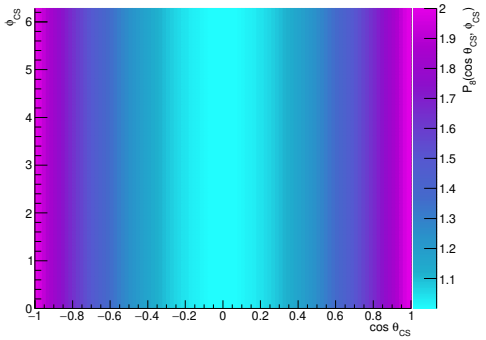
(f) $P_5(\cos\theta_{\mathrm{CS}}, \phi_{\mathrm{CS}})$.

Fig. 6.1.: Analytical polynomials P_0 to P_5 as a function of $\cos\theta_{\mathrm{CS}}$ and ϕ_{CS} as defined in equation 6.5.



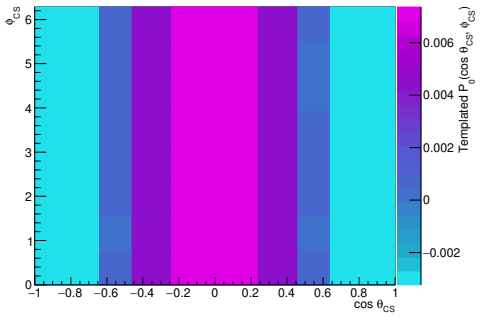
(a) $P_6(\cos\theta_{\mathrm{CS}}, \phi_{\mathrm{CS}})$.

(b) $P_7(\cos\theta_{\mathrm{CS}}, \phi_{\mathrm{CS}})$.

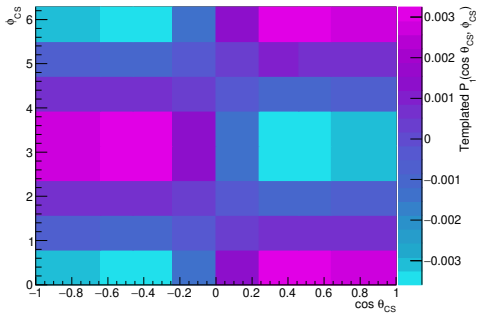


(c) $P_8(\cos\theta_{\mathrm{CS}}, \phi_{\mathrm{CS}})$.

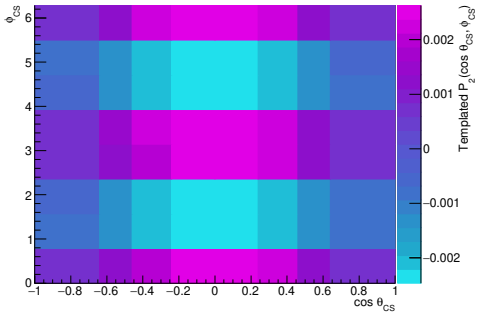
Fig. 6.2.: Analytical polynomials P_6 to P_8 as a function of $\cos\theta_{\mathrm{CS}}$ and ϕ_{CS} as defined in equation 6.5.



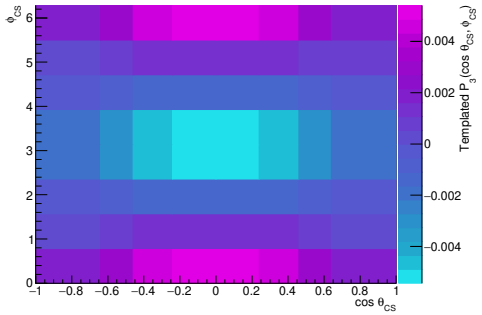
(a) Templated $P_0(\cos\theta_{\mathrm{CS}}, \phi_{\mathrm{CS}})$.



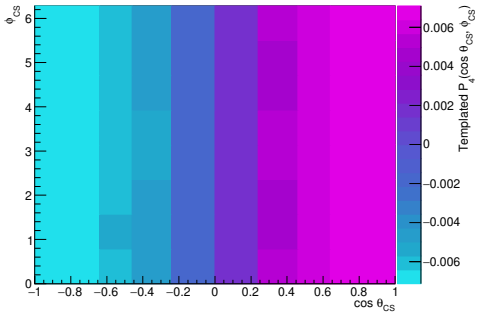
(b) Templated $P_1(\cos\theta_{\mathrm{CS}}, \phi_{\mathrm{CS}})$.



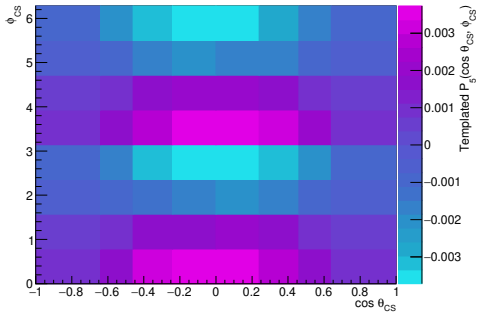
(c) Templated $P_2(\cos\theta_{\mathrm{CS}}, \phi_{\mathrm{CS}})$.



(d) Templated $P_3(\cos\theta_{\mathrm{CS}}, \phi_{\mathrm{CS}})$.

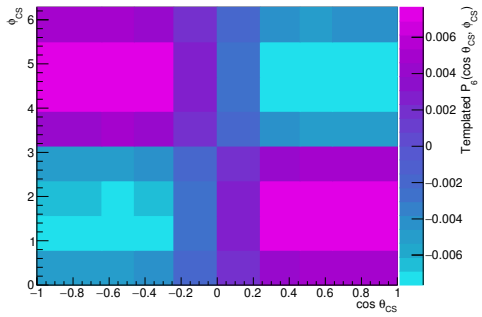


(e) Templated $P_4(\cos\theta_{\mathrm{CS}}, \phi_{\mathrm{CS}})$.

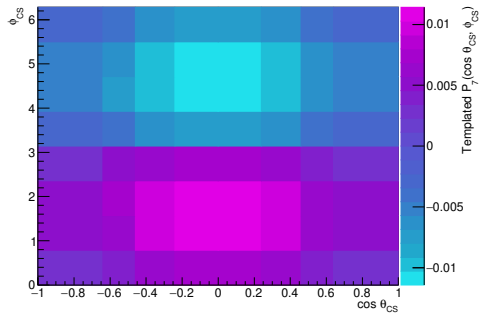


(f) Templated $P_5(\cos\theta_{\mathrm{CS}}, \phi_{\mathrm{CS}})$.

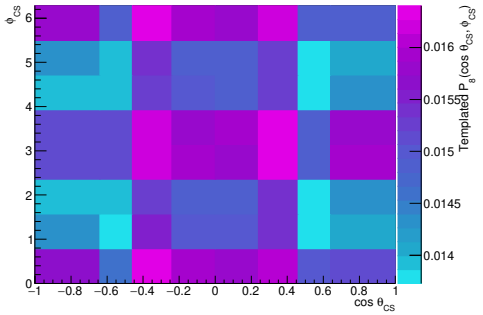
Fig. 6.3.: Templated polynomials (templates) of P_0 to P_5 as a function of $\cos\theta_{\mathrm{CS}}$ and ϕ_{CS}. The first bin in $p_{T,Z}$ and $p_{T,ll}$ (i.e. t^0_{00} to t^0_{50} in equation 6.8) is displayed.



(a) Templated $P_6(\cos\theta_{\mathrm{CS}}, \phi_{\mathrm{CS}})$.



(b) Templated $P_7(\cos\theta_{\mathrm{CS}}, \phi_{\mathrm{CS}})$.



(c) Templated $P_8(\cos\theta_{\mathrm{CS}}, \phi_{\mathrm{CS}})$.

Fig. 6.4.: Templated polynomials (templates) of P_6 to P_8 as a function of $\cos\theta_{\mathrm{CS}}$ and ϕ_{CS}. The first bin in $p_{T,Z}$ and $p_{T,ll}$ (i.e. t^0_{60} to t^0_{80} in equation 6.8) is displayed.

by the Poisson probability $P(N^n_{\text{MC,eff}}|\gamma^n N^n_{\text{MC,eff}})$. A total of $N_{\text{bins}} = 64 \cdot 6 \cdot 25 = 9600$ γ^n parameters describe the statistical limitations in each bin in the two-dimensional Collins-Soper distribution, the rapidity and the transverse momentum, respectively.

Adopting the symbology used in the previous ATLAS analysis [68, 72], the number of expected events per bin n can be expressed as the sum over all signal templates, normalised to the integrated luminosity, and background templates (which are already normalised). The appropriate cross section and angular coefficients A_i are also part of the normalisation, but they are left as a floating parameter to be determined in the fitting procedure, which will be explained in section 6.3 together with constraints on the nuisance parameters β and γ:

$$N^n_{\text{exp}}(A, \sigma, \theta) = \left\{ \sum_{j=1}^{N_{\text{Z bins}}} \sigma_j \cdot \mathfrak{L} \cdot \left[t^n_{8,j}(\beta) + \sum_{i=0}^{7} A_{ij} \cdot t^n_{ij}(\beta) \right] + \sum_{B \in \text{ bkgs}} T^n_B(\beta) \right\} \cdot \gamma^n. \tag{6.9}$$

In this equation $N^n_{\text{exp}}(A, \sigma, \theta)$ represents the expected number of events in (reconstructed) bin n, A_{ij} are the A_i coefficients in $p_{T,Z}$ and y_Z (true) bin j, A is set of all A_{ij}, σ_j is the differential cross section in $p_{T,Z}$ and y_Z bin $j \in [1, N_{\text{Z bins}}]$, $\mathfrak{L}$ is the integrated luminosity corresponding to approximately $139\,\text{fb}^{-1}$ and t^n_{ij} are the templates defined in equation 6.8, which depend on the nuisance parameters $\beta \in \theta$. Finally, T^n_B are the background templates and $\gamma^n \in \theta$ the nuisance parameters per analysis bin that represent the statistical limitation of the simulated number of events.

The expression for the likelihood function of interest $\mathcal{L}$ that will be used in the fit can finally be built as the product of all contributions introduced above. For each analysis bin n, the probability to observe N^n_{obs} events given an expectation of $N^n_{\text{exp}}(A, \sigma, \theta)$ is multiplied by the probability distributions that constrain the nuisance parameters. That is the Poisson distribution to observe $N^n_{\text{MC,eff}}$ simulated events given statistical fluctuations γ^n and the smearing described by a Gaussian distribution for each nuisance parameter β^m:

$$\mathcal{L}(A, \sigma, \theta|N_{\text{obs}}) = \prod_{n}^{N_{\text{bins}}} \left\{ P(N^n_{\text{obs}}|N^n_{\text{exp}}(A, \sigma, \theta)) P(N^n_{\text{MC,eff}}|\gamma^n N^n_{\text{MC,eff}}) \right\} \cdot \prod_{m}^{M} G(0|\beta^m, 1) \tag{6.10}$$

The products are calculated for all (true) bins in $p_{T,Z}$, y_Z, $\cos\theta^Z_{\text{CS}}$ and ϕ^Z_{CS} and all $\beta^m \in \left\{\beta^0, ..., \beta^M\right\}$. In case of this measurement it is $N_{\text{bins}} = 25 \times 6 \times 8 \times 8 = 9600$.

6.3 Maximum Likelihood Fit

To determine the best estimator for each parameter of interest, i.e. the angular coefficients and cross section per bin j in $p_{T,Z}$ and y_Z, the likelihood ratio [138] is constructed for the observed number of events N_{obs} [72]. For simplicity the cross section σ_j is included in the A_{ij} and $\hat{A}$ expressions:

$$\Lambda(A_{ij}) = \frac{\mathcal{L}(\hat{A}(A_{ij}), \hat{\theta}(A_{ij}))}{\mathcal{L}(\hat{A}, \hat{\theta})}. \tag{6.11}$$

In this equation $\hat{A}$ and $\hat{\theta}$ are the estimators for the angular coefficients including the unpolarised cross section and the nuisance parameters, respectively. Note that the numerator of the likelihood is maximised for a specific angular coefficient or cross section, while the denominator is maximised across all coefficients and nuisance parameters. The maximisation is performed by minimising the negative logarithm of the likelihood ratio $q_{A_{ij}} = -2\log\Lambda(A_{ij})$ using a Newton minimisation algorithm [171] in a custom framework [158]. Uncertainties are defined by the test statistic, where $q_{A^{\pm}_{ij}} = \pm 1$ (corresponding to the $\pm 1\sigma$ confidence interval) and $A^{\pm}_{ij} = \hat{A}_{ij} \pm 1\sigma^{\pm}$. According to Wilk's theorem [172], this likelihood ratio asymptotically follows a χ^2 distribution. This means the results of the minimisation of the likelihood ratio are best estimators for all angular coefficients and the unpolarised cross section in all true bins in rapidity and transverse momentum as well as the uncertainties on the estimators.

6.4 Validation

In order to validate the procedure used to extract the angular coefficients, it is useful to construct an *Asimov*[4] dataset. This is a dataset where real data is replaced by its simulated prediction, i.e. the expectation value is identical to the observed data [174]. By construction the resulting extracted coefficients should be identical to the reference angular coefficients obtained by the moments method discussed in chapter 1.3.2 as the moments are derived from the NLO simulation used for the construction of the Asimov dataset.

The relative difference of the Asimov results compared to the reference coefficients from the simulated POWHEGBOX + PYTHIA 8 Monte Carlo samples are shown in figure 6.5 for the electron channel in the first rapidity bin of the dilepton pair. Clearly, the agreement between both methods is very accurate to a high degree so that there

[4] Named after the American writer and professor at Boston University Isaac Asimov, who wrote the short story "Franchise", in which one voter should represent the entire electorate [173].

are no visible deviations. The same holds true for the other rapidity bins and the muon channel. A discussion of the shapes of the angular coefficients will occur in chapter 6.9.2. Additionally, note that the unpolarised cross section cannot be determined by the moments method and is not shown here. The uncertainty bars include all systematic and statistical uncertainties in case of the Asimov dataset and only (Monte Carlo) statistical uncertainties in case of the moments method.

6.5 Fit Quality

In order to assess the quality of a fit, it is useful to study the goodness of the fit using Pearson's χ^2-test [175] in relation to the degrees of freedom of the fit. The χ^2 is the quadratic sum of differences between the observed data points o_i and the expected values e_i with a variance σ_i^2 for each data point i [138]:

$$\chi^2 = \sum_{i=1}^{n} \frac{(o_i - e_i)^2}{\sigma_i^2}. \tag{6.12}$$

This is set in relation to the total number of degrees of freedom $N_{\text{d.o.f.}}$ of the fit

$$N_{\text{d.o.f.}} = N_{\text{bins}} - N_{\text{fit parameters}}, \tag{6.13}$$

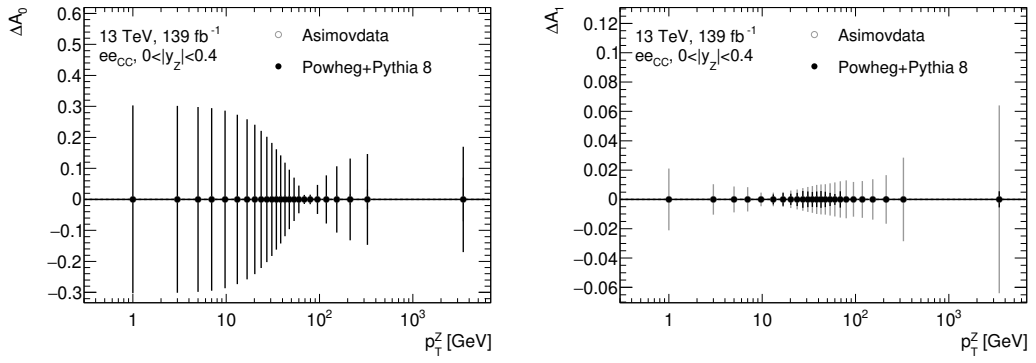
which is the difference of the number of bins to fit N_{bins} and the number of free parameters $N_{\text{fit parameters}}$. The goodness of a fit can be evaluated by the ratio of $\chi^2/N_{\text{d.o.f.}}$. Large values, i.e. $\gg 1$, indicate large differences between the fit and the data points, which can stem from an unsuited fitting model or divergence in the fit minimisation. Extremely small values can indicate *overfitting*, i.e. a model that almost perfectly describes each data point including statistical fluctuations.

In case of the electron channel and the muon channel the degrees of freedom are determined to be

$$N_{\text{d.o.f.}} = 25 \cdot 6 \cdot 64 - 25 \cdot 6 \cdot 9 = 8250, \tag{6.14}$$

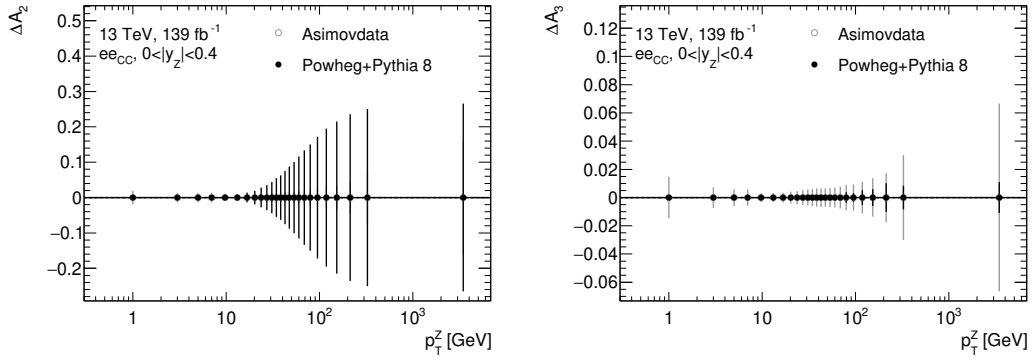
i.e. 25 bins in transverse momentum, 6 bins in rapidity, 64 bins in the two-dimensional Collins-Soper distributions and $8 + 1 = 9$ angular coefficients (including the unpolarised cross section) in each bin of transverse momentum and rapidity. Tests on the Asimov dataset in both channels expectedly result in $\chi^2 = 0$.

In real data, for muons the goodness of the fit is determined to be $\chi^2/N_{\text{d.o.f.}} = 8554.78/8250 \approx 1.04$, which indicates a very good fit quality. For the electron channel the fit on data results in $\chi^2/N_{\text{d.o.f.}} = 14396.4/8250 \approx 1.75$, which points to some deviations between the fit and the data, however, not on a significant level. Since the convergence of the fit is also influenced by the nuisance parameters, a re-



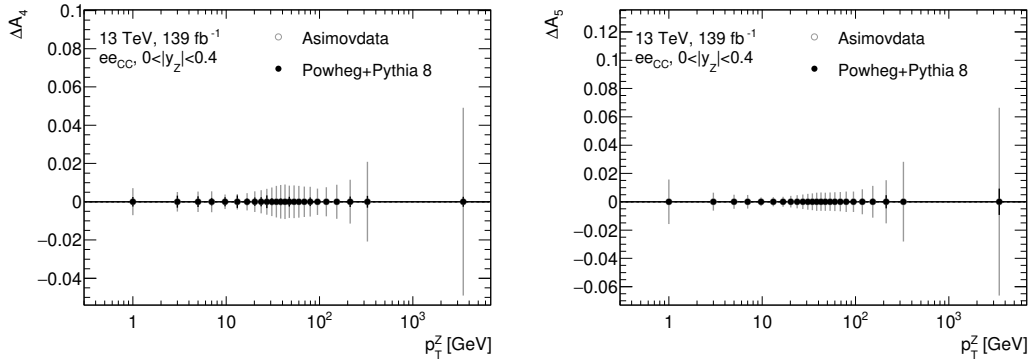
(a) A_0.

(b) A_1.



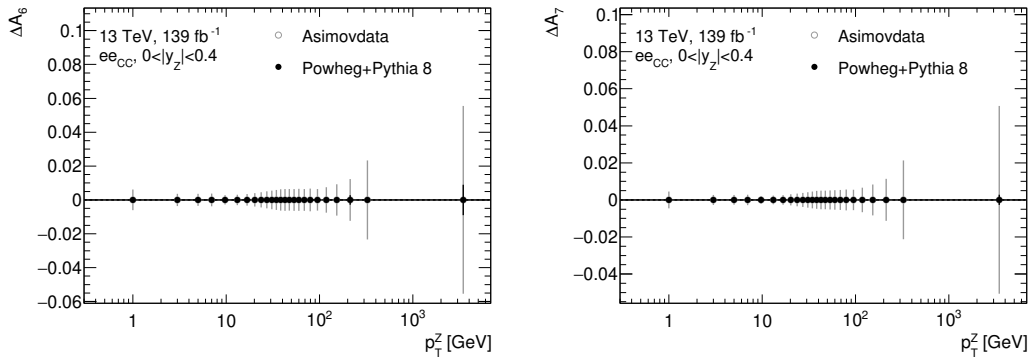
(c) A_2.

(d) A_3.



(e) A_4.

(f) A_5.



(g) A_6.

(h) A_7.

Fig. 6.5.: Absolute difference between extracted angular coefficients from Asimovdata and the expectation from the moments method derived from the same simulated sample shown in the lowest rapidity bin in the electron channel. Identical results have been achieved in other bins and the muon channel.

evaluation of the $\chi^2/N_{\text{d.o.f.}}$ is needed once multijet uncertainties are better described, as shown in section 6.6.

6.6 Uncertainties

The details of the uncertainties that affect the measurement have been discussed in section 5.5. However, in particular uncertainties such as the PDF uncertainty are expected to be reduced considerably since modelling effects are removed by the unfolding procedure. The uncertainties discussed in this section are decomposed into individual nuisance parameters that are affected by the fitting procedure. The following discussion focusses on a fit in each analysis channel individually. Each nuisance parameter θ that enters the likelihood function in equation 6.11 represents the imperfect knowledge of some modelling assumptions (for instance the energy scale etc.), i.e. $\theta = \theta_0 \pm \Delta\theta$ [176]. This means a Gaussian distribution of each nuisance parameters around θ_0 is assumed. In particular $\Delta\theta = 1\sigma$ is defined, following conventions, so that each nuisance parameter follows a normal distribution. Minimising the likelihood ratio results in best-fit values of $\hat{\theta}$, which can be different from θ_0. It is useful to study so-called *pull* distributions g, defined as

$$g = \frac{(\hat{\theta} - \theta_0)}{\Delta\theta}. \tag{6.15}$$

In this equation g is expected to follow a normal distribution if the best-fit value $\hat{\theta}$ is identical to the pre-fit value θ_0. If the statistical power of the fit is sufficiently large, $\Delta\theta$ can be *constrained*, i.e. reduced in size, which effectively means a reduction in systematic uncertainty. Additionally, if $\hat{\theta}$ is not identical to θ_0, the nuisance parameter is *pulled*, i.e. not centred around 0. As most nuisance parameters are derived from centrally (by ATLAS) provided uncertainties based on Run 2 studies, in most cases no significant constraint or pull is expected with the exception of statistical fluctuations.

Finally, the best-fit values for all nuisance parameters (i.e. all systematic sources) are added accounting for correlations in the covariance matrix. This results in total uncertainties that can be broken down by category and studied for each angular coefficient and the unpolarised cross section in each analysis bin individually.

6.6.1 Electron Channel

The uncertainties in the electron channel are broken down into the categories introduced in section 5.5 for closer study. Figures 6.6, 6.7 and 6.8 depict the pull

distributions of each nuisance parameter individually with their technical names[5] below each data entry. In case of the uncertainties on the scale factors of the electron identification overall pull distributions exhibit some expected fluctuations. Note that some individual nuisance parameters are missing if they do not affect the kinematic region of the fit. The uncertainties on the reconstruction efficiency in figure 6.7(c) show a similar behaviour with the exception of parameter `EL_EFF_Reco_CorrUncertaintyNP2`, which accounts for correlated systematic effects and is pulled outside of the $\pm 1\sigma$ band. However, as it is not strongly constrained, it is not incompatible with pre-fit assumptions. The trigger nuisance parameters in figure 6.7(d) also exhibit some fluctuations but no significant pulls.

Figure 6.8(a) depicts the pull distributions for the PDF uncertainties. The PDF is decomposed into individual nuisance parameters and its uncertainty is derived from variations that are attached to each one, which can be accessed by the LHA PDF Tool [168]. The variation is derived by reweighting the nominal PDF weight to the variation of the nuisance parameters. An upper limit of this ratio of 100 is enforced to avoid unphysically large variations. This means the fluctuations visible are well within expectations. The multijet uncertainties, however, in figure 6.8(b) highlight remaining challenges in assessing the uncertainty on the estimate correctly. While the central values of each nuisance parameter are not pulled very strongly, the constraints are unexpectedly large (while still non-zero). It indicates that the statistical fluctuations in the data and the simulation that are propagated as the estimate on the multijet distributions may be too conservative. As the overall impact of this particular uncertainty is extremely small, this observation does not affect the overall measurement in a noticeable way. Even if a relative uncertainty of 100% was applied to the multijet estimate, its overall contribution to the uncertainty would remain small. Its relative background contribution ranges between $< 10^{-3}$ up to approximately 0.5% in sparsely populated regions, which means a 100% relative uncertainty on the estimate in regions with small contributions would not change the overall sensitivity, while such an uncertainty in more sparsely populated regions would still be small compared to the statistical uncertainty from data and simulation.

Finally, the pull distributions in figure 6.8(c) highlight a particularly interesting effect of the measurement in that it is able to constrain the energy resolution uncertainties due to the precise measurement of the angular information in ϕ_{CS} (more precise than a measurement of energies or momentum used for the calibration), which is independent of the Z boson pole mass. The other nuisance parameters exhibit some fluctuations but are overall well within expectations with the exception of

[5] The naming scheme has been defined by the ATLAS E/Gamma group. Most names indicate the origin of the nuisance parameter, however, the full naming scheme is explained in the internal documentation [177].

the EG_SCALE_ZEESYST parameter, which represents the systematic uncertainty of a potential miscalibration of the energy scale (using the Z boson pole mass). The analytical decomposition of the cross section into the angular coefficients depends on the energy scale and can thus strongly constrain uncertainties from such a source.

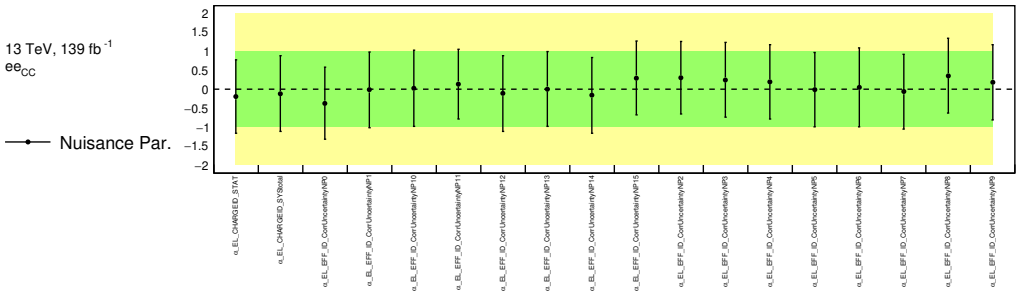
The following figures 6.9 and 6.10 depict the absolute measured uncertainties on a representative set of the measured angular coefficients as well as the effect of different rapidity regions using the example of A_4. Importantly, the statistical uncertainty from data is depicted in blue and the total systematic uncertainty is shown in black. In all cases it is clear that statistical uncertainties on the data dominate the overall measurement in each individual bin. Moreover, with the exception of the energy scale uncertainty at $40\,\mathrm{GeV}$ to $50\,\mathrm{GeV}$ in A_4 and A_0 the systematic uncertainty is dominated almost exclusively by the Monte Carlo statistical uncertainty. Other uncertainty sources are far less dominant, in particular the uncertainties derived from the multijet estimate. The difference in uncertainties between lower and higher rapidity regions is also clearly visible. Due to reduced numbers of events in data and expectation at higher rapidities the overall uncertainty increases considerably depending on the coefficient under consideration. In addition, the PDF uncertainties also increase at higher rapidities as explained in section 5.5. The dominant sources of uncertainties are expected in a measurement such as this with 150 analysis bins. In case of an integration over the rapidity, statistical uncertainties are expected to be drastically reduced.

Figure 6.11 depicts the relative uncertainties[6] on the measurement of the unpolarised cross section at low rapidity (left) and high rapidity (right). Overall, a similar conclusion can be drawn as in the case of the angular coefficients. However, at lower rapidity there are also significant contributions of uncertainties due to the identification efficiency as well as uncertainties on the energy scale, both of which dominate over the statistical uncertainty of the Monte Carlo sample in some transverse momentum bins.

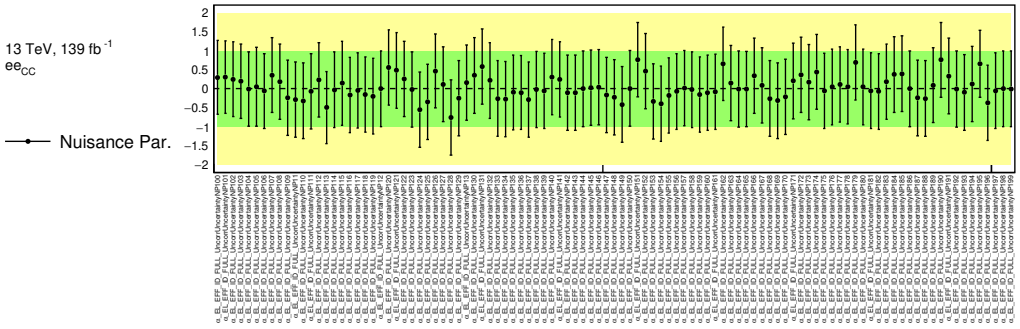
6.6.2 Muon Channel

The number of nuisance parameters[7] in the muon channel is drastically smaller than in the electron channel. This results from different schemes, defined by ATLAS E/Gamma and Muon groups, used. In case of the electron channel systematic sources are decomposed into a large number of individual coefficients, most of which are uncorrelated and affect only certain kinematic regions.

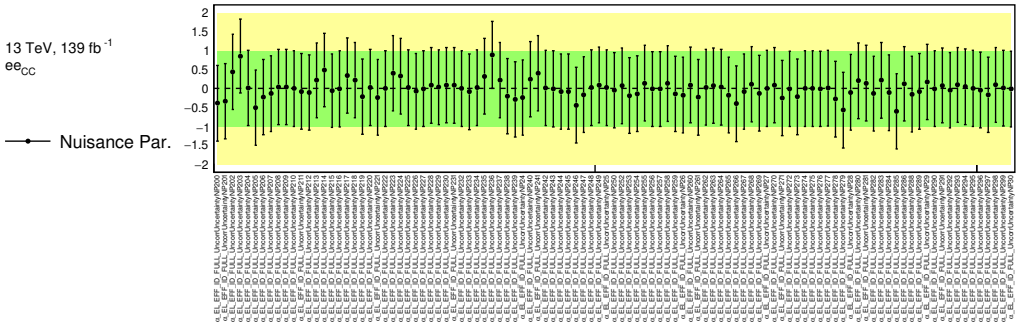
[6] In case of the cross section the relative uncertainties are shown since its range on the y-axis is larger than the ranges of all angular coefficients which are closer together and thus easier to compare.
[7] The full naming convention is documented by the ATLAS Muon group internally [178].



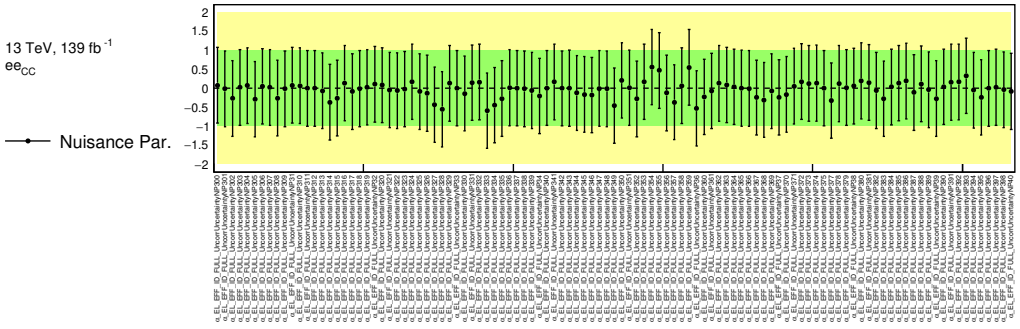
(a) Nuisance parameters related to (charge) identification efficiency uncertainties.



(b) Nuisance parameters related to identification efficiency uncertainties.

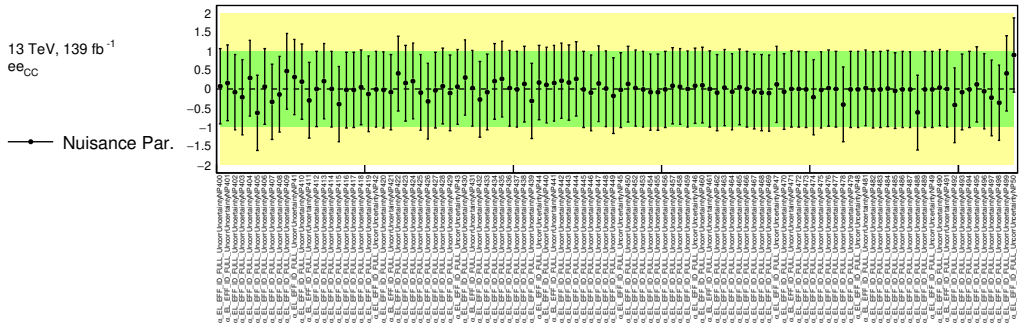


(c) Nuisance parameters related to identification efficiency uncertainties.

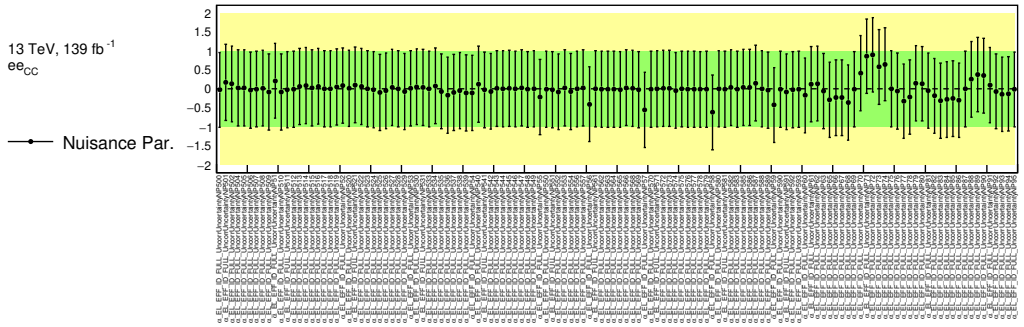


(d) Nuisance parameters related to identification efficiency uncertainties.

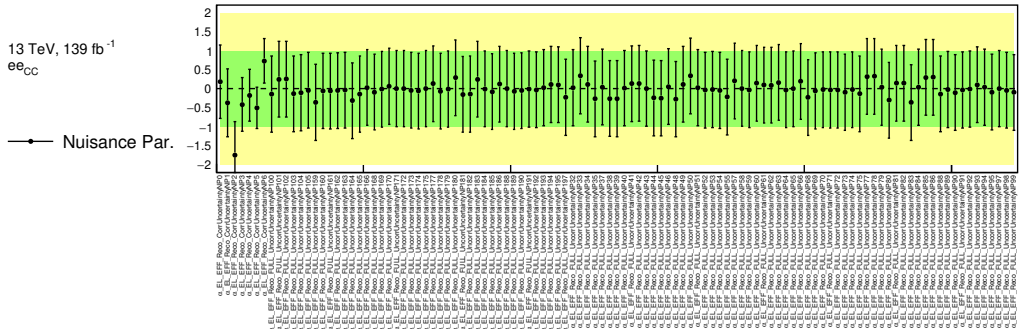
Fig. 6.6.: Pulls of electron nuisance parameters. Note that the vertical axis shows the dimensionless pull g.



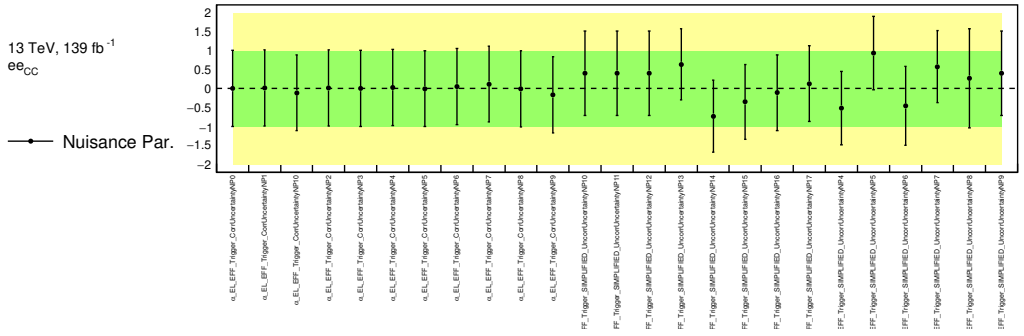
(a) Nuisance parameters related to identification efficiency uncertainties.



(b) Nuisance parameters related to identification efficiency uncertainties.

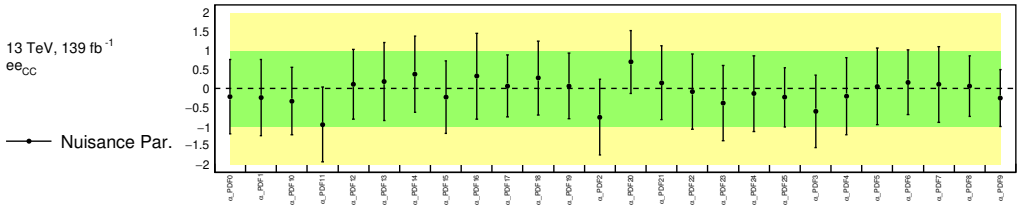


(c) Nuisance parameters related to reconstruction efficiency uncertainties.

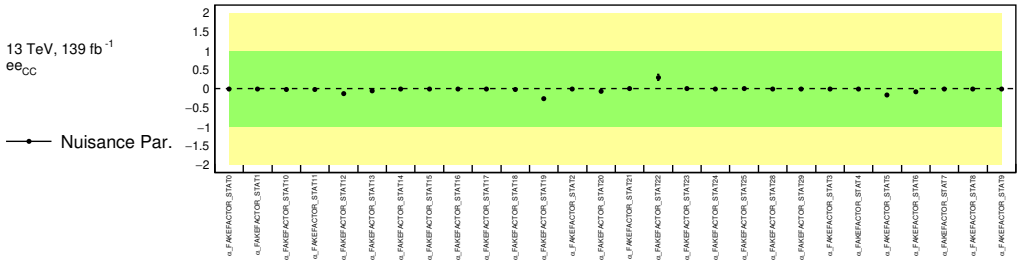


(d) Nuisance parameters related to trigger efficiency uncertainties.

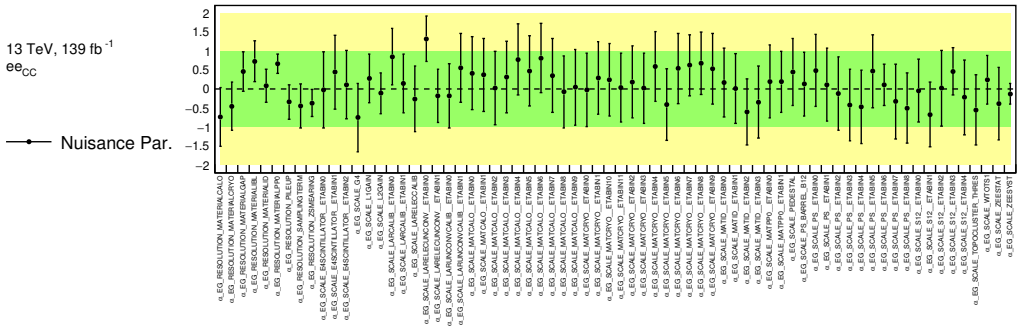
Fig. 6.7.: Pulls of electron nuisance parameters. Note that the vertical axis shows the dimensionless pull g.



(a) Nuisance parameters related to PDF uncertainties.

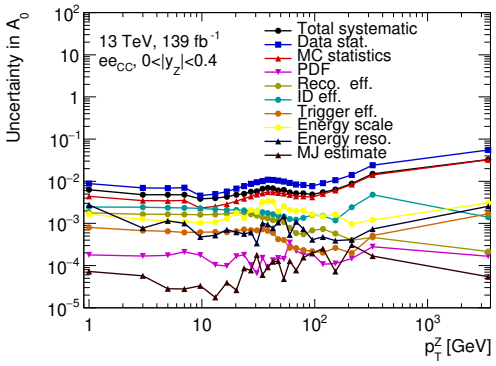


(b) Nuisance parameters related to multijet estimate uncertainties.

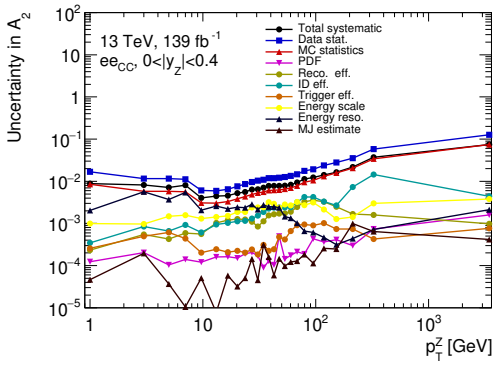


(c) Nuisance parameters related to energy scale and resolution uncertainties.

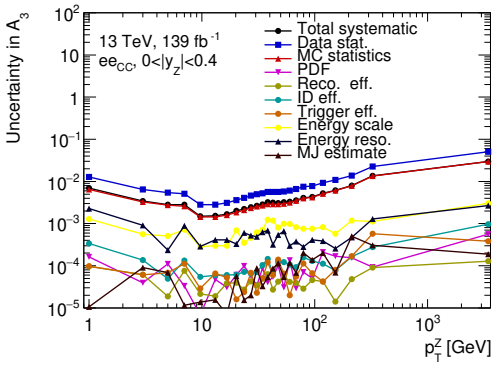
Fig. 6.8.: Pulls of electron nuisance parameters. Note that the vertical axis shows the dimensionless pull g.



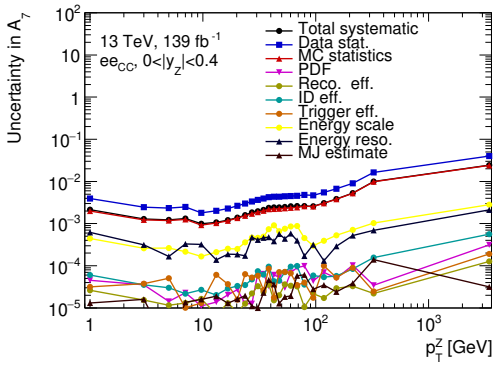
(a) Uncertainty on A_0.



(b) Uncertainty on A_2.

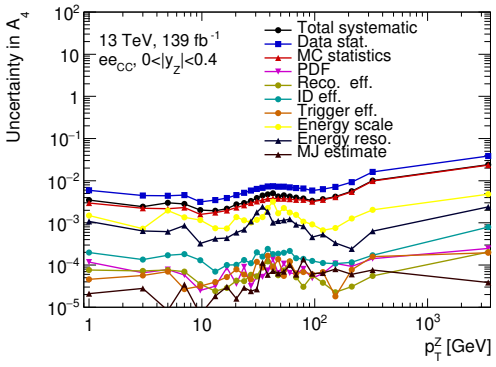


(c) Uncertainty on A_3.



(d) Uncertainty on A_7.

Fig. 6.9.: Breakdown of absolute uncertainties on angular coefficients as a function of the Z boson transverse momentum (denoted p_T^Z) in the electron channel.



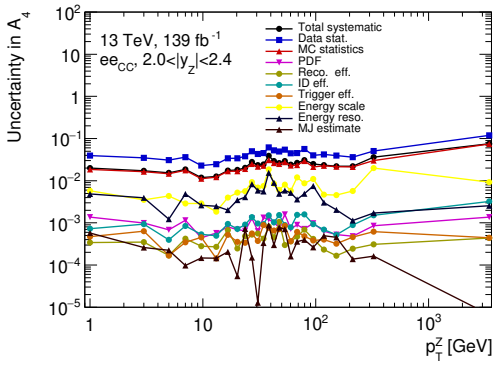


Fig. 6.10.: Breakdown of absolute uncertainties on the A_4 coefficient as a function of the Z boson transverse momentum (denoted p_T^Z) in different rapidity ranges in the electron channel.

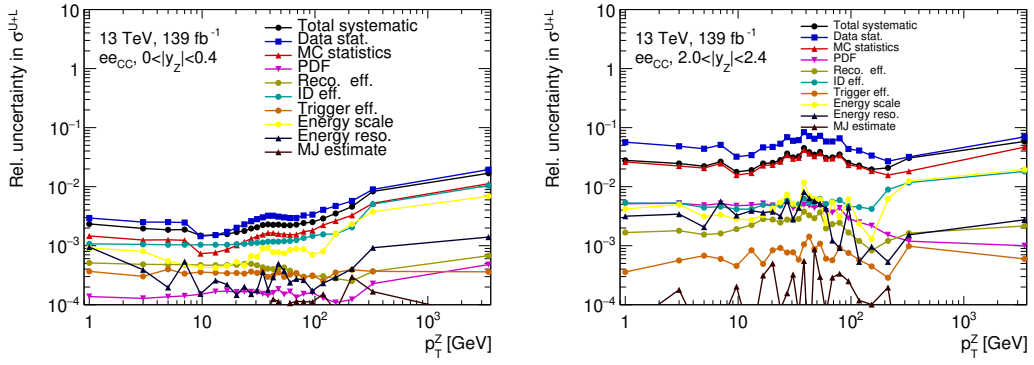


Fig. 6.11.: Breakdown of relative uncertainties on the unpolarised cross section as a function of the Z boson transverse momentum (denoted p_T^Z) in different rapidity ranges in the electron channel.

In case of the muon uncertainties a scheme has been chosen in which the number of nuisance parameters in the decomposition is smaller and less granular. They are depicted in figure 6.12 where all categories of uncertainty sources are included. The pull distributions of PDF uncertainties follow a similar pattern as in the electron channel and are well within expectations. This also holds true for most of the efficiency-related nuisance parameters with the exception of the trigger-related uncertainties, `MUON_EFF_TrigStatUncertainty` and `MUON_EFF_TrigSysUncertainty`. The former is pulled out of scale to approximately $g = -2.6$ and both of them exhibit a significant constraint. This indicates that a more detailed breakdown of nuisance parameters might be beneficial to assess whether the constraining power is real or an artefact of a simpler scheme. In addition, a detailed breakdown will also highlight the origin of the strong pull more clearly. The momentum resolution related nuisance parameter `MUON_CB` also shows a very strong constraint which can be traced to the same origin as the electron channel, i.e. the sensitivity of this measurement to the momentum resolution. Overall, most of the uncertainty sources under consideration follow the expectations with respect to the pre-fit assumptions. The individual parameters that show a stronger pull and/or constraint are related to non-leading uncertainty sources and might also benefit from a more detailed uncertainty scheme, such as `MUON_SCALE` or the trigger-related nuisance parameters in particular.

Overall, the uncertainties depicted in figures 6.13 and 6.14 follow similar patterns as in the electron channel. Expectedly the statistical uncertainties from data and simulation dominate for all angular coefficients and increase towards higher rapidity and transverse momentum. Efficiencies from the muon reconstruction efficiency contribute considerably only at low rapidity in A_0. However, in all other cases non-statistical uncertainty sources do not contribute significantly. This is different for the unpolarised cross section in figure 6.15, where the relative uncertainty at high rapidity is still dominated statistically. However, at low rapidity there are

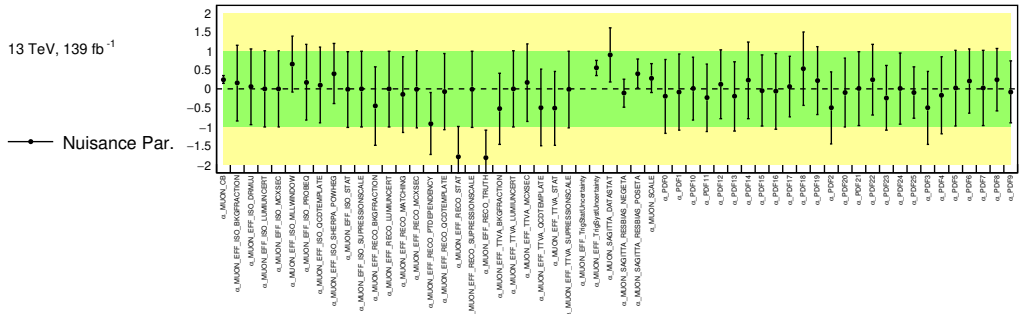


Fig. 6.12.: Pulls of muon nuisance parameters. Note that the vertical axis shows the dimensionless pull g and `MUON_EFF_TrigStatUncertainty` is out of scale.

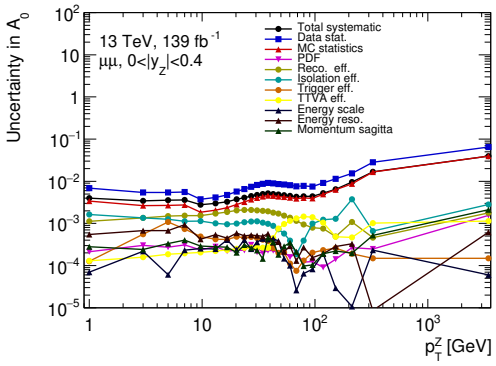
sizeable contributions from the scale factor uncertainties, in particular the isolation efficiency.

6.7 Compatibility

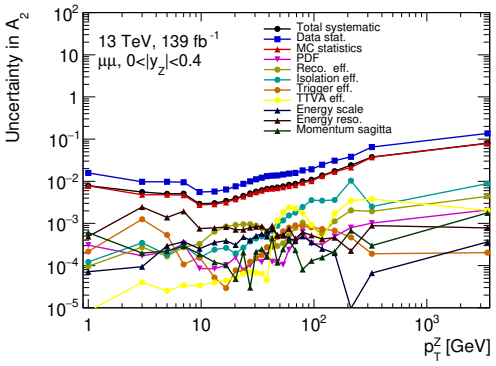
Before combining both analysis channels to maximise the sensitivity of the measurement, it is necessary to evaluate their compatibility. This can be done comparing the difference in the extracted coefficients. It is important to note, though, that the uncertainty bars shown in this compatibility test are partially correlated as both include PDF uncertainties. As these are non-leading systematic uncertainty sources this is not expected to change the overall comparison for compatibility. To validate the method, the first section depicts the absolute difference in the extracted coefficients in the Asimov dataset, i.e. simulation only to show the validity of the method.

6.7.1 Validation

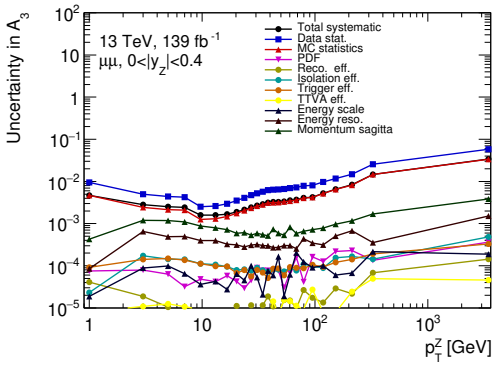
Figures 6.16, 6.17 and 6.18 depict the difference in each A_i coefficient and the unpolarised cross section in the simulated Asimov dataset between the electron and the muon channels in different regions. The open data points are centred on 0, while the black data points represent the ΔA_i between the electron and the muon channels. In all cases, as expected, the results from both channels agree to a very high degree of precision, well within the uncertainty bands. However, the agreement is not fully perfect and exhibits some minor fluctuations likely due to the limited statistical accuracy of the simulations as well as bin-to-bin migrations between neighbouring bins in transverse momentum. As the events selected in both channels are uncorrelated to each other minor fluctuations within uncertainties are expected. Overall this highlights the accuracy of the extraction procedure and supports its validity. The uncertainty bars contain all statistical and systematic



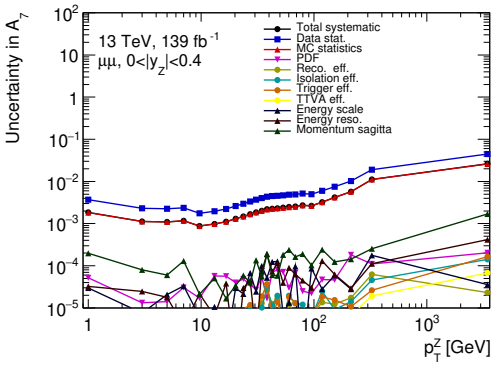
(a) Uncertainty on A_0.



(b) Uncertainty on A_2.

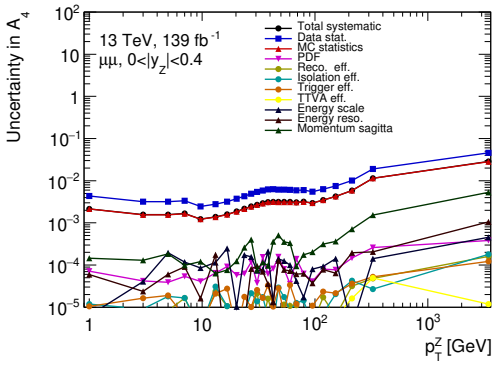


(c) Uncertainty on A_3.



(d) Uncertainty on A_7.

Fig. 6.13.: Breakdown of absolute uncertainties on angular coefficients as a function of the Z boson transverse momentum (denoted p_T^Z) in the muon channel.



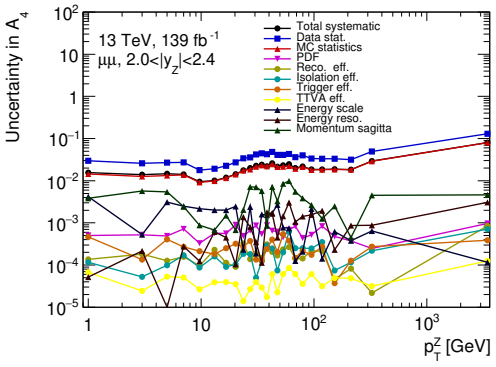


Fig. 6.14.: Breakdown of absolute uncertainties on the A_4 coefficient as a function of the Z boson transverse momentum (denoted p_T^Z) in different rapidity ranges in the muon channel.

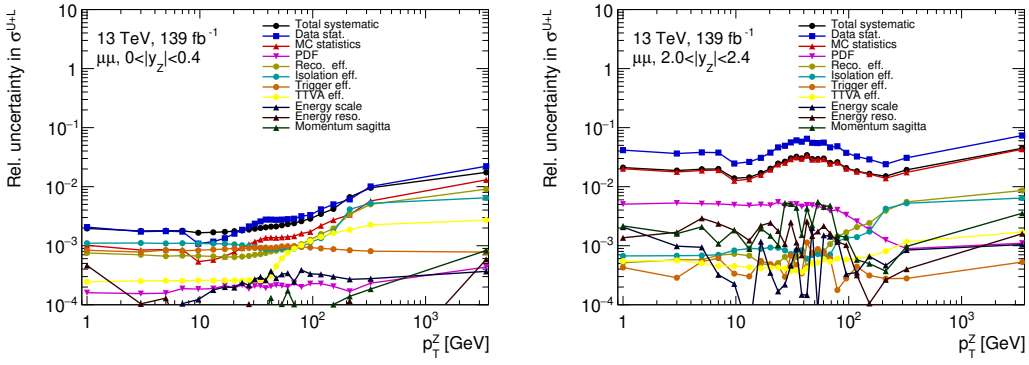
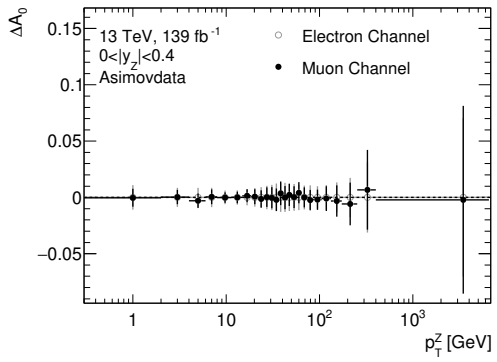


Fig. 6.15.: Breakdown of relative uncertainties on the unpolarised cross section as a function of the Z boson transverse momentum (denoted p_T^Z) in different rapidity ranges in the muon channel.

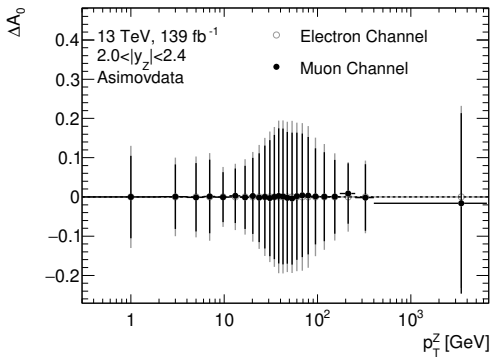
sources and highlight where the highest sensitivity is achieved for the different coefficients. Driven by statistical uncertainties, the total uncertainty increases on the coefficients in all cases at higher rapidity and transverse momenta but also in the region approximately between $10\,\mathrm{GeV}$ and $100\,\mathrm{GeV}$ in transverse momentum due to the fine, non-equidistant binning chosen. Expectedly, the same holds true for the relative uncertainty of the unpolarised cross section in figure 6.18.

6.7.2 Data Compatibility

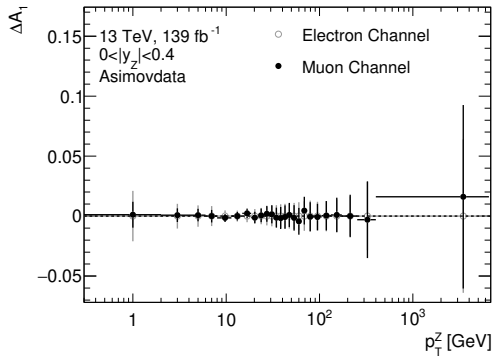
After validating the compatibility between the electron and muon channels in Asimovdata in the previous section, this section gives an overview of the compatibility between the channels in data. Figures 6.19, 6.20 and 6.21 depict all ΔA_i between the channels at low and high rapidity as well as the unpolarised cross section. Uncertainties are again partially correlated as both contain the relatively small contribution of the PDF uncertainties. Expectedly, there are more fluctuations and deviations visible between the channels compared to the purely simulation-based compatibility test. In most cases these fluctuations do not exhibit a systematic shape and are within the overall uncertainties. The difference between both channels are mostly of statistical nature as well as caused by bin-to-bin migrations. This is particularly noticeable as consecutive bins that fluctuate up and down. Some coefficients are affected by small differences in shape between channels, such as A_0 at low transverse momentum or A_3 at high transverse momentum. The A_4 coefficient, which is of particular interest for measurements of the weak mixing angle, overall mostly exhibits statistical fluctuations within uncertainties. While the lowest bin in transverse momentum at low rapidity shows a significant deviation between both channels, this is not observable at higher rapidity where the coefficient is most sensitive to the weak mixing angle due to reduced dilution effects. Additionally, some shape differences can also be observed in the unpolarised cross section in figure 6.21,



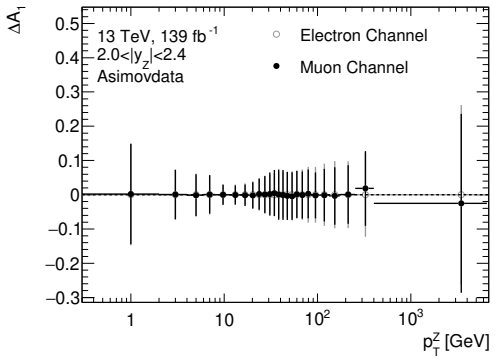
(a) Absolute difference in A_0 in $0 < |y_Z| < 0.4$.



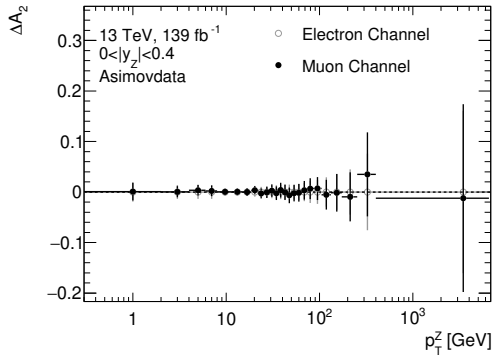
(b) Absolute difference in A_0 in $2.0 < |y_Z| < 2.4$.



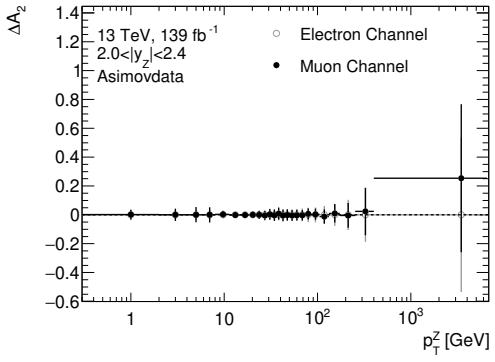
(c) Absolute difference in A_1 in $0 < |y_Z| < 0.4$.



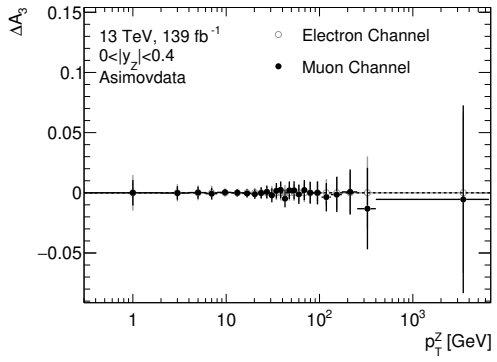
(d) Absolute difference in A_1 in $2.0 < |y_Z| < 2.4$.



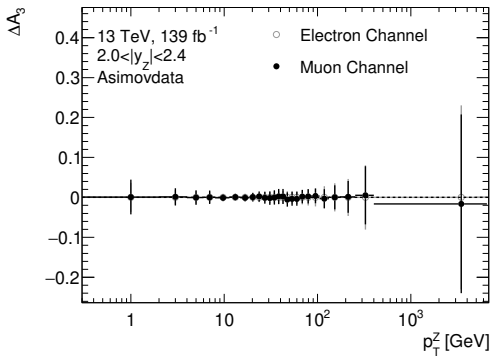
(e) Absolute difference in A_2 in $0 < |y_Z| < 0.4$.



(f) Absolute difference in A_2 in $2.0 < |y_Z| < 2.4$.

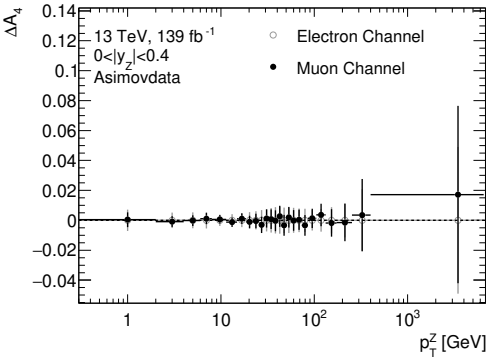


(g) Absolute difference in A_3 in $0 < |y_Z| < 0.4$.

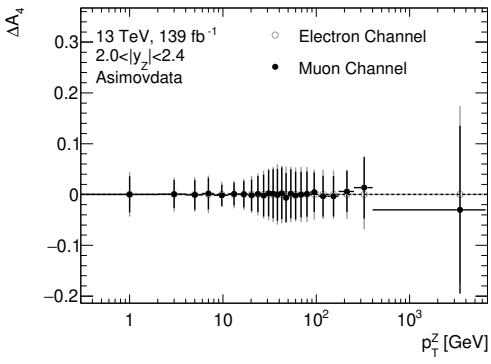


(h) Absolute difference in A_3 in $2.0 < |y_Z| < 2.4$.

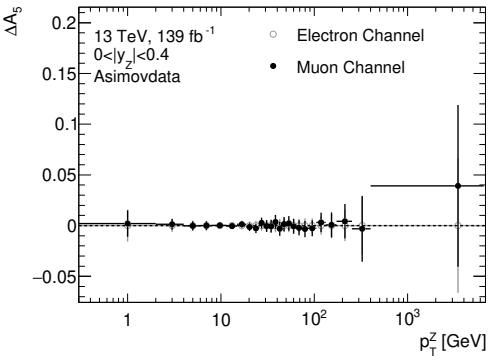
Fig. 6.16.: Closure test between electron and muon channel in Asimovdata as a function of the Z boson transverse momentum (denoted p_T^Z) in different rapidity ranges. All systematic and statistical uncertainties are included.



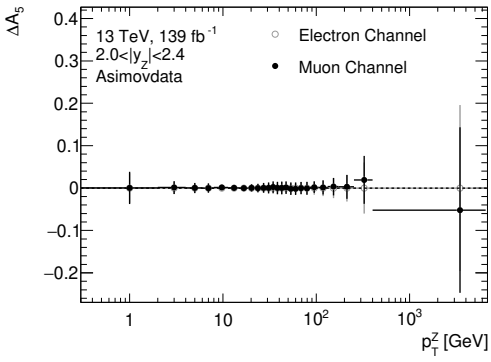
(a) Absolute difference in A_4 in $0 < |y_Z| < 0.4$.



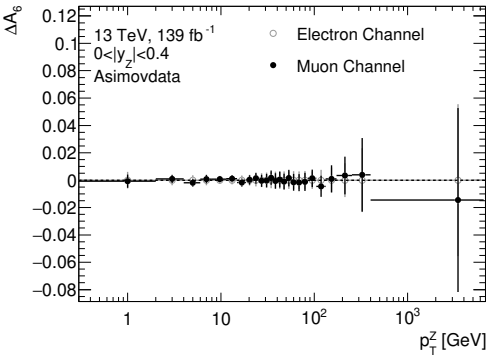
(b) Absolute difference in A_4 in $2.0 < |y_Z| < 2.4$.



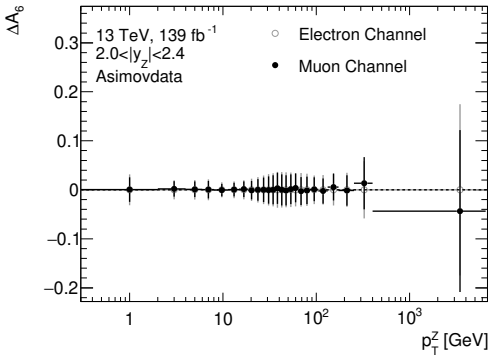
(c) Absolute difference in A_5 in $0 < |y_Z| < 0.4$.



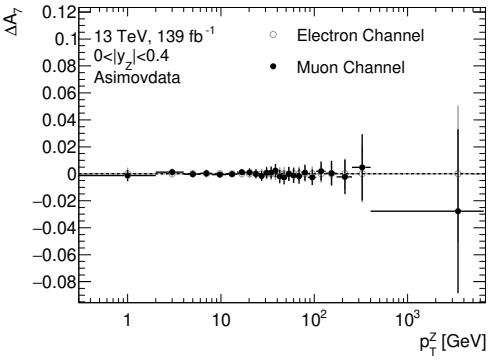
(d) Absolute difference in A_5 in $2.0 < |y_Z| < 2.4$.



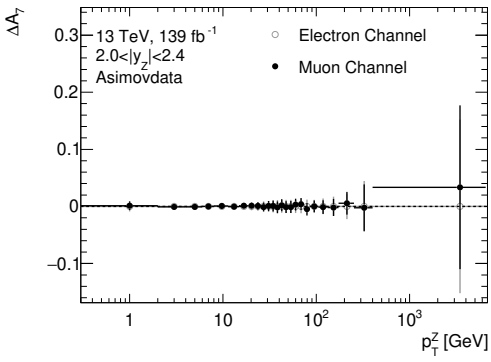
(e) Absolute difference in A_6 in $0 < |y_Z| < 0.4$.



(f) Absolute difference in A_6 in $2.0 < |y_Z| < 2.4$.



(g) Absolute difference in A_7 in $0 < |y_Z| < 0.4$.



(h) Absolute difference in A_7 in $2.0 < |y_Z| < 2.4$.

Fig. 6.17.: Closure test between electron and muon channel in Asimovdata as a function of the Z boson transverse momentum (denoted p_T^Z) in different rapidity ranges. All systematic and statistical uncertainties are included.

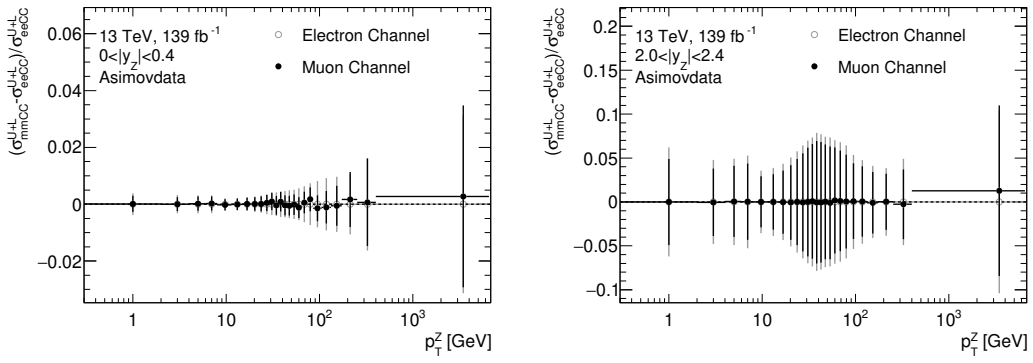


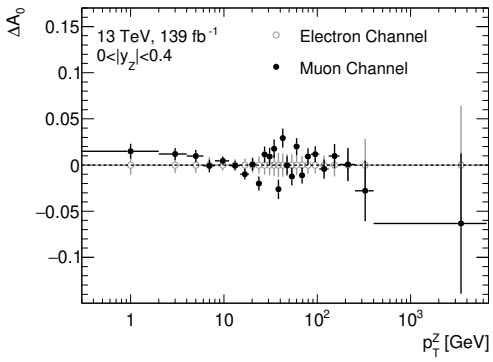
Fig. 6.18.: Closure test shown as the relative difference between electron and muon channel in Asimovdata as a function of the Z boson transverse momentum (denoted p_T^Z) in different rapidity ranges. All systematic and statistical uncertainties are included.

especially at low rapidity where the muon cross section is lower than the electron cross section at low transverse momentum but larger at high transverse momentum. Bin-to-bin migrations are also more noticeable in case of the higher rapidity. The sizes of uncertainties follow a similar pattern as in the case of the Asimov dataset. Overall, some differences between the channels should be studied further once muon systematic effects are understood to a high precision. Nonetheless, these deviations only affect certain regions in phase space and are thus no obstacle to a combination of both channels to maximise sensitivity.

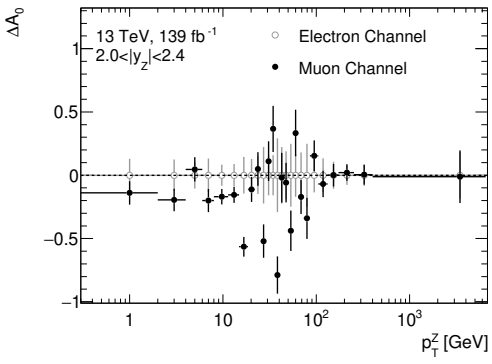
6.8 Individual Results

The following figures 6.22 and 6.23 depict a comparison of extracted angular coefficients in different regions between electron channel and muon channel. This first comparison focusses on the shapes of the individual channels before combining them and comparing them to the predictions and discussing the shapes in the next section. Overall, this highlights that many of the deviations and fluctuations observed in the compatibility test are of statistical nature or due to bin-to-bin migrations rather than systematic shifts and supports the dominating agreement between both channels.

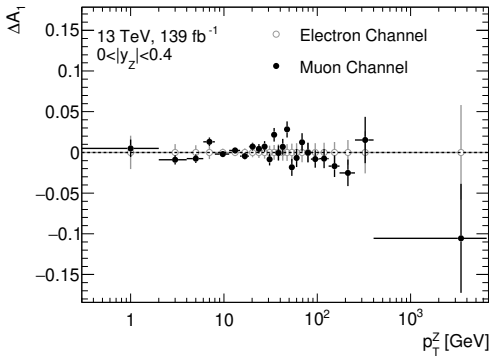
In figure 6.24 the comparison of the unpolarised cross section between electrons and muons shows the observations made in the compatibility test. While at low rapidity visually there is not much difference between channels, their high statistical and systematic accuracy leads to a more significant deviation between the channels compared to the larger deviations seen at higher rapidity. In the latter case, these deviations are mostly covered by uncertainties in case of low transverse momenta, but at higher momenta they appear to be more significant. A clearer understanding



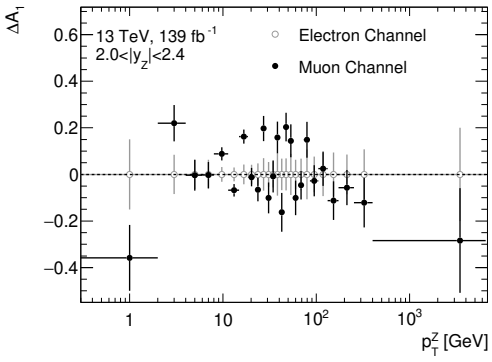
(a) Absolute difference in A_0 in $0 < |y_Z| < 0.4$.



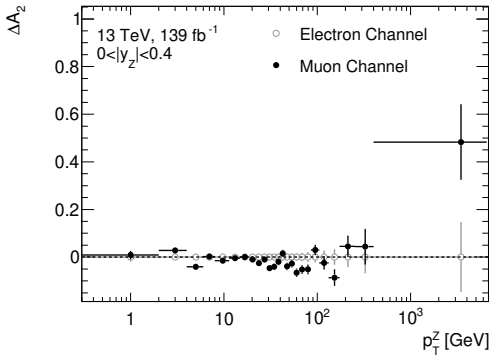
(b) Absolute difference in A_0 in $2.0 < |y_Z| < 2.4$.



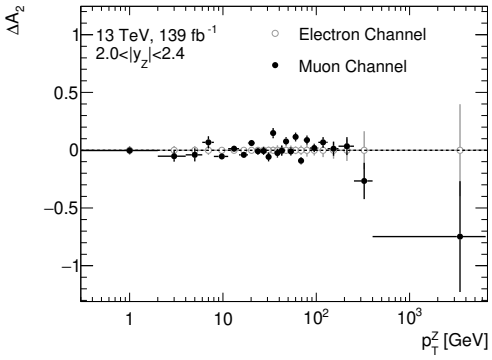
(c) Absolute difference in A_1 in $0 < |y_Z| < 0.4$.



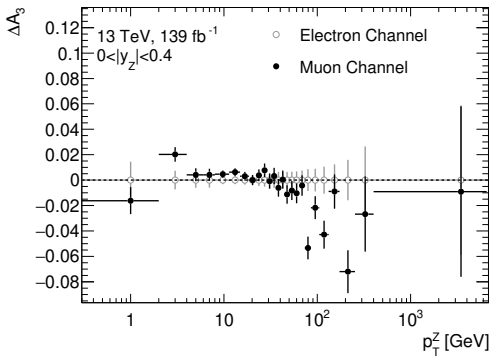
(d) Absolute difference in A_1 in $2.0 < |y_Z| < 2.4$.



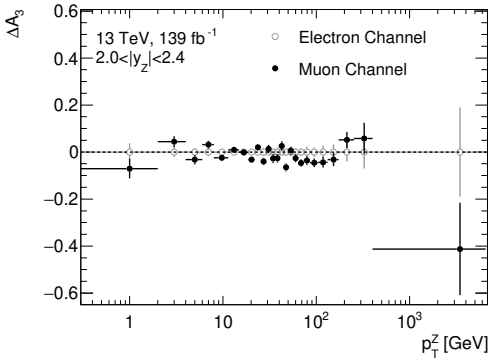
(e) Absolute difference in A_2 in $0 < |y_Z| < 0.4$.



(f) Absolute difference in A_2 in $2.0 < |y_Z| < 2.4$.

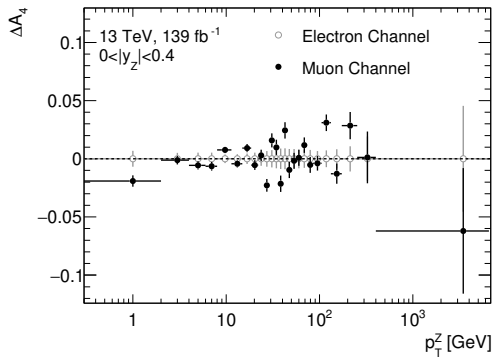


(g) Absolute difference in A_3 in $0 < |y_Z| < 0.4$.

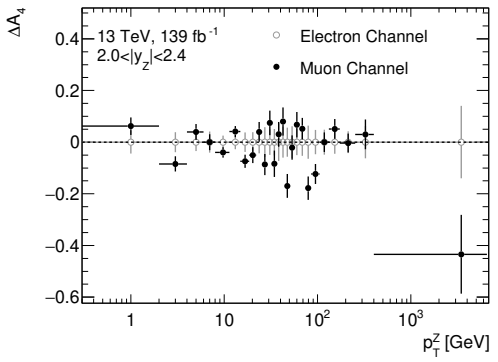


(h) Absolute difference in A_3 in $2.0 < |y_Z| < 2.4$.

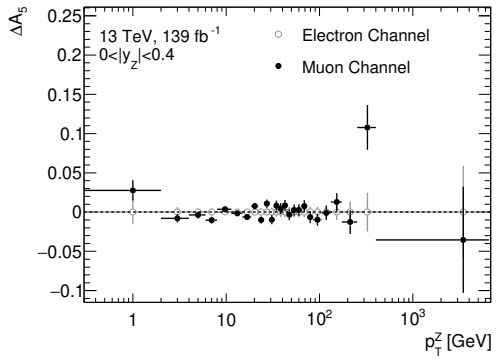
Fig. 6.19.: Absolute difference in extracted angular coefficients between electron and muon channel as a function of the Z boson transverse momentum (denoted p_T^Z) in different rapidity ranges. All systematic and statistical uncertainties are included.



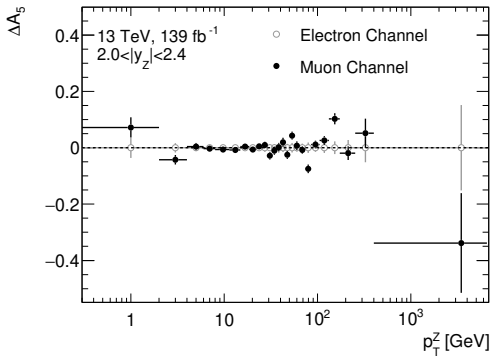
(a) Absolute difference in A_4 in $0 < |y_Z| < 0.4$.



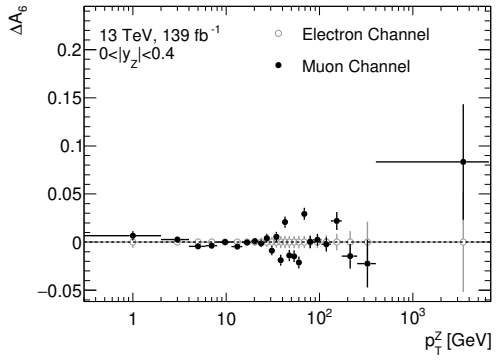
(b) Absolute difference in A_4 in $2.0 < |y_Z| < 2.4$.



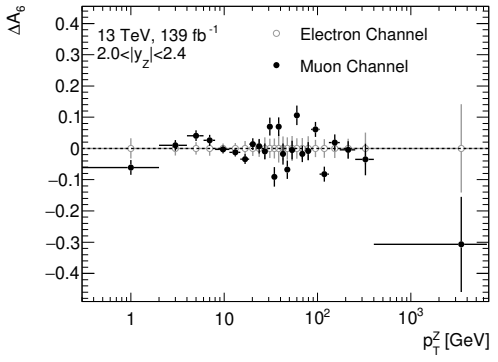
(c) Absolute difference in A_4 in $0 < |y_Z| < 0.4$.



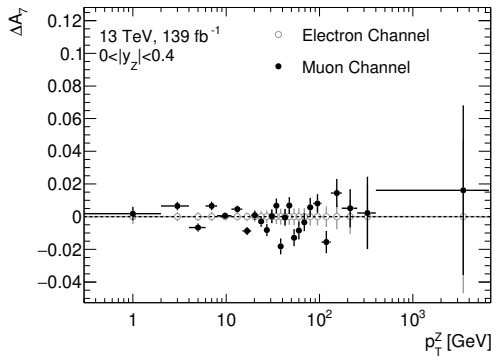
(d) Absolute difference in A_5 in $2.0 < |y_Z| < 2.4$.



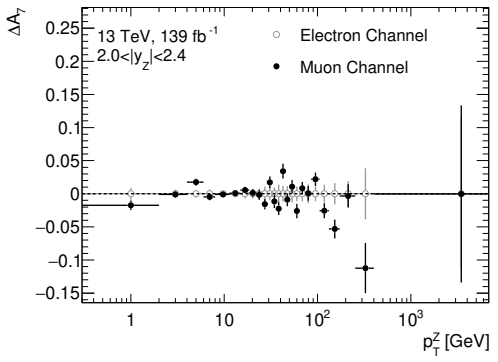
(e) Absolute difference in A_6 in $0 < |y_Z| < 0.4$.



(f) Absolute difference in A_6 in $2.0 < |y_Z| < 2.4$.



(g) Absolute difference in A_7 in $0 < |y_Z| < 0.4$.



(h) Absolute difference in A_7 in $2.0 < |y_Z| < 2.4$.

Fig. 6.20.: Absolute difference in extracted angular coefficients between electron and muon channel as a function of the Z boson transverse momentum (denoted p_T^Z) in different rapidity ranges. All systematic and statistical uncertainties are included.

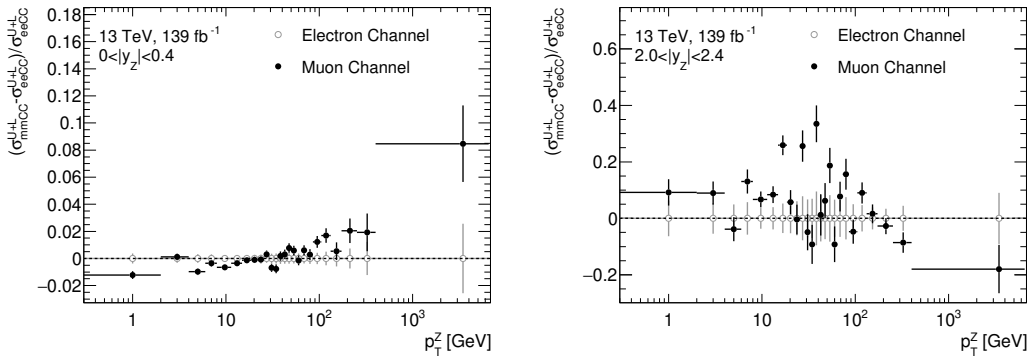


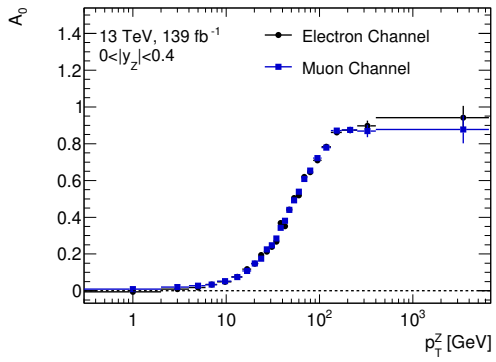
Fig. 6.21.: Relative difference in the measured cross section between electron and muon channel as a function of the Z boson transverse momentum (denoted p_T^Z) in different rapidity ranges. All systematic and statistical uncertainties are included.

is expected once muon systematic uncertainties are decomposed in a more detailed way. However, special attention will be required to be placed on the electron energy calibration compared to the muon momentum calibration as a function of the dilepton transverse momentum as well as the absolute size of the multijet estimate in the electron channel. While the control distributions in figures 5.12 do not exhibit an unexpected distribution of the estimate, its relative contribution increases towards high transverse momenta and as such - as it is subtracted in the extraction - could lead to some regions where it is over- or underestimated.

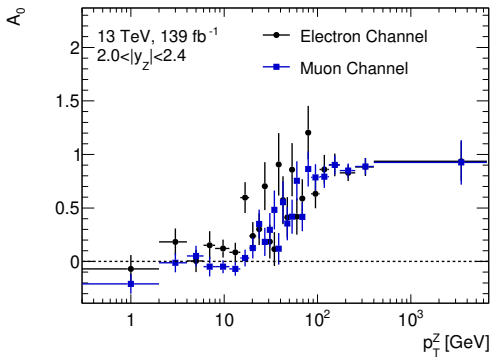
Additional observations can be made comparing the angular coefficients. For instance, in most cases in the highest bin of transverse momentum of the individual A_i coefficients the electron channel has a larger value than the muon channel with few exceptions. The highest bin in transverse momentum is also the one affected by the largest statistical fluctuations, but this, combined with the deviation in the measured cross section in figure 6.24, supports the need for close inspection once muon systematic sources are broken down in a more detailed way. Most other deviations do not appear to follow clear systematic shifts. This means a combination of both channels in the next section can be done as the channels are compatible with each other, in particular in the statistically most relevant regions.

6.9 Combined Results

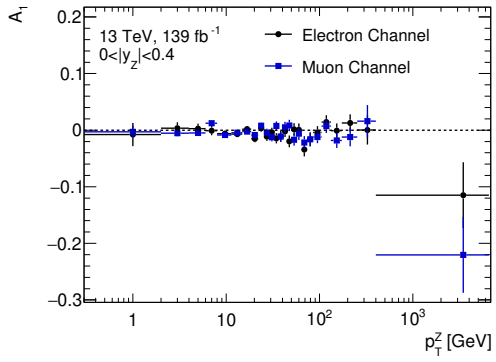
After establishing the validity of the fitting procedure as well as the compatibility of both channels individually, they can be combined in a single fit to maximise the sensitivity of the measurement. This is achieved by accounting for the covariance of



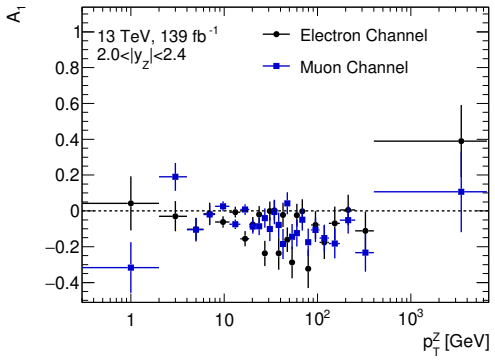
(a) Measured A_0 in $0 < |y_Z| < 0.4$.



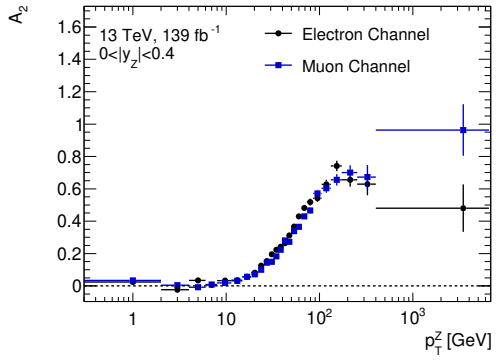
(b) Measured A_0 in $2.0 < |y_Z| < 2.4$.



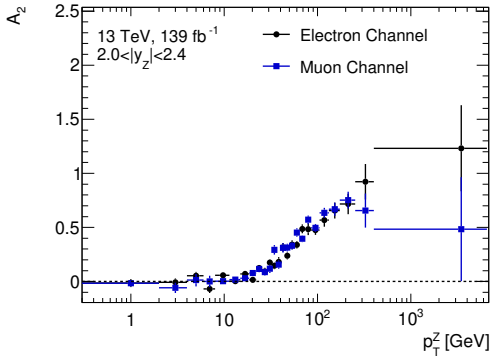
(c) Measured A_1 in $0 < |y_Z| < 0.4$.



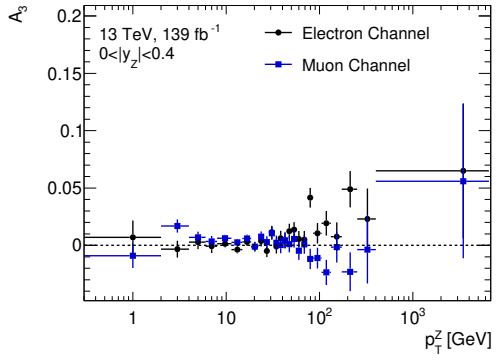
(d) Measured A_1 in $2.0 < |y_Z| < 2.4$.



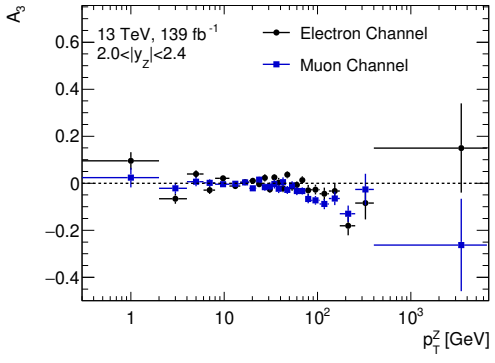
(e) Measured A_2 in $0 < |y_Z| < 0.4$.



(f) Measured A_2 in $2.0 < |y_Z| < 2.4$.

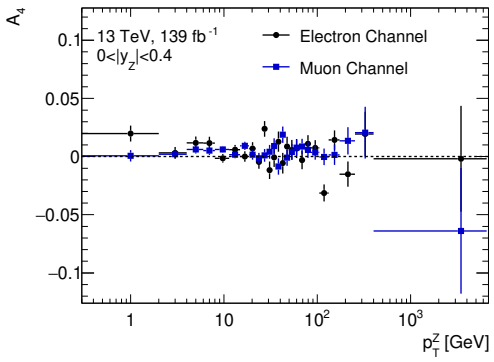


(g) Measured A_3 in $0 < |y_Z| < 0.4$.

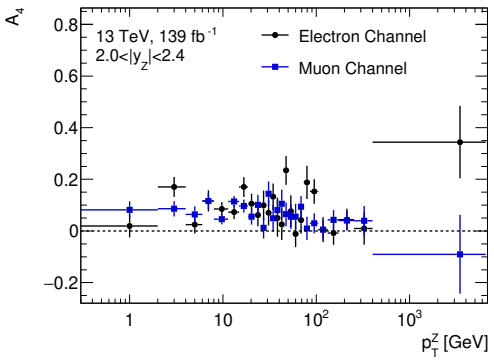


(h) Measured A_3 in $2.0 < |y_Z| < 2.4$.

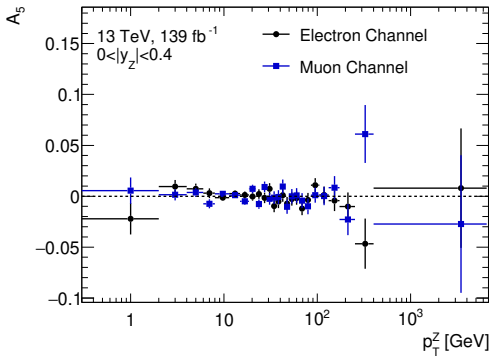
Fig. 6.22.: Extracted angular coefficients in the electron and muon channels as a function of the Z boson transverse momentum (denoted p_T^Z) in different rapidity ranges. All systematic and statistical uncertainty sources are included.



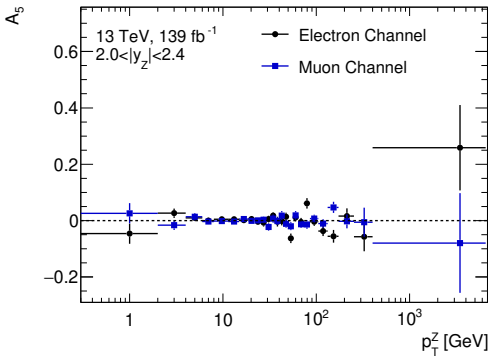
(a) Measured A_4 in $0 < |y_Z| < 0.4$.



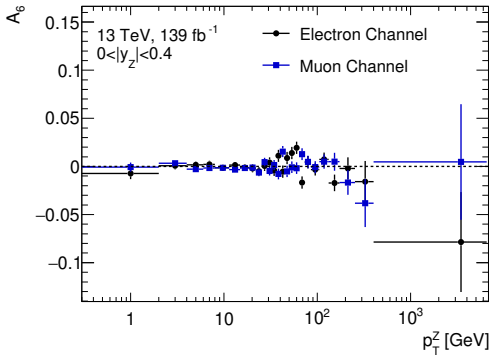
(b) Measured A_4 in $2.0 < |y_Z| < 2.4$.



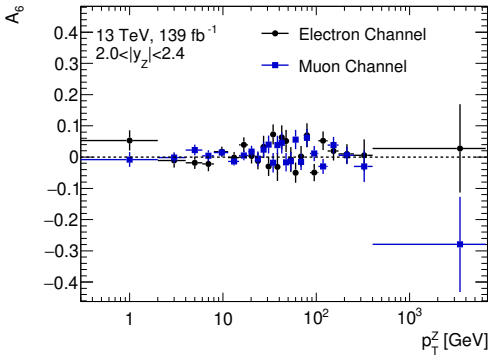
(c) Measured A_5 in $0 < |y_Z| < 0.4$.



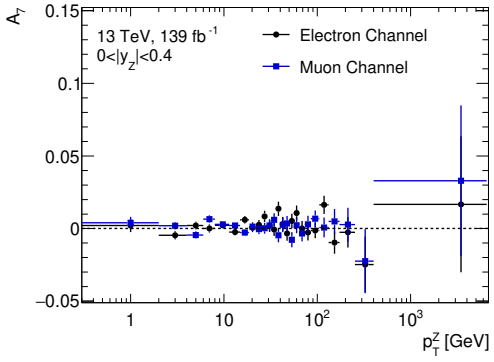
(d) Measured A_5 in $2.0 < |y_Z| < 2.4$.



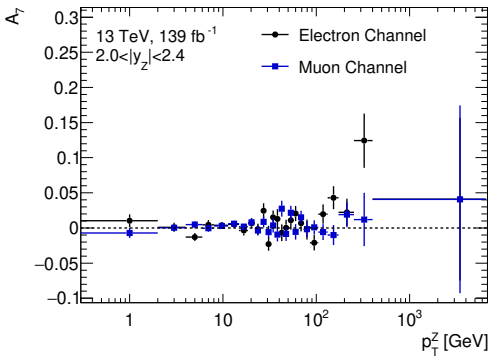
(e) Measured A_6 in $0 < |y_Z| < 0.4$.



(f) Measured A_6 in $2.0 < |y_Z| < 2.4$.



(g) Measured A_7 in $0 < |y_Z| < 0.4$.



(h) Measured A_7 in $2.0 < |y_Z| < 2.4$.

Fig. 6.23.: Extracted angular coefficients in the electron and muon channels as a function of the Z boson transverse momentum (denoted p_T^Z) in different rapidity ranges. All systematic and statistical uncertainty sources are included.

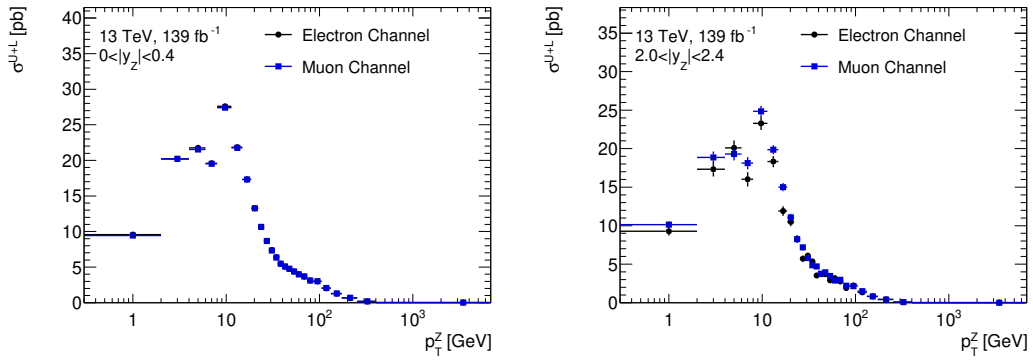


Fig. 6.24.: Measured cross section in the electron and muon channels as a function of the Z boson transverse momentum (denoted p_T^Z) in different rapidity ranges. All systematic and statistical uncertainty sources are included.

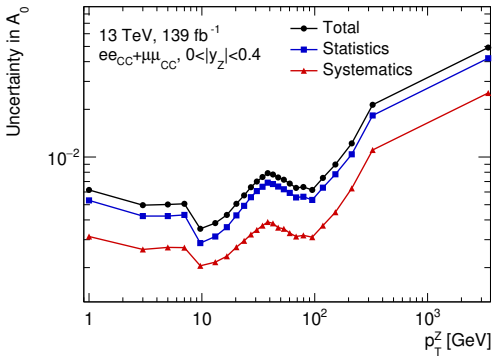
uncertainties. The combined fit has a larger number of degrees of freedom than a single channel, for the number of bins is effectively doubled

$$N_{\text{d.o.f.}} = 25 \cdot 6 \cdot 64 \cdot 2 - 25 \cdot 6 \cdot 9 = 17850. \tag{6.16}$$

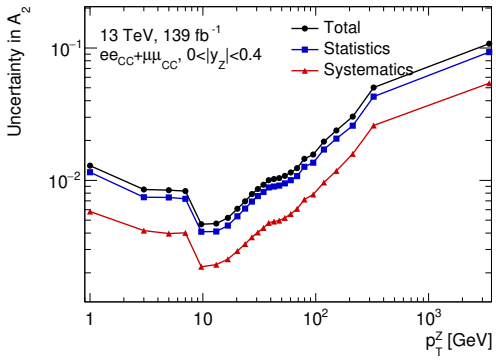
The fit on data results in an overall $\chi^2/N_{\text{d.o.f.}} = 26818.3/17850 \approx 1.5$, which is in line with expectations given the increased $\chi^2/N_{\text{d.o.f.}}$ from the electron channel. Overall, this does not indicate major problems in the fit, but it should still be studied once remaining minor effects such as the multijet uncertainties are completely understood.

6.9.1 Uncertainties

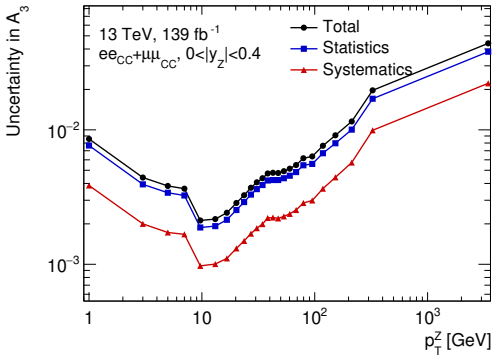
For simplicity the following representative distributions 6.25 and 6.26 are only split into statistical and systematic uncertainties on the individual angular coefficients. Coefficients and kinematic regions not shown follow the same behaviour. Detailed pull plots are in appendix F and do not exhibit major deviations from what has been observed in the individual fits. The figures below depict the final precision for exemplary coefficients in line with observations from the individual channels, for instance with respect to the statistical uncertainties as a function of the transverse momentum. In particular, even with the combined statistical power of both channels, data statistical uncertainties still by far dominate the total uncertainties in all cases. The relative uncertainty on the unpolarised cross section shows a similar behaviour. However, there are some kinematic regions at low rapidity at $p_{T,Z} \approx 10\,\text{GeV}$ where systematic effects dominate (mostly driven by the Monte Carlo statistical limitation and the electron identification, in line with the observations from the electron channel).



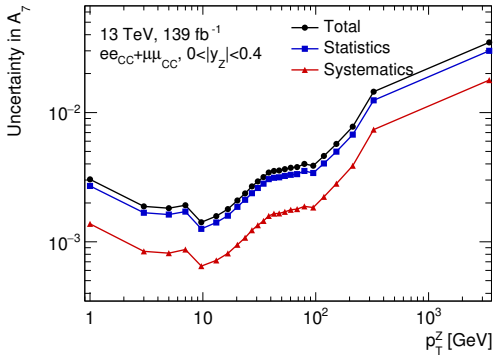
(a) Uncertainty on A_0.



(b) Uncertainty on A_2.

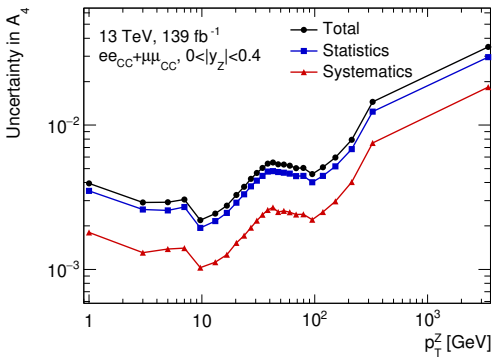


(c) Uncertainty on A_3.



(d) Uncertainty on A_7.

Fig. 6.25.: Breakdown of absolute uncertainties on the extracted angular coefficients into statistical and systematic sources as a function of the Z boson transverse momentum (denoted p_T^Z). The combination of the electron and the muon channels is depicted.



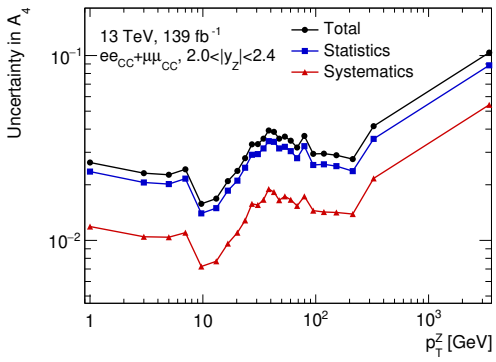


Fig. 6.26.: Breakdown of absolute uncertainties on the extracted A_4 coefficient into statistical and systematic sources as a function of the Z boson transverse momentum (denoted p_T^Z) in different rapidity ranges. The combination of the electron and the muon channels is depicted.

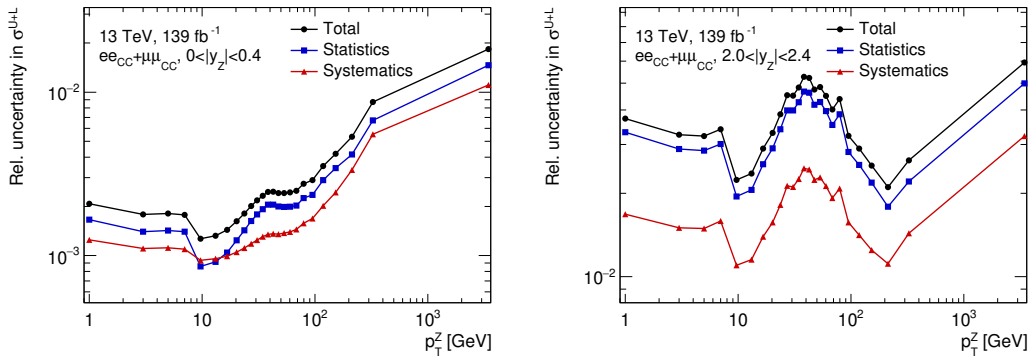


Fig. 6.27.: Breakdown of relative uncertainties on the measured cross section into statistical and systematic sources as a function of the Z boson transverse momentum (denoted p_T^Z) in different rapidity ranges. The combination of the electron and the muon channels is depicted.

6.9.2 Final Results

The final results of this measurement are shown in figures 6.28, 6.29 and 6.30, which depict the measured angular coefficients and the unpolarised cross section including all systematic sources discussed compared to the expectation from the POWHEGBOX + PYTHIA 8 generator[8]. Full results for all bins in data are presented in appendix G. The prediction is calculated at NLO in QCD and does thus not reflect effects of NNLO or higher order. NNLO expectations are depicted in section 1.3.2.4. This is noticeable, for instance, in A_0 and A_2, which at NLO are expected to fulfil the Lam-Tung relation $A_0 - A_2 = 0$. However, at higher orders in QCD this relation is broken and the data supports this expectation. Kinematically this is caused by the non-coplanarity of the quark plane and the hadron plane in the Collins-Soper system due to the non-zero transverse momentum of the dilepton system, which leads to $A_0 \geq A_2$ as observed in the data [70]. Furthermore, the coefficients A_5, A_6 and A_7 are expected to be non-zero only at NNLO in QCD or higher orders as seen in section 1.3.2.4. In particular in the case of A_6 around $50\,\mathrm{GeV}$ in transverse momentum this is clearly visible and supports this expectation. The distributions presented also highlight that some coefficients more strongly depend on the rapidity than others, e.g. A_0 or A_2 do not appear to benefit significantly from a rapidity differential measurement, while there are very clear trends for A_1, A_3 and A_4 towards larger absolute values at higher rapidity. In part, for instance for A_4, this can be explained by reduced dilution effects, i.e. less ambiguity about which proton provided the quark and which one the anti-quark in the $q\bar{q} \to Z$ production process as sea quarks in the proton statistically carry lower momenta. The apparent deviation between data and expectation in A_3 at high transverse momenta and low rapidity is not yet understood and demands further study.

[8] Uncertainties on the prediction originate in the statistical uncertainty of the Monte Carlo sample only.

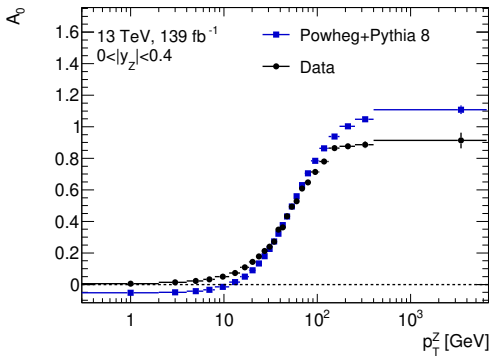
The precise shape of the angular coefficients is rooted in the phase space considered, which defines the scale at which the coefficients are probed, in particular defined by the mass window of the Z pole mass. Moreover, as stated before, the accuracy in QCD also strongly impacts the expectation on the shape and the relative behaviour of the coefficients to each other. In addition to the dilution effects which are higher at lower rapidity and thus affect the shape of the coefficients, the effect of low and high transverse momenta can also be estimated for some of the coefficients using formula 1.45 and 1.56 which reveal that, for instance, A_1 and A_4 are expected to vanish at very high transverse momenta, which is also supported by the data with the exception of statistical fluctuations and bin-to-bin migrations. Besides, at NLO in QCD approaching the limit of $p_{T,Z} = 0\,\mathrm{GeV}$ all coefficients with the exception of A_4, representing the forward-backward asymmetry, are expected to vanish, while at higher orders some coefficients receive a small non-zero contribution from NNLO and higher orders [70].

Overall, statistical fluctuations and bin-to-bin migrations (also observed in the previous measurement at ATLAS [68]), in particular in sparsely populated regions hide some systematic effects between the NLO expectation and the data. Future measurements that integrate over the dilepton rapidity will also benefit from higher statistical accuracy. In addition, a regularisation method which aims to account for bin-to-bin migration effects in particular between bins in transverse momentum could help sharpening the shape of the angular coefficients in data. Nonetheless, this measurement already shows a very high statistical and systematic accuracy at which the angular coefficients are measured, which will in particular aid comparisons to theoretical predictions as they can be probed to a high precision.

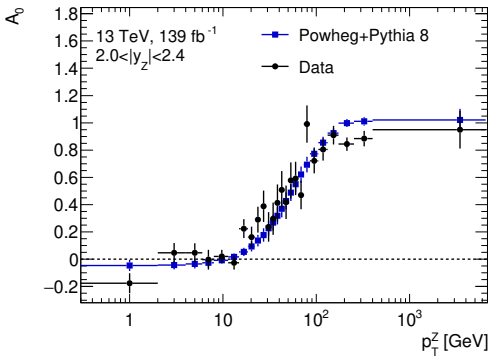
Finally, the high precision of the unpolarised cross section measurement is visible in figure 6.28. Expectedly, towards very high transverse momenta the cross section approaches 0 as it is statistically unlikely for such a large transverse momentum to be created. The same effect is true for higher rapidity regions, however, the distribution (i.e. the integration over the transverse momentum shown) does not decrease as sharply as the transverse momentum. The shape of the cross section as a function of the transverse momentum is strongly sculpted by the centre-of-mass energy and the mass window around the Z boson pole mass. A non-zero transverse momentum of the Z boson can be caused either by non-zero transverse momenta of the initial partons in the protons or small angles between the colliding protons. One of the main production processes of a Z boson at the LHC is $gq \to Z + q$, i.e. the production with a jet. Since the transverse momentum must be conserved, they are produced mostly back-to-back in the transverse plane, which sculpts the cross section observed here. The shape is also influenced by the non-equidistant binning which leads to the double-peak like structure. Compared to the predictions from POWHEGBOX + PYTHIA 8 the mismodelling of the transverse momentum is clearly

visible and consistent with the control distributions shown in section 5.6. The shape of the relative difference between the prediction and the data in the cross section as a function of the transverse momentum is consistent with the observed behaviour, for instance in an analysis of Z boson transverse momentum of the CMS collaboration [179]. The unpolarised cross section shown is independent of selections on final state leptons and as such more sensitive to the rapidity dependence on the transverse momentum compared to measurements such as a recent measurement of the ATLAS collaboration [180], where this dependence is effectively removed by the fiducial lepton selections. This has also been shown in the measurement of the Z boson transverse momentum at $\sqrt{s} = 8\,\mathrm{TeV}$ in ATLAS [181].

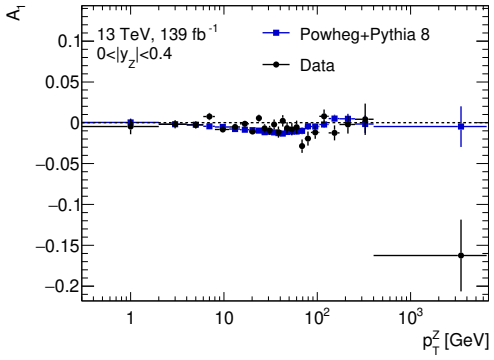
The measurement of the unpolarised cross section differential in rapidity and transverse momentum is a crucial part in a better understanding of Z boson production and thus improving theoretical predictions with a higher accuracy. Such a precise understanding is also essential for simulations and other theoretical predictions to better model the Z boson transverse momentum as discussed in chapter 5, where the mismodelling in the POWHEGBOX + PYTHIA 8 simulation is clearly visible. To conclude, the data clearly support the observations already made by ATLAS at $\sqrt{s} = 8\,\mathrm{TeV}$ [68], in particular the breaking of the Lam-Tung relation as well as the non-zero coefficients A_5, A_6 and A_7. The achievable accuracy of the measurement expectedly surpasses the previous one, however, some of this additional accuracy is expected to show only in a rapidity-integrated measurement. This measurement is a baseline for continued rigorous study of the data and also for a statistical evaluation of the deviations observed. Theoretical predictions can be compared to a high precision to draw further conclusions on existing models.



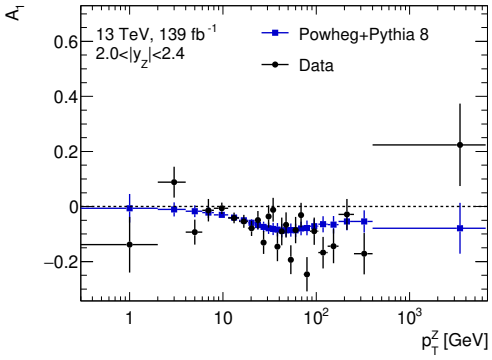
(a) Measured A_0 in $0 < |y_Z| < 0.4$.



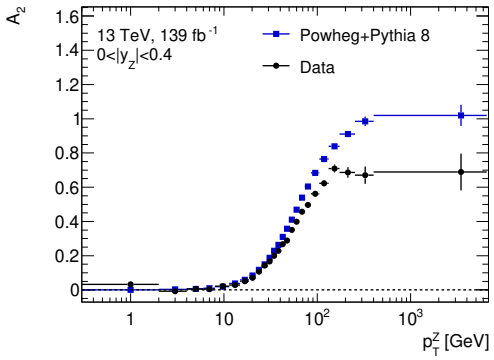
(b) Measured A_0 in $2.0 < |y_Z| < 2.4$.



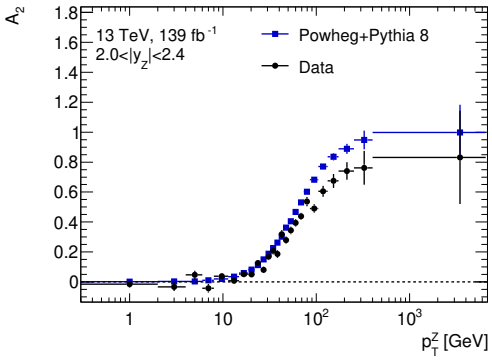
(c) Measured A_1 in $0 < |y_Z| < 0.4$.



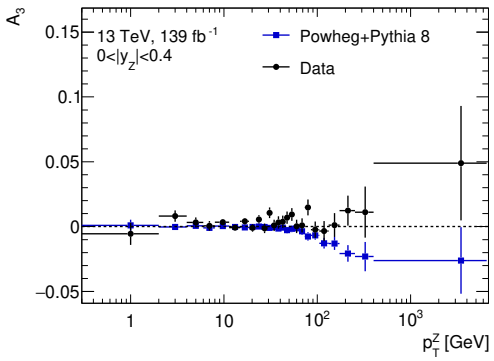
(d) Measured A_1 in $2.0 < |y_Z| < 2.4$.



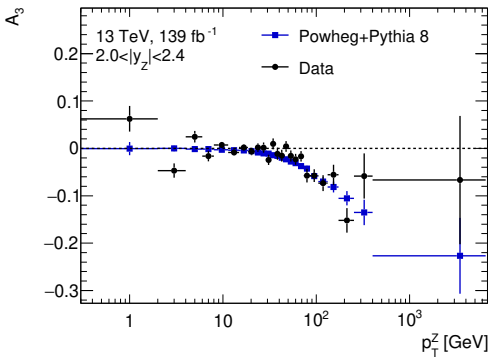
(e) Measured A_2 in $0 < |y_Z| < 0.4$.



(f) Measured A_2 in $2.0 < |y_Z| < 2.4$.

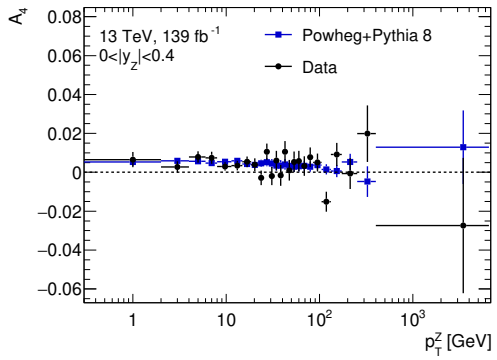


(g) Measured A_3 in $0 < |y_Z| < 0.4$.

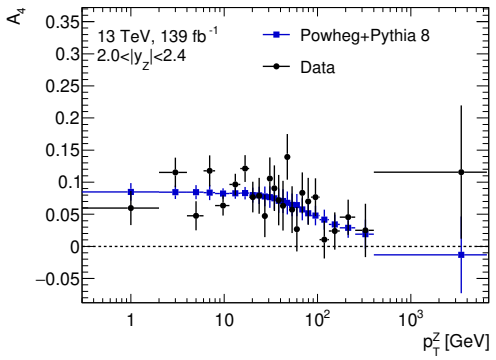


(h) Measured A_3 in $2.0 < |y_Z| < 2.4$.

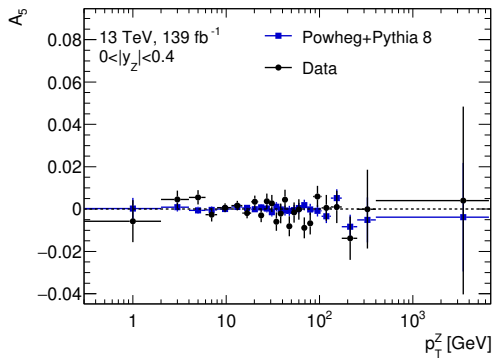
Fig. 6.28.: Extracted angular coefficients from the combination of electron and muon channels as a function of the Z boson transverse momentum (denoted p_T^Z) in different rapidity ranges. All systematic and statistical uncertainty sources are included.



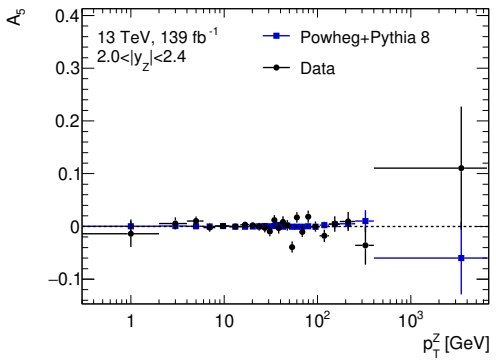
(a) Measured A_4 in $0 < |y_Z| < 0.4$.



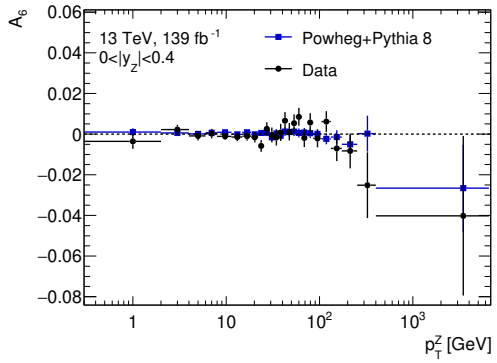
(b) Measured A_4 in $2.0 < |y_Z| < 2.4$.



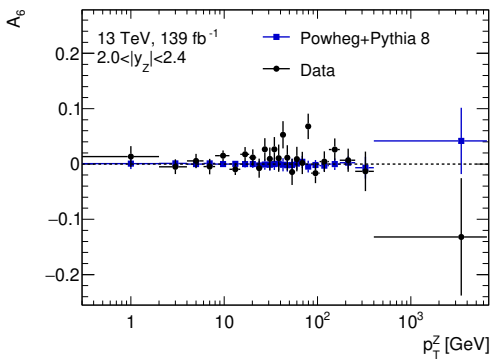
(c) Measured A_5 in $0 < |y_Z| < 0.4$.



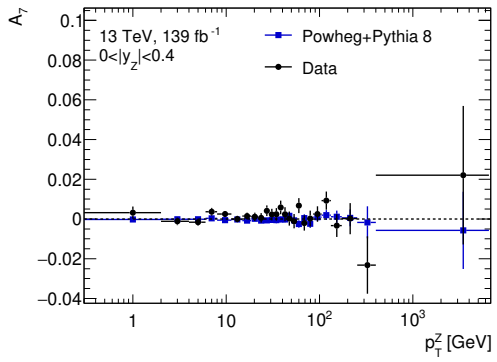
(d) Measured A_5 in $2.0 < |y_Z| < 2.4$.



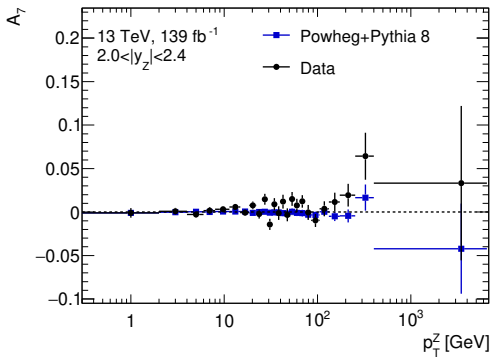
(e) Measured A_6 in $0 < |y_Z| < 0.4$.



(f) Measured A_6 in $2.0 < |y_Z| < 2.4$.

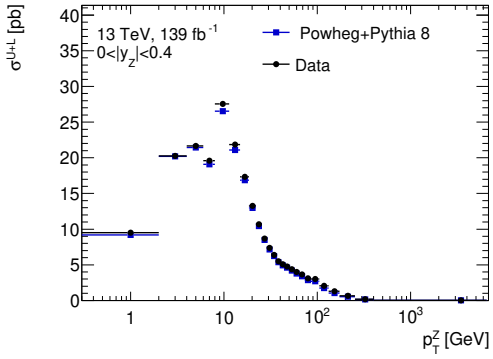


(g) Measured A_7 in $0 < |y_Z| < 0.4$.

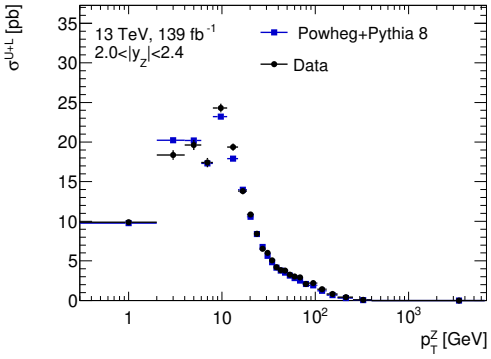


(h) Measured A_7 in $2.0 < |y_Z| < 2.4$.

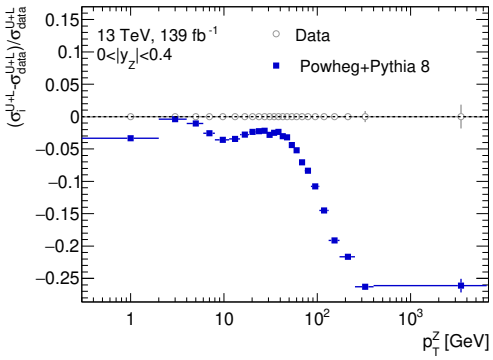
Fig. 6.29.: Extracted angular coefficients from the combination of electron and muon channels as a function of the Z boson transverse momentum (denoted p_T^Z) in different rapidity ranges. All systematic and statistical uncertainty sources are included.



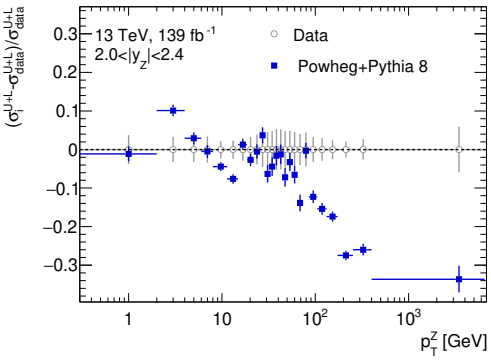
(a) Measured unpolarised cross section in $0 < |y_Z| < 0.4$.



(b) Measured unpolarised cross section in $2.0 < |y_Z| < 2.4$.



(c) Relative difference in the unpolarised cross section between data and prediction in $0 < |y_Z| < 0.4$.



(d) Relative difference in the unpolarised cross section between data and prediction in $2.0 < |y_Z| < 2.4$

Fig. 6.30.: Measured unpolarised cross section from the combination of electron and muon channels as a function of the Z boson transverse momentum (denoted p_T^Z) in different rapidity ranges. All systematic and statistical uncertainty sources are included.

6.10 Outlook

In this chapter the first measurement of the full set of angular coefficients including the unpolarised cross section at $\sqrt{s} = 13\,\text{TeV}$ has been presented. Expectedly, the additional statistical power and increased production cross section compared to the previous ATLAS measurement benefits the accuracy of the measurement significantly. This greatly helps future detailed tests of theoretical predictions in perturbative QCD and in particular higher order effects such as the breaking of the Lam-Tung relation as well as non-zero coefficients A_5, A_6 and A_7.

Nonetheless, some minor aspects remain to be studied in further detail such as a precise understanding of multijet uncertainties in the electron channel, which currently are unexpectedly strongly constrained. Uncertainties attached to the background prediction in the simulation are also to be included, however, their impact is estimated to be at a similar order of magnitude as the multijet uncertainties.

With the currently ongoing Run 3 at the LHC and with the prospect of the High-Luminosity LHC for Run 4 and beyond, statistical uncertainties will be reduced significantly. Assuming a total of approximately $350\,\text{fb}^{-1}$ of integrated luminosity collected after[9] Run 3 [182], a reduction factor in the statistical uncertainties of about 1.6 will be achieved compared to a Run 2 measurement alone (not taking into account the different production cross sections of the Z boson due to the centre-of-mass energy of $\sqrt{s} = 13.6\,\text{TeV}$ in Run 3 and $\sqrt{s} = 8\,\text{TeV}$ in Run 1). Within the context of the overall systematic breakdown this already closes the gap between data statistical uncertainties and systematic uncertainties significantly and in some regions even below the level of current systematic uncertainties. Beyond Run 3 the goal of the High-Luminosity LHC upgrade is to collect up to $3000\,\text{fb}^{-1}$ [182] or more data. This would reduce statistical uncertainties compared to Run 2 alone by more than a factor of 4.5, thus alleviating the current statistical limitation of the measurement. For this to result in a reduction of total uncertainties below the current systematic level the number of simulated events needs to be increased accordingly. Studying the uncertainties presented in this chapter also reveals that other systematic sources, in particular energy/momentum scale and resolution uncertainties but also some efficiency-related uncertainties (depending on the coefficient and the region) would become more dominant. However, as an increase in data recorded also benefits energy and momentum calibrations in achieving a higher precision, a significant overall reduction in uncertainties seems reasonable to expect.

In order to maximise the sensitivity of coefficients that are particularly sensitive to dilution effects, such as A_4, the addition of electrons in the ATLAS forward region,

[9] This includes all proton-proton data from Run 1 to Run 3 at different centre-of-mass energies.

i.e. between $2.5 < |\eta| < 4.9$, is expected to greatly benefit the overall sensitivity of the measurement. This is also crucial for the highest accuracy possible in the measurement of the weak mixing angle from the angular coefficients. A simulation-based sensitivity study for a Run 2 measurement in the central channels presented here is discussed in the following chapter.

Part IV

Towards the Weak Mixing Angle

7 Motivation and Strategy

> *The important thing is not to stop questioning.*
>
> **— Albert Einstein**

The previous chapter has illustrated the precision of a measurement of angular coefficients at the ATLAS experiments and how they are a key element in tests of perturbative QCD. Beyond the measurement of the coefficients themselves it is possible to also determine the effective weak mixing angle which is closely connected to the A_4 coefficient, as described in chapter 1.3.3. This can be achieved by a parametrisation of the coefficient as a linear function of the effective leptonic weak mixing angle $\sin^2\theta^l_{\text{eff}}$, which is fitted instead of the coefficient it replaces.

A critical measurement such as one determining the weak mixing angle requires the best theoretical predictions to compare to as well as an in-depth understanding of electroweak schemes and corrections and in particular a correct description of the dilepton transverse momentum by the simulation. This effort is still ongoing so that an extraction of the weak mixing angle in data in this thesis will not be shown but rather a study on the expected sensitivity employing the simulation used in the measurement of the angular coefficients. This section will highlight the strategy for determining the weak mixing angle from the angular coefficients and will closely inspect expected statistical and systematic uncertainties which can be used to derive an estimate on the sensitivity of such a measurement in particular in comparison to other measurements such as the one at $\sqrt{s} = 8\,\text{TeV}$ by ATLAS [65]. The study aims to highlight the potential of a measurement of the effective leptonic weak mixing angle at ATLAS as well as aspects of the measurement that could be a focus of optimisation going forward.

To this end, predictions using the DYTURBO [76] tool will be derived using different PDF sets as the linearisation of the A_4 coefficient depends on the PDF set chosen. This allows to compare the effect of different PDF sets as well as a test for consistency in the extraction procedure, but it is also a significant source of expected uncertainties (which are propagated from the PDF variations). For the extraction, an Asimov dataset is used. This means that this study is independent of background estimates or mismodellings in the simulation (such as the dilepton transverse momentum) as the predictions and (pseudo-)measurements are defined to be identical. The binning in mass, rapidity and transverse momentum is chosen to be consistent with the

previous measurement at $\sqrt{s} = 8\,\text{TeV}$ at ATLAS. Crucially, additional off-pole bins in the mass are introduced and the transverse momentum will be integrated over to exploit the dependence of A_4 (and thus the weak mixing angle) on the mass and the rapidity.

In a first step, A_4 will be determined in this binning to highlight statistical and systematic uncertainties that are expected to propagate also to the weak mixing angle, which will be extracted in a second step. This already provides crucial insights into the expected statistical and systematic power of a measurement of the effective leptonic weak mixing angle at ATLAS in Run 2 using the angular coefficients in central electron and muon channels and will set such a future measurement in data into context with other measurements as the overall aim is the highest precision possible also in view of the tensions shown by the two most precise measurements thus far.

Notes on Contributions of the Author The results presented in this chapter utilise the same software tools discussed in section 4. In addition, the DYTURBO [76] software has been used to calculate the predictions used throughout this chapter. The main effort was focussed on adapting the software frameworks and tools to extract an estimate for the sensitivity of a measurement of the weak mixing angle. Particular focus was placed on deriving the uncertainty estimates for different PDF sets, their plausibility and comparability to the previous ATLAS measurement [65]. All work presented has been conducted by the author unless explicitly mentioned otherwise given the considerations provided before.

8 Expected Sensitivity of the Weak Mixing Angle Extraction

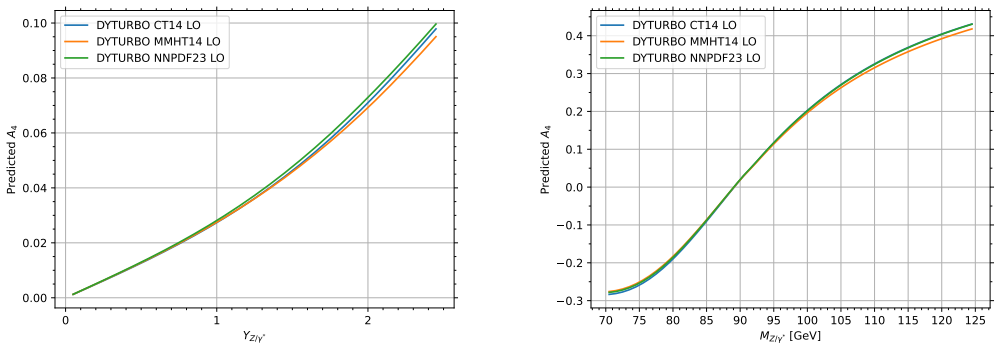
> *What stands in the way becomes the way.*
>
> **— Marcus Aurelius**

The relevance of the weak mixing angle in particular in electroweak physics has been discussed in section 1.3.3. Using similar methods as outlined in the previous section, in this chapter the expected precision of a measurement of the effective leptonic weak mixing angle will be presented and discussed.

8.1 Methodology

As explained in section 1.3.3 the A_3, A_4 and A_7 angular coefficients measured in the previous chapter are sensitive to the effective leptonic weak mixing angle $\sin^2\theta^l_{\text{eff}} = \kappa_l \sin^2\theta_W$. For leptons in the $\overline{MS}$ scheme the effective weak mixing angle can be approximated as $\sin\theta^l_{\text{eff}} = \sin^2\theta_W + 0.00032$ [14]. However, the extraction of these angular coefficients in section 6 shows that A_3 is non-zero only at high transverse momenta of the Z boson and A_7 overall very close to zero. As such they are much reduced in their sensitivity due to the sparse population of the high-momentum phase space and small values. For this reason this study focusses on the extraction of the weak mixing angle solely from the A_4 coefficient. It varies with the mass and the rapidity of the final state dilepton pair[1]. The variation in the mass visible in figure 8.1(b) is caused by the interference of vector and axial vector coupling terms, which is described by the weak mixing angle. At lower masses photon contributions increase, thus it is expected that the asymmetry actually approaches zero for decreasing masses [183]. At the Z pole mass the asymmetry is also close to zero due to the inverse effect, i.e. dominating Z contributions. Finally, at high masses A_4 is expected to become approximately constant due to the interference of both bosons. In figure 8.1(a) it is clearly visible that A_4 is expected to increase with the dilepton rapidity. This can be explained by a decrease in dilution effects at higher rapidities, i.e. the boson is more often produced in the direction of the incoming

[1] As shown in the previous chapter, A_4 also varies as a function of the transverse momentum of the dilepton pair. To increase statistical sensitivity it is beneficial to integrate over the dilepton transverse momentum in order to maximise the variation of A_4 as a function of the dilepton rapidity and mass shown in figure 8.1.



(a) Predicted $A_4(Y_{Z/\gamma^*})$ for $0\,\text{GeV} < p_{T,Z/\gamma^*} < 6500\,\text{GeV}$ and $70\,\text{GeV} < M_{Z/\gamma^*} < 125\,\text{GeV}$.

(b) Predicted $A_4(M_{Z/\gamma^*})$ for $0\,\text{GeV} < p_{T,Z/\gamma^*} < 6500\,\text{GeV}$ and $0 < |Y_{Z/\gamma^*}| < 2.5$.

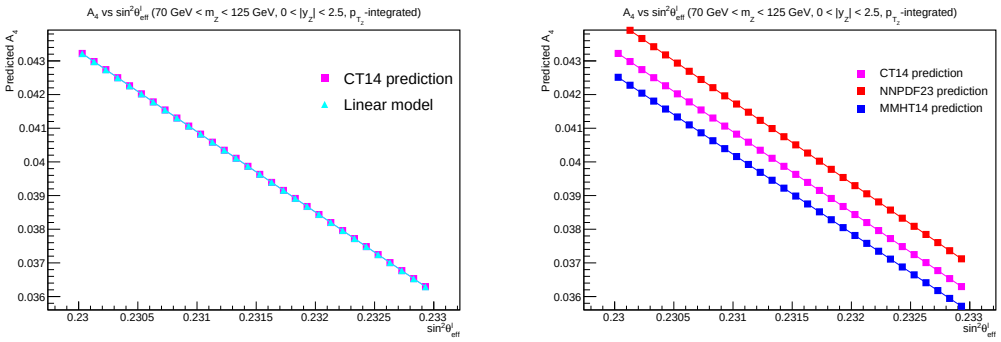
Fig. 8.1.: A_4 coefficient as predicted by DYTURBO at LO in QCD and LO in electroweak theory as a function of the Z/γ^* mass M_{Z/γ^*} and rapidity Y_{Z/γ^*} for different PDF sets. No uncertainties are depicted.

quark, which statistically has a higher momentum than the anti-quark in a proton. This effect can also be seen in figure 6.29 for A_4 which increases towards higher rapidity (thus increasing experimental sensitivity). This effect is also illustrated in this CMS proposal [184] to measure A_{FB}. In both cases three different sets of PDFs are shown at LO in QCD and electroweak theory to illustrate the dependence of the prediction on the PDF set chosen. The PDFs are denoted as "CT14" for the CT14 NNLO PDF set [52], "MMHT14" for the MMHT 2014 PDF set [185] and "NNPDF23" for the NNPDF 2.3 PDF set [186].

The A_4 coefficient is closely connected to the forward-backward asymmetry A_{FB} which has been defined in section 1.3.3, via $A_{\text{FB}} = \frac{3}{8}A_4$ in full lepton phase space. As indicated in formulas 1.60 and 1.63, it is expected that A_{FB} and thus A_4 are approximately linearly dependant on the weak mixing angle. Simulating[2] this behaviour with DYTURBO at leading order in QCD and electroweak theory, this relation can be visualised in figure 8.2. DYTURBO is a program that computes LO electroweak predictions of angular coefficients and cross sections at up to NNLO in QCD (however, this study is based on NLO predictions for computational reasons). It provides fixed order and resummed QCD calculations of the Z boson production.

The simulation clearly exhibits the linearity between A_4 and the weak mixing angle. This is complemented in figure 8.2(a) by a linear model of the form $A_4(\sin^2\theta^l_{\text{eff}}) = a\sin^2\theta^l_{\text{eff}} + b$, where the free parameters in this case have been fixed by the lowest and highest entries of the prediction. The dependence of these predictions on the

[2] The electroweak input parameters to DYTURBO were set to $G_F = 1.166\,378\,7 \times 10^{-5}\,\text{GeV}^{-2}$, $M_Z = 91.1876\,\text{GeV}$, $M_W = 80.385\,\text{GeV}$, $\Gamma_Z = 2.4952\,\text{GeV}$ and $\alpha_{\text{e.m.}}(M_Z) = 0.00775996$.



(a) Comparison of the CT14 prediction and a linear interpolation model.

(b) Comparison of the CT14, NNPDF23 and MMHT14 PDF predictions.

Fig. 8.2.: Prediction of A_4 as a function of the effective leptonic weak mixing angle calculated with DYTURBO at LO in QCD and LO in electroweak theory. The linear model is calculated from the lowest and highest entry of the CT14 graph.

PDF set used can be seen in figure 8.2(b), where three sets are compared. While all of them exhibit a linear behaviour, there is an absolute shift between each.

This is the motivation to extract the weak mixing angle from A_4 using a linear parametrisation directly in the likelihood function $\mathcal{L}$ in equation 6.10 as

$$A_{4,j}(\sin^2\theta^l_{\text{eff}}, \theta) = a_j(\theta) \cdot \sin^2\theta^l_{\text{eff}} + b_j(\theta) \tag{8.1}$$

within each analysis bin j. The two parameters $a_j(\theta)$ and $b_j(\theta)$ depend on the set of nuisance parameters θ. The precise prediction of A_4 as a function of the weak mixing angle also depends on the PDF set chosen as different sets directly influence parton flavour and momentum compositions as illustrated in figure 8.2(b). The PDF sets are interfaced using the LHA PDF Tool [168].

Extracting the weak mixing angle builds upon the previously discussed measurement of the angular coefficients. The binning of the dilepton variables is changed, however, to achieve the best sensitivity by maximising the statistical power within each bin. Since coefficient A_4 only varies marginally as a function of the dilepton transverse momentum, the latter variable is integrated over and only bins in the dilepton rapidity are kept. In addition, a very coarse binning in the dilepton mass is introduced to differentiate between the pole and the side-band regions of the Z boson. As depicted in figure 8.1(b), A_4 is expected to vary across mass regions. This means the binning for this sensitivity study is defined as

$$\begin{aligned} |y_Z^{\text{boundary}}| &\in \{0,\ 0.8,\ 1.6,\ 2.5\} \\ m_Z^{\text{boundary}} &\in \{70,\ 80,\ 100,\ 125\}\,\text{GeV}. \end{aligned} \tag{8.2}$$

The fitting procedure differs from the extraction of the angular coefficients only in that the A_4 coefficient is replaced by the linear model dependant on $\sin^2\theta^l_{\text{eff}}$ as well as the different binning defined above. For the purpose of this sensitivity study an Asimov dataset is constructed and used. The method allows to determine an expected sensitivity of a measurement without using data. In particular, corrections to the dilepton transverse momentum or other precision corrections as well as the multijet estimate are not necessary to estimate the statistical and systematic uncertainties[3] of such a measurement. The same fitting framework [158] is used to minimise the likelihood ratio defined in equation 6.11 but with A_4 replaced as defined in equation 8.1 using a Newton minimisation algorithm [171].

8.2 Extraction of the A_4 Coefficient

The first step towards a measurement of the weak mixing angle is to extract the angular coefficient A_4 and to understand its uncertainties. Importantly, this step is useful as a consistency test in particular with respect to the uncertainties, but it is independent of the actual measurement of the weak mixing angle in which A_4 is replaced by the linear interpolation in the likelihood fit. This step differs from the extraction in the previous chapter in that it uses a binning integrated over the transverse momentum and a coarse binning in the rapidity and mass. The expected yields of this adapted binning are shown in table 8.1 and follow similar observations made before, specifically higher yields in the muon channel.

The expected values for A_4, extracted from a fit on the Asimov dataset, and the breakdown of statistical and systematic uncertainties in each region are listed in tables 8.2 and 8.3 for the electron channel and the muon channel, respectively, using the POWHEGBOX + PYTHIA 8 generator. Clearly, both the expected central values and the expected uncertainties vary drastically between different regions in the dilepton mass and rapidity. The behaviour of the central value follows the expectations derived from figures 8.1(b) and 8.1(a) earlier which already highlight the dependence of A_4 on the dilepton mass and rapidity. Central values are expectedly compatible between both analysis channels. Statistical uncertainties are naturally at a minimum around the Z pole where the the number of events is at its maximum. As already seen in the data analysis in chapter 5 and the extraction in chapter 6, more expected data in the muon channel increases its statistical power compared to the electron channel. On the systematic side the limited number of events of the simulation is a leading contribution in both channels. However, the electron channel is affected by significantly higher uncertainties on the scale and resolution compared to the

[3] Uncertainties related to the application of such corrections or the multijet estimate are not considered with this method.

muon channel, so that these uncertainties even exceed the ones from statistical limitations of the simulation ("MC Statistics"). PDF related uncertainties ("PDF (meas.)") exhibit variations in size across the rapidity and mass regions as they depend on the phase space considered, but they are smaller in relative size than the leading systematic contributions. Finally, lepton efficiency-related uncertainties impact the extraction to varying degrees and are strongly dependant on the kinematic region. Overall, they affect the electron channel more drastically than the muon channel. The results from the extraction of the angular coefficients in chapter 6 indicate that muon uncertainties are expected to benefit from an uncertainty scheme with a more detailed breakdown of individual uncertainty sources. This could also affect the uncertainties presented in this chapter, however, it is not expected to have a major impact. Crucially, this comparison of uncertainty breakdowns also highlights that, while the central rapidity and pole mass regions exhibit the smallest absolute uncertainties, in relative terms, in particular the higher rapidity regions benefit from smaller relative uncertainties. This shows that these regions are more sensitive to such a measurement than the central regions due to the shape of A_4.

	A_4								
Rapidity	$0 < \|Y_Z\| < 0.8$			$0.8 < \|Y_Z\| < 1.6$			$1.6 < \|Y_Z\| < 2.5$		
Mass [GeV]	$70-80$	$80-100$	$100-125$	$70-80$	$80-100$	$100-125$	$70-80$	$80-100$	$100-125$
Muon Channel	1.34	33.52	1.29	1.43	33.07	1.25	0.69	14.20	0.54
Electron Channel	1.08	27.75	1.12	0.89	21.16	0.83	0.38	7.95	0.29

Tab. 8.1.: Expected yields in units of 10^6 events in each analysis region considered (only signal simulation is used).

A_4									
Absolute Rapidity	$0-0.8$			$0.8-1.6$			$1.6-2.5$		
Mass [GeV]	$70-80$	$80-100$	$100-125$	$70-80$	$80-100$	$100-125$	$70-80$	$80-100$	$100-125$
Central Value	-579	94	728	-1962	320	2404	-4350	684	5120
Total Uncertainty	88	18	49	130	19	46	229	25	127
Systematic Uncertainty	58	17	37	106	18	30	159	20	89
Statistical Uncertainty	66	6	33	74	6	36	165	15	91
MC Statistics	32	3	16	36	3	17	79	7	43
Energy Scale	39	15	28	53	17	16	113	15	65
Energy Resolution	27	3	17	80	5	15	66	9	27
PDF (meas.)	7	1	3	26	1	9	31	5	29
ID Eff.	8	4	4	12	4	2	22	3	11
Reco. Eff.	3	2	1	3	2	1	8	1	7
Trigger Eff.	4	2	2	8	3	1	14	1	1
Charge ID Eff.	0	0	0	1	0	0	1	0	2

Tab. 8.2.: Expected central values and uncertainties of A_4 in the electron channel extracted from the Asimov dataset based on the POWHEGBOX + PYTHIA 8 simulation. The central value and the uncertainties are shown in units of 10^{-4}. Values are rounded and can thus appear as 0.

A_4									
Absolute Rapidity	$0-0.8$			$0.8-1.6$			$1.6-2.5$		
Mass [GeV]	$70-80$	$80-100$	$100-125$	$70-80$	$80-100$	$100-125$	$70-80$	$80-100$	$100-125$
Central Value	-579	95	723	-1966	320	2406	-4351	684	5122
Total Uncertainty	59	6	31	64	11	37	136	15	85
Systematic Uncertainty	30	3	16	37	9	22	76	11	48
Statistical Uncertainty	51	5	27	53	5	30	114	11	70
MC Statistics	25	2	13	26	3	15	56	6	35
Momentum Scale	6	1	3	14	9	11	26	0	6
Momentum Resolution	12	1	6	11	0	6	14	3	12
PDF (meas.)	6	0	4	18	1	9	27	5	29
Iso. Eff.	1	1	2	1	1	3	3	0	3
Reco. Eff.	0	0	0	0	0	1	1	0	1
TTVA Eff.	0	0	0	0	0	0	0	0	0
Sagitta	7	1	3	7	1	3	30	7	10

Tab. 8.3.: Expected central values and uncertainties of A_4 in the muon channel extracted from the Asimov dataset based on the POWHEGBOX + PYTHIA 8 simulation. The central value and the uncertainties are shown in units of 10^{-4}. Values are rounded and can thus appear as 0.

8.3 Expected Sensitivity of a Weak Mixing Angle Measurement

As explained in previous sections, the A_4 coefficient in the likelihood function of the extraction can be replaced by a linear parametrisation in the weak mixing angle, as defined in equation 8.1. This reparametrisation is then fitted instead of the A_4 coefficient shown in the previous section using the same method explained before. Crucially, the linearisation is done for three different values, closely around the LEP and SLD combination [6] of 0.23153. A variation of $\pm 100 \cdot 10^{-5}$ around this value is used so that prediction for $A_{4,j}$ and the linear constants a_j and b_j are derived for each analysis bin j. Uncertainties are taken into account by nuisance parameters θ that vary the central value of A_4. The final value of $\sin^2\theta^l_{\text{eff}}$ is obtained as a weighted[4] average of the fitted value in each analysis bin.

The predictions calculated with DYTURBO depend on the PDF sets that are chosen, which also induce a significant overall theoretical uncertainty (denoted as "PDF (pred.)") on such a measurement as the parametrisation of A_4 as a function of the weak mixing angle is very sensitive to the PDF chosen, as shown in figure 8.2(b). For this study three sets, CT14, MMHT14 and NNPDF23, have been chosen to provide comparability to earlier measurements and to ensure that ATLAS Run 2 data has not been used in the determination of these PDFs, which could introduce biases.

The results of the extraction are shown in tables 8.4 and 8.5 for the electron channel and the muon channel, respectively. In addition to the statistical and systematic uncertainties discussed previously, uncertainties on the PDF used in the predictions as well as uncertainties due to the QCD scale, which also introduce variations in the parametrisation of A_4, are included in the sensitivity estimate. Importantly, the uncertainties from the PDF in the predictions need to be differentiated from the PDF uncertainty from the actual measurement (denoted as "PDF (meas.)") both of which are assumed to be uncorrelated to each other. Since this study is based on simulation only, the central value is expected to be compatible with the values used in the generation of the simulations. For the POWHEGBOX + PYTHIA 8 samples the standard value is $\sin^2\theta_W = 0.23113$. This is translated to an effective weak mixing angle $\sin^2\theta^l_{\text{eff}} = \sin^2\theta_W + 0.00032 = 0.23145$ used in the simulation. In both channels the extraction using the CT14 and MMHT14 PDF sets return this central value to a close approximation. The NNPDF23 PDF set induces a systematic shift of this value of approximately $30 \cdot 10^{-5}$, however, in all cases the central value returned from the extraction is perfectly compatible with the central value induced in the simulation.

[4] Weighted by the number of events in each bin to accurately reflect statistical importance.

Compared to the previous measurement by ATLAS [65], expectedly the statistical uncertainties are significantly reduced due to the larger dataset available. In total the expected uncertainties follow a similar pattern as the ones in the extraction of A_4. This means a higher precision is expected from the muon channel due to lower statistical uncertainties and lower systematic uncertainties, driven by higher precision in scale and resolution, which are two of the dominant uncertainty sources in the electron channel. The large uncertainty from the energy scale and resolution in the electron channel is unexpected (considering their smaller impact on the angular coefficients and in comparison to the muon channel) and motivates future closer studies of their impact on the measurement.

Importantly, some systematic uncertainties cannot be determined by this study on simulation. Those are uncertainties connected to the reweighting of the dilepton transverse momentum, necessary due to the mismodelling of this distribution compared to data. Moreover, uncertainties from additional electroweak corrections on the simulation as well as uncertainties due to the background, such as the multijet background, are not estimated. All of these uncertainties do not affect this Asimov study, where the simulated signal is treated as data. They are of lesser significance compared to uncertainties such as the uncertainty from the PDF in the predictions, statistical uncertainties (both in data and simulation) and scale/resolution-related uncertainties. The PDF uncertainties from predictions are derived from eigenvector variations of the respective PDF set with DYTURBO. The resulting number of nuisance parameters (a single nuisance parameter representing both, one upward and downward variation) is 50 for NNPDF23, 28 for CT14 and 25 for MMHT14. The QCD scale uncertainties are determined as the variations of both, the factorisation and renormalisation scales, μ_F and μ_R, respectively, between $50 - 200\%$ of their nominal values also in DYTUBRO.

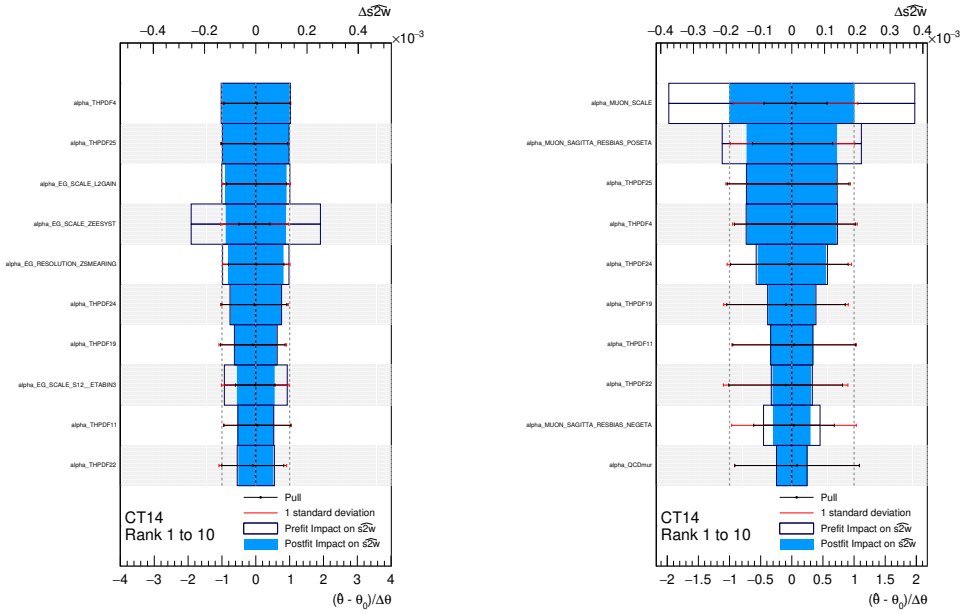
In order to understand the effect of uncertainties on the weak mixing angle in more detail, figures 8.3, 8.4 and 8.5 depict the systematic nuisance parameters with the highest impact on the weak mixing angle estimates, denoted $\mathrm{s\hat{2}w}$, for the CT14, the MMHT14 and the NNPDF23 PDF sets, respectively, for both channels. The nuisance parameters are denoted by their technical names, which are identical to the naming scheme from the extraction of the angular coefficients in the previous chapter, with the addition of nuisance parameters for the PDF in the predictions (α_{THPDF}) and the QCD scale (α_{QCDmur} for μ_R and α_{QCDmuf} for μ_F). The rankings are shown with the most impactful nuisance parameters at the top and the least (of the top ten highest impacting ones) at the bottom. The top x-axis shows the actual impact on the s$\hat{2}$w estimator, i.e. the measured weak mixing angle, and the bottom x-axis the pull of each nuisance parameter. The pull distributions are represented by the black data points with the black uncertainty bars with the addition of a red uncertainty bar for reference showing the $\pm 1\sigma$ width. The

impact on the weak mixing angle is shown as blue box with an unfilled black box highlighting the impact before the likelihood fit. In case of the muon channel the ranking is dominated by the nuisance parameters from the PDF variations for the predictions in line with the observation of their overall dominating impact on the sensitivity estimate. Additionally, renormalisation scale-related nuisance parameters and nuisance parameters from the sagitta uncertainty also exhibit a significant overall uncertainty on the estimator. This is particularly noticeable in the extraction using PDF set CT14 where the momentum scale uncertainties are significantly larger than in the other cases. In case of using the NNPDF23 set, the sagitta-related uncertainties are significantly larger, which is reflected both in the systematic breakdown as well as in the ranking presented. In comparison, unexpectedly large uncertainties from the energy scale and resolution in the electron channel dominate the overall ranking. Nuisance parameters from the PDF set chosen exhibit a significant impact as well, but only in the case of the CT14 PDF set the most impactful nuisance parameters are originated in the PDF for the parametrisation, which is again compatible with the overall systematic breakdown. In comparison, in case of the MMHT14 PDF set the ranking is dominated almost exclusively by scale and resolution-related nuisance parameters. Overall, this emphasises the need to better understand the origin of these large uncertainties in order to maximise the overall sensitivity achievable.

Comparing the individual uncertainties to the previous ATLAS measurement [65], it becomes clear that some uncertainties are expected to shrink, in particular the ones related to statistical uncertainties. In other cases, for instance in case of the energy scale and resolution in the electron channel, closer inspections and optimisations are necessary to achieve a competitive sensitivity on the weak mixing angle. However, a detailed comparison matching each source of uncertainties between measurements is also of limited value as the systematic breakdown is affected by correlations between uncertainty sources. For instance, the size uncertainty from the PDF (predictions) affects the size of other types of uncertainties. This is visible in table 8.4, where the NNPDF23 PDF set exhibits smaller uncertainties in the PDF (predictions), however, uncertainties from the energy resolution are inflated. It is important to note that these correlations do not change the overall uncertainty breakdown into statistical and systematic uncertainties, but they only highlight the challenge of detailed comparisons between measurements and sensitivity estimates.

Finally, it is insightful to estimate the sensitivity of a combined measurement in the electron and muon channels, where correlated uncertainties are taken into account (such as the PDF uncertainties). In case of the CT14 PDF set the combined Asimov-based sensitivity estimate is

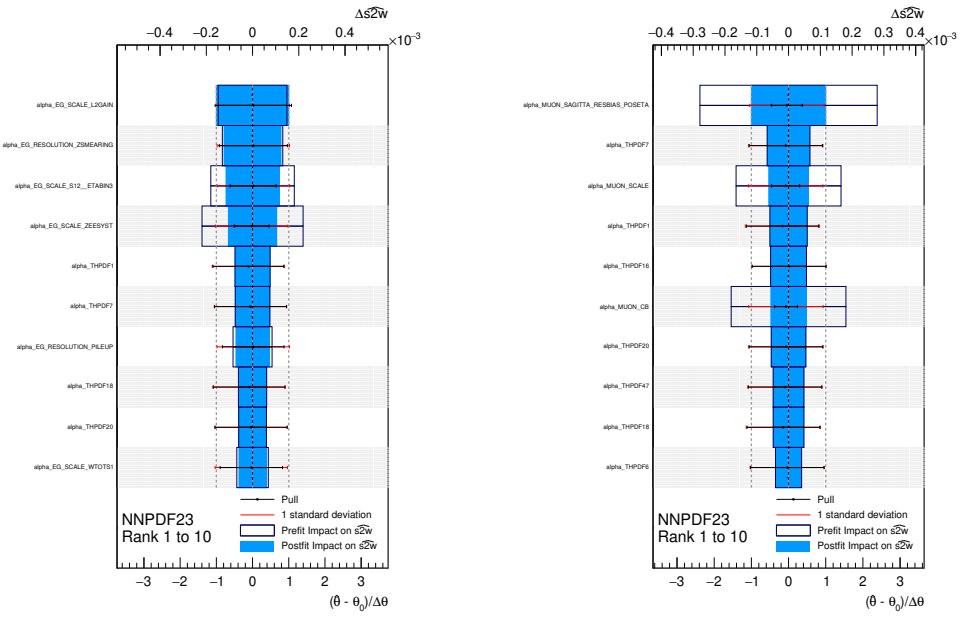
$$\sin^2\theta^l_{\text{eff, Asimov}} = 0.23145 \pm 0.00013\ \text{(stat.)}\ \pm 0.00034\ \text{(sys.)}\ = 0.23145 \pm 0.00036.$$



(a) Ranking in the electron channel.

(b) Ranking in the muon channel.

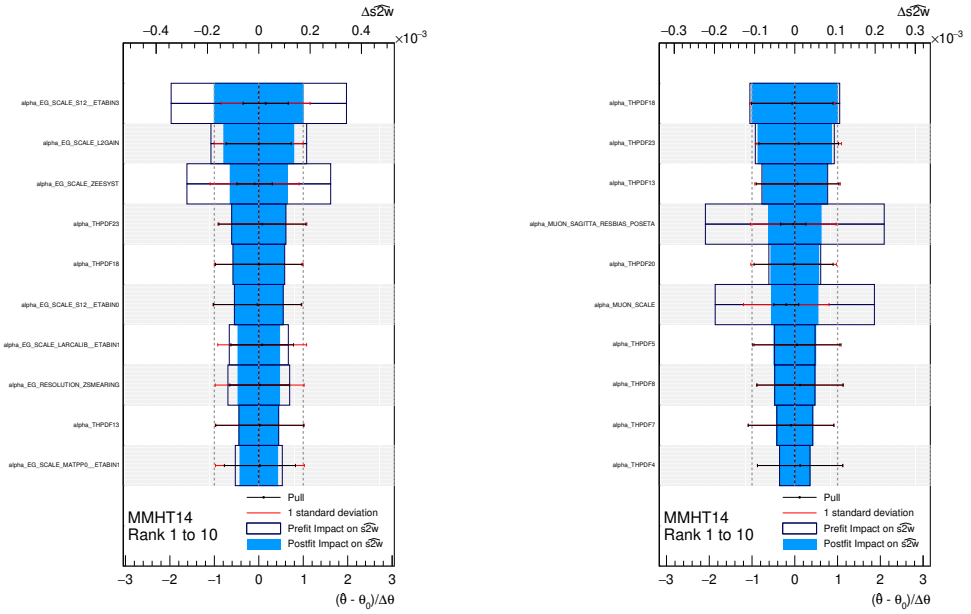
Fig. 8.3.: Highest ranking nuisance parameters in terms of their impact on the total uncertainty on the estimator for the effective weak mixing angle $\mathrm{s}\hat{2}\mathrm{w}$ using the CT14 PDF set. The upper x-axis represents the impact on the weak mixing angle and the lower x-axis represents the scale for the pull defined in equation 6.15, which is represented by the black data point and the black uncertainty bar. For reference, an uncertainty bar of one standard deviation is shown in red. The centre dashed line is located at 0, while the other dashed lines represent the $\pm 1\sigma$ distance from 0. Finally, the black unfilled boxes represent the impact of a particular nuisance parameter on the estimator (scaled at the top x-axis) before the fit and the blue filled boxes show the impact after the fit.



(a) Ranking in the electron channel.

(b) Ranking in the muon channel.

Fig. 8.4.: Highest ranking nuisance parameters in terms of their impact on the total uncertainty on the estimator for the effective weak mixing angle $\mathrm{s}\hat{2}\mathrm{w}$ using the NNPDF23 PDF set. The upper x-axis represents the impact on the weak mixing angle and the lower x-axis represents the scale for the pull defined in equation 6.15, which is represented by the black data point and the black uncertainty bar. For reference, an uncertainty bar of one standard deviation is shown in red. The centre dashed line is located at 0, while the other dashed lines represent the $\pm 1\sigma$ distance from 0. Finally, the black unfilled boxes represent the impact of a particular nuisance parameter on the estimator (scaled at the top x-axis) before the fit and the blue filled boxes show the impact after the fit.



(a) Ranking in the electron channel.

(b) Ranking in the muon channel.

Fig. 8.5.: Highest ranking nuisance parameters in terms of their impact on the total uncertainty on the estimator for the effective weak mixing angle $\hat{s^2_w}$ using the MMHT14 PDF set. The upper x-axis represents the impact on the weak mixing angle and the lower x-axis represents the scale for the pull defined in equation 6.15, which is represented by the black data point and the black uncertainty bar. For reference, an uncertainty bar of one standard deviation is shown in red. The centre dashed line is located at 0, while the other dashed lines represent the $\pm 1\sigma$ distance from 0. Finally, the black unfilled boxes represent the impact of a particular nuisance parameter on the estimator (scaled at the top x-axis) before the fit and the blue filled boxes show the impact after the fit.

	CT14	MMHT14	NNPDF23
Central Value	0.23149	0.23154	0.23188
Total	53	53	59
Stat.	22	22	21
Syst.	48	48	55
Uncertainties from Measurement			
PDF (meas.)	7	7	8
Energy Scale	30	33	31
Energy Resol.	14	13	18
ID Eff.	4	5	6
Reco. Eff	1	1	1
Trig. Eff.	4	4	5
Charge MisID	0	0	0
Uncertainties from Predictions			
MC Stat.	11	11	14
PDF (pred.)	30	27	22
QCD Scale	14	12	4

Tab. 8.4.: Expected central value and uncertainties on the effective weak mixing angle extracted from the POWHEGBOX + PYTHIA 8 Asimov dataset using different PDFs in the electron channel. The parametrisation is calculated using DYTURBO at NLO in QCD and LO in electroweak theory. The POWHEGBOX standard value for the effective weak mixing angle is $\sin^2\theta^l_{\text{eff}} = 0.23145$. Uncertainties are shown in units of 10^{-5}. Values are rounded and can thus appear as 0.

	CT14	MMHT14	NNPDF23
Central Value	0.231**44**	0.231**54**	0.231**81**
Total	38	34	43
Stat.	17	17	17
Syst.	34	29	39
Uncertainties from Measurement			
PDF (meas.)	6	7	7
Momentum Scale	14	9	8
Momentum Resol.	4	2	5
Iso. Eff.	1	0	1
Reco. Eff	0	0	0
Trig. Eff.	1	1	2
TTVA Eff.	0	0	0
Sagitta	5	4	10
Uncertainties from Predictions			
MC Stat.	8	8	12
PDF (pred.)	27	23	21
QCD Scale	13	10	2

Tab. 8.5.: Expected central value and uncertainties on the effective weak mixing angle extracted from the POWHEGBOX + PYTHIA 8 Asimov dataset using different PDFs in the muon channel. The parametrisation is calculated using DYTURBO at NLO in QCD and LO in electroweak theory. The POWHEGBOX standard value for the effective weak mixing angle is $\sin^2\theta^l_{\text{eff}} = 0.23145$. Uncertainties are shown in units of 10^{-5}. Values are rounded and can thus appear as 0.

A simplified estimate for the missing uncertainties can be done using the uncertainties from the previous ATLAS measurement (in units of 10^{-5}). Adding them quadratically to the derived sensitivity estimate results in

$$\begin{aligned}(\Delta \sin^2\theta^l_{\text{eff, Asimov}}[10^{-5}])^2 &= 36^2 \text{ (tot. estimate)} \\ &+ 3^2 \text{ (electroweak corrections)} \\ &+ 1^2 \text{ ($p_{T,Z}$ corrections)} \\ &+ 1^2 \text{ (Bkg.)} \\ &\approx 36^2.\end{aligned} \tag{8.3}$$

This supports the expectation that the missing uncertainties do not significantly contribute to the total uncertainty and thus the expected sensitivity of this measurement. The expected sensitivity of these central channels alone is almost identical to the total sensitivity of the previous ATLAS measurement (which includes the more sensitive forward region). This simple estimate presented here for the electron and muon channels indicates a potential improvement in the sensitivity of approximately 26% compared to the previous ATLAS measurement. If the electron channel including forward electrons follows a similar improvement, this would result in a total reduction of the uncertainties to approximately $26 \cdot 10^{-5}$. This surpasses the sensitivity reached at the Tevatron [86] of $33 \cdot 10^{-5}$ and is competitive to LEP/SLD measurements, as shown in figure 1.7(a), where some of the previous measurements are compared to the ATLAS $\sqrt{s} = 8\,\text{TeV}$ measurement. A direct comparison of the sensitivity estimates derived in this chapter to the preliminary ATLAS results at $\sqrt{s} = 8\,\text{TeV}$ is presented in figure 8.6, where the individual central channels, their combination as well as the combination of all channels including the central-forward channel are presented. It visualises the potential improvements achievable with the Run 2 dataset in ATLAS which are expected to provide valuable insights into the current tensions observed between other sensitive measurements.

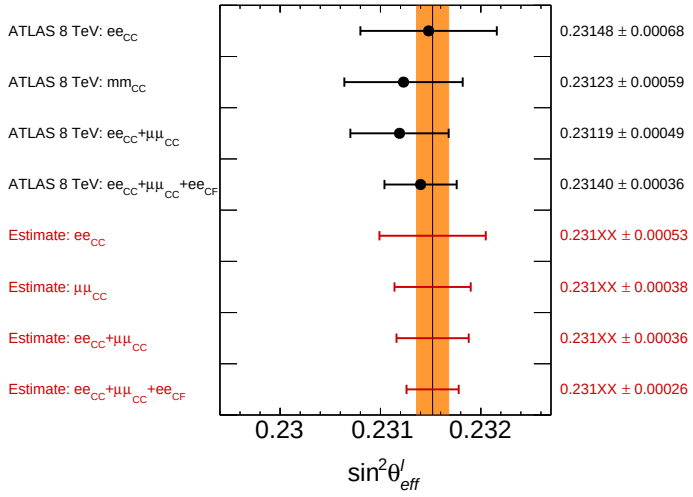


Fig. 8.6.: Comparison of sensitivity estimates of this thesis to the preliminary ATLAS measurement at $\sqrt{s} = 8\,\text{TeV}$ [65]. The current world average [6] is shown as the orange band with the black central line.

8.4 Outlook

The first sensitivity estimate on a measurement of the effective leptonic weak mixing angle using the angular coefficient A_4 and the ATLAS Run 2 dataset has shown the potential of such a measurement and its competitiveness compared to other experimental results. Given that the electron energy scale and resolution uncertainties appear unexpectedly large at the moment, an estimate can be derived for how a reduction of these uncertainties impacts the overall sensitivity of the measurement. Assuming electron energy scale and resolution uncertainties can be brought to the level of the $\sqrt{s} = 8\,\text{TeV}$ measurement at ATLAS (i.e. absolute uncertainties of $4 \cdot 10^{-5}$ on the energy scale and $6 \cdot 10^{-5}$ on the resolution) this would reduce the total systematic uncertainties in the electron channel (for the CT14 PDF set) to approximately $38 \cdot 10^{-5}$ and thus the total uncertainty in the electron channel to approximately $44 \cdot 10^{-5}$. However, in the final estimate for the combination of the two central channels a significant improvement in the electron energy scale and resolution could reduce the total systematic uncertainty to approximately $32 \cdot 10^{-5}$ (from $34 \cdot 10^{-5}$), which shows an improvement of individual systematic uncertainties is not sufficient for a significant overall improvement. This would require additional reductions of systematic uncertainties, in particular uncertainties from the predictions, for instance in the statistical uncertainty of the simulation as well as the PDF uncertainties of the prediction.

As the current estimate already indicates that a measurement of the effective leptonic weak mixing angle is expected to be dominated by systematic uncertainties, a

reduction of statistical uncertainties alone using data collected at Run 3 or beyond during the High-Luminosity LHC era will not be sufficient to push the boundary towards the highest possible sensitivity. Using the sensitivity estimate of a measurement combined in the central channels $\sin^2\theta^l_{\text{eff, Asimov}} = 0.23145 \pm 0.00013$ (stat.) $\pm$ 0.00034 (sys.) , even a reduction of statistical uncertainties to a negligible level would reduce overall uncertainties only towards $34 \cdot 10^{-5}$.

This shows that, while improvements of such a measurement using significantly more data are possible, a reduction of systematic uncertainties at the same time is crucial for the highest sensitivity. Many experimental systematic sources are expected to be reduced with additional data collected as this allows for the highest precision possible, for instance in the energy or momentum calibrations. Nonetheless, one of the most significant challenges are the PDF uncertainties of the predictions. It is expected that more recent PDF sets will reduce the overall PDF-related uncertainties, however, a quantification of this reduction is non-trivial. While it remains important to account for potential correlations between PDF sets derived from ATLAS Run 2 data, PDF sets such as the CT18 PDF set family [187] (which correspond to updated versions of the CT14 PDF sets) show that higher precisions in the description of parton density functions are achievable. This will positively impact future measurements of the weak mixing angle at ATLAS and other experiments both in the near term for a Run 2 measurement and in the long term for the High-Luminosity LHC. The High-Luminosity upgrade will also contribute to reductions in PDF uncertainties of the predictions by providing experimental results to derive new PDF sets.

9 Conclusion of the Study

> *There are two possible outcomes: If the result confirms the hypothesis, then you've made a measurement. If the result is contrary to the hypothesis, then you've made a discovery.*
>
> **— Enrico Fermi**

The study on the expected sensitivity of an ATLAS measurement of the effective weak mixing angle using the full Run 2 dataset at $\sqrt{s} = 13\,\mathrm{TeV}$ highlights the gains of such a measurement compared to previous iterations. The most significant driver of this improvement compared to Run 1 will be the increased statistical power of the large dataset. For the central electron and muon channels a sensitivity improvement of approximately 26% is expected resulting in a total sensitivity of $36 \cdot 10^{-5}$.

Due to the dilution effects in proton-proton collisions, an additional channel including forward electrons is expected to significantly benefit the overall sensitivity as well, as visible in figure 8.6, where the previous ATLAS measurement is shown. The ATLAS forward region is challenging to calibrate and understand, which is why the addition of this channel requires further in-depth study. If similar improvements can be made in this channel as well, the overall sensitivity is expected to reach approximately $26 \cdot 10^{-5}$. Given the tension of two of the most precise measurements to date, such a precision would be greatly beneficial in understanding this discrepancy in more detail.

This estimate does not take into account potential improvement on the PDFs used for the extraction which are some of the main drivers of the total uncertainty. Newer PDF sets are continued to be released and are expected to decrease the total uncertainty even more. Finally, while additional data collected in future ATLAS runs cannot reduce the total uncertainty on a measurement of the weak mixing angle indefinitely, its impact on higher precision in energy and momentum calibrations as well as more precise PDF sets is crucial for future high-precision measurements. This shows that higher luminosities and the exploitation of additional sensitive phase space regions such as the ATLAS forward region will drive the statistical and experimental improvements of a measurement of the weak mixing angle at ATLAS. The next chapter will introduce a new trigger module for the High-Luminosity LHC in the

ATLAS forward region to be used to trigger mainly electrons (and jets), which will play a crucial role in maximising the sensitivity of such a measurement.

Part V

Preparation for the High-Luminosity Era

10 Future Upgrades to ATLAS for the High-Luminosity Large Hadron Collider

> *Before anything else, preparation is the key to success.*
>
> **— Alexander Graham Bell**

Numerous upgrades to ATLAS are planned in order to measure fundamental processes even more precisely than currently possible with ATLAS data and to expand the possibility for searches for new physics. These upgrades are intended to coincide with the upgrade of the Large Hadron Collider to the *High-Luminosity LHC* (HL-LHC) at the end of this decade. In this chapter one particular upgrade project, the so-called *forward Feature EXtractor* (fFEX), is discussed in detail and set in the broader context of the upgraded ATLAS detector. As its name implies, it covers the forward region of ATLAS ($2.5 < |\eta| < 4.9$) and will be part of the upgraded trigger system, thus enabling significant gains in collected data that includes forward objects. This is expected to particularly benefit measurements such as the determination of the weak mixing angle presented in the previous chapter.

10.1 The High-Luminosity LHC

As the experiments at the LHC gather more data, the relative increase of each additional block of integrated luminosity compared to the total integrated luminosity at the current LHC is reduced over time. In particular, measurements such as the ones presented in previous chapters, i.e. the extraction of angular coefficients and in particular of the weak mixing angle, rely on very large numbers of events to achieve the best possible sensitivity. In some cases they are dominated by the statistical uncertainties alone, and in other cases systematic uncertainties can be reduced by larger datasets, for instance to improve the energy calibration.

For this reason the High-Luminosity LHC project is underway to drastically increase the average instantaneous luminosity and consequently to significantly shorten the

time until additional data taken noticeably impacts sensitivities of the measurements. It is expected that the average number of interactions per bunch crossing will rise from approximately 40 during Run 2 to up to 200 during Run 4[1] and beyond [182].

Research and development are ongoing for the upgrade project. First data is expected to be delivered by the HL-LHC nearing the end of the decade. Naturally, the experiments at the LHC have their own upgrade programmes to add further improvements to their detectors but also to replace and upgrade components to be able to deal with the drastic increase in instantaneous luminosity, which could not be handled with current detector technologies. This affects in particular the increase in instantaneous luminosity and results in larger numbers of simultaneous collisions. Sophisticated systems are necessary to be able to efficiently disentangle simultaneous collisions and select interesting events. In addition, higher radiation combined with the large levels of radiation (and radiation damage) already received during previous runs require a hardening of some of the most affected subsystems such as the tracker which is closest to the beam pipe.

10.2 Upgrades to the ATLAS Detector

As indicated in the previous section, the ATLAS detector will be upgraded in numerous ways to be able to efficiently record high quality data delivered by the HL-LHC. Most detector systems will be affected by these upgrades. In the following, a general overview of the major parts of the project will be given. The projects that will upgrade electronic systems for the liquid argon and tile calorimeters are not explicitly discussed. The significant upgrade to the trigger and data acquisition system will be outlined in the next section.

Inner Tracking Detector The current inner detector described in chapter 2.2.2 will be fully replaced by the new *Inner Tracking detector* (ITk) [188, 189]. It will be completely silicon-based with at least 9 tracking layers and cover a region up to $|\eta| = 4.0$ compared to the coverage of the current tracking system up to $|\eta| = 2.5$. Its segmentation will be finer and the overall amount of material reduced compared to the current system. This design is chosen to maximise the efficiency to correctly reconstruct the high number of tracks and to withstand high doses of radiation expected in the HL-LHC environment.

High-Granularity Timing Detector Between the upgraded tracking system and the end-caps of the detector a new *High-Granularity Timing Detector* (HGTD) [190]

[1] Run 4 is expected to be the first run of data taking after the HL-LHC upgrade.

is planned to be employed. It will cover a range of $2.4 < |\eta| < 4.0$ and allow to better discriminate primary vertices during a bunch crossing. This is essential to disentangle individual inelastic interactions and in particular potentially interesting hard-scattered signal interactions from background pileup interactions. For this reason, timing information with a resolution of less than $70\,\mathrm{ps}$ will be determined in the HGTD, which will allow for a significantly better separation of these individual interactions.

Muon System During the shutdown between Run 2 and Run 3 a significant upgrade has already been inserted in the ATLAS detector in the form of the New Small Wheel (NSW) built from small-strip Thin Gap Chambers (sTGC). It is used for tracking and triggering muons in the forward region and critical to suppress background in high-luminosity environments. For Run 4 and beyond additional muon chambers [191] will be installed in the barrel region. Additionally, some MDT chambers will be replaced and a significant fraction of the electronic system will be overhauled to include muon chambers in the new trigger system.

10.3 Upgrades to the ATLAS Trigger System

The ATLAS Trigger system will also undergo significant upgrades [192] in order to be able to efficiently trigger interesting events in a much more challenging environment than ever before. As mentioned previously, the number of simultaneous inelastic scatterings between protons is expected to increase approximately fivefold from 40 to 200 between Run 2 and the High-Luminosity LHC runs. Moreover, the output rate of the full trigger system will be approximately $10\,\mathrm{kHz}$, which is almost 10 times higher than the rate of the Run 2 system.

The upgrades to the trigger system are deployed in two stages, the first stage of upgrades is already used for the currently ongoing Run 3. The second stage will be included in the next long shutdown of the LHC after which the trigger system will be almost completely replaced compared to Run 2. Since this thesis focusses on electrons and positrons as decay products, the discussion will centre around the systems that trigger these objects.

Triggering electrons during Run 2 could be done using the *Level-1 Calo* system depicted in figure 2.8. The Level-1 Calorimeter trigger was also used as input to the *Level-1 Topological Trigger* system built to determine topological relations to other objects so that the final trigger decision was calculated in the *Central Trigger Processor*. This means it was possible to trigger on single electrons or electron pairs in the ATLAS central region. In the forward region in Run 2 it was only possible to

trigger on jet objects [193]. The Run 2 trigger chains have been used in the analysis presented in chapters 5 and 6. The upgrade of the trigger system for the currently ongoing Run 3 of the LHC has already significantly changed the architecture of the trigger system. While for the initial period the Run 2 system is still used, in the long term new systems will soon replace the Run 2 hardware. With these new systems, naturally, it is also possible to trigger central electron objects as well as central and forward jets. However, it is also possible to trigger electron objects in the forward region of the detector, covering a range up to $|\eta| < 4.9$ using the *jet Feature EXtractor* (jFEX), a system focussed on triggering jet objects also capable of triggering electron objects in the forward region. This already allows to define trigger chains of signatures that correspond to high rapidity Z bosons that decay into electron pairs, where one electron is registered in the central barrel region and one in this forward region.

The caveat of the Run 3 system is that the granularity used for the trigger in the *ElectroMagnetic EndCap* (EMEC), *Hadronic EndCap* (HEC) and *Forward CALorimeter* (FCAL) systems does not correspond to the full detector granularity of the liquid argon calorimeter. For this reason there will be a new trigger system that efficiently covers the full ATLAS forward region ($2.5 < |\eta| < 4.9$) and that receives the full calorimeter granularity of the EMEC, the HEC and the FCAL to allow for maximum precision in the selection of electron, tau and jet objects in the forward region. This forward feature extractor (fFEX) is depicted in figure 10.1 alongside the other feature extractors of the new *Level-0 Calorimeter Trigger* (denoted as "L0Calo") as the first trigger stage, replacing the Level-1 trigger system. Besides the fFEX and the jFEX, these are the *electron Feature EXtractor* (eFEX) and the *global Feature EXtractor* (gFEX). For leptonic Z boson decays in particular the eFEX is relevant to select electron signatures in the central ATLAS region. The L0Calo system is only one aspect of the complete trigger system. It is complemented by the *L0Muon Trigger*, which is composed of multiple subsystems (Barrel and Endcap systems as well as processors for the *New Small Wheel* (NSW) and *Monitored Drift Tubes* (MDTs)) to effectively trigger muons. The L0Muon trigger passes muon track candidates to the *Muon-Central-Trigger-Processor Interface* (MUCTPI) and the *Central Trigger Processor* (CTP). The MUCTPI removes candidates that have been counted twice by the barrel and endcap sector logics and determines the number of candidates for different thresholds in transverse momentum. The L0Calo system also passes on its identified candidates to the *Global Trigger*, which receives all candidates of the previous systems including spatial and energy or momentum variables as well as any other discriminatory variables. It combines these candidates with additional calorimeter information to refine selections of electron, photon, muon, tau and jet objects. The final Level-0 trigger decision is calculated in the Central Trigger Processor, which receives information at a rate of $40\,\mathrm{MHz}$. If an event is accepted, the *Front-End LInk eXchange* (FELIX) system reads out all detectors at $1\,\mathrm{MHz}$ and

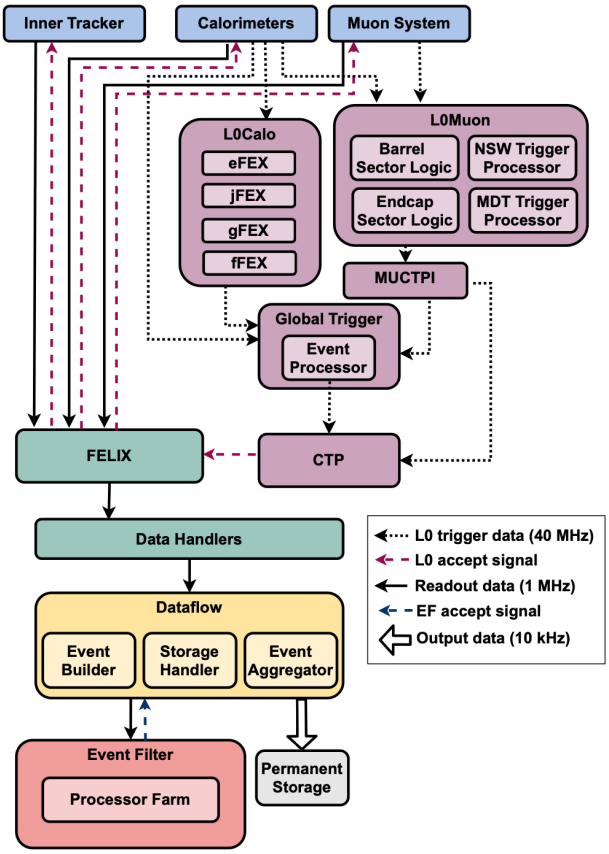


Fig. 10.1.: Overview of the Run 4 trigger system [194].

passes the information to the *Data Handlers* and the *Dataflow* system, which contains the *Event Builder*, *Storage Handler* and *Event Aggregator*. Together they comprise the Data Acquisition (DAQ) system. A CPU-based processor farm in the *Event Filter* then calculates the final trigger decision using all processed information (based on the tracking, calorimeter and muon system information) to achieve an "accept"-rate of approximately $10\,\mathrm{kHz}$. For each accepted event all information is saved in the *Permanent Storage* for future analysis. The following section will focus in more detail on the forward feature extractor and highlight technical considerations.

10.4 The Forward Feature Extractor

As mentioned in the previous section, fFEX will be part of the new Level-0 Calorimeter trigger system and will be required to efficiently trigger electromagnetic objects in the full ATLAS forward region ($2.5 < |\eta| < 4.9$) as well as jet objects in the FCAL ($|\eta| > 3.2$) and hadronically decaying taus in $2.5 < |\eta| < 4.0$ (corresponding to the coverage of the tracker). The study of the weak mixing angle presented in this thesis has explained the benefit of forward electrons used for such precision analyses that

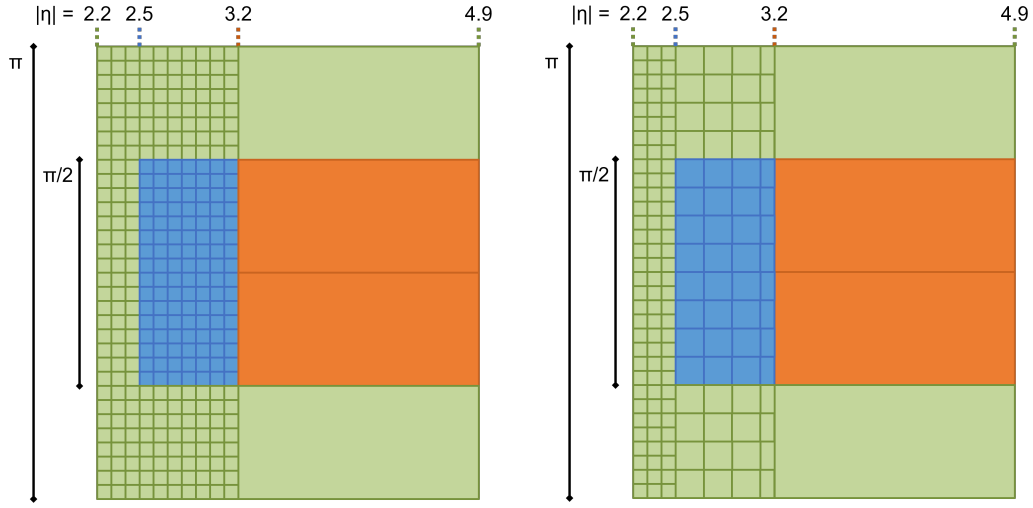
reduce the dilution effects from the proton PDF. Jets, which originate from quarks, in the forward region are expected to be particularly sensitive to processes such as vector boson fusion, where two vector bosons are radiated from quarks and fuse into a Higgs boson that decays into other particles. It is expected that the jets originating from the quarks that radiate the vector bosons enter the detector at high rapidities due to their large longitudinal momentum.

Having established the physical motivation for the fFEX system, it is important to outline the technical specifications. As the project is still ongoing, some changes are anticipated between the current state and the final deployment in ATLAS during Run 4. However, fundamental considerations and specifications are not expected to change considerably. The basis for the following discussion is the ATLAS specification report [195] of the system, which at the time of writing this thesis is not yet publicly accessible. The fFEX will receive the full granularity of the liquid argon calorimeter in the forward region, i.e. all individual calorimeter cells in each longitudinal and transverse segmentation.

The system will be constructed from four individual modules, each containing two *Field Programmable Gate Arrays* (FPGAs) necessary for computations on input data (in particular the energies of all cells). FPGAs are specialised hardware that are built from programmable logic and can be customised to efficiently and quickly compute algorithms that need to be implemented in firmware beforehand. The trigger algorithms discussed in the next chapter will need to be executable in real-time on these FPGAs. For maximum parallelisation each module is intended to cover one half in the azimuthal angle ϕ (i.e. $\Delta\phi = \pi$) of either side of the forward calorimeters, i.e. each individual FPGA will be dedicated to efficiently compute trigger decisions in one quadrant of one side of the forward region. This is schematically shown in figure 10.2, which illustrates the coverage of a single FPGA for both the electromagnetic and the hadronic calorimeter sections. As each fFEX module contains two FPGAs, each one covers $\Delta\phi = \frac{\pi}{2}$, as illustrated in the figures by the orange and blue regions as *core region*. In order to efficiently trigger in the full azimuthal angle, it is necessary to also consider the *environment* of each FPGA which extends its coverage to $\Delta\phi = \pi$, meaning it receives information on either side of the core region to calculate variables for electron, tau and jet trigger candidates. The next section will discuss how the forward calorimeter region is constructed.

10.4.1 The ATLAS Forward Region

After the general outline of the geometry and the function of the ATLAS detector in chapter 2, this section provides more details on the so-called *forward region* of the detector.



(a) Coverage in the electromagnetic calorimeter parts.

(b) Coverage in the hadronic calorimeter parts.

Fig. 10.2.: Schematic overview of the coverage of each FPGA in the fFEX system [195]. Individual cells in the FCAL systems are not depicted explicitly.

Generally, the calorimeters in the forward region are more challenging to utilise efficiently than the calorimeters in the central regions with $|\eta| < 2.5$ due to their coarser and non-uniform structure across the full region between $2.5 < |\eta| < 4.9$. The forward region of the ATLAS liquid argon calorimeter is divided into three distinct calorimeter systems, the Electromagnetic Endcap (Inner Wheel), the Hadronic Endcap and the Forward Calorimeter. Each system consists of individual layers, the EMEC Inner Wheel has two layers, the HEC four and the FCAL three layers. All utilise liquid argon as active medium to read out signals. The segmentation into cells of the liquid argon calorimeters in ATLAS can for instance be seen in figure 10.3. Cells are the finest segmentation of the calorimeters in contrast to supercells which are composite objects formed from multiple cells, also depicted in the figure. The fine segmentation is needed to resolve showers in the calorimeters as precisely as possible, both spatially and energetically. The layers have a similar purpose, in particular resolving shower developments in depth, which are expected to drastically differ between electrons or photons and jets. Hadronic showers are expected to be broader and deeper in the calorimeter compared to electromagnetic showers [196]. The EMEC is thus designed to provide precise measurements of electromagnetic showers using lead as absorber material, while the HEC is using copper as absorber to stop hadronic showers. Finally, the first layer of the FCAL serves as electromagnetic calorimeter and uses copper as absorber whereas the second and third layers are made from tungsten to stop hadronic showers.

The segmentation into cells in each calorimeter is defined in table 10.1. One important distinction between the EMEC/HEC and the FCAL is the geometry of the individual cells. In the EMEC/HEC they are arranged in a projective way in η and

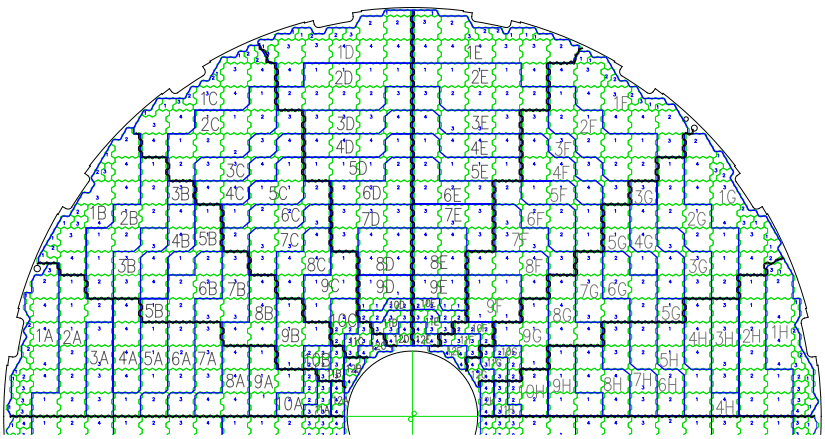


Fig. 10.3.: Segmentation of a calorimeter into individual cells using the example of one half of one hemisphere of the first layer of the FCAL. Cell boundaries are defined by green lines. Supercell boundaries are depicted as blue lines [197].

ϕ, while in the FCAL cells are arranged in regular carthesian coordinates in x and y (both following the previously introduced ATLAS coordinate system). Furthermore, cells in the HEC, which is behind the EMEC and is used in particular to measure hadronic showers, are four times the size of cells in the EMEC and arranged in such a way that cell boundaries align.

Finally, there is an overlap between the EMEC/HEC systems and the FCAL to ensure continuity of energy measurements. This is depicted in figure 10.4, which shows a cross-sectional view of the overlapping calorimeters as well as additional supporting structures of the detector. This figure highlights the consideration that the overlap between the EMEC/HEC and FCAL systems leads to a small region around $|\eta| \approx 3.2$ where parts of the electromagnetic layer of the FCAL1 are actually contained within the HEC and thus act as a hadronic layer in reality. This is relevant in order to be able to accurately calculate information on electromagnetically or hadronically interacting objects.

The geometric challenge can be visualised by studying cell centres in either η and ϕ space or in x and y space as depicted in figures 10.5 and 10.6, respectively, both of which show the same two halves of one side of the forward region. Clearly, the EMEC/HEC systems follow a different geometric arrangement of cells compared to the FCAL system. Specifically, the EMEC/HEC cells follow a regular pattern in $\eta \times \phi$ space, while FCAL cells follow a regular pattern in $x \times y$ space. This is crucial to

Calorimeter	Layer	η coverage	$\Delta\eta \times \Delta\phi$
EMEC	EME1	$2.2 < \lvert\eta\rvert < 2.4$	$0.025/4 \times \pi/32$
		$2.4 < \lvert\eta\rvert < 2.5$	$0.025 \times \pi/32$
		$2.5 < \lvert\eta\rvert < 3.2$	$0.1 \times \pi/32$
	EME2	$2.2 < \lvert\eta\rvert < 2.5$	$0.025 \times \pi/128$
		$2.5 < \lvert\eta\rvert < 3.2$	$0.1 \times \pi/128$
	EME3	$2.2 < \lvert\eta\rvert < 2.5$	$0.050 \times \pi/128$
HEC	HEC0/1/2/3	$2.2 < \lvert\eta\rvert < 2.5$	$0.1 \times \pi/32$
		$2.5 < \lvert\eta\rvert < 3.2$	$0.2 \times \pi/16$
			$\Delta x \times \Delta y$
FCAL	FCAL1	$3.1 < \lvert\eta\rvert < 3.15$	$1.5\,\text{cm} \times 1.3\,\text{cm}$
		$3.15 < \lvert\eta\rvert < 4.3$	$3.0\,\text{cm} \times 2.6\,\text{cm}$
		$4.3 < \lvert\eta\rvert < 4.83$	$1.5\,\text{cm} \times 1.3\,\text{cm}$
	FCAL2	$3.2 < \lvert\eta\rvert < 3.24$	$1.7\,\text{cm} \times 2.1\,\text{cm}$
		$3.24 < \lvert\eta\rvert < 4.5$	$3.3\,\text{cm} \times 4.2\,\text{cm}$
		$4.5 < \lvert\eta\rvert < 4.81$	$1.7\,\text{cm} \times 2.1\,\text{cm}$
	FCAL3	$3.29 < \lvert\eta\rvert < 3.32$	$2.7\,\text{cm} \times 2.4\,\text{cm}$
		$3.32 < \lvert\eta\rvert < 4.6$	$5.4\,\text{cm} \times 4.7\,\text{cm}$
		$4.6 < \lvert\eta\rvert < 4.75$	$2.7\,\text{cm} \times 2.4\,\text{cm}$

Tab. 10.1.: Sizes and layers of calorimeters in the forward region distinguished by pseudorapidity [198]. Note that the information is only provided for the region of $|\eta| > 2.2$ and other detector subsystems are not shown. Note that technical names of the FCAL layers have been adapted to correspond to figure 10.4.

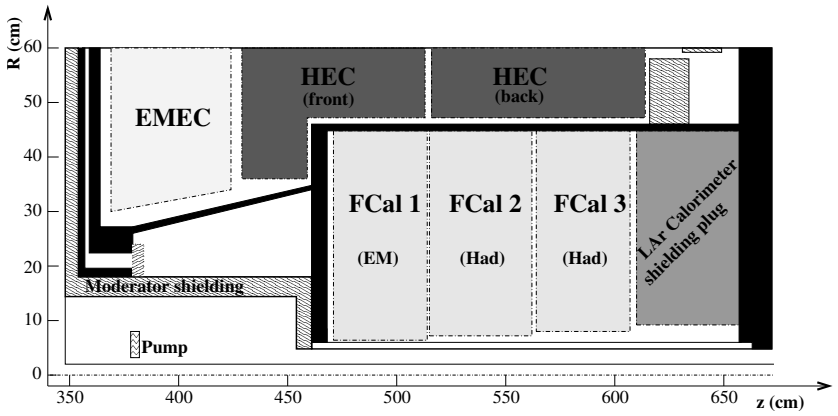


Fig. 10.4.: Schematic cross-sectional view of the ATLAS forward calorimeters in the $r - z$ plane depicting the different calorimeter systems and supporting structures [96].

take into account for efficient trigger algorithms and in particular when the overlap between both systems is considered since the consistent definition of identification and isolation variables is non-trivial.

10.4.2 Firmware Considerations

At the time of writing this thesis different FPGA types are considered to be used on the four fFEX modules. Besides the computational power, the data throughput in form of input and output links is also an important benchmark that will decide the final choice of FPGA and the board design. This process is a close collaboration between hardware experts for the fFEX and industry partners that can provide the necessary hardware as well as experts of other systems that operate upstream (i.e. before fFEX receives data) and downstream (i.e. systems that receive fFEX output). This is an iterative process where multiple prototypes will be constructed and tested for suitability on a hardware and firmware level.

Nonetheless, at the time of writing this thesis some higher-level considerations can already be made (but still subject to potential change). Before discussing the algorithms in the next chapter, it is useful to consider how such algorithms are implemented in firmware on the FPGAs. Such an overview is given in figure 10.7. Each FPGA will receive 96 fibre optic links from the *Liquid Argon Signal Processor* (LASP), which passes on information of individual cells of the liquid argon calorimeters. In the region below $|\eta| = 2.2$ cells are summed up into composite objects of the same size as in the region between $2.5 < |\eta| < 3.2$ in the EMEC and HEC. The high throughput at $40\,\mathrm{MHz}$ requires appropriate link speeds at $25.781\,25\,\mathrm{Gbit\,s^{-1}}$ per fibre link (with 96 input and 12 output links). The *Real-Time Data Path* (RTDP)

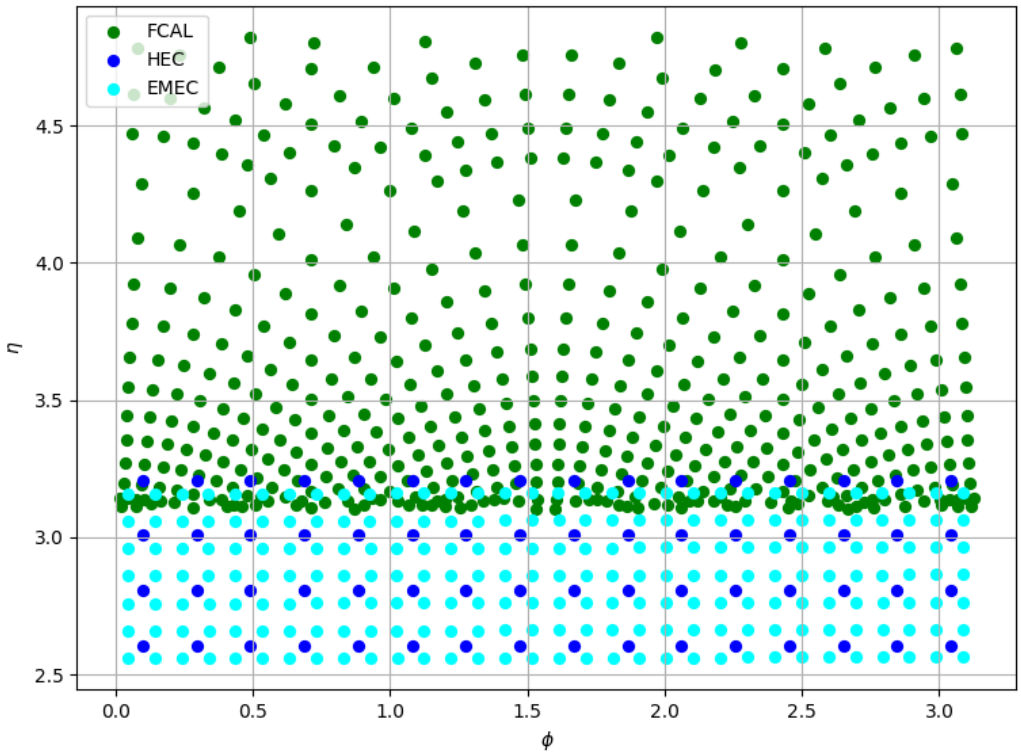


Fig. 10.5.: Distribution of geometric cell centres of the first (front facing towards the interaction region) layer of each calorimeter in η and ϕ. The upper half of the positive η region is depicted.

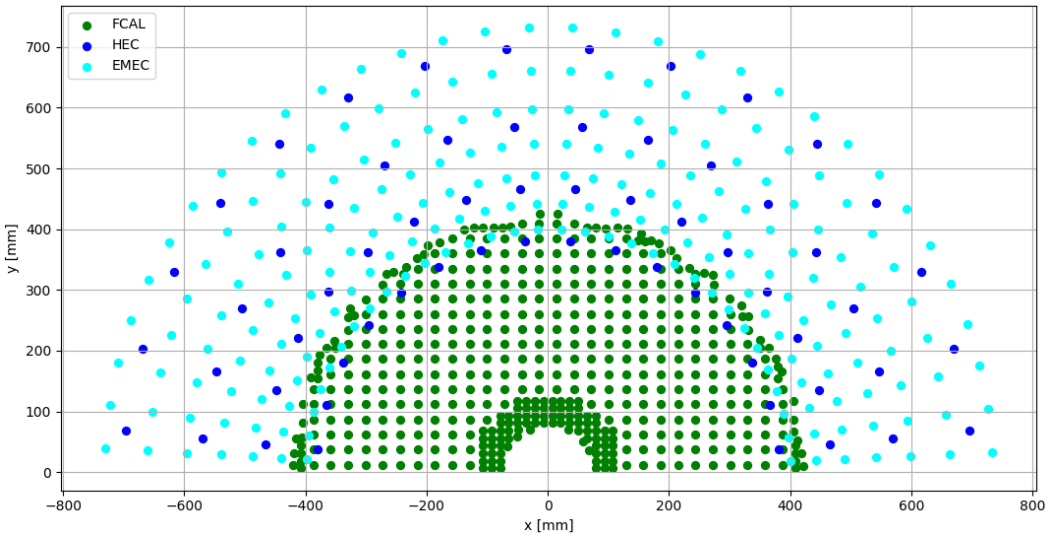


Fig. 10.6.: Distribution of geometric cell centres of the first (front facing towards the interaction region) layer of each calorimeter in x and y, projected onto the first layer of the FCAL. The upper half of the positive η region is depicted.

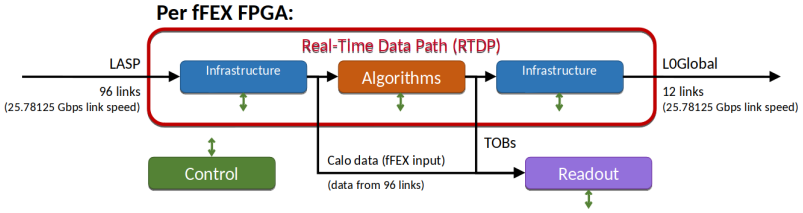


Fig. 10.7.: High-level firmware overview of a fFEX FPGA. Adapted from the ATLAS specification report [195].

describes the actual processing of data on the FPGA. Its total latency is expected to be approximately $0.7\,\mu$s with about $0.5\,\mu$s for the actual processing. The information is first received using certain infrastructure modules (blue box) before it is passed on to the actual algorithms (orange box) which forwards its output to infrastructure modules again. The latter pass the information onto L0Global using 12 fibre optic links at the same link speed as before. In addition, the input to and the output from the algorithms are passed onto another readout system (purple box), i.e. both the calorimeter information as well as trigger candidates, denoted as *trigger objects* (TOBs) to be passed forward to other systems. Each of the individual modules on the Real-Time Data Path as well as the readout system are steered by a separate control module (green box).

A more detailed overview of the algorithmic part of figure 10.7 is provided in figure 10.8 of the fFEX system. The diagram depicted is read from top to bottom and illustrates different general components of algorithmic firmware. Information from the liquid argon calorimeters is received and depicted as purple for the electromagnetic calorimeter information and blue for the hadronic calorimeter information. Firstly, during the *Masking* step the energy information from individual cells can be set to zero (which is used, for instance, in case of faulty cells). In the second step, the *Pileup Subtraction*, the additional energy deposited into the calorimeter system besides the hard scattering information is subtracted. After this, a *Noise Cut* can be applied, which removes all cells below a certain threshold to clear cells only containing electronic noise. In the fourth step the actual algorithms are executed in parallel. Jets, both with small radius and large radius (in η and ϕ space) receive energy sums of the electromagnetic and hadronic calorimeter cells, while forward taus and electrons receive all cells separated by calorimeter type. In addition, the total transverse energy, $\sum E_T$, and the missing transverse energy, MET, are calculated in parallel. The total transverse energy is the sum of transverse energy $E_{T,i}$ across all cells i and the missing transverse energy, MET or E_T^{miss}, is calculated in x and y components as $E_{x/y}^{\text{miss}} = -\sum_i E_{x/y,i}$. Finally, the outputs of all algorithms are passed on to create trigger objects, which are sorted by their transverse energy values to be provided

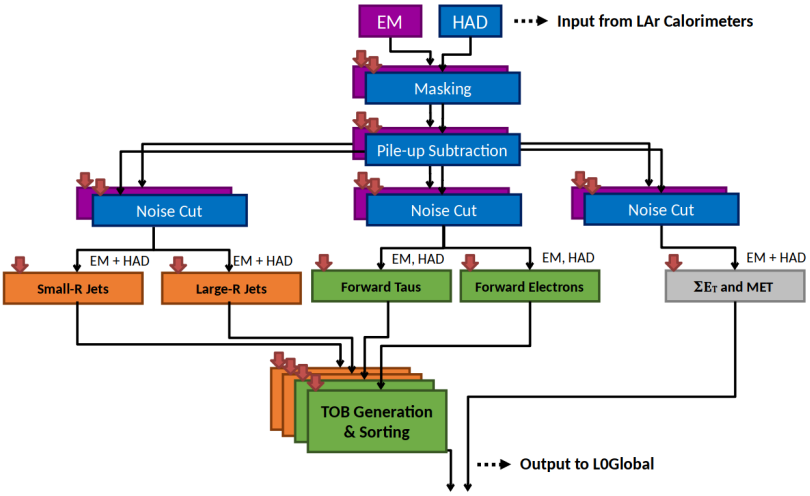


Fig. 10.8.: High-level overview of the fFEX trigger algorithms [195].

to the L0Global system. At all stages it is critical to assess the requirements needed for algorithms and calculations with respect to the implementations in firmware, in particular as calculations such as divisions are typically more resource-intensive than simple additions.

11 Development of Trigger Algorithms for the Forward Feature Extractor Module

> *In the midst of chaos, there is also opportunity.*
>
> **— Sun Tzu**

In order to efficiently exploit the potential of the upgrades made to the ATLAS trigger system, in particular in the forward region between $2.5 < |\eta| < 4.9$, specialised trigger algorithms are being developed. This chapter aims to highlight first studies on algorithms for the fFEX that are designed to trigger electrons or photons. An efficient trigger of electrons in the forward region in particular is expected to be greatly beneficial to future measurements of the weak mixing angle at ATLAS, as discussed in chapter 8. The algorithms presented here have been created by the author within the official ATLAS Athena [126] code base in C++ as a new software package and benefited from ATLAS software reviews leading to its inclusion on the Athena 21.3 and 21.9 releases.

11.1 Trigger Algorithms

One of the main challenges in the design of trigger algorithms is the efficient utilisation of limited resources on the available FPGA boards within the constricted latency available. In case of Run 4 the latency for processing is expected to be $0.5\,\mu\text{s}$ [195]. Since it is not possible to store each event in ATLAS due to bandwidth limitations, the Level-0 trigger system for the HL-LHC is anticipated to operate at a rate budget of $1\,\text{MHz}$. The precise allocation of the rate allowed in each subsystem is not clear at the time of writing this thesis, however, an upper limit for the fFEX system of $10\,\text{kHz}$ which corresponds to 1% of the total rate is assumed for the following studies. Since most collisions in ATLAS are not of interest (as collisions are dominated by processes not used for analyses), the main difficulty of trigger algorithms is to highly suppress this background while maximising the *efficiency* $\epsilon = \frac{\text{signal events triggered}}{\text{all signal events}}$ to successfully identify relevant signal signatures. The background suppression is crucial as the total rate is driven by statistically dominating background processes. Overall, trigger algorithms are a cornerstone of the data-taking process and need to be carefully designed since events that are

not triggered cannot be recovered later, in contrast to any selections applied during offline analyses.

11.1.1 Technical Prerequisites

The baseline for the following studies of efficiencies and rates of different algorithms are simulations of $Z \to e^+e^-$ as signal[1] and jet production as dominant background[2] (where a $20\,\mathrm{GeV}$ maximum p_T threshold has been applied on generator level jets), both simulated using the POWHEGBOX [145] and PYTHIA [144] generators. The information of individual calorimeter cells is only stored in the very storage-intensive *Event Summary Data* (ESD) format in the ATLAS processing chain described in section 2.2.7. For this reason the number of simulated events available is statistically limited to $250,000$ signal events and $850,000$ simulated events as background, both of which have been centrally provided by ATLAS. In all cases, considered *signal objects* are required to be spatially matched to true electrons from the simulation by $\Delta R = \sqrt{\Delta\eta^2 + \Delta\phi^2} < 0.2$. The instantaneous luminosity of these simulations corresponds to roughly the one during Run 2, i.e. an average of $\mu \approx 40$ simultaneous collisions per bunch crossing. While the anticipated pileup at the HL-LHC is expected to reach $\mu = 200$, the studies and considerations presented here serve as a first proof of principle and as first studies on optimisations on different types of algorithms. Nonetheless, as it is non-trivial to extrapolate the following results to conditions anticipated during Run 4, the algorithms presented need to be evaluated in a similar manner once such simulations are available. In order to simulate the algorithms presented, a custom software package has been developed that can be used within the ATLAS Athena software.

11.1.2 Sliding Window Algorithms

Iterative algorithms such as the clustering used during the reconstruction process described in chapter 2.3 have not been suitable for triggers in the past given their intensive hardware use. While more resources in the form of processing power and latency are available for the fFEX compared to Run 2 systems, it is nonetheless unclear whether iterative approaches can feasibly be implemented. Instead, the focus of the studies and discussion in this chapter will be a class of algorithms that use fixed numbers of cells within a given window, which lends itself especially well to parallelisation on the anticipated hardware.

[1] ATLAS dataset identifier: `mc16_13TeV.361106.PowhegPythia8EvtGen_AZNLOCTEQ6L1_Zee.recon.ESD.e3601_e5984_s3126_r10684.`

[2] ATLAS dataset identifier: `mc16_13TeV.361020.Pythia8EvtGen_A14NNPDF23LO_jetjet_JZ0W.recon.ESD.e3569_s3498_r11742.`

Such approaches are classified as *sliding window algorithms* [199] since a fixed sized window is evaluated at each possible position in the calorimeters. During the data taking of Run 2 between 2015 and 2018 and the recently started Run 3 these algorithms have been used extensively already and are known to provide high efficiencies at reasonable trigger rates if optimised properly.

Below, different approaches to this class of algorithms are presented and evaluated in terms of signal efficiency and expected background rate using simulations. The basic concept is visualised in Figure 11.1, where a rectangle of 4×4 cells encapsulates a core region of 2×2 cells. The *electromagnetic core* contains the sum of transverse energy E_T of all cells within the 2×2 central cell window, also longitudinally in the electromagnetic calorimeter layers, while the *electromagnetic isolation* is determined by the sum of the transverse energy of the 4×4 ring of cells excluding the core, also summed up for all electromagnetic layers. Finally, a *hadronic isolation* energy sum is determined as the sum of all cell transverse energies of cells within the 4×4 window in the hadronic calorimeter[3]. The example shown in figure 11.1 depicts this for cells that are arranged in a regular $\eta \times \phi$ pattern, but this can also be adjusted for cells arranged in a $x \times y$ pattern.

Since electromagnetic showers are expected to be compact with the bulk of their energy deposited in the electromagnetic parts of the calorimeters, the three energy sums can be used in a simple approach to differentiate between electromagnetic and hadronic showers by applying selection criteria of minimum energy thresholds in the electromagnetic core and maximum energy thresholds in each of the isolation energy sums.

Such a fixed-size window of cell energies can be determined at each position in the calorimeter. In order to prevent any double counting that could occur due to the evaluation of the window at each possible position, a local maximum criterion is enforced by comparing the central energy sum (in the 2×2 window, called *seed*) to the energy sums of surrounding window positions following a specific pattern. The coordinates depend on the reference frame chosen and are omitted in figure 11.2.

This way only unique objects are found and passed on to other trigger systems. However, the reality of the ATLAS calorimeter systems in the forward region does not follow such a simple and regular structure in all parts as indicated in table 10.1. For this reason, different approaches to the design of an efficient algorithm are presented. Some of the major aspects of these algorithms can be varied, such as the window size, the geometry ($\eta \times \phi$ or $x \times y$) and derived variables such as the energy sums, but also variables designed to describe shower properties [198] than can be

[3] Studies did not reveal any benefit in differentiating between a hadronic core of 2×2 cells and a hadronic isolation ring of 4×4 cells, which is often used in other sliding window algorithms.

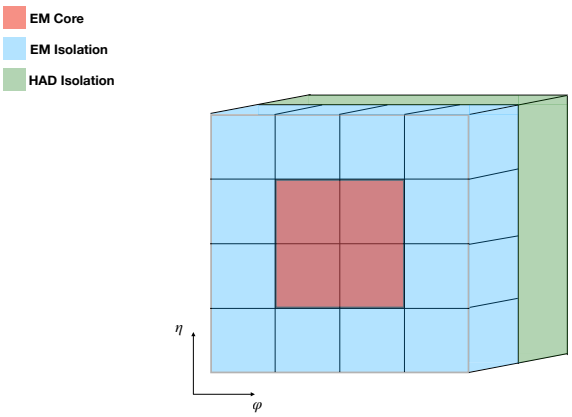


Fig. 11.1.: Conceptual overview of sliding window-type algorithms. Multiple energy sums are calculated, here in red the *electromagnetic core*, in blue the *electromagnetic isolation* and in green the *hadronic isolation* (no individual cells are shown for the hadronic isolation).

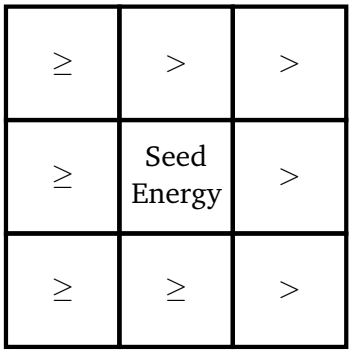


Fig. 11.2.: Schematic overview of the local maximum criteria used in sliding window algorithms presented in this chapter.

adjusted to fixed windows. In particular, defining consistent local maxima at the boundary between the EMEC/HEC region and the FCAL is important and enforced by giving preference to maxima in the EMEC/HEC regions due to the overlap with the FCAL and to avoid double counting between different detector parts.

In the following sections some variations of these approaches will be described and evaluated. In particular, the 4×4 window of cells will be evaluated in $\eta \times \phi$ as well as in $x \times y$ as the expected size of an electron shower, described by the Molière radius [200], fits inside the 2×2 core cells of the windows. Due to the expected radius of about $1.6\,\mathrm{cm}$ for both, copper and lead [14], an electromagnetic shower might even fit within one cell in the EMEC or the FCAL. However, as it is unlikely that electron candidates hit cells perfectly in their centre, the 2×2 window is chosen.

Importantly, these studies have been performed without any cell information below $|\eta| = 2.5$, leading to some inefficiencies at the boundaries. Current developments indicate that cell information will be available below this threshold to ensure that such boundary effects do not occur. Nonetheless, for the purpose of most of the studies presented below it is useful to focus on fiducial regions in the EMEC/HEC and the FCAL to avoid any influence from boundaries at $|\eta| = 2.5$ or $|\eta| = 4.9$ and also the transition between the two calorimeter regions. If not explicitly stated otherwise, fiducial regions are considered for these studies: $2.7 < |\eta| < 3.0$ for the EMEC/HEC and $3.4 < |\eta| < 4.4$ for the FCAL. The system that will be deployed in ATLAS for the HL-LHC is expected to use noise suppression on individual cells to maximise computational efficiency. While the method used for this is not fully defined yet, a conservative threshold of $\pm 100\,\mathrm{MeV}$ per cell is applied as a noise suppression. Due to the way a signal is formed from the charges in the calorimeters, negative energies must be counted as well, so that the noise suppression removes a small energy range around zero.

11.1.3 Legacy-like Sliding Window Algorithm

The simplest approach to trigger candidates of electrons and photons is to extend the same concept that has been applied in the central ATLAS region during Run 2 to the forward region. Crucially, the size of the window is based on the size of cells in the inner wheel of the electromagnetic endcap calorimeter. Whether a cell is counted towards a window depends on its geometric centre. Specifically, a core window of $0.2 \times 2\frac{\pi}{64}$ in η and ϕ in the electromagnetic layers of the calorimeters leading to energy sums of

$$E_T^{\text{core}} = \sum_{\text{cell}_i \in (0.2 \times 2\frac{\pi}{64} \in \text{EM layers})} E_{T,i} \tag{11.1}$$

needs to be identified in which the energy exceeds $5\,\mathrm{GeV}$. Additional isolation criteria are applied in a window of $0.4 \times 4\frac{\pi}{64}$ in η and ϕ in the electromagnetic layer to exclude broader showers that typically originate from hadronic particles

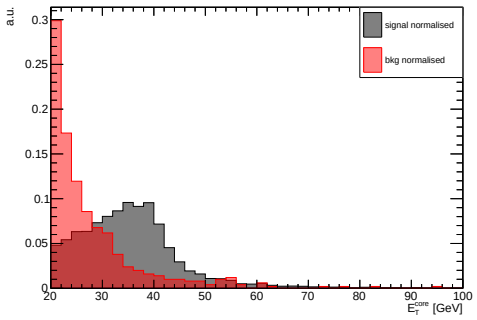
$$E_T^{\text{EM Iso.}} = \sum_{\text{cell}_i \in (0.4\times 4\frac{\pi}{64} \in \text{EM layers}) \wedge \text{cell}_i \notin (0.2\times 2\frac{\pi}{64} \in \text{EM layers})} E_{T,i}. \tag{11.2}$$

Finally, the hadronic layer behind the electromagnetic layer is used to enforce another isolation criterion to exclude showers that reach deeper into the hadronic calorimeter, which is also a differentiation between electromagnetic and hadronic showers. Since cells in the HEC and the hadronic layers of the FCAL are larger than the front-facing cells of the electromagnetic layers, only a fraction $f = I/A$ of the energy deposition is counted towards the window defined by the intersection I of the cell area with the window area A

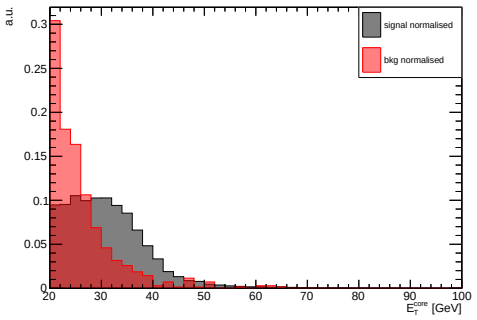
$$E_T^{\text{Had Iso.}} = \sum_{\text{cell}_i \in (0.4\times 4\frac{\pi}{64} \in \text{Had. layers})} f \cdot E_{T,i}. \tag{11.3}$$

The normalised distributions of the three energy sums are shown in figure 11.3. In case of the transverse energy the Jacobian peak of the electrons from the Z boson decay is clearly visible in the EMEC at approximately $45\,\mathrm{GeV}$, while the distribution is more smeared out in the FCAL. Expectedly, the background distribution is steeply falling towards higher energies as QCD production processes decrease with higher energies as well. The electromagnetic isolation energy is also more distinguished in the EMEC than in the FCAL. However, in both cases the signal is contained in a smaller energy window, as expected from a compact electromagnetic shower. Finally, the hadronic energies compared between the HEC and the FCAL are more similar than the other variables, which highlights the challenge to separate signal and background with this variable. Nonetheless, the background distribution is shifted towards higher energies with a long tail as expected from a hadronic shower in the hadronic calorimeters.

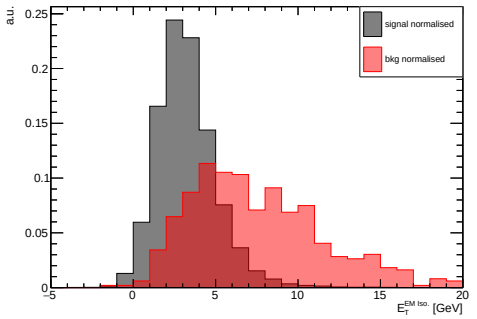
In view of the distributions depicted in figure 11.3, selections on each variable have been defined to ensure a high signal efficiency while removing as much background contributions as possible. The electromagnetic isolation is required to be $E_T^{\text{EM Iso.}} < 10\,\mathrm{GeV}$ both in the EMEC and the FCAL. Additionally, the hadronic isolation must be $E_T^{\text{Had. Iso.}} < 1\,\mathrm{GeV}$ in the HEC and $E_T^{\text{Had. Iso.}} < 0.5\,\mathrm{GeV}$ in the FCAL.



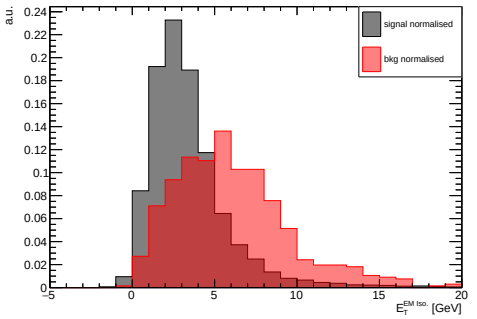
(a) E_T^{core} in the EMEC/HEC.



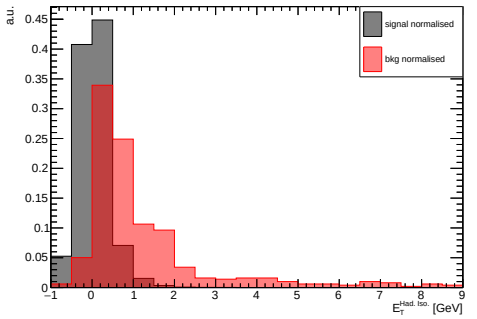
(b) E_T^{core} in the FCAL.



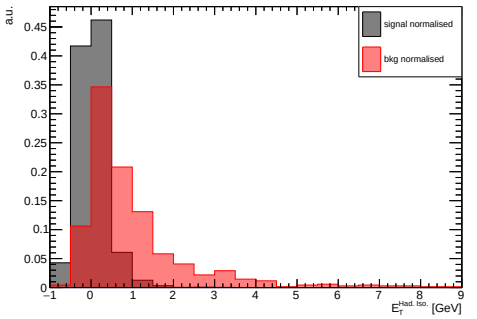
(c) $E_T^{\text{EM Iso.}}$ in the EMEC/HEC.



(d) $E_T^{\text{EM Iso.}}$ in the FCAL.



(e) $E_T^{\text{Had. Iso.}}$ in the EMEC/HEC.



(f) $E_T^{\text{Had. Iso.}}$ in the FCAL.

Fig. 11.3.: Normalised distributions of energy sums for signal and background of the legacy-like sliding window algorithm in the EMEC/HEC and FCAL fiducial regions for core energies $E_T^{\text{core}} > 20\,\text{GeV}$.

11.1.4 Geometry-aware Sliding Window Algorithm

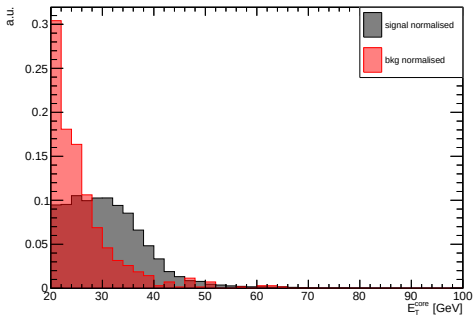
As the layout of cells in the FCAL system is vastly different from the layout in the EMEC and HEC, it is useful to consider a variation of the sliding window algorithm of the previous section exploiting the different geometries. This is done by using the same sliding window algorithm described before in the EMEC and HEC and a sliding window of size $3.0\,\mathrm{cm} \times 2.6\,\mathrm{cm}$ in $x \times y$ in the FCAL. This size reflects the dominant cell size in the first layer of the FCAL and allows for a consistent definition of the three energy variables introduced before, i.e.

$$\begin{aligned} E_T^{\text{core}} &= \sum_{\text{cell}_i \in (3.0\,\text{cm} \times 2.6\,\text{cm} \in \text{EM layer})} E_{T,i} \\ E_T^{\text{EM Iso.}} &= \sum_{\text{cell}_i \in (6.0\,\text{cm} \times 5.2\,\text{cm} \in \text{EM layer}) \wedge \text{cell}_i \notin (3.0\,\text{cm} \times 2.6\,\text{cm} \in \text{EM layer})} E_{T,i} \\ E_T^{\text{Had Iso.}} &= \sum_{\text{cell}_i \in (6.0\,\text{cm} \times 5.2\,\text{cm} \in \text{Had. layers})} f \cdot E_{T,i}. \end{aligned} \tag{11.4}$$

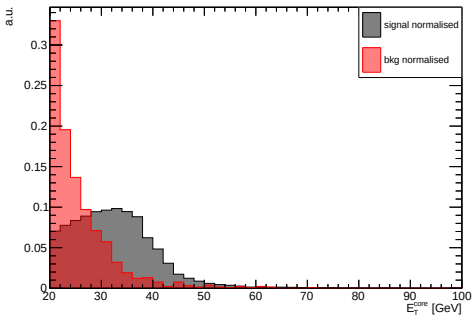
The expected size of an electromagnetic shower is still captured by these windows accounting for the appropriate projection of the Molière radius onto the $x \times y$ plane. Normalised comparisons between the signal and background distributions for the legacy and the geometry-aware algorithms are shown in figure 11.4 for the FCAL (as EMEC/HEC distributions are identical to ones of the legacy-like algorithm). In the transition between the EMEC/HEC calorimeter and the FCAL calorimeter preference is given to the $\eta \times \phi$ window until $|\eta| < 3.4$ in case conflicting local maxima between the EMEC/HEC and FCAL regions are found. This is motivated by the geometric arrangement of the detectors shown in figure 10.4.

The energy distributions on the right overall show a similar pattern compared to the distributions of the legacy algorithms shown on the left. However, a close comparison reveals that the transverse energy, in particular the Jacobian peak of the signal, is better resolved and distinguishable between signal and background in case of the geometry-aware algorithm. In addition, the distributions of the electromagnetic isolation energy have less overlap and are thus easier to separate. In case of the hadronic energy no obvious improvement is visible in the FCAL. Nevertheless, since two of the crucial energy sums could be improved, the following discussion will focus on this geometry-aware sliding window algorithm.

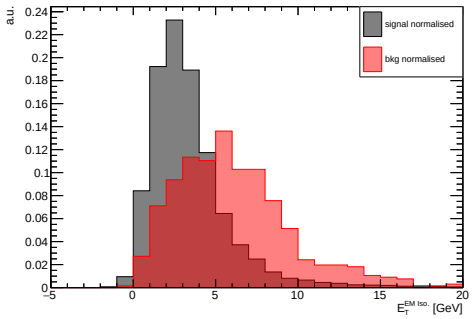
Efficient separation between signal and background in the EMEC and HEC is achieved by identical selections on the energy variables employing the previously defined thresholds. In the FCAL increased separation allows to use the same thresholds with increased signal efficiency and background rejection.



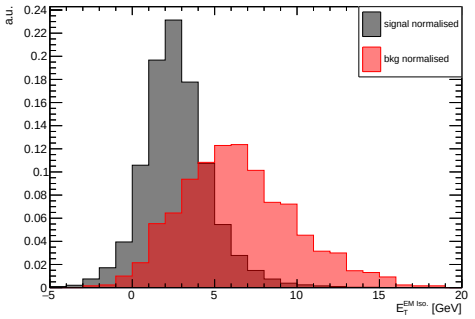
(a) E_T^{core} in the legacy algorithm.



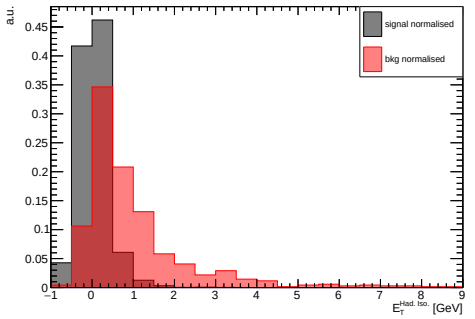
(b) E_T^{core} in the geometry-aware algorithm.



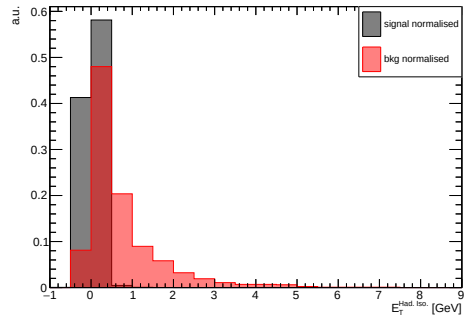
(c) $E_T^{\text{EM Iso.}}$ in the legacy algorithm.



(d) $E_T^{\text{EM Iso.}}$ in the geometry-aware algorithm.

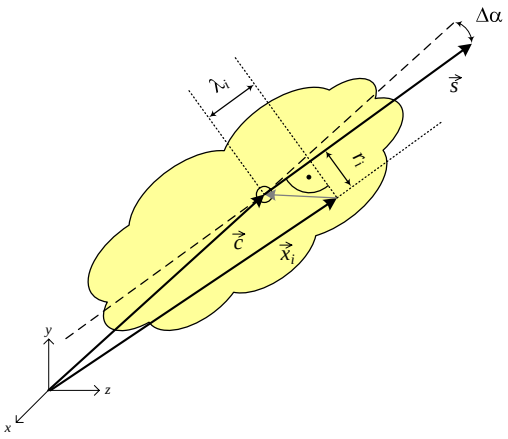


(e) $E_T^{\text{Had. Iso.}}$ in the legacy algorithm.



(f) $E_T^{\text{Had. Iso.}}$ in the geometry-aware algorithm.

Fig. 11.4.: Normalised distributions of energy sums for signal and background of the legacy and the geometry-aware sliding window algorithms in the FCAL fiducial regions for core energies $E_T^{\text{core}} > 20\,\text{GeV}$.



$\vec{c}$ *centre of gravity of cluster, measured from the nominal vertex* $(x = 0, y = 0, z = 0)$ *in ATLAS*

$\vec{x}_i$ *geometrical centre of a calorimeter cell in the cluster, measured from the nominal detector centre of ATLAS*

$\vec{s}$ *particle direction of flight (shower axis)*

$\Delta\alpha$ *angular distance* $\Delta\alpha = \angle(\vec{c}, \vec{s})$ *between cluster centre of gravity and shower axis* $\vec{s}$

λ_i *distance of cell at* $\vec{x}_i$ *from the cluster centre of gravity measured along shower axis* $\vec{s}$ $(\lambda_i < 0$ *is possible)*

r_i *radial (shortest) distance of cell at* $\vec{x}_i$ *from shower axis* $\vec{s}$ $(r_i \geq 0)$

Fig. 11.5.: Schematic view of geometric moments of a topological cluster in the ATLAS detector [198].

11.1.5 Shower Shape Variables

The previously introduced energy sums already clearly exhibit different shapes between signal and background. Nevertheless, it is useful to study additional derived parameters that utilise physical properties describing the shower evolution in the calorimeter, since those can further expose differences between electromagnetic signal and hadronic background. These so-called *shower shape variables* are used in the offline identification algorithms in ATLAS [136]. They are depicted in figure 11.5 and are sometimes also called geometric *cluster moments*. The diagram depicts such a cluster in yellow with its barycentre ("centre of gravity"), its geometric centre as well as its shower axis, angles and distances describing its physical properties.

Usually these variables are calculated with respect to a topological cluster of cells, depicted in figure 11.5, which has been determined iteratively. However, it is still possible to approximate them using a fixed-sized window as introduced previously. Specifically, the variables of interest are listed in table 11.1 together with their physical description. A comparison between signal and background using these variables is shown in figure 11.6. The overall aim is to identify variables that provide an improved separation between signal and background compared to the simple energy sums. All distributions are based on the geometry-aware sliding windows, but similar distributions can be calculated for the legacy algorithm as shown in appendix H.1.

The two most powerful variables for separation of electromagnetic showers and hadronic showers are depicted in the first and second row of figure 11.6. The fraction of energy carried by the most energetic cell compared to the rest of the cells in the window f_{max} is expectedly clearly able to separate between the two types of showers.

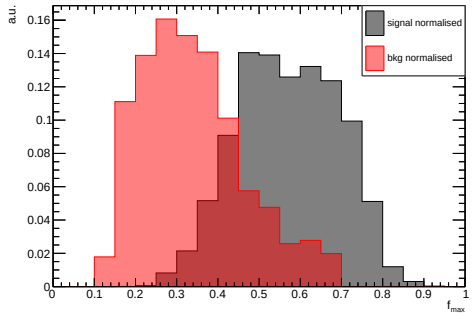
This can be explained by the relative compactness of an electromagnetic shower compared to a hadronic shower. Secondly, the depth of the shower barycentre d_z in the z direction[4] (along the beam axis) is also able to distinguish between electromagnetic and hadronic showers. The latter extend further into the calorimeter, in particular into the hadronic calorimeter parts and thus the depth of the barycentre can extend much deeper than the barycentre of electromagnetic showers, which are clearly much more focussed closer to the front-facing surface of the calorimeter. The third row depicts the variance of the shower along the z axis σ_z^2, which is closely connected to the depth of the barycentre and thus shows a similar behaviour as the previous distributions. Finally, the variance σ_r^2 is determined along the $r = \sqrt{x^2 + y^2}$ axis, which provides information about the width of the shower. While electromagnetic and hadronic showers are separated in particular in the EMEC/HEC, the overall separation power of this parameter appears much reduced compared to the ones discussed before.

Category	Description	Symbol
Shower depth	Depth of the shower barycentre along the beam axis.	d_z
Maximum cell energy	Fraction of total energy carried by the cell with the highest energy.	f_{max}
Longitudinal second momentum	Variance of the weighted distance of each cell towards the energetic barycentre of the window along the beam axis.	σ_z^2
Transverse second momentum	Variance of the weighted distance of each cell towards the energetic barycentre of the window in transverse direction.	σ_r^2

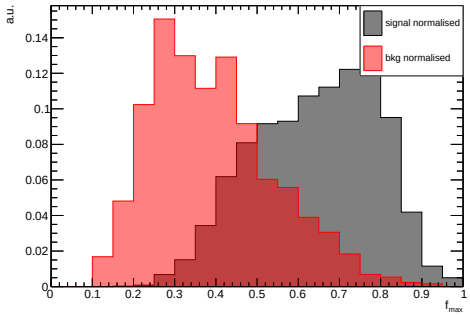
Tab. 11.1.: List of shower shape variables, their meaning and symbol. The definition of each variable can be found in appendix H.2.

Four of these additional distributions are utilised for improved signal and background discrimination. Due to the limitation in available simulated events, the thresholds for separation of signal and background are determined visually from the distributions rather than by a grid search. In particular, the shower depth $d_z < 60\,\text{mm}$ in the EMEC/HEC and $d_z < 40\,\text{mm}$ in the FCAL achieve a high separation. To that end, a selection of $f_{\text{max}} > 0.3$ in the EMEC/HEC and $f_{\text{max}} > 0.4$ in the FCAL provide a balance between high signal efficiency and improved background rejection.

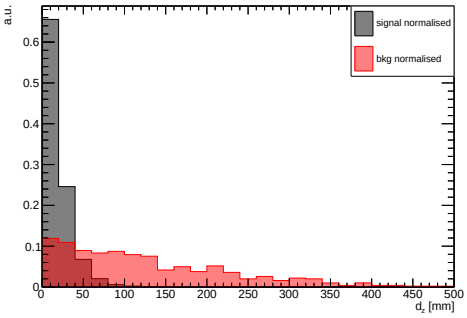
[4] This definition is different from the definition used in offline identification methods which uses the shower axis. The simplification is made to reduce computational complexity in view of the implementation in firmware on FPGAs.



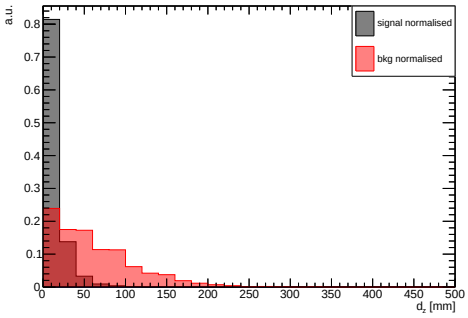
(a) f_{max} in the EMEC/HEC.



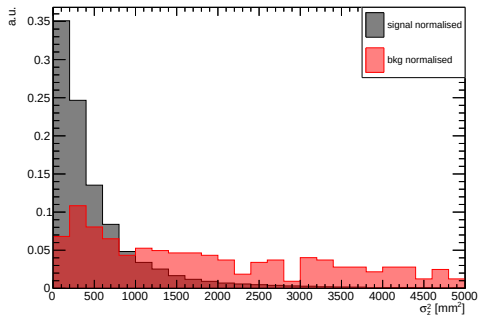
(b) f_{max} in the FCAL.



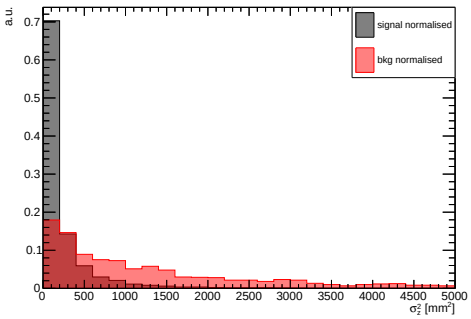
(c) d_z in the EMEC/HEC.



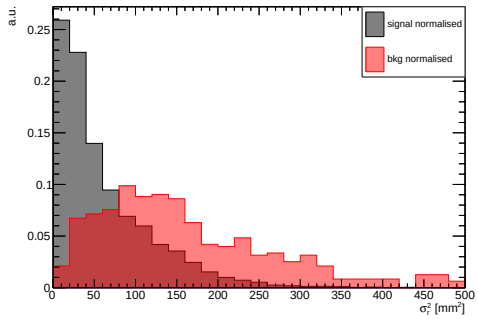
(d) d_z in the FCAL.



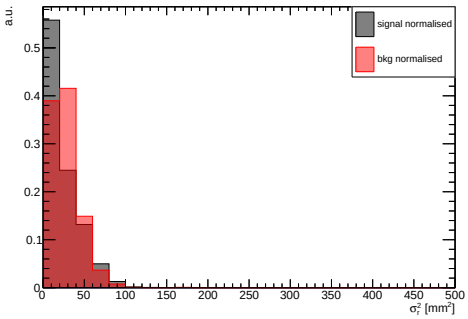
(e) σ_z^2 in the EMEC/HEC.



(f) σ_z^2 in the FCAL.



(g) σ_r^2 in the EMEC/HEC.



(h) σ_r^2 in the FCAL.

Fig. 11.6.: Normalised distributions of shower shape variables for signal and background of the geometry-aware sliding window algorithm in the EMEC/HEC and FCAL fiducial regions for core energies $E_T^{\text{core}} > 20\,\text{GeV}$.

11.1.6 Neural Networks

The algorithms discussed so far are all limited by their one-dimensional selection approach. With powerful FPGAs that include optimised architecture for neural networks such as the Xilinx Versal AI Engine Technology [201], multivariate selection approaches such as neural networks can realistically assumed to be executable on modern FPGA hardware to improve the classification. For this approach, both *Boosted Decision Trees* (BDTs) and neural networks have been studied and found to be of comparable performance. For this reason, the focus will be on a simple neural network architecture, which is the type of architecture suitable for modern FPGAs. The study has been performed using the TMVA (Toolkit for MultiVariate Analysis) in ROOT [202].

Artificial neural networks have become the de-facto standard in many classification tasks in the last decade due to their versatility and adaptability. The theoretical and mathematical background for these networks are provided for instance by Ng et al. [203]. Neural networks are models that can be trained to distinguish between signal and background objects by providing labelled simulations. During this training process weights at individual neurons of such a network are updated using backpropagation. Through this training process, a neural network will transform its input into different internal representations where signal and background can most effectively be distinguished and finally combined into a single output in case of a binary classification such as the one under consideration for the trigger algorithms.

The number of simulated events is sparse[5] after a basic selection of $E_T^{\text{core}} > 15\,\text{GeV}$ is applied to create a representative source for training the architecture of the neural network. For this reason its structure is a simple multilayer perceptron with a single hidden layer containing nine neurons to ensure convergence of the loss function, in this case the mean squared error (i.e. the quadratic difference between true and predicted categories over the sample size).

Importantly, to maximise the usage of the available number of events, a two-fold cross-training is performed, where events are split by even/odd event numbers (random numbers assigned by the generator). The neural network is trained on one set and tested on the other one. Another network uses the opposite, complimentary approach.

Finally, all of the energy sums and shower shape variables are considered as input variables. However, due to the sparsity of the simulation used for training only

[5] In total $31,598$ signal events and 1136 background events in the EMEC/HEC region as well as $19,847$ signal events and 1575 background events in the FCAL region were left.

the variables that provide the best separation between signal and background are kept. This has been determined by an importance ranking by TMVA with respect to the MLP classifier in a test using all variables introduced in previous sections. The importance I_i of a variable i is the sum of squared neuron weights $w_{ij}^{(1)}$ between each input variable and the hidden layer, separately multiplied by the normalised squared sample mean $\bar{x}_i$ of this variable

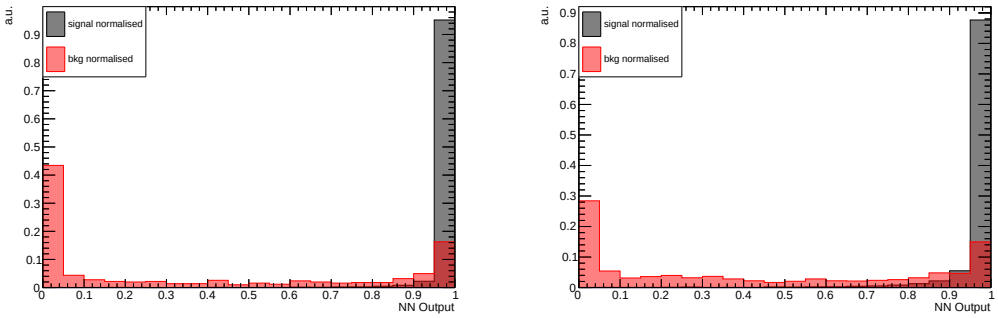
$$I_i = \bar{x}_i^2 \sum_{j=0}^{n_h} (w_{ij}^{(1)})^2, \tag{11.5}$$

where n_h is the number of neurons in the hidden layer. Importantly, the core energy of the window is excluded to reduce a potential bias of the network to learn specific energies[6]. The variables with the highest importance have been found to be the hadronic isolation $E_T^{\text{Had. Iso.}}$, the electromagnetic isolation $E_T^{\text{EM Iso.}}$, the shower depth d_z and the fraction of energy of the most energetic cell f_{max}. This is supported by a study of the correlation between variables shown in appendix H.3, which show that these four variables exhibit a stronger correlation in background than in the signal, which can be exploited by a neural network. A preselection of $E_T^{\text{core}} > 20\,\text{GeV}$ is enforced to avoid a bias towards very low energetic electrons, which typically cannot be triggered anyway.

The training of the different networks (two for each cross-training and two for the EMEC/HEC and the FCAL) was done using the Adam optimiser [204] at a learning rate of 0.02 with a decay rate of 0.01 in order not to skip the global minimum over 600 epochs using the full sample as batch size. As an activation function $\tanh(x) = \frac{e^x - e^{-x}}{e^x + e^{-x}}$ was used, where x is the weighted sum of a neuron. The development of the mean squared error loss on the training and testing sample did not indicate major effects of overtraining.

The distributions in figure 11.7 depict the output of the neural networks in the EMEC/HEC and the FCAL. A very good separation can be achieved, however, some residual background contribution remains. A selection of *NN output* > 0.9 in both cases drastically reduces background contributions while keeping most of the signal. A detailed performance evaluation of the network in comparison with the other algorithms presented is shown in the next section.

[6] A residual bias due to correlations between the energy and isolation and shower shape variables cannot be removed by this method.



(a) Network output for the EMEC/HEC. (b) Network output for the FCAL.

Fig. 11.7.: Normalised distributions of the neural network output for signal and background of the geometry-aware sliding window algorithm in the EMEC/HEC and FCAL fiducial regions for core energies $E_T^{\text{core}} > 20\,\text{GeV}$.

11.2 Performance Evaluation

Each of the algorithms presented has to be benchmarked in order to evaluate their expected performance using simulations. In this section three measures of performance will be compared:

- A **single electron trigger rate curve** is a benchmark of an expected trigger rate as a function of the single electron trigger threshold in $p_T = \sqrt{E_T^{\text{core},2} - m_e^2}$ (where m_e is the electron mass). Hardware limitations will dictate upper limits on the rate budget for the fFEX system so that lower p_T thresholds at identical rates are preferable to capture as much electron phase space of interesting signal processes as possible.

- The **single electron trigger efficiency** is a measure of how many true electrons in a given phase space region are correctly identified and selected by a trigger algorithm with a given threshold on the sum of the electromagnetic core E_T^{core}. This threshold is determined by the target rate which serves as a lower boundary in p_T.

- The **Receiver Operating Characteristic** (ROC) curve is a common measure to evaluate the performance of an algorithm. It shows the true positive rate $\text{TPR} = \frac{\text{No. of true electrons triggered}}{\text{No. of all true electrons}}$ as a function of the false positive rate $\text{FPR} = \frac{\text{No. of background objects triggered}}{\text{No. of all background objects}}$ for a given region in phase space.

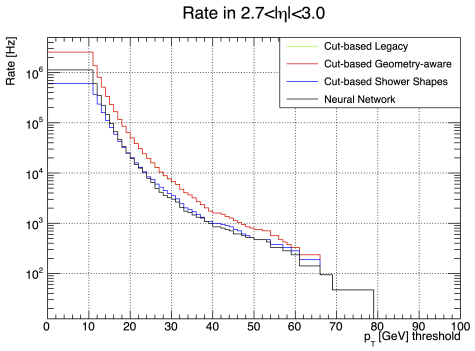
Figure 11.8 depicts the three performance measures introduced above for the EMEC/HEC region on the left and for the FCAL region on the right. The logarithmic rate distribution in the first row for the EMEC/HEC region are identical between the legacy sliding window and the geometry-aware sliding window. The lowest p_T

thresholds at identical rates in most cases can be achieved by the neural network but also by the cut-based shower shape approach. The neural network exhibits a lower rate in particular towards higher transverse momenta where simple one-dimensional selections on variables may not be sufficient. This is also explainable by the training during which the network was only exposed to candidates with a $p_T > 20\,\mathrm{GeV}$. In the FCAL the benefit of using a geometry-aware algorithm becomes clear as the legacy algorithm leads to higher rates for most p_T thresholds, while the addition of shower shapes in both regions expectedly reduces the rate further. The second row compares the true electron efficiencies ϵ at identical rates of $5\,\mathrm{kHz}$ each in both the EMEC/HEC region and the FCAL region. Expectedly, the neural network achieves the highest efficiency at the lowest transverse momentum where the cut-based shower shape approach is a close contender. In all cases the sparsity of signal events is clearly visible at high transverse momenta where statistical fluctuations become very large. The efficiency curve in the FCAL also again clearly highlights the challenge in the legacy sliding window algorithm which is purely based on η and ϕ geometry in the FCAL environment. A perfect algorithm would follow a step-function at the threshold of where a rate of $5\,\mathrm{kHz}$ was identified with a threshold as low as possible. The efficiency curves in the EMEC/HEC approach such a step-function to a closer degree than the curves in the FCAL region as the EMEC/HEC region follows a more regular structure of cell geometry (compared to cells of various sizes in the FCAL).

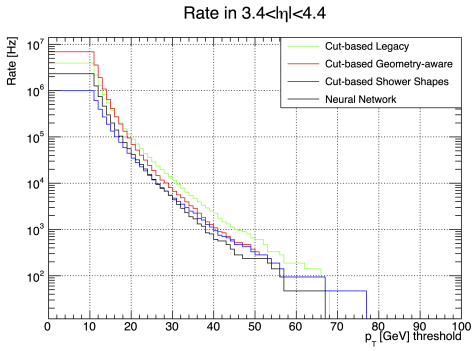
Finally, the last row compares the ROC curve[7] of the neural networks to the cut-based selections and also indicates which true positive and false positive rates are achieved by the selection of 0.9 on the network output. Generally, the best algorithms are desired to have high true positive rates and low false positive rates (i.e. the closer to the top left corner the better). The neural network outperforms all other algorithms, however, not necessarily by a significant margin. The relatively high false positive rates of the sliding window algorithms purely based on energy sums are clearly visible, while selections on shower shapes already drastically improve the performance. The performance of the neural network in the EMEC/HEC is expectedly better than in the FCAL, where electronic noise is higher [205] and cells are arranged more irregularly than in the EMEC/HEC region. This complements the observations made from the rate and efficiency curves.

After the comparison of the EMEC/HEC and FCAL fiducial regions, it is also useful to study the efficiency as a function of the pseudorapidity to highlight inefficient detector regions. This is done by calculating the efficiency at identical rates, in this case $10\,\mathrm{kHz}$, and adding $10\,\mathrm{GeV}$ onto the p_T threshold to be close to the plateau that most algorithms reach while reducing stark statistical fluctuations. The insights

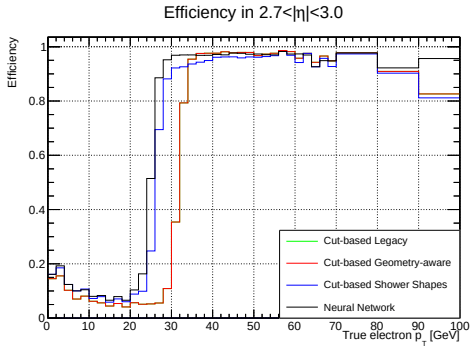
[7] Note that only the neural network performance is shown as a curve (the black point symbolises a selection of > 0.9 on the network output). All other algorithms are displayed as a single point only as they are constructed from fixed selections.



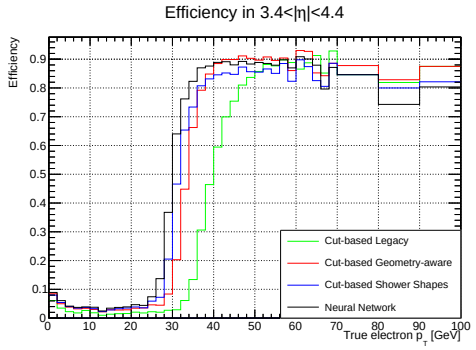
(a) Rates as a function of the p_T threshold in the EMEC/HEC.



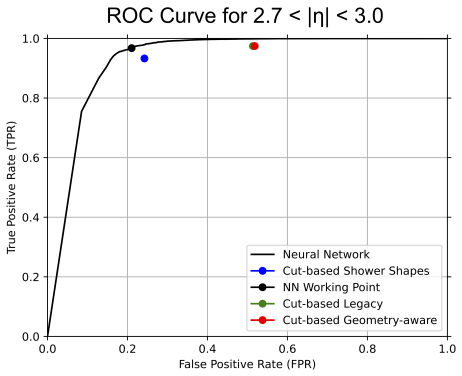
(b) Rates as a function of the p_T threshold in the FCAL.



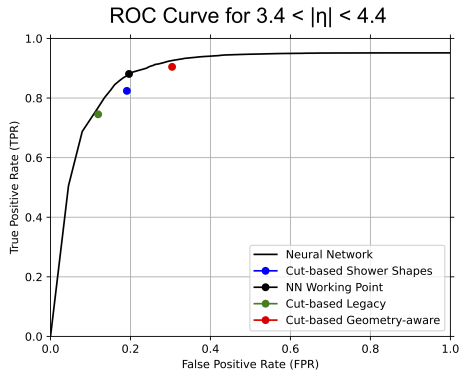
(c) Efficiencies as a function of the true p_T using a trigger threshold matched to a rate of $5\,\mathrm{kHz}$ in the EMEC/HEC.



(d) Efficiencies as a function of the true p_T using a trigger threshold matched to a rate of $5\,\mathrm{kHz}$ in the FCAL.



(e) True and false positive rates in the EMEC/HEC for a trigger threshold of $p_T > 20\,\mathrm{GeV}$.



(f) True and false positive rates in the FCAL for a trigger threshold of $p_T > 20\,\mathrm{GeV}$.

Fig. 11.8.: Comparisons of performance measures in the EMEC/HEC (left) and the FCAL (right) fiducial regions. Note that in the EMEC/HEC regions by definition the legacy (green) and geometry-aware (red) sliding window algorithms are identical so that only the red curve is visible.

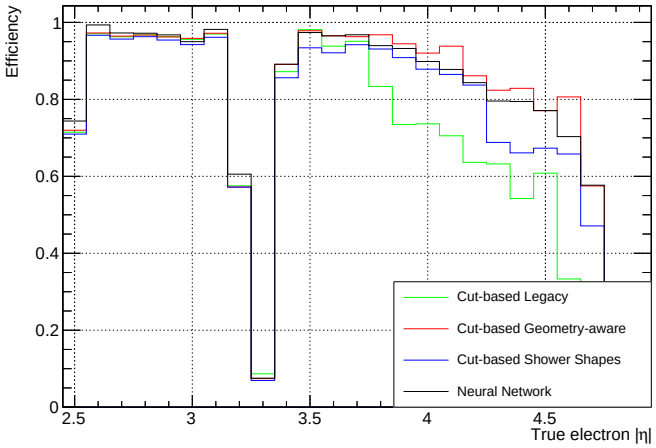
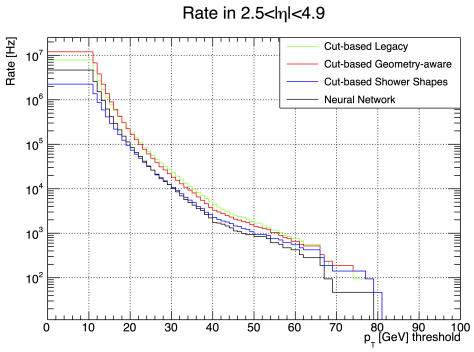


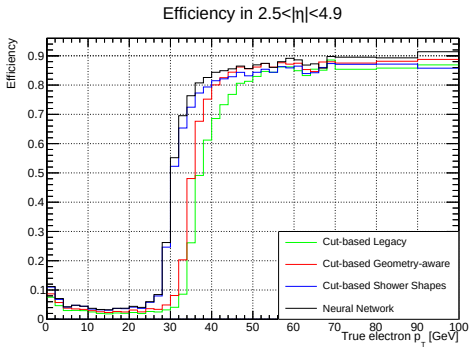
Fig. 11.9.: Efficiencies as a function of the true absolute pseudorapidity $|\eta|$ using a trigger threshold matched to a rate of $10\,\mathrm{kHz}$ in the plateau (p_T threshold $+10\,\mathrm{GeV}$).

that can be derived from this in figure 11.9 are aligned with the ones explained previously. In particular in the FCAL there appears to be an increase in efficiency when considering a $x \times y$ geometry compared to the legacy approach. The benefit of using shower shape variables also seems to be reduced at high pseudorapidities in the FCAL, in particular above $|\eta| > 4.3$, where cell sizes are smaller compared to the rest of the FCAL. Importantly, drops in efficiencies are expectedly observed at the high and low edges of the fFEX coverage, where no cell information has been available. Additionally, the challenging transition between the EMEC/HEC regions and the FCAL region causes a significant drop in efficiency. However, as this transition is also excluded from usage in most offline analyses this does not give rise to concern.

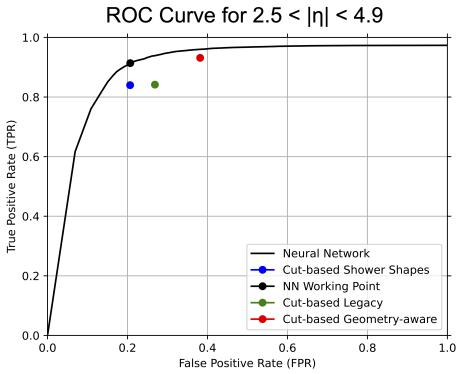
Finally, figure 11.10 depicts the expected rates and efficiencies at $10\,\mathrm{kHz}$ as well as the ROC curve for the full forward region of $|\eta| > 2.5$. The ranking in performance, both in efficiency and rates, between the individual algorithms does not change. The neural network outperforms the others in most parts, closely followed by the cut-based approach using shower shapes and the legacy algorithm exhibiting the weakest performance. The combined statistical power of the full forward region leads to more statistically stable performance evaluations at low rates and high efficiencies compared to the individual regions supporting the observations made in each region separately before. The ROC curve also highlights again the separation power of the neural network compared to other methods as it clearly outperforms those for all TPRs and FPRs.



(a) Rates as a function of the p_T threshold.



(b) Efficiencies as a function of the true p_T using a trigger threshold matched to a rate of $10\,\mathrm{kHz}$.



(c) True and false positive rates in the FCAL for a trigger threshold of $p_T > 20\,\mathrm{GeV}$.

Fig. 11.10.: Comparisons of performance measures in the full forward region.

11.3 Outlook

This chapter has shown the potential of sliding-window based algorithms used in the ATLAS forward region utilising different approaches to maximise signal and background separation. While these studies are statistically limited, there is a clear indication that the $x \times y$ geometry of the FCAL can be exploited by adapting sliding windows to this different type of geometry. Additionally, variables describing shower properties appear to provide a significant increase in separation power compared to simple energy sums used in legacy-like algorithms. Finally, using neural networks to enhance the selection of energy sums and shower shape variables seems to also improve algorithm performance. Due to the statistical limitations it is important to study the performance of each algorithm type once more simulated events are available to clarify whether each performance improvement is statistically significant and to utilise the additional statistical power to further tune algorithm parameters, such as the evaluation of whether to use one or two hadronic isolation variables. The influence of pileup on these algorithms as well as sophisticated noise-reduction mechanisms are additional aspects that are important to understand once a larger simulated sample size is available.

Another study performed by Layh [206] utilises cell energy information directly in a convolutional network using the YOLO [207] algorithm to reduce algorithmic inefficiencies of a sliding window-based approach and increase algorithm performance further still.

Crucially, in all cases it is important to consider limitations by hardware and firmware to be employed in the fFEX system, which will ultimately define the maximum complexity achievable by any algorithm to be deployed. Recent developments in FPGA hardware with dedicated modules to be used for neural networks [201] support the assumption of implementing complex multivariate methods in the fFEX trigger. This is a topic of ongoing study and is expected to be iterated until the deployment for Run 4 in ATLAS.

Finally, the inclusion of the fFEX module to trigger electron objects in the forward region is expected to be greatly beneficial to a measurement of the weak mixing angle as discussed in chapter 8. In particular, the ability to define trigger chains that include signatures of high-rapidity Z boson decays into an electron and a positron will contribute to a drastic reduction of statistical uncertainties of such a measurement. A planned integrated luminosity of more than $3000\,\mathrm{fb}^{-1}$ at the end of the HL-LHC [182] corresponds to a more than ten-fold reduction of statistical uncertainties compared to the ATLAS 8 TeV measurement (based on the integrated luminosity of Run 1), thus rendering it one of the smallest uncertainty contributions

of such a measurement assuming similar systematic uncertainties. In order to leverage this large amount of data it is crucial to efficiently trigger electron objects in particular in the very sensitive forward region given the significantly larger number of simultaneous collisions. As the tracking system will be extended up to $|\eta| = 4.0$, fFEX will provide the foundation to identify candidate seeds which can be refined by the additional tracking information. It will complement the trigger systems of the central regions and thus enable selecting high-rapidity dilepton topologies unprecedented to ATLAS.

Part VI

Conclusion

> *Not all those who wander are lost.*
>
> **— J. R. R. Tolkien**

In the introduction of this thesis Steven Weinberg was quoted to highlight the inherent unpredictability attached to fundamental research. By its nature it requires exploration, trial and error and patience. In this thesis these attributes are reflected in the first measurement of the full set of angular coefficients at $\sqrt{s} = 13\,\text{TeV}$ and the subsequent estimate of a measurement of the weak mixing angle to improve theoretical predictions and to shed light on experimental tensions.

The first measurement of the full set of angular coefficients at $\sqrt{s} = 13\,\text{TeV}$ has been presented differentially in the dilepton rapidity and transverse momentum. At the same time the differential unpolarised cross section of the Z/γ^* production was measured. The large ATLAS Run 2 dataset has enabled a high statistical accuracy, which can be improved even further in a measurement integrated over the rapidity range. Nonetheless, as a trade-off to the fine granularity in dilepton rapidity and transverse momentum, statistical uncertainties dominate over the systematic uncertainties. The latter are mainly caused by limitations in simulated events available as well as by contributions from energy/momentum scale and resolution effects and the electron identification in some regions of phase space. The extracted results of the electron and muon channels are compatible with each other within uncertainties in most regions, with few individual outliers from fluctuations. No systematic difference between the channels in the angular coefficients has been found, however, at low transverse momenta of the dilepton pair some deviations are observed which require closer inspection. The combined results compared to the prediction from POWHEGBOX + PYTHIA 8 at NLO in QCD support observations made in previous measurements, in particular the breaking of the Lam-Tung relation as

well as non-zero coefficients A_5 to A_7. Lastly, the high accuracy of the measurement of the unpolarised cross section with relative uncertainties ranging from $< 0.2\%$ at low rapidity and transverse momentum to approximately 6% at high rapidity enables more accurate predictions of the Z/γ^* transverse momentum for generators such as POWHEGBOX + PYTHIA 8.

The expected sensitivity of a measurement of the effective leptonic weak mixing angle from the angular coefficient A_4 using the electron and muon channels and comparable PDF sets to the previous measurements shows that an accuracy of $36 \cdot 10^{-5}$ can be achieved. Assuming the electron energy scale and resolution uncertainties can be improved and recent PDF sets reduce the related modelling uncertainty, an even higher precision will be reachable. Conservatively estimating a similar relative improvement of the precision of a measurement using the central-forward channel in addition to the central channels when compared to the previous ATLAS measurement at $\sqrt{s} = 8\,\mathrm{TeV}$, the expected precision surpasses the Tevatron combined results and becomes competitive to the LEP/SLD results, which are the most precise measurements to date.

In order to reach the highest precision possible in such measurements, in the final part of the thesis algorithms to identify electromagnetic objects with the fFEX module of the upgraded ATLAS trigger system for the High-Luminosity LHC have been developed and presented. The challenge of the ATLAS forward region in $|\eta| > 2.5$ with different geometric arrangements of calorimeter cells led to the development of algorithms utilising these geometries individually as well as sophisticated variables parametrising the shape of electromagnetic and hadronic showers. Neural networks in combination with these shower variables exhibit promising results when evaluated in terms of their efficiency and background rejection. These developments are the baseline for the continued evaluation of the best electromagnetic trigger algorithms taking into account limited resources on the hardware. Overall, the new fFEX system utilising such algorithms will contribute immensely to the statistical power of measurements of the weak mixing angle as it can capture the decay topology of high-rapidity Z/γ^* bosons when combined with central trigger systems.

All in all, the measurements and developments in the context of the neutral current Drell-Yan process presented in this thesis highlight its central role in electroweak physics. In particular the angular coefficients as gateways to both QCD production processes and the weak mixing angle prove to be a powerful tool to probe these processes to the highest precision. The results of this thesis can be used to benchmark theoretical predictions. In particular they motivate further study and understanding of a measurement of the weak mixing angle at ATLAS. With measurements building on top of the one presented in this thesis and together with the high statistical power of the data collected at the LHC and the HL-LHC in the future an unprecedented

precision will be achieved. This will be a central contribution to modern electroweak physics in particular within the context of the recent tensions observed in this sector. Such measurements are of explorative nature reaching into unknown regions of modern science. These wanderings do not mean particle physics is lost, but steadily on its way to new understanding.

Bibliography

[1] M. Chalmers. *Still seeking solutions*. In: *CERN Courier* (2021) (cit. on p. 1).

[2] ATLAS Collaboration. *Observation of a new particle in the search for the Standard Model Higgs boson with the ATLAS detector at the LHC*. In: *Phys. Lett. B* 716 (2012), pp. 1–29. arXiv: 1207.7214 [hep-ex] (cit. on pp. 1, 9, 20).

[3] CMS Collaboration. *Observation of a New Boson at a Mass of 125 GeV with the CMS Experiment at the LHC*. In: *Phys. Lett. B* 716 (2012), pp. 30–61. arXiv: 1207.7235 [hep-ex] (cit. on pp. 1, 9, 20).

[4] Y. Fukuda et al. *Evidence for oscillation of atmospheric neutrinos*. In: *Phys. Rev. Lett.* 81 (1998), pp. 1562–1567. arXiv: hep-ex/9807003 (cit. on pp. 1, 20).

[5] SNO Collaboration. *Direct evidence for neutrino flavor transformation from neutral current interactions in the Sudbury Neutrino Observatory*. In: *Phys. Rev. Lett.* 89 (2002), p. 011301. arXiv: nucl-ex/0204008 (cit. on pp. 1, 20).

[6] ALEPH, DELPHI, L3, OPAL, SLD, LEP Electroweak Working Group, SLD Electroweak Group, SLD Heavy Flavour Group. *Precision electroweak measurements on the Z resonance*. In: *Phys. Rept.* 427 (2006), pp. 257–454. arXiv: hep-ex/0509008 (cit. on pp. 2, 27, 28, 39, 42, 185, 194).

[7] D. Griffiths. *Introduction to elementary particles*. Wiley-VCH, 2008 (cit. on pp. 7, 21).

[8] M. E. Peskin and D. V. Schroeder. *An Introduction to quantum field theory*. Reading, USA: Addison-Wesley, 1995 (cit. on pp. 7, 15, 16).

[9] A. Kulesza. *Standard Model of particle physics*. Lecture at 53. Herbstschule für Hochenergiephysik, Maria Laach. 2022 (cit. on p. 7).

[10] S. L. Glashow. *Partial Symmetries of Weak Interactions*. In: *Nucl. Phys.* 22 (1961), pp. 579–588 (cit. on pp. 7, 16).

[11] S. Weinberg. *A Model of Leptons*. In: *Phys. Rev. Lett.* 19 (1967), pp. 1264–1266 (cit. on pp. 7, 16).

[12] A. Salam. *Weak and Electromagnetic Interactions*. In: *Conf. Proc. C* 680519 (1968), pp. 367–377 (cit. on pp. 7, 16).

[13] G. 't Hooft and M. J. G. Veltman. *Regularization and Renormalization of Gauge Fields*. In: *Nucl. Phys. B* 44 (1972), pp. 189–213 (cit. on p. 7).

[14] R. L. Workman et al. *Review of Particle Physics*. In: *PTEP* 2022 (2022), p. 083C01 (cit. on pp. 8, 10, 12, 39, 177, 219).

[15]K. Chilikin et al. *Experimental constraints on the spin and parity of the $Z(4430)^+$*. In: *Phys. Rev. D* 88.7 (2013), p. 074026. arXiv: 1306.4894 [hep-ex] (cit. on p. 9).

[16]LHCb Collaboration. *Observation of $J/\psi p$ Resonances Consistent with Pentaquark States in $\Lambda_b^0 \to J/\psi K^- p$ Decays*. In: *Phys. Rev. Lett.* 115 (2015), p. 072001. arXiv: 1507.03414 [hep-ex] (cit. on p. 9).

[17]F. Englert and R. Brout. *Broken Symmetry and the Mass of Gauge Vector Mesons*. In: *Phys. Rev. Lett.* 13 (1964). Ed. by J. C. Taylor, pp. 321–323 (cit. on pp. 9, 18).

[18]P. W. Higgs. *Broken symmetries, massless particles and gauge fields*. In: *Phys. Lett.* 12 (1964), pp. 132–133 (cit. on pp. 9, 18).

[19]P. W. Higgs. *Broken Symmetries and the Masses of Gauge Bosons*. In: *Phys. Rev. Lett.* 13 (1964). Ed. by J. C. Taylor, pp. 508–509 (cit. on pp. 9, 18).

[20]G. S. Guralnik, C. R. Hagen, and T. W. B. Kibble. *Global Conservation Laws and Massless Particles*. In: *Phys. Rev. Lett.* 13 (1964). Ed. by J. C. Taylor, pp. 585–587 (cit. on pp. 9, 18).

[21]P. W. Higgs. *Spontaneous Symmetry Breakdown without Massless Bosons*. In: *Phys. Rev.* 145 (1966), pp. 1156–1163 (cit. on pp. 9, 18).

[22]T. W. B. Kibble. *Symmetry breaking in non-Abelian gauge theories*. In: *Phys. Rev.* 155 (1967). Ed. by J. C. Taylor, pp. 1554–1561 (cit. on pp. 9, 18).

[23]P. A. M. Dirac. *The quantum theory of the emission and absorption of radiation*. In: *Proceedings of the Royal Society of London. Series A, Containing Papers of a Mathematical and Physical Character* 114.767 (1927), pp. 243–265 (cit. on pp. 11, 21).

[24]R. P. Feynman. *Space-time approach to nonrelativistic quantum mechanics*. In: *Rev. Mod. Phys.* 20 (1948), pp. 367–387 (cit. on p. 11).

[25]E. Fermi. *Quantum Theory of Radiation*. In: *Rev. Mod. Phys.* 4.1 (1932), pp. 87–132 (cit. on p. 11).

[26]S. Tomonaga. *On a relativistically invariant formulation of the quantum theory of wave fields*. In: *Prog. Theor. Phys.* 1 (1946), pp. 27–42 (cit. on p. 11).

[27]J. S. Schwinger. *On Quantum electrodynamics and the magnetic moment of the electron*. In: *Phys. Rev.* 73 (1948), pp. 416–417 (cit. on p. 11).

[28]E. Noether. *Invariante Variationsprobleme*. ger. In: *Nachrichten von der Gesellschaft der Wissenschaften zu Göttingen, Mathematisch-Physikalische Klasse* 1918 (1918), pp. 235–257 (cit. on p. 12).

[29]R. P. Feynman, R. B. Leighton, and M. Sands. *The Feynman lectures on physics; New millennium ed.* Originally published 1963-1965. New York, NY: Basic Books, 2010 (cit. on p. 13).

[30]G. 't Hooft. *Dimensional regularization and the renormalization group*. In: *Nuclear Physics B* 61 (1973), pp. 455–468 (cit. on p. 14).

[31]S. Weinberg. *New Approach to the Renormalization Group*. In: *Phys. Rev. D* 8 (10 1973), pp. 3497–3509 (cit. on p. 14).

[32]M. D. Schwartz. *Quantum Field Theory and the Standard Model*. Cambridge University Press, Mar. 2014 (cit. on p. 14).

[33]C.-N. Yang and R. L. Mills. *Conservation of Isotopic Spin and Isotopic Gauge Invariance*. In: *Phys. Rev.* 96 (1954). Ed. by J.-P. Hsu and D. Fine, pp. 191–195 (cit. on pp. 14, 15).

[34]H. Fritzsch, M. Gell-Mann, and H. Leutwyler. *Advantages of the Color Octet Gluon Picture*. In: *Phys. Lett. B* 47 (1973), pp. 365–368 (cit. on p. 14).

[35]M. Gell-Mann. *A Schematic Model of Baryons and Mesons*. In: *Phys. Lett.* 8 (1964), pp. 214–215 (cit. on p. 14).

[36]Y. Ne'eman. *Derivation of strong interactions from a gauge invariance*. In: *Nucl. Phys.* 26 (1961). Ed. by R. Ruffini and Y. Verbin, pp. 222–229 (cit. on p. 14).

[37]R. Brock et al. *Handbook of perturbative QCD: Version 1.0*. In: *Rev. Mod. Phys.* 67 (1995), pp. 157–248 (cit. on p. 15).

[38]P. Skands. *Introduction to QCD*. In: *Theoretical Advanced Study Institute in Elementary Particle Physics: Searching for New Physics at Small and Large Scales*. 2013, pp. 341–420. arXiv: 1207.2389 [hep-ph] (cit. on p. 15).

[39]L. D. Faddeev and V. N. Popov. *Feynman Diagrams for the Yang-Mills Field*. In: *Phys. Lett. B* 25 (1967). Ed. by J.-P. Hsu and D. Fine, pp. 29–30 (cit. on p. 15).

[40]G. Dissertori. *The Determination of the Strong Coupling Constant*. In: *Adv. Ser. Direct. High Energy Phys.* 26 (2016), pp. 113–128. arXiv: 1506.05407 [hep-ex] (cit. on p. 15).

[41]S. Dawson. *Introduction to electroweak symmetry breaking*. In: *ICTP Summer School in High-Energy Physics and Cosmology*. June 1998, pp. 1–83. arXiv: hep-ph/9901280 (cit. on p. 16).

[42]C. Hays. *Lecture: Electroweak Physics*. 2016 (cit. on p. 16).

[43]A. Pich. *The Standard model of electroweak interactions*. In: *2006 European School of High-Energy Physics*. 2007, pp. 1–49. arXiv: 0705.4264 [hep-ph] (cit. on p. 16).

[44]H. Yukawa. *Quantum Theory of Nonlocal Fields. 1. Free Fields*. In: *Phys. Rev.* 77 (1950), pp. 219–226 (cit. on p. 19).

[45]J. Oort. *Some Problems Concerning the Structure and Dynamics of the Galactic System and the Elliptical Nebulae NGC 3115 and 4494*. In: *The Astrophysical Journal* 91 (Apr. 1940), p. 273 (cit. on p. 20).

[46]E. Hubble. *A Relation between Distance and Radial Velocity among Extra-Galactic Nebulae*. In: *Proceedings of the National Academy of Science* 15.3 (Mar. 1929), pp. 168–173 (cit. on p. 20).

[47]E. Fermi. *Nuclear physics: a course given by Enrico Fermi at the University of Chicago*. University of Chicago Press, 1950 (cit. on p. 21).

[48]J. D. Bjorken. *Asymptotic Sum Rules at Infinite Momentum*. In: *Phys. Rev.* 179 (1969), pp. 1547–1553 (cit. on p. 22).

[49]J. M. Campbell, J. W. Huston, and W. J. Stirling. *Hard Interactions of Quarks and Gluons: A Primer for LHC Physics*. In: *Rept. Prog. Phys.* 70 (2007), p. 89. arXiv: hep-ph/0611148 (cit. on p. 23).

[50]D. E. Soper. *Parton distribution functions*. In: *Nucl. Phys. B Proc. Suppl.* 53 (1997). Ed. by C. Bernard, M. Golterman, M. Ogilvie, and J. Potvin, pp. 69–80. arXiv: hep-lat/9609018 (cit. on p. 23).

[51]J. C. Collins, D. E. Soper, and G. F. Sterman. *Factorization of Hard Processes in QCD*. In: *Adv. Ser. Direct. High Energy Phys.* 5 (1989), pp. 1–91. arXiv: hep-ph/0409313 (cit. on p. 23).

[52]S. Dulat, T.-J. Hou, J. Gao, et al. *New parton distribution functions from a global analysis of quantum chromodynamics*. In: *Phys. Rev. D* 93.3 (2016), p. 033006. arXiv: 1506.07443 [hep-ph] (cit. on pp. 23, 24, 178).

[53]H. L. Lai, J. Botts, J. Huston, et al. *Global QCD analysis and the CTEQ parton distributions*. In: *Phys. Rev. D* 51 (1995), pp. 4763–4782. arXiv: hep-ph/9410404 (cit. on p. 24).

[54]L. A. Harland-Lang, A. D. Martin, P. Motylinski, and R. S. Thorne. *Parton distributions in the LHC era: MMHT 2014 PDFs*. In: *The European Physical Journal C* 75.5 (2015) (cit. on pp. 24, 86).

[55]L. Del Debbio, S. Forte, J. I. Latorre, A. Piccione, and J. Rojo. *Unbiased determination of the proton structure function F(2)**p with faithful uncertainty estimation*. In: *JHEP* 03 (2005), p. 080. arXiv: hep-ph/0501067 (cit. on p. 24).

[56]F. D. Aaron et al. *Combined Measurement and QCD Analysis of the Inclusive e+- p Scattering Cross Sections at HERA*. In: *JHEP* 01 (2010), p. 109. arXiv: 0911.0884 [hep-ex] (cit. on p. 24).

[57]Y. L. Dokshitzer. *Calculation of the Structure Functions for Deep Inelastic Scattering and e+ e- Annihilation by Perturbation Theory in Quantum Chromodynamics.* In: *Sov. Phys. JETP* 46 (1977), pp. 641–653 (cit. on p. 24).

[58]G. Altarelli and G. Parisi. *Asymptotic Freedom in Parton Language*. In: *Nucl. Phys. B* 126 (1977), pp. 298–318 (cit. on p. 24).

[59]L. N. Lipatov. *The parton model and perturbation theory*. In: *Yad. Fiz.* 20 (1974), pp. 181–198 (cit. on p. 24).

[60]V. N. Gribov and L. N. Lipatov. *Deep inelastic e p scattering in perturbation theory*. In: *Sov. J. Nucl. Phys.* 15 (1972), pp. 438–450 (cit. on p. 24).

[61]M. Rieger. *Search for $t\bar{t}H$ Production in the $H \to b\bar{b}$ Decay Channel*. Springer Cham (cit. on p. 26).

[62]S. D. Drell and T.-M. Yan. *Massive Lepton Pair Production in Hadron-Hadron Collisions at High-Energies*. In: *Phys. Rev. Lett.* 25 (1970). [Erratum: Phys.Rev.Lett. 25, 902 (1970)], pp. 316–320 (cit. on p. 25).

[63]P. Reinertsen. *Precise measurement of the weak mixing angle from leptonic polarization asymmetries at the SLD experiment*. In: *Nuclear Physics B - Proceedings Supplements* 76.1 (1999). Tau Lepton Physics, pp. 45–54 (cit. on p. 28).

[64]T. Aaltonen et al. *High-precision measurement of the W boson mass with the CDF II detector*. In: *Science* 376.6589 (2022), pp. 170–176 (cit. on p. 28).

[65]ATLAS Collaboration. *Measurement of the effective leptonic weak mixing angle using electron and muon pairs from Z-boson decay in the ATLAS experiment at $\sqrt{s} = 8$ TeV*. Tech. rep. Geneva: CERN, 2018 (cit. on pp. 28, 38, 40, 41, 175, 176, 186, 187, 194).

[66]E. Mirkes. *Angular decay distribution of leptons from W bosons at NLO in hadronic collisions*. In: *Nucl. Phys. B* 387 (1992), pp. 3–85 (cit. on pp. 29, 32, 33).

[67]E. Mirkes and J. Ohnemus. *W and Z polarization effects in hadronic collisions*. In: *Phys. Rev. D* 50 (9 1994), pp. 5692–5703 (cit. on pp. 29, 32, 34).

[68]ATLAS Collaboration. *Measurement of the angular coefficients in Z-boson events using electron and muon pairs from data taken at $\sqrt{s} = 8$ TeV with the ATLAS detector*. In: *Journal of High Energy Physics* 2016.8 (2016) (cit. on pp. 29, 31, 32, 36, 97, 107, 129–131, 139, 165, 166).

[69]J. C. Collins and D. E. Soper. *Angular Distribution of Dileptons in High-Energy Hadron Collisions*. In: *Phys. Rev. D* 16 (1977), p. 2219 (cit. on p. 30).

[70]J.-C. Peng, W.-C. Chang, R. E. McClellan, and O. Teryaev. *Interpretation of angular distributions of Z-boson production at colliders*. In: *Physics Letters B* 758 (2016), pp. 384–388 (cit. on pp. 31, 34–36, 164, 165).

[71]E. Richter-Was and Z. Was. *Separating electroweak and strong interactions in Drell–Yan processes at LHC: leptons angular distributions and reference frames*. In: *Eur. Phys. J. C* 76.8 (2016), p. 473. arXiv: 1605.05450 [hep-ph] (cit. on p. 30).

[72]ATLAS Collaboration. *Probing QCD dynamics with measurement of polarisation angular coefficients in $Z \to ll$ process with ATLAS detector*. Tech. rep. Geneva: CERN, 2014 (cit. on pp. 32, 35, 131, 132, 139, 140).

[73]C. S. Lam and W.-K. Tung. *Systematic approach to inclusive lepton pair production in hadronic collisions*. In: *Phys. Rev. D* 18 (7 1978), pp. 2447–2461 (cit. on p. 35).

[74]C. S. Lam and W.-K. Tung. *Parton-model relation without quantum-chromodynamic modifications in lepton pair production*. In: *Phys. Rev. D* 21 (9 1980), pp. 2712–2715 (cit. on p. 35).

[75]A. Vallier. *Private communication*. 2023 (cit. on p. 37).

[76]S. Camarda, M. Boonekamp, G. Bozzi, et al. *DYTurbo: fast predictions for Drell–Yan processes*. In: *The European Physical Journal C* 80.3 (2020) (cit. on pp. 37, 175, 176).

[77]S. Falciano et al. *Angular Distributions of Muon Pairs Produced by 194-GeV/c Negative Pions*. In: *Z. Phys. C* 31 (1986), p. 513 (cit. on p. 36).

[78]M. Guanziroli et al. *Angular Distributions of Muon Pairs Produced by Negative Pions on Deuterium and Tungsten*. In: *Z. Phys. C* 37 (1988), p. 545 (cit. on p. 36).

[79]J. S. Conway et al. *Experimental Study of Muon Pairs Produced by 252-GeV Pions on Tungsten*. In: *Phys. Rev. D* 39 (1989), pp. 92–122 (cit. on p. 36).

[80]J. G. Heinrich et al. *Higher twist effects in the reaction pi- N —> mu+ mu- X at 253-GeV/c*. In: *Phys. Rev. D* 44 (1991), pp. 1909–1932 (cit. on p. 36).

[81]CMS Collaboration. *Angular coefficients of Z bosons produced in pp collisions at $\sqrt{s}$ = 8 TeV and decaying to $\mu^+\mu^-$ as a function of transverse momentum and rapidity*. In: *Phys. Lett. B* 750 (2015), pp. 154–175. arXiv: 1504.03512 [hep-ex] (cit. on p. 36).

[82]LHCb Collaboration. *First Measurement of the $Z \to \mu^+\mu^-$ Angular Coefficients in the Forward Region of pp Collisions at $\sqrt{s} = 13$ TeV*. In: *Phys. Rev. Lett.* 129 (9 2022), p. 091801 (cit. on p. 36).

[83]J. Erler and M. J. Ramsey-Musolf. *The Weak mixing angle at low energies*. In: *Phys. Rev. D* 72 (2005), p. 073003. arXiv: hep-ph/0409169 (cit. on pp. 40, 42).

[84]CMS Collaboration. *Measurement of the weak mixing angle using the forward-backward asymmetry of Drell-Yan events in pp collisions at 8 TeV*. In: *Eur. Phys. J. C* 78.9 (2018), p. 701. arXiv: 1806.00863 [hep-ex] (cit. on pp. 40, 41).

[85]LHCb Collaboration. *Measurement of the forward-backward asymmetry in $Z/\gamma^* \to \mu^+\mu^-$ decays and determination of the effective weak mixing angle*. In: *JHEP* 11 (2015), p. 190. arXiv: 1509.07645 [hep-ex] (cit. on p. 40).

[86]CDF Collaboration, D0 Collaboration. *Tevatron Run II combination of the effective leptonic electroweak mixing angle*. In: *Physical Review D* 97.11 (2018) (cit. on pp. 42, 193).

[87]N. Berger et al. *Measuring the weak mixing angle with the P2 experiment at MESA*. In: *J. Univ. Sci. Tech. China* 46.6 (2016), pp. 481–487. arXiv: 1511.03934 [physics.ins-det] (cit. on pp. 42, 43).

[88]C. S. Wood, S. C. Bennett, D. Cho, et al. *Measurement of parity nonconservation and an anapole moment in cesium*. In: *Science* 275 (1997), pp. 1759–1763 (cit. on p. 42).

[89]P. L. Anthony et al. *Precision measurement of the weak mixing angle in Moller scattering*. In: *Phys. Rev. Lett.* 95 (2005), p. 081601. arXiv: hep-ex/0504049 (cit. on p. 42).

[90]D. Androic et al. *First Determination of the Weak Charge of the Proton*. In: *Phys. Rev. Lett.* 111.14 (2013), p. 141803. arXiv: 1307.5275 [nucl-ex] (cit. on p. 42).

[91]A. Aktas et al. *A Determination of electroweak parameters at HERA*. In: *Phys. Lett. B* 632 (2006), pp. 35–42. arXiv: hep-ex/0507080 (cit. on p. 42).

[92]G. P. Zeller et al. *A Precise Determination of Electroweak Parameters in Neutrino Nucleon Scattering*. In: *Phys. Rev. Lett.* 88 (2002). [Erratum: Phys.Rev.Lett. 90, 239902 (2003)], p. 091802. arXiv: hep-ex/0110059 (cit. on p. 42).

[93]J. Benesch et al. *The MOLLER Experiment: An Ultra-Precise Measurement of the Weak Mixing Angle Using M\oller Scattering*. In: (Nov. 2014). arXiv: 1411.4088 [nucl-ex] (cit. on p. 42).

[94]J. P. Chen, H. Gao, T. K. Hemmick, Z. E. Meziani, and P. A. Souder. *A White Paper on SoLID (Solenoidal Large Intensity Device)*. In: (Sept. 2014). arXiv: 1409.7741 [nucl-ex] (cit. on p. 42).

[95]D. Becker et al. *The P2 experiment*. In: *Eur. Phys. J. A* 54.11 (2018), p. 208. arXiv: 1802.04759 [nucl-ex] (cit. on p. 42).

[96]ATLAS Collaboration. *The ATLAS Experiment at the CERN Large Hadron Collider*. In: *Journal of Instrumentation* 3.08 (2008), S08003 (cit. on pp. 45, 47, 48, 50–52, 54, 57, 210).

[97]O. S. Brüning, P. Collier, P Lebrun, et al. *LHC Design Report*. CERN Yellow Reports: Monographs. Geneva: CERN, 2004 (cit. on pp. 45, 47).

[98]ATLAS Collaboration. *Luminosity Run 2 Public Results*. URL: https://twiki.cern.ch/twiki/bin/view/AtlasPublic/LuminosityPublicResultsRun2 (visited on Apr. 1, 2023) (cit. on p. 46).

[99]J. Haffner. *The CERN accelerator complex. Complexe des accelerateurs du CERN*. In: (2013). General Photo (cit. on p. 46).

[100]J. T. Boyd. *LHC Run-2 and future prospects*. In: *CERN Yellow Rep. School Proc.* 5 (2022). Ed. by C. Duhr and M. Mulders, p. 247. arXiv: 2001.04370 [hep-ex] (cit. on pp. 46, 47).

[101]CMS Collaboration. *The CMS Experiment at the CERN LHC*. In: *JINST* 3 (2008), S08004 (cit. on p. 47).

[102]LHCb Collaboration. *The LHCb Detector at the LHC*. In: *JINST* 3 (2008), S08005 (cit. on p. 47).

[103]ALICE Collaboration. *The ALICE experiment at the CERN LHC*. In: *JINST* 3 (2008), S08002 (cit. on p. 47).

[104]ATLAS Collaboration. *Reconstruction of primary vertices at the ATLAS experiment in Run 1 proton–proton collisions at the LHC*. In: *Eur. Phys. J. C* 77.5 (2017), p. 332. arXiv: 1611.10235 [physics.ins-det] (cit. on p. 47).

[105]J. Pequenao. *Computer generated image of the whole ATLAS detector*. 2008 (cit. on p. 48).

[106]I. Neutelings. *CMS coordinate system*. 2017. URL: https://tikz.net/axis3d_cms/ (visited on Mar. 30, 2023) (cit. on p. 49).

[107]ATLAS Collaboration. *ATLAS inner detector: Technical Design Report, 1*. Technical design report. ATLAS. Geneva: CERN, 1997 (cit. on pp. 50–52).

[108]ATLAS Collaboration. *Operation and performance of the ATLAS semiconductor tracker*. In: *JINST* 9 (2014), P08009. arXiv: 1404.7473 [hep-ex] (cit. on pp. 50, 52).

[109]J. Pequenao. *Computer generated image of the ATLAS inner detector*. 2008 (cit. on p. 51).

[110]ATLAS Collaboration. *ATLAS Insertable B-Layer Technical Design Report*. Tech. rep. 2010 (cit. on p. 50).

[111]J. Pequenao. *Computer generated image of the ATLAS calorimeter*. 2008 (cit. on p. 53).

[112]ATLAS Collaboration. *ATLAS liquid-argon calorimeter: Technical Design Report*. Technical design report. ATLAS. Geneva: CERN, 1996 (cit. on pp. 53, 55).

[113]C. W. Fabjan and F Gianotti. *Calorimetry for Particle Physics*. In: *Rev. Mod. Phys.* 75 (2003), pp. 1243–1286 (cit. on pp. 53, 55).

[114]Z. Meng. *Performance of the ATLAS liquid argon calorimeter*. In: *Physics at the LHC 2010*. Dec. 2010, pp. 406–408 (cit. on pp. 54, 55).

[115]ATLAS Collaboration. *ATLAS tile calorimeter: Technical Design Report*. Technical design report. ATLAS. Geneva: CERN, 1996 (cit. on p. 55).

[116]B. Dowler, J. Pinfold, J. Soukup, et al. *Performance of the ATLAS hadronic end-cap calorimeter in beam tests*. In: *Nuclear Instruments and Methods in Physics Research Section A: Accelerators, Spectrometers, Detectors and Associated Equipment* 482.1 (2002), pp. 94–124 (cit. on p. 56).

[117]T. Zakareishvili. *Study of energy response and resolution of the ATLAS tile calorimeter to hadrons of energies from 16 to 30 GeV*. In: (2020) (cit. on p. 56).

[118]ATLAS Collaboration. *ATLAS barrel toroid: Technical Design Report*. Technical design report. ATLAS. Geneva: CERN, 1997 (cit. on p. 56).

[119]ATLAS Collaboration. *Muon reconstruction and identification efficiency in ATLAS using the full Run 2 pp collision data set at $\sqrt{s} = 13$ TeV*. In: *Eur. Phys. J. C* 81.7 (2021), p. 578. arXiv: 2012.00578 [hep-ex] (cit. on pp. 57, 68, 69).

[120]ATLAS Collaboration. *Luminosity determination in pp collisions at $\sqrt{s}$ = 8 TeV using the ATLAS detector at the LHC*. In: *Eur. Phys. J. C* 76.12 (2016), p. 653. arXiv: 1608.03953 [hep-ex] (cit. on p. 58).

[121]V. Cindro et al. *The ATLAS beam conditions monitor*. In: *JINST* 3 (2008), P02004 (cit. on p. 58).

[122]ATLAS Collaboration. *Luminosity determination in pp collisions at $\sqrt{s} = 13$ TeV using the ATLAS detector at the LHC*. In: (Dec. 2022). arXiv: 2212.09379 [hep-ex] (cit. on pp. 58, 104).

[123]ATLAS Collaboration. *Operation of the ATLAS trigger system in Run 2*. In: *JINST* 15.10 (2020), P10004. arXiv: 2007.12539 [physics.ins-det] (cit. on pp. 58, 59).

[124]ATLAS Collaboration. *ATLAS level-1 trigger: Technical Design Report*. Technical design report. ATLAS. Geneva: CERN, 1998 (cit. on p. 58).

[125]ATLAS Collaboration. *ATLAS high-level trigger, data-acquisition and controls: Technical Design Report*. Technical design report. ATLAS. Geneva: CERN, 2003 (cit. on p. 58).

[126]ATLAS Collaboration. *Athena*. Version 21.0.127. May 2021 (cit. on pp. 59, 80, 87, 215).

[127]G. Barrand, I. Belyaev, P. Binko, et al. *GAUDI: The software architecture and framework for building LHCb data processing applications*. In: (2000) (cit. on p. 59).

[128]ATLAS Collaboration. *Schematic of the ATLAS Trigger and Data Acquisition system in Run 2 with specific focus given to the components of the L1 Trigger system*. https://twiki.cern.ch/twiki/pub/AtlasPublic/ApprovedPlotsDAQ/tdaq-run2-schematic2017.png. 2017 (cit. on p. 60).

[129]I. Bird, P. Buncic, F. Carminati, et al. *Update of the Computing Models of the WLCG and the LHC Experiments*. Tech. rep. 2014 (cit. on pp. 59, 61).

[130]R. Brun, F. Rademakers, and S. Panacek. *ROOT, an object oriented data analysis framework*. In: (2000) (cit. on p. 61).

[131]J. Pequenao and P. Schaffner. *How ATLAS detects particles: diagram of particle paths in the detector*. 2013 (cit. on p. 62).

[132]ATLAS Collaboration. *ATLAS b-jet identification performance and efficiency measurement with $t\bar{t}$ events in pp collisions at $\sqrt{s} = 13$ TeV*. In: *Eur. Phys. J. C* 79.11 (2019), p. 970. arXiv: 1907.05120 [hep-ex] (cit. on p. 63).

[133]T. G. Cornelissen, M. Elsing, I. Gavrilenko, et al. *The global χ^2 track fitter in ATLAS*. In: *J. Phys.: Conf. Ser.* 119 (2008), p. 032013 (cit. on p. 64).

[134]K. Grimm, S. Boutle, D. Casper, et al. *Primary vertex reconstruction at the ATLAS experiment*. Tech. rep. 4. Geneva: CERN, 2017 (cit. on p. 64).

[135]ATLAS Collaboration. *Electron and photon energy calibration with the ATLAS detector using 2015-2016 LHC proton-proton collision data*. In: *Journal of Instrumentation* 14.03 (2019), P03017 (cit. on pp. 64, 105).

[136]ATLAS Collaboration. *Electron reconstruction and identification in the ATLAS experiment using the 2015 and 2016 LHC proton-proton collision data at $\sqrt{s}$ = 13 TeV*. In: *Eur. Phys. J. C* 79.8 (2019), p. 639. arXiv: 1902.04655 [physics.ins-det] (cit. on pp. 64–66, 224).

[137]ATLAS Collaboration. *Muon reconstruction performance of the ATLAS detector in proton–proton collision data at $\sqrt{s}$ =13 TeV*. In: *Eur. Phys. J. C* 76.5 (2016), p. 292. arXiv: 1603.05598 [hep-ex] (cit. on pp. 67–69, 106).

[138]G. Cowan. *Statistical data analysis*. Oxford University Press, USA, 1998 (cit. on pp. 71, 140, 141).

[139]J. von Neumann. *Various techniques used in connection with random digits.* In: *National Bureau of Standards*. Applied Math Series 12 (1951), pp. 36–38 (cit. on p. 71).

[140]S. Camarda, L. Cieri, and G. Ferrera. *Drell–Yan lepton-pair production: qT resummation at N3LL accuracy and fiducial cross sections at N3LO*. In: *Phys. Rev. D* 104.11 (2021), p. L111503. arXiv: 2103.04974 [hep-ph] (cit. on p. 72).

[141]C. Duhr, F. Dulat, and B. Mistlberger. *Charged current Drell-Yan production at N^3LO*. In: *JHEP* 11 (2020), p. 143. arXiv: 2007.13313 [hep-ph] (cit. on p. 72).

[142]C. Duhr and B. Mistlberger. *Lepton-pair production at hadron colliders at N^3LO in QCD*. In: *JHEP* 03 (2022), p. 116. arXiv: 2111.10379 [hep-ph] (cit. on p. 72).

[143]J. Alwall, A. Ballestrero, P. Bartalini, et al. *A standard format for Les Houches Event Files*. In: *Computer Physics Communications* 176.4 (2007), pp. 300–304 (cit. on p. 73).

[144]T. Sjöstrand, S. Mrenna, and P. Skands. *A brief introduction to PYTHIA 8.1*. In: *Computer Physics Communications* 178.11 (2008), pp. 852–867 (cit. on pp. 73, 84, 216).

[145]S. Alioli, P. Nason, C. Oleari, and E. Re. *A general framework for implementing NLO calculations in shower Monte Carlo programs: the POWHEG BOX*. In: *JHEP* 06 (2010), p. 043. arXiv: 1002.2581 [hep-ph] (cit. on pp. 73, 84, 216).

[146]D. J. Lange. *The EvtGen particle decay simulation package*. In: *Nucl. Instrum. Meth. A* 462 (2001). Ed. by S. Erhan, P. Schlein, and Y. Rozen, pp. 152–155 (cit. on pp. 73, 84).

[147]E. Barberio and Z. Was. *PHOTOS: A Universal Monte Carlo for QED radiative corrections. Version 2.0*. In: *Comput. Phys. Commun.* 79 (1994), pp. 291–308 (cit. on pp. 74, 84).

[148]S. P. Baranov, O. Duenger, H. Shooshtari, and J. A. M. Vermaseren. *LPAIR: A generator for lepton pair production*. In: *Workshop on Physics at HERA*. 1991 (cit. on p. 74).

[149]M. Bähr, S. Gieseke, M. A. Gigg, et al. *Herwig++ physics and manual*. In: *The European Physical Journal C* 58.4 (2008), pp. 639–707 (cit. on p. 74).

[150]S. Agostinelli et al. *Geant4 - a simulation toolkit*. In: *Nuclear Instruments and Methods in Physics Research Section A: Accelerators, Spectrometers, Detectors and Associated Equipment* 506.3 (2003), pp. 250–303 (cit. on p. 74).

[151]J. McFayden. *ATLAS MC generation - Integration into software and production*. 2016 (cit. on p. 74).

[152]J. Catmore. *The ATLAS data processing chain: from collisions to papers*. 2016 (cit. on p. 74).

[153]Z. Marshall and the ATLAS Collaboration. *Simulation of Pile-up in the ATLAS Experiment*. In: *Journal of Physics: Conference Series* 513.2 (2014), p. 022024 (cit. on p. 74).

[154]H. Kolanoski and N. Wermes. *Track reconstruction and momentum measurement*. In: *Particle Detectors: Fundamentals and Applications*. Oxford University Press, June 2020 (cit. on p. 76).

[155]ATLAS Collaboration. *Studies of the muon momentum calibration and performance of the ATLAS detector with pp collisions at $\sqrt{s}$=13 TeV*. 2022. arXiv: 2212.07338 [hep-ex] (cit. on p. 76).

[156]ATLAS ZAi Analysis Group. *ntuplecode_13TeV*. URL: https://gitlab.cern.ch/aiteam/ntuplecode_13TeV (cit. on p. 80).

[157]ATLAS ZAi Analysis Group. *AiDY*. URL: https://gitlab.cern.ch/aiteam/aidy (cit. on pp. 80, 129).

[158]A. Armbruster. *Faster Than Light (FTL) Fitting Framework*. Internal Gitlab Repository (cit. on pp. 81, 140, 180).

[159]ATLAS Collaboration. *Total Integrated Luminosity and Data Quality in 2015-2018*. 2019. URL: https://twiki.cern.ch/twiki/bin/view/AtlasPublic/LuminosityPublicResultsRun2#Online_Luminosity_Summary_Plots (visited on Mar. 30, 2023) (cit. on p. 84).

[160]H.-L. Lai, M. Guzzi, J. Huston, et al. *New parton distributions for collider physics*. In: *Phys. Rev. D* 82 (7 2010), p. 074024 (cit. on pp. 84, 86).

[161]ATLAS Collaboration. *Example ATLAS tunes of Pythia8, Pythia6 and Powheg to an observable sensitive to Z boson transverse momentum*. Tech. rep. Geneva: CERN, 2013 (cit. on p. 84).

[162]J. Pumplin, D. R. Stump, J. Huston, et al. *New Generation of Parton Distributions with Uncertainties from Global QCD Analysis*. In: *Journal of High Energy Physics* 2002.07 (2002), p. 012 (cit. on p. 84).

[163]A. Hoecker. *Physics at the LHC Run-2 and Beyond. Physics at the LHC Run-2 and Beyond*. In: (2017), pp. 153–212. arXiv: 1611.07864 (cit. on p. 85).

[164]F. Déliot and P. V. Mulders. *Top quark physics at the LHC*. In: *Comptes Rendus Physique* 21.1 (2020), pp. 45–60 (cit. on p. 85).

[165]A. V. Manohar, P. Nason, G. P. Salam, and G. Zanderighi. *The photon content of the proton*. In: *Journal of High Energy Physics* 2017.12 (2017) (cit. on p. 86).

[166]R. D. Ball, V. Bertone, S. Carrazza, et al. *Parton distributions with LHC data*. In: *Nuclear Physics B* 867.2 (2013), pp. 244–289 (cit. on p. 86).

[167]R. D. Ball, V. Bertone, S. Carrazza, et al. *Parton distributions with QED corrections*. In: *Nuclear Physics B* 877.2 (2013), pp. 290–320 (cit. on p. 86).

[168]A. Buckley, J. Ferrando, S. Lloyd, et al. *LHAPDF6: parton density access in the LHC precision era*. In: *The European Physical Journal C* 75.3 (2015) (cit. on pp. 107, 144, 179).

[169]ATLAS Collaboration. *Measurements of differential Z boson production cross sections in proton-proton collisions at $\sqrt{s} = 13$ TeV*. In: *Journal of High Energy Physics* 2019.12 (2019) (cit. on pp. 110, 113).

[170]M. Kohl. *Measurement of the Angular coefficients in Z-boson production at $\sqrt{s} = 13$ TeV with the ATLAS experiment*. 2019 (cit. on pp. 113, 118).

[171]J. Nocedal and S. Wright. *Numerical optimization*. 2. ed. Springer series in operations research and financial engineering. New York, NY: Springer, 2006 (cit. on pp. 140, 180).

[172]S. S. Wilks. *The Large-Sample Distribution of the Likelihood Ratio for Testing Composite Hypotheses*. In: *The Annals of Mathematical Statistics* 9.1 (1938), pp. 60 –62 (cit. on p. 140).

[173]I. Asimov. *Franchise (short story)*. In: *If: Worlds of Science Fiction* (1955) (cit. on p. 140).

[174]G. Cowan, K. Cranmer, E. Gross, and O. Vitells. *Asymptotic formulae for likelihood-based tests of new physics*. In: *The European Physical Journal C* 71.2 (2011) (cit. on p. 140).

[175]K. Pearson. *X. On the criterion that a given system of deviations from the probable in the case of a correlated system of variables is such that it can be reasonably supposed to have arisen from random sampling*. July 1900 (cit. on p. 141).

[176]M. Pinamonti. *Statistical methods at ATLAS and CMS*. Presentation at Higgs Toppings Workshop. 2018 (cit. on p. 143).

[177]ATLAS Collaboration. *Energy scale and resolution systematics: summary and correlations*. Tech. rep. Geneva: CERN, 2017 (cit. on p. 144).

[178]ATLAS Muon Combined Performance Group. *MCPAnalysisGuidelinesMC16*. 2022. URL: `https://twiki.cern.ch/twiki/bin/viewauth/AtlasProtected/MCPAnalysisGuidelinesMC16` (visited on Mar. 30, 2023) (cit. on p. 145).

[179]CMS Collaboration. *Measurements of differential Z boson production cross sections in proton-proton collisions at $\sqrt{s} = 13$ TeV*. In: *Journal of High Energy Physics* 2019.12 (2019) (cit. on p. 166).

[180]ATLAS Collaboration. *Measurement of the transverse momentum distribution of Drell-Yan lepton pairs in proton-proton collisions at $\sqrt{s} = 13$ TeV with the ATLAS detector*. 2020. arXiv: `1912.02844 [hep-ex]` (cit. on p. 166).

[181]ATLAS Collaboration. *A precise measurement of the Z-boson double-differential transverse momentum and rapidity distributions in the full phase space of the decay leptons with the ATLAS experiment at $\sqrt{s} = 8$ TeV*. Tech. rep. 2023 (cit. on p. 166).

[182]O. Aberle et al. *High-Luminosity Large Hadron Collider (HL-LHC): Technical design report*. CERN Yellow Reports: Monographs. Geneva: CERN, 2020 (cit. on pp. 170, 202, 234).

[183]Z. Zhao, S. Yang, M. Ruan, M. Liu, and L. Han. *Measurement of the effective weak mixing angle at the CEPC*. 2022. arXiv: `2204.09921 [hep-ex]` (cit. on p. 177).

[184]CMS Collaboration. *A proposal for the measurement of the weak mixing angle at the HL-LHC*. Tech. rep. Geneva: CERN, 2017 (cit. on p. 178).

[185]L. A. Harland-Lang, A. D. Martin, P. Motylinski, and R. S. Thorne. *Parton distributions in the LHC era: MMHT 2014 PDFs*. In: *The European Physical Journal C* 75.5 (2015) (cit. on p. 178).

[186]R. D. Ball, V. Bertone, S. Carrazza, et al. *Parton distributions with LHC data*. In: *Nuclear Physics B* 867.2 (2013), pp. 244–289 (cit. on p. 178).

[187]T.-J. Hou et al. *New CTEQ global analysis of quantum chromodynamics with high-precision data from the LHC*. In: *Phys. Rev. D* 103.1 (2021), p. 014013. arXiv: 1912.10053 [hep-ph] (cit. on p. 195).

[188]ATLAS Collaboration. *Expected tracking and related performance with the updated ATLAS Inner Tracker layout at the High-Luminosity LHC*. Tech. rep. Geneva: CERN, 2021 (cit. on p. 202).

[189]ATLAS Collaboration. *Technical Design Report for the ATLAS Inner Tracker Pixel Detector*. Tech. rep. Geneva: CERN, 2017 (cit. on p. 202).

[190]ATLAS Collaboration. *Technical Design Report: A High-Granularity Timing Detector for the ATLAS Phase-II Upgrade*. Tech. rep. Geneva: CERN, 2020 (cit. on p. 202).

[191]ATLAS Collaboration. *Technical Design Report for the Phase-II Upgrade of the ATLAS Muon Spectrometer*. Tech. rep. Geneva: CERN, 2017 (cit. on p. 203).

[192]ATLAS Collaboration. *Technical Design Report for the Phase-II Upgrade of the ATLAS TDAQ System*. Tech. rep. Geneva: CERN, 2017 (cit. on p. 203).

[193]ATLAS Collaboration. *The ATLAS Level-1 Calorimeter Trigger*. Tech. rep. Geneva: CERN, 2008 (cit. on p. 204).

[194]ATLAS Collaboration. *Technical Design Report for the Phase-II Upgrade of the ATLAS Trigger and Data Acquisition System - Event Filter Tracking Amendment*. Tech. rep. Geneva: CERN, 2022 (cit. on p. 205).

[195]ATLAS Collaboration. *Forward Feature EXtractor (fFEX) User Requirements, Specifications and Preliminary Design Documen*. Tech. rep. Version 1.1. Geneva: CERN, 2023 (cit. on pp. 206, 207, 212, 213, 215).

[196]S. Masciocchi. *Electromagnetic and hadronic calorimeters*. Presentation at Graduate Days 2017 in Heidelberg. 2017 (cit. on p. 207).

[197]J. Rutherfoord. *Private communication*. 2018 (cit. on p. 208).

[198]ATLAS Collaboration. *Topological cell clustering in the ATLAS calorimeters and its performance in LHC Run 1*. In: *The European Physical Journal C* 77.7 (2017) (cit. on pp. 209, 217, 224).

[199]E. F. Eisenhandler. *ATLAS Level-1 Calorimeter Trigger Algorithms*. Tech. rep. Geneva: CERN, 2004 (cit. on p. 217).

[200]W. R. Nelson, T. M. Jenkins, R. C. McCall, and J. K. Cobb. *Electron-Induced Cascade Showers in Copper and Lead at 1 GeV*. In: *Phys. Rev.* 149 (1 1966), pp. 201–208 (cit. on p. 219).

[201]Advanced Micro Devices Inc. *White paper: AI Engines and Their Applications*. Tech. rep. WP506 (v1.2). 2022 (cit. on pp. 227, 234).

[202]A. Hoecker, P. Speckmayer, J. Stelzer, et al. *TMVA - Toolkit for Multivariate Data Analysis*. 2009. arXiv: physics/0703039 [physics.data-an] (cit. on p. 227).

[203]A. Ng and T. Ma. *CS229 Lecture Notes*. 2023 (cit. on p. 227).

[204]D. P. Kingma and J. Ba. *Adam: A Method for Stochastic Optimization*. 2017. arXiv: 1412.6980 [cs.LG] (cit. on p. 228).

[205]ATLAS Collaboration. *Performance of the electronic readout of the ATLAS liquid argon calorimeters*. In: *Journal of Instrumentation* 5.09 (2010) (cit. on p. 230).

[206]D. Layh. *MEDUSA and CALONet - High-Speed Data Transmission and a Deep Learning-based Algorithm for an upgrade of the ATLAS Trigger*. 2023 (cit. on p. 234).

[207]J. Redmon, S. Divvala, R. Girshick, and A. Farhadi. *You Only Look Once: Unified, Real-Time Object Detection*. 2016. arXiv: 1506.02640 [cs.CV] (cit. on p. 234).

List of Figures

1.1 Examples of Feynman diagrams of the reaction $f\bar{f} \to Z/\gamma^* \to f'\bar{f}'$. Diagrams depicted possess identical initial and final states but can be distinguished by the type of interaction, i.e. scattering or annihilation processes. 13
1.2 Examples of higher order contributions to the process $f\bar{f} \to Z/\gamma^* \to f'\bar{f}'$. 14
1.3 Schematic diagram of a collision of protons A and B [49]. 23
1.4 CT14NNLO parton density function at different momentum transfers Q^2 [52]. Uncertainties are not shown. 24
1.5 Schematic diagram illustrating a simplified overview of the different processes during and after a proton-proton interaction [61]. 26
1.6 Leading order Drell-Yan neutral current process. 26
1.7 Tensions of electroweak precision measurements. 28
1.8 Schematic overview of Collins-Soper frame adapted from Peng et al. [70]. Note that angles θ and ϕ depicted here are defined as $\theta = \theta_{\mathrm{CS}}$ and $\phi = \phi_{\mathrm{CS}}$ in the text. 31
1.9 Predictions of all angular coefficients at NLO and NNLO compared between centre-of-mass energies of $8\,\mathrm{TeV}$ and $13\,\mathrm{TeV}$ provided by A. Vallier [75], using DYTURBO [76] and the CT14NNLO PDF set with electroweak input parameters $G_F = 1.166\,378\,7 \times 10^{-5}\,\mathrm{GeV}^{-2}$, $M_Z = 91.1876\,\mathrm{GeV}$ and $M_W = 80.379\,\mathrm{GeV}$. Only statistical uncertainties of the simulation are shown. 37
1.10 Measurements of angular coefficients by the ATLAS collaboration at $\sqrt{s} = 8\,\mathrm{TeV}$ [65]. 38
1.11 Simulated A_4 as function of the dilepton mass with and without Z/γ^* interference [65]. 41
1.12 Scale dependence of the weak mixing angle illustrated [87] with completed measurements in black, prospective measurements in blue (centred on the theory prediction) and the theory prediction in dark blue. . 43

2.1 Overview of the accelerator complex at CERN, focussed on the Large Hadron Collider and its different stages [99]. 46
2.2 Computer generated overview of the ATLAS detector, shown here in a cut-away view with labels of major detector systems [105]. 48

2.3 Coordinate system used for the ATLAS detector. Adapted from Neutelings [106]. 49
2.4 Computer generated images of the ATLAS tracking system [109]. . . . 51
2.5 Computer generated cut-away view of the ATLAS calorimeter systems [111]. 53
2.6 Schematic overview of a section of the liquid argon calorimeter highlighting the accordion structure and the segmentation into individual cells [96]. 54
2.7 Cross-sectional schematic diagram [96] of a part of the muon system in the ATLAS detector. The barrel (B) and end-cap (E) inner (I), middle (M) and outer (O) layers (L) are coloured. Dashed lines indicate the hypothetical path of an infinite-momentum muon. 57
2.8 Schematic overview of the trigger and data acquisition system in ATLAS during Run 2. Adapted from ATLAS [128]. 60
2.9 Schematic overview of expected signatures of different types of particles in the ATLAS detector [131]. 62
2.10 Schematic overview [136] of the different components of an electron candidate signature in the ATLAS detector used in the reconstruction. The solid red line represents an electron, while the dashed red line represents a photon emitted by the electron in the tracker. The beam spot is the region where the two colliding beams interact. 65
2.11 Electron identification efficiencies for different working points [136]. . 66
2.12 Muon identification efficiencies for different working points [137]. The efficiency in data is shown and compared to a Monte Carlo simulation for reference. 68

5.1 Integrated luminosity delivered by the LHC (green), recorded by ATLAS (yellow) and useable for analysis (blue) over the whole data-taking period [159]. 84
5.2 Product of acceptance and efficiency in different dilepton variables for both analysis channels. The shapes of these distributions can be derived from the underlying kinematic distributions and constraints by the detector. 96
5.3 Schematic overview of the different regions used to determine the fake factors and their respective selection criteria. The *on pole* and *off pole* requirements are determined by the dilepton mass of the electron pair in an event. In contrast, the *pass ID* and *pass anti-ID* requirements are applied to the lepton of interest individually, while the second lepton must always fulfil the *pass anti-ID* requirement. 99

5.4 Fake contribution in the four different regions used for the estimate. Coloured histograms are stacked and data is shown in black. The ratio of data and expectation (simulation and multijet estimate) is shown below. Note that in all regions except the signal region this is 1 by design. The signal region includes (statistical and systematic) uncertainties in the grey band. 101
5.5 Fake factors with uncertainties as a function of the electron transverse momentum in different bins of the electron pseudorapidity. Fake factors for both leptons are shown, the one which has been triggered on the left and the one which has not been triggered on the right. 103
5.6 Comparison of data (black points) to expectation (stacked histograms) in the distributions of the transverse momentum of both leptons in both channels (the one with a larger p_T is shown in the left column, the other one in the right column, the electron channel is shown in the first row, the muon channel in the second row). The inclusive bin in the dilepton rapidity ($0 < |y_{ll}| < 2.4$) integrated over the dilepton transverse momentum in the mass window around the Z boson pole mass is depicted.
Below each histogram the ratio of the data and the sum of expectations is shown, where the grey band represents the combination of all uncertainties including the uncertainty on the integrated luminosity. . 111
5.7 Comparison of uncertainties in the distributions of the transverse momentum of both leptons in both channels (the one with a larger p_T is shown in the left column, the other one in the right column, the electron channel is shown in the first row, the muon channel in the second row). The uncertainty on the integrated luminosity of about 1.7% is not shown as it affects only the normalisation. The inclusive bin in the dilepton rapidity ($0 < |y_{ll}| < 2.4$) integrated over the dilepton transverse momentum in the mass window around the Z boson pole mass is depicted. 112
5.8 Comparison of data (black points) to expectation (stacked histograms) in the distributions of the pseudorapidity of both leptons in both channels (the one with a larger p_T is shown in the left column, the other one in the right column, the electron channel is shown in the first row, the muon channel in the second row). The inclusive bin in the dilepton rapidity ($0 < |y_{ll}| < 2.4$) integrated over the dilepton transverse momentum in the mass window around the Z boson pole mass is depicted.
Below each histogram the ratio of the data and the sum of expectations is shown, where the grey band represents the combination of all uncertainties including the uncertainty on the integrated luminosity. . 114

5.9 Comparison of uncertainties in the distributions of the pseudorapidity of both leptons in both channels (the one with a larger p_T is shown in the left column, the other one in the right column, the electron channel is shown in the first row, the muon channel in the second row). The uncertainty on the integrated luminosity of about 1.7% is not shown as it affects only the normalisation. The inclusive bin in the dilepton rapidity ($0 < |y_{ll}| < 2.4$) integrated over the dilepton transverse momentum in the mass window around the Z boson pole mass is depicted. 115
5.10 Comparison of data (black points) to expectation (stacked histograms) in the distributions of the azimuthal angle of both leptons in both channels (the one with a larger p_T is shown in the left column, the other one in the right column, the electron channel is shown in the first row, the muon channel in the second row). The inclusive bin in the dilepton rapidity ($0 < |y_{ll}| < 2.4$) integrated over the dilepton transverse momentum in the mass window around the Z boson pole mass is depicted. Below each histogram the ratio of the data and the sum of expectations is shown, where the grey band represents the combination of all uncertainties including the uncertainty on the integrated luminosity. . 116
5.11 Comparison of uncertainties in the distributions of the azimuthal angle of both leptons in both channels (the one with a larger p_T is shown in the left column, the other one in the right column, the electron channel is shown in the first row, the muon channel in the second row). The uncertainty on the integrated luminosity of about 1.7% is not shown as it affects only the normalisation. The inclusive bin in the dilepton rapidity ($0 < |y_{ll}| < 2.4$) integrated over the dilepton transverse momentum in the mass window around the Z boson pole mass is depicted. 117
5.12 Comparison of data (black points) to expectation (stacked histograms) in the dilepton kinematic distributions in the electron channel. The inclusive bin in the dilepton rapidity ($0 < |y_{ll}| < 2.4$) integrated over the dilepton transverse momentum in the mass window around the Z boson pole mass is depicted.
Below each histogram the ratio of the data and the sum of expectations is shown, where the grey band represents the combination of all uncertainties. 119
5.13 Comparison of uncertainties in dilepton distributions in the electron channel. The uncertainty on the integrated luminosity of about 1.7% is not shown as it affects only the normalisation. Depicted is the inclusive bin in the dilepton rapidity ($0 < |y_{ll}| < 2.4$) integrated over the dilepton transverse momentum in the mass window around the Z boson pole mass. 120

5.14 Comparison of data (black points) to expectation (stacked histograms) in the dilepton kinematic distributions in the muon channel. The inclusive bin in the dilepton rapidity ($0 < |y_{ll}| < 2.4$) integrated over the dilepton transverse momentum in the mass window around the Z boson pole mass is depicted.
Below each histogram the ratio of the data and the sum of expectations is shown, where the grey band represents the combination of all uncertainties. 121
5.15 Comparison of uncertainties in dilepton distributions in the muon channel. The uncertainty on the integrated luminosity of about 1.7% is not shown as it affects only the normalisation. The inclusive bin in the dilepton rapidity ($0 < |y_{ll}| < 2.4$) integrated over the dilepton transverse momentum in the mass window around the Z boson pole mass is depicted. 122
5.16 Comparison of data (black points) to expectation (stacked histograms) in the Collins-Soper distributions in both channels (the electron channel is shown in the first row, the muon channel in the second row). The inclusive bin in the dilepton rapidity ($0 < |y_{ll}| < 2.4$) integrated over the dilepton transverse momentum in the mass window around the Z boson pole mass is depicted.
Below each histogram the ratio of the data and the sum of expectations is shown, where the grey band represents the combination of all uncertainties. 123
5.17 Comparison of uncertainties in the Collins-Soper distributions in both channels (the electron channel is shown in the first row, the muon channel in the second row). The uncertainty on the integrated luminosity of about 1.7% is not shown as it affects only the normalisation. The inclusive bin in the dilepton rapidity ($0 < |y_{ll}| < 2.4$) integrated over the dilepton transverse momentum in the mass window around the Z boson pole mass is depicted. 124
5.18 Comparison of uncertainties on Collins-Soper distributions in the muon channel between low dilepton rapidity and high dilepton rapidity regions. 126
5.19 Comparison of Collins-Soper distributions in the electron channel between low dilepton momentum and high dilepton momentum regions. 127

6.1 Analytical polynomials P_0 to P_5 as a function of $\cos\theta_{\mathrm{CS}}$ and ϕ_{CS} as defined in equation 6.5. 135
6.2 Analytical polynomials P_6 to P_8 as a function of $\cos\theta_{\mathrm{CS}}$ and ϕ_{CS} as defined in equation 6.5. 136
6.3 Templated polynomials (templates) of P_0 to P_5 as a function of $\cos\theta_{\mathrm{CS}}$ and ϕ_{CS}. The first bin in $p_{T,Z}$ and $p_{T,ll}$ (i.e. t^0_{00} to t^0_{50} in equation 6.8) is displayed. 137

6.4 Templated polynomials (templates) of P_6 to P_8 as a function of $\cos\theta_{\mathrm{CS}}$ and ϕ_{CS}. The first bin in $p_{T,Z}$ and $p_{T,ll}$ (i.e. t^0_{60} to t^0_{80} in equation 6.8) is displayed. 138
6.5 Absolute difference between extracted angular coefficients from Asimovdata and the expectation from the moments method derived from the same simulated sample shown in the lowest rapidity bin in the electron channel. Identical results have been achieved in other bins and the muon channel. 142
6.6 Pulls of electron nuisance parameters. Note that the vertical axis shows the dimensionless pull g. 146
6.7 Pulls of electron nuisance parameters. Note that the vertical axis shows the dimensionless pull g. 147
6.8 Pulls of electron nuisance parameters. Note that the vertical axis shows the dimensionless pull g. 148
6.9 Breakdown of absolute uncertainties on angular coefficients as a function of the Z boson transverse momentum (denoted p_T^Z) in the electron channel. 149
6.10 Breakdown of absolute uncertainties on the A_4 coefficient as a function of the Z boson transverse momentum (denoted p_T^Z) in different rapidity ranges in the electron channel. 149
6.11 Breakdown of relative uncertainties on the unpolarised cross section as a function of the Z boson transverse momentum (denoted p_T^Z) in different rapidity ranges in the electron channel. 150
6.12 Pulls of muon nuisance parameters. Note that the vertical axis shows the dimensionless pull g and `MUON_EFF_TrigStatUncertainty` is out of scale. 151
6.13 Breakdown of absolute uncertainties on angular coefficients as a function of the Z boson transverse momentum (denoted p_T^Z) in the muon channel. 152
6.14 Breakdown of absolute uncertainties on the A_4 coefficient as a function of the Z boson transverse momentum (denoted p_T^Z) in different rapidity ranges in the muon channel. 152
6.15 Breakdown of relative uncertainties on the unpolarised cross section as a function of the Z boson transverse momentum (denoted p_T^Z) in different rapidity ranges in the muon channel. 153
6.16 Closure test between electron and muon channel in Asimovdata as a function of the Z boson transverse momentum (denoted p_T^Z) in different rapidity ranges. All systematic and statistical uncertainties are included. 154
6.17 Closure test between electron and muon channel in Asimovdata as a function of the Z boson transverse momentum (denoted p_T^Z) in different rapidity ranges. All systematic and statistical uncertainties are included. 155

6.18 Closure test shown as the relative difference between electron and muon channel in Asimovdata as a function of the Z boson transverse momentum (denoted p_T^Z) in different rapidity ranges. All systematic and statistical uncertainties are included. 156
6.19 Absolute difference in extracted angular coefficients between electron and muon channel as a function of the Z boson transverse momentum (denoted p_T^Z) in different rapidity ranges. All systematic and statistical uncertainties are included. 157
6.20 Absolute difference in extracted angular coefficients between electron and muon channel as a function of the Z boson transverse momentum (denoted p_T^Z) in different rapidity ranges. All systematic and statistical uncertainties are included. 158
6.21 Relative difference in the measured cross section between electron and muon channel as a function of the Z boson transverse momentum (denoted p_T^Z) in different rapidity ranges. All systematic and statistical uncertainties are included. 159
6.22 Extracted angular coefficients in the electron and muon channels as a function of the Z boson transverse momentum (denoted p_T^Z) in different rapidity ranges. All systematic and statistical uncertainty sources are included. 160
6.23 Extracted angular coefficients in the electron and muon channels as a function of the Z boson transverse momentum (denoted p_T^Z) in different rapidity ranges. All systematic and statistical uncertainty sources are included. 161
6.24 Measured cross section in the electron and muon channels as a function of the Z boson transverse momentum (denoted p_T^Z) in different rapidity ranges. All systematic and statistical uncertainty sources are included. 162
6.25 Breakdown of absolute uncertainties on the extracted angular coefficients into statistical and systematic sources as a function of the Z boson transverse momentum (denoted p_T^Z). The combination of the electron and the muon channels is depicted. 163
6.26 Breakdown of absolute uncertainties on the extracted A_4 coefficient into statistical and systematic sources as a function of the Z boson transverse momentum (denoted p_T^Z) in different rapidity ranges. The combination of the electron and the muon channels is depicted. 163
6.27 Breakdown of relative uncertainties on the measured cross section into statistical and systematic sources as a function of the Z boson transverse momentum (denoted p_T^Z) in different rapidity ranges. The combination of the electron and the muon channels is depicted. 164

6.28 Extracted angular coefficients from the combination of electron and muon channels as a function of the Z boson transverse momentum (denoted p_T^Z) in different rapidity ranges. All systematic and statistical uncertainty sources are included. 167
6.29 Extracted angular coefficients from the combination of electron and muon channels as a function of the Z boson transverse momentum (denoted p_T^Z) in different rapidity ranges. All systematic and statistical uncertainty sources are included. 168
6.30 Measured unpolarised cross section from the combination of electron and muon channels as a function of the Z boson transverse momentum (denoted p_T^Z) in different rapidity ranges. All systematic and statistical uncertainty sources are included. 169

8.1 A_4 coefficient as predicted by DYTURBO at LO in QCD and LO in electroweak theory as a function of the Z/γ^* mass M_{Z/γ^*} and rapidity Y_{Z/γ^*} for different PDF sets. No uncertainties are depicted. 178
8.2 Prediction of A_4 as a function of the effective leptonic weak mixing angle calculated with DYTURBO at LO in QCD and LO in electroweak theory. The linear model is calculated from the lowest and highest entry of the CT14 graph. 179
8.3 Highest ranking nuisance parameters in terms of their impact on the total uncertainty on the estimator for the effective weak mixing angle $\mathrm{s}\hat{2}\mathrm{w}$ using the CT14 PDF set. The upper x-axis represents the impact on the weak mixing angle and the lower x-axis represents the scale for the pull defined in equation 6.15, which is represented by the black data point and the black uncertainty bar. For reference, an uncertainty bar of one standard deviation is shown in red. The centre dashed line is located at 0, while the other dashed lines represent the $\pm 1\sigma$ distance from 0. Finally, the black unfilled boxes represent the impact of a particular nuisance parameter on the estimator (scaled at the top x-axis) before the fit and the blue filled boxes show the impact after the fit. 188

8.4 Highest ranking nuisance parameters in terms of their impact on the total uncertainty on the estimator for the effective weak mixing angle $\hat{\mathrm{s2w}}$ using the NNPDF23 PDF set. The upper x-axis represents the impact on the weak mixing angle and the lower x-axis represents the scale for the pull defined in equation 6.15, which is represented by the black data point and the black uncertainty bar. For reference, an uncertainty bar of one standard deviation is shown in red. The centre dashed line is located at 0, while the other dashed lines represent the $\pm 1\sigma$ distance from 0. Finally, the black unfilled boxes represent the impact of a particular nuisance parameter on the estimator (scaled at the top x-axis) before the fit and the blue filled boxes show the impact after the fit. 189
8.5 Highest ranking nuisance parameters in terms of their impact on the total uncertainty on the estimator for the effective weak mixing angle $\hat{\mathrm{s2w}}$ using the MMHT14 PDF set. The upper x-axis represents the impact on the weak mixing angle and the lower x-axis represents the scale for the pull defined in equation 6.15, which is represented by the black data point and the black uncertainty bar. For reference, an uncertainty bar of one standard deviation is shown in red. The centre dashed line is located at 0, while the other dashed lines represent the $\pm 1\sigma$ distance from 0. Finally, the black unfilled boxes represent the impact of a particular nuisance parameter on the estimator (scaled at the top x-axis) before the fit and the blue filled boxes show the impact after the fit. 190
8.6 Comparison of sensitivity estimates of this thesis to the preliminary ATLAS measurement at $\sqrt{s} = 8\,\mathrm{TeV}$ [65]. The current world average [6] is shown as the orange band with the black central line. 194

10.1 Overview of the Run 4 trigger system [194]. 205
10.2 Schematic overview of the coverage of each FPGA in the fFEX system [195]. Individual cells in the FCAL systems are not depicted explicitly. 207
10.3 Segmentation of a calorimeter into individual cells using the example of one half of one hemisphere of the first layer of the FCAL. Cell boundaries are defined by green lines. Supercell boundaries are depicted as blue lines [197]. 208
10.4 Schematic cross-sectional view of the ATLAS forward calorimeters in the $r - z$ plane depicting the different calorimeter systems and supporting structures [96]. 210
10.5 Distribution of geometric cell centres of the first (front facing towards the interaction region) layer of each calorimeter in η and ϕ. The upper half of the positive η region is depicted. 211

10.6 Distribution of geometric cell centres of the first (front facing towards the interaction region) layer of each calorimeter in x and y, projected onto the first layer of the FCAL. The upper half of the positive η region is depicted. 211
10.7 High-level firmware overview of a fFEX FPGA. Adapted from the ATLAS specification report [195]. 212
10.8 High-level overview of the fFEX trigger algorithms [195]. 213

11.1 Conceptual overview of sliding window-type algorithms. Multiple energy sums are calculated, here in red the *electromagnetic core*, in blue the *electromagnetic isolation* and in green the *hadronic isolation* (no individual cells are shown for the hadronic isolation). 218
11.2 Schematic overview of the local maximum criteria used in sliding window algorithms presented in this chapter. 218
11.3 Normalised distributions of energy sums for signal and background of the legacy-like sliding window algorithm in the EMEC/HEC and FCAL fiducial regions for core energies $E_T^{\text{core}} > 20\,\text{GeV}$. 221
11.4 Normalised distributions of energy sums for signal and background of the legacy and the geometry-aware sliding window algorithms in the FCAL fiducial regions for core energies $E_T^{\text{core}} > 20\,\text{GeV}$. 223
11.5 Schematic view of geometric moments of a topological cluster in the ATLAS detector [198]. 224
11.6 Normalised distributions of shower shape variables for signal and background of the geometry-aware sliding window algorithm in the EMEC/HEC and FCAL fiducial regions for core energies $E_T^{\text{core}} > 20\,\text{GeV}$. 226
11.7 Normalised distributions of the neural network output for signal and background of the geometry-aware sliding window algorithm in the EMEC/HEC and FCAL fiducial regions for core energies $E_T^{\text{core}} > 20\,\text{GeV}$. 229
11.8 Comparisons of performance measures in the EMEC/HEC (left) and the FCAL (right) fiducial regions. Note that in the EMEC/HEC regions by definition the legacy (green) and geometry-aware (red) sliding window algorithms are identical so that only the red curve is visible. 231
11.9 Efficiencies as a function of the true absolute pseudorapidity $|\eta|$ using a trigger threshold matched to a rate of $10\,\text{kHz}$ in the plateau (p_T threshold $+10\,\text{GeV}$). 232
11.10 Comparisons of performance measures in the full forward region. . . . 233

C.1 Acceptance and efficiency separated in different dilepton variables for both analysis channels. The shapes of these distributions can be derived from the underlying kinematic distributions and constraints by the detector. 275

F.1 Pulls of electron nuisance parameters for the Asimov dataset. Note that the vertical axis shows the dimensionless pull g. 291
F.2 Pulls of electron nuisance parameters for the Asimov dataset. Note that the vertical axis shows the dimensionless pull g. 292
F.3 Pulls of electron nuisance parameters for the Asimov dataset. Note that the vertical axis shows the dimensionless pull g. 293
F.4 Pulls of muon nuisance parameters for the Asimov dataset. Note that the vertical axis shows the dimensionless pull g. 294
F.5 Pulls of electron and muon nuisance parameters in the combined fit. Note that the vertical axis shows the dimensionless pull g. 295
F.6 Pulls of electron and muon nuisance parameters in the combined fit. Note that the vertical axis shows the dimensionless pull g. 296
F.7 Pulls of electron and muon nuisance parameters in the combined fit. Note that the vertical axis shows the dimensionless pull g. 297

H.1 Normalised distributions of shower shape variables for signal and background of the legacy sliding window algorithm in the EMEC/HEC and FCAL fiducial regions for core energies $E_T^{\text{core}} > 20\,\text{GeV}$. 307
H.2 Normalised distributions of shower shape variables for signal and background of the legacy sliding window algorithm in the EMEC/HEC and FCAL fiducial regions for core energies $E_T^{\text{core}} > 20\,\text{GeV}$. 308
H.3 Correlation Matrices of shower shape, sliding window and kinematic variables. Empty boxes represent 0. The variable E_T^{pair} representing the energy of the highest energetic 2x1 cell pair within the 2x2 core is added. 310

List of Tables

1.1 Overview of fermion properties in the Standard Model by fermion type and generation. All values have been taken from the Particle Data Group [14] and mass values are rounded. The *current quark mass* values used for the Up, Down and Strange quarks are quoted in the $\overline{MS}$ scheme (which will be discussed in more detail in section 1.1.2.2), while the Top quark mass has been measured from decays. 10

1.2 Overview of bosons and their properties in the Standard Model. All values have been taken from the Particle Data Group [14]. 10

2.1 Technical parameters of the LHC comparing the design values to Run 1 and Run 2. Data taken from Duhr et al. [100]. Crossing angle for Run 1 taken from the dedicated ATLAS publication [104]. 47

5.1 List of all processes generated using the Monte Carlo method with their respective generators, PDF sets and cross section σ_{tot} as set in the generator. Processes are generated for different lepton flavours separately and contain at least one lepton in the final state. Note that all processes use EvtGen to more accurately reflect particle decays. An estimate of the cross section of the multijet contribution is also shown which includes dijet production, production of W bosons with jets etc. The estimate is based on dijet production alone, which dominates the total cross section. 86

5.2 Selection of transverse momenta p_T in the electron channel, split into the leading and subleading candidates with respect to the trigger chains that have been fulfilled. The subscripts indicate which electron candidate fulfilled the single-electron trigger (SLT), while DLT24 and DLT17 differentiate which di-electron trigger has been fulfilled. 90

5.3 Selection of transverse momenta p_T in the muon channel, split into the leading and subleading candidates with respect to the trigger chains that have been fulfilled. The subscripts indicate which muon candidate fulfilled the single-muon trigger (SLT), while DLT22 and DLT14 differentiate which di-muon trigger has been fulfilled. 92

5.4 Numbers of events in the electron channel after applying each selection step for $80\,\text{GeV} < m_{ll} < 102\,\text{GeV}$ and $0 < |y_{ll}| < 2.4$. Simulated events are scaled to $\mathfrak{L} = 139\,\text{fb}^{-1}$. 95

5.5 Numbers of events in the muon channel after applying each selection step for $80\,\text{GeV} < m_{ll} < 102\,\text{GeV}$ and $0 < |y_{ll}| < 2.4$. Simulated events are scaled to $\mathfrak{L} = 139\,\text{fb}^{-1}$ 96
5.6 Numbers of events in the electron channel after applying the full selection for $80\,\text{GeV} < m_{ll} < 102\,\text{GeV}$ and different bins in rapidity. Simulated events are scaled to $\mathfrak{L} = 139\,\text{fb}^{-1}$. Ratios of data to the sum of expectations and the multijet fraction with respect to the data are listed. 109
5.7 Numbers of events in the muon channel after applying the full selection for $80\,\text{GeV} < m_{ll} < 102\,\text{GeV}$ and different bins in rapidity. Simulated events are scaled to $\mathfrak{L} = 139\,\text{fb}^{-1}$. Ratios of data to the sum of expectations are listed. 109

8.1 Expected yields in units of 10^6 events in each analysis region considered (only signal simulation is used). 182
8.2 Expected central values and uncertainties of A_4 in the electron channel extracted from the Asimov dataset based on the POWHEGBOX + PYTHIA 8 simulation. The central value and the uncertainties are shown in units of 10^{-4}. Values are rounded and can thus appear as 0. 183
8.3 Expected central values and uncertainties of A_4 in the muon channel extracted from the Asimov dataset based on the POWHEGBOX + PYTHIA 8 simulation. The central value and the uncertainties are shown in units of 10^{-4}. Values are rounded and can thus appear as 0. 184
8.4 Expected central value and uncertainties on the effective weak mixing angle extracted from the POWHEGBOX + PYTHIA 8 Asimov dataset using different PDFs in the electron channel. The parametrisation is calculated using DYTURBO at NLO in QCD and LO in electroweak theory. The POWHEGBOX standard value for the effective weak mixing angle is $\sin^2\theta^l_{\text{eff}} = 0.23145$. Uncertainties are shown in units of 10^{-5}. Values are rounded and can thus appear as 0. 191
8.5 Expected central value and uncertainties on the effective weak mixing angle extracted from the POWHEGBOX + PYTHIA 8 Asimov dataset using different PDFs in the muon channel. The parametrisation is calculated using DYTURBO at NLO in QCD and LO in electroweak theory. The POWHEGBOX standard value for the effective weak mixing angle is $\sin^2\theta^l_{\text{eff}} = 0.23145$. Uncertainties are shown in units of 10^{-5}. Values are rounded and can thus appear as 0. 192

10.1 Sizes and layers of calorimeters in the forward region distinguished by pseudorapidity [198]. Note that the information is only provided for the region of $|\eta| > 2.2$ and other detector subsystems are not shown. Note that technical names of the FCAL layers have been adapted to correspond to figure 10.4. 209

11.1 List of shower shape variables, their meaning and symbol. The definition of each variable can be found in appendix H.2. 225

A.1 All datasets used for the analysis of the angular coefficients and their technical identifiers. 271

A.2 All Monte Carlo simulations used for the analysis of the angular coefficients as well as the sensitivity study and their technical identifiers. The `<r-tag>` is different for three different simulation campaigns: `r9364` for MC16a (for 2015 and 2016), `r10201` for MC16d (for 2017) and `r10724` for MC16e (for 2018). The different campaigns reflect the detector conditions during the different periods (mainly the number of simultaneous proton collisions per bunch crossing). 272

B.1 Technical names of trigger chains used for the STDM4 ATLAS data format. 273

D.1 Numbers of events in the electron channel for data and prediction as well as the ratio of data to expectation and the fraction of multijet events in different analysis bins. If ranges of mass, rapidity or transverse momentum are not explicitly given, they are assumed to be inclusive. . 277

D.2 Numbers of events in the muon channel for data and prediction as well as the ratio of data to expectation in different analysis bins. If ranges of mass, rapidity or transverse momentum are not explicitly given, they are assumed to be inclusive. 279

E.1 Optimised bin boundaries in the Collins-Soper variables $\cos\theta_{\mathrm{CS}}$ and ϕ_{CS} for all bins used in the analysis. 283

G.1 Results of the combined fit in all bins of transverse momentum and $0 < y_{ll} < 0.4$. 300

G.2 Results of the combined fit in all bins of transverse momentum and $0.4 < y_{ll} < 0.8$. 301

G.3 Results of the combined fit in all bins of transverse momentum and $0.8 < y_{ll} < 1.2$. 302

G.4 Results of the combined fit in all bins of transverse momentum and $1.2 < y_{ll} < 1.6$. 303

G.5 Results of the combined fit in all bins of transverse momentum and $1.6 < y_{ll} < 2.0$. 304

G.6 Results of the combined fit in all bins of transverse momentum and $2.0 < y_{ll} < 2.4$. 305

A

Datasets and Monte Carlo Simulation

Year	Name
2015	data15_13TeV.periodD.physics_Main.PhysCont.DAOD_STDM4.grp23_v01_p4238
2015	data15_13TeV.periodE.physics_Main.PhysCont.DAOD_STDM4.grp23_v01_p4238
2015	data15_13TeV.periodF.physics_Main.PhysCont.DAOD_STDM4.grp23_v01_p4238
2015	data15_13TeV.periodG.physics_Main.PhysCont.DAOD_STDM4.grp23_v01_p4238
2015	data15_13TeV.periodH.physics_Main.PhysCont.DAOD_STDM4.grp23_v01_p4238
2015	data15_13TeV.periodJ.physics_Main.PhysCont.DAOD_STDM4.grp23_v01_p4238
2016	data16_13TeV.periodA.physics_Main.PhysCont.DAOD_STDM4.grp23_v01_p4238
2016	data16_13TeV.periodB.physics_Main.PhysCont.DAOD_STDM4.grp23_v01_p4238
2016	data16_13TeV.periodC.physics_Main.PhysCont.DAOD_STDM4.grp23_v01_p4238
2016	data16_13TeV.periodD.physics_Main.PhysCont.DAOD_STDM4.grp23_v01_p4238
2016	data16_13TeV.periodE.physics_Main.PhysCont.DAOD_STDM4.grp23_v01_p4238
2016	data16_13TeV.periodF.physics_Main.PhysCont.DAOD_STDM4.grp23_v01_p4238
2016	data16_13TeV.periodG.physics_Main.PhysCont.DAOD_STDM4.grp23_v01_p4238
2016	data16_13TeV.periodI.physics_Main.PhysCont.DAOD_STDM4.grp23_v01_p4238
2016	data16_13TeV.periodK.physics_Main.PhysCont.DAOD_STDM4.grp23_v01_p4238
2016	data16_13TeV.periodL.physics_Main.PhysCont.DAOD_STDM4.grp23_v01_p4238
2017	data17_13TeV.periodB.physics_Main.PhysCont.DAOD_STDM4.grp23_v01_p4238
2017	data17_13TeV.periodC.physics_Main.PhysCont.DAOD_STDM4.grp23_v01_p4238
2017	data17_13TeV.periodD.physics_Main.PhysCont.DAOD_STDM4.grp23_v01_p4238
2017	data17_13TeV.periodE.physics_Main.PhysCont.DAOD_STDM4.grp23_v01_p4238
2017	data17_13TeV.periodF.physics_Main.PhysCont.DAOD_STDM4.grp23_v01_p4238
2017	data17_13TeV.periodH.physics_Main.PhysCont.DAOD_STDM4.grp23_v01_p4238
2017	data17_13TeV.periodI.physics_Main.PhysCont.DAOD_STDM4.grp23_v01_p4238
2017	data17_13TeV.periodK.physics_Main.PhysCont.DAOD_STDM4.grp23_v01_p4238
2018	data18_13TeV.periodC.physics_Main.PhysCont.DAOD_STDM4.grp23_v01_p4238
2018	data18_13TeV.periodD.physics_Main.PhysCont.DAOD_STDM4.grp23_v01_p4238
2018	data18_13TeV.periodF.physics_Main.PhysCont.DAOD_STDM4.grp23_v01_p4238
2018	data18_13TeV.periodI.physics_Main.PhysCont.DAOD_STDM4.grp23_v01_p4238
2018	data18_13TeV.periodK.physics_Main.PhysCont.DAOD_STDM4.grp23_v01_p4238
2018	data18_13TeV.periodL.physics_Main.PhysCont.DAOD_STDM4.grp23_v01_p4238
2018	data18_13TeV.periodM.physics_Main.PhysCont.DAOD_STDM4.grp23_v01_p4238

Tab. A.1.: All datasets used for the analysis of the angular coefficients and their technical identifiers.

Process	Simulation Identifier
$Z \to e^+e^-$	mc16_13TeV.361107.PowhegPythia8EvtGen_AZNLOCTEQ6L1_Zmumu.deriv.DAOD_STDM4.e3601_s3126_<r-tag>_p4239
$Z \to \mu^+\mu^-$	mc16_13TeV.361106.PowhegPythia8EvtGen_AZNLOCTEQ6L1_Zee.deriv.DAOD_STDM4.e3601_s3126_<r-tag>_p4239
$Z \to \tau^+\tau^-$	mc16_13TeV.361108.PowhegPythia8EvtGen_AZNLOCTEQ6L1_Ztautau.deriv.DAOD_STDM4.e3601_s3126_<r-tag>_p4237
$t\bar{t} \to X$	mc16_13TeV.410470.PhPy8EG_A14_ttbar_hdamp258p75_nonallhad.deriv.DAOD_STDM4.e6337_s3126_<r-tag>_p4237
$t/\bar{t} \to X$	mc16_13TeV.410644.PowhegPythia8EvtGen_A14_singletop_schan_lept_top.deriv.DAOD_STDM4.e6527_s3126_<r-tag>_p4237
	mc16_13TeV.410645.PowhegPythia8EvtGen_A14_singletop_schan_lept_antitop.deriv.DAOD_STDM4.e6527_s3126_<r-tag>_p4237
	mc16_13TeV.410658.PhPy8EG_A14_tchan_BW50_lept_top.deriv.DAOD_STDM4.e6671_s3126_<r-tag>_p4237
	mc16_13TeV.410659.PhPy8EG_A14_tchan_BW50_lept_antitop.deriv.DAOD_STDM4.e6671_s3126_<r-tag>_p4237
$Wt/W\bar{t} \to X$	mc16_13TeV.410646.PowhegPythia8EvtGen_A14_Wt_DR_inclusive_top.deriv.DAOD_STDM4.e6552_s3126_<r-tag>_p4237
	mc16_13TeV.410647.PowhegPythia8EvtGen_A14_Wt_DR_inclusive_antitop.deriv.DAOD_STDM4.e6552_s3126_<r-tag>_p4237
Multiboson	mc16_13TeV.361600.PowhegPy8EG_CT10nloME_AZNLOCTEQ6L1_WWlvlv.deriv.DAOD_STDM4.e4616_s3126_<r-tag>_p4237
	mc16_13TeV.361601.PowhegPy8EG_CT10nloME_AZNLOCTEQ6L1_WZlvll_mll4.deriv.DAOD_STDM4.e4475_s3126_<r-tag>_p4237
	mc16_13TeV.361603.PowhegPy8EG_CT10nloME_AZNLOCTEQ6L1_ZZllll_mll4.deriv.DAOD_STDM4.e4475_s3126_<r-tag>_p4237
	mc16_13TeV.361604.PowhegPy8EG_CT10nloME_AZNLOCTEQ6L1_ZZvvll_mll4.deriv.DAOD_STDM4.e4475_s3126_<r-tag>_p4237
	mc16_13TeV.361606.PowhegPy8EG_CT10nloME_AZNLOCTEQ6L1_WWlvqq.deriv.DAOD_STDM4.e4711_s3126_<r-tag>_p4237
	mc16_13TeV.361607.PowhegPy8EG_CT10nloME_AZNLOCTEQ6L1_WZqqll_mll20.deriv.DAOD_STDM4.e4711_s3126_<r-tag>_p4237
	mc16_13TeV.361609.PowhegPy8EG_CT10nloME_AZNLOCTEQ6L1_WZlvqq_mqq20.deriv.DAOD_STDM4.e4711_s3126_<r-tag>_p42377
	mc16_13TeV.361610.PowhegPy8EG_CT10nloME_AZNLOCTEQ6L1_ZZqqll_mqq20mll20.deriv.DAOD_STDM4.e4711_s3126_<r-tag>_p4237
Photon induced	mc16_13TeV.363695.HepMCAsciiEG_Lpair_BSY_SDiss_ggTOee_60M200_LeptonFilter.deriv.DAOD_STDM4.e7595_s3126_<r-tag>_p4237
	mc16_13TeV.363699.HepMCAsciiEG_Lpair_BSY_SDiss_ggTOmumu_60M200_LeptonFilter.deriv.DAOD_STDM4.e7595_s3126_<r-tag>_p4237
	mc16_13TeV.363254.Herwig7EvtGen_BudnevQED_ggTOee_60M200_LeptonFilter.deriv.DAOD_STDM4.e7607_s3126_<r-tag>_p4237
	mc16_13TeV.363256.Herwig7EvtGen_BudnevQED_ggTOmumu_60M200_LeptonFilter.deriv.DAOD_STDM4.e7607_s3126_<r-tag>_p4237
	mc16_13TeV.363673.Pythia8EvtGen_NNPDF23QED_ggTOee_60M200_LeptonFilter.deriv.DAOD_STDM4.e7595_s3126_<r-tag>_p4237
	mc16_13TeV.363677.Pythia8EvtGen_NNPDF23QED_ggTOmumu_60M200_LeptonFilter.deriv.DAOD_STDM4.e7595_s3126_<r-tag>_p4237

Tab. A.2.: All Monte Carlo simulations used for the analysis of the angular coefficients as well as the sensitivity study and their technical identifiers. The <r-tag> is different for three different simulation campaigns: r9364 for MC16a (for 2015 and 2016), r10201 for MC16d (for 2017) and r10724 for MC16e (for 2018). The different campaigns reflect the detector conditions during the different periods (mainly the number of simultaneous proton collisions per bunch crossing).

B STDM4 Preselection

For the ATLAS STDM4 data format there is logical "or" selection applied for the trigger chains presented in table B.1 and one of the following requirements:

- One reconstructed muon candidate with $p_T > 15\,\mathrm{GeV}$ in $|\eta| < 2.6$ passing basic track quality requirements outlined by the Muon Combined Performance Group.

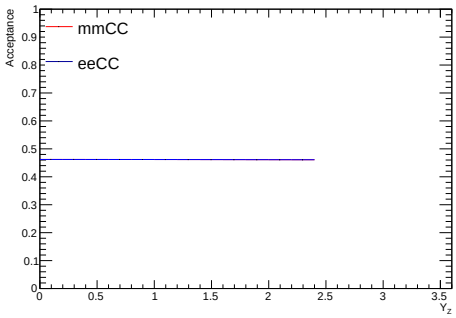
- One reconstructed electron candidate with $p_T > 20\,\mathrm{GeV}$ in $|\eta| < 2.6$ passing the `IsEMLoose` or the `LHLoose` identification requirement.

Trigger name	
HLT_e120_lhloose	HLT_e120_lhloosemc
HLT_e120_lhloose_nod0	HLT_e120_loose
HLT_e140_lhloose	HLT_e140_lhloose_nod0
HLT_e140_loose	HLT_e20_lhmedium_nod0_2g10_loose
HLT_e20_lhmedium_nod0_g35_loose	HLT_e24_lhmedium_iloose_L1EM18VH
HLT_e24_lhmedium_iloose_L1EM20VH	HLT_e24_lhmedium_L1EM18VH
HLT_e24_lhmedium_L1EM20VH	HLT_e24_lhmedium_L1EM20VHI
HLT_e24_lhmedium_nod0_L1EM15VH_g25_medium	HLT_e24_lhmedium_nod0_L1EM20VH
HLT_e24_lhtight_iloose	HLT_e24_lhtight_iloose_L1EM20VH
HLT_e24_lhtight_nod0_ivarloose	HLT_e24_lhvloose_nod0_L1EM20VH
HLT_e24_medium_iloose_L1EM18VH	HLT_e24_medium_iloose_L1EM20VH
HLT_e24_tight_iloose	HLT_e24_tight_iloose_L1EM20VH
HLT_e26_lhtight_iloose	HLT_e26_lhtight_nod0_ivarloose
HLT_e26_tight_iloose	HLT_e300_etcut
HLT_e60_lhmedium	HLT_e60_lhmedium_nod0
HLT_e60_medium	HLT_mu20_iloose_L1MU15
HLT_mu24_iloose_L1MU15	HLT_mu24_iloose
HLT_mu24_imedium	HLT_mu24_ivarmedium
HLT_mu24_L1MU15	HLT_mu26_imedium
HLT_mu26_ivarmedium	HLT_mu26_medium
HLT_mu40	HLT_mu50
HLT_mu60_0eta105_msonly	

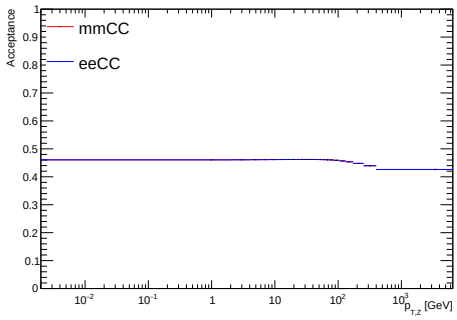
Tab. B.1.: Technical names of trigger chains used for the STDM4 ATLAS data format.

C

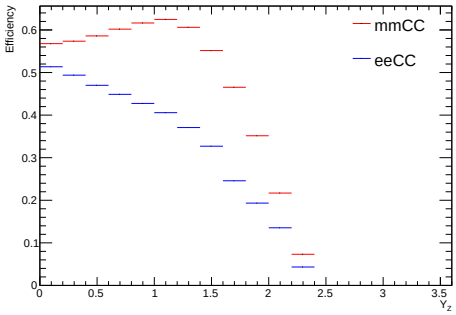
Acceptance and Efficiency



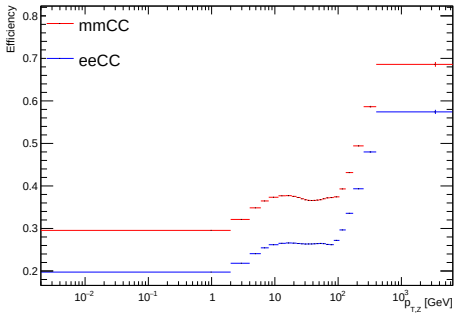
(a) Acceptance as a function of the Z boson rapidity.



(b) Acceptance as a function of the Z boson transverse momentum.



(c) Efficiency as a function of the Z boson rapidity.



(d) Efficiency as a function of the Z boson transverse momentum.

Fig. C.1.: Acceptance and efficiency separated in different dilepton variables for both analysis channels. The shapes of these distributions can be derived from the underlying kinematic distributions and constraints by the detector.

D

Cutflows

Tab. D.1.: Numbers of events in the electron channel for data and prediction as well as the ratio of data to expectation and the fraction of multijet events in different analysis bins. If ranges of mass, rapidity or transverse momentum are not explicitly given, they are assumed to be inclusive.

Region	Data	Signal	Non-Fiducial	Top+EW	Multijet	Data/Exp.	MJ Fraction
Inclusive	6.042×10^{7}	5.706×10^{7}	377633	214830	309522	1.04	5.1×10^{-3}
$0 - 6500.0$ GeV, $0 - 0.4$	1.556×10^{7}	1.465×10^{7}	89060.6	62390.6	68775.7	1.05	4.4×10^{-3}
$0 - 6500.0$ GeV, $0.4 - 0.8$	1.403×10^{7}	1.321×10^{7}	85034.6	55132.1	66181.7	1.05	4.7×10^{-3}
$0 - 6500.0$ GeV, $0.8 - 1.2$	1.240×10^{7}	1.172×10^{7}	81341.8	43902.7	72466.3	1.04	5.8×10^{-3}
$0 - 6500.0$ GeV, $1.2 - 1.6$	1.001×10^{7}	9.510×10^{6}	66298.7	30263.3	52303.7	1.04	5.2×10^{-3}
$0 - 6500.0$ GeV, $1.6 - 2.0$	6.070×10^{6}	5.733×10^{6}	41474.2	17314.9	33468.1	1.04	5.5×10^{-3}
$0 - 6500.0$ GeV, $2.0 - 2.4$	2.353×10^{6}	2.239×10^{6}	14423.5	5826.47	16326.4	1.03	6.9×10^{-3}
$0 - 2.0$ GeV	2.351×10^{6}	2.298×10^{6}	13079.6	2093.04	1621.6	1.02	6.9×10^{-4}
$0 - 2.0$ GeV, $0 - 0.4$	6.102×10^{5}	5.827×10^{5}	3085.11	613.315	373.511	1.04	6.1×10^{-4}
$0 - 2.0$ GeV, $0.4 - 0.8$	5.448×10^{5}	5.224×10^{5}	2969.97	530.073	505.433	1.03	9.3×10^{-4}
$0 - 2.0$ GeV, $0.8 - 1.2$	4.937×10^{5}	4.816×10^{5}	2851.18	460.886	489.944	1.02	9.9×10^{-4}
$0 - 2.0$ GeV, $1.2 - 1.6$	3.937×10^{5}	3.950×10^{5}	2328.49	310.327	253.338	0.989	6.4×10^{-4}
$0 - 2.0$ GeV, $1.6 - 2.0$	2.193×10^{5}	2.233×10^{5}	1333.34	131.104	124.836	0.975	5.7×10^{-4}
$0 - 2.0$ GeV, $2.0 - 2.4$	8.892×10^{4}	9.323×10^{4}	511.551	47.3354	625.29	0.942	7.0×10^{-3}
$2.0 - 4.0$ GeV	5.377×10^{6}	5.297×10^{6}	30659.9	2694.97	4437	1.01	8.3×10^{-4}
$2.0 - 4.0$ GeV, $0 - 0.4$	1.391×10^{6}	1.348×10^{6}	7300.6	736.388	2226.7	1.02	1.6×10^{-3}
$2.0 - 4.0$ GeV, $0.4 - 0.8$	1.241×10^{6}	1.205×10^{6}	6940.42	678.29	1132.51	1.02	9.1×10^{-4}
$2.0 - 4.0$ GeV, $0.8 - 1.2$	1.125×10^{6}	1.109×10^{6}	6693.81	596.281	1004.42	1.01	8.9×10^{-4}
$2.0 - 4.0$ GeV, $1.2 - 1.6$	9.089×10^{5}	9.111×10^{5}	5430.93	411.019	552.619	0.991	6.1×10^{-4}
$2.0 - 4.0$ GeV, $1.6 - 2.0$	5.081×10^{5}	5.147×10^{5}	3159.83	194.942	457.799	0.980	9.0×10^{-4}
$2.0 - 4.0$ GeV, $2.0 - 2.4$	2.022×10^{5}	2.094×10^{5}	1134.27	78.0517	469.97	0.958	2.3×10^{-3}
$4.0 - 6.0$ GeV	6.023×10^{6}	5.883×10^{6}	35643.5	2785.34	6613.19	1.02	1.1×10^{-3}
$4.0 - 6.0$ GeV, $0 - 0.4$	1.552×10^{6}	1.501×10^{6}	8401.52	770.892	1660.86	1.03	1.1×10^{-3}
$4.0 - 6.0$ GeV, $0.4 - 0.8$	1.385×10^{6}	1.342×10^{6}	8038.84	665.752	1417.71	1.02	1.0×10^{-3}
$4.0 - 6.0$ GeV, $0.8 - 1.2$	1.259×10^{6}	1.231×10^{6}	7828.17	599.28	1870.35	1.01	1.5×10^{-3}
$4.0 - 6.0$ GeV, $1.2 - 1.6$	1.022×10^{6}	1.011×10^{6}	6390.92	421.197	1120.79	1.00	1.1×10^{-3}
$4.0 - 6.0$ GeV, $1.6 - 2.0$	5.786×10^{5}	5.722×10^{5}	3715.23	247.171	538.579	1.00	9.3×10^{-4}
$4.0 - 6.0$ GeV, $2.0 - 2.4$	2.250×10^{5}	2.258×10^{5}	1268.83	81.0465	44.8692	0.990	2.0×10^{-4}
$6.0 - 8.0$ GeV	5.555×10^{6}	5.340×10^{6}	33936.7	2854.85	7934.92	1.03	1.4×10^{-3}
$6.0 - 8.0$ GeV, $0 - 0.4$	1.431×10^{6}	1.365×10^{6}	8030.58	789.723	1911.74	1.04	1.3×10^{-3}
$6.0 - 8.0$ GeV, $0.4 - 0.8$	1.277×10^{6}	1.219×10^{6}	7643.74	701.32	2251.76	1.04	1.8×10^{-3}
$6.0 - 8.0$ GeV, $0.8 - 1.2$	1.157×10^{6}	1.114×10^{6}	7440.75	587.067	2021.11	1.03	1.7×10^{-3}
$6.0 - 8.0$ GeV, $1.2 - 1.6$	9.462×10^{5}	9.186×10^{5}	6029.84	463.264	1935.18	1.02	2.0×10^{-3}
$6.0 - 8.0$ GeV, $1.6 - 2.0$	5.374×10^{5}	5.216×10^{5}	3565.05	224.143	755.874	1.02	1.4×10^{-3}
$6.0 - 8.0$ GeV, $2.0 - 2.4$	2.059×10^{5}	2.013×10^{5}	1226.77	89.3365	141.143	1.02	6.9×10^{-4}
$8.0 - 11.4$ GeV	7.783×10^{6}	7.372×10^{6}	48902.1	5388.67	15795.7	1.05	2.0×10^{-3}
$8.0 - 11.4$ GeV, $0 - 0.4$	2.004×10^{6}	1.892×10^{6}	11590.4	1515.75	3984.28	1.05	2.0×10^{-3}
$8.0 - 11.4$ GeV, $0.4 - 0.8$	1.787×10^{6}	1.688×10^{6}	10932.8	1287.27	3494.48	1.05	2.0×10^{-3}
$8.0 - 11.4$ GeV, $0.8 - 1.2$	1.614×10^{6}	1.530×10^{6}	10727.6	1107.43	3937.54	1.04	2.4×10^{-3}
$8.0 - 11.4$ GeV, $1.2 - 1.6$	1.327×10^{6}	1.265×10^{6}	8784.82	859.567	2583.91	1.04	1.9×10^{-3}
$8.0 - 11.4$ GeV, $1.6 - 2.0$	7.609×10^{5}	7.210×10^{5}	5144.52	457.342	1066.63	1.05	1.4×10^{-3}
$8.0 - 11.4$ GeV, $2.0 - 2.4$	2.893×10^{5}	2.748×10^{5}	1721.94	161.311	745.45	1.04	2.6×10^{-3}
$11.4 - 14.9$ GeV	6.097×10^{6}	5.745×10^{6}	39679.6	6285.13	17909.9	1.05	2.9×10^{-3}
$11.4 - 14.9$ GeV, $0 - 0.4$	1.571×10^{6}	1.481×10^{6}	9368.78	1762.85	4179.42	1.05	2.7×10^{-3}
$11.4 - 14.9$ GeV, $0.4 - 0.8$	1.404×10^{6}	1.322×10^{6}	8915.61	1539.01	3682.61	1.05	2.6×10^{-3}
$11.4 - 14.9$ GeV, $0.8 - 1.2$	1.253×10^{6}	1.182×10^{6}	8611.05	1283.13	3971.44	1.05	3.2×10^{-3}
$11.4 - 14.9$ GeV, $1.2 - 1.6$	1.036×10^{6}	9.800×10^{5}	7144.67	975.731	3274.62	1.05	3.2×10^{-3}
$11.4 - 14.9$ GeV, $1.6 - 2.0$	6.041×10^{5}	5.654×10^{5}	4222.41	532.862	1772.06	1.06	2.9×10^{-3}
$11.4 - 14.9$ GeV, $2.0 - 2.4$	2.284×10^{5}	2.141×10^{5}	1417.03	191.547	1033.52	1.05	4.5×10^{-3}
$14.9 - 18.5$ GeV	4.782×10^{6}	4.513×10^{6}	32160.1	7090	17799.9	1.05	3.7×10^{-3}
$14.9 - 18.5$ GeV, $0 - 0.4$	1.231×10^{6}	1.166×10^{6}	7634.79	1983.42	3752.39	1.04	3.0×10^{-3}
$14.9 - 18.5$ GeV, $0.4 - 0.8$	1.106×10^{6}	1.046×10^{6}	7233.39	1754.17	3693.92	1.04	3.3×10^{-3}
$14.9 - 18.5$ GeV, $0.8 - 1.2$	9.738×10^{5}	9.187×10^{5}	6823.88	1448.44	3675.98	1.05	3.8×10^{-3}
$14.9 - 18.5$ GeV, $1.2 - 1.6$	8.077×10^{5}	7.621×10^{5}	5749.29	1086.23	3212.33	1.05	4.0×10^{-3}
$14.9 - 18.5$ GeV, $1.6 - 2.0$	4.819×10^{5}	4.504×10^{5}	3530.34	608.331	2003.26	1.06	4.2×10^{-3}
$14.9 - 18.5$ GeV, $2.0 - 2.4$	1.814×10^{5}	1.699×10^{5}	1188.36	209.415	1462.05	1.05	8.1×10^{-3}
$18.5 - 22.0$ GeV	3.618×10^{6}	3.421×10^{6}	24455.3	7456.37	14396	1.04	4.0×10^{-3}
$18.5 - 22.0$ GeV, $0 - 0.4$	9.314×10^{5}	8.840×10^{5}	5768.17	2118.31	3347.52	1.04	3.6×10^{-3}
$18.5 - 22.0$ GeV, $0.4 - 0.8$	8.416×10^{5}	7.961×10^{5}	5515.48	1832.64	3063.09	1.04	3.6×10^{-3}
$18.5 - 22.0$ GeV, $0.8 - 1.2$	7.309×10^{5}	6.905×10^{5}	5206.52	1516.11	3006.45	1.04	4.1×10^{-3}
$18.5 - 22.0$ GeV, $1.2 - 1.6$	6.043×10^{5}	5.712×10^{5}	4281.65	1112.14	2293.19	1.04	3.8×10^{-3}
$18.5 - 22.0$ GeV, $1.6 - 2.0$	3.695×10^{5}	3.479×10^{5}	2781.89	656.477	2158.46	1.05	5.8×10^{-3}
$18.5 - 22.0$ GeV, $2.0 - 2.4$	1.401×10^{5}	1.309×10^{5}	901.587	220.69	646.834	1.06	4.6×10^{-3}

22.0 − 25.5 GeV	2.876×10^6	2.720×10^6	19321.4	7869.22	12042.8	1.04	4.2×10^{-3}
22.0 − 25.5 GeV, 0 − 0.4	7.395×10^5	7.027×10^5	4571.58	2195.21	2699.31	1.04	3.7×10^{-3}
22.0 − 25.5 GeV, 0.4 − 0.8	6.714×10^5	6.366×10^5	4313.49	1965.77	1222.49	1.04	1.8×10^{-3}
22.0 − 25.5 GeV, 0.8 − 1.2	5.768×10^5	5.461×10^5	4120.6	1574.87	2070.82	1.04	3.6×10^{-3}
22.0 − 25.5 GeV, 1.2 − 1.6	4.754×10^5	4.488×10^5	3360.01	1203.96	2620.52	1.04	5.5×10^{-3}
22.0 − 25.5 GeV, 1.6 − 2.0	2.998×10^5	2.800×10^5	2204.67	695.951	2447.66	1.05	8.2×10^{-3}
22.0 − 25.5 GeV, 2.0 − 2.4	1.133×10^5	1.062×10^5	751.107	233.448	1028.62	1.05	9.1×10^{-3}
22.5 − 29.0 GeV	2.323×10^6	2.197×10^6	15550.7	8092.93	12383.4	1.04	5.3×10^{-3}
22.5 − 29.0 GeV, 0 − 0.4	5.957×10^5	5.673×10^5	3703.9	2279.86	2516.84	1.03	4.2×10^{-3}
22.5 − 29.0 GeV, 0.4 − 0.8	5.435×10^5	5.153×10^5	3489.93	2020.35	2485.54	1.04	4.6×10^{-3}
22.5 − 29.0 GeV, 0.8 − 1.2	4.648×10^5	4.388×10^5	3257.99	1612.7	3457.26	1.04	7.4×10^{-3}
22.5 − 29.0 GeV, 1.2 − 1.6	3.800×10^5	3.583×10^5	2709.86	1216.45	2093.26	1.04	5.5×10^{-3}
22.5 − 29.0 GeV, 1.6 − 2.0	2.456×10^5	2.296×10^5	1785.24	720.174	1329.73	1.05	5.4×10^{-3}
22.5 − 29.0 GeV, 2.0 − 2.4	9.317×10^4	8.750×10^4	603.751	243.392	863.754	1.04	9.3×10^{-3}
29.0 − 32.6 GeV	1.954×10^6	1.839×10^6	13075.9	8483.51	11538.9	1.04	5.9×10^{-3}
29.0 − 32.6 GeV, 0 − 0.4	5.012×10^5	4.740×10^5	3077.08	2410.59	2582.77	1.04	5.2×10^{-3}
29.0 − 32.6 GeV, 0.4 − 0.8	4.573×10^5	4.327×10^5	2899.6	2125.89	2598.01	1.04	5.7×10^{-3}
29.0 − 32.6 GeV, 0.8 − 1.2	3.904×10^5	3.670×10^5	2782.77	1688.81	2324.65	1.04	6.0×10^{-3}
29.0 − 32.6 GeV, 1.2 − 1.6	3.169×10^5	2.963×10^5	2258.59	1247.47	2403.49	1.05	7.6×10^{-3}
29.0 − 32.6 GeV, 1.6 − 2.0	2.080×10^5	1.943×10^5	1513.35	751.889	1725.86	1.05	8.3×10^{-3}
29.0 − 32.6 GeV, 2.0 − 2.4	7.983×10^4	7.472×10^4	544.464	258.857	0	1.06	0.
32.6 − 36.4 GeV	1.686×10^6	1.587×10^6	11133.1	9104	16409.2	1.04	9.7×10^{-3}
32.6 − 36.4 GeV, 0 − 0.4	4.328×10^5	4.087×10^5	2619.56	2605.75	3175.2	1.04	7.3×10^{-3}
32.6 − 36.4 GeV, 0.4 − 0.8	3.961×10^5	3.741×10^5	2518.7	2294.86	3268.67	1.04	8.3×10^{-3}
32.6 − 36.4 GeV, 0.8 − 1.2	3.375×10^5	3.168×10^5	2331.76	1826.3	3822.68	1.04	1.1×10^{-2}
32.6 − 36.4 GeV, 1.2 − 1.6	2.685×10^5	2.523×10^5	1886.13	1325.03	2696.26	1.04	1.0×10^{-2}
32.6 − 36.4 GeV, 1.6 − 2.0	1.808×10^5	1.689×10^5	1302.69	778.767	2131.23	1.04	1.2×10^{-2}
32.6 − 36.4 GeV, 2.0 − 2.4	7.065×10^4	6.607×10^4	474.274	273.304	1377.05	1.04	1.9×10^{-2}
36.4 − 40.4 GeV	1.457×10^6	1.363×10^6	9506.23	9519.54	17199	1.04	1.2×10^{-2}
36.4 − 40.4 GeV, 0 − 0.4	3.724×10^5	3.503×10^5	2177.67	2715.03	3536.46	1.04	9.5×10^{-3}
36.4 − 40.4 GeV, 0.4 − 0.8	3.428×10^5	3.222×10^5	2154.07	2418.88	3368.01	1.04	9.8×10^{-3}
36.4 − 40.4 GeV, 0.8 − 1.2	2.921×10^5	2.725×10^5	2004.74	1949.74	4413.63	1.04	1.5×10^{-2}
36.4 − 40.4 GeV, 1.2 − 1.6	2.294×10^5	2.138×10^5	1603.89	1349.33	3448.83	1.04	1.5×10^{-2}
36.4 − 40.4 GeV, 1.6 − 2.0	1.577×10^5	1.460×10^5	1158.99	804.355	1705.93	1.05	1.1×10^{-2}
36.4 − 40.4 GeV, 2.0 − 2.4	6.272×10^4	5.813×10^4	406.877	282.207	872.816	1.05	1.4×10^{-2}
40.4 − 44.9 GeV	1.337×10^6	1.242×10^6	8660.11	10440.6	20553	1.04	1.5×10^{-2}
40.4 − 44.9 GeV, 0 − 0.4	3.415×10^5	3.196×10^5	2019.3	2992.49	4676.01	1.04	1.4×10^{-2}
40.4 − 44.9 GeV, 0.4 − 0.8	3.158×10^5	2.943×10^5	1954.27	2670.76	4679.34	1.04	1.5×10^{-2}
40.4 − 44.9 GeV, 0.8 − 1.2	2.682×10^5	2.496×10^5	1799.1	2110.86	4928.38	1.04	1.8×10^{-2}
40.4 − 44.9 GeV, 1.2 − 1.6	2.078×10^5	1.913×10^5	1460.02	1475.77	3425.19	1.05	1.6×10^{-2}
40.4 − 44.9 GeV, 1.6 − 2.0	1.445×10^5	1.332×10^5	1046.15	880.406	2083.9	1.05	1.4×10^{-2}
40.4 − 44.9 GeV, 2.0 − 2.4	5.896×10^4	5.439×10^4	381.27	310.284	824.462	1.05	1.4×10^{-2}
44.9 − 50.2 GeV	1.257×10^6	1.159×10^6	7985.66	12008.1	22837.8	1.05	1.8×10^{-2}
44.9 − 50.2 GeV, 0 − 0.4	3.212×10^5	2.983×10^5	1850.76	3486.74	5450.14	1.04	1.7×10^{-2}
44.9 − 50.2 GeV, 0.4 − 0.8	2.982×10^5	2.767×10^5	1822.03	3091.04	5188.38	1.04	1.7×10^{-2}
44.9 − 50.2 GeV, 0.8 − 1.2	2.537×10^5	2.338×10^5	1703.26	2461.33	5210.61	1.04	2.1×10^{-2}
44.9 − 50.2 GeV, 1.2 − 1.6	1.917×10^5	1.752×10^5	1339.84	1665.93	3236.03	1.06	1.7×10^{-2}
44.9 − 50.2 GeV, 1.6 − 2.0	1.359×10^5	1.234×10^5	932.478	965.759	2723.26	1.06	2.0×10^{-2}
44.9 − 50.2 GeV, 2.0 − 2.4	5.650×10^4	5.161×10^4	337.292	337.281	1029.37	1.06	1.8×10^{-2}
50.2 − 56.4 GeV	1.146×10^6	1.043×10^6	7186.72	13341.3	21716.1	1.06	1.9×10^{-2}
50.2 − 56.4 GeV, 0 − 0.4	2.926×10^5	2.688×10^5	1668.08	3834.85	4429.97	1.05	1.5×10^{-2}
50.2 − 56.4 GeV, 0.4 − 0.8	2.726×10^5	2.499×10^5	1654.09	3523.13	4999.2	1.05	1.8×10^{-2}
50.2 − 56.4 GeV, 0.8 − 1.2	2.335×10^5	2.121×10^5	1531.3	2748.35	4342.66	1.06	1.9×10^{-2}
50.2 − 56.4 GeV, 1.2 − 1.6	1.720×10^5	1.547×10^5	1162.33	1804.17	4440.06	1.06	2.6×10^{-2}
50.2 − 56.4 GeV, 1.6 − 2.0	1.232×10^5	1.106×10^5	848.777	1051.32	2274.39	1.07	1.8×10^{-2}
50.2 − 56.4 GeV, 2.0 − 2.4	5.205×10^4	4.711×10^4	322.135	379.5	1445.11	1.06	2.8×10^{-2}
56.4 − 63.9 GeV	1.037×10^6	9.333×10^5	6376.72	14867.1	18240.7	1.07	1.8×10^{-2}
56.4 − 63.9 GeV, 0 − 0.4	2.661×10^5	2.410×10^5	1466.63	4365.49	3861.81	1.06	1.5×10^{-2}
56.4 − 63.9 GeV, 0.4 − 0.8	2.473×10^5	2.242×10^5	1456.64	3878.57	4488.4	1.06	1.8×10^{-2}
56.4 − 63.9 GeV, 0.8 − 1.2	2.124×10^5	1.909×10^5	1369.11	3106.46	5317.62	1.06	2.5×10^{-2}
56.4 − 63.9 GeV, 1.2 − 1.6	1.535×10^5	1.371×10^5	1040.1	1989.71	2448.37	1.08	1.6×10^{-2}
56.4 − 63.9 GeV, 1.6 − 2.0	1.104×10^5	9.791×10^4	753.582	1136.76	1155.61	1.09	1.0×10^{-2}
56.4 − 63.9 GeV, 2.0 − 2.4	4.703×10^4	4.210×10^4	290.663	390.069	1146.75	1.07	2.4×10^{-2}
63.9 − 73.4 GeV	9.353×10^5	8.229×10^5	5704.8	16500.6	17190.2	1.08	1.8×10^{-2}
63.9 − 73.4 GeV, 0 − 0.4	2.417×10^5	2.132×10^5	1347.68	4923.89	3773.39	1.08	1.6×10^{-2}
63.9 − 73.4 GeV, 0.4 − 0.8	2.229×10^5	1.968×10^5	1300.54	4340.7	3774.58	1.08	1.7×10^{-2}
63.9 − 73.4 GeV, 0.8 − 1.2	1.921×10^5	1.693×10^5	1196.59	3428.98	4814.87	1.07	2.5×10^{-2}
63.9 − 73.4 GeV, 1.2 − 1.6	1.397×10^5	1.219×10^5	926.002	2219.95	2682.19	1.09	1.9×10^{-2}
63.9 − 73.4 GeV, 1.6 − 2.0	9.771×10^4	8.538×10^4	661.755	1181.67	1572.94	1.10	1.6×10^{-2}
63.9 − 73.4 GeV, 2.0 − 2.4	4.115×10^4	3.634×10^4	272.237	405.414	883.862	1.09	2.1×10^{-2}
73.4 − 85.4 GeV	7.931×10^5	6.789×10^5	4682.35	17109.4	16296.1	1.11	2.1×10^{-2}
73.4 − 85.4 GeV, 0 − 0.4	2.052×10^5	1.761×10^5	1087.67	5152.72	3860.16	1.10	1.9×10^{-2}
73.4 − 85.4 GeV, 0.4 − 0.8	1.882×10^5	1.614×10^5	1077.39	4466.08	3556.44	1.10	1.9×10^{-2}
73.4 − 85.4 GeV, 0.8 − 1.2	1.625×10^5	1.393×10^5	995.207	3530.94	3282.8	1.10	2.0×10^{-2}
73.4 − 85.4 GeV, 1.2 − 1.6	1.214×10^5	1.030×10^5	753.505	2348.13	2986.06	1.11	2.5×10^{-2}
73.4 − 85.4 GeV, 1.6 − 2.0	8.253×10^4	7.042×10^4	561.116	1219.01	1789.96	1.12	2.2×10^{-2}
73.4 − 85.4 GeV, 2.0 − 2.4	3.320×10^4	2.872×10^4	207.461	392.535	843.504	1.10	2.5×10^{-2}
85.4 − 105.0 GeV	7.835×10^5	6.498×10^5	4335.28	19632.9	14813.8	1.14	1.9×10^{-2}
85.4 − 105.0 GeV, 0 − 0.4	2.027×10^5	1.685×10^5	996.674	5972.37	3894.62	1.13	1.9×10^{-2}
85.4 − 105.0 GeV, 0.4 − 0.8	1.852×10^5	1.539×10^5	971.053	5090.26	4178.56	1.13	2.3×10^{-2}

$85.4 - 105.0$ GeV, $0.8 - 1.2$	1.586×10^{5}	1.318×10^{5}	912.111	3999.13	2434.7	1.14	1.5×10^{-2}
$85.4 - 105.0$ GeV, $1.2 - 1.6$	1.219×10^{5}	1.000×10^{5}	725.687	2665.15	1993.44	1.16	1.6×10^{-2}
$85.4 - 105.0$ GeV, $1.6 - 2.0$	8.363×10^{4}	6.913×10^{4}	527.182	1469.45	1852.5	1.15	2.2×10^{-2}
$85.4 - 105.0$ GeV, $2.0 - 2.4$	3.154×10^{4}	2.641×10^{4}	202.576	436.508	483.295	1.15	1.5×10^{-2}
$105.0 - 132.0$ GeV	5.659×10^{5}	4.497×10^{5}	2763.71	14590.5	11111.3	1.18	2.0×10^{-2}
$105.0 - 132.0$ GeV, $0 - 0.4$	1.458×10^{5}	1.158×10^{5}	633.899	4335.37	2917.95	1.18	2.0×10^{-2}
$105.0 - 132.0$ GeV, $0.4 - 0.8$	1.344×10^{5}	1.069×10^{5}	609.63	3850.64	2422.44	1.18	1.8×10^{-2}
$105.0 - 132.0$ GeV, $0.8 - 1.2$	1.120×10^{5}	8.908×10^{4}	575.552	2904.18	2874.98	1.17	2.6×10^{-2}
$105.0 - 132.0$ GeV, $1.2 - 1.6$	8.841×10^{4}	6.974×10^{4}	464.715	2006.73	1574.28	1.20	1.8×10^{-2}
$105.0 - 132.0$ GeV, $1.6 - 2.0$	6.288×10^{4}	4.997×10^{4}	356.499	1164.08	722.339	1.20	1.1×10^{-2}
$105.0 - 132.0$ GeV, $2.0 - 2.4$	2.241×10^{4}	1.824×10^{4}	123.413	329.493	622.832	1.16	2.8×10^{-2}
$132.0 - 173.0$ GeV	3.793×10^{5}	2.884×10^{5}	1688.7	8958.81	4607.17	1.25	1.2×10^{-2}
$132.0 - 173.0$ GeV, $0 - 0.4$	9.706×10^{4}	7.366×10^{4}	394.155	2620.8	558.948	1.26	5.8×10^{-3}
$132.0 - 173.0$ GeV, $0.4 - 0.8$	8.982×10^{4}	6.879×10^{4}	373.583	2332.22	313.229	1.25	3.5×10^{-3}
$132.0 - 173.0$ GeV, $0.8 - 1.2$	7.435×10^{4}	5.668×10^{4}	341.479	1787.71	1795.79	1.23	2.4×10^{-2}
$132.0 - 173.0$ GeV, $1.2 - 1.6$	5.831×10^{4}	4.368×10^{4}	279.876	1195.24	920.789	1.27	1.6×10^{-2}
$132.0 - 173.0$ GeV, $1.6 - 2.0$	4.404×10^{4}	3.329×10^{4}	217.03	780.996	667.966	1.26	1.5×10^{-2}
$132.0 - 173.0$ GeV, $2.0 - 2.4$	1.575×10^{4}	1.228×10^{4}	82.5787	241.839	355.653	1.22	2.3×10^{-2}
$173.0 - 253.0$ GeV	2.233×10^{5}	1.605×10^{5}	872.188	5160.63	5154.08	1.30	2.3×10^{-2}
$173.0 - 253.0$ GeV, $0 - 0.4$	5.683×10^{4}	4.091×10^{4}	197.639	1458.02	1052.61	1.30	1.9×10^{-2}
$173.0 - 253.0$ GeV, $0.4 - 0.8$	5.391×10^{4}	3.915×10^{4}	182.226	1381.05	973.972	1.29	1.8×10^{-2}
$173.0 - 253.0$ GeV, $0.8 - 1.2$	4.504×10^{4}	3.229×10^{4}	187.017	1042.7	1078.6	1.30	2.4×10^{-2}
$173.0 - 253.0$ GeV, $1.2 - 1.6$	3.183×10^{4}	2.270×10^{4}	144.548	653.768	1247.33	1.29	3.9×10^{-2}
$173.0 - 253.0$ GeV, $1.6 - 2.0$	2.535×10^{4}	1.815×10^{4}	119.054	460.995	744.096	1.30	2.9×10^{-2}
$173.0 - 253.0$ GeV, $2.0 - 2.4$	1.029×10^{4}	7.298×10^{3}	41.7039	164.091	57.4771	1.36	5.6×10^{-3}
$253.0 - 400.0$ GeV	6.989×10^{4}	4.766×10^{4}	238.578	1973.12	564.597	1.39	8.1×10^{-3}
$253.0 - 400.0$ GeV, $0 - 0.4$	1.826×10^{4}	1.242×10^{4}	57.8218	582.321	0	1.40	0.
$253.0 - 400.0$ GeV, $0.4 - 0.8$	1.768×10^{4}	1.215×10^{4}	58.0318	532.317	0	1.39	0.
$253.0 - 400.0$ GeV, $0.8 - 1.2$	1.489×10^{4}	1.019×10^{4}	45.8721	417.943	460.45	1.34	3.1×10^{-2}
$253.0 - 400.0$ GeV, $1.2 - 1.6$	8.346×10^{3}	5.718×10^{3}	37.3108	213.063	209.409	1.35	2.5×10^{-2}
$253.0 - 400.0$ GeV, $1.6 - 2.0$	7.598×10^{3}	5.025×10^{3}	28.7782	167.927	116.396	1.42	1.5×10^{-2}
$253.0 - 400.0$ GeV, $2.0 - 2.4$	3.128×10^{3}	2.152×10^{3}	10.7639	59.5471	121.456	1.33	3.9×10^{-2}
$400.0 - 6500.0$ GeV	1.251×10^{4}	8.248×10^{3}	34.5641	529.484	738.677	1.31	5.9×10^{-2}
$400.0 - 6500.0$ GeV, $0 - 0.4$	3.562×10^{3}	2.402×10^{3}	10.5619	168.495	212.252	1.28	6.0×10^{-2}
$400.0 - 6500.0$ GeV, $0.4 - 0.8$	3.471×10^{3}	2.315×10^{3}	9.04223	161.022	0	1.40	0.
$400.0 - 6500.0$ GeV, $0.8 - 1.2$	2.819×10^{3}	1.854×10^{3}	4.36332	113.056	489.894	1.15	1.7×10^{-1}
$400.0 - 6500.0$ GeV, $1.2 - 1.6$	1.178×10^{3}	7.576×10^{2}	5.70995	43.9446	0	1.46	0.
$400.0 - 6500.0$ GeV, $1.6 - 2.0$	1.121×10^{3}	6.869×10^{2}	4.25624	32.9983	65.1329	1.42	5.8×10^{-2}
$400.0 - 6500.0$ GeV, $2.0 - 2.4$	3.610×10^{2}	2.322×10^{2}	0.630443	9.96738	0	1.49	0.

Tab. D.2.: Numbers of events in the muon channel for data and prediction as well as the ratio of data to expectation in different analysis bins. If ranges of mass, rapidity or transverse momentum are not explicitly given, they are assumed to be inclusive.

Region ($p_{T,ll}, y_{ll}$)	Data	Signal	Non-Fiducial	Top+EW	Data/Exp.
Inclusive	8.407×10^{7}	8.109×10^{7}	505692	266785	1.03
$0 - 6500.0$ GeV, $0 - 0.4$	1.715×10^{7}	1.658×10^{7}	93358.7	62081.7	1.02
$0 - 6500.0$ GeV, $0.4 - 0.8$	1.768×10^{7}	1.707×10^{7}	99722	61634.2	1.03
$0 - 6500.0$ GeV, $0.8 - 1.2$	1.805×10^{7}	1.744×10^{7}	107730	57886.3	1.02
$0 - 6500.0$ GeV, $1.2 - 1.6$	1.634×10^{7}	1.574×10^{7}	103785	47354.7	1.03
$0 - 6500.0$ GeV, $1.6 - 2.0$	1.110×10^{7}	1.065×10^{7}	75198.3	28944.3	1.03
$0 - 6500.0$ GeV, $2.0 - 2.4$	3.766×10^{6}	3.604×10^{6}	25898.5	8883.94	1.04
$0 - 2.0$ GeV	3.446×10^{6}	3.447×10^{6}	17292.9	1159.64	0.994
$0 - 2.0$ GeV, $0 - 0.4$	7.463×10^{5}	7.310×10^{5}	3289.21	283.215	1.02
$0 - 2.0$ GeV, $0.4 - 0.8$	7.553×10^{5}	7.434×10^{5}	3546.58	287.337	1.01
$0 - 2.0$ GeV, $0.8 - 1.2$	7.518×10^{5}	7.510×10^{5}	3723.61	262.561	0.996
$0 - 2.0$ GeV, $1.2 - 1.6$	6.451×10^{5}	6.548×10^{5}	3470.54	195.07	0.980
$0 - 2.0$ GeV, $1.6 - 2.0$	4.109×10^{5}	4.232×10^{5}	2427.93	103.579	0.965
$0 - 2.0$ GeV, $2.0 - 2.4$	1.364×10^{5}	1.436×10^{5}	834.996	27.881	0.944
$2.0 - 4.0$ GeV	7.762×10^{6}	7.817×10^{6}	40549.1	2628.75	0.988
$2.0 - 4.0$ GeV, $0 - 0.4$	1.649×10^{6}	1.640×10^{6}	7611.42	623.37	1.00
$2.0 - 4.0$ GeV, $0.4 - 0.8$	1.683×10^{6}	1.676×10^{6}	8163.55	623.132	0.999
$2.0 - 4.0$ GeV, $0.8 - 1.2$	1.690×10^{6}	1.701×10^{6}	8767.57	574.24	0.988
$2.0 - 4.0$ GeV, $1.2 - 1.6$	1.473×10^{6}	1.497×10^{6}	8264.74	465.04	0.978
$2.0 - 4.0$ GeV, $1.6 - 2.0$	9.510×10^{5}	9.747×10^{5}	5772.17	252.643	0.970
$2.0 - 4.0$ GeV, $2.0 - 2.4$	3.156×10^{5}	3.283×10^{5}	1969.7	90.325	0.955
$4.0 - 6.0$ GeV	8.553×10^{6}	8.532×10^{6}	46797.6	3139.79	0.997
$4.0 - 6.0$ GeV, $0 - 0.4$	1.787×10^{6}	1.771×10^{6}	8772.39	709.104	1.00
$4.0 - 6.0$ GeV, $0.4 - 0.8$	1.833×10^{6}	1.816×10^{6}	9442.1	707.463	1.00
$4.0 - 6.0$ GeV, $0.8 - 1.2$	1.856×10^{6}	1.853×10^{6}	10083.2	669.227	0.996
$4.0 - 6.0$ GeV, $1.2 - 1.6$	1.646×10^{6}	1.649×10^{6}	9482.62	585.671	0.992
$4.0 - 6.0$ GeV, $1.6 - 2.0$	1.074×10^{6}	1.081×10^{6}	6718.82	360.682	0.987

$4.0 - 6.0$ GeV, $2.0 - 2.4$	3.577×10^5	3.623×10^5	2298.5	107.639	0.981
$6.0 - 8.0$ GeV	7.829×10^6	7.665×10^6	44400.4	3535.37	1.02
$6.0 - 8.0$ GeV, $0 - 0.4$	1.618×10^6	1.582×10^6	8284.04	782.467	1.02
$6.0 - 8.0$ GeV, $0.4 - 0.8$	1.664×10^6	1.624×10^6	8816.78	805.259	1.02
$6.0 - 8.0$ GeV, $0.8 - 1.2$	1.694×10^6	1.661×10^6	9503.58	793.316	1.01
$6.0 - 8.0$ GeV, $1.2 - 1.6$	1.520×10^6	1.491×10^6	9131.23	649.812	1.01
$6.0 - 8.0$ GeV, $1.6 - 2.0$	1.001×10^6	9.812×10^5	6454.98	386.147	1.01
$6.0 - 8.0$ GeV, $2.0 - 2.4$	3.329×10^5	3.264×10^5	2209.74	118.373	1.01
$8.0 - 11.4$ GeV	1.090×10^7	1.052×10^7	64313.6	6777.28	1.03
$8.0 - 11.4$ GeV, $0 - 0.4$	2.236×10^6	2.162×10^6	12077.6	1486.84	1.03
$8.0 - 11.4$ GeV, $0.4 - 0.8$	2.304×10^6	2.224×10^6	12710.8	1526.45	1.03
$8.0 - 11.4$ GeV, $0.8 - 1.2$	2.353×10^6	2.275×10^6	13914.9	1482.82	1.03
$8.0 - 11.4$ GeV, $1.2 - 1.6$	2.127×10^6	2.053×10^6	13228.9	1267.79	1.03
$8.0 - 11.4$ GeV, $1.6 - 2.0$	1.409×10^6	1.355×10^6	9257.51	758.99	1.03
$8.0 - 11.4$ GeV, $2.0 - 2.4$	4.671×10^5	4.474×10^5	3123.83	254.387	1.04
$11.4 - 14.9$ GeV	8.497×10^6	8.154×10^6	52675	8015.45	1.03
$11.4 - 14.9$ GeV, $0 - 0.4$	1.732×10^6	1.672×10^6	9867.01	1792.32	1.03
$11.4 - 14.9$ GeV, $0.4 - 0.8$	1.785×10^6	1.720×10^6	10421.7	1779.54	1.03
$11.4 - 14.9$ GeV, $0.8 - 1.2$	1.831×10^6	1.760×10^6	11290.3	1754.01	1.03
$11.4 - 14.9$ GeV, $1.2 - 1.6$	1.666×10^6	1.597×10^6	10841	1479.47	1.04
$11.4 - 14.9$ GeV, $1.6 - 2.0$	1.115×10^6	1.057×10^6	7663.78	928.172	1.05
$11.4 - 14.9$ GeV, $2.0 - 2.4$	3.689×10^5	3.478×10^5	2591.2	281.933	1.05
$14.9 - 18.5$ GeV	6.633×10^6	6.377×10^6	42825.9	9092.58	1.03
$14.9 - 18.5$ GeV, $0 - 0.4$	1.343×10^6	1.302×10^6	7934.1	2013.27	1.02
$14.9 - 18.5$ GeV, $0.4 - 0.8$	1.384×10^6	1.340×10^6	8420.86	2048.82	1.03
$14.9 - 18.5$ GeV, $0.8 - 1.2$	1.426×10^6	1.375×10^6	9227.7	1969.75	1.03
$14.9 - 18.5$ GeV, $1.2 - 1.6$	1.306×10^6	1.250×10^6	8767.83	1676.75	1.04
$14.9 - 18.5$ GeV, $1.6 - 2.0$	8.830×10^5	8.360×10^5	6396.64	1065.24	1.05
$14.9 - 18.5$ GeV, $2.0 - 2.4$	2.915×10^5	2.746×10^5	2078.8	318.759	1.05
$18.5 - 22.0$ GeV	4.987×10^6	4.806×10^6	32923.7	9534.51	1.03
$18.5 - 22.0$ GeV, $0 - 0.4$	1.003×10^6	9.758×10^5	6030.17	2113.12	1.02
$18.5 - 22.0$ GeV, $0.4 - 0.8$	1.035×10^6	1.005×10^6	6431.68	2146.32	1.02
$18.5 - 22.0$ GeV, $0.8 - 1.2$	1.071×10^6	1.035×10^6	7001.17	2067.98	1.03
$18.5 - 22.0$ GeV, $1.2 - 1.6$	9.803×10^5	9.405×10^5	6814.99	1744.66	1.03
$18.5 - 22.0$ GeV, $1.6 - 2.0$	6.739×10^5	6.400×10^5	4975.33	1119.4	1.04
$18.5 - 22.0$ GeV, $2.0 - 2.4$	2.237×10^5	2.104×10^5	1670.36	343.032	1.05
$22.0 - 25.5$ GeV	3.951×10^6	3.806×10^6	26056.9	10052.5	1.03
$22.0 - 25.5$ GeV, $0 - 0.4$	7.898×10^5	7.694×10^5	4771.47	2253.51	1.02
$22.0 - 25.5$ GeV, $0.4 - 0.8$	8.156×10^5	7.918×10^5	5102.68	2262.61	1.02
$22.0 - 25.5$ GeV, $0.8 - 1.2$	8.459×10^5	8.181×10^5	5545.61	2167.23	1.02
$22.0 - 25.5$ GeV, $1.2 - 1.6$	7.761×10^5	7.422×10^5	5398.49	1835.99	1.04
$22.0 - 25.5$ GeV, $1.6 - 2.0$	5.417×10^5	5.144×10^5	3905.56	1172.08	1.04
$22.0 - 25.5$ GeV, $2.0 - 2.4$	1.814×10^5	1.696×10^5	1333.12	361.103	1.06
$22.5 - 29.0$ GeV	3.174×10^6	3.058×10^6	20959.2	10346.5	1.03
$22.5 - 29.0$ GeV, $0 - 0.4$	6.328×10^5	6.159×10^5	3804.29	2310.7	1.02
$22.5 - 29.0$ GeV, $0.4 - 0.8$	6.521×10^5	6.331×10^5	4052.2	2313.23	1.02
$22.5 - 29.0$ GeV, $0.8 - 1.2$	6.777×10^5	6.549×10^5	4427.88	2242.46	1.02
$22.5 - 29.0$ GeV, $1.2 - 1.6$	6.213×10^5	5.958×10^5	4300.82	1907.06	1.03
$22.5 - 29.0$ GeV, $1.6 - 2.0$	4.410×10^5	4.186×10^5	3229.32	1199.45	1.04
$22.5 - 29.0$ GeV, $2.0 - 2.4$	1.494×10^5	1.399×10^5	1144.73	373.561	1.06
$29.0 - 32.6$ GeV	2.651×10^6	2.552×10^6	17467.1	10860.8	1.03
$29.0 - 32.6$ GeV, $0 - 0.4$	5.266×10^5	5.117×10^5	3182.73	2469.39	1.02
$29.0 - 32.6$ GeV, $0.4 - 0.8$	5.431×10^5	5.266×10^5	3378.24	2441.57	1.02
$29.0 - 32.6$ GeV, $0.8 - 1.2$	5.637×10^5	5.447×10^5	3659.53	2354.62	1.02
$29.0 - 32.6$ GeV, $1.2 - 1.6$	5.188×10^5	4.963×10^5	3582.11	1948.04	1.03
$29.0 - 32.6$ GeV, $1.6 - 2.0$	3.718×10^5	3.536×10^5	2727.99	1270.62	1.04
$29.0 - 32.6$ GeV, $2.0 - 2.4$	1.276×10^5	1.194×10^5	936.463	376.575	1.06
$32.6 - 36.4$ GeV	2.284×10^6	2.194×10^6	14791.9	11483.9	1.03
$32.6 - 36.4$ GeV, $0 - 0.4$	4.500×10^5	4.382×10^5	2654.17	2603.13	1.01
$32.6 - 36.4$ GeV, $0.4 - 0.8$	4.666×10^5	4.521×10^5	2865.77	2592.95	1.02
$32.6 - 36.4$ GeV, $0.8 - 1.2$	4.848×10^5	4.670×10^5	3124.29	2486.79	1.03
$32.6 - 36.4$ GeV, $1.2 - 1.6$	4.459×10^5	4.249×10^5	3037.95	2059.31	1.04
$32.6 - 36.4$ GeV, $1.6 - 2.0$	3.244×10^5	3.061×10^5	2310.43	1324.78	1.05
$32.6 - 36.4$ GeV, $2.0 - 2.4$	1.124×10^5	1.053×10^5	799.244	416.926	1.06
$36.4 - 40.4$ GeV	1.965×10^6	1.881×10^6	12615.8	11987.4	1.03
$36.4 - 40.4$ GeV, $0 - 0.4$	3.866×10^5	3.752×10^5	2291.28	2748.05	1.02
$36.4 - 40.4$ GeV, $0.4 - 0.8$	4.019×10^5	3.873×10^5	2459.16	2682.2	1.02
$36.4 - 40.4$ GeV, $0.8 - 1.2$	4.152×10^5	3.985×10^5	2629.05	2616.79	1.03
$36.4 - 40.4$ GeV, $1.2 - 1.6$	3.835×10^5	3.645×10^5	2586.79	2153.85	1.04
$36.4 - 40.4$ GeV, $1.6 - 2.0$	2.797×10^5	2.631×10^5	1942.9	1364.79	1.05
$36.4 - 40.4$ GeV, $2.0 - 2.4$	9.847×10^4	9.246×10^4	706.621	421.748	1.05
$40.4 - 44.9$ GeV	1.802×10^6	1.713×10^6	11650.4	13276.7	1.04
$40.4 - 44.9$ GeV, $0 - 0.4$	3.545×10^5	3.412×10^5	2126.69	3011.11	1.02
$40.4 - 44.9$ GeV, $0.4 - 0.8$	3.693×10^5	3.541×10^5	2243.78	3044.2	1.03
$40.4 - 44.9$ GeV, $0.8 - 1.2$	3.789×10^5	3.617×10^5	2402.84	2862.59	1.03
$40.4 - 44.9$ GeV, $1.2 - 1.6$	3.496×10^5	3.293×10^5	2395.42	2376.43	1.05
$40.4 - 44.9$ GeV, $1.6 - 2.0$	2.569×10^5	2.400×10^5	1834.36	1497.26	1.06
$40.4 - 44.9$ GeV, $2.0 - 2.4$	9.231×10^4	8.622×10^4	647.369	485.103	1.06
$44.9 - 50.2$ GeV	1.695×10^6	1.598×10^6	10914.2	15170.3	1.04
$44.9 - 50.2$ GeV, $0 - 0.4$	3.337×10^5	3.183×10^5	1962.22	3544.9	1.03

$44.9 - 50.2$ GeV, $0.4 - 0.8$	3.496×10^5	3.319×10^5	2122.14	3514.19	1.04
$44.9 - 50.2$ GeV, $0.8 - 1.2$	3.548×10^5	3.358×10^5	2254.14	3245.93	1.04
$44.9 - 50.2$ GeV, $1.2 - 1.6$	3.273×10^5	3.066×10^5	2216.09	2675.42	1.05
$44.9 - 50.2$ GeV, $1.6 - 2.0$	2.408×10^5	2.239×10^5	1719.31	1656.16	1.06
$44.9 - 50.2$ GeV, $2.0 - 2.4$	8.891×10^4	8.193×10^4	640.309	533.68	1.07
$50.2 - 56.4$ GeV	1.543×10^6	1.440×10^6	9832.37	16894.6	1.05
$50.2 - 56.4$ GeV, $0 - 0.4$	3.034×10^5	2.860×10^5	1731.48	3977.19	1.04
$50.2 - 56.4$ GeV, $0.4 - 0.8$	3.180×10^5	2.993×10^5	1889.43	3960.07	1.04
$50.2 - 56.4$ GeV, $0.8 - 1.2$	3.227×10^5	3.016×10^5	2028.64	3651.37	1.05
$50.2 - 56.4$ GeV, $1.2 - 1.6$	2.987×10^5	2.770×10^5	2030.22	2927.96	1.06
$50.2 - 56.4$ GeV, $1.6 - 2.0$	2.179×10^5	2.009×10^5	1567.76	1800.25	1.07
$50.2 - 56.4$ GeV, $2.0 - 2.4$	8.222×10^4	7.552×10^4	584.84	577.734	1.07
$56.4 - 63.9$ GeV	1.410×10^6	1.299×10^6	8827.48	18896.9	1.06
$56.4 - 63.9$ GeV, $0 - 0.4$	2.774×10^5	2.581×10^5	1577.87	4549.81	1.05
$56.4 - 63.9$ GeV, $0.4 - 0.8$	2.925×10^5	2.712×10^5	1740.69	4475.54	1.05
$56.4 - 63.9$ GeV, $0.8 - 1.2$	2.933×10^5	2.708×10^5	1857.89	4112.51	1.06
$56.4 - 63.9$ GeV, $1.2 - 1.6$	2.732×10^5	2.500×10^5	1770.27	3232.81	1.07
$56.4 - 63.9$ GeV, $1.6 - 2.0$	1.975×10^5	1.804×10^5	1362.61	1928.31	1.08
$56.4 - 63.9$ GeV, $2.0 - 2.4$	7.588×10^4	6.894×10^4	518.147	597.912	1.08
$63.9 - 73.4$ GeV	1.289×10^6	1.162×10^6	7912.71	21130.5	1.08
$63.9 - 73.4$ GeV, $0 - 0.4$	2.541×10^5	2.303×10^5	1416.51	5128.03	1.07
$63.9 - 73.4$ GeV, $0.4 - 0.8$	2.672×10^5	2.417×10^5	1546.88	5065.65	1.08
$63.9 - 73.4$ GeV, $0.8 - 1.2$	2.677×10^5	2.414×10^5	1612.46	4591.17	1.08
$63.9 - 73.4$ GeV, $1.2 - 1.6$	2.509×10^5	2.252×10^5	1642.07	3615.14	1.09
$63.9 - 73.4$ GeV, $1.6 - 2.0$	1.802×10^5	1.611×10^5	1236.37	2078.35	1.10
$63.9 - 73.4$ GeV, $2.0 - 2.4$	6.934×10^4	6.204×10^4	458.427	652.181	1.10
$73.4 - 85.4$ GeV	1.092×10^6	9.619×10^5	6779.54	21660.6	1.10
$73.4 - 85.4$ GeV, $0 - 0.4$	2.153×10^5	1.906×10^5	1207.48	5303.38	1.09
$73.4 - 85.4$ GeV, $0.4 - 0.8$	2.241×10^5	1.990×10^5	1339.77	5147.08	1.09
$73.4 - 85.4$ GeV, $0.8 - 1.2$	2.280×10^5	2.004×10^5	1395.94	4743.69	1.10
$73.4 - 85.4$ GeV, $1.2 - 1.6$	2.145×10^5	1.879×10^5	1412.62	3728.38	1.11
$73.4 - 85.4$ GeV, $1.6 - 2.0$	1.519×10^5	1.330×10^5	1013.06	2108.93	1.12
$73.4 - 85.4$ GeV, $2.0 - 2.4$	5.806×10^4	5.098×10^4	410.676	629.165	1.12
$85.4 - 105.0$ GeV	1.046×10^6	8.884×10^5	6482.7	24331.2	1.14
$85.4 - 105.0$ GeV, $0 - 0.4$	2.068×10^5	1.762×10^5	1125.66	5938.24	1.13
$85.4 - 105.0$ GeV, $0.4 - 0.8$	2.137×10^5	1.818×10^5	1250.11	5725.97	1.13
$85.4 - 105.0$ GeV, $0.8 - 1.2$	2.186×10^5	1.859×10^5	1342.7	5318.43	1.14
$85.4 - 105.0$ GeV, $1.2 - 1.6$	2.069×10^5	1.747×10^5	1347.91	4253	1.15
$85.4 - 105.0$ GeV, $1.6 - 2.0$	1.468×10^5	1.241×10^5	1039.37	2428.46	1.15
$85.4 - 105.0$ GeV, $2.0 - 2.4$	5.313×10^4	4.569×10^4	376.938	667.122	1.14
$105.0 - 132.0$ GeV	7.280×10^5	5.903×10^5	4337.51	17624.1	1.19
$105.0 - 132.0$ GeV, $0 - 0.4$	1.426×10^5	1.154×10^5	762.258	4171.79	1.18
$105.0 - 132.0$ GeV, $0.4 - 0.8$	1.477×10^5	1.204×10^5	811.093	4103.06	1.18
$105.0 - 132.0$ GeV, $0.8 - 1.2$	1.517×10^5	1.231×10^5	874.149	3805.24	1.19
$105.0 - 132.0$ GeV, $1.2 - 1.6$	1.436×10^5	1.162×10^5	917.443	3132.39	1.19
$105.0 - 132.0$ GeV, $1.6 - 2.0$	1.053×10^5	8.512×10^4	716.214	1885.12	1.20
$105.0 - 132.0$ GeV, $2.0 - 2.4$	3.719×10^4	3.001×10^4	256.357	526.459	1.21
$132.0 - 173.0$ GeV	4.706×10^5	3.658×10^5	2879.72	10491	1.24
$132.0 - 173.0$ GeV, $0 - 0.4$	9.042×10^4	6.981×10^4	483.627	2365.98	1.24
$132.0 - 173.0$ GeV, $0.4 - 0.8$	9.508×10^4	7.401×10^4	525.638	2377.55	1.24
$132.0 - 173.0$ GeV, $0.8 - 1.2$	9.688×10^4	7.556×10^4	590.7	2254.26	1.24
$132.0 - 173.0$ GeV, $1.2 - 1.6$	9.284×10^4	7.231×10^4	610.088	1893.93	1.24
$132.0 - 173.0$ GeV, $1.6 - 2.0$	7.021×10^4	5.444×10^4	499.321	1231.73	1.25
$132.0 - 173.0$ GeV, $2.0 - 2.4$	2.521×10^4	1.972×10^4	170.346	367.554	1.24
$173.0 - 253.0$ GeV	2.676×10^5	1.979×10^5	1717.6	5961.94	1.30
$173.0 - 253.0$ GeV, $0 - 0.4$	5.005×10^4	3.708×10^4	282.95	1285.61	1.30
$173.0 - 253.0$ GeV, $0.4 - 0.8$	5.445×10^4	4.031×10^4	312.159	1341.73	1.30
$173.0 - 253.0$ GeV, $0.8 - 1.2$	5.461×10^4	4.053×10^4	334.977	1267.34	1.30
$173.0 - 253.0$ GeV, $1.2 - 1.6$	5.218×10^4	3.859×10^4	377.908	1090.21	1.30
$173.0 - 253.0$ GeV, $1.6 - 2.0$	4.062×10^4	2.992×10^4	311.606	724.486	1.31
$173.0 - 253.0$ GeV, $2.0 - 2.4$	1.567×10^4	1.149×10^4	97.9985	252.577	1.32
$253.0 - 400.0$ GeV	8.043×10^4	5.619×10^4	564.913	2196.25	1.36
$253.0 - 400.0$ GeV, $0 - 0.4$	1.538×10^4	1.067×10^4	91.5525	479.848	1.37
$253.0 - 400.0$ GeV, $0.4 - 0.8$	1.711×10^4	1.203×10^4	100.731	517.756	1.35
$253.0 - 400.0$ GeV, $0.8 - 1.2$	1.661×10^4	1.160×10^4	111.671	473.128	1.36
$253.0 - 400.0$ GeV, $1.2 - 1.6$	1.525×10^4	1.072×10^4	128.182	380.004	1.36
$253.0 - 400.0$ GeV, $1.6 - 2.0$	1.160×10^4	7.964×10^3	97.0446	256.878	1.39
$253.0 - 400.0$ GeV, $2.0 - 2.4$	4.477×10^3	3.208×10^3	35.7317	88.6322	1.34
$400.0 - 6500.0$ GeV	1.341×10^4	9.027×10^3	124.231	536.6	1.38
$400.0 - 6500.0$ GeV, $0 - 0.4$	2.908×10^3	1.944×10^3	20.5102	137.296	1.38
$400.0 - 6500.0$ GeV, $0.4 - 0.8$	3.277×10^3	2.220×10^3	27.478	144.523	1.37
$400.0 - 6500.0$ GeV, $0.8 - 1.2$	2.812×10^3	1.960×10^3	25.8397	118.816	1.34
$400.0 - 6500.0$ GeV, $1.2 - 1.6$	2.442×10^3	1.574×10^3	28.4754	80.5489	1.45
$400.0 - 6500.0$ GeV, $1.6 - 2.0$	1.489×10^3	9.964×10^2	17.9002	41.8293	1.41
$400.0 - 6500.0$ GeV, $2.0 - 2.4$	4.770×10^2	3.334×10^2	4.02776	13.5864	1.36

E

Binning of 2D Collins-Soper Distributions

Tab. E.1.: Optimised bin boundaries in the Collins-Soper variables $\cos\theta_{\mathrm{CS}}$ and ϕ_{CS} for all bins used in the analysis.

Region ($p_{T,ll}$, y_{ll})	$\cos\theta_{\mathrm{CS}}$									ϕ_{CS}								
$0-2.0$ GeV, $0-0.4$	-1	-0.64	-0.46	-0.24	0	0.24	0.46	0.64	1	0	0.79	1.6	2.4	3.1	3.9	4.7	5.5	6.3
$0-2.0$ GeV, $0.4-0.8$	-1	-0.62	-0.41	-0.21	0	0.21	0.41	0.62	1	0	0.79	1.6	2.4	3.1	3.9	4.7	5.5	6.3
$0-2.0$ GeV, $0.8-1.2$	-1	-0.69	-0.50	-0.21	0	0.21	0.50	0.69	1	0	0.79	1.6	2.4	3.1	3.9	4.7	5.5	6.3
$0-2.0$ GeV, $1.2-1.6$	-1	-0.63	-0.49	-0.32	0	0.32	0.49	0.63	1	0	0.79	1.6	2.4	3.1	3.9	4.7	5.5	6.3
$0-2.0$ GeV, $1.6-2.0$	-1	-0.45	-0.28	-0.12	0	0.12	0.28	0.45	1	0	0.79	1.6	2.4	3.1	3.9	4.7	5.5	6.3
$0-2.0$ GeV, $2.0-2.4$	-1	-0.19	-0.11	-0.050	0	0.050	0.11	0.19	1	0	0.79	1.6	2.4	3.1	3.9	4.7	5.5	6.3
$2.0-4.0$ GeV, $0-0.4$	-1	-0.64	-0.46	-0.24	0	0.24	0.46	0.64	1	0	0.75	1.6	2.4	3.1	3.9	4.7	5.5	6.3
$2.0-4.0$ GeV, $0.4-0.8$	-1	-0.61	-0.41	-0.21	0	0.21	0.41	0.61	1	0	0.75	1.6	2.4	3.1	3.9	4.7	5.5	6.3
$2.0-4.0$ GeV, $0.8-1.2$	-1	-0.68	-0.49	-0.21	0	0.21	0.49	0.68	1	0	0.75	1.6	2.4	3.1	3.9	4.7	5.5	6.3
$2.0-4.0$ GeV, $1.2-1.6$	-1	-0.62	-0.48	-0.32	0	0.32	0.48	0.62	1	0	0.75	1.6	2.4	3.1	3.9	4.7	5.5	6.3
$2.0-4.0$ GeV, $1.6-2.0$	-1	-0.45	-0.28	-0.12	0	0.12	0.28	0.45	1	0	0.75	1.6	2.4	3.1	3.9	4.7	5.5	6.3
$2.0-4.0$ GeV, $2.0-2.4$	-1	-0.20	-0.12	-0.050	0	0.050	0.12	0.20	1	0	0.75	1.6	2.4	3.1	3.9	4.7	5.5	6.3
$4.0-6.0$ GeV, $0-0.4$	-1	-0.64	-0.46	-0.24	0	0.24	0.46	0.64	1	0	0.75	1.6	2.4	3.1	3.9	4.7	5.5	6.3

$4.0 - 6.0$ GeV, $0.4 - 0.8$	-1	-0.60	-0.41	-0.21	0	0.21	0.41	0.60	1	0	0.75	1.6	2.4	3.1	3.9	4.7	5.5	6.3
$4.0 - 6.0$ GeV, $0.8 - 1.2$	-1	-0.67	-0.48	-0.20	0	0.20	0.48	0.67	1	0	0.75	1.6	2.4	3.1	3.9	4.7	5.5	6.3
$4.0 - 6.0$ GeV, $1.2 - 1.6$	-1	-0.62	-0.48	-0.31	0	0.31	0.48	0.62	1	0	0.75	1.6	2.4	3.1	3.9	4.7	5.5	6.3
$4.0 - 6.0$ GeV, $1.6 - 2.0$	-1	-0.45	-0.28	-0.12	0	0.12	0.28	0.45	1	0	0.72	1.6	2.4	3.1	3.9	4.7	5.6	6.3
$4.0 - 6.0$ GeV, $2.0 - 2.4$	-1	-0.20	-0.12	-0.050	0	0.050	0.12	0.20	1	0	0.75	1.6	2.4	3.1	3.9	4.7	5.5	6.3
$6.0 - 8.0$ GeV, $0 - 0.4$	-1	-0.63	-0.45	-0.24	0	0.24	0.45	0.63	1	0	0.75	1.6	2.4	3.1	3.9	4.7	5.5	6.3
$6.0 - 8.0$ GeV, $0.4 - 0.8$	-1	-0.60	-0.40	-0.21	0	0.21	0.40	0.60	1	0	0.75	1.6	2.4	3.1	3.9	4.7	5.5	6.3
$6.0 - 8.0$ GeV, $0.8 - 1.2$	-1	-0.67	-0.47	-0.20	0	0.20	0.47	0.67	1	0	0.75	1.6	2.4	3.1	3.9	4.7	5.5	6.3
$6.0 - 8.0$ GeV, $1.2 - 1.6$	-1	-0.62	-0.47	-0.31	0	0.31	0.47	0.62	1	0	0.75	1.6	2.4	3.1	3.9	4.7	5.5	6.3
$6.0 - 8.0$ GeV, $1.6 - 2.0$	-1	-0.45	-0.28	-0.12	0	0.12	0.28	0.45	1	0	0.72	1.6	2.4	3.1	3.9	4.7	5.6	6.3
$6.0 - 8.0$ GeV, $2.0 - 2.4$	-1	-0.20	-0.12	-0.050	0	0.050	0.12	0.20	1	0	0.72	1.6	2.4	3.1	3.9	4.7	5.6	6.3
$8.0 - 11.4$ GeV, $0 - 0.4$	-1	-0.63	-0.44	-0.23	0	0.23	0.44	0.63	1	0	0.79	1.6	2.4	3.1	3.9	4.7	5.5	6.3
$8.0 - 11.4$ GeV, $0.4 - 0.8$	-1	-0.59	-0.39	-0.20	0	0.20	0.39	0.59	1	0	0.75	1.6	2.4	3.1	3.9	4.7	5.5	6.3
$8.0 - 11.4$ GeV, $0.8 - 1.2$	-1	-0.66	-0.45	-0.19	0	0.19	0.45	0.66	1	0	0.75	1.6	2.4	3.1	3.9	4.7	5.5	6.3
$8.0 - 11.4$ GeV, $1.2 - 1.6$	-1	-0.61	-0.47	-0.31	0	0.31	0.47	0.61	1	0	0.75	1.6	2.4	3.1	3.9	4.7	5.5	6.3
$8.0 - 11.4$ GeV, $1.6 - 2.0$	-1	-0.45	-0.28	-0.12	0	0.12	0.28	0.45	1	0	0.72	1.6	2.4	3.1	3.9	4.7	5.6	6.3
$8.0 - 11.4$ GeV, $2.0 - 2.4$	-1	-0.20	-0.12	-0.050	0	0.050	0.12	0.20	1	0	0.75	1.6	2.4	3.1	3.9	4.7	5.5	6.3
$11.4 - 14.9$ GeV, $0 - 0.4$	-1	-0.62	-0.44	-0.23	0	0.23	0.44	0.62	1	0	0.79	1.6	2.4	3.1	3.9	4.7	5.5	6.3
$11.4 - 14.9$ GeV, $0.4 - 0.8$	-1	-0.58	-0.39	-0.20	0	0.20	0.39	0.58	1	0	0.79	1.6	2.4	3.1	3.9	4.7	5.5	6.3
$11.4 - 14.9$ GeV, $0.8 - 1.2$	-1	-0.65	-0.43	-0.19	0	0.19	0.43	0.65	1	0	0.79	1.6	2.4	3.1	3.9	4.7	5.5	6.3
$11.4 - 14.9$ GeV, $1.2 - 1.6$	-1	-0.61	-0.46	-0.30	0	0.30	0.46	0.61	1	0	0.79	1.6	2.4	3.1	3.9	4.7	5.5	6.3
$11.4 - 14.9$ GeV, $1.6 - 2.0$	-1	-0.45	-0.28	-0.12	0	0.12	0.28	0.45	1	0	0.75	1.6	2.4	3.1	3.9	4.7	5.5	6.3
$11.4 - 14.9$ GeV, $2.0 - 2.4$	-1	-0.20	-0.12	-0.050	0	0.050	0.12	0.20	1	0	0.75	1.6	2.4	3.1	3.9	4.7	5.5	6.3
$14.9 - 18.5$ GeV, $0 - 0.4$	-1	-0.60	-0.42	-0.22	0	0.22	0.42	0.60	1	0	0.82	1.6	2.3	3.1	4.0	4.7	5.5	6.3

$14.9 - 18.5$ GeV, $0.4 - 0.8$	-1	-0.57	-0.38	-0.19	0	0.19	0.38	0.57	1	0	0.79	1.6	2.4	3.1	3.9	4.7	5.5	6.3
$14.9 - 18.5$ GeV, $0.8 - 1.2$	-1	-0.63	-0.42	-0.18	0	0.18	0.42	0.63	1	0	0.82	1.6	2.3	3.1	4.0	4.7	5.5	6.3
$14.9 - 18.5$ GeV, $1.2 - 1.6$	-1	-0.60	-0.46	-0.30	0	0.30	0.46	0.60	1	0	0.79	1.6	2.4	3.1	3.9	4.7	5.5	6.3
$14.9 - 18.5$ GeV, $1.6 - 2.0$	-1	-0.45	-0.28	-0.12	0	0.12	0.28	0.45	1	0	0.75	1.6	2.4	3.1	3.9	4.7	5.5	6.3
$14.9 - 18.5$ GeV, $2.0 - 2.4$	-1	-0.20	-0.12	-0.060	0	0.060	0.12	0.20	1	0	0.75	1.6	2.4	3.1	3.9	4.7	5.5	6.3
$18.5 - 22.0$ GeV, $0 - 0.4$	-1	-0.59	-0.41	-0.21	0	0.21	0.41	0.59	1	0	0.82	1.6	2.3	3.1	4.0	4.7	5.5	6.3
$18.5 - 22.0$ GeV, $0.4 - 0.8$	-1	-0.56	-0.37	-0.19	0	0.19	0.37	0.56	1	0	0.82	1.6	2.3	3.1	4.0	4.7	5.5	6.3
$18.5 - 22.0$ GeV, $0.8 - 1.2$	-1	-0.62	-0.40	-0.17	0	0.17	0.40	0.62	1	0	0.82	1.6	2.3	3.1	4.0	4.7	5.5	6.3
$18.5 - 22.0$ GeV, $1.2 - 1.6$	-1	-0.59	-0.45	-0.29	0	0.29	0.45	0.59	1	0	0.82	1.6	2.3	3.1	4.0	4.7	5.5	6.3
$18.5 - 22.0$ GeV, $1.6 - 2.0$	-1	-0.46	-0.28	-0.12	0	0.12	0.28	0.46	1	0	0.75	1.6	2.4	3.1	3.9	4.7	5.5	6.3
$18.5 - 22.0$ GeV, $2.0 - 2.4$	-1	-0.20	-0.12	-0.060	0	0.060	0.12	0.20	1	0	0.75	1.6	2.4	3.1	3.9	4.7	5.5	6.3
$22.0 - 25.5$ GeV, $0 - 0.4$	-1	-0.58	-0.40	-0.21	0	0.21	0.40	0.58	1	0	0.82	1.6	2.3	3.1	4.0	4.7	5.5	6.3
$22.0 - 25.5$ GeV, $0.4 - 0.8$	-1	-0.55	-0.36	-0.18	0	0.18	0.36	0.55	1	0	0.82	1.6	2.3	3.1	4.0	4.7	5.5	6.3
$22.0 - 25.5$ GeV, $0.8 - 1.2$	-1	-0.60	-0.38	-0.17	0	0.17	0.38	0.60	1	0	0.85	1.6	2.3	3.1	4.0	4.7	5.4	6.3
$22.0 - 25.5$ GeV, $1.2 - 1.6$	-1	-0.58	-0.44	-0.29	0	0.29	0.44	0.58	1	0	0.82	1.6	2.3	3.1	4.0	4.7	5.5	6.3
$22.0 - 25.5$ GeV, $1.6 - 2.0$	-1	-0.46	-0.28	-0.12	0	0.12	0.28	0.46	1	0	0.75	1.6	2.4	3.1	3.9	4.7	5.5	6.3
$22.0 - 25.5$ GeV, $2.0 - 2.4$	-1	-0.20	-0.12	-0.060	0	0.060	0.12	0.20	1	0	0.75	1.6	2.4	3.1	3.9	4.7	5.5	6.3
$22.5 - 29.0$ GeV, $0 - 0.4$	-1	-0.57	-0.39	-0.20	0	0.20	0.39	0.57	1	0	0.85	1.6	2.3	3.1	4.0	4.7	5.4	6.3
$22.5 - 29.0$ GeV, $0.4 - 0.8$	-1	-0.54	-0.36	-0.18	0	0.18	0.36	0.54	1	0	0.85	1.6	2.3	3.1	4.0	4.7	5.4	6.3
$22.5 - 29.0$ GeV, $0.8 - 1.2$	-1	-0.59	-0.37	-0.16	0	0.16	0.37	0.59	1	0	0.85	1.6	2.3	3.1	4.0	4.7	5.4	6.3
$22.5 - 29.0$ GeV, $1.2 - 1.6$	-1	-0.58	-0.43	-0.29	0	0.29	0.43	0.58	1	0	0.85	1.6	2.3	3.1	4.0	4.7	5.4	6.3
$22.5 - 29.0$ GeV, $1.6 - 2.0$	-1	-0.46	-0.27	-0.12	0	0.12	0.27	0.46	1	0	0.75	1.6	2.4	3.1	3.9	4.7	5.5	6.3
$22.5 - 29.0$ GeV, $2.0 - 2.4$	-1	-0.21	-0.12	-0.060	0	0.060	0.12	0.21	1	0	0.75	1.6	2.4	3.1	3.9	4.7	5.5	6.3
$29.0 - 32.6$ GeV, $0 - 0.4$	-1	-0.56	-0.38	-0.20	0	0.20	0.38	0.56	1	0	0.85	1.6	2.3	3.1	4.0	4.7	5.4	6.3

29.0 – 32.6 GeV, 0.4 – 0.8	−1	−0.53	−0.35	−0.17	0	0.17	0.35	0.53	1	0	0.85	1.6	2.3	3.1	4.0	4.7	5.4	6.3
29.0 – 32.6 GeV, 0.8 – 1.2	−1	−0.58	−0.35	−0.16	0	0.16	0.35	0.58	1	0	0.88	1.6	2.3	3.1	4.0	4.7	5.4	6.3
29.0 – 32.6 GeV, 1.2 – 1.6	−1	−0.57	−0.43	−0.28	0	0.28	0.43	0.57	1	0	0.88	1.6	2.3	3.1	4.0	4.7	5.4	6.3
29.0 – 32.6 GeV, 1.6 – 2.0	−1	−0.45	−0.27	−0.12	0	0.12	0.27	0.45	1	0	0.79	1.6	2.4	3.1	3.9	4.7	5.5	6.3
29.0 – 32.6 GeV, 2.0 – 2.4	−1	−0.21	−0.12	−0.060	0	0.060	0.12	0.21	1	0	0.75	1.6	2.4	3.1	3.9	4.7	5.5	6.3
32.6 – 36.4 GeV, 0 – 0.4	−1	−0.55	−0.37	−0.19	0	0.19	0.37	0.55	1	0	0.88	1.6	2.3	3.1	4.0	4.7	5.4	6.3
32.6 – 36.4 GeV, 0.4 – 0.8	−1	−0.52	−0.34	−0.17	0	0.17	0.34	0.52	1	0	0.85	1.6	2.3	3.1	4.0	4.7	5.4	6.3
32.6 – 36.4 GeV, 0.8 – 1.2	−1	−0.57	−0.34	−0.16	0	0.16	0.34	0.57	1	0	0.88	1.6	2.3	3.1	4.0	4.7	5.4	6.3
32.6 – 36.4 GeV, 1.2 – 1.6	−1	−0.56	−0.42	−0.27	0	0.27	0.42	0.56	1	0	0.88	1.6	2.3	3.1	4.0	4.7	5.4	6.3
32.6 – 36.4 GeV, 1.6 – 2.0	−1	−0.45	−0.27	−0.12	0	0.12	0.27	0.45	1	0	0.79	1.6	2.4	3.1	3.9	4.7	5.5	6.3
32.6 – 36.4 GeV, 2.0 – 2.4	−1	−0.21	−0.12	−0.060	0	0.060	0.12	0.21	1	0	0.75	1.6	2.4	3.1	3.9	4.7	5.5	6.3
36.4 – 40.4 GeV, 0 – 0.4	−1	−0.55	−0.37	−0.18	0	0.18	0.37	0.55	1	0	0.88	1.6	2.3	3.1	4.0	4.7	5.4	6.3
36.4 – 40.4 GeV, 0.4 – 0.8	−1	−0.52	−0.33	−0.17	0	0.17	0.33	0.52	1	0	0.88	1.6	2.3	3.1	4.0	4.7	5.4	6.3
36.4 – 40.4 GeV, 0.8 – 1.2	−1	−0.56	−0.33	−0.15	0	0.15	0.33	0.56	1	0	0.88	1.6	2.3	3.1	4.0	4.7	5.4	6.3
36.4 – 40.4 GeV, 1.2 – 1.6	−1	−0.56	−0.42	−0.27	0	0.27	0.42	0.56	1	0	0.91	1.6	2.2	3.1	4.1	4.7	5.4	6.3
36.4 – 40.4 GeV, 1.6 – 2.0	−1	−0.44	−0.26	−0.11	0	0.11	0.26	0.44	1	0	0.82	1.6	2.4	3.1	3.9	4.7	5.5	6.3
36.4 – 40.4 GeV, 2.0 – 2.4	−1	−0.21	−0.12	−0.060	0	0.060	0.12	0.21	1	0	0.75	1.6	2.4	3.1	3.9	4.7	5.5	6.3
40.4 – 44.9 GeV, 0 – 0.4	−1	−0.55	−0.36	−0.18	0	0.18	0.36	0.55	1	0	0.91	1.6	2.2	3.1	4.1	4.7	5.4	6.3
40.4 – 44.9 GeV, 0.4 – 0.8	−1	−0.52	−0.33	−0.16	0	0.16	0.33	0.52	1	0	0.91	1.6	2.2	3.1	4.1	4.7	5.4	6.3
40.4 – 44.9 GeV, 0.8 – 1.2	−1	−0.56	−0.33	−0.15	0	0.15	0.33	0.56	1	0	0.91	1.6	2.2	3.1	4.1	4.7	5.4	6.3
40.4 – 44.9 GeV, 1.2 – 1.6	−1	−0.56	−0.41	−0.26	0	0.26	0.41	0.56	1	0	0.94	1.6	2.2	3.1	4.1	4.7	5.3	6.3
40.4 – 44.9 GeV, 1.6 – 2.0	−1	−0.43	−0.25	−0.11	0	0.11	0.25	0.43	1	0	0.82	1.6	2.3	3.1	4.0	4.7	5.5	6.3
40.4 – 44.9 GeV, 2.0 – 2.4	−1	−0.21	−0.12	−0.060	0	0.060	0.12	0.21	1	0	0.79	1.6	2.4	3.1	3.9	4.7	5.5	6.3
44.9 – 50.2 GeV, 0 – 0.4	−1	−0.55	−0.35	−0.18	0	0.18	0.35	0.55	1	0	0.94	1.6	2.2	3.1	4.1	4.7	5.3	6.3

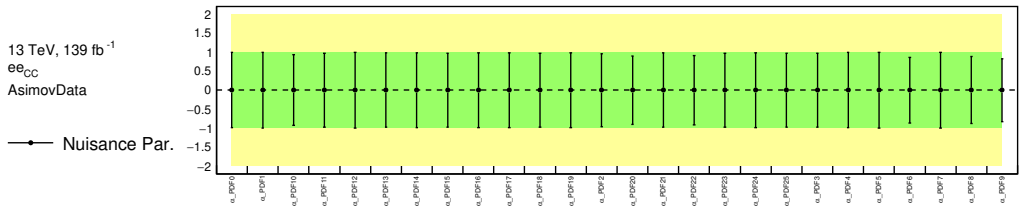
44.9 – 50.2 GeV, 0.4 – 0.8	−1	−0.52	−0.32	−0.16	0	0.16	0.32	0.52	1	0	0.94	1.6	2.2	3.1	4.1	4.7	5.3	6.3
44.9 – 50.2 GeV, 0.8 – 1.2	−1	−0.57	−0.32	−0.15	0	0.15	0.32	0.57	1	0	0.94	1.6	2.2	3.1	4.1	4.7	5.3	6.3
44.9 – 50.2 GeV, 1.2 – 1.6	−1	−0.57	−0.41	−0.26	0	0.26	0.41	0.57	1	0	0.97	1.6	2.2	3.1	4.1	4.7	5.3	6.3
44.9 – 50.2 GeV, 1.6 – 2.0	−1	−0.43	−0.25	−0.11	0	0.11	0.25	0.43	1	0	0.85	1.6	2.3	3.1	4.0	4.7	5.4	6.3
44.9 – 50.2 GeV, 2.0 – 2.4	−1	−0.21	−0.12	−0.060	0	0.060	0.12	0.21	1	0	0.79	1.6	2.4	3.1	3.9	4.7	5.5	6.3
50.2 – 56.4 GeV, 0 – 0.4	−1	−0.57	−0.35	−0.17	0	0.17	0.35	0.57	1	0	0.97	1.6	2.2	3.1	4.1	4.7	5.3	6.3
50.2 – 56.4 GeV, 0.4 – 0.8	−1	−0.54	−0.32	−0.16	0	0.16	0.32	0.54	1	0	0.94	1.6	2.2	3.1	4.1	4.7	5.3	6.3
50.2 – 56.4 GeV, 0.8 – 1.2	−1	−0.59	−0.32	−0.15	0	0.15	0.32	0.59	1	0	0.97	1.6	2.2	3.1	4.1	4.7	5.3	6.3
50.2 – 56.4 GeV, 1.2 – 1.6	−1	−0.59	−0.41	−0.25	0	0.25	0.41	0.59	1	0	1.0	1.6	2.1	3.1	4.1	4.7	5.3	6.3
50.2 – 56.4 GeV, 1.6 – 2.0	−1	−0.43	−0.24	−0.11	0	0.11	0.24	0.43	1	0	0.88	1.6	2.3	3.1	4.0	4.7	5.4	6.3
50.2 – 56.4 GeV, 2.0 – 2.4	−1	−0.21	−0.12	−0.060	0	0.060	0.12	0.21	1	0	0.82	1.6	2.4	3.1	3.9	4.7	5.5	6.3
56.4 – 63.9 GeV, 0 – 0.4	−1	−0.60	−0.36	−0.17	0	0.17	0.36	0.60	1	0	1.0	1.6	2.1	3.1	4.1	4.7	5.3	6.3
56.4 – 63.9 GeV, 0.4 – 0.8	−1	−0.57	−0.33	−0.16	0	0.16	0.33	0.57	1	0	0.97	1.6	2.2	3.1	4.1	4.7	5.3	6.3
56.4 – 63.9 GeV, 0.8 – 1.2	−1	−0.63	−0.33	−0.15	0	0.15	0.33	0.63	1	0	1.0	1.6	2.2	3.1	4.1	4.7	5.3	6.3
56.4 – 63.9 GeV, 1.2 – 1.6	−1	−0.62	−0.43	−0.26	0	0.26	0.43	0.62	1	0	1.0	1.6	2.1	3.1	4.2	4.7	5.2	6.3
56.4 – 63.9 GeV, 1.6 – 2.0	−1	−0.44	−0.24	−0.11	0	0.11	0.24	0.44	1	0	0.94	1.6	2.2	3.1	4.1	4.7	5.3	6.3
56.4 – 63.9 GeV, 2.0 – 2.4	−1	−0.22	−0.12	−0.060	0	0.060	0.12	0.22	1	0	0.85	1.6	2.3	3.1	4.0	4.7	5.4	6.3
63.9 – 73.4 GeV, 0 – 0.4	−1	−0.65	−0.39	−0.18	0	0.18	0.39	0.65	1	0	1.0	1.6	2.1	3.1	4.1	4.7	5.3	6.3
63.9 – 73.4 GeV, 0.4 – 0.8	−1	−0.61	−0.35	−0.16	0	0.16	0.35	0.61	1	0	1.0	1.6	2.1	3.1	4.1	4.7	5.3	6.3
63.9 – 73.4 GeV, 0.8 – 1.2	−1	−0.68	−0.36	−0.15	0	0.15	0.36	0.68	1	0	1.0	1.6	2.1	3.1	4.1	4.7	5.3	6.3
63.9 – 73.4 GeV, 1.2 – 1.6	−1	−0.67	−0.46	−0.27	0	0.27	0.46	0.67	1	0	1.1	1.6	2.1	3.1	4.2	4.7	5.2	6.3
63.9 – 73.4 GeV, 1.6 – 2.0	−1	−0.47	−0.25	−0.11	0	0.11	0.25	0.47	1	0	0.97	1.6	2.2	3.1	4.1	4.7	5.3	6.3
63.9 – 73.4 GeV, 2.0 – 2.4	−1	−0.22	−0.12	−0.060	0	0.060	0.12	0.22	1	0	0.91	1.6	2.3	3.1	4.0	4.7	5.4	6.3
73.4 – 85.4 GeV, 0 – 0.4	−1	−0.70	−0.42	−0.20	0	0.20	0.42	0.70	1	0	1.0	1.6	2.1	3.1	4.2	4.7	5.2	6.3

73.4 – 85.4 GeV, 0.4 – 0.8	−1	−0.66	−0.38	−0.18	0	0.18	0.38	0.66	1	0	1.0	1.6	2.1	3.1	4.1	4.7	5.3	6.3
73.4 – 85.4 GeV, 0.8 – 1.2	−1	−0.73	−0.39	−0.17	0	0.17	0.39	0.73	1	0	1.0	1.6	2.1	3.1	4.1	4.7	5.3	6.3
73.4 – 85.4 GeV, 1.2 – 1.6	−1	−0.73	−0.50	−0.29	0	0.29	0.50	0.73	1	0	1.1	1.6	2.1	3.1	4.2	4.7	5.2	6.3
73.4 – 85.4 GeV, 1.6 – 2.0	−1	−0.52	−0.28	−0.12	0	0.12	0.28	0.52	1	0	1.0	1.6	2.1	3.1	4.1	4.7	5.3	6.3
73.4 – 85.4 GeV, 2.0 – 2.4	−1	−0.24	−0.13	−0.060	0	0.060	0.13	0.24	1	0	0.97	1.6	2.2	3.1	4.1	4.7	5.3	6.3
85.4 – 105.0 GeV, 0 – 0.4	−1	−0.76	−0.47	−0.22	0	0.22	0.47	0.76	1	0	1.0	1.6	2.1	3.1	4.1	4.7	5.2	6.3
85.4 – 105.0 GeV, 0.4 – 0.8	−1	−0.72	−0.43	−0.20	0	0.20	0.43	0.72	1	0	1.0	1.6	2.1	3.1	4.1	4.7	5.3	6.3
85.4 – 105.0 GeV, 0.8 – 1.2	−1	−0.76	−0.43	−0.19	0	0.19	0.43	0.76	1	0	1.0	1.6	2.1	3.1	4.1	4.7	5.3	6.3
85.4 – 105.0 GeV, 1.2 – 1.6	−1	−0.79	−0.55	−0.33	0	0.33	0.55	0.79	1	0	1.1	1.6	2.1	3.1	4.2	4.7	5.2	6.3
85.4 – 105.0 GeV, 1.6 – 2.0	−1	−0.61	−0.33	−0.14	0	0.14	0.33	0.61	1	0	1.0	1.6	2.1	3.1	4.1	4.7	5.2	6.3
85.4 – 105.0 GeV, 2.0 – 2.4	−1	−0.27	−0.15	−0.070	0	0.070	0.15	0.27	1	0	1.0	1.6	2.1	3.1	4.1	4.7	5.2	6.3
105.0 – 132.0 GeV, 0 – 0.4	−1	−0.79	−0.51	−0.24	0	0.24	0.51	0.79	1	0	1.0	1.6	2.1	3.1	4.1	4.7	5.3	6.3
105.0 – 132.0 GeV, 0.4 – 0.8	−1	−0.76	−0.47	−0.22	0	0.22	0.47	0.76	1	0	1.0	1.6	2.1	3.1	4.1	4.7	5.3	6.3
105.0 – 132.0 GeV, 0.8 – 1.2	−1	−0.77	−0.46	−0.20	0	0.20	0.46	0.77	1	0	0.97	1.6	2.2	3.1	4.1	4.7	5.3	6.3
105.0 – 132.0 GeV, 1.2 – 1.6	−1	−0.83	−0.61	−0.36	0	0.36	0.61	0.83	1	0	1.0	1.6	2.1	3.1	4.1	4.7	5.2	6.3
105.0 – 132.0 GeV, 1.6 – 2.0	−1	−0.70	−0.40	−0.17	0	0.17	0.40	0.70	1	0	1.0	1.6	2.1	3.1	4.1	4.7	5.2	6.3
105.0 – 132.0 GeV, 2.0 – 2.4	−1	−0.31	−0.17	−0.080	0	0.080	0.17	0.31	1	0	1.1	1.6	2.1	3.1	4.1	4.7	5.2	6.3
132.0 – 173.0 GeV, 0 – 0.4	−1	−0.80	−0.54	−0.26	0	0.26	0.54	0.80	1	0	0.97	1.6	2.2	3.1	4.1	4.7	5.3	6.3
132.0 – 173.0 GeV, 0.4 – 0.8	−1	−0.78	−0.51	−0.24	0	0.24	0.51	0.78	1	0	0.97	1.6	2.2	3.1	4.1	4.7	5.3	6.3
132.0 – 173.0 GeV, 0.8 – 1.2	−1	−0.77	−0.48	−0.22	0	0.22	0.48	0.77	1	0	0.97	1.6	2.2	3.1	4.1	4.7	5.3	6.3
132.0 – 173.0 GeV, 1.2 – 1.6	−1	−0.85	−0.65	−0.39	0	0.39	0.65	0.85	1	0	0.97	1.6	2.2	3.1	4.1	4.7	5.3	6.3
132.0 – 173.0 GeV, 1.6 – 2.0	−1	−0.77	−0.45	−0.19	0	0.19	0.45	0.77	1	0	1.0	1.6	2.2	3.1	4.1	4.7	5.3	6.3
132.0 – 173.0 GeV, 2.0 – 2.4	−1	−0.40	−0.22	−0.10	0	0.10	0.22	0.40	1	0	1.1	1.6	2.1	3.1	4.1	4.7	5.2	6.3
173.0 – 253.0 GeV, 0 – 0.4	−1	−0.79	−0.55	−0.27	0	0.27	0.55	0.79	1	0	0.91	1.6	2.2	3.1	4.1	4.7	5.4	6.3

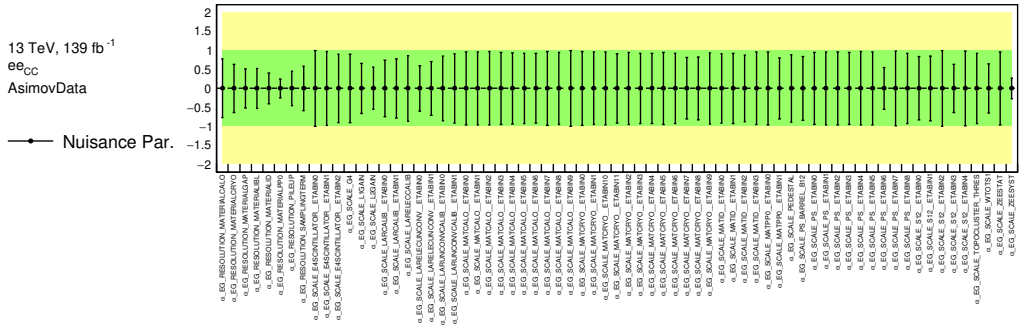
173.0 – 253.0 GeV, 0.4 – 0.8	−1	−0.78	−0.53	−0.26	0	0.26	0.53	0.78	1	0	0.94	1.6	2.2	3.1	4.1	4.7	5.3	6.3
173.0 – 253.0 GeV, 0.8 – 1.2	−1	−0.75	−0.50	−0.23	0	0.23	0.50	0.75	1	0	0.91	1.6	2.3	3.1	4.0	4.7	5.4	6.3
173.0 – 253.0 GeV, 1.2 – 1.6	−1	−0.84	−0.66	−0.39	0	0.39	0.66	0.84	1	0	0.91	1.6	2.3	3.1	4.0	4.7	5.4	6.3
173.0 – 253.0 GeV, 1.6 – 2.0	−1	−0.74	−0.45	−0.20	0	0.20	0.45	0.74	1	0	0.97	1.6	2.2	3.1	4.1	4.7	5.3	6.3
173.0 – 253.0 GeV, 2.0 – 2.4	−1	−0.51	−0.28	−0.12	0	0.12	0.28	0.51	1	0	1.0	1.6	2.1	3.1	4.1	4.7	5.2	6.3
253.0 – 400.0 GeV, 0 – 0.4	−1	−0.76	−0.55	−0.28	0	0.28	0.55	0.76	1	0	0.85	1.6	2.3	3.1	4.0	4.7	5.4	6.3
253.0 – 400.0 GeV, 0.4 – 0.8	−1	−0.76	−0.53	−0.27	0	0.27	0.53	0.76	1	0	0.85	1.6	2.3	3.1	4.0	4.7	5.4	6.3
253.0 – 400.0 GeV, 0.8 – 1.2	−1	−0.74	−0.52	−0.26	0	0.26	0.52	0.74	1	0	0.88	1.6	2.3	3.1	4.0	4.7	5.4	6.3
253.0 – 400.0 GeV, 1.2 – 1.6	−1	−0.82	−0.63	−0.37	0	0.37	0.63	0.82	1	0	0.82	1.6	2.4	3.1	3.9	4.6	5.5	6.3
253.0 – 400.0 GeV, 1.6 – 2.0	−1	−0.72	−0.49	−0.23	0	0.23	0.49	0.72	1	0	0.91	1.6	2.3	3.1	4.0	4.6	5.4	6.3
253.0 – 400.0 GeV, 2.0 – 2.4	−1	−0.64	−0.38	−0.17	0	0.17	0.38	0.64	1	0	1.0	1.7	2.2	3.1	4.1	4.6	5.3	6.3
400.0 – 6500.0 GeV, 0 – 0.4	−1	−0.74	−0.51	−0.29	0	0.29	0.51	0.74	1	0	0.79	1.6	2.4	3.1	3.9	4.7	5.5	6.3
400.0 – 6500.0 GeV, 0.4 – 0.8	−1	−0.74	−0.52	−0.27	0	0.27	0.52	0.74	1	0	0.79	1.6	2.4	3.1	3.9	4.7	5.5	6.3
400.0 – 6500.0 GeV, 0.8 – 1.2	−1	−0.75	−0.51	−0.27	0	0.27	0.51	0.75	1	0	0.85	1.6	2.4	3.1	3.9	4.7	5.4	6.3
400.0 – 6500.0 GeV, 1.2 – 1.6	−1	−0.77	−0.55	−0.29	0	0.29	0.55	0.77	1	0	0.82	1.8	2.5	3.1	3.8	4.5	5.5	6.3
400.0 – 6500.0 GeV, 1.6 – 2.0	−1	−0.72	−0.49	−0.25	0	0.25	0.49	0.72	1	0	0.82	1.6	2.3	3.1	4.0	4.7	5.5	6.3
400.0 – 6500.0 GeV, 2.0 – 2.4	−1	−0.72	−0.49	−0.23	0	0.23	0.49	0.72	1	0	0.97	1.7	2.3	3.1	4.0	4.6	5.3	6.3

F

Additional Pull Distributions

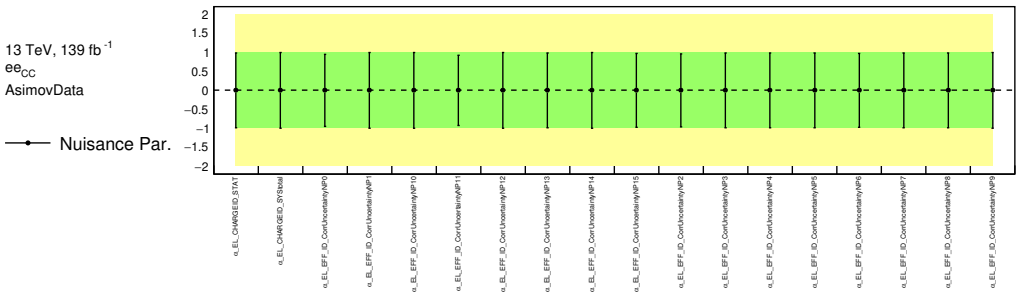


(a) Nuisance parameters related to PDF uncertainties.

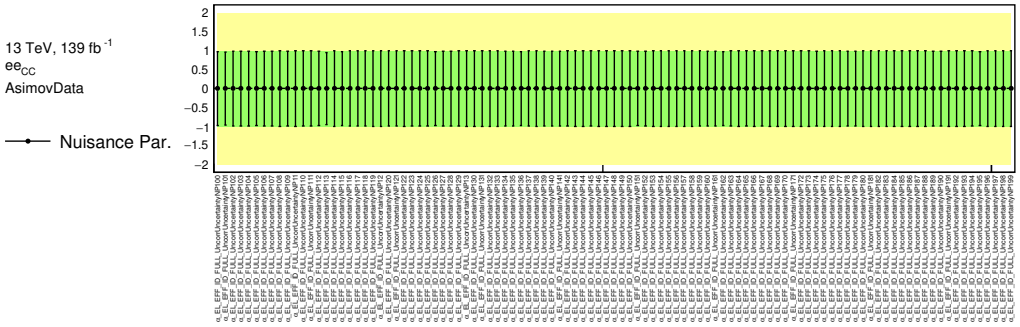


(b) Nuisance parameters related to energy scale and resolution uncertainties.

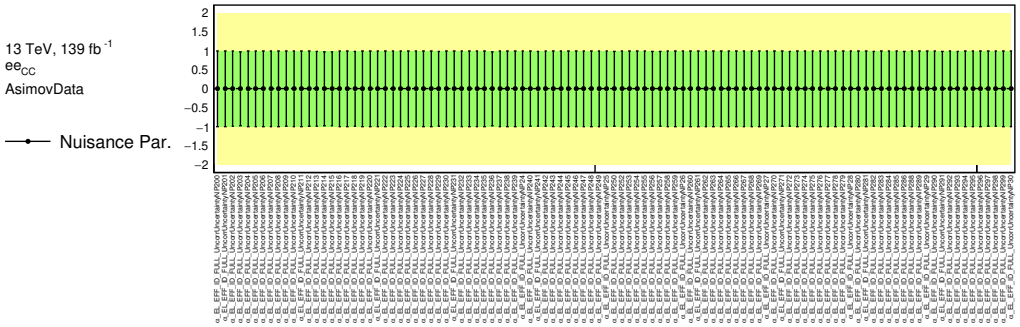
Fig. F.1.: Pulls of electron nuisance parameters for the Asimov dataset. Note that the vertical axis shows the dimensionless pull g.



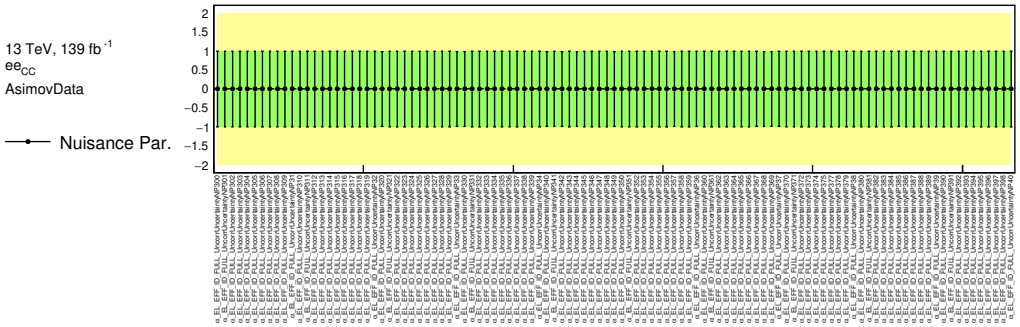
(a) Nuisance parameters related to (charge) identification efficiency uncertainties.



(b) Nuisance parameters related to identification efficiency uncertainties.

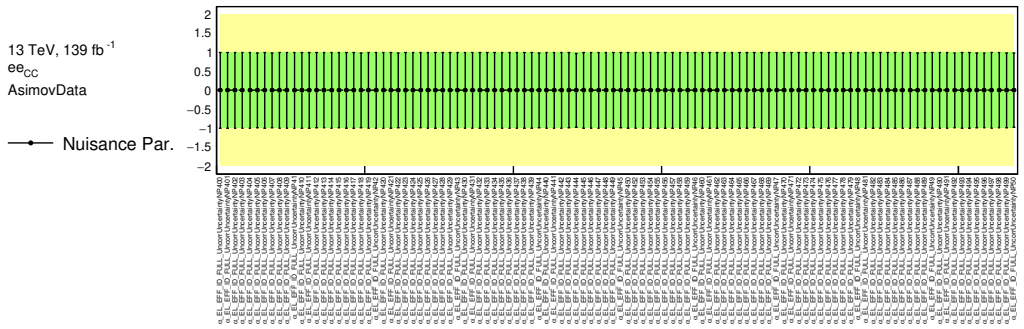


(c) Nuisance parameters related to identification efficiency uncertainties.

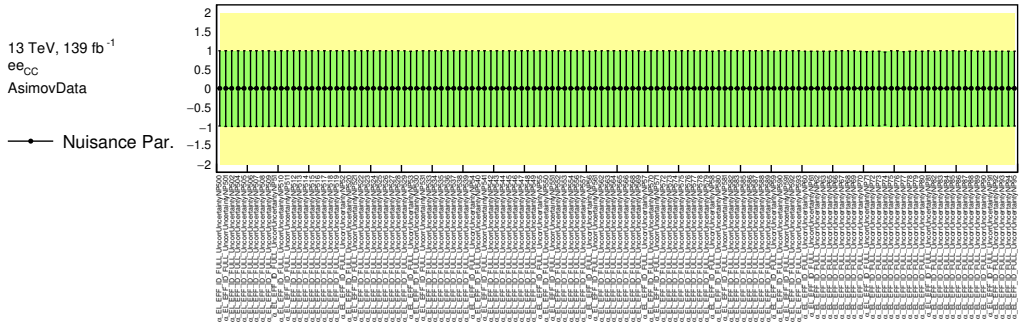


(d) Nuisance parameters related to identification efficiency uncertainties.

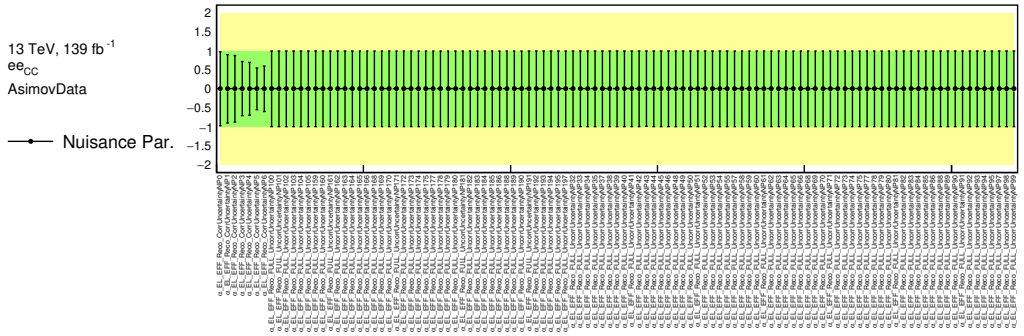
Fig. F.2.: Pulls of electron nuisance parameters for the Asimov dataset. Note that the vertical axis shows the dimensionless pull g.



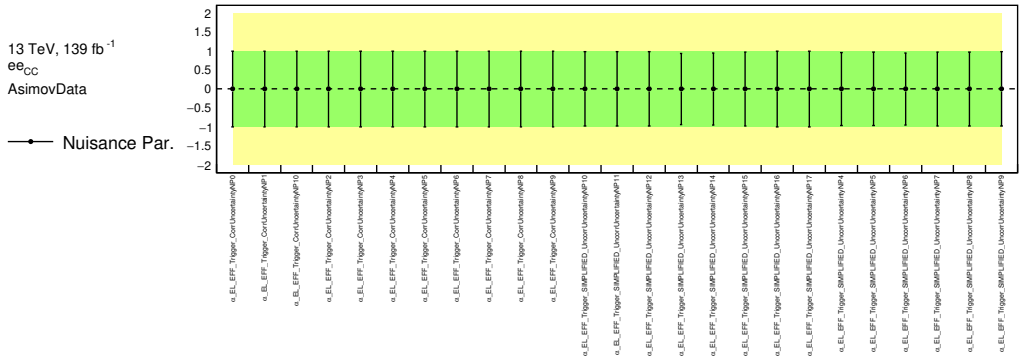
(a) Nuisance parameters related to identification efficiency uncertainties.



(b) Nuisance parameters related to identification efficiency uncertainties.



(c) Nuisance parameters related to reconstruction efficiency uncertainties.



(d) Nuisance parameters related to trigger efficiency uncertainties.

Fig. F.3.: Pulls of electron nuisance parameters for the Asimov dataset. Note that the vertical axis shows the dimensionless pull g.

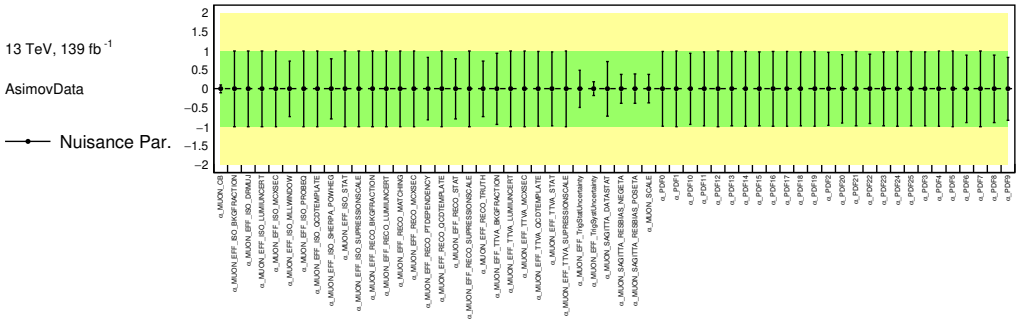
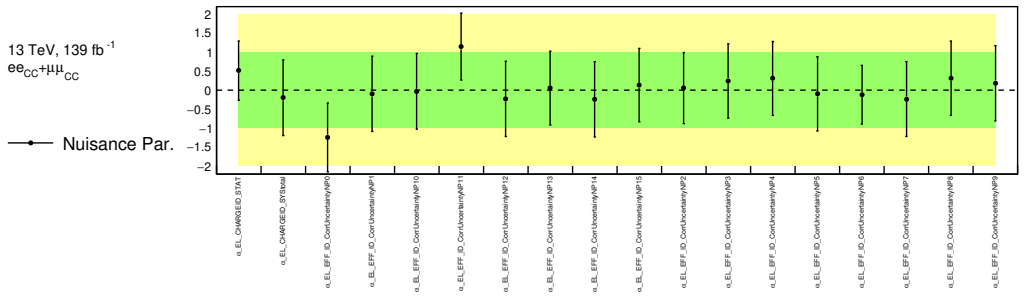
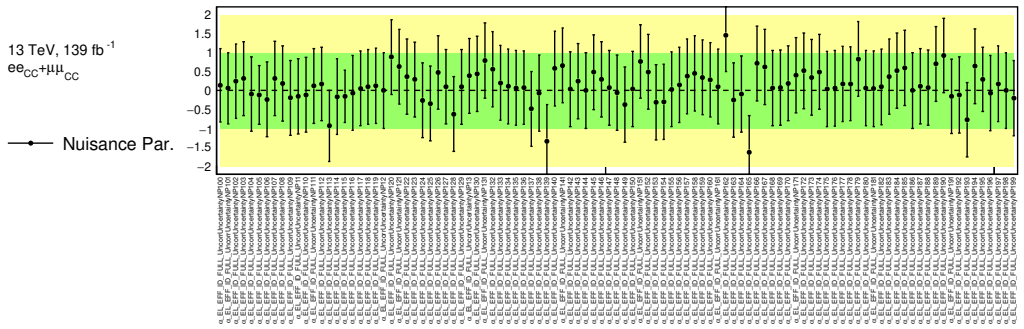


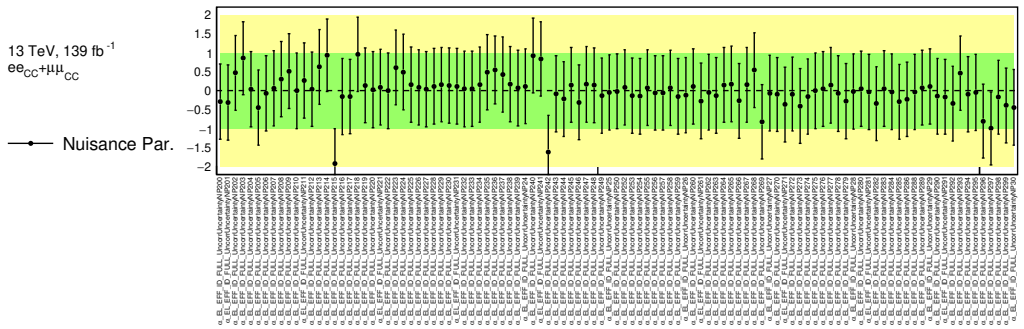
Fig. F.4.: Pulls of muon nuisance parameters for the Asimov dataset. Note that the vertical axis shows the dimensionless pull g.



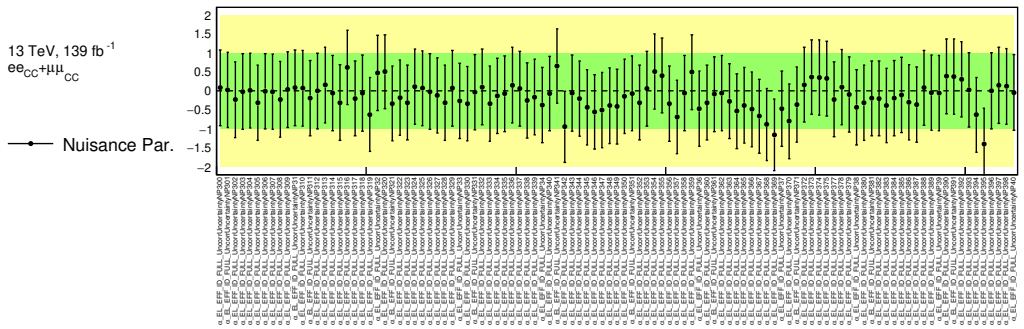
(a) Nuisance parameters related to (charge) identification efficiency uncertainties.



(b) Nuisance parameters related to identification efficiency uncertainties.

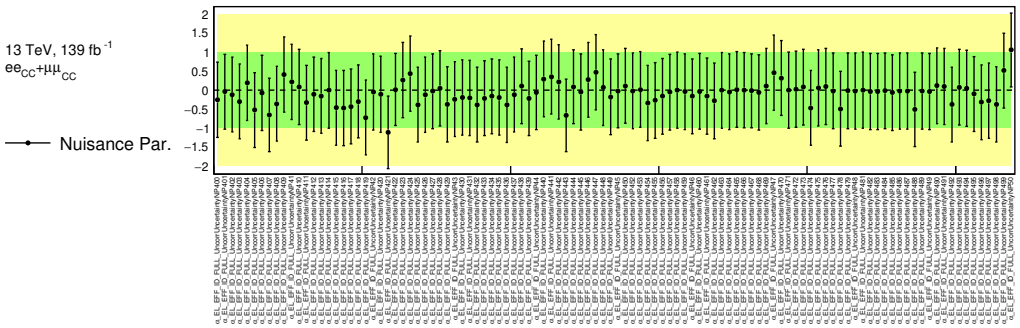


(c) Nuisance parameters related to identification efficiency uncertainties.

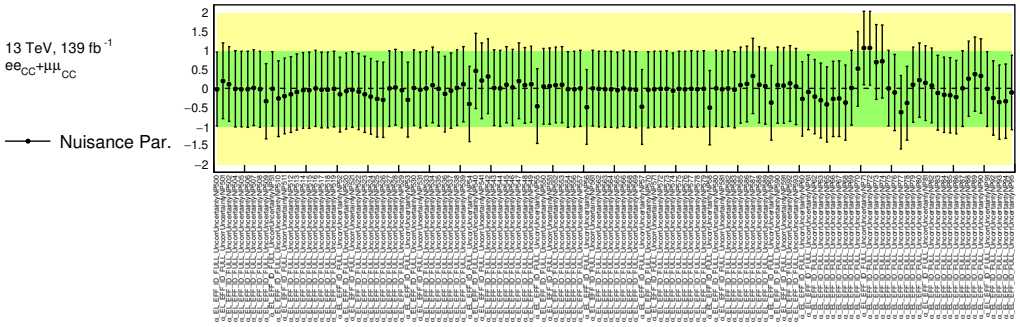


(d) Nuisance parameters related to identification efficiency uncertainties.

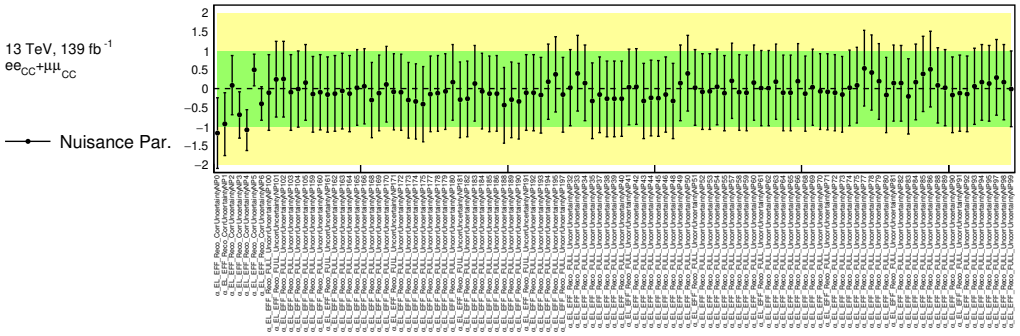
Fig. F.5.: Pulls of electron and muon nuisance parameters in the combined fit. Note that the vertical axis shows the dimensionless pull g.



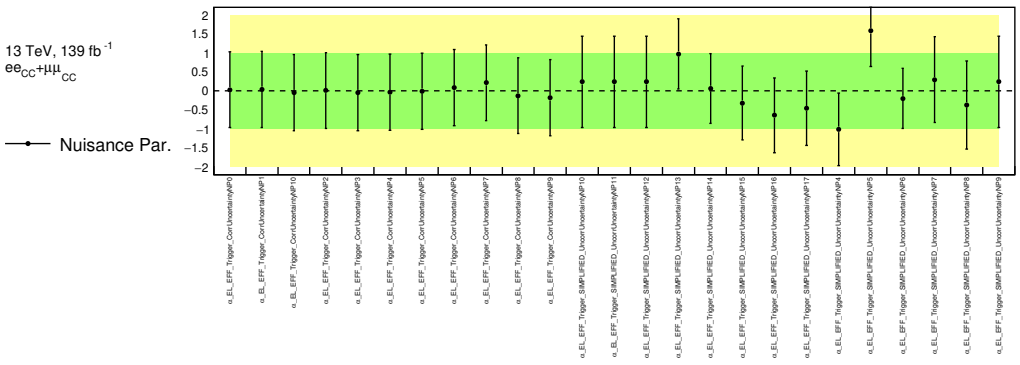
(a) Nuisance parameters related to identification efficiency uncertainties.



(b) Nuisance parameters related to identification efficiency uncertainties.

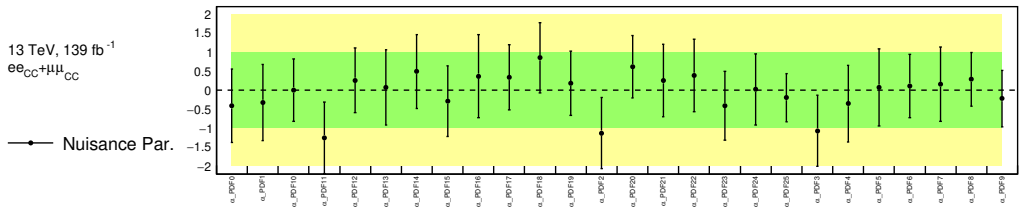


(c) Nuisance parameters related to reconstruction efficiency uncertainties.

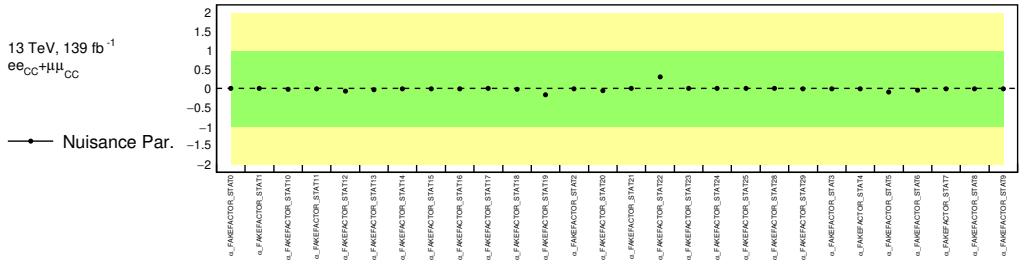


(d) Nuisance parameters related to trigger efficiency uncertainties.

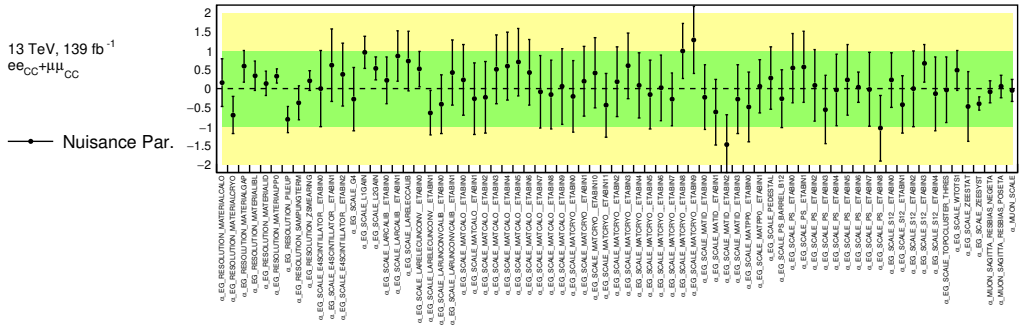
Fig. F.6.: Pulls of electron and muon nuisance parameters in the combined fit. Note that the vertical axis shows the dimensionless pull g.



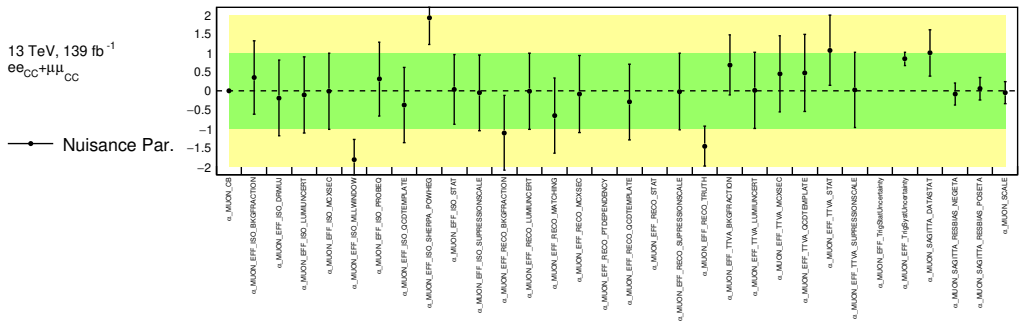
(a) Nuisance parameters related to PDF uncertainties.



(b) Nuisance parameters related to multijet uncertainties.



(c) Nuisance parameters related to energy scale and resolution uncertainties.



(d) Nuisance parameters related to muon-specific uncertainties.

Fig. F.7.: Pulls of electron and muon nuisance parameters in the combined fit. Note that the vertical axis shows the dimensionless pull g.

G

Detailed Breakdown of Combined Measured Angular Coefficients and Cross Section

Transverse Momentum	A_0	A_1	A_2	A_3	A_4	A_5	A_6	A_7	$\sigma^{\mathrm{U+L}}$[pb]
$0 < p_{T,ll} < 2.0$ GeV	0.0056 ± 0.0062	-0.0047 ± 0.0094	0.0319 ± 0.0129	-0.0055 ± 0.0086	0.0065 ± 0.0039	-0.0057 ± 0.0099	-0.0035 ± 0.0037	0.0032 ± 0.0030	9.5086 ± 0.0197
$2.0 < p_{T,ll} < 4.0$ GeV	0.0145 ± 0.0050	-0.0018 ± 0.0050	-0.0074 ± 0.0085	0.0081 ± 0.0044	0.0027 ± 0.0029	0.0045 ± 0.0042	0.0023 ± 0.0023	-0.0012 ± 0.0019	20.2778 ± 0.0362
$4.0 < p_{T,ll} < 6.0$ GeV	0.0220 ± 0.0050	-0.0027 ± 0.0044	0.0054 ± 0.0084	0.0032 ± 0.0038	0.0079 ± 0.0029	0.0055 ± 0.0034	-0.0008 ± 0.0022	-0.0016 ± 0.0018	21.6616 ± 0.0392
$6.0 < p_{T,ll} < 8.0$ GeV	0.0330 ± 0.0051	0.0076 ± 0.0043	0.0051 ± 0.0083	0.0006 ± 0.0037	0.0075 ± 0.0031	-0.0026 ± 0.0032	0.0003 ± 0.0024	0.0036 ± 0.0019	19.6001 ± 0.0348
$8.0 < p_{T,ll} < 11.4$ GeV	0.0493 ± 0.0035	-0.0083 ± 0.0026	0.0212 ± 0.0047	0.0034 ± 0.0021	0.0030 ± 0.0022	0.0007 ± 0.0021	-0.0011 ± 0.0018	0.0025 ± 0.0014	27.5379 ± 0.0349
$11.4 < p_{T,ll} < 14.9$ GeV	0.0724 ± 0.0038	-0.0051 ± 0.0028	0.0282 ± 0.0047	-0.0008 ± 0.0022	0.0034 ± 0.0024	0.0016 ± 0.0022	-0.0014 ± 0.0020	-0.0000 ± 0.0016	21.8426 ± 0.0289
$14.9 < p_{T,ll} < 18.5$ GeV	0.1087 ± 0.0043	-0.0012 ± 0.0031	0.0510 ± 0.0052	0.0041 ± 0.0024	0.0054 ± 0.0028	-0.0019 ± 0.0025	-0.0010 ± 0.0022	0.0015 ± 0.0018	17.3502 ± 0.0250
$18.5 < p_{T,ll} < 22.0$ GeV	0.1431 ± 0.0051	-0.0108 ± 0.0037	0.0702 ± 0.0061	-0.0010 ± 0.0029	0.0038 ± 0.0033	0.0035 ± 0.0029	-0.0015 ± 0.0026	0.0011 ± 0.0021	13.2746 ± 0.0216
$22.0 < p_{T,ll} < 25.5$ GeV	0.1777 ± 0.0057	0.0056 ± 0.0043	0.1061 ± 0.0070	0.0056 ± 0.0033	-0.0028 ± 0.0037	-0.0029 ± 0.0033	-0.0058 ± 0.0029	0.0006 ± 0.0024	10.6715 ± 0.0193
$22.5 < p_{T,ll} < 29.0$ GeV	0.2127 ± 0.0064	-0.0068 ± 0.0050	0.1420 ± 0.0079	-0.0013 ± 0.0037	0.0106 ± 0.0042	0.0036 ± 0.0037	0.0026 ± 0.0033	0.0041 ± 0.0027	8.6794 ± 0.0175
$29.0 < p_{T,ll} < 32.6$ GeV	0.2393 ± 0.0070	-0.0092 ± 0.0056	0.1666 ± 0.0086	0.0107 ± 0.0041	-0.0019 ± 0.0047	0.0027 ± 0.0040	-0.0004 ± 0.0036	0.0022 ± 0.0029	7.3751 ± 0.0161
$32.6 < p_{T,ll} < 36.4$ GeV	0.2712 ± 0.0075	-0.0021 ± 0.0061	0.1992 ± 0.0093	0.0010 ± 0.0044	0.0060 ± 0.0050	-0.0059 ± 0.0043	-0.0017 ± 0.0039	0.0023 ± 0.0032	6.3757 ± 0.0148
$36.4 < p_{T,ll} < 40.4$ GeV	0.3483 ± 0.0079	-0.0115 ± 0.0067	0.2284 ± 0.0100	0.0033 ± 0.0047	-0.0016 ± 0.0054	-0.0021 ± 0.0047	0.0009 ± 0.0042	0.0058 ± 0.0034	5.4999 ± 0.0135
$40.4 < p_{T,ll} < 44.9$ GeV	0.3615 ± 0.0078	0.0024 ± 0.0070	0.2672 ± 0.0102	0.0038 ± 0.0048	0.0105 ± 0.0055	0.0045 ± 0.0047	0.0066 ± 0.0043	0.0024 ± 0.0035	5.0767 ± 0.0125
$44.9 < p_{T,ll} < 50.2$ GeV	0.4326 ± 0.0074	-0.0065 ± 0.0071	0.2890 ± 0.0104	0.0069 ± 0.0048	0.0010 ± 0.0053	-0.0082 ± 0.0047	0.0012 ± 0.0043	0.0002 ± 0.0036	4.7720 ± 0.0115
$50.2 < p_{T,ll} < 56.4$ GeV	0.4927 ± 0.0072	-0.0079 ± 0.0075	0.3513 ± 0.0108	0.0093 ± 0.0049	0.0054 ± 0.0053	-0.0016 ± 0.0048	0.0053 ± 0.0043	-0.0011 ± 0.0037	4.3796 ± 0.0106
$56.4 < p_{T,ll} < 63.9$ GeV	0.5273 ± 0.0068	-0.0053 ± 0.0079	0.3981 ± 0.0115	0.0002 ± 0.0051	0.0058 ± 0.0052	-0.0002 ± 0.0048	0.0085 ± 0.0044	0.0067 ± 0.0037	3.9952 ± 0.0097
$63.9 < p_{T,ll} < 73.4$ GeV	0.6085 ± 0.0064	-0.0286 ± 0.0082	0.4569 ± 0.0124	0.0010 ± 0.0055	0.0032 ± 0.0050	-0.0089 ± 0.0049	-0.0019 ± 0.0044	-0.0020 ± 0.0038	3.6660 ± 0.0091
$73.4 < p_{T,ll} < 85.4$ GeV	0.6479 ± 0.0065	-0.0193 ± 0.0085	0.4964 ± 0.0145	0.0148 ± 0.0062	0.0078 ± 0.0050	-0.0068 ± 0.0052	0.0057 ± 0.0046	0.0003 ± 0.0040	3.1231 ± 0.0086
$85.4 < p_{T,ll} < 105.0$ GeV	0.7137 ± 0.0062	-0.0117 ± 0.0078	0.5612 ± 0.0157	-0.0024 ± 0.0063	0.0050 ± 0.0046	0.0059 ± 0.0051	-0.0021 ± 0.0044	0.0025 ± 0.0039	3.0145 ± 0.0087
$105.0 < p_{T,ll} < 132.0$ GeV	0.7796 ± 0.0074	0.0079 ± 0.0083	0.6224 ± 0.0196	-0.0034 ± 0.0076	-0.0151 ± 0.0051	0.0006 ± 0.0061	0.0061 ± 0.0051	0.0093 ± 0.0046	2.0526 ± 0.0072
$132.0 < p_{T,ll} < 173.0$ GeV	0.8651 ± 0.0090	-0.0123 ± 0.0092	0.7095 ± 0.0238	0.0012 ± 0.0091	0.0092 ± 0.0060	0.0009 ± 0.0076	-0.0070 ± 0.0063	-0.0033 ± 0.0057	1.2818 ± 0.0054
$173.0 < p_{T,ll} < 253.0$ GeV	0.8760 ± 0.0122	-0.0021 ± 0.0110	0.6867 ± 0.0304	0.0124 ± 0.0116	-0.0007 ± 0.0079	-0.0138 ± 0.0103	-0.0083 ± 0.0086	0.0002 ± 0.0078	0.6711 ± 0.0036
$253.0 < p_{T,ll} < 400.0$ GeV	0.8860 ± 0.0214	0.0043 ± 0.0191	0.6700 ± 0.0502	0.0112 ± 0.0197	0.0198 ± 0.0145	-0.0001 ± 0.0186	-0.0251 ± 0.0162	-0.0232 ± 0.0145	0.1944 ± 0.0017
$400.0 < p_{T,ll} < 6500.0$ GeV	0.9130 ± 0.0491	-0.1625 ± 0.0440	0.6889 ± 0.1077	0.0489 ± 0.0441	-0.0274 ± 0.0348	0.0040 ± 0.0443	-0.0402 ± 0.0393	0.0221 ± 0.0348	0.0343 ± 0.0006

Tab. G.1.: Results of the combined fit in all bins of transverse momentum and $0 < y_{ll} < 0.4$.

Transverse Momentum	A_0	A_1	A_2	A_3	A_4	A_5	A_6	A_7	$\sigma^{\mathrm{U+L}}$[pb]
$0 < p_{T,ll} < 2.0$ GeV	0.0170 ± 0.0064	0.0086 ± 0.0110	0.0174 ± 0.0134	0.0108 ± 0.0098	0.0162 ± 0.0042	-0.0089 ± 0.0110	-0.0039 ± 0.0040	0.0001 ± 0.0031	9.4755 ± 0.0216
$2.0 < p_{T,ll} < 4.0$ GeV	0.0108 ± 0.0052	-0.0035 ± 0.0057	-0.0088 ± 0.0094	0.0004 ± 0.0050	0.0140 ± 0.0031	0.0055 ± 0.0046	0.0019 ± 0.0025	0.0013 ± 0.0019	20.2138 ± 0.0401
$4.0 < p_{T,ll} < 6.0$ GeV	0.0367 ± 0.0053	0.0006 ± 0.0051	0.0096 ± 0.0096	0.0056 ± 0.0043	0.0055 ± 0.0031	-0.0047 ± 0.0036	-0.0015 ± 0.0024	-0.0008 ± 0.0019	21.4814 ± 0.0436
$6.0 < p_{T,ll} < 8.0$ GeV	0.0333 ± 0.0053	-0.0010 ± 0.0050	-0.0049 ± 0.0094	-0.0024 ± 0.0041	0.0151 ± 0.0033	0.0066 ± 0.0034	0.0035 ± 0.0026	0.0035 ± 0.0020	19.4501 ± 0.0384
$8.0 < p_{T,ll} < 11.4$ GeV	0.0565 ± 0.0035	-0.0091 ± 0.0030	0.0220 ± 0.0051	0.0022 ± 0.0023	0.0130 ± 0.0023	0.0003 ± 0.0022	0.0012 ± 0.0019	0.0002 ± 0.0014	27.2454 ± 0.0371
$11.4 < p_{T,ll} < 14.9$ GeV	0.0656 ± 0.0038	-0.0046 ± 0.0031	0.0243 ± 0.0050	0.0035 ± 0.0023	0.0172 ± 0.0026	-0.0001 ± 0.0023	0.0013 ± 0.0021	0.0015 ± 0.0016	21.6254 ± 0.0304
$14.9 < p_{T,ll} < 18.5$ GeV	0.1186 ± 0.0043	-0.0185 ± 0.0035	0.0452 ± 0.0055	0.0020 ± 0.0026	0.0087 ± 0.0030	0.0034 ± 0.0025	0.0026 ± 0.0024	0.0020 ± 0.0018	17.1019 ± 0.0263
$18.5 < p_{T,ll} < 22.0$ GeV	0.1375 ± 0.0051	-0.0086 ± 0.0041	0.0704 ± 0.0064	0.0035 ± 0.0030	0.0128 ± 0.0035	-0.0030 ± 0.0030	0.0032 ± 0.0028	-0.0002 ± 0.0021	13.1349 ± 0.0229
$22.0 < p_{T,ll} < 25.5$ GeV	0.1890 ± 0.0059	-0.0198 ± 0.0048	0.0971 ± 0.0073	-0.0024 ± 0.0035	0.0161 ± 0.0040	-0.0006 ± 0.0034	-0.0027 ± 0.0032	-0.0023 ± 0.0024	10.5348 ± 0.0205
$22.5 < p_{T,ll} < 29.0$ GeV	0.2130 ± 0.0066	-0.0073 ± 0.0056	0.1362 ± 0.0083	-0.0038 ± 0.0040	0.0039 ± 0.0046	0.0048 ± 0.0038	0.0003 ± 0.0036	0.0031 ± 0.0027	8.5557 ± 0.0186
$29.0 < p_{T,ll} < 32.6$ GeV	0.2490 ± 0.0072	-0.0200 ± 0.0062	0.1552 ± 0.0090	0.0008 ± 0.0043	0.0174 ± 0.0050	-0.0074 ± 0.0041	0.0084 ± 0.0039	0.0012 ± 0.0030	7.2443 ± 0.0171
$32.6 < p_{T,ll} < 36.4$ GeV	0.2949 ± 0.0077	-0.0223 ± 0.0067	0.1822 ± 0.0097	0.0047 ± 0.0046	0.0128 ± 0.0054	-0.0031 ± 0.0045	0.0015 ± 0.0042	-0.0078 ± 0.0032	6.2535 ± 0.0157
$36.4 < p_{T,ll} < 40.4$ GeV	0.3380 ± 0.0081	-0.0145 ± 0.0073	0.2401 ± 0.0103	-0.0071 ± 0.0049	0.0120 ± 0.0057	-0.0047 ± 0.0048	-0.0035 ± 0.0046	0.0072 ± 0.0035	5.4324 ± 0.0143
$40.4 < p_{T,ll} < 44.9$ GeV	0.3807 ± 0.0080	-0.0188 ± 0.0075	0.2410 ± 0.0105	0.0134 ± 0.0050	0.0076 ± 0.0058	-0.0058 ± 0.0048	0.0015 ± 0.0047	-0.0018 ± 0.0036	4.9927 ± 0.0130
$44.9 < p_{T,ll} < 50.2$ GeV	0.4104 ± 0.0075	-0.0180 ± 0.0076	0.2939 ± 0.0104	0.0127 ± 0.0049	0.0072 ± 0.0056	0.0030 ± 0.0047	0.0051 ± 0.0047	0.0044 ± 0.0036	4.7142 ± 0.0119
$50.2 < p_{T,ll} < 56.4$ GeV	0.4746 ± 0.0073	-0.0427 ± 0.0079	0.3211 ± 0.0108	0.0050 ± 0.0050	0.0139 ± 0.0056	-0.0033 ± 0.0048	-0.0019 ± 0.0047	0.0013 ± 0.0037	4.2890 ± 0.0107
$56.4 < p_{T,ll} < 63.9$ GeV	0.5287 ± 0.0069	-0.0171 ± 0.0083	0.3979 ± 0.0113	0.0092 ± 0.0052	0.0124 ± 0.0054	-0.0026 ± 0.0049	-0.0039 ± 0.0048	-0.0014 ± 0.0037	3.9275 ± 0.0098
$63.9 < p_{T,ll} < 73.4$ GeV	0.5967 ± 0.0066	-0.0206 ± 0.0084	0.4396 ± 0.0122	-0.0014 ± 0.0055	0.0197 ± 0.0053	0.0055 ± 0.0049	-0.0020 ± 0.0047	-0.0006 ± 0.0038	3.6096 ± 0.0091
$73.4 < p_{T,ll} < 85.4$ GeV	0.6543 ± 0.0067	-0.0311 ± 0.0087	0.4833 ± 0.0141	0.0134 ± 0.0062	0.0077 ± 0.0053	-0.0085 ± 0.0052	0.0016 ± 0.0049	0.0071 ± 0.0040	3.0636 ± 0.0084
$85.4 < p_{T,ll} < 105.0$ GeV	0.7228 ± 0.0065	-0.0178 ± 0.0079	0.5515 ± 0.0153	0.0319 ± 0.0063	0.0087 ± 0.0048	0.0041 ± 0.0050	0.0071 ± 0.0047	0.0051 ± 0.0038	2.9611 ± 0.0085
$105.0 < p_{T,ll} < 132.0$ GeV	0.8036 ± 0.0077	-0.0168 ± 0.0084	0.6319 ± 0.0191	-0.0212 ± 0.0076	-0.0005 ± 0.0053	0.0042 ± 0.0060	-0.0021 ± 0.0053	-0.0006 ± 0.0045	2.0219 ± 0.0070
$132.0 < p_{T,ll} < 173.0$ GeV	0.8724 ± 0.0094	-0.0199 ± 0.0092	0.7303 ± 0.0233	-0.0041 ± 0.0091	0.0186 ± 0.0062	-0.0098 ± 0.0075	-0.0005 ± 0.0064	-0.0016 ± 0.0056	1.2516 ± 0.0052
$173.0 < p_{T,ll} < 253.0$ GeV	0.8807 ± 0.0123	-0.0056 ± 0.0111	0.6650 ± 0.0299	-0.0170 ± 0.0115	0.0238 ± 0.0080	-0.0111 ± 0.0100	-0.0113 ± 0.0086	-0.0060 ± 0.0076	0.6566 ± 0.0035
$253.0 < p_{T,ll} < 400.0$ GeV	0.9083 ± 0.0211	-0.0100 ± 0.0187	0.6460 ± 0.0492	-0.0182 ± 0.0195	0.0151 ± 0.0142	0.0033 ± 0.0182	-0.0126 ± 0.0157	-0.0174 ± 0.0140	0.1883 ± 0.0016
$400.0 < p_{T,ll} < 6500.0$ GeV	0.9521 ± 0.0477	-0.0443 ± 0.0418	0.6770 ± 0.1053	-0.0769 ± 0.0429	-0.0194 ± 0.0330	-0.0626 ± 0.0430	-0.0121 ± 0.0377	0.0626 ± 0.0336	0.0332 ± 0.0006

Tab. G.2.: Results of the combined fit in all bins of transverse momentum and $0.4 < y_{ll} < 0.8$.

Transverse Momentum	A_0	A_1	A_2	A_3	A_4	A_5	A_6	A_7	$\sigma^{\mathrm{U+L}}$[pb]
$0 < p_{T,ll} < 2.0$ GeV	0.0018 ± 0.0076	-0.0034 ± 0.0120	0.0119 ± 0.0148	-0.0049 ± 0.0123	0.0280 ± 0.0043	-0.0131 ± 0.0137	0.0048 ± 0.0041	0.0026 ± 0.0033	9.4013 ± 0.0254
$2.0 < p_{T,ll} < 4.0$ GeV	0.0297 ± 0.0065	0.0047 ± 0.0062	0.0095 ± 0.0123	0.0055 ± 0.0062	0.0250 ± 0.0032	0.0108 ± 0.0056	-0.0005 ± 0.0026	0.0018 ± 0.0020	19.9600 ± 0.0493
$4.0 < p_{T,ll} < 6.0$ GeV	0.0173 ± 0.0067	-0.0108 ± 0.0056	-0.0076 ± 0.0131	-0.0014 ± 0.0053	0.0255 ± 0.0032	-0.0057 ± 0.0044	0.0016 ± 0.0025	-0.0002 ± 0.0020	21.1119 ± 0.0542
$6.0 < p_{T,ll} < 8.0$ GeV	0.0351 ± 0.0065	-0.0043 ± 0.0054	0.0102 ± 0.0125	0.0061 ± 0.0049	0.0254 ± 0.0034	0.0059 ± 0.0041	-0.0023 ± 0.0027	-0.0013 ± 0.0021	19.1196 ± 0.0463
$8.0 < p_{T,ll} < 11.4$ GeV	0.0538 ± 0.0040	-0.0111 ± 0.0032	0.0175 ± 0.0064	0.0012 ± 0.0027	0.0263 ± 0.0024	-0.0004 ± 0.0024	-0.0009 ± 0.0020	0.0024 ± 0.0015	26.6773 ± 0.0405
$11.4 < p_{T,ll} < 14.9$ GeV	0.0777 ± 0.0042	-0.0180 ± 0.0033	0.0325 ± 0.0058	0.0003 ± 0.0027	0.0249 ± 0.0027	-0.0023 ± 0.0025	-0.0014 ± 0.0022	-0.0001 ± 0.0017	21.1292 ± 0.0321
$14.9 < p_{T,ll} < 18.5$ GeV	0.0949 ± 0.0047	-0.0204 ± 0.0037	0.0451 ± 0.0063	0.0055 ± 0.0029	0.0214 ± 0.0031	0.0030 ± 0.0028	-0.0006 ± 0.0025	0.0021 ± 0.0019	16.7617 ± 0.0276
$18.5 < p_{T,ll} < 22.0$ GeV	0.1473 ± 0.0056	-0.0221 ± 0.0045	0.0772 ± 0.0074	0.0019 ± 0.0035	0.0214 ± 0.0037	-0.0068 ± 0.0033	0.0043 ± 0.0029	0.0035 ± 0.0023	12.7882 ± 0.0240
$22.0 < p_{T,ll} < 25.5$ GeV	0.1641 ± 0.0064	-0.0261 ± 0.0053	0.1157 ± 0.0085	-0.0045 ± 0.0040	0.0184 ± 0.0042	0.0052 ± 0.0038	-0.0019 ± 0.0033	-0.0009 ± 0.0026	10.2680 ± 0.0218
$22.5 < p_{T,ll} < 29.0$ GeV	0.1971 ± 0.0072	-0.0308 ± 0.0062	0.1140 ± 0.0098	0.0079 ± 0.0046	0.0247 ± 0.0048	0.0019 ± 0.0043	0.0055 ± 0.0038	0.0081 ± 0.0029	8.3302 ± 0.0199
$29.0 < p_{T,ll} < 32.6$ GeV	0.2565 ± 0.0079	-0.0392 ± 0.0069	0.1834 ± 0.0106	-0.0083 ± 0.0051	0.0239 ± 0.0053	0.0013 ± 0.0047	0.0099 ± 0.0041	0.0034 ± 0.0032	7.0487 ± 0.0184
$32.6 < p_{T,ll} < 36.4$ GeV	0.2847 ± 0.0084	-0.0195 ± 0.0076	0.1939 ± 0.0114	0.0068 ± 0.0055	0.0086 ± 0.0057	-0.0001 ± 0.0051	-0.0055 ± 0.0045	0.0030 ± 0.0035	6.0840 ± 0.0169
$36.4 < p_{T,ll} < 40.4$ GeV	0.3238 ± 0.0088	-0.0537 ± 0.0081	0.2196 ± 0.0119	-0.0009 ± 0.0058	0.0245 ± 0.0061	0.0040 ± 0.0054	-0.0015 ± 0.0048	-0.0092 ± 0.0038	5.2926 ± 0.0154
$40.4 < p_{T,ll} < 44.9$ GeV	0.3795 ± 0.0087	-0.0202 ± 0.0083	0.2510 ± 0.0120	0.0080 ± 0.0058	0.0162 ± 0.0062	-0.0050 ± 0.0054	0.0088 ± 0.0049	0.0150 ± 0.0039	4.8306 ± 0.0139
$44.9 < p_{T,ll} < 50.2$ GeV	0.4172 ± 0.0081	-0.0307 ± 0.0083	0.2963 ± 0.0117	0.0057 ± 0.0055	0.0299 ± 0.0059	0.0036 ± 0.0053	0.0016 ± 0.0049	0.0042 ± 0.0039	4.5609 ± 0.0125
$50.2 < p_{T,ll} < 56.4$ GeV	0.4799 ± 0.0077	-0.0348 ± 0.0085	0.3630 ± 0.0119	0.0004 ± 0.0056	0.0079 ± 0.0059	0.0040 ± 0.0052	-0.0036 ± 0.0050	0.0023 ± 0.0040	4.1914 ± 0.0112
$56.4 < p_{T,ll} < 63.9$ GeV	0.5291 ± 0.0073	-0.0477 ± 0.0088	0.3886 ± 0.0124	0.0106 ± 0.0057	0.0272 ± 0.0057	-0.0041 ± 0.0053	0.0058 ± 0.0050	0.0060 ± 0.0040	3.7974 ± 0.0101
$63.9 < p_{T,ll} < 73.4$ GeV	0.5748 ± 0.0068	-0.0354 ± 0.0089	0.4450 ± 0.0131	0.0017 ± 0.0059	0.0118 ± 0.0054	-0.0056 ± 0.0052	0.0018 ± 0.0049	0.0101 ± 0.0040	3.4811 ± 0.0093
$73.4 < p_{T,ll} < 85.4$ GeV	0.6483 ± 0.0069	-0.0359 ± 0.0092	0.4875 ± 0.0151	-0.0009 ± 0.0066	0.0121 ± 0.0054	-0.0021 ± 0.0055	-0.0075 ± 0.0051	0.0057 ± 0.0042	2.9661 ± 0.0086
$85.4 < p_{T,ll} < 105.0$ GeV	0.7265 ± 0.0066	-0.0453 ± 0.0082	0.5545 ± 0.0162	-0.0104 ± 0.0067	0.0139 ± 0.0049	-0.0028 ± 0.0053	0.0027 ± 0.0048	-0.0050 ± 0.0040	2.8635 ± 0.0085
$105.0 < p_{T,ll} < 132.0$ GeV	0.7960 ± 0.0080	-0.0451 ± 0.0089	0.6082 ± 0.0205	-0.0161 ± 0.0081	0.0231 ± 0.0055	-0.0067 ± 0.0064	-0.0045 ± 0.0057	0.0067 ± 0.0048	1.9352 ± 0.0071
$132.0 < p_{T,ll} < 173.0$ GeV	0.8679 ± 0.0099	-0.0298 ± 0.0097	0.7581 ± 0.0247	-0.0057 ± 0.0096	0.0079 ± 0.0065	-0.0096 ± 0.0079	0.0041 ± 0.0069	0.0024 ± 0.0059	1.2015 ± 0.0053
$173.0 < p_{T,ll} < 253.0$ GeV	0.8807 ± 0.0132	-0.0506 ± 0.0116	0.6974 ± 0.0314	-0.0450 ± 0.0121	0.0093 ± 0.0085	-0.0060 ± 0.0105	-0.0035 ± 0.0091	0.0009 ± 0.0079	0.6313 ± 0.0036
$253.0 < p_{T,ll} < 400.0$ GeV	0.9161 ± 0.0230	-0.0141 ± 0.0200	0.7315 ± 0.0515	0.0088 ± 0.0208	-0.0253 ± 0.0153	-0.0102 ± 0.0192	0.0155 ± 0.0167	-0.0151 ± 0.0147	0.1784 ± 0.0017
$400.0 < p_{T,ll} < 6500.0$ GeV	0.9992 ± 0.0520	-0.0205 ± 0.0465	0.8441 ± 0.1139	-0.0853 ± 0.0480	-0.0143 ± 0.0358	-0.0517 ± 0.0474	-0.0001 ± 0.0400	0.0188 ± 0.0358	0.0296 ± 0.0006

Tab. G.3.: Results of the combined fit in all bins of transverse momentum and $0.8 < y_{ll} < 1.2$.

Transverse Momentum	A_0	A_1	A_2	A_3	A_4	A_5	A_6	A_7	$\sigma^{\mathrm{U+L}}$[pb]
$0 < p_{T,ll} < 2.0$ GeV	0.0283 ± 0.0107	-0.0220 ± 0.0144	0.0082 ± 0.0165	-0.0020 ± 0.0153	0.0411 ± 0.0050	-0.0085 ± 0.0168	-0.0048 ± 0.0045	-0.0010 ± 0.0036	9.2855 ± 0.0312
$2.0 < p_{T,ll} < 4.0$ GeV	-0.0034 ± 0.0093	-0.0012 ± 0.0074	-0.0301 ± 0.0157	-0.0014 ± 0.0076	0.0385 ± 0.0037	0.0061 ± 0.0068	0.0036 ± 0.0028	-0.0010 ± 0.0022	19.6401 ± 0.0608
$4.0 < p_{T,ll} < 6.0$ GeV	0.0235 ± 0.0095	-0.0065 ± 0.0064	0.0273 ± 0.0166	0.0109 ± 0.0064	0.0413 ± 0.0037	-0.0118 ± 0.0052	0.0044 ± 0.0027	0.0019 ± 0.0022	20.8355 ± 0.0669
$6.0 < p_{T,ll} < 8.0$ GeV	0.0281 ± 0.0093	-0.0098 ± 0.0061	-0.0149 ± 0.0163	0.0011 ± 0.0059	0.0432 ± 0.0039	0.0052 ± 0.0048	0.0015 ± 0.0029	-0.0003 ± 0.0023	18.5866 ± 0.0563
$8.0 < p_{T,ll} < 11.4$ GeV	0.0531 ± 0.0055	-0.0106 ± 0.0035	0.0271 ± 0.0081	0.0028 ± 0.0032	0.0428 ± 0.0027	-0.0021 ± 0.0028	-0.0027 ± 0.0021	0.0016 ± 0.0017	25.9795 ± 0.0467
$11.4 < p_{T,ll} < 14.9$ GeV	0.0659 ± 0.0057	-0.0185 ± 0.0036	0.0271 ± 0.0072	-0.0007 ± 0.0031	0.0399 ± 0.0030	0.0027 ± 0.0029	0.0000 ± 0.0023	0.0050 ± 0.0019	20.4394 ± 0.0361
$14.9 < p_{T,ll} < 18.5$ GeV	0.1055 ± 0.0063	-0.0256 ± 0.0040	0.0531 ± 0.0077	0.0011 ± 0.0035	0.0432 ± 0.0034	-0.0016 ± 0.0032	0.0059 ± 0.0026	0.0005 ± 0.0021	16.2101 ± 0.0310
$18.5 < p_{T,ll} < 22.0$ GeV	0.1416 ± 0.0075	-0.0358 ± 0.0049	0.0737 ± 0.0092	-0.0062 ± 0.0042	0.0399 ± 0.0041	-0.0012 ± 0.0039	0.0042 ± 0.0031	-0.0008 ± 0.0025	12.3166 ± 0.0272
$22.0 < p_{T,ll} < 25.5$ GeV	0.1641 ± 0.0087	-0.0314 ± 0.0058	0.0852 ± 0.0107	0.0046 ± 0.0049	0.0305 ± 0.0047	-0.0066 ± 0.0044	0.0054 ± 0.0035	0.0050 ± 0.0029	9.8913 ± 0.0249
$22.5 < p_{T,ll} < 29.0$ GeV	0.1980 ± 0.0098	-0.0406 ± 0.0068	0.1418 ± 0.0123	0.0014 ± 0.0057	0.0324 ± 0.0054	0.0100 ± 0.0051	0.0018 ± 0.0040	0.0046 ± 0.0033	8.0122 ± 0.0229
$29.0 < p_{T,ll} < 32.6$ GeV	0.2461 ± 0.0108	-0.0457 ± 0.0077	0.1634 ± 0.0136	-0.0070 ± 0.0063	0.0360 ± 0.0059	0.0005 ± 0.0056	0.0066 ± 0.0044	0.0009 ± 0.0036	6.7785 ± 0.0215
$32.6 < p_{T,ll} < 36.4$ GeV	0.2918 ± 0.0116	-0.0554 ± 0.0085	0.1999 ± 0.0146	-0.0058 ± 0.0068	0.0368 ± 0.0064	-0.0103 ± 0.0061	0.0097 ± 0.0048	0.0047 ± 0.0040	5.8381 ± 0.0199
$36.4 < p_{T,ll} < 40.4$ GeV	0.3225 ± 0.0122	-0.0283 ± 0.0093	0.1897 ± 0.0156	-0.0001 ± 0.0073	0.0291 ± 0.0070	0.0099 ± 0.0066	0.0079 ± 0.0052	0.0048 ± 0.0043	5.0311 ± 0.0183
$40.4 < p_{T,ll} < 44.9$ GeV	0.3754 ± 0.0120	-0.0672 ± 0.0094	0.2693 ± 0.0151	-0.0063 ± 0.0072	0.0297 ± 0.0070	-0.0084 ± 0.0065	0.0012 ± 0.0052	0.0099 ± 0.0044	4.6610 ± 0.0167
$44.9 < p_{T,ll} < 50.2$ GeV	0.4381 ± 0.0114	-0.0499 ± 0.0094	0.3124 ± 0.0146	-0.0047 ± 0.0069	0.0357 ± 0.0069	0.0062 ± 0.0063	0.0117 ± 0.0051	0.0026 ± 0.0044	4.3592 ± 0.0151
$50.2 < p_{T,ll} < 56.4$ GeV	0.4734 ± 0.0109	-0.0559 ± 0.0096	0.3100 ± 0.0149	0.0115 ± 0.0069	0.0384 ± 0.0068	0.0084 ± 0.0063	0.0054 ± 0.0052	0.0061 ± 0.0045	3.9670 ± 0.0135
$56.4 < p_{T,ll} < 63.9$ GeV	0.5439 ± 0.0100	-0.0573 ± 0.0099	0.4339 ± 0.0150	-0.0159 ± 0.0069	0.0291 ± 0.0066	-0.0066 ± 0.0062	0.0085 ± 0.0051	0.0028 ± 0.0045	3.6449 ± 0.0120
$63.9 < p_{T,ll} < 73.4$ GeV	0.5826 ± 0.0090	-0.0496 ± 0.0102	0.4404 ± 0.0158	-0.0024 ± 0.0071	0.0257 ± 0.0063	-0.0149 ± 0.0061	-0.0028 ± 0.0051	0.0116 ± 0.0045	3.3144 ± 0.0107
$73.4 < p_{T,ll} < 85.4$ GeV	0.6228 ± 0.0084	-0.0602 ± 0.0106	0.4819 ± 0.0177	-0.0144 ± 0.0077	0.0247 ± 0.0061	-0.0001 ± 0.0064	0.0052 ± 0.0053	0.0008 ± 0.0047	2.8193 ± 0.0096
$85.4 < p_{T,ll} < 105.0$ GeV	0.7177 ± 0.0075	-0.0599 ± 0.0094	0.5722 ± 0.0184	-0.0280 ± 0.0076	0.0330 ± 0.0053	-0.0208 ± 0.0060	0.0054 ± 0.0049	0.0030 ± 0.0045	2.7262 ± 0.0093
$105.0 < p_{T,ll} < 132.0$ GeV	0.7998 ± 0.0086	-0.0625 ± 0.0099	0.6448 ± 0.0231	-0.0417 ± 0.0091	0.0269 ± 0.0057	-0.0050 ± 0.0072	0.0023 ± 0.0057	-0.0032 ± 0.0053	1.8375 ± 0.0076
$132.0 < p_{T,ll} < 173.0$ GeV	0.8448 ± 0.0105	-0.0432 ± 0.0107	0.5988 ± 0.0290	-0.0372 ± 0.0110	0.0134 ± 0.0068	0.0038 ± 0.0092	0.0032 ± 0.0072	0.0034 ± 0.0068	1.1107 ± 0.0056
$173.0 < p_{T,ll} < 253.0$ GeV	0.8792 ± 0.0138	-0.0478 ± 0.0129	0.7542 ± 0.0361	-0.0710 ± 0.0139	0.0094 ± 0.0088	-0.0034 ± 0.0123	0.0106 ± 0.0098	0.0018 ± 0.0092	0.5858 ± 0.0038
$253.0 < p_{T,ll} < 400.0$ GeV	0.9503 ± 0.0253	-0.0291 ± 0.0232	0.7420 ± 0.0645	-0.0528 ± 0.0251	0.0567 ± 0.0169	0.0059 ± 0.0243	-0.0233 ± 0.0197	0.0180 ± 0.0185	0.1579 ± 0.0017
$400.0 < p_{T,ll} < 6500.0$ GeV	0.9530 ± 0.0669	-0.0895 ± 0.0593	0.9309 ± 0.1532	-0.2807 ± 0.0635	0.0738 ± 0.0464	0.0008 ± 0.0661	0.0291 ± 0.0556	-0.0305 ± 0.0491	0.0251 ± 0.0006

Tab. G.4.: Results of the combined fit in all bins of transverse momentum and $1.2 < y_{ll} < 1.6$.

Transverse Momentum	A_0	A_1	A_2	A_3	A_4	A_5	A_6	A_7	$\sigma^{\mathrm{U+L}}$[pb]
$0 < p_{T,ll} < 2.0$ GeV	-0.0070 ± 0.0190	-0.0499 ± 0.0311	-0.0084 ± 0.0185	0.0040 ± 0.0227	0.0438 ± 0.0088	-0.0002 ± 0.0212	-0.0021 ± 0.0070	-0.0099 ± 0.0041	9.2643 ± 0.0604
$2.0 < p_{T,ll} < 4.0$ GeV	-0.0087 ± 0.0164	0.0096 ± 0.0156	-0.0183 ± 0.0224	0.0082 ± 0.0112	0.0730 ± 0.0068	-0.0021 ± 0.0086	0.0054 ± 0.0044	0.0014 ± 0.0026	19.3457 ± 0.1108
$4.0 < p_{T,ll} < 6.0$ GeV	0.0286 ± 0.0170	-0.0259 ± 0.0131	0.0273 ± 0.0258	-0.0082 ± 0.0091	0.0473 ± 0.0068	0.0001 ± 0.0064	0.0030 ± 0.0043	0.0024 ± 0.0026	20.3397 ± 0.1219
$6.0 < p_{T,ll} < 8.0$ GeV	0.0397 ± 0.0171	0.0015 ± 0.0122	-0.0206 ± 0.0257	0.0122 ± 0.0083	0.0674 ± 0.0073	0.0038 ± 0.0059	-0.0055 ± 0.0047	0.0038 ± 0.0028	17.9257 ± 0.1066
$8.0 < p_{T,ll} < 11.4$ GeV	0.0385 ± 0.0101	-0.0239 ± 0.0065	0.0255 ± 0.0118	0.0005 ± 0.0042	0.0516 ± 0.0049	-0.0005 ± 0.0033	0.0057 ± 0.0033	-0.0017 ± 0.0019	25.1426 ± 0.0900
$11.4 < p_{T,ll} < 14.9$ GeV	0.0751 ± 0.0106	-0.0187 ± 0.0064	0.0261 ± 0.0097	0.0027 ± 0.0040	0.0711 ± 0.0053	0.0009 ± 0.0034	0.0044 ± 0.0037	0.0045 ± 0.0022	19.6644 ± 0.0721
$14.9 < p_{T,ll} < 18.5$ GeV	0.0964 ± 0.0118	-0.0420 ± 0.0071	0.0563 ± 0.0099	-0.0050 ± 0.0044	0.0473 ± 0.0060	-0.0013 ± 0.0037	-0.0033 ± 0.0041	0.0027 ± 0.0025	15.5733 ± 0.0628
$18.5 < p_{T,ll} < 22.0$ GeV	0.1425 ± 0.0141	-0.0457 ± 0.0088	0.0580 ± 0.0120	0.0073 ± 0.0054	0.0712 ± 0.0072	0.0010 ± 0.0045	0.0016 ± 0.0049	-0.0000 ± 0.0030	11.6523 ± 0.0556
$22.0 < p_{T,ll} < 25.5$ GeV	0.1841 ± 0.0162	-0.0446 ± 0.0104	0.1085 ± 0.0140	-0.0070 ± 0.0063	0.0401 ± 0.0083	-0.0074 ± 0.0052	0.0028 ± 0.0056	0.0014 ± 0.0034	9.3738 ± 0.0514
$22.5 < p_{T,ll} < 29.0$ GeV	0.2084 ± 0.0183	-0.0484 ± 0.0123	0.1370 ± 0.0163	0.0073 ± 0.0073	0.0701 ± 0.0095	0.0034 ± 0.0059	0.0043 ± 0.0063	0.0017 ± 0.0039	7.6062 ± 0.0477
$29.0 < p_{T,ll} < 32.6$ GeV	0.2448 ± 0.0202	-0.0584 ± 0.0139	0.1548 ± 0.0178	-0.0085 ± 0.0081	0.0426 ± 0.0104	-0.0083 ± 0.0065	0.0015 ± 0.0070	0.0107 ± 0.0043	6.3695 ± 0.0443
$32.6 < p_{T,ll} < 36.4$ GeV	0.2965 ± 0.0218	-0.0547 ± 0.0153	0.1782 ± 0.0188	-0.0101 ± 0.0087	0.0514 ± 0.0112	-0.0042 ± 0.0071	-0.0045 ± 0.0076	0.0109 ± 0.0047	5.4857 ± 0.0412
$36.4 < p_{T,ll} < 40.4$ GeV	0.3510 ± 0.0232	-0.0368 ± 0.0162	0.2649 ± 0.0191	-0.0033 ± 0.0091	0.0567 ± 0.0120	-0.0059 ± 0.0075	0.0084 ± 0.0079	0.0048 ± 0.0050	4.7858 ± 0.0381
$40.4 < p_{T,ll} < 44.9$ GeV	0.3658 ± 0.0232	-0.1104 ± 0.0168	0.2438 ± 0.0184	-0.0112 ± 0.0089	0.0485 ± 0.0119	0.0043 ± 0.0075	0.0135 ± 0.0081	0.0008 ± 0.0052	4.3326 ± 0.0344
$44.9 < p_{T,ll} < 50.2$ GeV	0.4321 ± 0.0222	-0.0478 ± 0.0158	0.3100 ± 0.0166	-0.0058 ± 0.0083	0.0378 ± 0.0115	-0.0037 ± 0.0072	-0.0068 ± 0.0078	0.0094 ± 0.0050	4.1161 ± 0.0308
$50.2 < p_{T,ll} < 56.4$ GeV	0.4714 ± 0.0219	-0.0776 ± 0.0160	0.3142 ± 0.0162	-0.0133 ± 0.0081	0.0338 ± 0.0115	-0.0079 ± 0.0072	0.0224 ± 0.0078	0.0057 ± 0.0052	3.7178 ± 0.0272
$56.4 < p_{T,ll} < 63.9$ GeV	0.5238 ± 0.0207	-0.0702 ± 0.0159	0.4221 ± 0.0157	-0.0174 ± 0.0079	0.0448 ± 0.0110	-0.0006 ± 0.0069	0.0065 ± 0.0075	0.0077 ± 0.0050	3.4235 ± 0.0236
$63.9 < p_{T,ll} < 73.4$ GeV	0.5674 ± 0.0189	-0.0765 ± 0.0162	0.4510 ± 0.0162	-0.0218 ± 0.0080	0.0473 ± 0.0106	-0.0064 ± 0.0068	-0.0058 ± 0.0073	0.0114 ± 0.0050	3.1071 ± 0.0198
$73.4 < p_{T,ll} < 85.4$ GeV	0.6478 ± 0.0175	-0.0922 ± 0.0174	0.4856 ± 0.0185	-0.0066 ± 0.0088	0.0394 ± 0.0105	-0.0071 ± 0.0071	0.0058 ± 0.0074	0.0049 ± 0.0053	2.6075 ± 0.0158
$85.4 < p_{T,ll} < 105.0$ GeV	0.7166 ± 0.0135	-0.0731 ± 0.0159	0.5362 ± 0.0197	-0.0409 ± 0.0088	0.0283 ± 0.0086	0.0012 ± 0.0066	-0.0039 ± 0.0066	0.0109 ± 0.0049	2.4933 ± 0.0129
$105.0 < p_{T,ll} < 132.0$ GeV	0.7996 ± 0.0127	-0.0758 ± 0.0166	0.5991 ± 0.0251	-0.0455 ± 0.0106	0.0433 ± 0.0086	-0.0111 ± 0.0078	0.0016 ± 0.0074	0.0044 ± 0.0058	1.6726 ± 0.0093
$132.0 < p_{T,ll} < 173.0$ GeV	0.8549 ± 0.0131	-0.0720 ± 0.0168	0.7259 ± 0.0311	-0.0619 ± 0.0128	0.0246 ± 0.0092	0.0130 ± 0.0097	0.0092 ± 0.0086	0.0039 ± 0.0071	1.0101 ± 0.0063
$173.0 < p_{T,ll} < 253.0$ GeV	0.8624 ± 0.0164	-0.0110 ± 0.0181	0.7721 ± 0.0398	-0.0856 ± 0.0159	0.0388 ± 0.0112	-0.0153 ± 0.0128	-0.0297 ± 0.0113	-0.0017 ± 0.0095	0.5156 ± 0.0040
$253.0 < p_{T,ll} < 400.0$ GeV	0.9356 ± 0.0298	-0.0503 ± 0.0283	0.8132 ± 0.0683	-0.1682 ± 0.0280	0.0399 ± 0.0202	-0.0320 ± 0.0248	-0.0010 ± 0.0216	0.0269 ± 0.0186	0.1312 ± 0.0016
$400.0 < p_{T,ll} < 6500.0$ GeV	0.9317 ± 0.0841	-0.0697 ± 0.0741	0.6896 ± 0.1812	-0.1396 ± 0.0749	-0.0065 ± 0.0582	0.0513 ± 0.0717	-0.0598 ± 0.0631	0.0311 ± 0.0561	0.0156 ± 0.0005

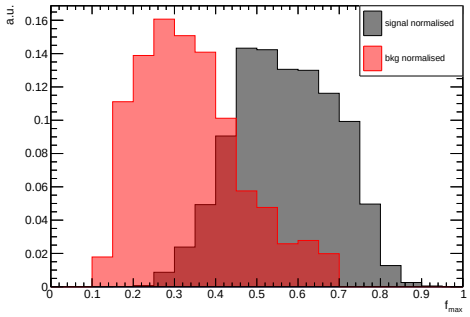
Tab. G.5.: Results of the combined fit in all bins of transverse momentum and $1.6 < y_{ll} < 2.0$.

Transverse Momentum	A_0	A_1	A_2	A_3	A_4	A_5	A_6	A_7	$\sigma^{\mathrm{U+L}}$[pb]
$0 < p_{T,ll} < 2.0$ GeV	-0.1759 ± 0.0740	-0.1386 ± 0.1012	-0.0153 ± 0.0234	0.0624 ± 0.0270	0.0597 ± 0.0264	-0.0140 ± 0.0248	0.0134 ± 0.0189	-0.0010 ± 0.0055	9.8757 ± 0.3676
$2.0 < p_{T,ll} < 4.0$ GeV	0.0471 ± 0.0711	0.0885 ± 0.0559	-0.0330 ± 0.0267	-0.0468 ± 0.0152	0.1151 ± 0.0231	0.0056 ± 0.0114	-0.0050 ± 0.0133	0.0008 ± 0.0039	18.3619 ± 0.5974
$4.0 < p_{T,ll} < 6.0$ GeV	0.0466 ± 0.0704	-0.0933 ± 0.0453	0.0467 ± 0.0287	0.0246 ± 0.0123	0.0477 ± 0.0227	0.0104 ± 0.0085	0.0054 ± 0.0129	-0.0029 ± 0.0038	19.6405 ± 0.6319
$6.0 < p_{T,ll} < 8.0$ GeV	-0.0035 ± 0.0731	-0.0136 ± 0.0407	-0.0427 ± 0.0288	-0.0163 ± 0.0112	0.1176 ± 0.0242	-0.0021 ± 0.0078	-0.0046 ± 0.0139	0.0016 ± 0.0041	17.4081 ± 0.5926
$8.0 < p_{T,ll} < 11.4$ GeV	0.0207 ± 0.0488	-0.0067 ± 0.0205	0.0378 ± 0.0134	0.0073 ± 0.0058	0.0637 ± 0.0157	0.0009 ± 0.0045	0.0150 ± 0.0096	0.0032 ± 0.0028	24.2940 ± 0.5432
$11.4 < p_{T,ll} < 14.9$ GeV	-0.0253 ± 0.0505	-0.0417 ± 0.0193	0.0075 ± 0.0114	-0.0087 ± 0.0054	0.0964 ± 0.0168	-0.0002 ± 0.0045	-0.0095 ± 0.0104	0.0059 ± 0.0031	19.3794 ± 0.4568
$14.9 < p_{T,ll} < 18.5$ GeV	0.2243 ± 0.0695	-0.0540 ± 0.0237	0.0518 ± 0.0133	0.0019 ± 0.0065	0.1211 ± 0.0209	0.0032 ± 0.0055	0.0175 ± 0.0130	-0.0006 ± 0.0039	13.8196 ± 0.4010
$18.5 < p_{T,ll} < 22.0$ GeV	0.1617 ± 0.0770	-0.0794 ± 0.0279	0.0499 ± 0.0152	-0.0067 ± 0.0075	0.0768 ± 0.0238	0.0022 ± 0.0063	0.0117 ± 0.0148	0.0076 ± 0.0045	10.8708 ± 0.3588
$22.0 < p_{T,ll} < 25.5$ GeV	0.2904 ± 0.0948	-0.0492 ± 0.0330	0.1261 ± 0.0184	0.0017 ± 0.0090	0.0787 ± 0.0278	-0.0007 ± 0.0074	-0.0075 ± 0.0172	-0.0022 ± 0.0052	8.4260 ± 0.3248
$22.5 < p_{T,ll} < 29.0$ GeV	0.3886 ± 0.1153	-0.1310 ± 0.0417	0.0809 ± 0.0216	0.0015 ± 0.0107	0.0473 ± 0.0331	-0.0025 ± 0.0088	0.0263 ± 0.0205	0.0147 ± 0.0063	6.5157 ± 0.2943
$29.0 < p_{T,ll} < 32.6$ GeV	0.2376 ± 0.1081	-0.0362 ± 0.0403	0.1682 ± 0.0222	-0.0243 ± 0.0108	0.1055 ± 0.0332	-0.0097 ± 0.0088	0.0092 ± 0.0205	-0.0142 ± 0.0063	6.0111 ± 0.2707
$32.6 < p_{T,ll} < 36.4$ GeV	0.2969 ± 0.1185	-0.0119 ± 0.0432	0.2075 ± 0.0243	0.0095 ± 0.0116	0.0906 ± 0.0356	0.0119 ± 0.0096	0.0266 ± 0.0221	0.0090 ± 0.0069	5.0756 ± 0.2447
$36.4 < p_{T,ll} < 40.4$ GeV	0.4129 ± 0.1354	-0.1463 ± 0.0521	0.1873 ± 0.0260	-0.0115 ± 0.0127	0.0721 ± 0.0393	-0.0030 ± 0.0106	0.0104 ± 0.0246	-0.0012 ± 0.0078	4.2206 ± 0.2223
$40.4 < p_{T,ll} < 44.9$ GeV	0.5081 ± 0.1390	-0.0908 ± 0.0505	0.3191 ± 0.0275	-0.0153 ± 0.0125	0.0633 ± 0.0387	0.0085 ± 0.0106	0.0527 ± 0.0246	0.0120 ± 0.0079	3.8234 ± 0.1995
$44.9 < p_{T,ll} < 50.2$ GeV	0.4179 ± 0.1219	-0.0668 ± 0.0457	0.2801 ± 0.0238	0.0040 ± 0.0113	0.1394 ± 0.0355	0.0019 ± 0.0099	0.0112 ± 0.0227	-0.0033 ± 0.0075	3.7840 ± 0.1793
$50.2 < p_{T,ll} < 56.4$ GeV	0.5776 ± 0.1320	-0.1934 ± 0.0527	0.3441 ± 0.0253	-0.0160 ± 0.0118	0.0572 ± 0.0364	-0.0391 ± 0.0105	-0.0144 ± 0.0235	0.0150 ± 0.0079	3.2586 ± 0.1577
$56.4 < p_{T,ll} < 63.9$ GeV	0.5920 ± 0.1229	-0.0859 ± 0.0478	0.3950 ± 0.0249	-0.0229 ± 0.0115	0.0268 ± 0.0346	0.0171 ± 0.0101	0.0089 ± 0.0221	0.0076 ± 0.0077	3.0286 ± 0.1360
$63.9 < p_{T,ll} < 73.4$ GeV	0.4707 ± 0.1047	-0.0313 ± 0.0442	0.4380 ± 0.0236	-0.0167 ± 0.0110	0.0832 ± 0.0318	-0.0106 ± 0.0094	0.0018 ± 0.0202	0.0123 ± 0.0072	2.9185 ± 0.1172
$73.4 < p_{T,ll} < 85.4$ GeV	0.9909 ± 0.1362	-0.2465 ± 0.0623	0.5363 ± 0.0308	-0.0575 ± 0.0144	0.0701 ± 0.0367	0.0185 ± 0.0114	0.0681 ± 0.0230	-0.0004 ± 0.0087	2.0888 ± 0.0915
$85.4 < p_{T,ll} < 105.0$ GeV	0.7207 ± 0.0901	-0.0897 ± 0.0498	0.4906 ± 0.0280	-0.0577 ± 0.0134	0.0768 ± 0.0294	-0.0003 ± 0.0097	-0.0167 ± 0.0180	-0.0096 ± 0.0074	2.1887 ± 0.0706
$105.0 < p_{T,ll} < 132.0$ GeV	0.8042 ± 0.0810	-0.1676 ± 0.0574	0.6054 ± 0.0359	-0.0735 ± 0.0168	0.0105 ± 0.0295	-0.0179 ± 0.0116	0.0042 ± 0.0186	0.0038 ± 0.0086	1.4374 ± 0.0416
$132.0 < p_{T,ll} < 173.0$ GeV	0.9090 ± 0.0682	-0.1441 ± 0.0617	0.6745 ± 0.0464	-0.0558 ± 0.0213	0.0239 ± 0.0289	0.0045 ± 0.0146	0.0262 ± 0.0199	0.0116 ± 0.0106	0.8218 ± 0.0207
$173.0 < p_{T,ll} < 253.0$ GeV	0.8443 ± 0.0492	-0.0286 ± 0.0559	0.7409 ± 0.0586	-0.1521 ± 0.0259	0.0454 ± 0.0275	0.0093 ± 0.0181	0.0069 ± 0.0208	0.0193 ± 0.0130	0.4217 ± 0.0089
$253.0 < p_{T,ll} < 400.0$ GeV	0.8839 ± 0.0568	-0.1716 ± 0.0749	0.7619 ± 0.1126	-0.0583 ± 0.0476	0.0249 ± 0.0415	-0.0360 ± 0.0364	-0.0132 ± 0.0358	0.0642 ± 0.0270	0.0833 ± 0.0022
$400.0 < p_{T,ll} < 6500.0$ GeV	0.9491 ± 0.1380	0.2238 ± 0.1498	0.8315 ± 0.3112	-0.0668 ± 0.1355	0.1157 ± 0.1038	0.1104 ± 0.1167	-0.1319 ± 0.1061	0.0332 ± 0.0887	0.0073 ± 0.0004

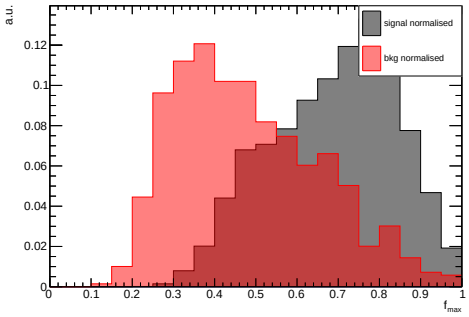
Tab. G.6.: Results of the combined fit in all bins of transverse momentum and $2.0 < y_{ll} < 2.4$.

H Shower Shape Variables

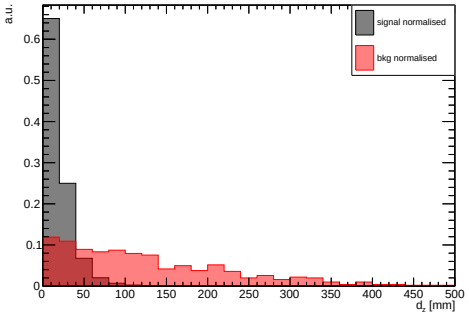
H.1 Legacy Shower Shape Variables



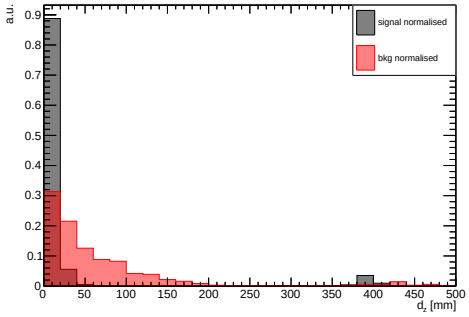
(a) f_{max} in the EMEC/HEC.



(b) f_{max} in the FCAL.

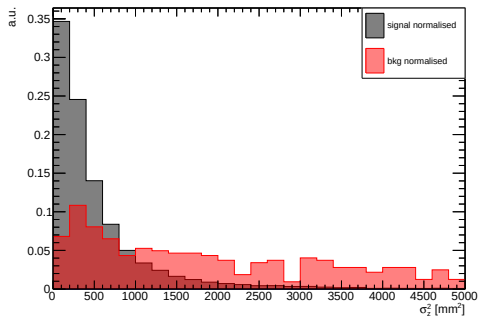


(c) d_z in the EMEC/HEC.

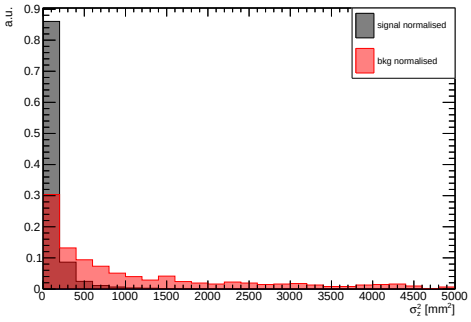


(d) d_z in the FCAL.

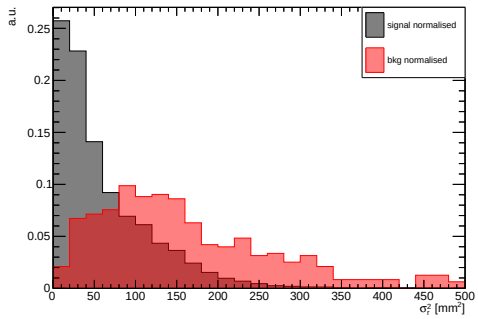
Fig. H.1.: Normalised distributions of shower shape variables for signal and background of the legacy sliding window algorithm in the EMEC/HEC and FCAL fiducial regions for core energies $E_T^{\text{core}} > 20\,\text{GeV}$.



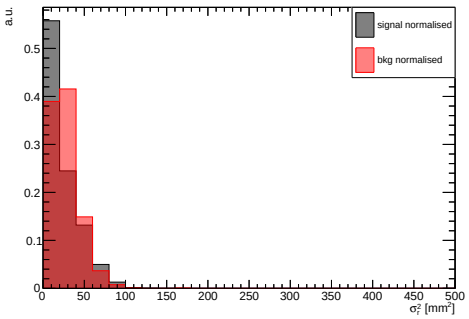
(a) σ_z^2 in the EMEC/HEC.



(b) σ_z^2 in the FCAL.



(c) σ_r^2 in the EMEC/HEC.



(d) σ_r^2 in the FCAL.

Fig. H.2.: Normalised distributions of shower shape variables for signal and background of the legacy sliding window algorithm in the EMEC/HEC and FCAL fiducial regions for core energies $E_T^{\text{core}} > 20\,\text{GeV}$.

H.2 Definition of Shower Shape Variables

The fraction of the energy of the highest-energetic cell to the rest of cells is defined as

$$f_{\text{max}} = \frac{\max(E_{T,i}; \text{cell}_i \in (0.4 \times 4\frac{\pi}{64}))}{\sum_{\text{cell}_i \in (0.4\times 4\frac{\pi}{64})} E_{T,i}}. \tag{H.1}$$

The depth of the shower centre in along the z axis is defined as

$$d_z = \frac{\sum_{\text{cell}_i \in (0.4\times 4\frac{\pi}{64})} E_{T,i}|z_{\text{cell,i}} - z_{\text{front}}|}{\sum_{\text{cell}_i \in (0.4\times 4\frac{\pi}{64})} E_{T,i}}, \tag{H.2}$$

where $z_{\text{cell,i}}$ is the depth in z of cell i and z_{front} is the z coordinate of the cell closest to the detector centre.

The weighted variance along the z axis is defined as

$$\sigma_z^2 = \sum_{\text{cell}_i \in (0.4\times 4\frac{\pi}{64})} (|z_{\text{cell,i}} - z_{\text{front}}| - \bar{\mu}_z)^2 (\frac{E_{T,i}}{E_{T,\text{all}}})^2, \tag{H.3}$$

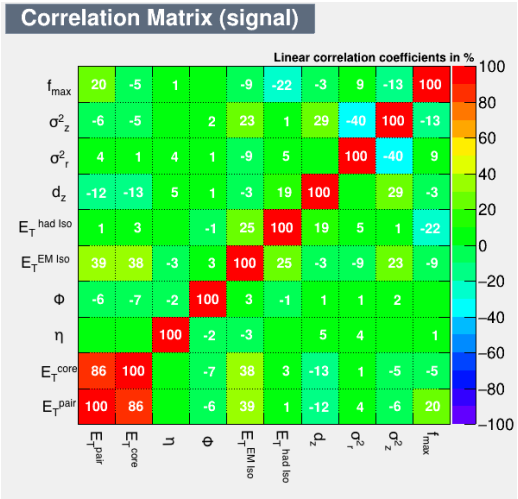
where $E_{T,\text{all}}$ is the sum of $E_{T,i}$ for all cells i in the window and $\bar{\mu}_z$ is the E_T weighted arithmetic mean in z of all cells in the window (with respect to the cell closest to the detector centre). $z_{\text{cell,i}}$ is the depth in z of cell i and z_{front} is the z coordinate of the cell closest to the detector centre.

The weighted variance in the transverse plane is defined as

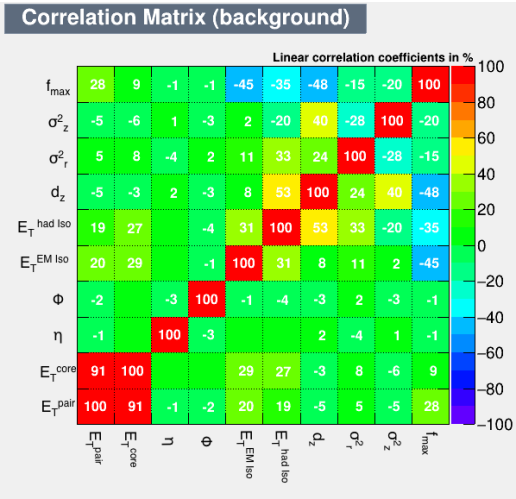
$$\sigma_r^2 = \sum_{\text{cell}_i \in (0.4\times 4\frac{\pi}{64})} (r_{\text{cell,i}} - \bar{\mu}_r)^2 (\frac{E_{T,i}}{E_{T,\text{all}}})^2, \tag{H.4}$$

where $r_{\text{cell,i}} = \sqrt{x_{\text{cell,i}}^2 + y_{\text{cell,i}}^2}$ is the radius in the transverse plane, $E_{T,\text{all}}$ is the sum of $E_{T,i}$ for all cells i in the window and $\bar{\mu}_r$ is the E_T weighted arithmetic mean r of all cells in the window.

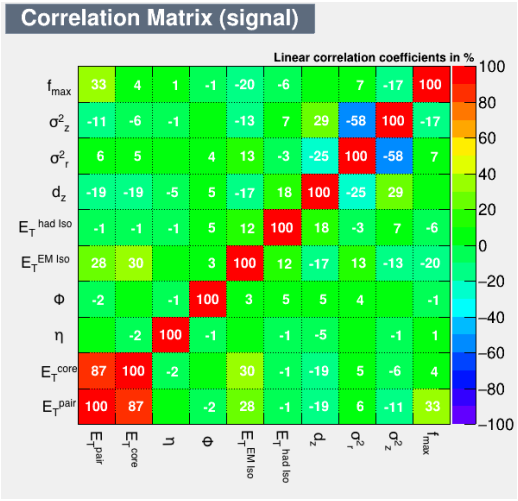
H.3 Correlation Matrices



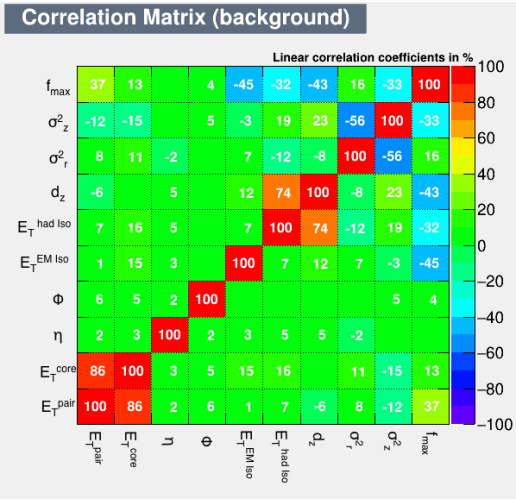
(a) Correlation in the signal in the EMEC/HEC.



(b) Correlation in the background in the EMEC/HEC.



(c) Correlation in the signal in the FCAL.



(d) Correlation in the background in the FCAL.

Fig. H.3.: Correlation Matrices of shower shape, sliding window and kinematic variables. Empty boxes represent 0. The variable E_T^{pair} representing the energy of the highest energetic 2x1 cell pair within the 2x2 core is added.

Danksagung

> *If I have seen further, it is by standing on the shoulders of giants.*
>
> **— Isaac Newton**

[In der elektronischen Version aus Datenschutzgründen entfernt]

Lebenslauf

[In der elektronischen Version aus Datenschutzgründen entfernt]